

AD 738203

AD

USAAMRDL TECHNICAL REPORT 71-42

**ADVANCED-GEOMETRY, GLASS-FIBER-REINFORCED
PLASTIC ROTOR BLADE TEST PROGRAM**

By

Donald J. Hoffstedt

September 1971

EUSTIS DIRECTORATE
U. S. ARMY AIR MOBILITY RESEARCH AND DEVELOPMENT LABORATORY
FORT EUSTIS, VIRGINIA

CONTRACT DAAJ02-67-C-0072
THE BOEING COMPANY, VERTOL DIVISION
BOEING CENTER
PHILADELPHIA, PENNSYLVANIA

Approved for public release;
distribution unlimited.



Reproduced by
**NATIONAL TECHNICAL
INFORMATION SERVICE**
Springfield, Va 22151



473

DISCLAIMERS

The findings in this report are not to be construed as an official Department of the Army position unless so designated by other authorized documents.

When Government drawings, specifications, or other data are used for any purpose other than in connection with a definitely related Government procurement operation, the U. S. Government thereby incurs no responsibility nor any obligation whatsoever; and the fact that the Government may have formulated, furnished, or in any way supplied the said drawings, specifications, or other data is not to be regarded by implication or otherwise as in any manner licensing the holder or any other person or corporation, or conveying any rights or permission, to manufacture, use, or sell any patented invention that may in any way be related thereto.

Trade names cited in this report do not constitute an official endorsement or approval of the use of such commercial hardware or software.

DISPOSITION INSTRUCTIONS

Destroy this report when no longer needed. Do not return it to the originator.

ACCOMPLISHED BY		
OFFICE	WRITE SECTION	<input checked="" type="checkbox"/>
NO	OFF SECTION	<input type="checkbox"/>
CHANGES		<input type="checkbox"/>
JUSTIFICATION		
BY		
DISTRIBUTION/AVAILABILITY CODES		
DET.	AVAIL. NO./YR	SERIAL
A		

UNCLASSIFIED

Security Classification

DOCUMENT CONTROL DATA - R & D

(Security classification of title, body of abstract and indexing annotation must be entered when the overall report is classified)

1. ORIGINATING ACTIVITY (Corporate author) The Boeing Company, Vertol Division Boeing Center, Philadelphia, Pennsylvania		2a. REPORT SECURITY CLASSIFICATION Unclassified	
		2b. GROUP	
3. REPORT TITLE ADVANCED-GEOMETRY, GLASS-FIBER-REINFORCED PLASTIC ROTOR BLADE TEST PROGRAM			
4. DESCRIPTIVE NOTES (Type of report and inclusive dates) Final Technical Report (June 1967 to February 1971)			
5. AUTHOR(S) (First name, middle initial, last name) Donald J. Hoffstedt			
6. REPORT DATE September 1971		7a. TOTAL NO. OF PAGES 470	7b. NO. OF REFS 22
8a. CONTRACT OR GRANT NO. DAAJ02-67-C-0072		8a. ORIGINATOR'S REPORT NUMBER(S) USAAMRDL Technical Report 71-42	
8b. PROJECT NO. Task IF163204DI5709		8b. OTHER REPORT NO(S) (Any other numbers that may be assigned this report) D210-10079-1	
10. DISTRIBUTION STATEMENT Approved for public release; distribution unlimited.			
11. SUPPLEMENTARY NOTES		12. SPONSORING MILITARY ACTIVITY Eustis Directorate, U.S. Army Air Mobility Research and Development Laboratory, Fort Eustis, Virginia	
13. ABSTRACT This report presents the results of a Boeing Company program with participation by USAAMRDL to design, tool, fabricate, bench test, and flight test glass-reinforced epoxy rotor blades. Blade design used S-glass reinforced epoxy, a mechanically trapped and bonded titanium root end attachment, and aerodynamic contours employing advanced airfoils, thickness taper, and planform taper. Fiberglass tooling was successfully employed, and fabrication and quality assurance techniques were developed for the prototype quantity of 12 rotor blades. Static and fatigue tests were conducted for both rotor blade elements and full-scale structure, and whirl test demonstration was completed. Exploratory flight testing was performed on a CH-47C prototype instrumented aircraft used as a "test-bed". Structural envelope improvements in gross weight, forward speed, and altitude were demonstrated. The thin tip contributed to higher advancing tip speed capability before encountering the impulsive noise threshold. At high advance ratios and advancing tip Mach numbers, a CH-47C helicopter equipped with AGB rotors: (1) will have decreased power requirements and (2) has demonstrated a higher lift-to-drag ratio in comparison to a metal rotor at equal solidity. The program demonstrated the feasibility of using composite materials for primary members in helicopter rotor blades of nonuniform geometric characteristics. It also proved the capability of achieving sound structure with improved strength-to-weight ratios.			

DD FORM 1473

REPLACES DD FORM 1473, 1 JAN 64, WHICH IS
OBSOLETE FOR ARMY USE.

UNCLASSIFIED

Security Classification

UNCLASSIFIED
Security Classification

14.	KEY WORDS	LINK A		LINK B		LINK C	
		ROLE	WT	ROLE	WT	ROLE	WT
	Advanced-Geometry Rotor Blades Glass-Reinforced Epoxy Rotor Blades Composite Rotor Blade Fabrication Composite Rotor Blade Tests Composite Rotor Blade Performance						

UNCLASSIFIED

Security Classification

9442-71



DEPARTMENT OF THE ARMY
U. S. ARMY AIR MOBILITY RESEARCH & DEVELOPMENT LABORATORY
EUSTIS DIRECTORATE
FORT EUSTIS, VIRGINIA 23604

This report was prepared by the Boeing Company, Vertol Division, under the terms of Contract DAAJ02-67-C-0072. It documents the research, development, and test efforts involved in designing, fabricating, and testing large, complex-geometry rotor blades made from composite material. Particular emphasis is given to an analysis of flight test data that was acquired during a 46-hour flight program on a CH-47C helicopter. Load and performance comparisons are made of the original predictions, the CH-47C helicopter equipped with standard rotors, and the CH-47C helicopter equipped with the advanced-geometry rotor system.

The program was generally successful but suffered frequent delays resulting from blade fabrication problems. A high one/rev vibration in conjunction with test vehicle power/transmission limitations precluded testing at speeds which could better exploit the capabilities of the AGB rotor system.

Results of the program indicate that additional research, development, and testing are required before composites can be specified as the primary material for use in manufacturing large, complex-geometry rotor blades in production quantities.

This report has been reviewed by this Directorate and is considered to be technically sound. The technical monitor for this contract was Mr. H. R. Young, Applied Aeronautics Division.

**Task 1F163204D15709
Contract DAAJ02-67-C-0072
USAAMRDL Technical Report 71-42
September 1971**

**ADVANCED-GEOMETRY, GLASS-FIBER-REINFORCED
PLASTIC ROTOR BLADE TEST PROGRAM**

Final Report

D210-10079-1

By

Donald J. Hoffstedt

Prepared by

**The Boeing Company, Vertol Division
Boeing Center
Philadelphia, Pennsylvania**

for

**EUSTIS DIRECTORATE
U.S. ARMY AIR MOBILITY RESEARCH AND DEVELOPMENT LABORATORY
FORT EUSTIS, VIRGINIA**

Approved for public release; distribution unlimited.

SUMMARY

This report presents the results of a program undertaken by The Boeing Company, with participation by the Eustis Directorate of the U.S. Army, to design, tool, fabricate, bench test, and flight test glass-reinforced epoxy rotor blades. Flight tests were conducted on a CH-47C Army helicopter.

The blade design used S-glass reinforced epoxy, a mechanically trapped and bonded titanium root end attachment, and aerodynamic contours employing advanced airfoils, thickness taper, and planform taper. Fiberglass tooling was successfully employed, and fabrication and quality assurance techniques were developed for the prototype quantity of 12 rotor blades. Static and fatigue tests were conducted for both rotor blade elements and full-scale structure, and whirl test demonstration was completed without encountering significant problems.

Exploratory flight testing was performed on a CH-47C prototype instrumented aircraft used as a "test-bed". Structural envelope improvements in gross weight, forward speed, and altitude were demonstrated, due in part to improvement in moment-stall-triggered rotor system response as compared to conventional metal blades. The thin tip contributed to higher advancing tip speed capability before encountering the impulsive noise threshold. At high advance ratios and advancing tip Mach numbers, a CH-47C helicopter equipped with AGB rotors: (1) will have decreased power requirements, and (2) has demonstrated a higher lift-to-drag ratio in comparison to a metal rotor at equal solidity.

The program has demonstrated the feasibility of using composite materials for primary members in helicopter rotor blades of nonuniform geometric characteristics. It also proved the capability of achieving sound structure with improved strength-to-weight ratios affording approximately 30 percent solidity improvements in the rotor disc at a weight penalty of approximately 12 percent.

FOREWORD

This report was prepared by The Boeing Company, Vertol Division, under Contract DAAJ02-67-C-0072 for the Eustis Directorate, U.S. Army Air Mobility Research and Development Laboratory, Fort Eustis, Virginia. Mr. H. Young was the U.S. Army Program Monitor.

The activities reported herein spanned a five-year period during which Mr. D. Hoffstedt and Mr. R. Pinckney were chiefly responsible for the design, fabrication and management of the blade development activity. Initial aerodynamic and dynamic efforts were performed by Messrs F. Davenport and F. Harris. Mr. W. Bates served as project engineer during the latter half of the program.

The program history and technology task results were supplied to Messrs J. Wisely and D. Reed, respectively, who assisted in the correlation and coordination of the data reported. Principal contributors to the total effort are listed below.

Program Manager	D. J. Hoffstedt
Project Engineer	W. E. Bates
Composite Materials Development	R. L. Pinckney
Manufacturing Development	R. Cox (Boeing-Wichita)
Quality Technology	W. Roettger
Acoustics	E. G. Schaeffer
Aerodynamics	W. W. Walls
	R. Wiesner
	R. F. Child
Control Systems	H. J. Neeb
Engineering Laboratories	H. J. Nonemaker
	J. W. Woolman
Flight Test	J. G. Kutkuhn
	F. J. Pearson
Helicopter Technology	H. A. Wahl
Rotor Development	H. E. Bishop
Stress Analysis	F. J. Ochs
	H. H. Steinmann
Structures	R. Gabel
Vibration	G. J. Wilson

TABLE OF CONTENTS

	<u>Page</u>
SUMMARY	iii
FOREWORD	v
LIST OF ILLUSTRATIONS	xi
LIST OF TABLES	xxx
LIST OF SYMBOLS	xxxiii
PROGRAM SYNOPSIS	xxxv
INTRODUCTION	1
BLADE DESIGN	5
DESIGN CRITERIA	5
AERODYNAMIC DESIGN OF THE ADVANCED-GEOMETRY BLADE	6
Airfoil Selection	6
Selection of Rotor Solidity	13
Twist and Planform Selection	13
Root Cutout Effects	14
MATERIAL SELECTION	16
MATERIAL TESTING AND ANALYSIS	16
STRUCTURAL DESIGN	20
Master Dimensions Program	20
Section Properties Program	20
Shear Center and Torsional Stiffness Program	22
Leone-Myklestad Programs	22
Strain and Margin-of-Safety Program	22
Special Condition Loading	22
DESIGN AND CONSTRUCTION OF THE ADVANCED-GEOMETRY BLADE	22
STRUCTURAL ANALYSIS OF THE ADVANCED-GEOMETRY BLADE	30
Design Properties	30
Calculated Blade Loads	30
Stress Analysis	39
Results of Stress Analysis	39
Conclusions	42
FABRICATION OF THE ADVANCED-GEOMETRY BLADE	48
INTRODUCTION	48
DESIGN AND FABRICATION OF TOOLS	48
Plaster Masters	52
Lifting and Handling Carrier	52
Honeycomb Core Machining Pattern	52
Upper Core Surface Milling Fixture	56
Lower Core Surface Milling Fixture	56
Core-Skin Assembly Bonding Jig	56
Spar Molding Jig	59
Blade Assembly Bonding Jig	61

<u>TABLE OF CONTENTS</u> (Continued)	<u>Page</u>
Erosion Strip Bond	65
Trailing-Edge Cusp Bonding	65
BLADE FABRICATION METHODS AND PROCEDURES	65
Titanium Detail Parts	65
Reinforced-Plastic Detail Parts	67
Spar Assembly	67
Core-Skin Assembly	69
Spar-Core Assembly	72
Spar-Core-Noseblock Assembly	74
Application of the Final Blade Skins	76
Application of Leading-Edge Erosion Strips	78
Application of the Trailing-Edge Cusp	82
Final Assembly Operations	82
FABRICATION PROBLEMS AND SOLUTIONS	82
Spar Fabrication	85
Corrective Tooling Measures	85
Corrective Processing Measures	87
Core-Skin Assembly Bonding	87
Spar-to-Core Assembly Bonding	89
Noseblock Assembly	91
Final Skin Assembly	91
MANUFACTURING EVALUATION	92
QUALITY CONTROL	94
INTRODUCTION	94
NONDESTRUCTIVE ULTRASONIC INSPECTION METHODS	94
Core-Skin Assembly Bonding	94
Spar Molding	96
Spar-to-Core Assembly Bonding	96
Final Assembly Bonding	96
Posttest Inspections	96
DIMENSIONAL INSPECTIONS	97
BLADE WEIGHT	97
STRUCTURAL TESTING	107
STATIC TESTS	107
Root End Ultimate Test	107
Blade Nonrotating Natural Frequency Test	109
Blade Section Moduli Test	110
Trailing-Edge Buckling Test	113
Static Proof Load Test	116
FATIGUE TESTS	119
Chordwise Airload Test	119
Tip Hardware Test	125
Root-End Test	127

<u>TABLE OF CONTENTS</u> (Continued)	<u>Page</u>
Outboard Blade Section Test	129
Inboard Blade Section Test	137
WHIRL TEST PROGRAM	148
INTRODUCTION	148
TEST CONFIGURATION	148
INSTRUMENTATION AND DATA	148
LIMITATIONS	148
BLADE TRACKING	149
STRESS AND MOTION SURVEY	149
STATIC THRUST PERFORMANCE	149
ENDURANCE TEST	149
TEST OBSERVATIONS	150
POSTTEST REMARKS	150
FLIGHT TEST PROGRAM	165
INTRODUCTION	165
AIRCRAFT CONFIGURATION	168
EQUIPMENT	170
INSTRUMENTATION	170
FLIGHT ENVELOPE AND LIMITATIONS	176
MECHANICAL INSTABILITY TESTS	176
BLADE TRACKING	178
FLIGHT TEST DATA ANALYSIS	179
ROTOR MOMENT STALL CHARACTERISTICS	179
Introduction	179
Definition of Moment Stall	179
Load Growth Rate	180
Summary of Flight Conditions Analyzed	183
Effect of RPM on Moment Stall	183
Effect of Altitude on Moment Stall	183
Effect of Sideslip Angle on Moment Stall	183
Pitch Link Load Comparison of CH-47C and CH-47C/AGB	188
Comparison Based on Moment Stall Parameters	195
Summary of Pitch Link Waveforms	197
Effect of Structural and Aerodynamic Damping	197
Principal Results and Observations	198
CONTROL SYSTEM AND ROTOR SHAFT LOADS	203
Introduction	203
Level-Flight Data	203
Maneuver Data	206
Test-Bed Limitations	206
Structural Flight Envelope - Level Flight	213
Bank Angle Envelope	216

<u>TABLE OF CONTENTS</u> (Continued)	<u>Page</u>
CGI Feasibility	218
Control System Steady Loads	222
BLADE LOADS	226
Introduction	226
Spanwise Moment Distributions	228
Scattergrams of Blade Parameters	239
Comparison of CH-47C and CH-47C/AGB Blade Loads for Equivalent C_T/σ	240
Load Phasing	246
Blade Life	251
Comparison of Design Allowables and Flight Stresses	262
Comparison of Structural Test Strain Levels and Flight Strains	264
Material Characteristic Changes Due to Fatigue Loading	266
Trailing-Edge Cracks in the Blade Transition Area	268
VIBRATION	274
Introduction	274
Vibration Test Conditions	275
Vibration Measurement Locations	275
Test Results	279
Comparison of CH-47C and CH-47C/AGB Vibration	288
One/Rev Vibration Investigation	296
Principal Results and Observations	306
PERFORMANCE	308
Performance Capabilities of the AGB Rotor Compared to the CH-47C Rotor	308
Performance Test Program	316
Discussion of Performance Test Results	326
FLYING QUALITIES	338
ACOUSTIC MEASUREMENTS	340
Comparison of CH-47B and CH-47C/AGB Rotor Noise Signatures	340
Test Conditions	343
Rotor Noise Analysis	343
CONCLUSIONS	344
General	344
Specific	344
RECOMMENDATIONS	346
LITERATURE CITED	347
APPENDIXES	
I. Blade Tracking History	349
II. Pitch Link Load Waveforms	358
III. Control and Rotor Shaft Loads	365
IV. Summary of Maneuvering Flight Test Conditions	389
V. Performance Support Data	397
DISTRIBUTION	425

LIST OF ILLUSTRATIONS

<u>Figure</u>		<u>Page</u>
1	CH-47C Helicopter With Advanced-Geometry Fiberglass Rotor Blades	3
2	Design Details of the Advanced-Geometry Blade	3
3	Rotor Blade Airfoil Aerodynamic Environment	8
4	Summary of Stall and Drag Rise Performance for Airfoils Tested in the Boeing Rotor Blade Profile Development Program . .	8
5	Profiles of Airfoils Tested in Boeing Supersonic Wind Tunnel	11
6	Summary of Stall and Drag Rise Characteristics for Several Airfoil Families	12
7	Calculated Effects of Blade Twist and Planform Taper on Power Required, Bending Moments, and Hub Shaking Force at 200 Knots	15
8	Effect of Root Cutout	15
9	Stress Curve for Unidirectional 1002S Epoxy-Resin Laminates Loaded in Tension-Tension Fatigue	18
10	Stress Curve for XP251S ± 45 -Degree Crossply Epoxy-Resin Laminates Loaded in Tension-Tension Fatigue	18
11	Stress Curve for BP907-143S Crossply Epoxy-Resin Laminates Loaded in Tension-Tension Fatigue	19
12	Strain Comparison of Unidirectional S-Glass and a Mixture of Unidirectional and Crossply S-Glass	19
13	Structural Design of the Advanced-Geometry Blade	21
14	Effects of Location of Tuning Weight on Blade Natural Frequencies	21
15	Physical Characteristics of the Advanced-Geometry Blade	21
16	Principal Steady and Vibratory Loadings of a Rotor Blade	25
17	Contours of the Advanced-Geometry Blade	25
18	Blade Spar Inner Torsion Wrap	26
19	Blade Spar Unidirectional Fibers	26
20	Blade Spar Outer Torsion Wrap	26
21	Exploded View of Blade Assembly	27

LIST OF ILLUSTRATIONS (Continued)

<u>Figure</u>		<u>Page</u>
22	Blade Root-End Attachment Joint	27
23	Assembly Buildup of the Advanced-Geometry Blade	28
24	Details of Fiber Orientation in the Blade	28
25	Details of the Blade Tip	28
26	Details of the Finished Advanced-Geometry Blade	29
27	Calculated Spanwise Variation of Centrifugal Force	31
28	Calculated Steady and Alternating Flapwise Bending Moments at 33,000 Pounds Gross Weight and 230 Rotor RPM	32
29	Calculated Steady and Alternating Chordwise Bending Moments at 33,000 Pounds Gross Weight and 230 Rotor RPM	33
30	Calculated Steady and Alternating Torsional Moments at 33,000 Pounds Gross Weight and 230 Rotor RPM	34
31	Calculated Steady and Alternating Flapwise Bending Moments at 44,000 Pounds Gross Weight and 243 Rotor RPM	35
32	Calculated Steady and Alternating Chordwise Bending Moments at 44,000 Pounds Gross Weight and 243 Rotor RPM	36
33	Calculated Steady and Alternating Torsional Moments at 44,000 Pounds Gross Weight and 243 Rotor RPM	37
34	Cyclic-Pitch Trim Schedule for the Advanced-Geometry Blade . . .	38
35	Calculated Radial Variation of Fatigue Strain Ratio for Spar, Torsion Wrap, and Skin Materials at 33,000 Pounds Gross Weight and 230 Rotor RPM	40
36	Calculated Radial Variation of Fatigue Strain Ratio for Spar, Torsion Wrap, and Skin Materials at 44,000 Pounds Gross Weight and 243 Rotor RPM	41
37	Calculated Alternating Strain at Blade Station 180, Check- point 2, in the XP251S Crossply Torsion Wrap	43
38	Calculated Alternating Strain at Blade Station 216 in the Torsion Wrap and Skin	44
39	Calculated Alternating Strain at Blade Station 288, Checkpoint 3, in the XP251S Crossply Torsion Wrap	45
40	Calculated Alternating Strain in the Crossply BP907-143S Skin and Unidirectional 1002S Spar With Torsion Wrap Deleted	46

LIST OF ILLUSTRATIONS (Continued)

<u>Figure</u>		<u>Page</u>
41	Major Fabrication Operations and Tooling Concepts	49
42	Fabrication of Plaster Masters	53
43	Rollover Carriers With Optical Alignment	54
44	Schematic Diagram of Tooling Transfers to Make Core Machining Patterns and Core Milling Fixture	55
45	Milling Fixture for Upper Core Surface	57
46	Milling Fixture for Lower Core Surface	58
47	Core-Skin Assembly Bonding Jig	58
48	Spar Molding Jig	60
49	Blade Assembly Bonding Jig - Multipurpose Use A.	63
50	Blade Assembly Bonding Jig - Multipurpose Use C.	64
51	Bonding of Erosion Strip	64
52	Bonding of Trailing-Edge Cusp	64
53	Machining of Rotor Blade Sockets	66
54	Spar Fabrication Tool Ready for Layup	68
55	Inner Torsion Wrap of No. 2 Root-End Specimen	70
56	Unidirectional Tape Layup of No. 2 Root-End Specimen After Cold-Compacting	70
57	Cured Spar Before Removal From Mold	71
58	Cured Spar After Removal From Mold	71
59	Chordwise Potting of Selected Cells of Honeycomb Core	73
60	Installation of Inboard Tool Support Block	73
61	Core-Skin Assembly Showing Buildup of Thickness	75
62	Tip-End View of Finished Spar-Core Assembly	75
63	Root-End View of Finished Spar-Core Assembly	75
64	Blade Assembly With Tooling Silicone Rubber in Place	77
65	Blade Assembly Filled and Faired With Syntactic Foam	77
66	Blade Assembly Ready for Application of Final Skins	77

LIST OF ILLUSTRATIONS (Continued)

<u>Figure</u>		<u>Page</u>
67	Tip-End View of Blade in Final Assembly With Caul Plate in Place	79
68	Root-End View of Blade in Final Assembly With Caul Plate in Place	79
69	Blade Assembly in Vacuum Bag for Cure of Outer Skins	80
70	Tip-End View of Blade Assembly in Vacuum Bag for Cure of Outer Skins	80
71	Tip-End View of Blade After Cure of Skins	81
72	Root-End View of Blade After Cure of Skins	81
73	Cured Blade Assembly Before Installation of Final Detail Parts	81
74	Installation of the Erosion Strip	83
75	Installation of the Leading- and Trailing-Edge Doublers	83
76	Machining the Root-End Taper	84
77	The Finished Advanced-Geometry Rotor Blade	84
78	Initial Spar Molding Deficiencies	86
79	Spar Damage From Thermal Expansion and Contraction	88
80	Evidence of Distortion and Chordal Movement of the Core- Skin Assembly Relative to the Spar	90
81	Blade Contour Adjustments With Syntactic Foam	90
82	Components Developed for Ultrasonic Inspection	99
83	Final Ultrasonic Probe With Phenolic Static Water Column	99
84	Ultrasonic Inspection of Blade Core-Skin Assembly	99
85	Inspection of the C-Shaped Spar	100
86	Inspection of the Spar-Core Assembly	100
87	Dimensional Inspection of the Finished Blade	101
88	Blade Measurements for Section Contour Check	101
89	Contour Variation of the Aft Blades	101
90	Ultimate Test of Root-End Section of the Advanced-Geometry Blade	108

LIST OF ILLUSTRATIONS (Continued)

<u>Figure</u>		<u>Page</u>
91	Spanwise Crack System in Test Root-End Section	108
92	Shaker Setup for Vibration of Blade in Flapwise Direction	108
93	Flapwise Natural Frequency Spectrum of the Advanced-Geometry Blade	111
94	Chordwise Natural Frequency Spectrum of the Advanced-Geometry Blade	111
95	Torsional Natural Frequency Spectrum of the Advanced-Geometry Blade	111
96	Setup for Test of Blade Section Moduli	112
97	Radial Variation of Flapwise Stiffness of the Advanced-Geometry Blade	114
98	Radial Variation of Chordwise Stiffness of the Advanced-Geometry Blade	114
99	Ultimate Chordwise Moment During Start of the Advanced-Geometry Blade	115
100	Placement of Weights on the Advanced-Geometry Blade at Stations 180, 252, and 350	117
101	Placement of Weights on the Advanced-Geometry Blade at Stations 180, 252, and 350	117
102	Radial Variation of Static Bending Moment in Analytical Design 42E	118
103	Static Proof Load Test of the Advanced-Geometry Blade	118
104	Setup for Chordwise Airload Fatigue Test	120
105	Envelope of Chordwise Variation of Aerodynamic Pressure on the Aft Rotor	121
106	Steady Shear Loads of the Advanced-Geometry Blade	121
107	Alternating Shear Loads of the Advanced-Geometry Blade	121
108	Steady Bending Moment of the Advanced-Geometry Blade	122
109	Alternating Bending Moment of the Advanced-Geometry Blade	122
110	Inboard Failure of Advanced-Geometry Blade Serial No. 107-1 During Chordwise Airload Fatigue Test	124
111	Outboard Failure of Advanced-Geometry Blade Serial No. 107-1 During Chordwise Airload Fatigue Test	124

LIST OF ILLUSTRATIONS (Continued)

<u>Figure</u>		<u>Page</u>
112	Setup for Fatigue Test of Tip Hardware	124
113	Details and Results of Fatigue Test of Tip Hardware	126
114	No. 1 Tool-Proving Root-End Test Section	128
115	Fatigue Failure of Root-End Socket	128
116	Fatigue-Life Curve for the Vertical Pin Joint	128
117	Setup for Fatigue Test of Outboard Blade Sections Serial Nos. 103-1 and 107-1.	130
118	Failure of Outboard End of Outboard Blade Section Serial No. 103-1	134
119	Ultrasonic Mapping of Bottom Surface of Outboard Blade Section Serial No. 107-1, End of Load Level 3	134
120	Stress Curve for Analytical and Test Results of Unidirectional 1002S Epoxy-Resin Laminates Loaded in Tension-Tension Fatigue	136
121	Stress Curve for Analytical and Test Results of XP251S ± 45 -Degree Crossply Epoxy-Resin Laminates Loaded in Tension-Tension Fatigue	136
122	Stress Curve for Analytical and Test Results of BP907-143S ± 45 -Degree Crossply Epoxy-Resin Laminates Loaded in Tension-Tension Fatigue	136
123	Setup for Fatigue Test of Inboard Blade Section Serial No. 103-1	138
124	Skin Failures on Bottom Surface of Inboard Blade Section Serial No. 103-1, End of Load Level 3	138
125	Closeup of Skin Failure on Top Surface at Inboard End of Inboard Blade Section Serial No. 103-1	138
126	Core Failure at Outboard End of Inboard Blade Section Serial No. 103-1	138
127	Stress Curve for Analytical and Test Results of Unidirectional 1002S Epoxy-Resin Laminates Loaded in Tension-Tension Fatigue	143
128	Stress Curve for Analytical and Test Results of XP251S ± 45 - Degree Crossply Epoxy-Resin Laminates Loaded in Tension- Tension Fatigue	143

LIST OF ILLUSTRATIONS (Continued)

<u>Figure</u>		<u>Page</u>
129	Stress Curve for Analytical and Test Results of BP907-143S ±45-Degree Crossply Epoxy-Resin Laminates Loaded in Tension-Tension Fatigue	143
130	Core Failure in Middle of Inboard Blade Serial No. 107-1	144
131	Stress Curve for Analytical and Test Results of Unidirectional 1002S Epoxy-Resin Laminates Loaded in Tension-Tension Fatigue After Rework	146
132	Stress Curve for Analytical and Test Results of XP251S ±45-Degree Crossply Epoxy-Resin Laminates Loaded in Tension-Tension Fatigue After Rework	146
133	Stress Curve for Analytical and Test Results of BP907-143S ±45-Degree Crossply Epoxy-Resin Laminates Loaded in Tension-Tension Fatigue After Rework	146
134	Failures of Inboard Blade Section Serial No. 107-1 After Rework	147
135	Whirl Tower With Advanced-Geometry Blades	152
136	Locations and Types of Strain Gages Installed on Advanced- Geometry Blade Serial No. 105-1	152
137	Locations of Gages on Whirl Tower Rotor Shaft	153
138	Installation of Blade Motion Transducers	154
139	Steady Flap Bending Moment in Whirl Test at 230 Rotor RPM . .	155
140	Alternating Flap Bending Moment in Whirl Test at 230 Rotor RPM	155
141	Steady Flap Bending Moment in Whirl Test at 245 Rotor RPM . .	156
142	Alternating Flap Bending Moment in Whirl Test at 245 Rotor RPM	156
143	Steady Chord Bending Moment in Whirl Test at 230	157
144	Alternating Chord Bending Moment in Whirl Test at 230 Rotor RPM	157
145	Steady Chord Bending Moment in Whirl Test at 245 Rotor RPM .	157
146	Alternating Chord Bending Moment in Whirl Test at 245 Rotor RPM	157

LIST OF ILLUSTRATIONS (Continued)

<u>Figure</u>		<u>Page</u>
147	Rotor Shaft Bending Moment Versus Collective Pitch in Whirl Test at 230 Rotor RPM	158
148	Rotor Shaft Bending Moment Versus Collective Pitch in Whirl Test at 245 Rotor RPM	158
149	Rotor Shaft Bending Moment Versus Collective Pitch in Whirl Test at 250 Rotor RPM	158
150	Rotor Shaft Bending Versus Cyclic Pitch in Whirl Test at 230 Rotor RPM	159
151	Rotor Shaft Bending Moment Versus Cyclic Pitch in Whirl Test at 245 Rotor RPM	159
152	Pitch Link Loads Versus Collective Pitch in Whirl Test at 230 Rotor RPM	160
153	Pitch Link Loads Versus Collective Pitch in Whirl Test at 245 Rotor RPM	160
154	Pitch Link Loads Versus Collective Pitch in Whirl Test at 250 Rotor RPM	160
155	Pitch Link Loads Versus Cyclic Pitch in Whirl Test at 230 Rotor RPM	161
156	Pitch Link Loads Versus Cyclic Pitch in Whirl Test at 245 Rotor RPM	161
157	Blade Flap and Pitch Angle Versus Collective Pitch in Whirl Test at 230 Rotor RPM	162
158	Blade Flap and Pitch Angle Versus Collective Pitch in Whirl Test at 245 Rotor RPM	162
159	Blade Flap and Pitch Angle Versus Collective Pitch in Whirl Test at 250 Rotor RPM	162
160	Blade Flap and Pitch Angle Versus Cyclic Pitch in Whirl Test at 230 Rotor RPM	163
161	Blade Flap and Pitch Angle Versus Cyclic Pitch in Whirl Test at 245 Rotor RPM	163
162	Blade Lag Versus Cyclic Pitch in Whirl Test	163
163	Blade Thrust Versus Collective Pitch in Whirl Test	164
164	Horsepower Versus Collective Pitch in Whirl Test	164

LIST OF ILLUSTRATIONS (Continued)

<u>Figure</u>		<u>Page</u>
165	Advanced-Geometry Blade Serial No. 106-1 Showing Peeled Tedlar, Bond Failure, and Missing Pieces	164
166	Orientation of Advanced-Geometry Blades on CH-47C Helicopter	169
167	Center-of-Gravity Envelope for the CH-47C Helicopter	171
168	Predicted Airspeed Capability for the CH-47C Helicopter With Advanced-Geometry Blades at 33,000 Pounds Gross Weight	177
169	Predicted Airspeed Capability for the CH-47C Helicopter With Advanced-Geometry Blades at 40,000 Pounds Gross Weight	177
170	Predicted Airspeed Capability for the CH-47C Helicopter With Advanced-Geometry Blades at 46,000 Pounds Gross Weight	177
171	Illustration of a Typical CH-47C Metal Blade Pitch Link Waveform During Moment Stall	181
172	Illustration of Typical CH-47C/AGB Pitch Link Waveforms	181
173	CH-47C Pitch Link Load Growth With Airspeed	182
174	CH-47C/AGB Pitch Link Load Growth With Airspeed	182
175	Summary of Flights Having Moment Stall	185
176	Illustration of the Effect of Altitude on Pitch Link Load Waveforms	186
177	Illustration of the Effect of RPM on Pitch Link Waveforms	186
178	Effect of Sideslip on Pitch Link Waveforms	187
179	Comparison of CH-47C and CH-47C/AGB Pitch Link Load Waveforms - Similar Flight Conditions	187
180	Comparison of CH-47C and CH-47C/AGB Aft Pitch Link Loads for Similar Flight Conditions	189
181	Comparison of CH-47C and CH-47C/AGB Aft Pitch Link Loads for Similar Flight Conditions	190
182	Comparison of CH-47C and CH-47C/AGB Aft Pitch Link Loads for Similar Flight Conditions	191
183	Comparison of CH-47C and CH-47C/AGB Pitch Link Load Waveforms - Equivalent C_T/σ	193

LIST OF ILLUSTRATIONS (Continued)

<u>Figure</u>		<u>Page</u>
184	Comparison of CH-47C and CH-47C/AGB Aft Pitch Link Loads at Equivalent C_T/σ	194
185	Nondimensional Comparison of CH-47C and CH-47C/AGB Aft Pitch Link Loads for Similar Flight Conditions and Equivalent C_T/σ	194
186	Moment Stall Inception Summary of Vertol Experience	196
187	A Comparison of Typical Pitch Link Load Decay Waveforms for the CH-47C Metal and CH-47C/AGB Blades	199
188	Typical Aft Pitch Link and Rotor Shaft Loads at 45,500 Pounds Gross Weight and 235 RPM	205
189	Typical Aft Pitch Link and Rotor Shaft Loads at 46,190 Pounds Gross Weight and 245 RPM	205
190	Comparison of Conventional and Advanced-Geometry Blades Through Maneuver Loads at Aft Pitch Links	207
191	Comparison of Conventional and Advanced-Geometry Blades Through Maneuver Loads on Aft Rotor Shaft	207
192	Speed Capability of CH-47C Helicopter With Advanced-Geometry Blades at 46,000 Pounds Gross Weight	209
193	Aft Pitch Link Loads for Flight 269 of CH-47C Helicopter Equipped With Advanced-Geometry Blades	209
194	Time History of Flight 269 Showing Effect of Negative, Long-Period Pitch Stability With Pitch Stability Augmentation System Off	212
195	Structural Airspeed Limits of CH-47C Helicopter Equipped With Advanced-Geometry Blades at 235 Rotor RPM	214
196	Structural Airspeed Limits of CH-47C Helicopter Equipped With Advanced-Geometry Blades at 245 Rotor RPM	214
197	Evaluation of Flight Envelope of CH-47C Helicopter Equipped With Advanced-Geometry Blades at 235 Rotor RPM	215
198	Evaluation of Flight Envelope of CH-47C Helicopter Equipped With Advanced-Geometry Blades at 245 Rotor RPM	215
199	Comparison of Conventional and Advanced-Geometry Blades Through Bank-Angle Envelope and Demonstrated Points	217

LIST OF ILLUSTRATIONS (Continued)

<u>Figure</u>		<u>Page</u>
200	Flight Test Turn Experience of CH-47C Helicopter Equipped With Advanced-Geometry Blades	217
201	Flapwise Bending Moment of Aft Advanced-Geometry Blade.	223
202	Feasibility of Cruise Guide Indicator With Advanced-Geometry Blades	223
203	Comparison of Aft Pitch Link Loads Conventional and Advanced-Geometry Blades	224
204	Aft Pivoting Actuator Loads on CH-47C Helicopter Equipped With Advanced-Geometry Blades	224
205	Aft Swiveling Actuator Loads on CH-47C Helicopter Equipped With Advanced-Geometry Blades	225
206	Aft Fixed Link Loads on CH-47C Helicopter Equipped With Advanced-Geometry Blades	225
207	Steady and Alternating Loads on Aft Pivoting Actuator of CH-47C Helicopter Equipped With Advanced-Geometry Blades . . .	227
208	Waveform of Loads on Aft Pivoting Actuator of CH-47C Helicopter Equipped With Advanced-Geometry Blades	227
209	Comparison of Predicted and Flight Test Steady Flapwise Bending Moments in Level Flight	230
210	Comparison of Predicted and Flight Test Alternating Flapwise Bending Moments in Level Flight	231
211	Comparison of Predicted and Flight Test Steady Chordwise Bending Moments in Level Flight	232
212	Comparison of Predicted and Flight Test Alternating Chordwise Bending Moments in Level Flight	234
213	Comparison of Predicted and Flight Test Steady Flapwise Moments in Maneuvering Flight	235
214	Comparison of Predicted and Flight Test Alternating Flapwise Bending Moments in Maneuvering Flight	236
215	Comparison of Predicted and Flight Test Steady Chordwise Bending Moments in Maneuvering Flight	237
216	Comparison of Predicted and Flight Test Alternating Chordwise Bending Moments in Maneuvering Flight	238

LIST OF ILLUSTRATIONS (Continued)

<u>Figure</u>		<u>Page</u>
217	Flap Bending at Station 32.8 of Aft Blade Socket on CH-47C Helicopter Equipped With Advanced-Geometry Blades	241
218	Flap Bending at Station 288 of Aft Blade Spar on CH-47C Helicopter Equipped With Advanced-Geometry Blades	242
219	Flap Bending at Station 288 of Aft Blade Spar on CH-47C Helicopter Equipped With Advanced-Geometry Blades	243
220	Trailing-Edge Tension at Station 198 of Aft Blade on CH-47C Helicopter Equipped With Advanced-Geometry Blades	244
221	Trailing-Edge Tension at Station 198 of Aft Blade on CH-47C Helicopter Equipped With Advanced-Geometry Blades	245
222	Comparison of CH-47C and CH-47C/AGB at Equivalent C_T/σ and Similar Flight Conditions, Forward Blade Flap Bending at Station 47	247
223	Comparison of CH-47C and CH-47C/AGB at Equivalent C_T/σ and Similar Flight Conditions, Aft Blade Flap Bending at Station 47	248
224	Comparison of CH-47C and CH-47C/AGB at Equivalent C_T/σ and Similar Flight Conditions, Aft Blade Flap Bending at Station 285	249
225	Comparison of CH-47C and CH-47C/AGB at Equivalent C_T/σ and Similar Flight Conditions, Aft Blade Trailing Edge Tension at Station 198	250
226	Alternating Load Phasing, Aft Blade Flap/Chord at Station 49.5	252
227	Alternating Load Phasing, Aft Blade Flap/Chord at Station 198	253
228	Alternating Load Phasing, Aft Blade Flap/Torsion at Station 288	254
229	Alternating Load Phasing, Aft Blade Torsion/Pitch Link at Station 288	255
230	S-N Curve for Unidirectional 1002S Epoxy Resin Laminates Loaded in Tension-Tension Fatigue	263
231	S-N Curve for XP251S±45° Crossply Epoxy Resin Laminates Loaded in Tension-Tension Fatigue	265

LIST OF ILLUSTRATIONS (Continued)

<u>Figure</u>		<u>Page</u>
232	S-N Curve for BP907-143S±45° Crossply Epoxy Resin Laminates Loaded in Tension-Tension Fatigue	265
233	Comparison of Flight Test and Structural Test Measured Strain - 33,000 and 40,000 Pounds Gross Weight	267
234	Comparison of Flight Test and Structural Test Measured Strain	269
235	Location of Blade Trailing Edge Cracks	270
236	Trailing Edge Cracks, Blade S/N 104-1	271
237	Trailing Edge Cracks, Blade S/N 106-1	272
238	Trailing Edge Cracks, Blade S/N 102-2	273
239	Ballast Diagrams - Advanced Geometry Blades	277
240	Ballast Diagram - CH-47C Vibration Compliance Program	277
241	CH-47C Detail Specification Limits	280
242	CH-47C Airframe Vibration With AGB Airspeed Sweep at 235 RPM	281
243	CH-47C Airframe Vibration With AGB Airspeed Sweep at 235 RPM	281
244	CH-47C Airframe Vibration With AGB RPM Sweep at 157 Knots (34,500 Pounds)	282
245	CH-47C Airframe Vibration With AGB RPM Sweep at 157 Knots (34,500 Pounds)	282
246	CH-47C Airframe Vibration With AGB Effect of Gross Weight at 235 RPM	284
247	CH-47C Airframe Vibration With AGB Effect of Gross Weight at 235 RPM	284
248	CH-47C Airframe Vibration With AGB Effect of Gross Weight at 235 RPM	285
249	CH-47C Airframe Vibration With AGB Effect of Altitude at 245 RPM	285
250	CH-47C Airframe Vibration With AGB Effect of Altitude at 245 RPM	285

LIST OF ILLUSTRATIONS (Continued)

<u>Figure</u>		<u>Page</u>
251	CH-47C Airframe Vibration With AGB Effect of Altitude at 245 RPM	285
252	CH-47C Airframe Vibration With AGB Effect of Altitude at 245 RPM	285
253	CH-47C Airframe Vibration With AGB Effect of Altitude at 245 RPM	286
254	Airframe Vibration With AGB Effect of RPM at 47,500 Pounds TOGW	286
255	Airframe Vibration With AGB Effect of RPM at 47,500 Pounds TOGW	286
256	Airframe Vibration With AGB Effect of RPM at 47,500 Pounds TOGW	286
257	Airframe Vibration With AGB Effect of Cyclic Trim	287
258	Airframe Vibration With AGB Effect of Cyclic Trim	287
259	Vibration Time History Effect of Cyclic Trim	289
260	Vibration Time History, Sta 95 Vertical Effect of Cyclic Trim, 100 Knots, 235 RPM	289
261	Vibration Time History, Sta 95 Lateral and Longitudinal Effect of Cyclic Trim, 100 Knots, 235 RPM	289
262	Maneuver Vibration With AGB Effect of Gross Weight	290
263	Maneuver Vibration With AGB Effect of Gross Weight	290
264	CH-47C Airframe Vibration Advanced Geometry Blades vs CH-47C Production Blades	291
265	CH-47C Airframe Vibration Advanced Geometry Blades vs CH-47C Production Blades	291
266	CH-47C Airframe Vibration Advanced Geometry Blades vs CH-47C Production Blades at 245 RPM Airspeed Sweep at 47,000 Pounds TOGW	293
267	CH-47C Airframe Vibration Advanced Geometry Blades vs CH-47C Production Blades at 245 RPM Airspeed Sweep at 47,000 Pounds TOGW	293
268	CH-47C Airframe Vibration Advanced Geometry Blades vs CH-47C Production Blades RPM Sweep at 157 Knots, 34,500 Pounds TOGW	294

LIST OF ILLUSTRATIONS (Continued)

<u>Figure</u>		<u>Page</u>
269	CH-47C Airframe Vibration Advanced Geometry Blades vs CH-47C Production Blades RPM Sweep at 157 Knots, 34, 500 Pounds TOGW	294
270	Cockpit Accelerations, Advanced Geometry Blades vs CH-47C Production Blades	295
271	Cockpit Vibration Displacements, Advanced Geometry Blades vs CH-47C Production Blades 47,000 Pounds TOGW, 235 RPM	295
272	Maneuver Vibration, Cockpit Vertical Advanced Geometry Blades vs CH-47C Production Blades, 34, 500 Pounds, TOGW, 235 RPM	297
273	Maneuver Vibration, Cockpit Lateral and Longitudinal Advanced Geometry Blades vs CH-47C Production Blades, 34, 500 Pounds TOGW, 235 RPM	297
274	Measured Twist, AGB Forward Rotor Blades	298
275	Measured Twist, AGB Aft Rotor Blades	298
276	Effective Twist, AGB Forward Rotor Blades	299
277	Effective Twist, AGB Aft Rotor Blades	299
278	Pitch Moment Variation, AGB Forward Rotor Blades	301
279	Pitch Moment Variation, AGB Aft Rotor Blades	301
280	AGB Calculated Track at 140 Knots	302
281	Effective Twist with T.E. Wedges, AGB Forward Rotor Blades	302
282	Effective Twist With T.E. Wedges, AGB Aft Rotor Blades	304
283	AGB Calculated Track at 140 Knots With T.E. Wedges	304
284	CH-47C 1/Rev Vibration With AGB Yawed Flight at 245 RPM	307
285	Rotor Blade Geometric Characteristics	311
286	CH-47C/AGB Rotor Figure of Merit - Hover Out of Ground Effect at 235 Rotor RPM	312
287	Comparison of Hover Capability Out of Ground Effect for Conventional and Advanced-Geometry Blades	312

LIST OF ILLUSTRATIONS (Continued)

<u>Figure</u>		<u>Page</u>
288	Comparison of Nondimensional Power Requirements of Conventional and Advanced-Geometry Blades	314
289	Comparison of Power Required With Conventional and Advanced-Geometry Blades at 3,000 Feet and Standard Temperature	314
290	CH-47C/AGB Rotor Comparison of Flight Test and Predicted Power Required at 33,000 Pounds and 230 RPM.	317
291	Longitudinal Cyclic Trim Schedules for CH-47C Helicopter Equipped With Advanced-Geometry Blades	317
292	Airspeed Position Error from Boom System Magnetic Tape on CH-47C Helicopter Equipped With Advanced-Geometry Blades	325
293	Airspeed Position Error from Ship System Magnetic Tape on CH-47C Helicopter Equipped With Advanced-Geometry Blades	325
294	Comparison of Predicted and Test Hover Power Required With Advanced-Geometry Blades	327
295	Comparison of Predicted and Test Hover Capability Out of Ground Effect With Advanced-Geometry Blades	327
296	Comparison of Hover Power Required Out of Ground Effect for Conventional and Advanced-Geometry Blades	329
297	Comparison of Hover Power Required Out of Ground Effect for Adjusted Conventional and Advanced-Geometry Blades	329
298	Test Results for Level-Flight Power Required With the Advanced-Geometry Blades at 235 Rotor RPM	330
299	Test Results for Level-Flight Power Required With the Advanced-Geometry Blades at 245 Rotor RPM	330
300	Comparison of Level-Flight Power Required for Conventional and Advanced-Geometry Blades at 235 Rotor RPM	331
301	Comparison of Level-Flight Power Required for Conventional and Advanced-Geometry Blades at 245 Rotor RPM	331
302	CH-47C/AGB Rotor Comparison of Level Flight Power Required at Constant Solidity (0.0845) - $N/\sqrt{\theta} = 245$ Rotor RPM	332

LIST OF ILLUSTRATIONS (Continued)

<u>Figure</u>		<u>Page</u>
303	Comparison of Speed Capability With Conventional and Advanced-Geometry Blades at 235 Rotor RPM	332
304	Comparison of Speed Capability With Conventional and Advanced-Geometry Blades at 245 Rotor RPM	332
305	Comparison of Speed Capability With Conventional and Advanced-Geometry Blades at 245 Rotor RPM at Higher Altitude	334
306	Comparison of Compressibility With Conventional and Advanced-Geometry Blades	334
307	Comparison of Predicted and Test Level-Flight Power Required With Advanced-Geometry Blades at 235 Rotor RPM	335
308	Comparison of Predicted and Test Level-Flight Power Required With Advanced-Geometry Blades at 245 Rotor RPM	335
309	Comparison of Predicted and Test Speed Capability With Advanced-Geometry Blades at 235 Rotor RPM	336
310	Comparison of Predicted and Test Speed Capability With Advanced-Geometry Blades at 245 Rotor RPM	336
311	Comparison of Minimum Power Required With Conventional and Advanced-Geometry Blades	337
312	Comparison of Single- and Dual-Engine Forward Climb Capability With Conventional and Advanced-Geometry Blades	337
313	Longitudinal Control Sensitivity of CH-47C and Advanced-Geometry Blades	339
314	Longitudinal Control Sensitivity of CH-47C and Advanced-Geometry Blades	339
315	CH-47C Helicopter With Advanced-Geometry Blades in Flight	341
316	Forward Flight Sound Pressure Levels - CH-47C and CH-47C/AGB	341
317	CH-47C Pitch Link Load Waveforms, Gross Weight = 40,000 Pounds, Rotor RPM = 235, Density Altitude = 6,000-7,500 Feet	359

LIST OF ILLUSTRATIONS (Continued)

<u>Figure</u>		<u>Page</u>
318	CH-47C/AGB Pitch Link Load Waveforms, Gross Weight = 46,000 Pounds, Rotor RPM = 235, Density Altitude = 3,000-5,600 Feet	360
319	CH-47C/AGB Pitch Link Load Waveforms, Gross Weight = 46,000 Pounds, Rotor RPM = 235, Density Altitude = 6,000-7,500 Feet	361
320	CH-47C/AGB Pitch Link Load Waveforms, Gross Weight = 46,000 Pounds, Rotor RPM = 235, Density Altitude = 9,400-11,000 Feet	362
321	CH-47C/AGB Pitch Link Load Waveforms, Gross Weight = 46,000 Pounds, Rotor RPM = 245, Density Altitude = 6,000-10,400 Feet	363
322	CH-47C/AGB Pitch Link Load Waveforms, Gross Weight = 50,000 Pounds, Rotor RPM = 245, Density Altitude = 2,500-10,000 Feet	364
323	Aft Pitch Link Loads on CH-47C Helicopter Equipped With Advanced-Geometry Blades	365
324	Aft Pitch Link Loads on CH-47C Helicopter Equipped With Advanced-Geometry Blades	366
325	Aft Pitch Link Loads on CH-47C Helicopter Equipped With Advanced-Geometry Blades	367
326	Aft Pitch Link Loads on CH-47C Helicopter Equipped With Advanced-Geometry Blades	368
327	Aft Pitch Link Loads on CH-47C Helicopter Equipped With Advanced-Geometry Blades	369
328	Aft Pitch Link Loads on CH-47C Helicopter Equipped With Advanced-Geometry Blades	370
329	Aft Pitch Link Loads on CH-47C Helicopter Equipped With Advanced-Geometry Blades	371
330	Aft Pitch Link Loads on CH-47C Helicopter Equipped With Advanced-Geometry Blades	372
331	Aft Rotor Shaft Bending Loads on CH-47C Helicopter Equipped With Advanced-Geometry Blades	373

LIST OF ILLUSTRATIONS (Continued)

<u>Figure</u>		<u>Page</u>
332	Aft Rotor Shaft Bending Loads on CH-47C Helicopter Equipped With Advanced-Geometry Blades	374
333	Aft Rotor Shaft Bending Loads on CH-47C Helicopter Equipped With Advanced-Geometry Blades	375
334	Aft Rotor Shaft Bending Loads on CH-47C Helicopter Equipped With Advanced-Geometry Blades	376
335	Aft Rotor Shaft Bending Loads on CH-47C Helicopter Equipped With Advanced-Geometry Blades	377
336	Aft Rotor Shaft Bending Loads on CH-47C Helicopter Equipped With Advanced-Geometry Blades	378
337	Aft Rotor Shaft Bending Loads on CH-47C Helicopter Equipped With Advanced-Geometry Blades	379
338	Aft Rotor Shaft Bending Loads on CH-47C Helicopter Equipped With Advanced-Geometry Blades	380
339	Aft Fixed Link Loads on CH-47C Helicopter Equipped With Advanced-Geometry Blades	381
340	Aft Fixed Link Loads on CH-47C Helicopter Equipped With Advanced-Geometry Blades	382
341	Aft Fixed Link Loads on CH-47C Helicopter Equipped With Advanced-Geometry Blades	383
342	Aft Fixed Link Loads on CH-47C Helicopter Equipped With Advanced-Geometry Blades	384
343	Aft Fixed Link Loads on CH-47C Helicopter Equipped With Advanced-Geometry Blades	385
344	Aft Fixed Link Loads on CH-47C Helicopter Equipped With Advanced-Geometry Blades	386
345	Aft Fixed Link Loads on CH-47C Helicopter Equipped With Advanced-Geometry Blades	387
346	Aft Fixed Link Loads on CH-47C Helicopter Equipped With Advanced-Geometry Blades	388

LIST OF TABLES

<u>Table</u>	<u>Page</u>
I Advanced-Geometry Blade (AGB) Rotor Configuration Description	4
II Airfoil Geometry and Aerodynamic Summary	9
III Summary of Effects of Twist and Planform Taper on the AGB Rotor	14
IV Preliminary Calculated Limits of the Blade Materials	30
V Twist-Angle Distribution of the Advanced-Geometry Blades	102
VI Trailing-Edge Cusp Angle of the Advanced-Geometry Blades	103
VII Section Contour Data on the Forward Advanced-Geometry Blades	104
VIII Section Contour Data on the Aft Advanced-Geometry Blades	105
IX Summary of Weights of the Advanced-Geometry Blades	106
X Details and Results of Chordwise Airload Fatigue Test of the Advanced-Geometry Blade	123
XI Cycle History of Chordwise Airload Fatigue Test of the Advanced-Geometry Blade	123
XII Loads Summary of Fatigue Test of Outboard Blade Sections	132
XIII Stress Summary of Fatigue Test of Outboard Blade Section Serial No. 107-1, Station 277	135
XIV Loads Summary of Fatigue Test of Inboard Blade Sections	139
XV Stress Summary of Fatigue Test of Inboard Blade Sections, Station 177	142
XVI Stress and Motion Survey Conditions	149
XVII Endurance Test Whirl Schedule	150
XVIII Program Data Flight Summary	166
XIX Supplementary Data Flight Summary	167
XX Availability of Instrumentation and Data Recording	172
XXI Summary of Flights Having Moment Stall Based Upon Waveform Analysis	184
XXII CH-47B/C Metal and Advanced-Geometry Fiberglass Rotor Blades, Uncoupled Natural Frequencies and Critical Damping Ratios	200

LIST OF TABLES (Continued)

<u>Table</u>		<u>Page</u>
XXIII	CH-47B/C Metal and Advanced-Geometry Fiberglass Rotor Blades, Design Parameters	201
XXIV	Advanced Geometry Blade Stress and Motion Level Flight Summary	204
XXV	CH-47/AGB Helicopter Pitch Stability Investigation	210
XXVI	Invalid Test Points Based on Pitch Stability Criteria	211
XXVII	Maximum Alternating Loads During Turn Maneuvers	218
XXVIII	Maximum Fatigue Load Summary, CH-47C/AGB Configuration, Aft Rotor	219
XXIX	Maximum Fatigue Load Summary, CH-47C/AGB Configuration, Forward Rotor	220
XXX	Summary of Alternating Load Phasing	256
XXXI	CH-47C Mission Profile, Basic Fatigue Loading Schedule	256
XXXII	Glass AGB Mission Profile	257
XXXIII	Fatigue Damage Summary - Spar at Sta. 288	257
XXXIV	Fatigue Damage Summary - Spar at Sta. 288	260
XXXV	Fatigue Damage Summary - Blade Socket	260
XXXVI	Fatigue Damage Summary - Trailing Edge Skin at Sta. 198	261
XXXVII	Fatigue Damage Summary - Trailing Edge Skin at Sta. 198	261
XXXVIII	CH-47C, B361, Advanced Geometry Blades	276
XXXIX	Vibration Instrumentation	278
XL	Pitch Link Rod End Bearing Clearance Measurements	305
XLI	AGB Rotor Test Conditions	309
XLII	Comparison of the Production CH-47C Rotor and AGB Rotor . . .	310
XLIII	Power Required at 165 Knots	315
XLIV	External Configuration, CH-47C/AGB Rotor Flight Test Aircraft, S/N 66-19103	318
XLV	Hover Out of Ground Effect Test Conditions (150-Foot Wheel Height)	320
XLVI	Level Flight Test Conditions	321
XLVII	Blade Tracking Results and Corresponding Pitch Link Adjustments	351

LIST OF TABLES (Continued)

XLVIII	Hover and Transition	389
XLIX	Climb	390
L	Left Turn	391
LI	Right Turn	392
LII	Sideslip	393
LIII	Partial Power Descent and Autorotation	395
LIV	Collective Pull-Up and Flare	396
LV	CH-47C/AGB Rotor Hover Power Required (Out of Ground Effect)	401
LVI	CH-47C/AGB Rotor - Level Flight Power Required.	406
LVII	CH 47C/AGB Rotor - Level Flight Power Required.	407
LVIII	CH-47C/AGB Rotor - Level Flight Power Required.	408
LIX	CH-47C/AGB Rotor - Acceleration Correction	409
LX	CH 47C/AGB Rotor - Rate of Climb Correction	410
LXI	CH-47C/AGB Rotor - Level Flight Power Required.	411
LXII	CH-47C/AGB Rotor - Acceleration Correction	412
LXIII	CH-47C/AGB Rotor - Rate of Climb Correction	413
LXIV	CH-47C/AGB Rotor - Level Flight Power Required.	414
LXV	CH-47C/AGB Rotor - Acceleration Correction	415
LXVI	CH-47C/AGB Rotor - Rate of Climb Correction	416
LXVII	CH-47C/AGB Rotor - Level Flight Power Required.	417
LXVIII	CH-47C/AGB Rotor - Acceleration Correction	418
LXIX	CH-47C/AGB Rotor - Rate of Climb Correction	419
LXX	CH-47C/AGB Rotor - Level Flight Power Required.	420
LXXI	CH-47C/AGB Rotor - Level Flight Power Required.	421
LXXII	CH-47C/AGB Rotor - Acceleration Correction	422
LXXIII	CH-47C/AGB Rotor - Rate of Climb Correction	423

LIST OF SYMBOLS (Continued)

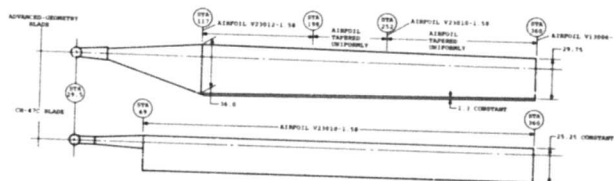
M_{DD}	drag divergence Mach number
n	number of cycles applied to the part
NBFM	narrowband frequency modulation
NDT	nondestructive test
N	rotor rpm
OGE	out of ground effect
P. L. L.	pitch link load, lb
T	thrust, lb
TAS	true airspeed
TOGW	takeoff gross weight
V_{ne}	velocity never exceed
V_T	tip velocity, fps
WBFM	wideband frequency modulation
WL	waterline, vertical distance above or below some arbitrary zero point in inches
W_O	natural frequency
W_1	damping
W_2	flutter parameter
α	angle of attack; is proportional to
ϵ	strain, microinches
μ	advance ratio
σ	solidity

PROGRAM SYNOPSIS

The Advanced Geometry Blade (AGB) Program performed under USAAVLABS Contract No. DAAJ02-67-C-0072 proved the feasibility of a composite material rotor blade for a large transport helicopter. It also demonstrated that composite material manufacturing techniques provide a high degree of freedom in tailoring aerodynamic, dynamic and structural properties anywhere along the blade.

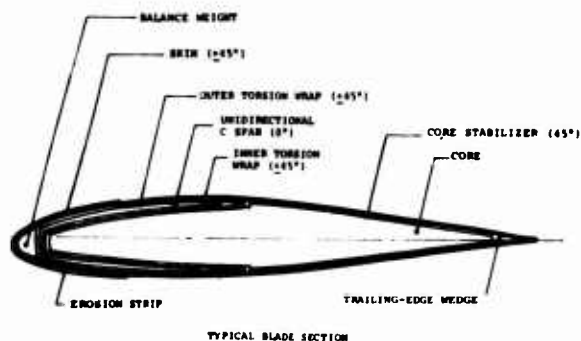
BLADE

The AGB is shown inflight on the CH-47C test aircraft. Relative to the standard CH-47C metal blade, the AGB has a wider, tapered chord producing a solidity increase from 0.067 to 0.0845, a tapered thickness for improved aerodynamic performance and increased torsional frequency, and thin tips to reduce tip drag.

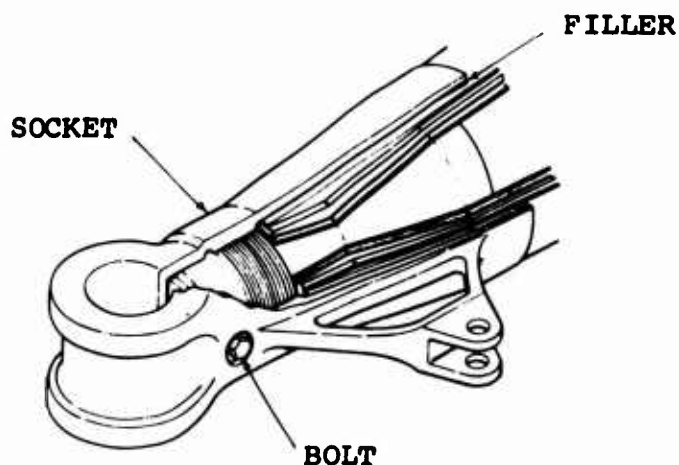


The airfoil section varies from 23012 inboard to 13A006 outboard. Such variations are unique for a large helicopter blade and were made possible only by the use of composite material fabrication techniques. The spanwise development of the airfoil section is nonlinear, and this fact alone would make the fabrication cost prohibitive by any other method.

In cross section, the main C-spar consists of an inner S-glass unidirectional fiber laminate which carries the centrifugal and bending loads, an inner and outer wrap of 45° oriented fibers plus a woven 0.020-inch S-glass cloth skin for torsional stiffness, an aluminum honeycomb core, a titanium erosion strip, and a continuous glass wedge trailing edge. The root end retention features a redundant design consisting



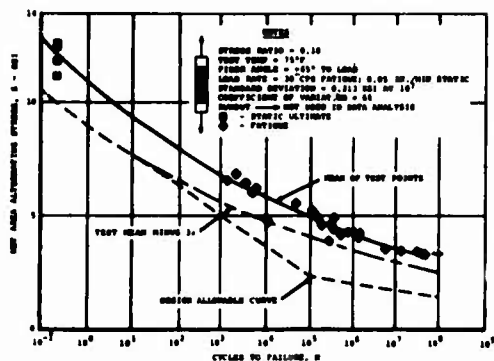
of an adhesive bond between an internal hour-glass shaped adapter and the glass spar, and a mechanical trap which sandwiches the fiberglass lay-up between the mismatched conical surfaces of the internal adapter and the external socket. A transparent 0.001-inch Tedlar film moisture barrier was applied to all exposed glass surfaces.



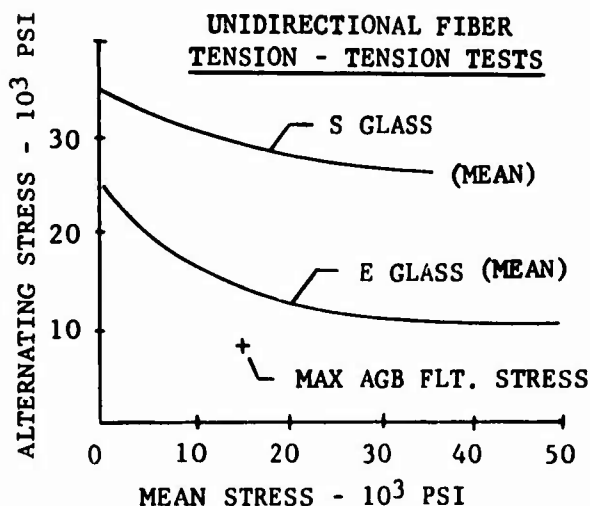
MATERIALS

S-glass composites were selected due to the high fatigue strength to density ratio (approximately 12.3×10^4 compared to 8.7×10^4 psi/lb/in.³ for steel) and a modulus to density ratio similar to the common engineering materials. The high strength to density ratio provided the maximum flexibility in meeting strength and weight requirements. Dynamic requirements of the AGB were nearly the same as the CH-47C, and the similarity of the fiberglass modulus to density ratio gave some assurance of meeting these requirements.

To establish the design allowables, an extensive materials test program was performed to determine the static and fatigue strength properties of the selected glass reinforced epoxy composite materials.



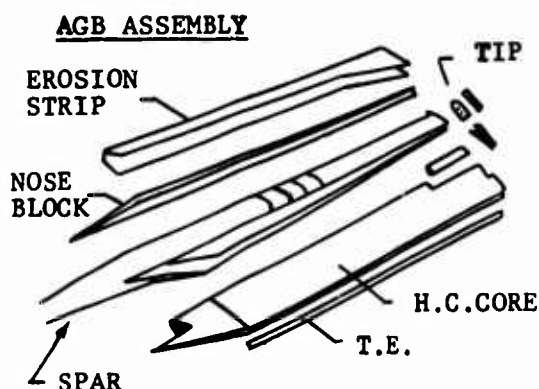
The mean and mean-minus-three sigma ($M-3\sigma$) values were established from statistical analysis of the test data. Design allowables between 10^5 and 10^8 cycles were obtained by reducing the ($M-3\sigma$) values by an estimated factor of 1.75 to account for environmental and other strength reducing factors experienced in full-scale hardware. The low cycle allowables were defined by a straight line passing through the allowable at 10^5 cycles and either tangent to the ($M-3\sigma$) curve or intersecting the static ultimate allowable, whichever produced the lowest values. Subsequent environmental testing and consideration of combined stresses justified the use of the 1.75 reduction factor in the high cycle range.



Although S-glass was used throughout, less expensive E-glass was considered. For the maximum predicted AGB loads, however, E-glass was marginal; and it was felt that the use of this material could jeopardize the success of the experimental program.

TOOLING AND FABRICATION

High-temperature-resistant glass fabric reinforced plastic tooling was used for the fabrication of the prototype quantity of 10 blades because of the ease of layup to the correct contours and relative capability for tool modification as opposed to metal tools. Tool leakage and warp control on large tools with high aspect ratio were early problem areas. These were resolved in subsequent tool development efforts. Program experience indicated that properly designed and fabricated reinforced plastic tooling provides a practical and successful means of fabricating a limited quantity of blades.



Engineering and quality control documents defined the material, facilities, manufacture, fabrication and assembly processing, and quality control requirements for the fabrication program. Principal blade fabrication operations included spar molding, core-skin assembly, spar-core bonding, spar-core noseblock bonding, final skin assembly and hardware attachments. All laminate molding and bonding operations were accomplished in an autoclave at prescribed temperature and pressure levels.

The progressive sequential assembly operations allowed step-by-step process and quality control assessments and evaluations to be made, thereby assuring the structural integrity of the finished product. Particular emphasis was given to the development and implementation of nondestructive ultrasonic and penetrating radiation (x-ray) inspection methods for these evaluations. Fabrication experience indicated that provisions for adequate holddown and constraint against chordal movement of the airfoil section part relative to the tool, and care in the use of vacuum pressure were two critical factors to be observed in fabrication operations.

PREFLIGHT TESTING

Two test blades were cut into sections for fatigue testing. The sections were weighted to obtain the desired bending moment distribution, subjected to a simulated centrifugal load and excited at their resonant frequency. No failures occurred

FIBERGLASS BLADE FATIGUE TEST SUMMARY

Run No.	Specimen	(F)	Flap Moment (in. lb.)	Chord Moment (in. lb.)	Steady Torque (in. lb.)	Alternating Torque (in. lb.)	Number of cycles	Frequency (Hz)
77 No. 1 Root End								
1	100%	90,000	1 71,000	126,000			10×10^6	0.2 10.4
2	100%	100,000	1 110,000	132,000			5×10^6	0.4
3	100%	100,000	1 171,000	140,000			1.25×10^6	7.5
S/N 103-1 Root End 150%								
1	150%	100,000	1 75,000				1.07×10^6	14.5
S/N 107-1 Root End 150%								
1	150%	100,000	1 75,000				1.51×10^6	12.5
S/N 103-1 100 in. Inboard								
1	100%	70,000	1 30,000	121,500			10×10^6	15.7 10.1
2	150%	70,000	1 54,000	130,500			5.02×10^6	10.6 15.3
3	200%	70,000	1 72,000	140,470			0.0075×10^6	12.0 12.7
4	100%	70,000	1 30,000	120,000			0.1750×10^6	12
S/N 107-1 100 in. Inboard								
1	100%	70,000	1 30,700	120,700			10×10^6	15.4
2	150%	70,000	1 54,000	130,500			1.23×10^6	
S/N 103-1 100 in. Outboard								
1	100%	61,500	1 27,700	11,000	110,500		1.04×10^6	
S/N 107-1 100 in. Outboard								
1	100%	61,500	1 25,000	110,000			10×10^6	13.0
2	150%	61,500	1 34,000	119,200			5×10^6	13.3
3	200%	61,500	1 40,000	125,000			1.30×10^6	13.3

below 1.69×10^6 cycles at 100% of design loads, and this failure (S/N 103-1 outboard) was due to excessive local loads where the specimen was attached to the test fixture. Otherwise, no failures occurred below 1.87×10^6 cycles at 150 percent of design load, at which point the titanium root end fitting failed.

A 50-hour whirl tower program was conducted during which only one minor problem was encountered. Bond failure of the leading-edge titanium erosion strip on the outboard blade sections was observed. The problem was traced

to a lack of adhesion between the primer and the metal. As an interim measure, the metal erosion strip was replaced by a polyurethane strip.

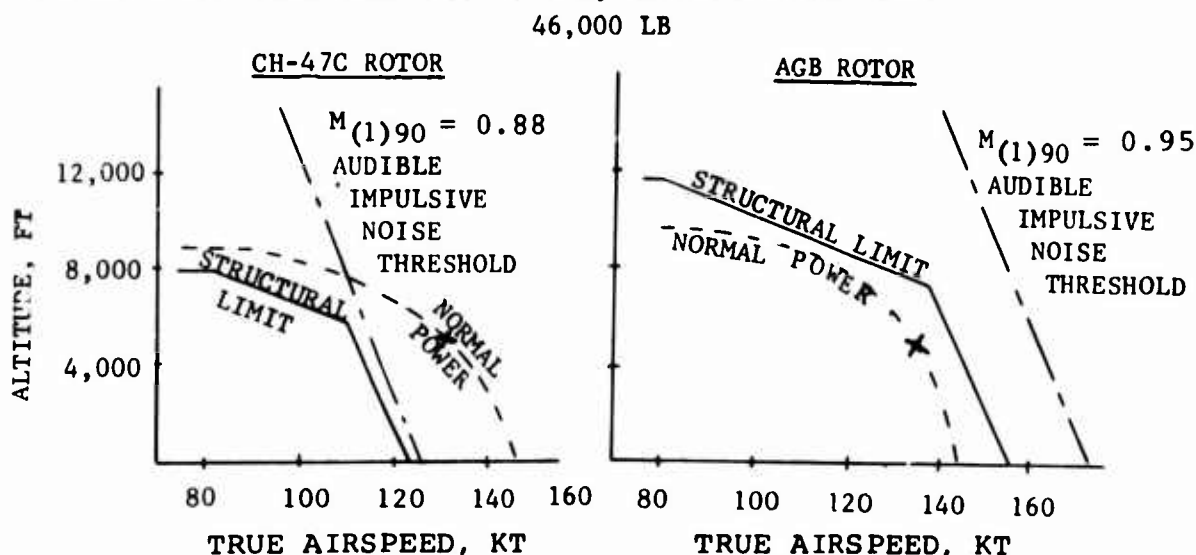
FLIGHT TESTING

Flight testing of the Advanced Geometry Blade was conducted on a CH-47C helicopter, S/N 66-19103 (B-361), at four gross weights from 33,000 to 50,000 pounds. Principal test objectives were to define:

- Aerodynamic performance of the AGB
- CH-47C flight envelope with the AGB
- CH-47C flying qualities, including vibration and external noise, with the AGB

PERFORMANCE

An overview comparing the speed capability of the production CH-47C and the CH-47C airframe with Advanced Geometry Blades is shown below.



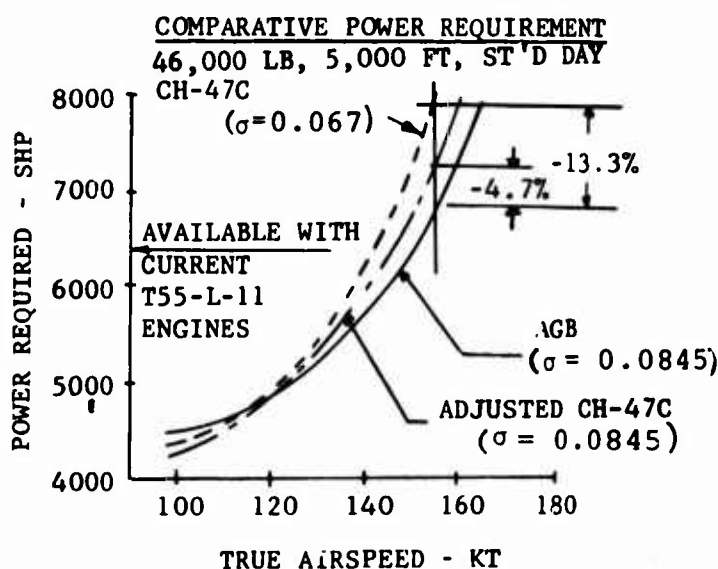
The operating envelopes shown derive from the following principal factors:

<u>Envelope</u>	<u>Principal Factors</u>
• Power envelope	Using normal power available from (2) T55-L-11 engines
• Structural envelope	Limited by control system endurance limit pitch link loads
• High impulsive noise threshold	Derives from compressibility effects at high advancing tip speeds

The power envelope of the high gross weight CH-47C with metal blades is beyond both the structural limit and the high-speed impulsive noise threshold, which can result in the aircraft exceeding the handbook structural limit and incurring undesirable fatigue damage and inducing high impulsive noise. The increased solidity and the thin tips of the AGB rotor correct this situation by placing the structural and noise envelopes outside the power envelope; thereby permitting the pilot to operate at power limit without encountering the other limits.

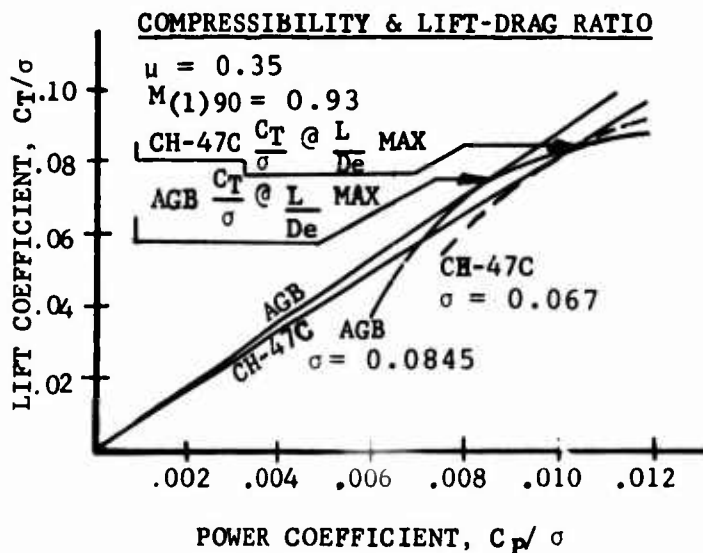
POWER ENVELOPE

The power envelope above shows a small speed advantage for the CH-47C with AGB rotor at 5000 ft. pressure altitude where the advancing tip Mach number is 0.91. As noted, a normal power-limited speed of 135 knots is obtained with the AGB compared to 132 knots with the metal blade. This benefit in performance will increase at higher Mach numbers, since the compressibility power requirements of the thin tip AGB at high advancing tip speeds (Mach numbers greater than 0.91) are significantly less than those of the metal blade. The following figure compares the level-flight power requirements of the AGB and metal blade rotor systems at 46,000 pounds and 5000 feet/standard. Metal blade performance is shown with present solidity (0.067) and at a solidity equal to the AGB (0.0845).



As noted at 155 knots (0.94 tip Mach number), the CH-47C equipped with the AGB rotor will require 13.3 percent less power than the current metal blade (0.067 solidity) and 4.7 percent less power than a metal blade with the same solidity as the AGB (0.0845). Due to the available power of the T55-L-11 engines installed in the test aircraft (6410 SHP at 5000 feet/standard), this potential speed improvement with the AGB could not be demonstrated.

The relationship of the maximum lift to drag ratio (L/D) at high speed is depicted in the following figure. As illustrated, the value of L/D for a rotorcraft is proportional to the slope of a line drawn from the origin tangent to the lift-power curve at a given airspeed and airframe drag. An increase in slope is equivalent to an increase in L/D . AGB demonstrated higher L/D at an advance ratio of 0.35 and a Mach number of 0.93; however, the lift coefficient (C_T/σ) at which the maximum L/D occurs is 12 percent lower than that of the metal blade CH-47C rotor. The relationship of C_T/σ at maximum L/D suggests that the AGB rotor at high airspeeds is optimum for operation at gross weights somewhat lower than the metal blade rotor at equal solidity. This reduction in C_T/σ for maximum L/D is attributed to the stall characteristics of the thin airfoils used over the outer 30 percent of the blade span and to the large root cutout of the AGB rotor.



NOISE ENVELOPE

An impulsive noise is generated by helicopters as the advancing blade tip Mach number approaches unity, implying that the sound-generating mechanism is related to compressibility. Based on data collected on the AGB rotor and the CH-47B/C rotors, the Mach number at which the noise becomes audible is related to blade airfoil drag divergence in the following way:

$$\begin{array}{lcl} \text{Mach Number for} & = & \text{Drag Divergence} + 0.045 \\ \text{Audible Impulsive Sound} & & \text{Mach Number} \end{array}$$

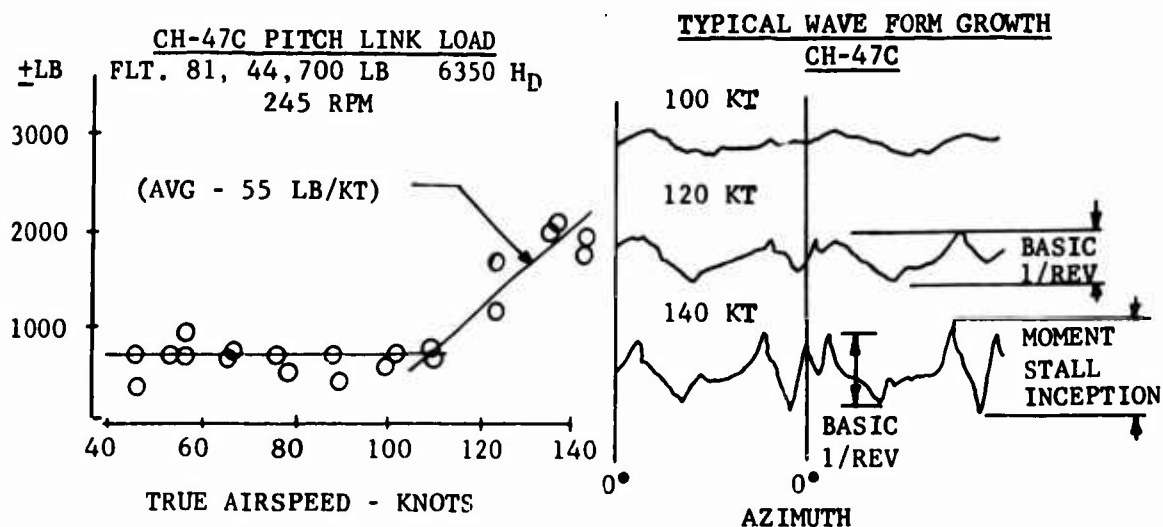
where: Mach number for drag divergence is a function of the critical advancing blade section coefficient of lift.

Accordingly, the audible impulsive noise threshold occurs at an advancing blade tip Mach number of 0.88 for the production CH-47C rotor, which has a 10 percent thick airfoil (V23010-1.58) at and near the blade tip. The audible impulsive noise threshold for the AGB rotor occurs at an advancing blade tip Mach number of 0.95.

The improved capability of the AGB rotor derives from the thickness ratio taper of the AGB airfoils over the outer 70 percent of the blade span. As an example, at 5000 feet altitude, the audible impulsive noise threshold occurs at 116 knots for the production CH-47C and at 161 knots for the AGB rotor.

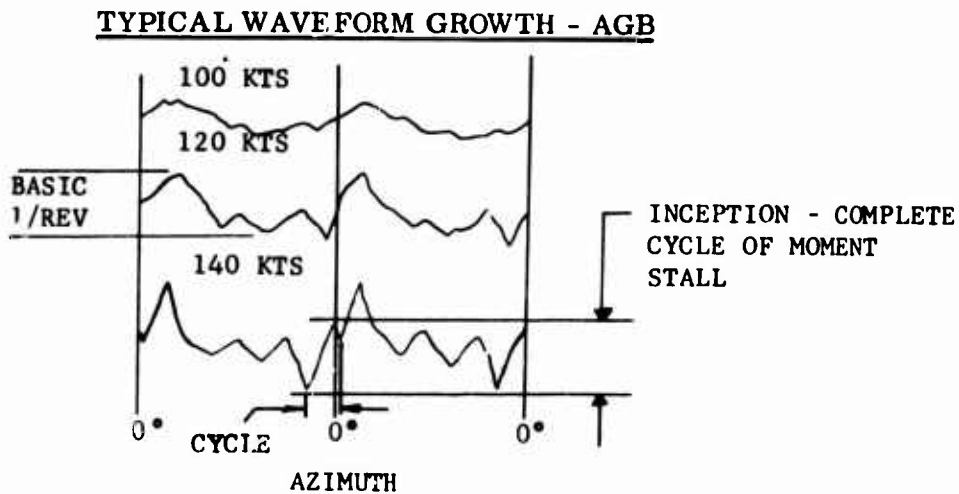
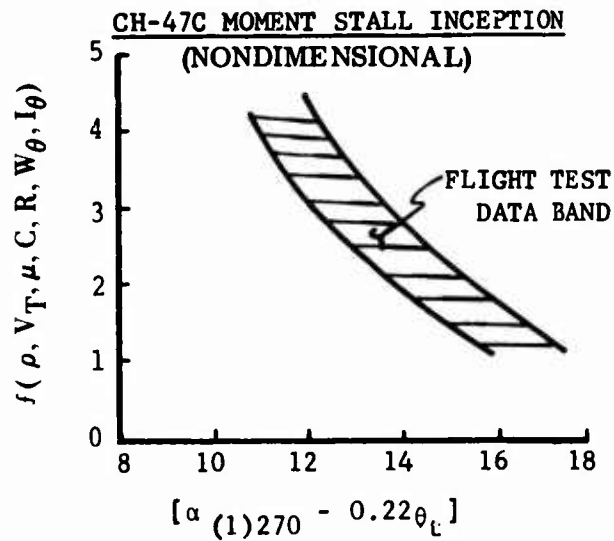
MOMENT STALL

Moment stall is a Boeing definition of stall flutter that recognizes the separate existence of two different stall phenomena - the most limiting being aerodynamic moment stall which excites the blade's torsional natural frequency, and second, aerodynamic lift stall which can similarly excite blade torsional response. Vertol's experience with conventional steel spar blades in full scale and model sizes has resulted in a definition of moment stall inception as the point of rapid increase in pitch link loads caused by a developing moment stall "spike" (at the blade's torsional frequency). The moment stall initiates in the fourth quadrant and controls the magnitude of the pitch link load. The following diagrams illustrate metal blade load growth rates and typical waveform growth.



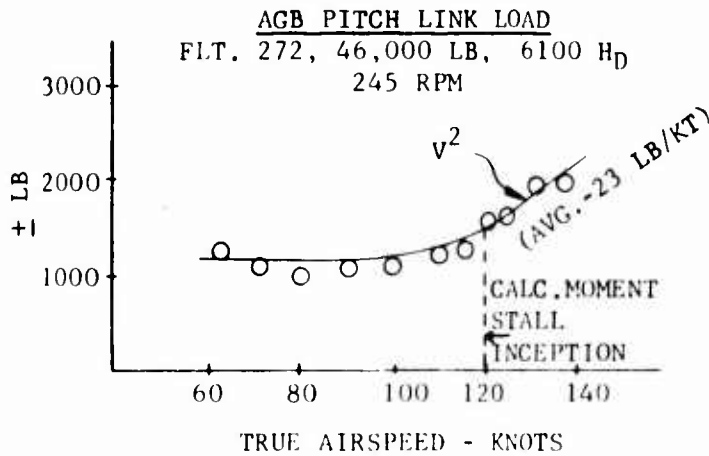
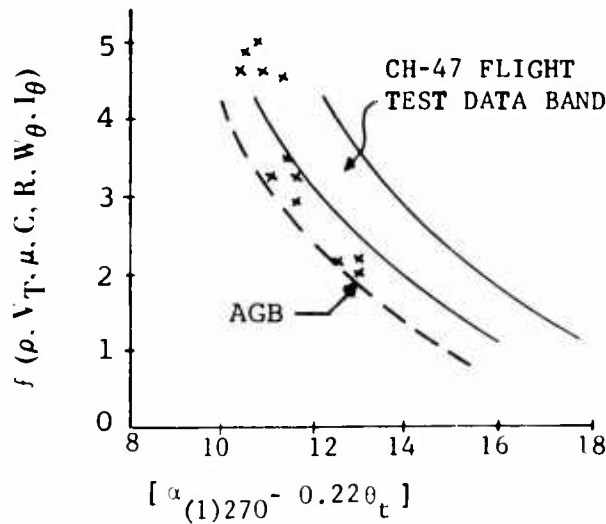
A large bank of such data has been nondimensionalized into a flutter parameter defining stall inception versus tip angle of attack at 270° azimuth.

The AGB pitch link load waveform has a different characteristic from that seen with the conventional metal blades. The moment stall spike appears in the waveform in the normal manner with increasing speed as a small cycle of torsional response well within the basic 1/rev waveform. As speed increases, the amplitude of the spike grows, eventually contributing to the peak-to-peak amplitude on the compression side but seldom dominating the 1/rev waveform. As a result, the inception of moment stall for the AGB blade was redefined to be that point at which a fully developed cycle of stall is first evident. The following figure displays an example of a typical waveform growth picture.



On a nondimensional basis, the AGB data shows evidence of an early stall inception point. This degradation is believed to be due to the 6 percent thin tip stalling earlier than the 10 percent CH-47C tip. Confirmation is seen in a comparison of waveforms at the same C_T/σ with evidence of stall showing up on the AGB blade before it does on the CH-47C blade.

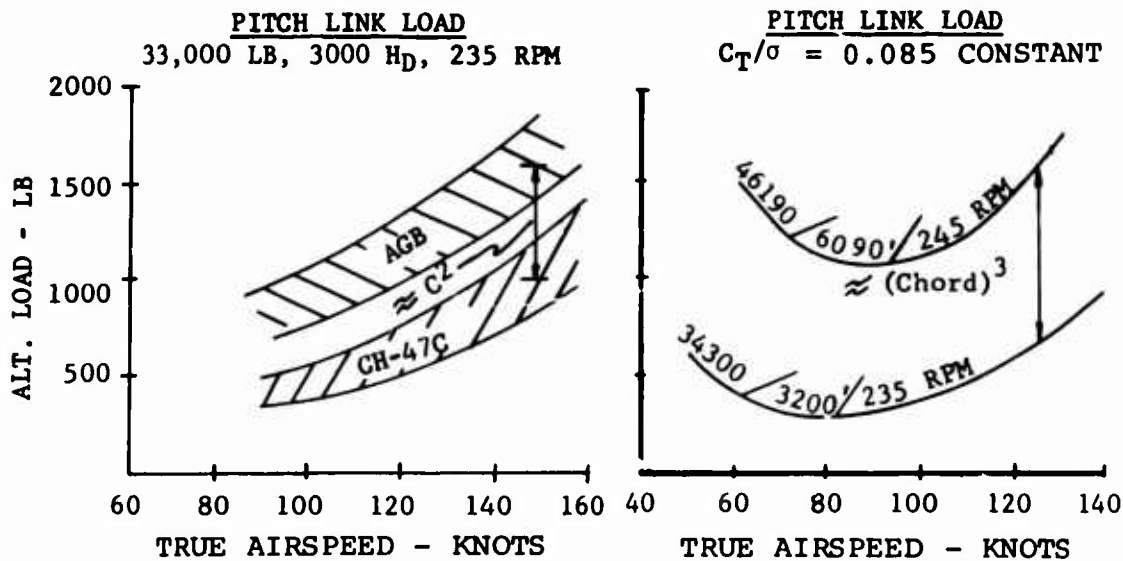
AGB MOMENT STALL INCEPTION
(Nondimensional)



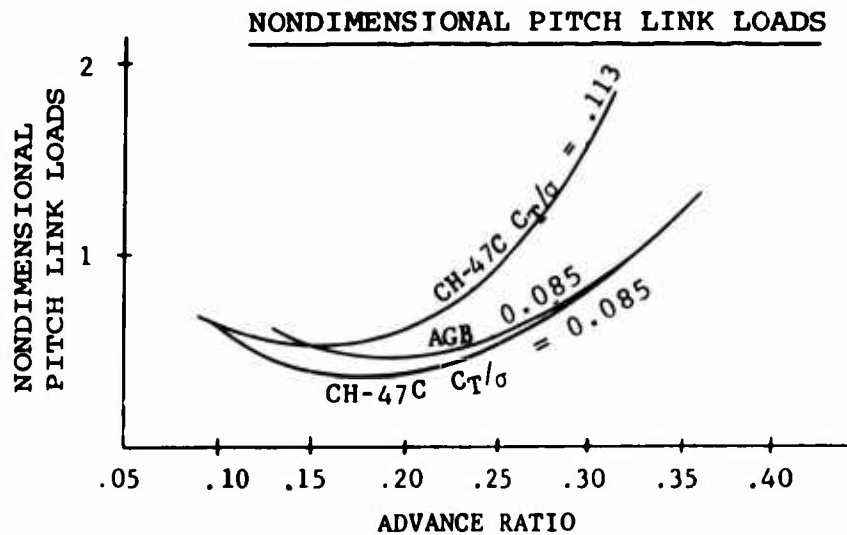
The pitch link load growth rate with airspeed for the AGB blade is much slower than occurs with the metal blade, more nearly approximating a (velocity)² trend. Utilizing the flutter parameter boundary established in the previous figure, the calculated moment stall limit is seen to occur at 120 knots, for the flight conditions shown.

The reason for the slower buildup is suspected to be from one or a combination of increased aerodynamic pitch damping from the wider chord (29 percent versus 24 percent critical), structural damping from the composite material (2.2 percent versus 1.7 percent), the pitch axis - A.C. relation (AGB 24 percent P. A.; CH-47C 19 percent P. A.), or different torsional natural frequencies (5.4 Ω /AGB; 6.4 Ω /CH-47C).

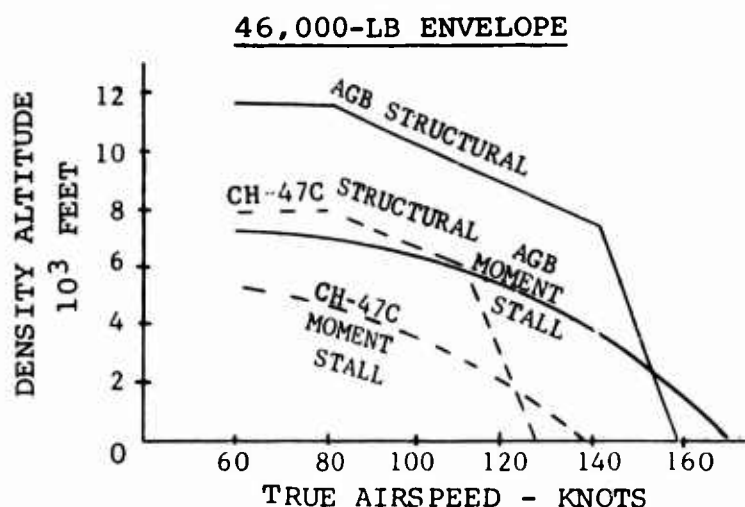
Below stall, the wider cord AGB blade develops higher pitch link loads in proportion to a (chord)² (thrust) relationship which can also be expressed in terms of a (chord)³ (CT/ σ) relationship.



If the same data is reduced to a nondimensional form using the expression $P.L.L. = K \left(\frac{C^2}{bR} \right) \left(\frac{T}{b} \right)$ and note $T = \frac{C_T}{\sigma} b \rho CR(V_T)^2$, we see that the pitching moment coefficients are approximately the same for both the AGB and CH-47C blades in unstalled flight regimes. When stall occurs on the CH-47C blade, the higher harmonic blade torsional response overrides the basic 1/rev loading, causing divergent control loads.



Depending on the relationship of power limits and nearness to stall, the increased chord of the AGB blade permits operation at lower C_T/σ than the CH-47C blade and avoids stall, thereby permitting improvement in the structural envelopes with little weight penalty as opposed to increasing metal blade chord.

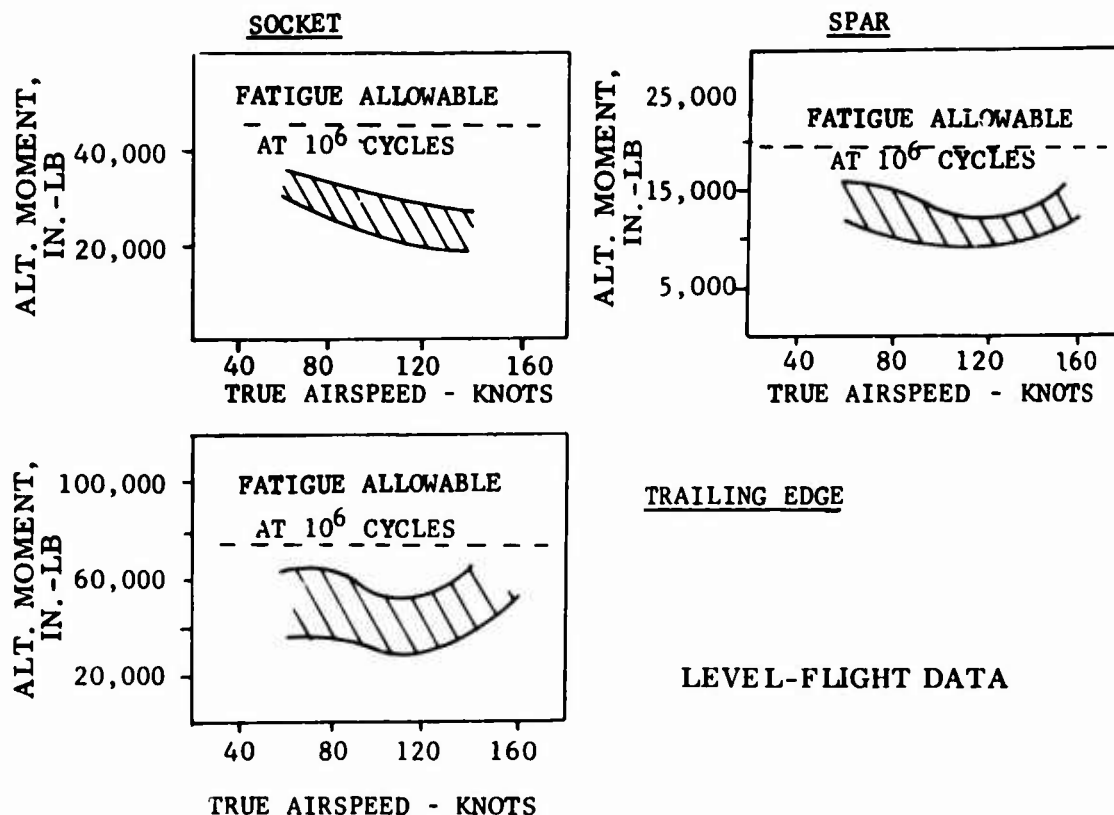


CONTROL AND BLADE LOADS

The stress and motion survey indicated that the most critical structural elements were in the aft rotor controls and the aft pitch links in particular. Blade loads were not critical and did not limit the level-flight envelope. As illustrated previously, a considerable improvement in the level-flight airspeed and gross weight capability was obtained with the AGB. Delay of moment stall, due to the increased solidity, and the lower pitch link load growth rate beyond the moment stall boundary are the primary reasons for the improved envelope.

Maximum alternating blade loads from flight data occurred in the aft rotor with the most critical locations being spar flapwise bending at station 288, blade socket flapwise bending at station 32.8 and blade trailing-edge tension at station 198. For all level-flight conditions, the loads at these locations were below the previously established fatigue allowables at 10^6 cycles.

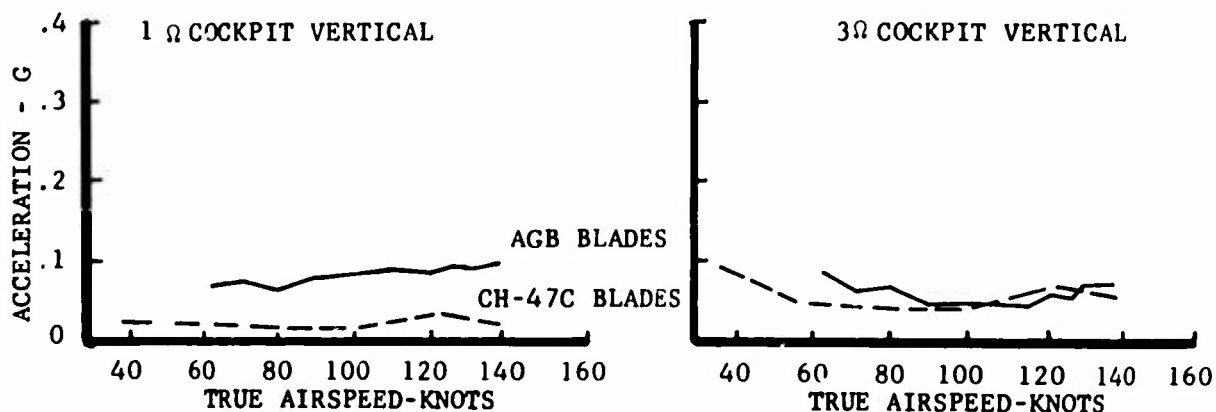
The fatigue allowables were exceeded in maneuvers, with the most critical location being the trailing-edge tension. Fatigue life considerations based on a modified CH-47C mission profile indicate a fatigue life of 4024 hours for the spar at station 228, 5850 hours for the blade's socket, and 938 hours for the trailing-edge skin at station 198. The most consistently damaging loads occurred in landing flares which, in the case of the trailing edge, accounted for 76 percent of the fatigue damage. No blade damage was observed during the flight program either visually or by means of ultrasonic inspection except at the trailing-edge transition area in the vicinity of station 94. Visually observable cracks occurred in the trailing edge of two forward blades and one aft blade. The cracks, which originated at discontinuities in the trailing edge, were not critical to the blade structure. Repairs were accomplished with blades on the aircraft, and no further discrepancies were noted.



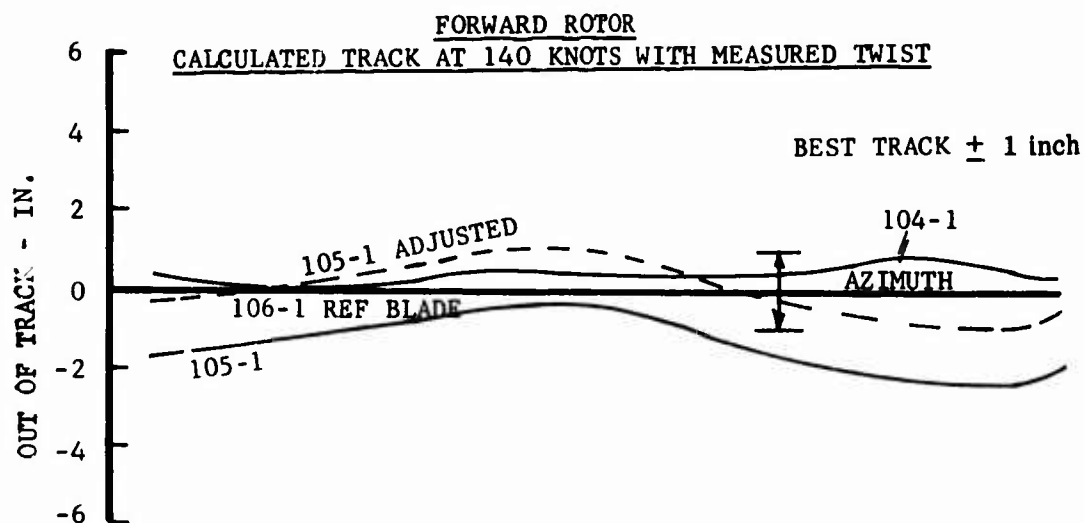
VIBRATION

Airframe vibration at the predominant 3/rev frequency with the Advanced Geometry Blades installed was comparable to the production CH-47C and within the model specification limits. The principal problem encountered was an excessive vibration at 1/rev.

Detailed inspection of the blades indicates that this difficulty was due to an approximately 1.5° twist discrepancy in one forward and one aft blade, together with deviations in the local pitching moment coefficients resulting from blade contour inaccuracies. Pitching moment coefficients can be corrected by local adjustments of the



trailing-edge cusp angle; however, as indicated by the following analytical results for the forward rotor, the twist effect alone is sufficient to produce an unacceptable track. Correction of this twist discrepancy in the fabrication process is necessary in order to hold blade twist within tolerable limits.



INTRODUCTION

The Vertol Division of The Boeing Company has completed a research and development program to design, fabricate, and fly advanced-geometry fiberglass rotor blades on the CH-47C helicopter (Figure 1). The primary objective of the program was to demonstrate the feasibility of utilizing composite materials in the fabrication of helicopter rotor blades and to improve the performance of the rotor system by a combination of increased solidity, improved airfoils and optimum blade geometry. A major factor in the selection of composites for the blade system was the degree of geometric freedom required for improved aerodynamic performance. A secondary objective of the program was to demonstrate that glass-fiber-reinforced epoxy could be used successfully in a fatigue-loaded primary structure.

The basic design criteria were similar to those for conventional rotor blades. However, the relative importance of some parameters assumed different proportions as a result of the application of composite materials. The criteria for torsional stiffness and shear strength were difficult to satisfy with glass-reinforced epoxy and played a major role in the materials selection process.

A materials test program was conducted to determine design properties and allowables. The program included static and fatigue tests on laminates, tubes, and sandwich beam specimens.

Configuration studies and parametric investigations to identify the blade which best satisfied the design criteria were included in the design phase. In addition, several analytical tools were developed.

The full-scale hardware structural test program included nonrotating natural frequency and section properties tests, static proof tests for trailing-edge buckling and ground flapping, static and fatigue tests of the root-end attachment and tip hardware, and fatigue tests of intermediate blade sections.

The whirl test program consisted of 50 hours of operation on the Boeing whirl tower. The blades were tracked for various combinations of collective pitch and rpm. A stress and motion survey was performed. The remainder of the program consisted of an endurance test in which combinations of collective and cyclic pitch were applied according to a regularly scheduled, repeating cycle.

The composite blades were flown on a CH-47C helicopter during the spring and summer of 1969 and accumulated approximately 46 hours of flight. Tests were conducted to investigate vibration, stress and motion, flying qualities, and performance.

The blade geometry was chosen on the basis of analysis and wind tunnel tests with the objective of obtaining maximum performance. In order to achieve optimum aerodynamic performance, the blade chord, airfoils and thickness ratio were varied along the span. One of the reasons for selecting fiberglass as the structural

material was that it afforded the geometric freedom required. It could be laid up on a mandrel of the desired shape and cured in an autoclave to the final geometry without the use of hard production-type tooling. Salient features of the AGB configuration are presented in Table I and depicted in Figure 2. A summary description of these features is presented below.

The blade is 30 feet long from the center of rotation to the tip and has a chord length of approximately 33.3 inches at the three-quarter radius. It also incorporates 6 degrees of linear twist. The chord length varies linearly between stations 48 and 117 and stations 117 and 360. The blade thickness variation is linear between stations 48 and 117, 117 and 198, and 198 and 360.

Five control stations were used to generate the entire blade configuration. The root-end control station (station 48) was circular in cross section with an outside diameter of approximately 7.7 inches. The pitch axis was located at the center of the circle. The second control station consisted of an NACA 23012 airfoil with a 36-inch chordline at blade station 117. The final three control stations were an NACA 23012 airfoil with a 33.917-inch chordline at station 198; an NACA 23010 airfoil with a 1.58-inch nose radius and a 32.54-inch chordline at station 252; and a Boeing airfoil, designated 13A006, with a 29.75-inch chordline at station 360. The pitch axis for all the airfoil sections was located at the quarter chord.

A combination of second- and third-degree surfaces was faired between the control stations utilizing a computer program. A trailing-edge cusp was added to the airfoil section to reduce the pitching moment characteristics.

A high fatigue strength-to-density ratio was another reason for selecting fiberglass. This ratio is approximately 8×10^4 psi/lb/in.³ for aluminum and 8.7×10^4 for steel, while fiberglass has a ratio of 12.3×10^4 . The ratio for fiberglass is based on a fatigue allowable of 8,000 psi alternating stress at 10^7 cycles and a density of 0.065 lb/in.³.

Fiberglass has a modulus-to-density ratio similar to that of the common engineering metals. The flap and chord natural frequencies could thus be made the same as metal blades which had flown successfully for many years. The dynamic requirements are the same as those for metal blades.

The orthotropic properties of fiberglass were another valuable asset. By changing the orientation of the fibers, the structure could be tailored to meet a wide range of strength and stiffness requirements.

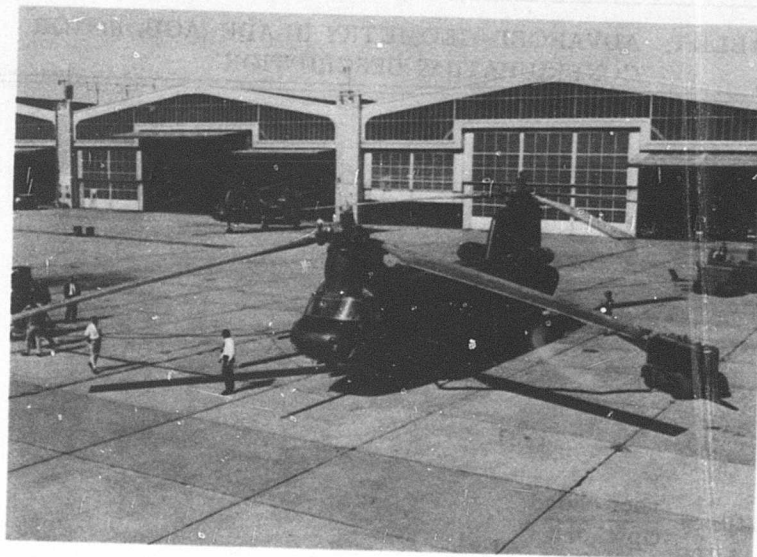


Figure 1. CH-47C Helicopter With Advanced-Geometry Fiberglass Rotor Blades.

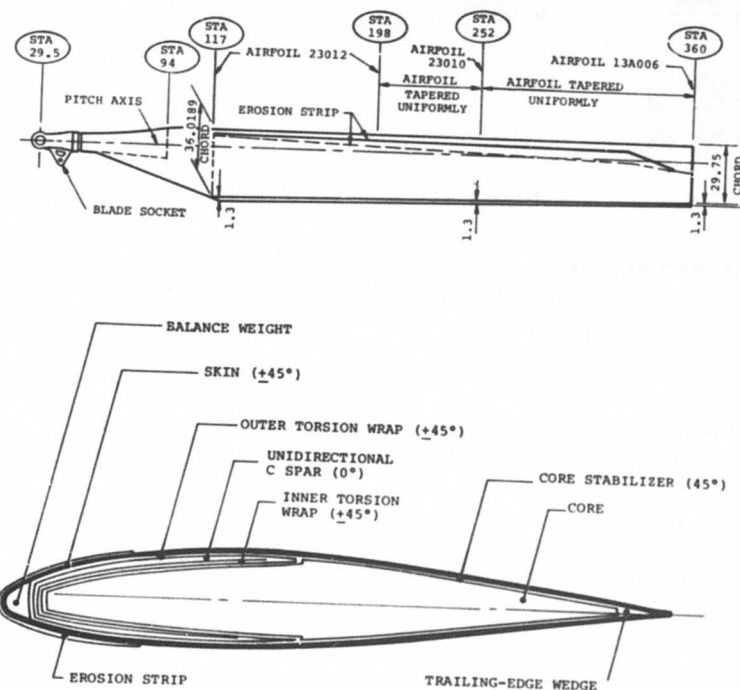


Figure 2. Design Details of the Advanced-Geometry Blade.

**TABLE I. ADVANCED-GEOMETRY BLADE (AGB) ROTOR
CONFIGURATION DESCRIPTION**

Rotor Radius - ft	30 ft				
Blade number per rotor	3				
Design rotor speed	230 RPM				
tipspeed	723 FPS				
Blade Chord at .75R	33.3 in.				
Chord taper ratio	1.31				
$\text{taper ratio} = \frac{\text{root chord}}{\text{tip chord}}$					
Root cutout	Inverse taper from 16% radius to 32% radius				
Rotor Solidity $\frac{bC_e}{\pi R}$	0.0845				
$C_e = \frac{\int CX^2 dx}{\int X^2 dx}$					
Blade twist	linear -6°				
Blade Control Station	48	117	198	252	360
Airfoil	circle	NACA23012	NACA23012	V23010-1.58	V13006-.7
	7.7-in.				
	diameter				
Chord not including trailing edge tab	-	36.0	33.917	32.54	29.75
including 1.3-in. trailing edge tab	-	37.3	34.217	33.84	31.05

BLADE DESIGN

DESIGN CRITERIA

The structural design criteria were in accordance with Reference 1. In addition to the specification requirements, the following criteria were established:

1. The blade shall be designed for 3,500 hours of service.
2. The steady stress in the fatigue cycle shall not be more than 20 percent of the ultimate strength of the material.
3. The metal fitting which mates with the vertical pin must be removable and replaceable, and mate with the CH-47B and C rotor hub.
4. Axes will be at the following locations:
 - a. Pitch axis - 25 percent chord
 - b. Static balance axis (center of gravity) - on or forward of the aerodynamic center
 - c. Dynamic balance axis - 1 percent of chord forward of the center of gravity at the three-quarter radius
 - d. Bending neutral axis - forward of the center of gravity
 - e. Shear center - 20 to 25 percent chord
5. Natural frequencies:
 - a. Flapwise
 - (1) First mode - 2.5 ± 0.05 per revolution
 - (2) Higher modes - a minimum of 0.2 per revolution away from any integer
 - b. Chordwise

All modes - a minimum of 0.2 per revolution away from integers
 - c. Torsional
 - (1) First mode - a minimum of 4.5 per revolution

- (2) All modes - removed by a minimum of 0.1 per revolution from any flap or chordwise mode

6. The blade weight shall be a maximum of 350 pounds.
7. The leading edge of the airfoil shall be protected against sand and rain erosion.

AERODYNAMIC DESIGN OF THE ADVANCED-GEOMETRY BLADE

An objective of the AGB program was to demonstrate improved performance capabilities of a pure helicopter.

To achieve the highest possible forward speeds for demonstrating the AGB, the program formulated in 1965 planned that the AGB rotor system be flown on a CH-47A helicopter with increased installed power. In addition, the test bed CH-47 airframe drag was to be reduced by removing the landing gear, fairing the pylons and fairing the fuselage ramp area. The actual flight test program conducted in 1969 utilized the CH-47C with T55-L-11 engines and up-rated transmissions, thereby providing the planned increased power; however, no drag reduction was provided.

The selection of composite materials for the AGB offered freedom from manufacturing constraints which usually prevent designers from specifying complex blade geometry for optimum performance. As a result of this selection, the AGB designer was able to specify complex airfoil, blade thickness, and blade planform variations desired for a high-performance, high-speed rotor. Presented in this section of the report is a brief summary of the rationale used in 1965 to select the AGB configuration. The items discussed include the selection rationale for

- airfoil and thickness distribution
- rotor solidity
- blade twist and planform
- root cutout

Airfoil Selection

The selection of airfoil sections capable of improving rotor performance without compromising lift capability or desired structural characteristics of the rotor blade was a major task in the development of the advanced geometry rotor blade. Efficient operation of the rotor at higher cruise speeds required airfoils well balanced for minimum airfoil drag at high Mach numbers and low angle of attack (experienced by an advancing blade), lift-drag properties at moderate Mach numbers and near

stall angles of attack (experienced by the retreating blade), and minimum airfoil pitching moment coefficient (C_{mac}) under all conditions.

Figure 3 summarizes the demands of the aerodynamic environment on rotor blade airfoils in terms of C_L and Mach number. Three critical regions are noted on the chart. Region A corresponds to high-gross-weight hover conditions and propulsive capability ($\psi = 0, 180^\circ$) in forward flight. Region B corresponds to the advancing tip where drag divergence due to compressibility can limit the aircraft speed. Region C corresponds to the high angle-of-attack region on the retreating side of the rotor disc. Here the effects of stall on control loads and vibration are the dominant influence.

Another method for analyzing airfoil suitability for helicopter use is shown in Figure 4, which plots $C_{L_{max}}$ at $M = 0.4$ (retreating blade stall criteria) against Mach number for $C_d = 0.018$ at $C_L = 0$ (advancing blade power criteria). Airfoils suitable for helicopters will have high values of both parameters.

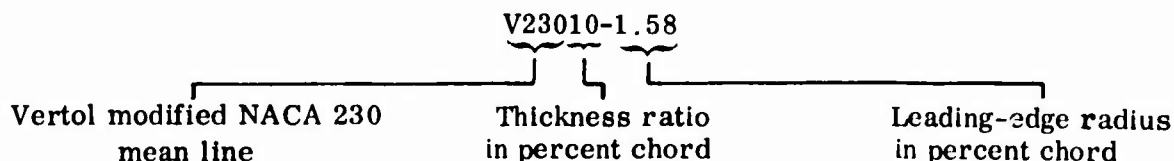
Model rotor system tests in 1964 showed that the standard NACA 0012 airfoil rotor blade begins to show a substantial compressibility lift penalty above a Mach number of 0.4. Similar tests of the standard NACA 23012 cambered airfoil showed a clear improvement in the lift capability; however, a penalty in drag rise Mach number resulted. Therefore, a development study was initiated to define airfoils which would be improvements in terms of the parameters of Figure 4 over the NACA 0012 airfoil.

Table II summarizes the gross geometric features of airfoil shapes and their effects on aerodynamic characteristics of interest. The features listed are not exhaustive; however, other possible variables (e.g., thickness distribution) are all much weaker in their effects than those tabulated. These important effects are covered in subsequent discussion.

The design study and wind tunnel tests resulted in the development of the Vertol 23010-1.58 airfoil section.* Flight tests of this airfoil section on the CH-47

*The Vertol airfoil designations, when different from standard NACA practice, have the following meanings:

The first three digits indicate the camber, as in the NACA 5-digit system. However, the Vertol profiles identified by prefix do not necessarily have the precise ordinates of the corresponding NACA mean line. For example, "130" means nose droop camber of about one-half the magnitude of the NACA 230. The next two digits indicate the thickness ratio, while the number after the hyphen is the leading-edge radius in percentage of chord.



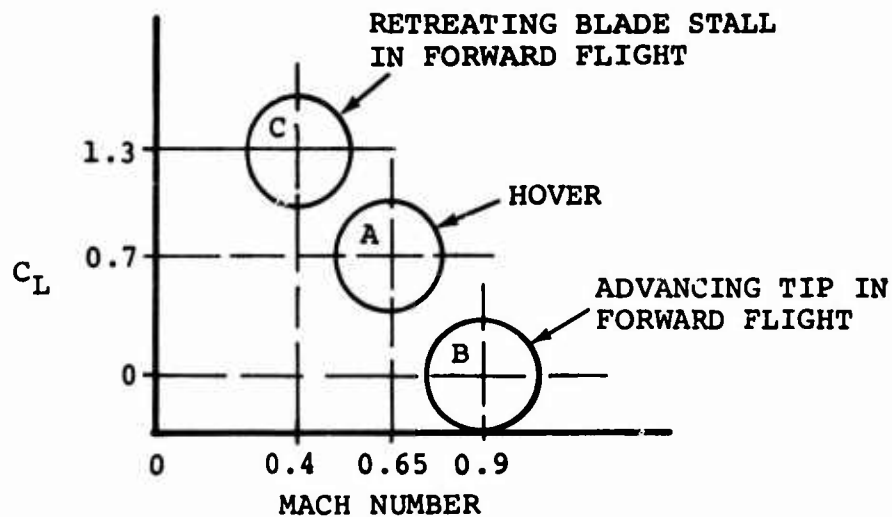


Figure 3. Rotor Blade Airfoil Aerodynamic Environment.

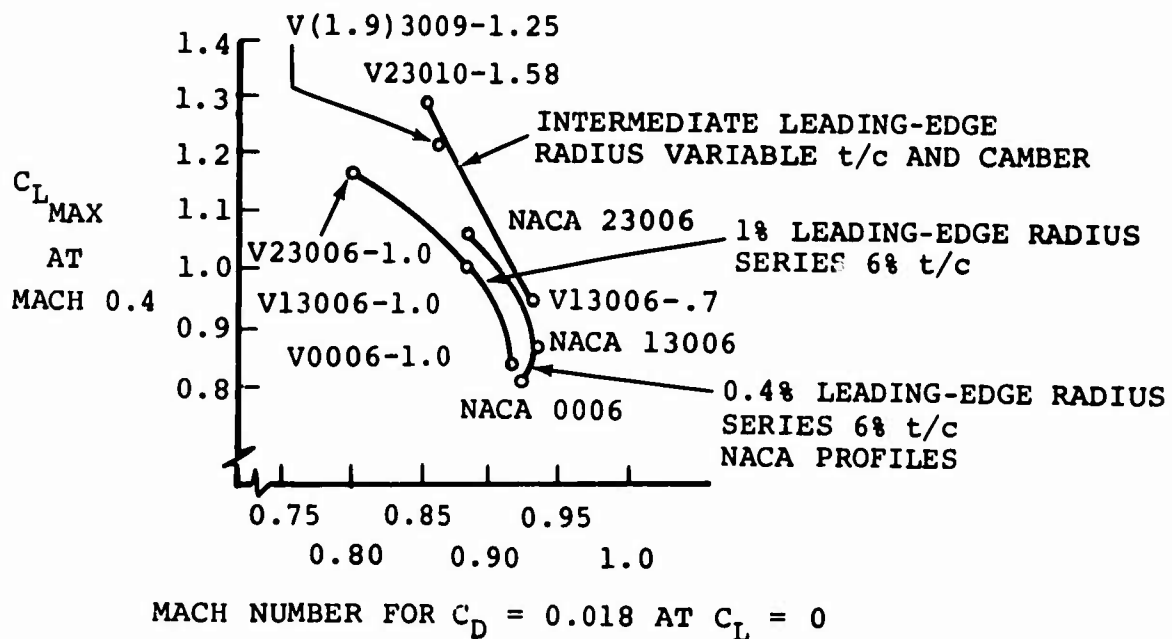


Figure 4. Summary of Stall and Drag Rise Performance for Airfoils Tested in the Boeing Rotor Blade Profile Development Program.

TABLE II. AIRFOIL GEOMETRY AND AERODYNAMIC SUMMARY						
Geometric Feature		Aerodynamic Characteristics				
		$C_{L_{max}}$	$C_{D_{min}}$	$\Delta C_{D_{lift}}$	$M_{DD} C_{L=0}$	$C_{m_{ac}}$
Thickness	Thick (greater than 12%)	Fair	Fair	Good	Poor	No effect
	Moderate (9 to 12%)	Good	Good	Good	Fair	No effect
	Thin (less than 9%)	Depends on camber, leading edge	Good	Depends on camber, leading edge	Good	No effect
Leading Edge	Blunt	Good	No effect	Good	No effect	No effect
	Sharp	Poor	No effect	Poor	No effect	No effect
Camber	None	Fair to poor	Good	Fair	Good	Good
	Uniform loading	Fair	Minute penalty	Fair to good	Fair	Unacceptable
	Trailing edge	Best	Unacceptable	Good	Unacceptable	Unacceptable
	Leading edge	Good	Slight penalty	Good	Fair	Fair (can be corrected to good)

helicopter confirmed the improvement in stall characteristics over the symmetrical NACA 0012 without a compromise of M for $C_d = 0.018$ at $C_L = 0$.

For efficient operation at higher Mach numbers above 0.9, a reduction in tip thickness ratio is required to avoid excessive power loss due to compressibility drag rise. Studies of existing airfoils showed that the NACA 0006 exhibited low section drag with increasing Mach number when unloaded ($C_L = 0$) but had poor lift capability (Figure 4). Applying nose droop camber to this section (transforming it to the NACA 23006) cured the lift problem but degraded the drag rise behavior (as evidenced by tests) which was the objective behind the thickness reduction.

Results obtained from two-dimensional wind tunnel tests (Reference 2) of thin forward camber airfoil section (23006) indicated that the reason for the drag degradation is that application of the 230 camber line to a 6 percent thickness form gives a lower surface contour that is very sensitive to negative angles of attack.

At this time, it was clear that new experimental data was needed as a basis for defining the proper camber and profile details for successful application of thin airfoils near the tips of rotor blades. It was anticipated that a better airfoil could be obtained by increasing the leading-edge radius and optimizing the camber. A program of airfoil optimization was then undertaken.

Two 6-percent t/c families of airfoils were selected for testing: one with an 0.4-percent leading-edge radius; the other with a 1.0-percent leading-edge radius. A systematic variation of camber was made by testing three airfoils for each family having: (1) 100 percent of NACA 230 camber, (2) 50 percent, (3) no camber.

When, during the course of testing, it became clear that the 1.0-percent leading-edge radius series suffered from unexpectedly early compressibility drag rise, two other airfoils were tested: (1) a 9-percent-thick airfoil for use as a transition profile between the 6-percent-thick tip and a 12-percent-thick inboard blade section, (2) a 6-percent-thick airfoil with 0.7-percent leading-edge radius. The airfoils described above are illustrated in Figure 5. The tests were conducted in the two-dimensional test section of the Boeing Supersonic Wind Tunnel. The test conditions ranged from 0.2 to 0.9 Mach number with Reynolds numbers equal to that of a 2-foot chord blade at 5,000 feet altitude (Reference 3).

A summary of the airfoils tested is given in Figure 6. The compromise acquired through the development of the Vertol 13006-.7 airfoil is evident (drag rise behavior nearly equal to that of the NACA 0006 with a $C_{L_{max}}$ only slightly poorer than that of the NACA 23006). The transition airfoil of a 9-percent t/c showed good drag-rise behavior and a high $C_{L_{max}}$. The three Vertol-developed airfoils are seen (Figure 6) to offer a combination of drag rise and high lift characteristics superior to both the NACA 230XX family and the NACA symmetrical 00XX airfoils.



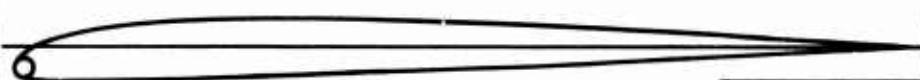
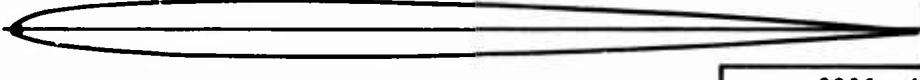
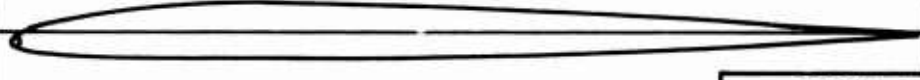
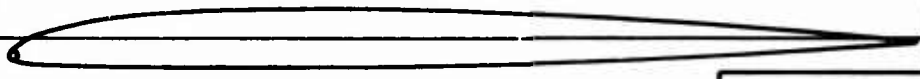
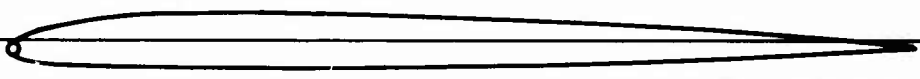

AIRFOIL FAMILY LEADING-EDGE RADIUS (% OF CHORD) (% OF 230 CAMBER)			PROFILE	DESIGNATION
1.0% LEADING-EDGE RADIUS SERIES 6% t/c	1.0%	0		0006-1.0
		50%		13006-1.0
		100%		23006-1.0
NACA 5-DIGIT SERIES 6% t/c	0.4%	0		0006-.4
		50%		13006-.4
		100%		23006-.4
MODIFIED AIRFOIL 6% t/c	0.7%	50%		13006-.7
INTERPOLATED AIRFOIL 9% t/c	1.25%	80%		(1.9)3009-1.25

Figure 5. Profiles of Airfoils Tested in the Boeing Supersonic Wind Tunnel.

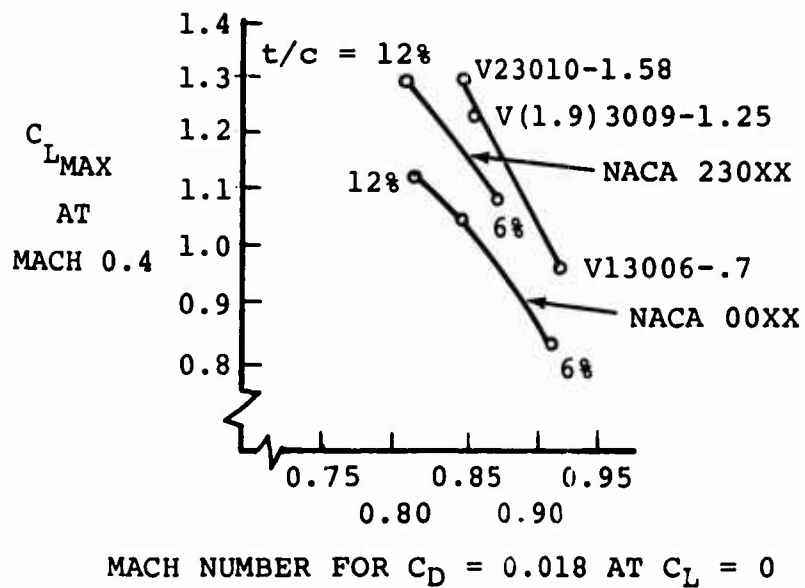


Figure 6. Summary of Stall and Drag Rise Characteristics for Several Airfoil Families.

In summary, the AGB airfoil selected for the root, the NACA23012, satisfied structural consideration of the design by providing a 12 percent thickness ratio and suitable aerodynamic characteristics for the low-Mach-number environment of the root. At 70 percent radius, the V23010-1.58 airfoil was selected for its high $C_{L_{max}}$ capability at Mach number of .4, thereby providing the best airfoil for retreating blade stall considerations. The V13006-.7 tip section was selected based on the high Mach number requirement of the advancing tip at high forward speeds.

Selection of Rotor Solidity

Rotor limitations prevent helicopters from achieving high lift capability at high cruise speeds. These rotor limitations derive principally from reverse flow, stall and compressibility effects which lead to high noise levels, high power requirements, high vibratory control loads and rotor trim control problems as forward speed is increased. The solidity of the AGB rotor system was selected with the objective of extending these limitations, thereby advancing the capability for increasing speed and increasing lifting capability of the pure helicopter.

When the program was formulated in 1965, increased power available and reduced drag was anticipated for the CH-47 vehicle tested which would permit speeds up to 200 knots at a gross weight of 33,000 pounds cruising at 3000 feet standard temperature conditions and at 230 rotor RPM. At a gross weight of 43,700 pounds, the estimated power limited speed capability was 180 knots. The rotor solidity was selected based on the estimated maximum lifting capability of a propelling rotor which is significantly reduced as forward speed is increased. Based on wind tunnel tests of model rotors and rotor stall theoretical analysis conducted in the 1965 time period, the maximum thrust coefficient (C_T'/σ) at 200 knots ($\mu = 0.47$) was estimated to be about 0.0775. At 180 knots ($\mu = 0.42$), the maximum thrust coefficient was estimated to be 0.085. The more critical limiting conditions associated with the 43,700-pound gross weight at 180 knots were used to select the AGB rotor solidity of 0.0845.

Twist and Planform Selection

Investigations of the effects of blade twist and planform taper on a rotor operating at 200 knots were conducted in 1965 in support of the AGB design. The general conclusions of these investigations were:

1. Power required is reduced when negative twist and planform taper ratios greater than one are utilized.
2. Flap bending moments increase when negative twist and planform taper are utilized.
3. Chordwise bending moments decrease for values of negative twist up to -3° and then increase with further negative twist. Alternating chordwise bending

moments increase with blade planform taper up to values of 1.4 and then decrease at higher values of planform taper.

4. Vertical 3/rev hub shaking forces increase when negative twist is utilized; they decrease when planform taper is utilized.

A summary of the effects of the -6° twist and the 1.3 taper ratio selected for the AGB rotor is presented in Table III. The values shown are taken from Figure 7, which shows the effects of twist from 0 to 11° and taper ratio from 1 to 1.6 on power, bending moments, and hub shaking forces.

TABLE III. SUMMARY OF EFFECTS OF TWIST AND PLANFORM TAPER ON THE AGB ROTOR			
Percent Change From 0 Twist or Taper Ratio = 1.0			
Item	Effects of -6° Twist at Taper Ratio = 1.0	Effects of 1.3 Taper Ratio at -6° Twist	Combined Effects of -6° Twist and 1.3 Taper Ratio
Power	8 1/2% decrease	1 1/2% decrease	10% decrease
Flap Bending Moment	11% increase	12% increase	23% increase
Chordwise Bending Moment	3% decrease	17% increase	14% increase
Vertical 3/Rev Hub Shaking Force	16% increase	8% decrease	8% increase

The selection of a -6° twist and a taper ratio of 1.3 for the AGB was based primarily on the performance benefit, which was calculated to be a 10 percent decrease in power required at 200 knots. The tapered planform was also selected to improve natural frequency. The bending moment and shaking force increases associated with this selection were considered inconsequential when compared to the performance improvement and the stress margins provided by the AGB design.

Root Cutout Effects

The inverse tapered root cutout geometry of the AGB was dictated by blade folding considerations. The effect of the root cutout on performance is depicted in Figure 8; the AGB inverse taper reduced the lift to drag (L/D) ratio of the AGB by about 10 percent compared to the L/D ratio of a blade with only 16 percent root cutout. The effects on flap bending and chordwise bending moments were negligible, and the 3/rev vertical shaking forces were estimated to increase by 10 percent.

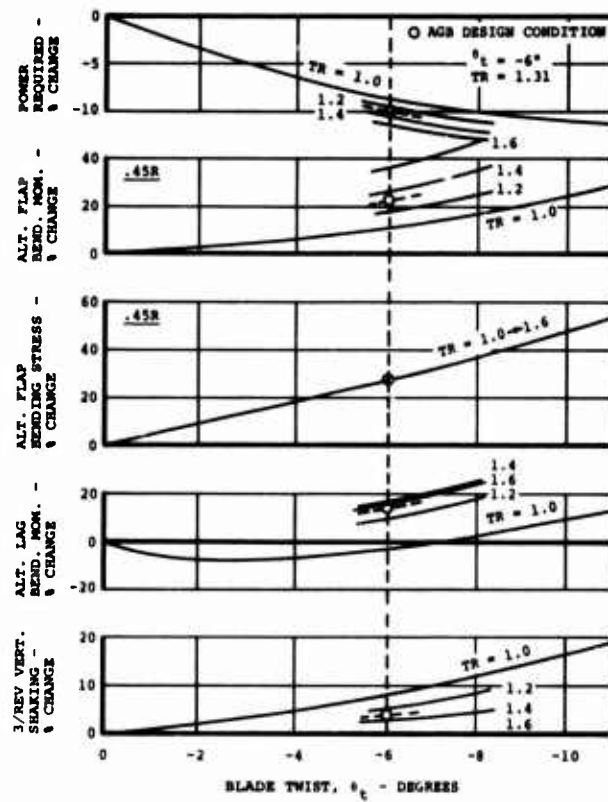


Figure 7. Calculated Effects of Blade Twist and Planform Taper on Power Required, Bending Moments, and Hub Shaking Force at 200 Knots.

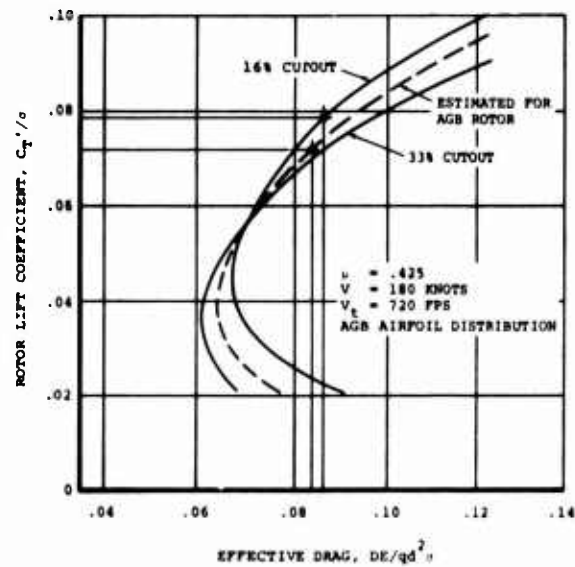


Figure 8. Effect of Root Cutout.

MATERIAL SELECTION

The aerodynamic configuration of the advanced-geometry blade included spanwise variations in chord length, thickness ratio, and airfoil sections. The primary reason for selecting fiberglass as the structural material was its flexibility in achieving this configuration, while exhibiting high fatigue strength-to-density ratio, acceptable modulus-to-density ratio, and the orthotropic properties of fiberglass.

Candidate composite materials were selected on the basis of Boeing data, Industry and Government literature, and vendor data. Those materials which had the required combination of strength, density, and moduli to meet the design criteria were considered. E-glass was eliminated in the early designs because its moduli and tensile strength were too low to meet the design requirements. As a result, S-glass was given primary emphasis, and promising S-glass materials were subjected to a series of screening tests. The purpose of this testing was to assure that the properties could be achieved with the actual blade fabrication process. Final selection of materials was made on the basis of the preliminary testing.

Scotchply 1002S was chosen for the blade spar, since its properties produced the desired flapwise natural frequency and bending strength. This material is an epoxy resin reinforced with nonwoven S994 filaments. The resin content, expressed as a percentage of the laminate weight, averaged 30.7. This resin content corresponds to a cured laminate density of 0.066 lb/in.³ and a fiber volume of 51 percent.

To satisfy the torsional criteria, the material with the highest shear strength and modulus was required. Scotchply XP251S oriented at ± 45 degrees to the pitch axis met the design requirements. This composite has a modified epoxy-resin matrix reinforced with S994 filaments. The average cured laminate density is 0.073 lb/in.³ with a fiber volume of 63 percent.

A tough material which could resist handling damage and bond well at relatively low curing pressures was required for the blade skin material. The composite selected was 143S glass cloth preimpregnated with American Cyanamid's BP907 resin system. The average cured laminate density was 0.066 lb/in.³ with a fiber volume of 63 percent.

MATERIAL TESTING AND ANALYSIS

After the blade materials had been selected on the basis of preliminary tests, it was necessary to perform an extensive materials test program to determine design properties and allowables for use in the design phase of the program. Test programs were conducted to obtain statistically significant data on the static and fatigue strength of the three blade materials. One program was conducted for the U.S. Army Aviation Materiel Laboratories under Contract DA44-177-AMC-440(T). Additional test data were generated under a company-funded effort.

A method of determining fatigue design allowables from coupon data was developed. The fatigue data were analyzed by regression analysis. Experience has shown that fatigue data fall on a straight line if plotted in a log-log field. A least-squares, best-fit line was established as the mean in this field. The equation of this line has the form $\log(\text{alternating stress}) = A + B \log(\text{number of cycles})$, where A and B are constants. From this equation, each data point was transposed to 10^7 cycles parallel to the mean line, where a standard deviation and a coefficient of variation were statistically determined. From data dispersion, it appeared that the coefficient of variation remained constant; therefore, at 10^6 , 10^5 , 10^4 , etc., the standard deviations were calculated. A mean-minus- 3σ line was determined by subtracting three times the corresponding standard deviation from the mean curve at the respective number of cycles. The design-allowable curve was obtained by dividing each ordinate of the mean-minus- 3σ curve between 10^5 and 10^8 cycles by a factor of 1.75. The 1.75 reduction factor is an engineering estimate based on experience with metals and is intended to account for all the strength-reduction factors experienced by full-scale hardware in a service environment. The low-cycle end of the design-allowable curve ($<10^5$ cycles) is a straight line which is either tangent to the mean-minus- 3σ line or intersects the static ultimate allowable at the quarter-cycle point, whichever is lower.

The coupon testing results are shown in Figures 9 through 11 for unidirectional 1002S, ± 45 -degree XP251S, and ± 45 -degree BP907-143S composites, respectively. The mean-of-data curve, test-mean-minus- 3σ curve, and design-allowable curve are indicated in the cited figures. All the laminates were tested at a stress ratio of 0.1 and a temperature of 75°F. The loading rate was 20 cycles per second.

Further fatigue testing was performed using a combination of 50 percent unidirectional 1002S and 50 percent ± 45 -degree XP251S. The results in terms of strain are plotted in Figure 12 and show that all the uni-crossply data fall into the scatter of the unidirectional material without resin degradation or delamination. Because of the modulus differential, the unidirectional material takes most of the load and is the fatigue-critical material; consequently, the crossply material acts as a relatively passive element in the combination. These data suggest that the uni-crossply combination should be designed to the limiting strain of the unidirectional material, provided that there is less than 50 percent crossply in the composite structure. Analysis of the structural and flight test results seems to support this conclusion, and the results are discussed in the relevant sections.

This coupon testing and data analysis of the uni-crossply combinations were performed after the flight test program. The effect on the structural analysis of the blade is considerable because the crossply (outer torsion wraps of the blade) was fatigue-critical when it was analyzed before flight testing.

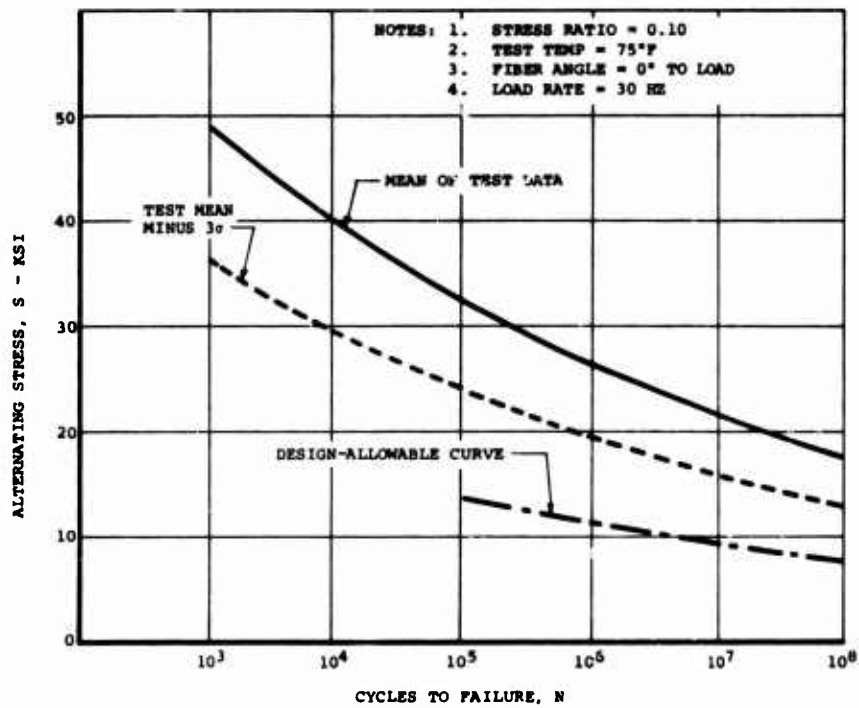


Figure 9. Stress Curve for Unidirectional 1002S Epoxy-Resin Laminates Loaded in Tension-Tension Fatigue.

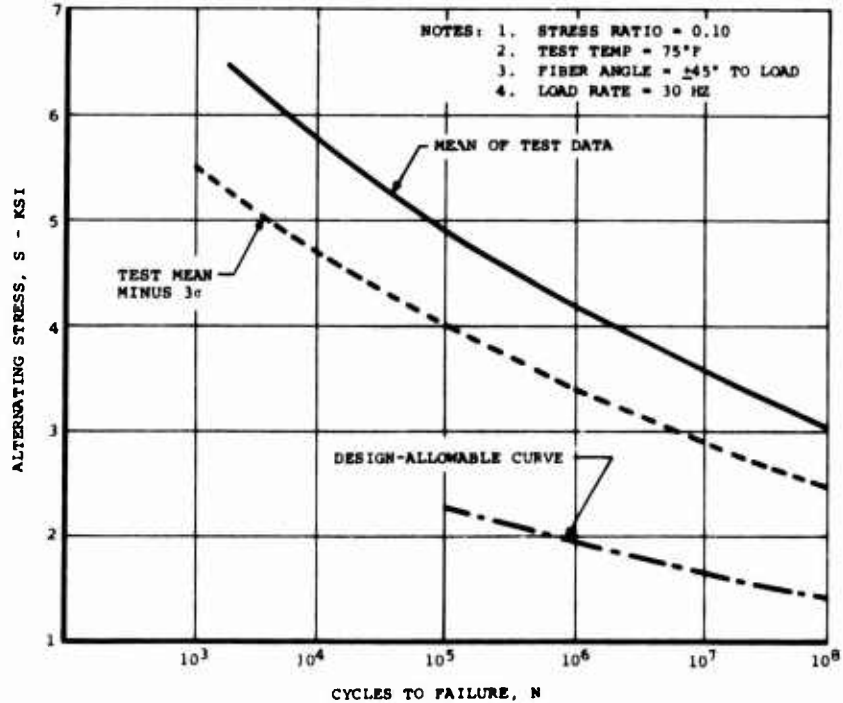


Figure 10. Stress Curve for XP251S ±45-Degree Crossply Epoxy-Resin Laminates Loaded in Tension-Tension Fatigue.

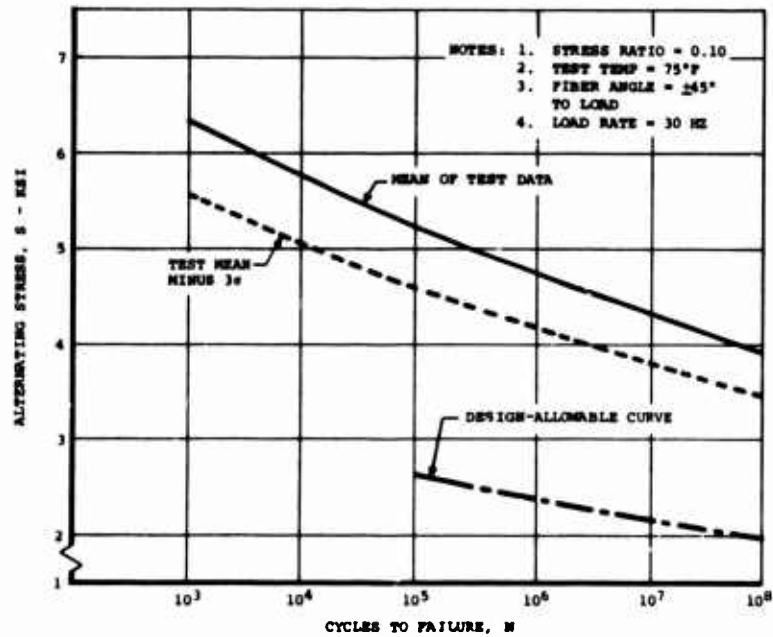


Figure 11. Stress Curve for BP907-143S Crossply Epoxy-Resin Laminates Loaded in Tension-Tension Fatigue.

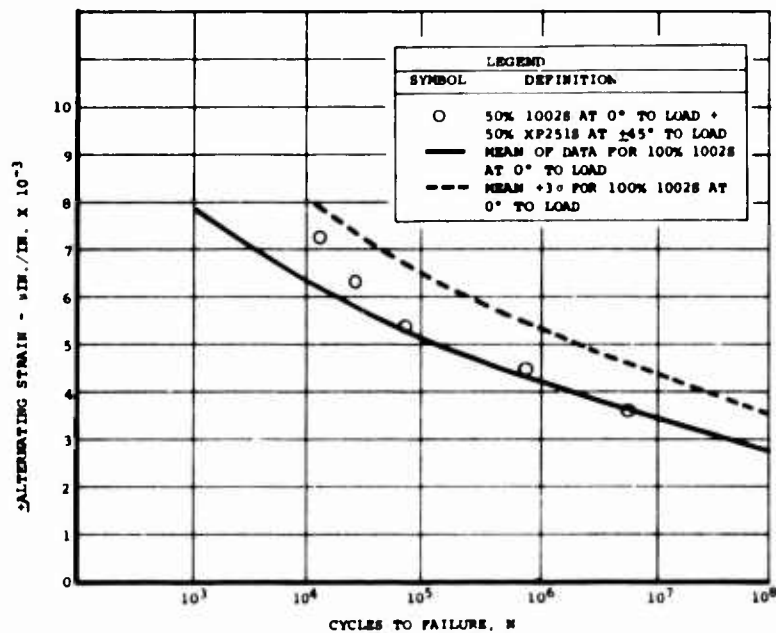


Figure 12. Strain Comparison of Unidirectional S-Glass and a Mixture of Unidirectional and Crossply S-Glass.

STRUCTURAL DESIGN

The preliminary design phase consisted of configuration studies to identify the most efficient arrangement of structural material within the airfoil cross section. Parametric evaluations to determine the effects of the spanwise distribution of properties on the blade's structural performance were also included in this phase.

Of the structural configurations which were investigated, the C-spar produced the maximum bending and torsional stiffness for the minimum balanced section weight. The selected structural geometry is illustrated in Figure 13.

Figure 14 shows the effects of the location of a tuning weight on the blade natural frequencies. Other studies showed that local flapwise stiffness changes had very little effect on the first-mode frequency and that the effect became more significant on the higher modes. It was determined that the most effective locations for the addition of torsional stiffness were the root-end spring and the midspan of the blade.

During the preliminary design phase, approximately 50 blade configurations were investigated. Included were variations in material thickness and orientations and various spanwise distributions of blade properties. Each configuration was evaluated for natural frequencies, loads, deflections, stresses or strains, and fatigue life or margin of safety. If any configuration failed to meet the design criteria at one step in the evaluation, the design was modified and the analytical process was repeated. Several analytical tools developed during the program are described in the following paragraphs.

Master Dimensions Program

Airfoil coordinates were used to generate a series of equations which represented the blade surface at the control stations. The equations for intermediate stations were developed by interpolation or by a series of third-degree equations. Material thicknesses and arrangements were described as offsets from the outer surface. A mathematical model of the entire blade, including the internal structure, was stored in the computer. Engineering information such as coordinates at all stations and area section properties for each material could then be extracted. The master dimensions model was also used to prepare blade section drawings and to prepare templates and plaster masters for blade tooling.

Section Properties Program

The information on area section properties, along with material densities and moduli and balance information, is input. The program calculates blade section properties and the amount of nose weight required to produce the desired balance axis location, as well as the pitching mass moment and the principal axis locations of the section.

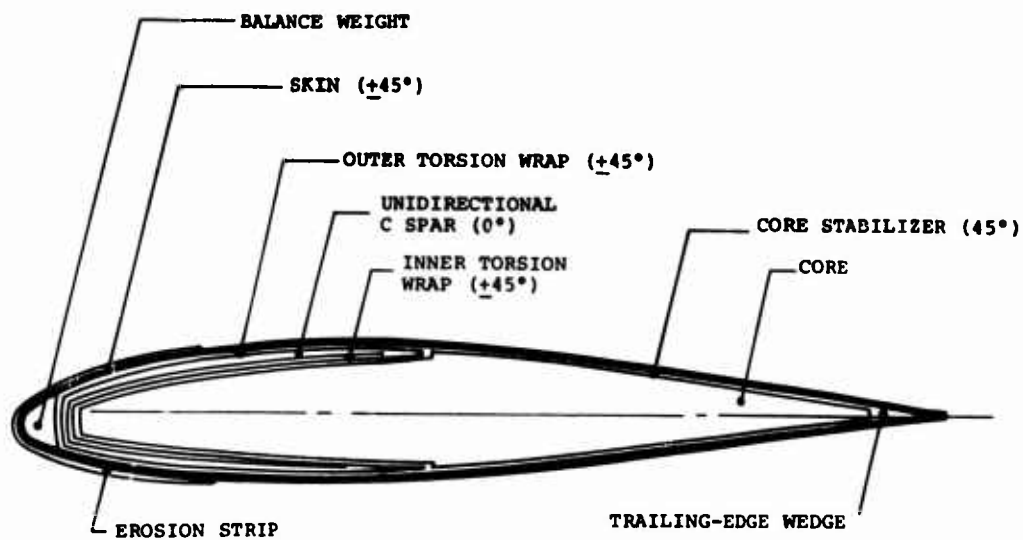


Figure 13. Structural Design of the Advanced-Geometry Blade.

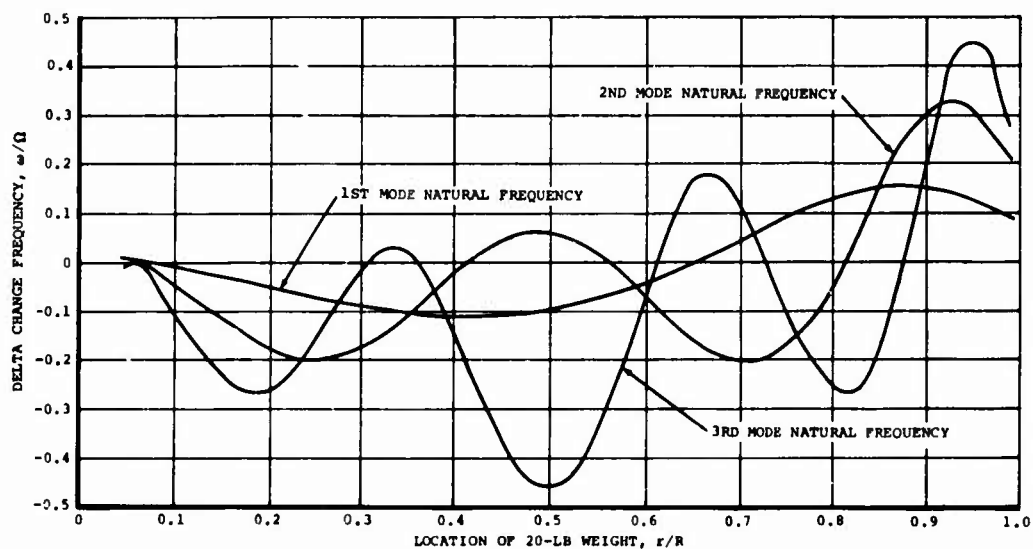


Figure 14. Effects of Location of Tuning Weight on Blade Natural Frequencies.

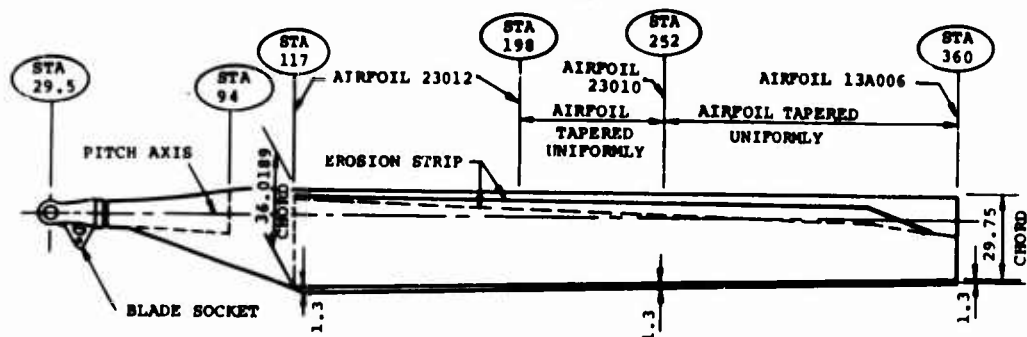


Figure 15. Physical Characteristics of the Advanced-Geometry Blade.

Shear Center and Torsional Stiffness Program

The blade section is idealized as a multicell torque box, and equations for shear flow are written for each cell. The material thicknesses are theoretically transformed into an equivalent thickness of the selected base material. A general torque equation is generated. Shear flows due to vertical shear and torsional loading, as well as the shear center and torsional stiffness, are calculated.

Leone-Myklestad Programs

These programs, which have been continually modified and updated since they were documented in References 4, 5, and 6, were used to determine blade natural frequencies and loading. Included in the modifications were provisions to account for nonuniform downwash, the addition of an air spring in the blade torsional natural frequency calculation, a stability analysis, and the updating of the torsional loading calculation.

Strain and Margin-of-Safety Program

Material allowables and blade section properties and loading are input to perform the bending stress analysis. The program calculates steady and alternating strains and margins of safety for each material present at selected checkpoints.

Special Condition Loading

Unit shears and moments are calculated. Average weight and flap stiffness in discrete spanwise locations are calculated from coordinates of the weight and flap stiffness distribution curves. Unit loads are calculated for starting, braking, shock torque, and ground flapping conditions.

DESIGN AND CONSTRUCTION OF THE ADVANCED-GEOMETRY BLADE

The advanced-geometry rotor blade is a composite structure using laminated, uni-directional, S-glass-fiber-reinforced epoxy materials, aluminum honeycomb core, and titanium attachments and fittings. It incorporates both a tapered planform and a tapered profile thickness while using cambered airfoil sections. The blade geometric characteristics are (refer to Figure 15):

Radius (from center of rotation)	30 feet
Root chord at station 117 - basic	36 inches
Root chord at station 117 - with cusp	37.30 inches
Tip chord - basic	29.75 inches

Tip chord - with cusp	31.05 inches
Thickness ratio, station 117 to station 198	0.12
Thickness ratio, station 198 to station 360	0.12 - 0.06
Airfoil, station 117 to station 198	Vertol 23012-1.58
Airfoil at station 252	Vertol 23010-1.58
Airfoil at station 360	Vertol 13006-.7
Twist	-6.0 degrees

Five control stations were used to generate the entire blade configuration. The root-end control station (station 48) was circular with an outside diameter of approximately 7.7 inches. The pitch axis was located at the center of the circle. The second control station consisted of an NACA 23012 airfoil with a 36-inch chordline at blade station 117. The final three control stations were an NACA 23012 airfoil with a 33.917-inch chordline at station 198; an NACA 23010 airfoil with a 1.58-inch nose radius and a 32.54-inch chordline at station 252; and a Boeing airfoil, designated 13A006, with a 29.75-inch chordline at station 360. The pitch axis for all the airfoil sections was located at the quarter chord.

The main lifting section of the blade extends from station 117 to the tip (station 360). A tapered transition section is used inboard of station 117 to the root-end socket vertical pin attachment joint. The attachment joint is designed to be compatible with the standard CH-47C rotor head. The major components of the blade are the spar, a stabilized core-skin assembly, leading-edge noseblock assembly, final profile skins, and root and tip attachments.

The main structural component is the fiberglass spar. The design uses inner and outer crossply torsional liners (alternately 45 degrees from the pitch axis) and a longitudinal, unidirectional core laminate placed between the torsional liners. The core laminate and torsional liners are tailored spanwise to produce the desired axial, flexural, and torsional stiffness. The spar changes from a round section at the socket outboard to an elliptical section and then to a C-section. The transition from a closed elliptical section begins at station 71, which enlarges to the C-section at station 94 and remains a C-section throughout the rest of the blade length. The root end of the fiberglass spar is molded around a conical, hourglass-shaped, titanium root-end fitting. A titanium tip anchor fitting is positioned within the outboard core laminate which wraps around it, providing a base attachment for tip balance weight studs. Both fittings become integral parts of the spar molding. The inboard end of the molded spar around the root-end fitting is circumferentially wrapped with unidirectional material and finish-machined to dimensionally match the internal cone surface of the root-end socket. The root-end socket attaches to

the root-end fitting by a thread and pin connection. The root-end configuration provides mechanical interlocking of the fiberglass spar to the fittings, providing redundancy for the adhesive joint. The largest portions of the flapwise, chordwise, torsional, and centrifugal tension loads are reacted by the spar structure.

The core-skin assembly is a sandwich structure using aluminum honeycomb core, oriented fiberglass skins, and a solid fiberglass trailing-edge wedge. It is contoured to fill all space within the C-spar from station 94 to the tip. It stabilizes the spar and is the box structure for the airfoil section aft of the spar. An external tapered transition section of this assembly abuts the trailing edge of the spar inboard of station 94. The density of the honeycomb core is varied to provide required shear fatigue properties. This subassembly is bonded to the internal spar surfaces outboard of station 94 and externally to the spar inboard of station 94. A premolded foam detail is used inboard at the external bond joint to fill and fair the gap between the contoured spar trailing edge and the vertical face of the inboard core extension. The leading edge of the core-skin assembly at the tip end is cut out for a molded fiberglass overbalance fitting which is contoured to fit the inside surface of the spar and is bonded to the spar concurrently with the core-skin assembly. This fitting provides the housing for the overbalance rod weight used for dynamic and static balance axes adjustments. The weight is retained by a stud in the tip anchor fitting.

The noseblock assembly is a spanwise family of 12 tapered and contoured molded fiberglass shells filled with a tungsten-powder-impregnated elastomeric compound. This provides the means for static balancing of the blade along its length (station 97 to station 356) by the proper selection of the density of the compound encapsulated in each shell. The filled shells are bonded to the leading edge of the spar. As assembled, they form the internal leading-edge shape of the airfoil sections.

The bonded spar, core-skin, and noseblock subassemblies are completely covered with oriented fiberglass skins joined at the leading and trailing edges of the blade. The orientation of the skins provides torsional shear-carrying capability. Molded fiberglass tip rib and tip end closure details are bonded in place concurrently with the final skinning operation. The tip rib provides a housing for the tip span and tracking weights. These weights are retained on four studs which attach to the tip anchor fitting. A molded fiberglass tip cover is flush-mounted to the open end of the tip rib and retained by four screws.

Titanium strips are bonded to the leading edge of the blade for protection from rain and sand erosion. An adjustable fiberglass cusp is bonded to the trailing edge of the blade. Fiberglass doublers are bonded to the leading- and trailing-edge skin joints in the inboard transition section of the blade. Machining of the cone at the root end of the molded spar and installation of the socket, incidence pin, and tip hardware complete the blade assembly.

Figures 16 through 26 show some of the problems and design solutions involved in the development of the advanced-geometry blade.

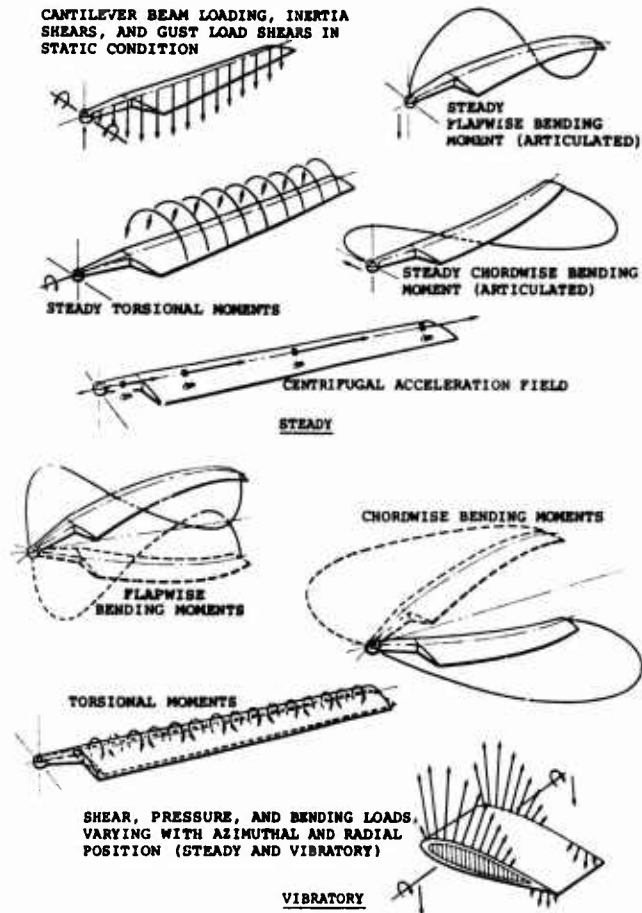


Figure 16. Principal Steady and Vibratory Loadings of a Rotor Blade.

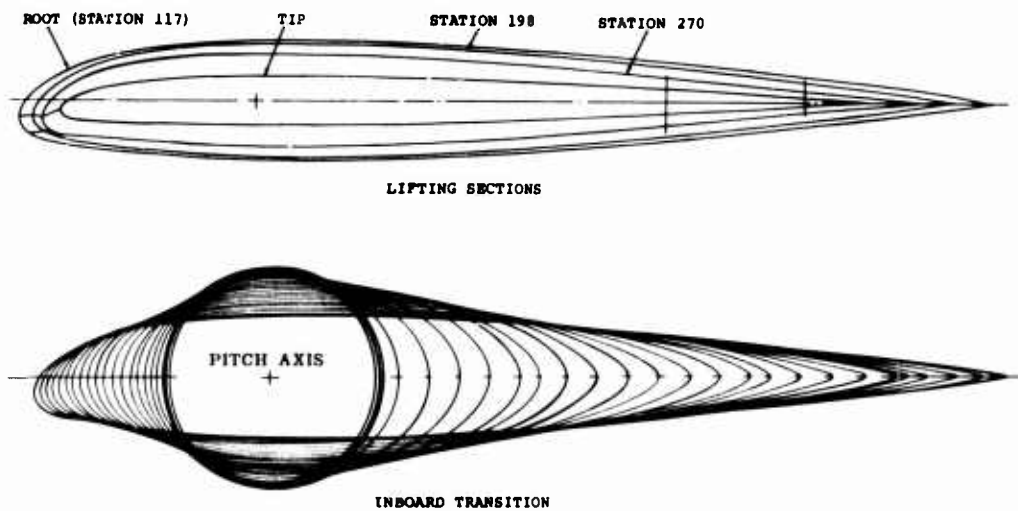


Figure 17. Contours of the Advanced-Geometry Blade.

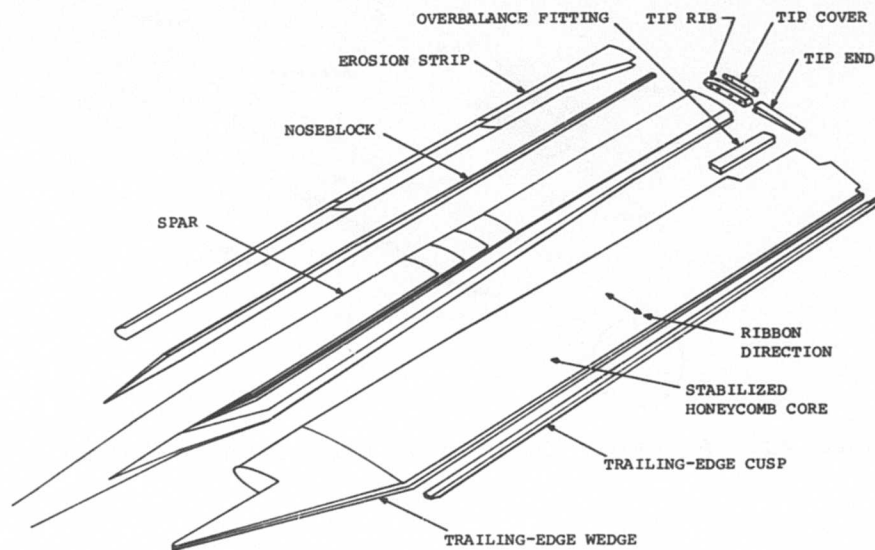


Figure 21. Exploded View of Blade Assembly.

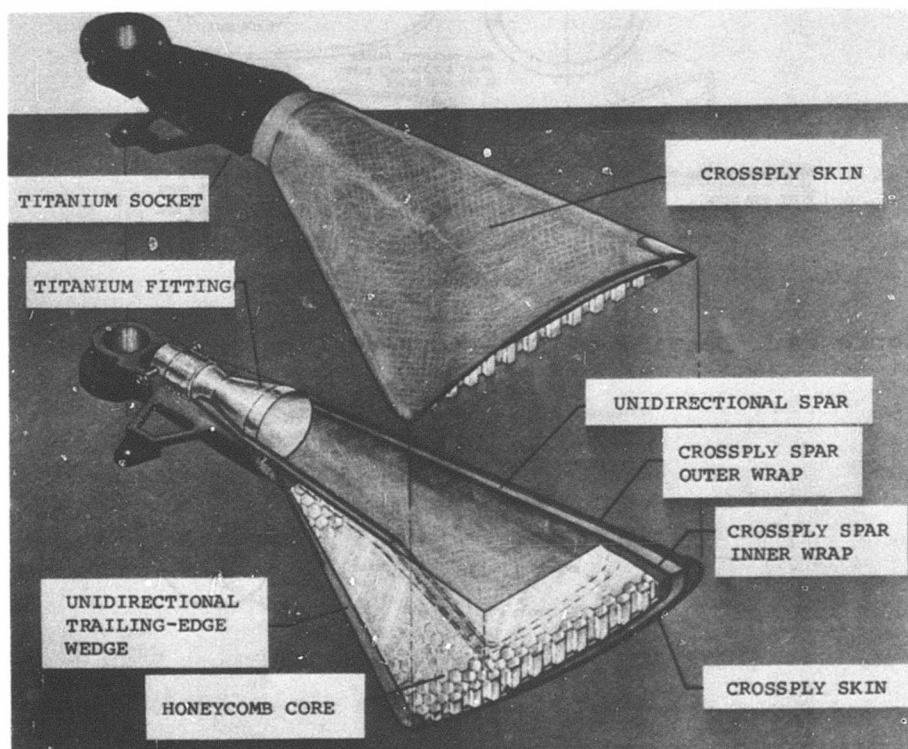


Figure 22. Blade Root-End Attachment Joint.

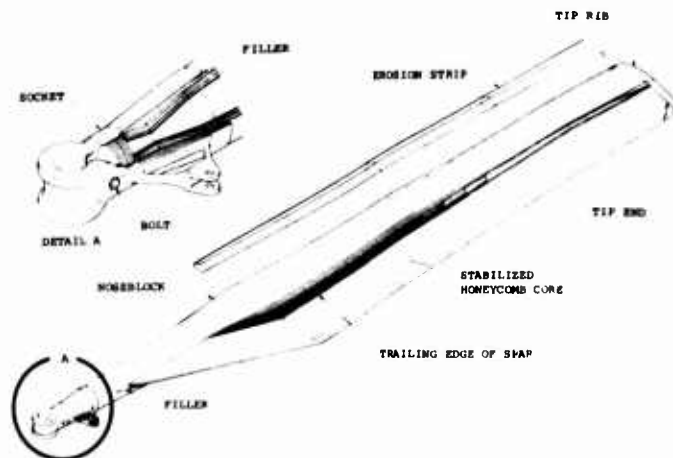


Figure 23. Assembly Buildup of the Advanced-Geometry Blade.

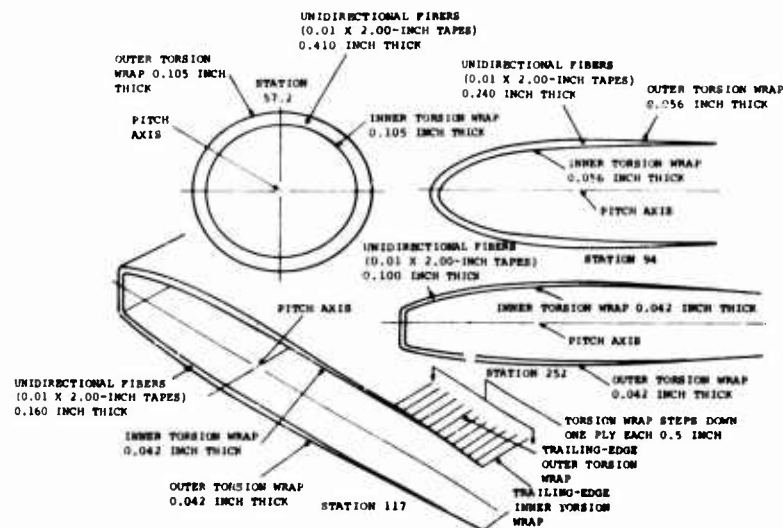


Figure 24. Details of Fiber Orientation in the Blade.

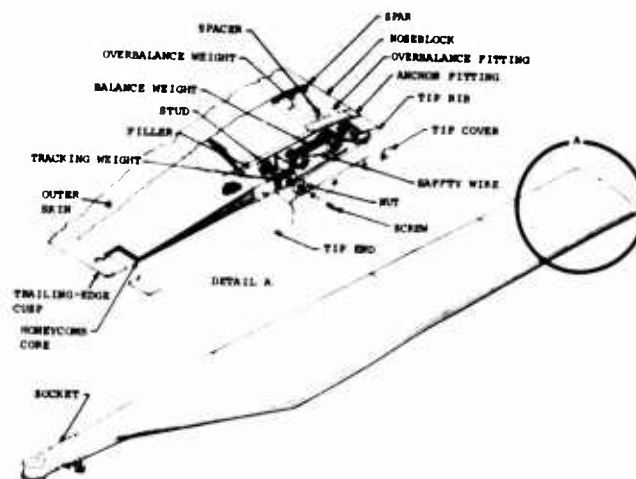


Figure 25. Details of the Blade Tip.

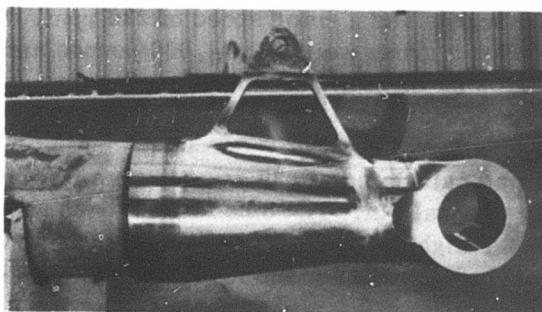
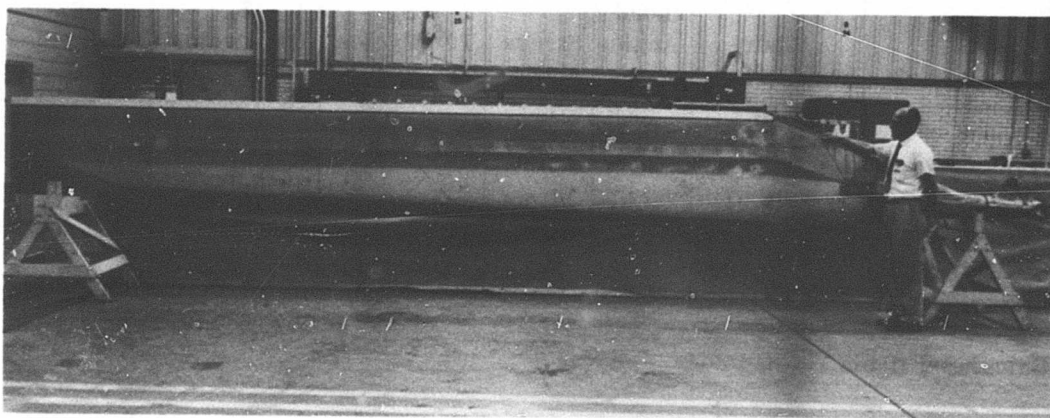


Figure 26. Details of the Finished Advanced-Geometry Blade.

STRUCTURAL ANALYSIS OF THE ADVANCED-GEOMETRY BLADE

Design Properties

The design data used in the preflight strength evaluation are presented in this section. The critical material property was fatigue strength. The fatigue allowables were derived from coupon data which were evaluated as described in the section MATERIAL TESTING AND ANALYSIS.

The following table shows the results of the analysis of these data for the three structural materials used in the blade: unidirectional 1002S glass (spar), BP907-143S ± 45 -degree crossply (skin), and XP251S ± 45 -degree crossply (torsion wrap). The allowables presented here differ from the results in the cited section of the report because all coupon testing was not completed at the time of this fatigue analysis. The preliminary endurance limits are shown in Table IV.

TABLE IV. PRELIMINARY CALCULATED LIMITS OF THE BLADE MATERIALS						
Material	Fiber Orientation	Load Angle (deg)	Stress Ratio	10^5 S_e Cycles (ksi)	10^6 S_e Cycles (ksi)	10^7 S_e Cycles (ksi)
1002S	Parallel	0	0.05	12.30	10.30	8.30
XP251S	Crossply	45	0.05	2.60	2.31	2.02
BP907-143S	Crossply	45	0.10	2.07	2.03	2.00

Calculated Blade Loads

The calculated centrifugal force and steady and vibratory flapwise and chordwise bending moments and torsional moments are shown in Figures 27 through 30 for a gross weight of 33,000 pounds and a rotor speed of 230 rpm. The calculated bending and torsional moments for a gross weight of 44,000 pounds and a rotor speed of 243 rpm are shown in Figures 31 through 33. These loads were calculated with computer program LO-2 for the following conditions.

The centrifugal force was calculated at 230 and 243 rpm for a blade weight of 376 pounds outboard of the vertical pin. The other blade loads were calculated for the aft rotor in forward level flight at sea level with a 17-inch-forward aircraft center of gravity. The trim schedule used for the loads calculations is shown in Figure 34.

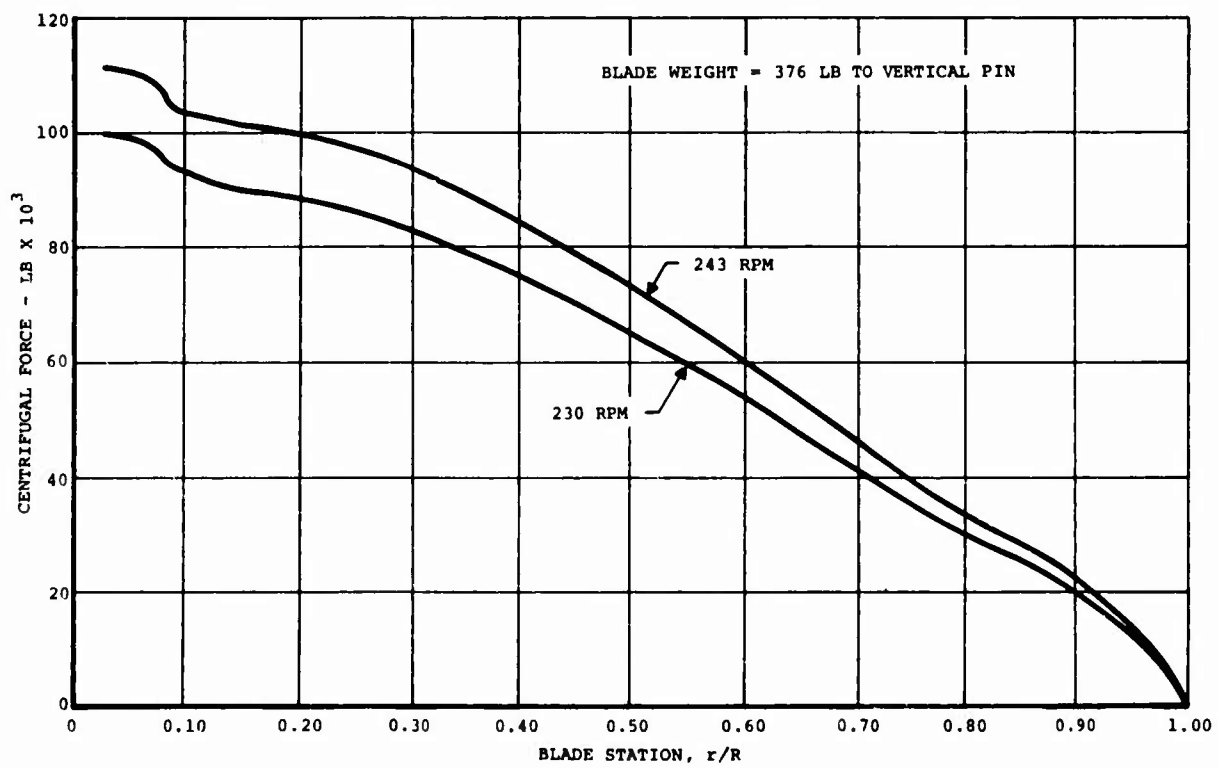


Figure 27. Calculated Spanwise Variation of Centrifugal Force.

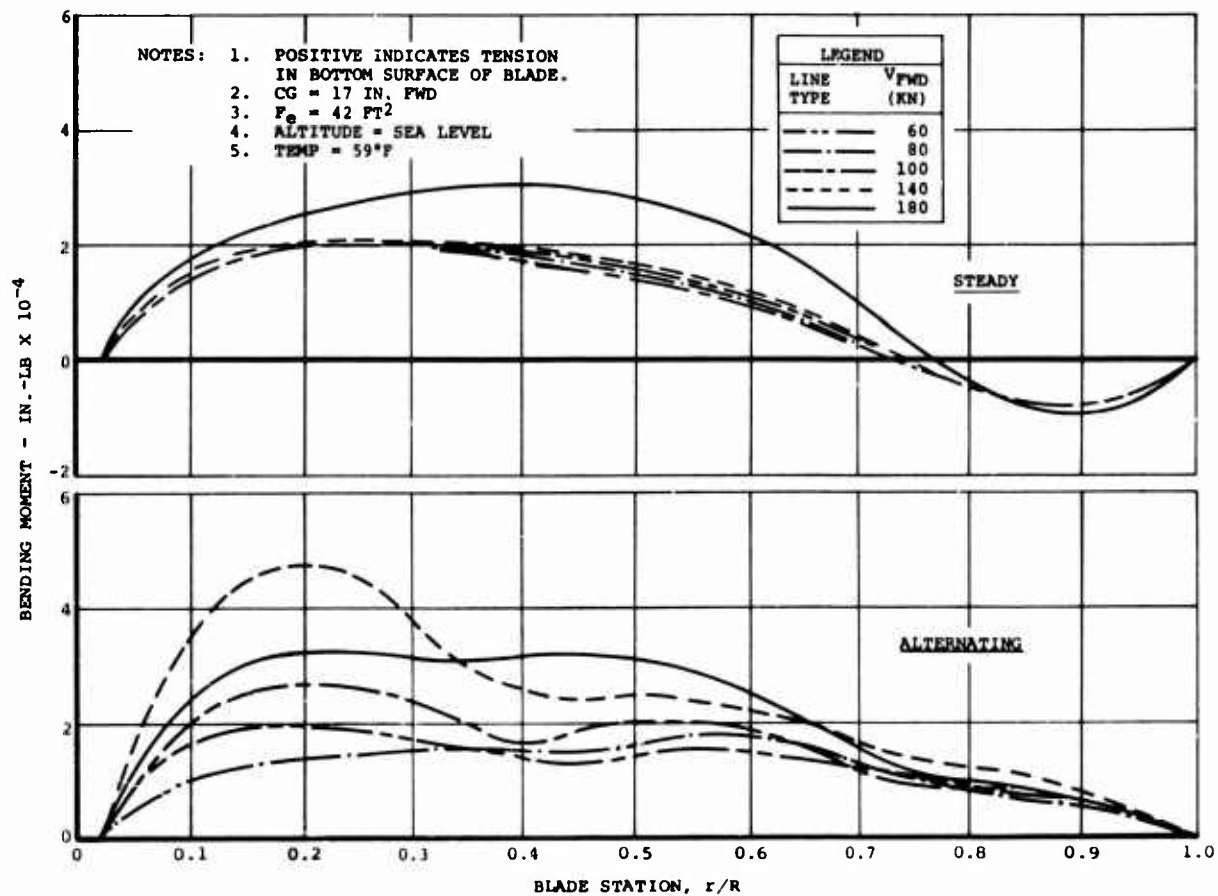


Figure 28. Calculated Steady and Alternating Flapwise Bending Moments at 33,000 Pounds Gross Weight and 230 Rotor RPM.

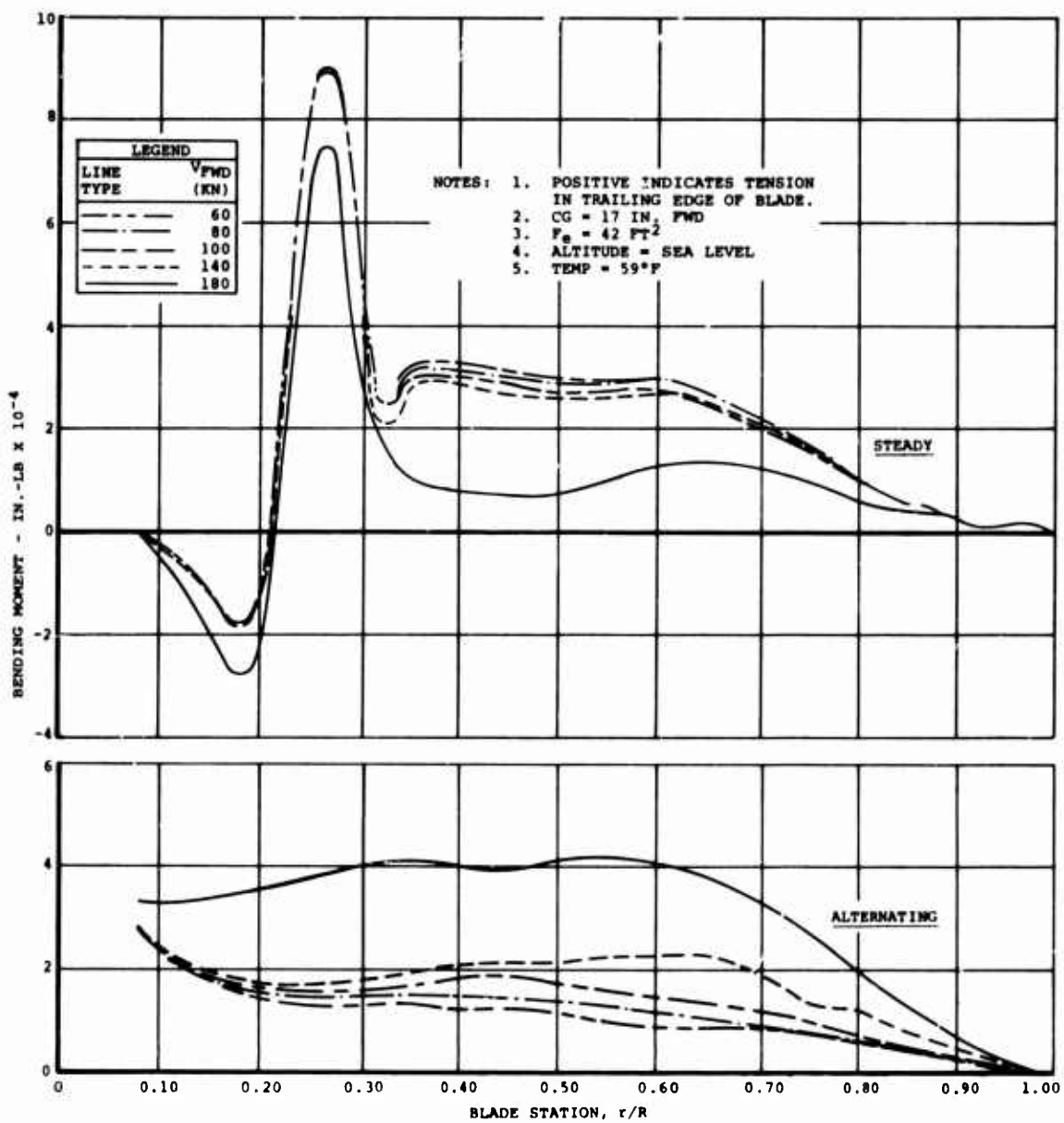


Figure 29. Calculated Steady and Alternating Chordwise Bending Moments at 33,000 Pounds Gross Weight and 230 Rotor RPM.

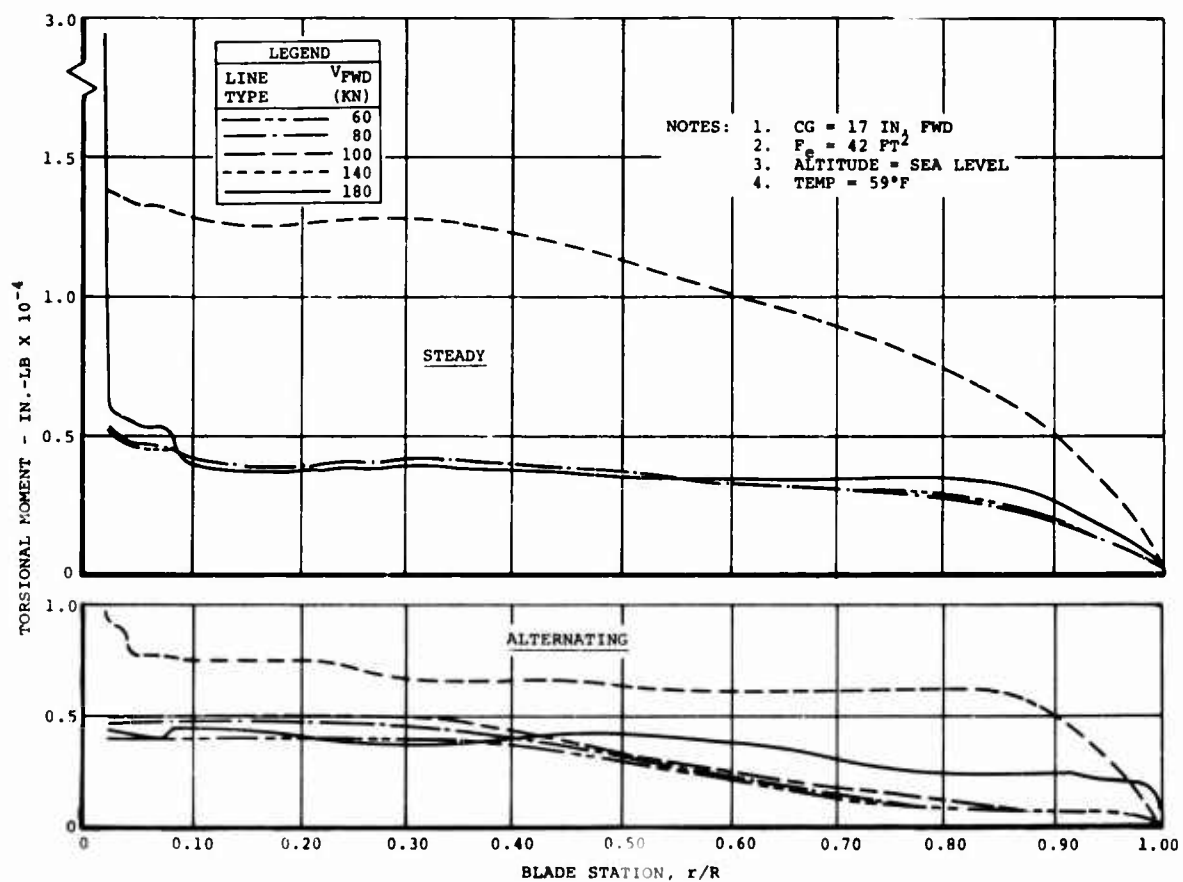


Figure 30. Calculated Steady and Alternating Torsional Moments at 33,000 Pounds Gross Weight and 230 Rotor RPM.

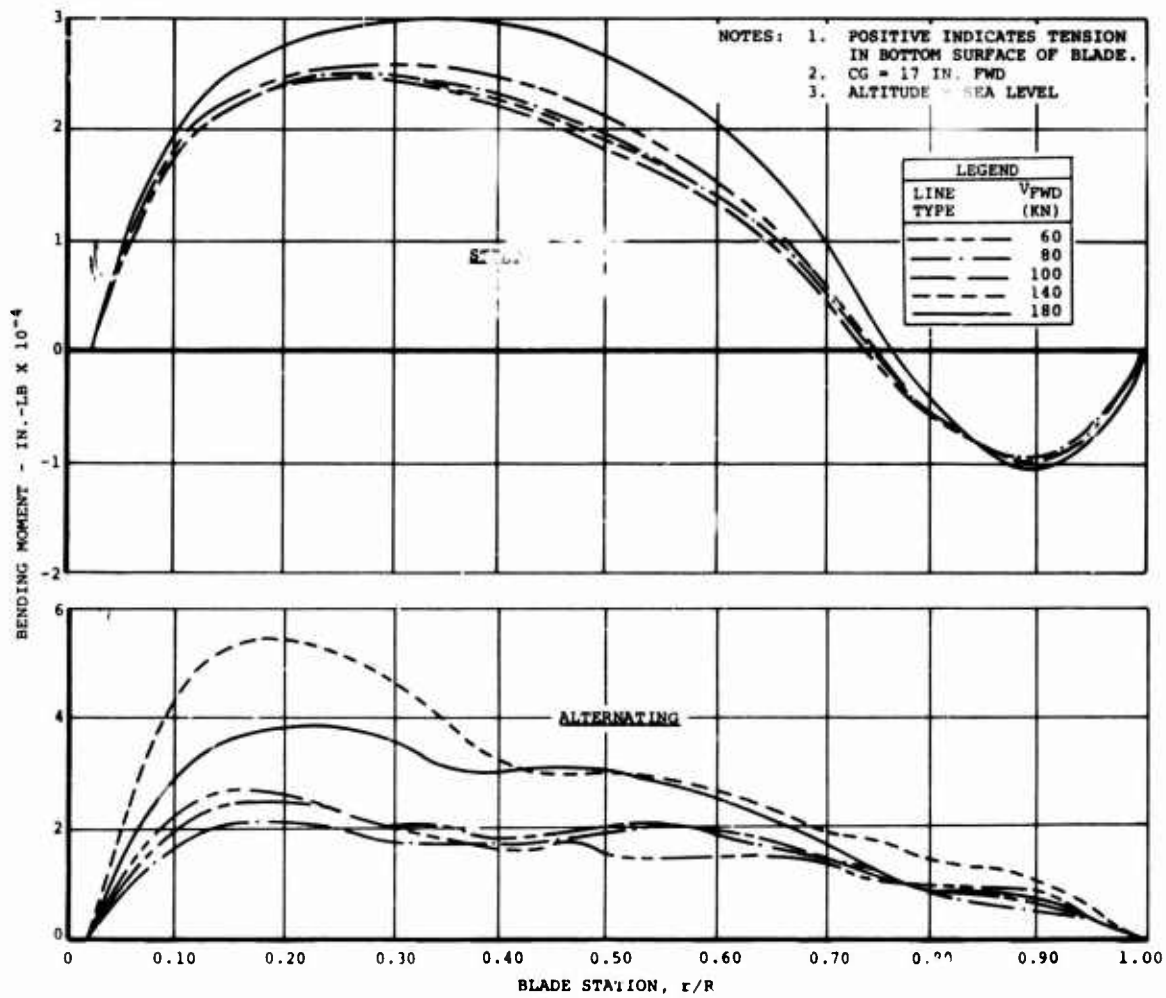


Figure 21. Calculated Steady and Alternating Flapwise Bending Moments at 44,000 Pounds Gross Weight and 243 Rotor RPM.

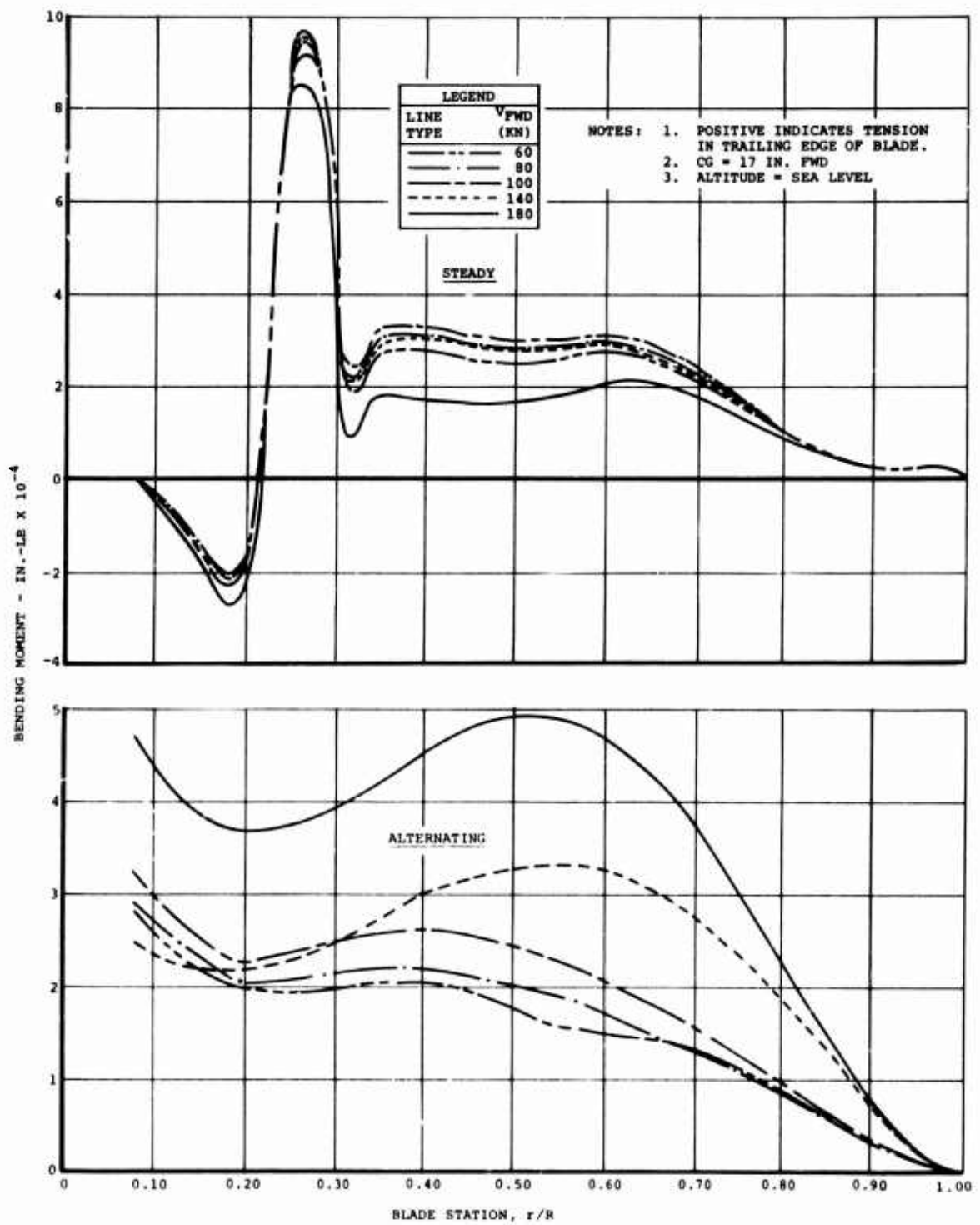


Figure 32. Calculated Steady and Alternating Chordwise Bending Moments at 44,000 Pounds Gross Weight and 243 Rotor RPM.

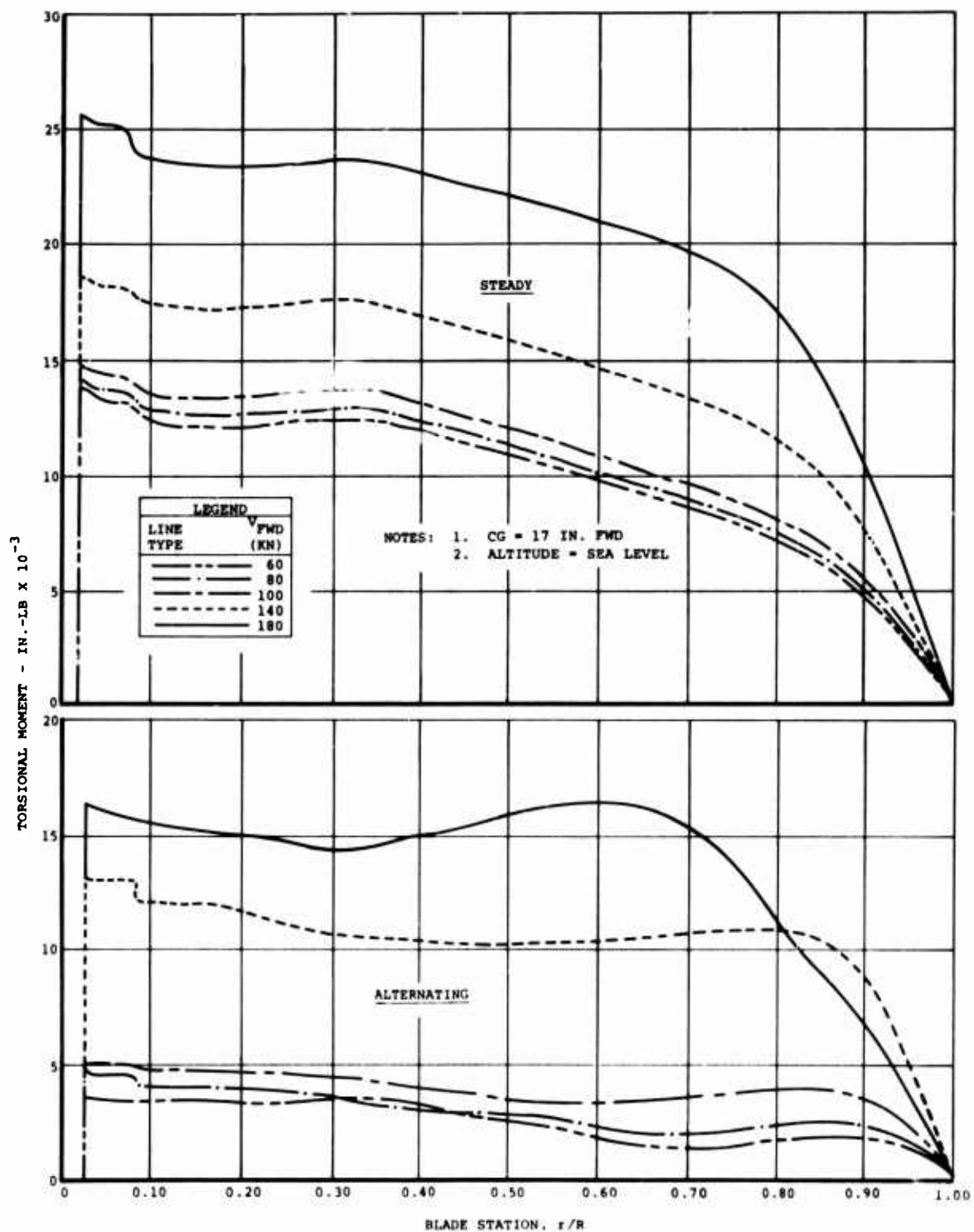


Figure 33. Calculated Steady and Alternating Torsional Moments at 44,000 Pounds Gross Weight and 243 Rotor RPM.

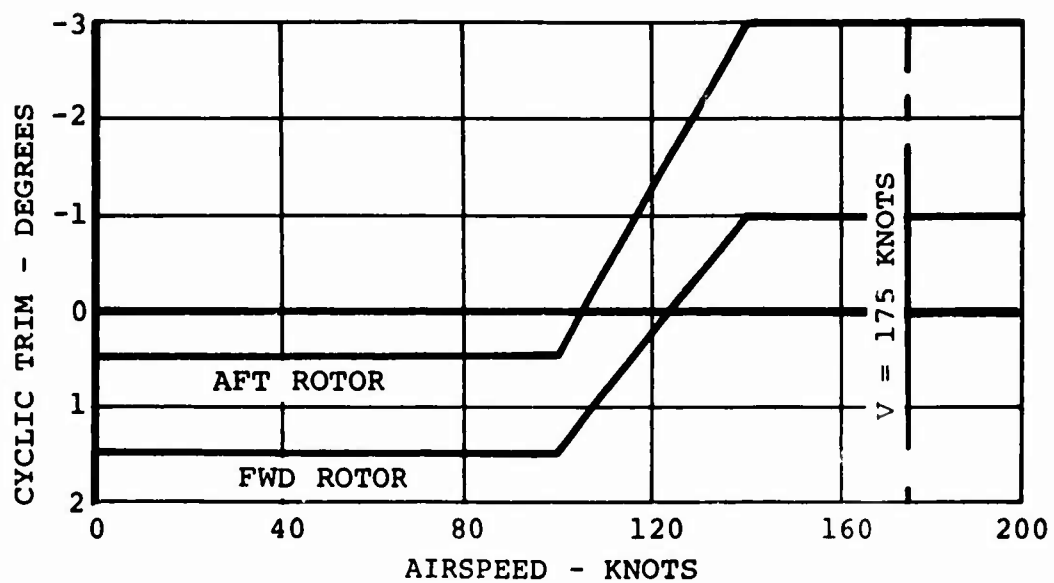


Figure 34. Cyclic-Pitch Trim Schedule for the Advanced-Geometry Blade.

Stress Analysis

The fatigue stress analysis was performed with computer program STRAIN. Representative blade stations and critical checkpoints at each station were selected, and the blade materials at the checkpoints were analyzed in terms of strain. The predicted steady strain was composed of the strain due to centrifugal force, the maximum steady flapwise bending moment, and the maximum steady chordwise bending moment. To account for phasing of the blade loads, the predicted alternating strain was calculated with the maximum alternating flapwise moment plus one-third of the maximum alternating chordwise moment. At the trailing edge, the predicted alternating strain was also determined from the maximum alternating chordwise moment plus one-third of the maximum alternating flapwise moment. The calculated alternating strain was then compared to the allowable alternating strain for the calculated steady strain at 10^5 , 10^6 , and 10^7 cycles.

Results of Stress Analysis

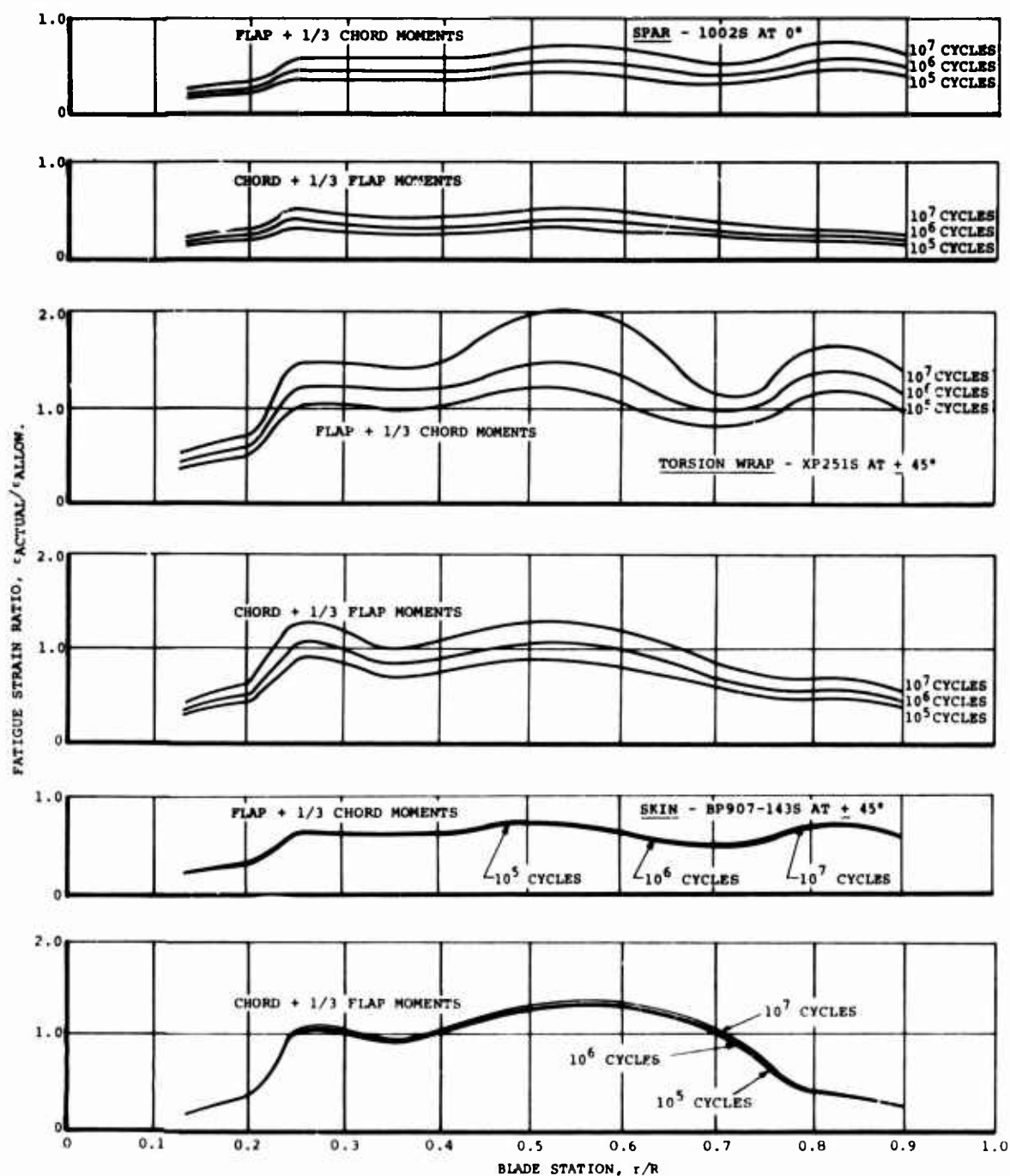
The results of the fatigue stress analysis are shown in Figure 35 for a gross weight of 33,000 pounds and in Figure 36 for a gross weight of 44,000 pounds. These curves indicate the radial variation of the maximum ratio of predicted alternating strain-to-allowable alternating strain for each material due to steady and alternating envelope loads.

Examination of Figure 35 for the 33,000-pound gross weight shows that:

- The spar had a fatigue life in excess of 10 million cycles.
- The most critical blade section for the outer torsion wrap was between blade stations 180 ($r/R = 0.50$) and 198 ($r/R = 0.55$).
- The outer skin was most fatigue-critical between blade stations 180 ($r/R = 0.50$) and 216 ($r/R = 0.60$).

At a gross weight of 44,000 pounds, the top graph of Figure 36 indicates that the spar had a fatigue life of over 10 million cycles except in the vicinity of blade station 306 ($r/R = 0.85$), where the fatigue life was almost 10 million cycles. The middle graph of Figure 36 shows that the outer torsion wrap was most fatigue-critical between blade stations 288 ($r/R = 0.80$) and 324 ($r/R = 0.90$). The bottom graph of Figure 36 indicates that the skin was most fatigue-critical between blade stations 180 and 216.

The outer torsion wrap and skin were analyzed on the basis of the aforementioned results at blade station 180 for a gross weight of 33,000 pounds and at blade stations 216 and 288 for a gross weight of 44,000 pounds, with predicted steady and alternating loads at various forward velocities instead of steady and alternating envelope loads.



NOTES. 1. CG = 17 IN. FWD
2. ALTITUDE = SEA LEVEL
3. $P_0 = 42 \text{ FT}^2$
4. ENVELOPE LOADS AT
0 TO 180 FNOTS

Figure 35. Calculated Radial Variation of Fatigue Strain Ratio for Spar, Torsion Wrap, and Skin Materials at 33,000 Pounds Gross Weight and 230 Rotor RPM.

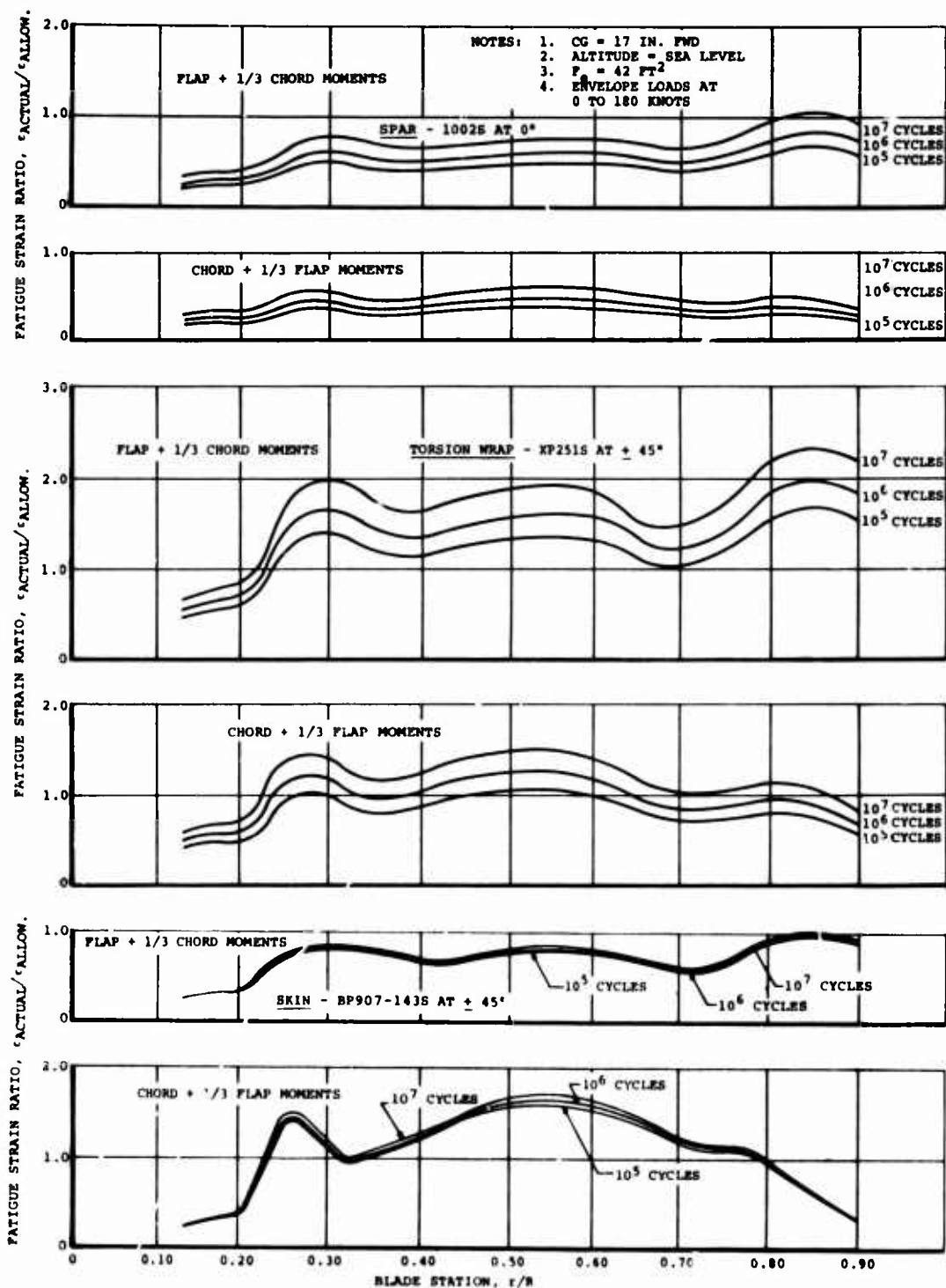


Figure 36. Calculated Radial Variation of Fatigue Strain Ratio for Spar, Torsion Wrap, and Skin Materials at 44,000 Pounds Gross Weight and 243 Rotor RPM.

Figure 37 shows the variation of predicted alternating strain and the allowable alternating strain at 10^5 , 10^6 , and 10^7 cycles with forward velocity for the outer torsion wrap at blade station 180 and the 33,000-pound gross weight. The decrease in fatigue life is evident as forward velocity increases. The analysis of the skin material indicated that the fatigue life was greater than 10 million cycles for the forward velocities of 80, 100, 140, and 180 knots. The variations of predicted alternating strain and the allowable alternating strain at 10^5 , 10^6 , and 10^7 cycles with forward velocity for the outer torsion wrap and skin at blade station 216 and the 44,000-pound gross weight are shown in Figure 38; a decrease in fatigue life is indicated as high-speed flight is attained. Figure 39 also shows a decrease in fatigue life with increase in forward velocity for the outer torsion wrap at blade station 288 and the 44,000-pound gross weight.

Figure 40 gives the variations of predicted alternating strain and allowable alternating strain of the spar and skin materials with forward velocity at the respective blade stations and gross weights mentioned previously. This analysis was performed with the stiffness and strength of the inner and outer torsion wraps deleted from the blade structure. The section properties were changed to account for this modification, but it was assumed that the natural frequencies and therefore the blade bending moments were unchanged.

At the 33,000-pound gross weight and blade station 180, the fatigue life of the spar was greater than 10 million cycles while the fatigue life of the skin decreased rapidly as the forward velocity approached 180 knots. At a gross weight of 44,000 pounds and blade station 216, the fatigue life of the spar was greater than 10 million cycles while the fatigue life of the skin decreased as forward velocity approached 140 knots. For the 44,000-pound gross weight and blade station 288, the fatigue life of the spar was greater than a million cycles while the fatigue life of the skin decreased rapidly as the forward velocity approached 120 knots.

Conclusions

The results of the blade fatigue stress analysis at the 33,000-pound gross weight indicated that the advanced-geometry fiberglass rotor blade was satisfactory for flight test operations based on the preliminary material allowables and the investigation at the critical station with reduced section properties. At a gross weight of 44,000 pounds, the results of the fatigue stress analysis showed that the blade was satisfactory for limited flight test operations. From the structural test results and because the material allowables were preliminary, it was felt that the blade was satisfactory for higher-gross-weight flight test operations. Because of the importance placed on predicted steady and alternating loads in the fatigue stress analysis and in the structural test loading requirements, it was recommended that flight test operations at the higher gross weight be exploratory in nature with special consideration given to blade loads and their duration.

- NOTES:
1. GROSS WEIGHT = 33,000 LB
 2. ROTOR RPM = 230
 3. CG = 17 IN. FWD
 4. PREDICTED ALTERNATING ϵ =
ALTERNATING FLAP ϵ + 1/3
ALTERNATING CHORD ϵ
 5. ALLOWABLE ALTERNATING ϵ
BASED ON PREDICTED STEADY ϵ

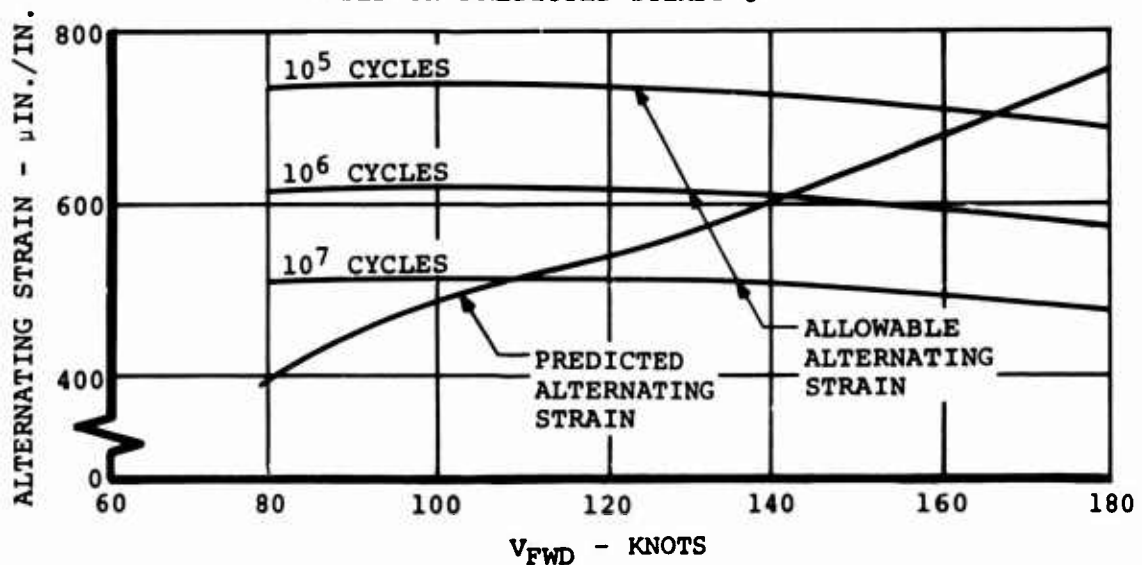
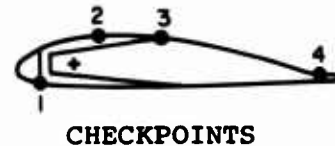


Figure 37. Calculated Alternating Strain at Blade Station 180, Checkpoint 2, in the XP251S Crossply Torsion Wrap.

- NOTES: 1. GROSS WEIGHT = 44,000 LB
 2. ROTOR RPM = 243
 3. CG = 17 IN. FWD
 4. PREDICTED ALTERNATING ϵ =
 ALTERNATING FLAP ϵ + 1/3
 ALTERNATING CHORD ϵ
 5. ALLOWABLE ALTERNATING ϵ
 BASED ON PREDICTED STEADY ϵ

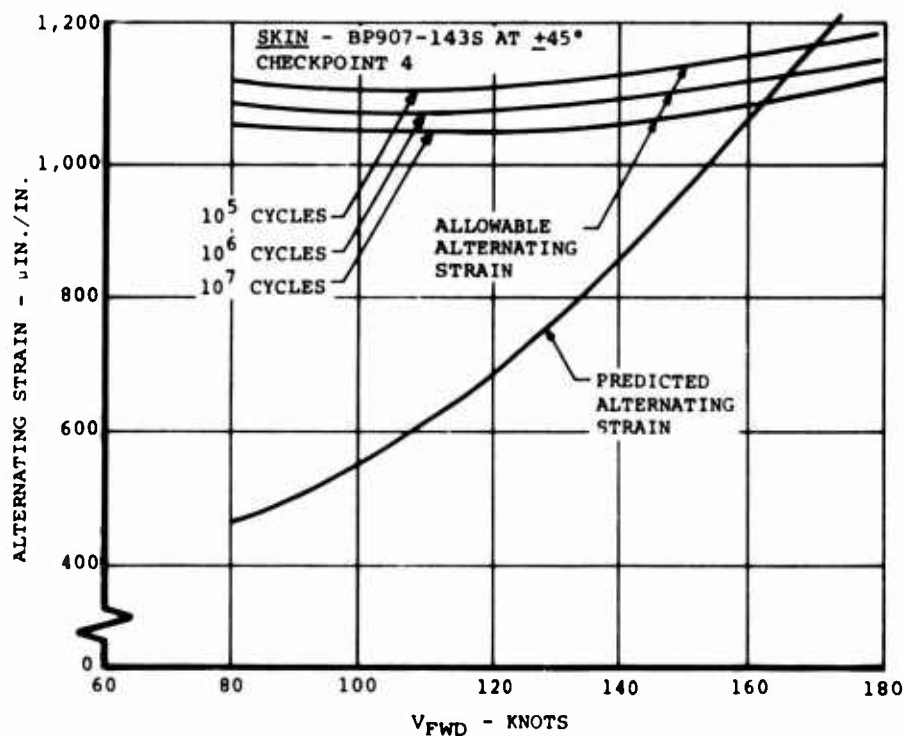
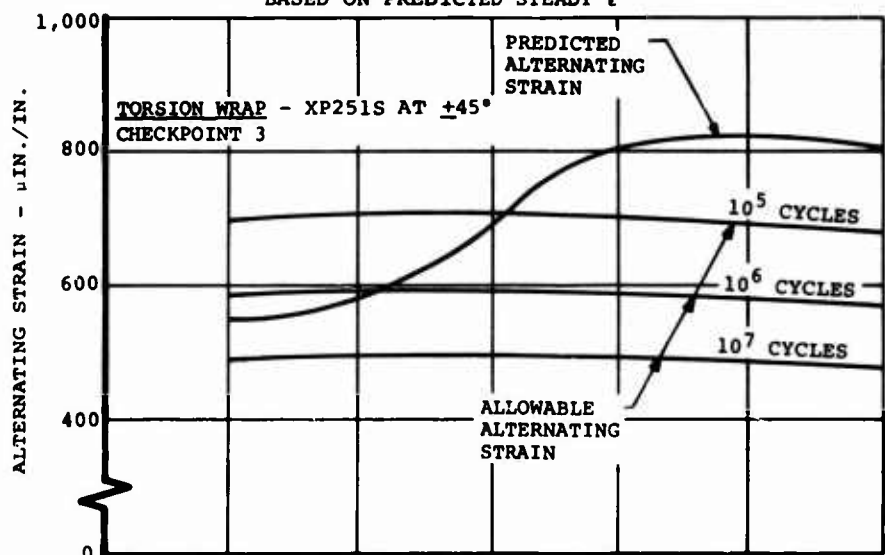


Figure 38. Calculated Alternating Strain at Blade Station 216 in the Torsion Wrap and Skin.

- NOTES:
1. GROSS WEIGHT = 44,000 LB
 2. ROTOR RPM = 243
 3. CG = 17 IN. FWD
 4. PREDICTED ALTERNATING ϵ =
ALTERNATING FLAP ϵ + 1/3
ALTERNATING CHORD ϵ
 5. ALLOWABLE ALTERNATING ϵ
BASED ON PREDICTED STEADY
 ϵ

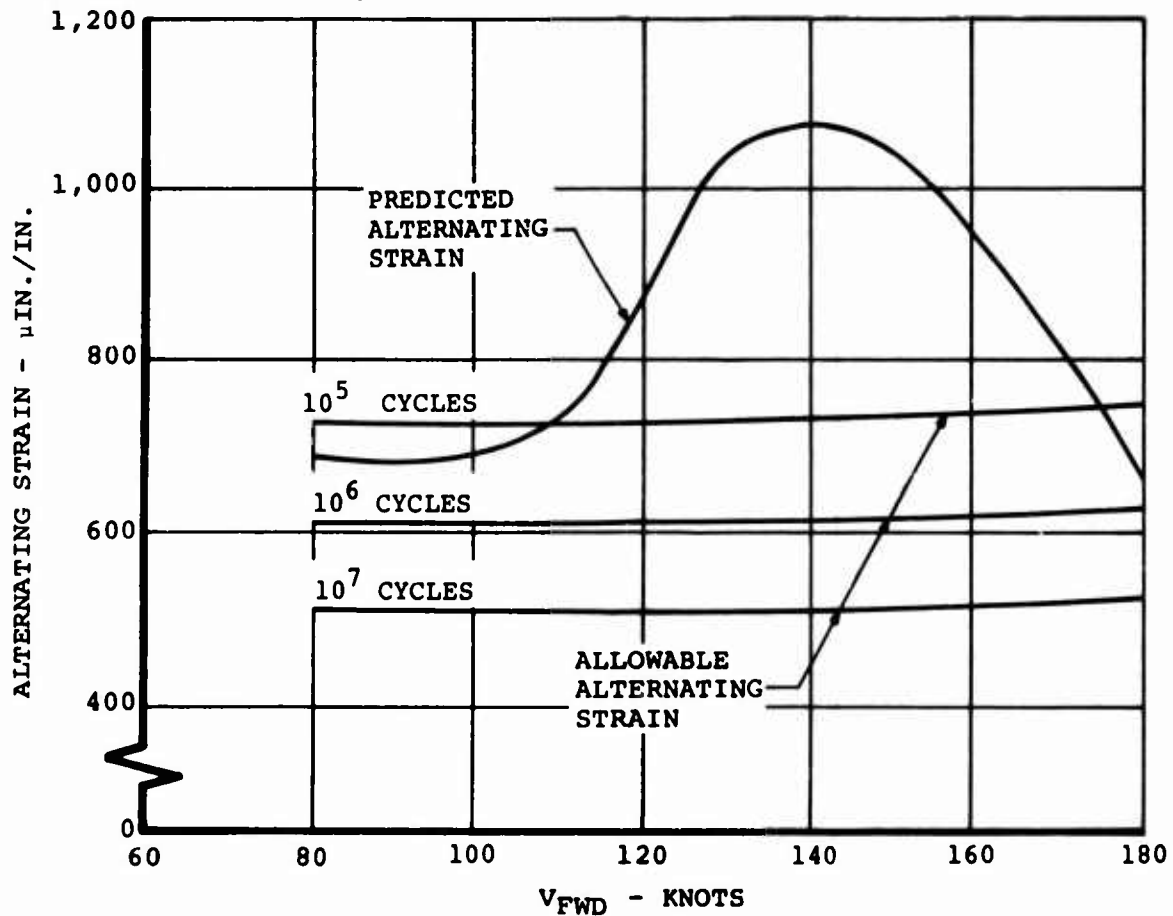
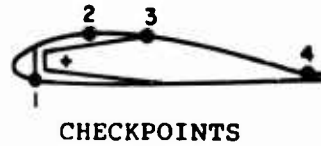


Figure 39. Calculated Alternating Strain at Blade Station 288, Checkpoint 3, in the XP251S Crossply Torsion Wrap.

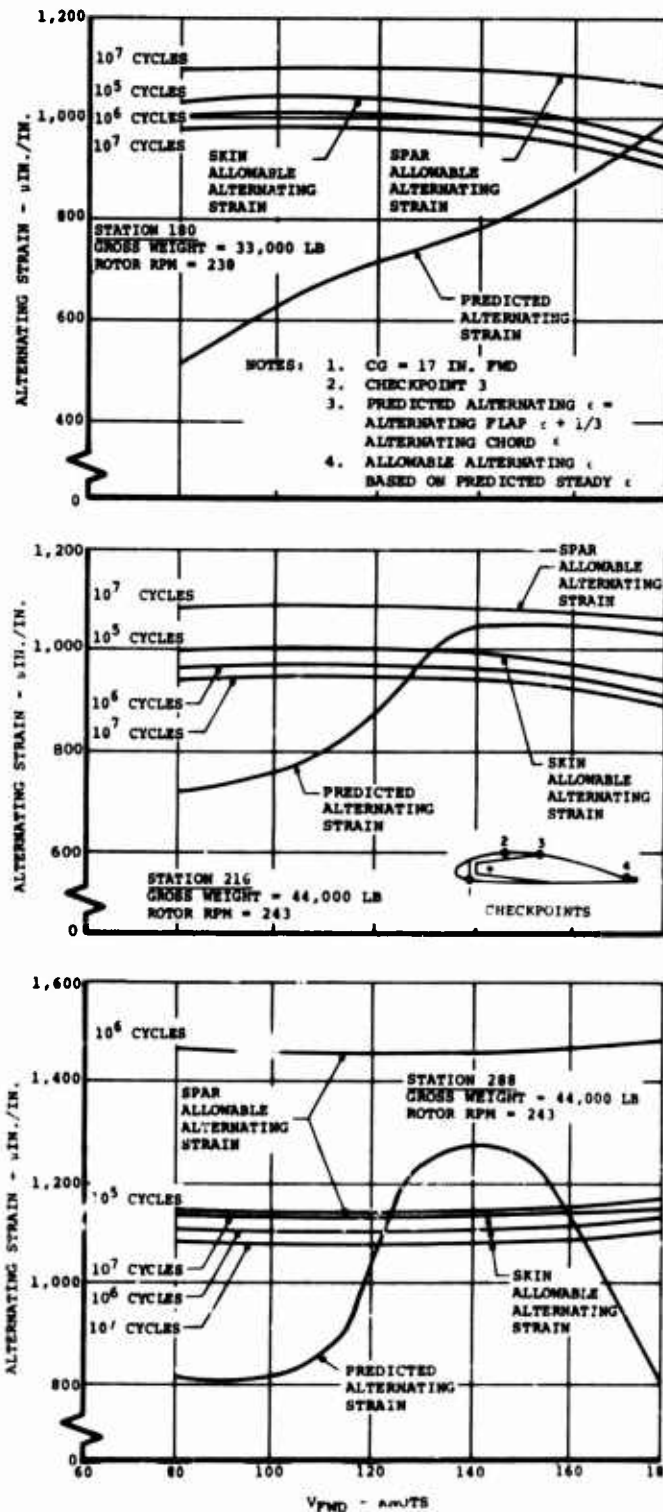


Figure 40. Calculated Alternating Strain in the Crossply BP907-143S Skin and Unidirectional 1002S Spar With Torsion Wrap Deleted.

No attempt was made to incorporate the effects of the uni-crossply fatigue results from the section on MATERIAL TESTING AND ANALYSIS into this analysis. The net effect would show that the outer torsion wrap was not fatigue-critical. In this fatigue analysis the torsion wrap would show the same results as the unidirectional 1002S spar shown in Figures 35 and 36.

FABRICATION OF THE ADVANCED-GEOMETRY BLADE

INTRODUCTION

The design of the advanced-geometry rotor blade and the engineering requirements for manufacture and quality control were established by The Boeing Company's Vertol Division. The design and development of all tooling and the development and implementation of processes and techniques for fabrication of the rotor blade assemblies were performed by the Manufacturing Development Department of Boeing's Wichita Division.

The objective was to fabricate 6 forward and 4 aft rotor blades. Two of the forward blades were designated for full-scale structural tests and the remaining 8 blades, 4 forward and 4 aft, for flight tests. Tool design and manufacturing methods were oriented to the limited quantity of prototype rotor blades to be built.

DESIGN AND FABRICATION OF TOOLS

Figure 41 shows sequential diagrams of the major fabrication operations and tooling concepts developed to build and assemble the blade to the design configuration. The major fabrication operations are:

1. Core machining
2. Stabilized core-skin assembly
3. Molding of spar assembly
4. Spar-to-core assembly bond
5. Noseblock assembly bond
6. Final skin operation
7. Erosion strip bond
8. Trailing-edge cusp bond

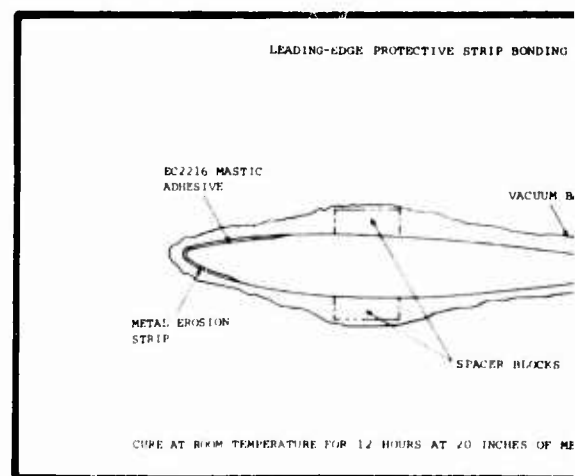
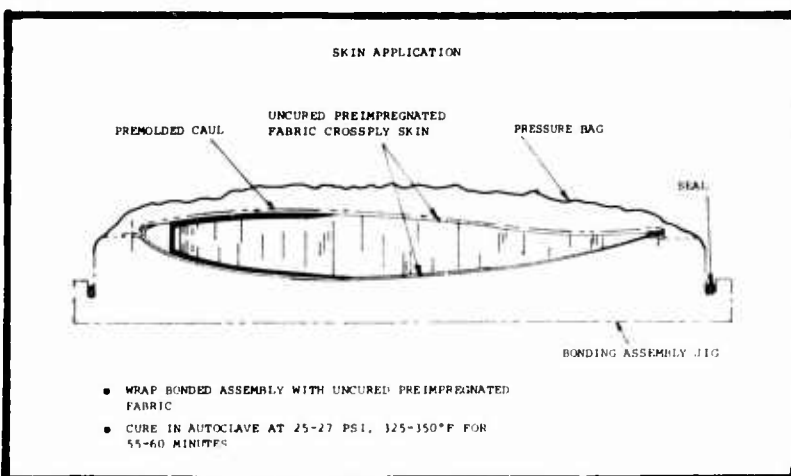
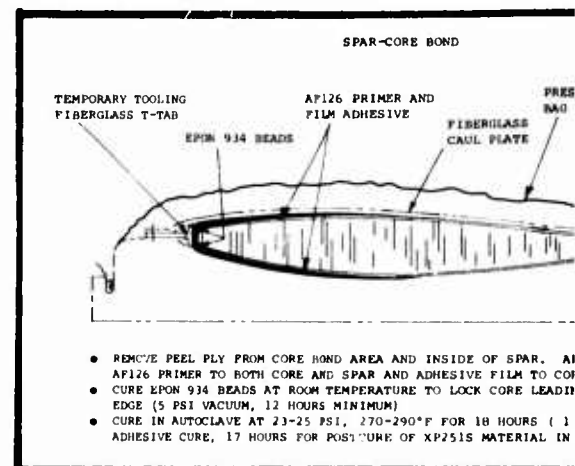
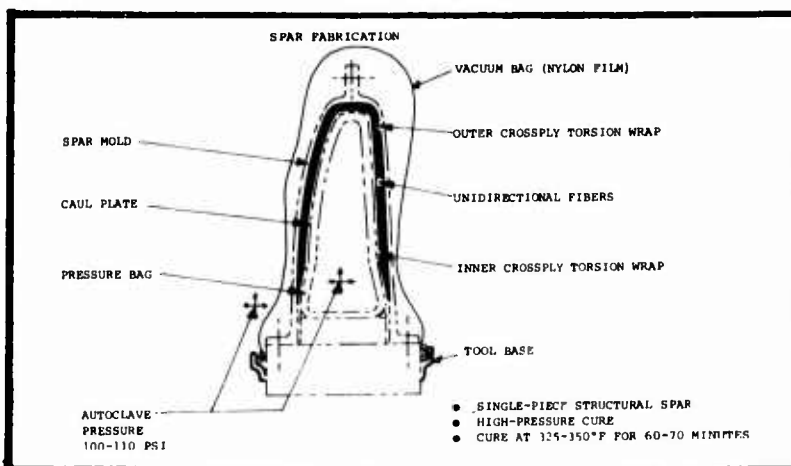
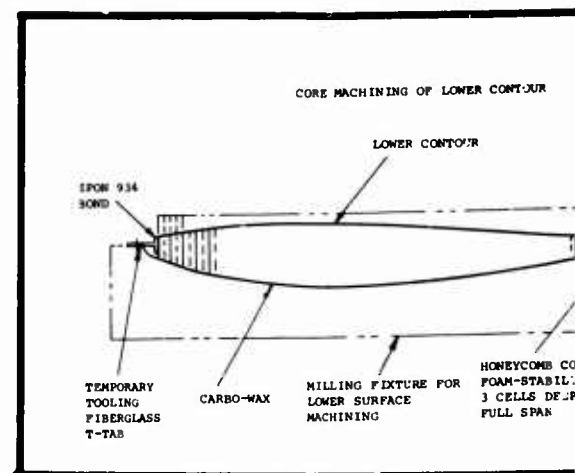
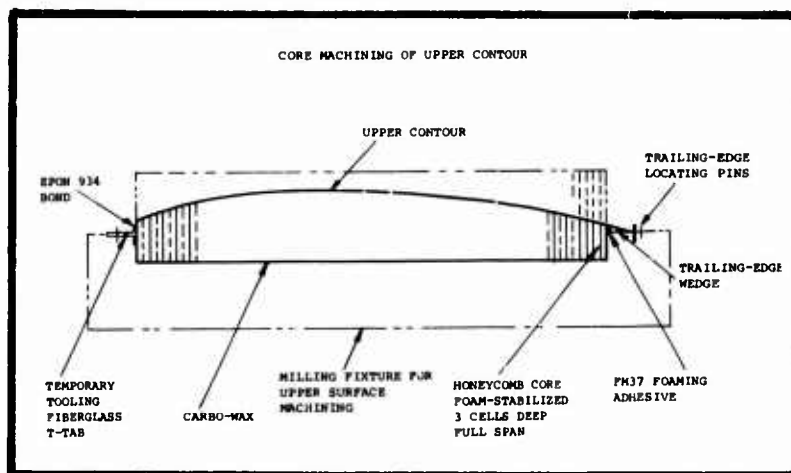
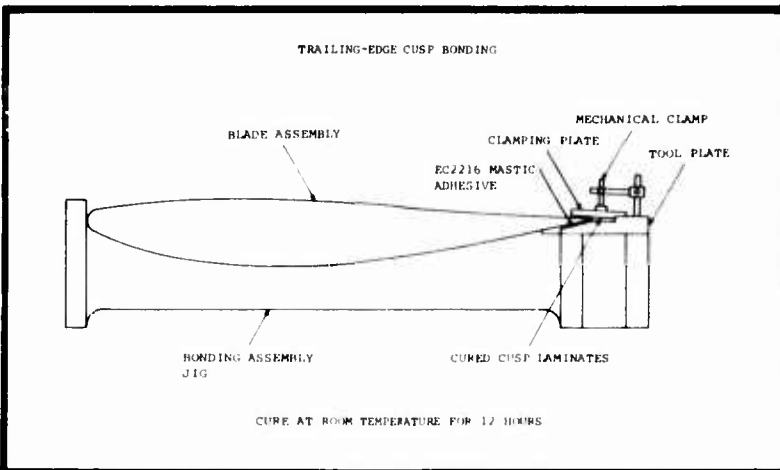
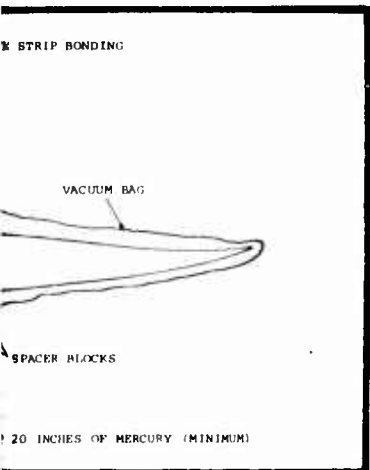
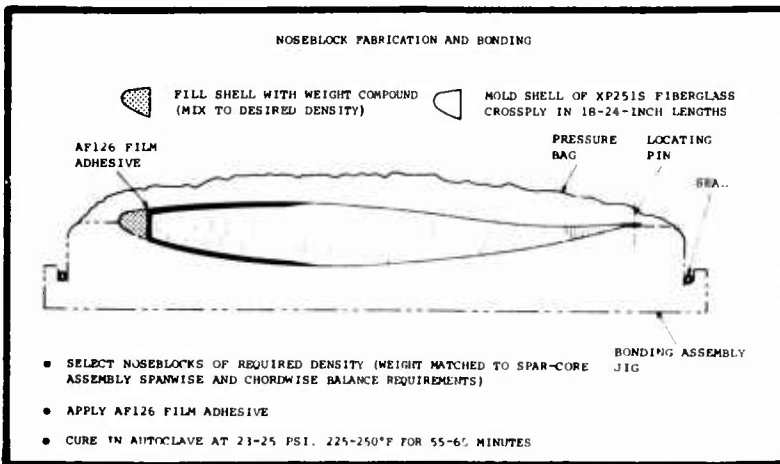
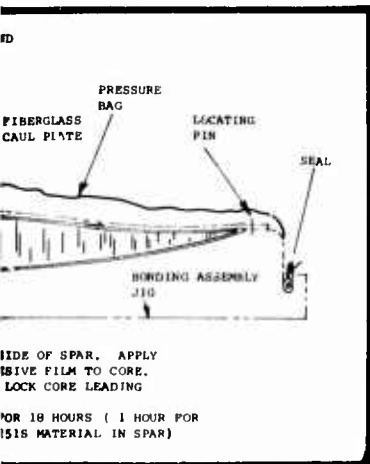
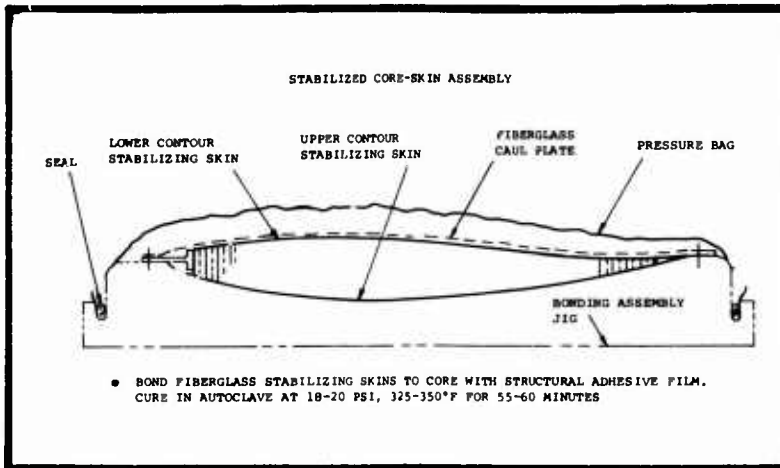
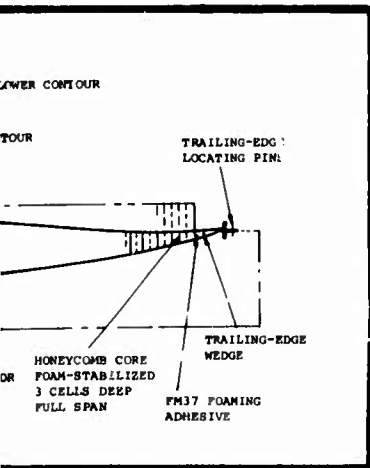


Figure 41. Major Fabrication Operation

13



Operations and Tooling Concepts.

Dimensional control requirements and the tapered planform and profile shape of the large, single-piece core (25 by 3 feet) required that it be machined with the core expanded. This dictated the use of large fixtures to assure adequate stabilization of the core during all machining, prefit, and handling operations. Cure and bonding operations for the stabilized core-skin assembly, spar-core bond, nose-block assembly bond, and final skin operation required bonding assembly jigs designed to fully support and align the parts, provide dimensional control, and function at required fluid pressures and high temperatures in an autoclave. To attain optimum control of upper airfoil surface contours, all jigs were designed so that all nesting of components during bonding was accomplished against the upper surface of the component.

The spar-molding bonding assembly jig provides the form upon which the composite metallic and fiberglass laminated spar can be laid up and cured. The tooling concept uses fixed outer shells for restraining and sizing the outside contour of the spar, floating inside caul shells, and an inflatable internal pressure bag. The concept provides for equalization of autoclave pressure upon the outer shells while simultaneously applying pressure to the internal bag, thus eliminating the need for heavily supported tools.

Tooling and fixtures employed for this program used materials and approaches calculated to best accomplish the desired objectives of producing a limited quantity of developmental rotor blades, namely, 6 left-hand forward blades and 4 right-hand aft blades.

To minimize tooling costs, certain tooling was fabricated to permit multipurpose operations throughout the program. This is discussed later.

Where possible, temperature-resistant, glass-fabric-reinforced epoxy resins were used as tooling materials to provide ready transfer of contours and configuration from plaster masters as opposed to complex machining of similar metal tools.

A master dimensioning computer program was used to develop tapes and readouts of numerical shape definition of external and internal contours for the blade from engineering design drawings⁷. The master dimensioning information was converted directly to sweep-template-controlled plaster masters from which transfer splashes, with appropriate allowance for component thickness, were obtained to control the desired tooling dimensions and configuration.

The major tools are described below for one blade configuration. Duplicate tooling was fabricated for the required opposite-hand blade configuration.

Plaster Masters (Figure 42)

Six plaster masters were fabricated to represent the following:

1. The upper and lower outer mold lines of the final blade
2. The upper and lower outer mold lines of the spar
3. The upper and lower inner mold lines of the spar

Approximately 63 numerical-tape-control-machined header templates were set upon each of the 6 base structures, aligned, and used as sweep templates for finalizing the plaster master surfaces.

Lifting and Handling Carrier (Figure 43)

Early in the tool fabrication effort it became evident that all transfers would require optical alignment references to be established on them. This was due to the size of transfers and molds and the prohibitive size of backup structures rigid enough to negate such a requirement.

Therefore, four carriers were fabricated, with built-in optical alignment features, for use in all major transfers and having rollover capability so these transfers could be turned over without damage.

A number of pipe frames were also fabricated, each of which used its own individual set of optical values for each new attachment. These values remained in use from the time of establishment through all subsequent alignments.

During use of the carriers as supports for the plaster laminating molds, it was necessary to free the carrier from the plaster so that the carrier could expand or contract on slide pins while still retaining its optical alignment capability.

Honeycomb Core Machining Pattern (Figure 44)

Two 30-foot-long male patterns (Keller pattern type), one for the upper surface and one for the lower surface, were required to contour-machine the bare honeycomb core. Since none of the plaster masters duplicated the entire core contour--the portion which fits inside of the spar was missing--a direct means of contour transfer was not possible. The required outside mold line of the core was created as follows. Female casts were taken from the male inside mold line of the spar plaster masters, and male laminated plugs were made from these casts. By positioning these plugs in the appropriate female outside mold line of the blade plaster master, the resultant void--difference between blade outside mold line and spar inside mold line--could be filled with a removable POR-ROK cast. The blade outside mold line plaster master with the FOR-ROK in place generated the female



Reproduced from
best available copy.

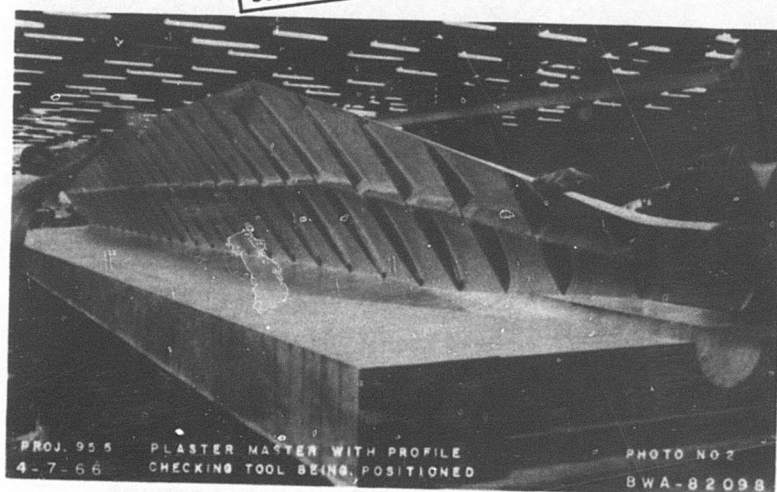


Figure 42. Fabrication of Plaster Masters.



Reproduced from
best available copy.

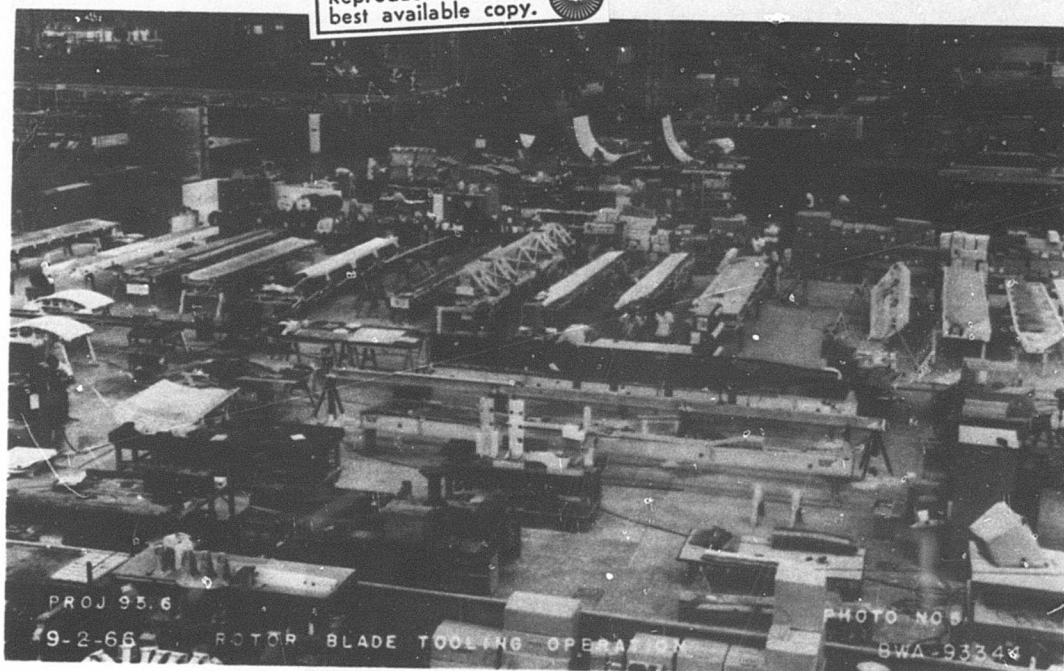


Figure 43. Rollover Carriers With Optical Alignment.

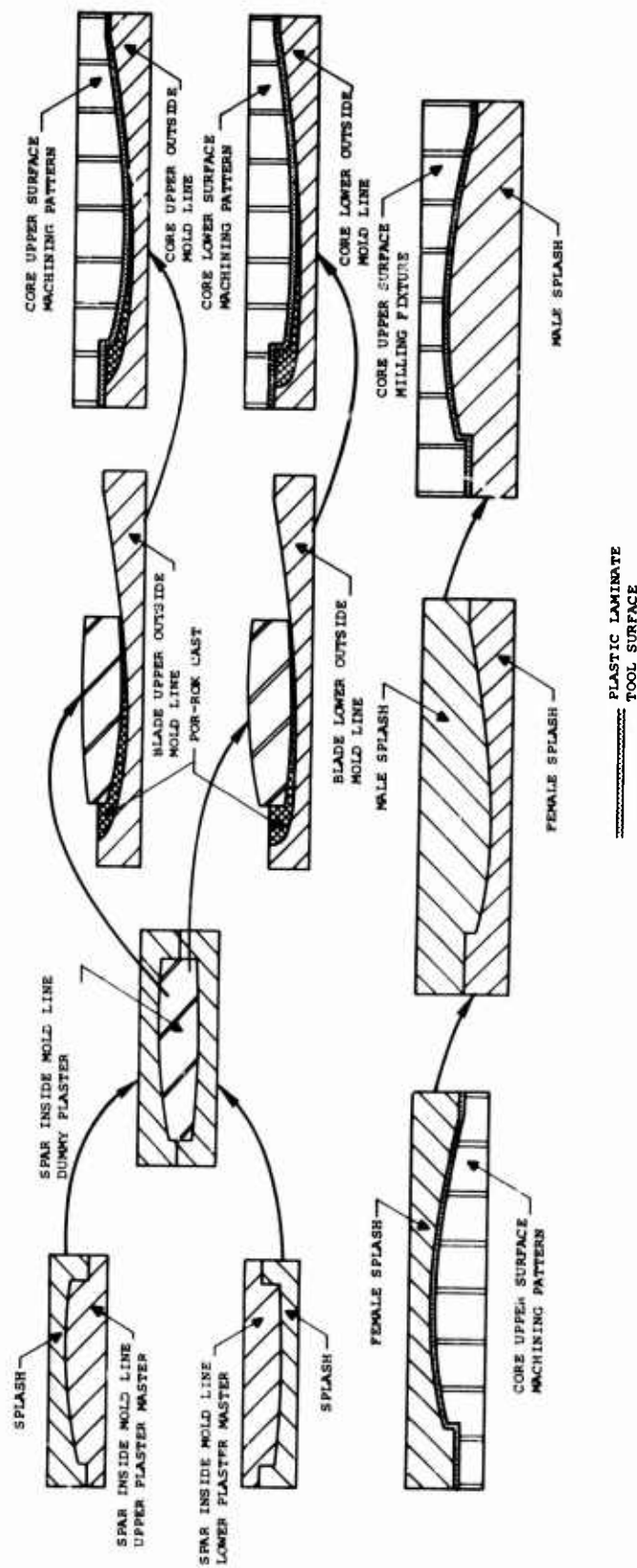


Figure 44. Schematic Diagram of Tooling Transfers to Make Core Machining Patterns and Core Milling Fixture.

outside mold line plaster master of the core. All of these transfers, as well as their final positioning, were accomplished with the aid of optical alignment systems installed on each transfer. The two male core machining pattern tools were fabricated by the molding of a plaster laminate on the female core outside mold line plaster master and reinforcing this laminate with a bonded, reinforced-plastic, box-type egg crate structure.

Upper Core Surface Milling Fixture (Figure 45)

The milling fixture was designed to hold and support the honeycomb core block on its flat, unmachined surface while the upper surface contour was being machined.

Initial engineering requirements specified the thickness of the honeycomb core material to be 7 inches. The all-aluminum milling fixtures were designed and fabricated to hold this thickness in a horizontal (to core face) position. A change in engineering requirements resulted in alteration of the fixture so that a 4-inch-thick core could be used. Thus, the honeycomb core resting surface was raised and positioned on an angle so that a minimum of material was removed from the honeycomb core surface at its greatest required final thickness.

The altered configuration resulted in the honeycomb core resting in the milling fixture with the cell walls at an approximate 4-degree angle to the fore-to-aft centerline of the core.

The milling fixture also served as a bonding tool for simultaneous foam splice-joining of the different-density honeycomb core sections and the precured trailing-edge wedge.

Lower Core Surface Milling Fixture (Figure 46)

This milling fixture was designed to hold the honeycomb core by its previously machined upper surface during machining of the lower surface. A female plaster splash was taken from the male upper core surface machining pattern tool; and through appropriate transfers, a male, upper core surface, plastic-faced plaster form was generated. The female nesting fixture was fabricated by molding a fiberglass-reinforced-plastic laminate on this form and reinforcing this laminate with a reinforced-plastic, box-type egg crate structure.

Core-Skin Assembly Bonding Jig (Figure 47)

The tool was fabricated by molding a fiberglass-reinforced-plastic laminate on a male, upper core surface, plaster form similar to that used to fabricate the lower core surface milling fixture. Appropriate allowances for skin thickness were incorporated in this male form. In this case, steel pipe was assembled as a box structure within the laminate on the back surface of the tool as reinforcement. The tool was fabricated with tool pinholes at approximately 24-inch spacing along the entire trailing-edge length to limit forward movement of the core during the cure

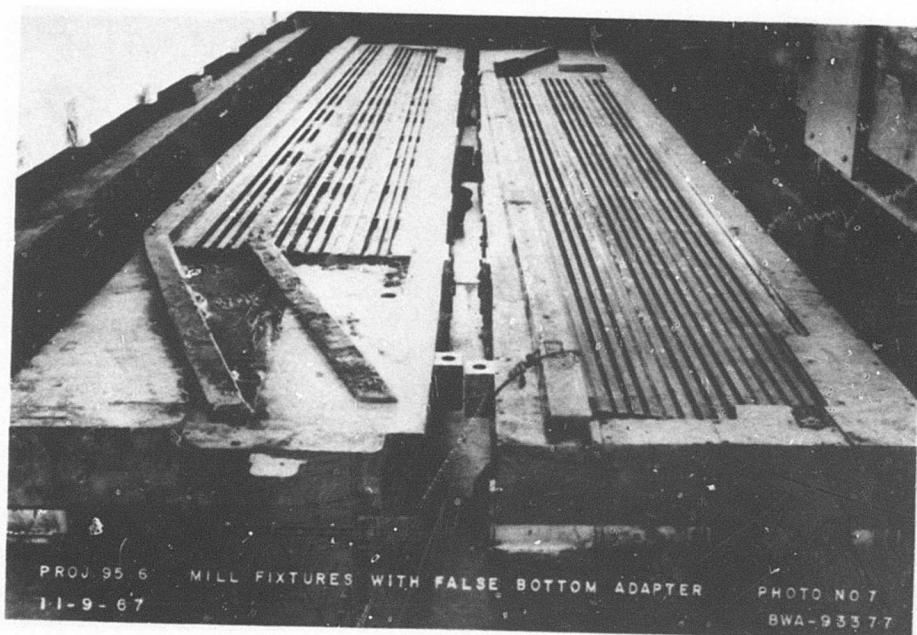
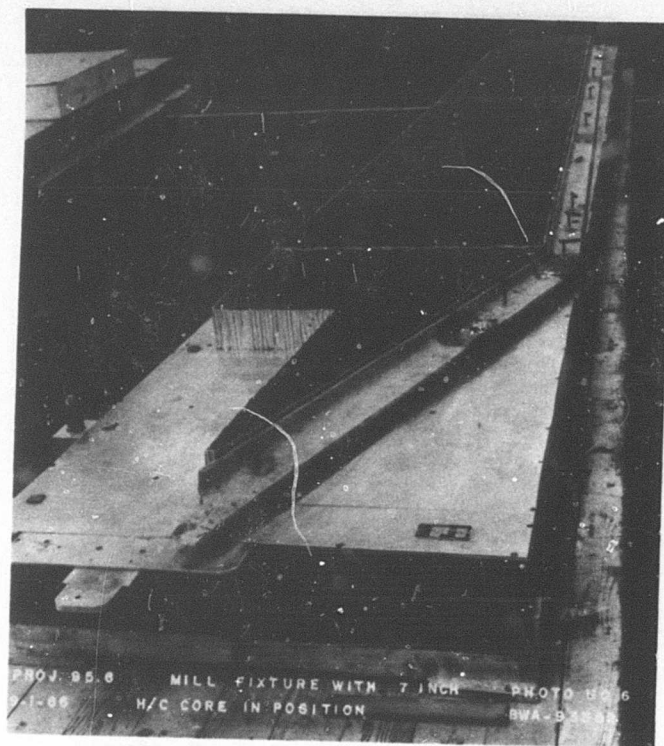


Figure 45. Milling Fixture for Upper Core Surface.

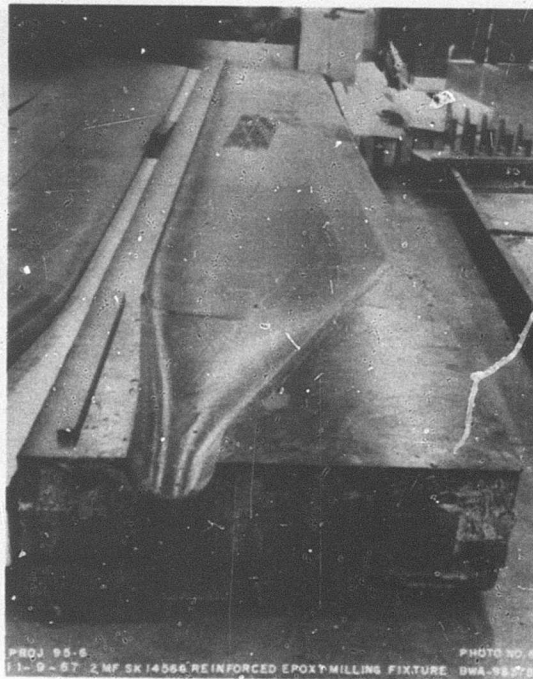


Figure 46. Milling Fixture for Lower Core Surface.

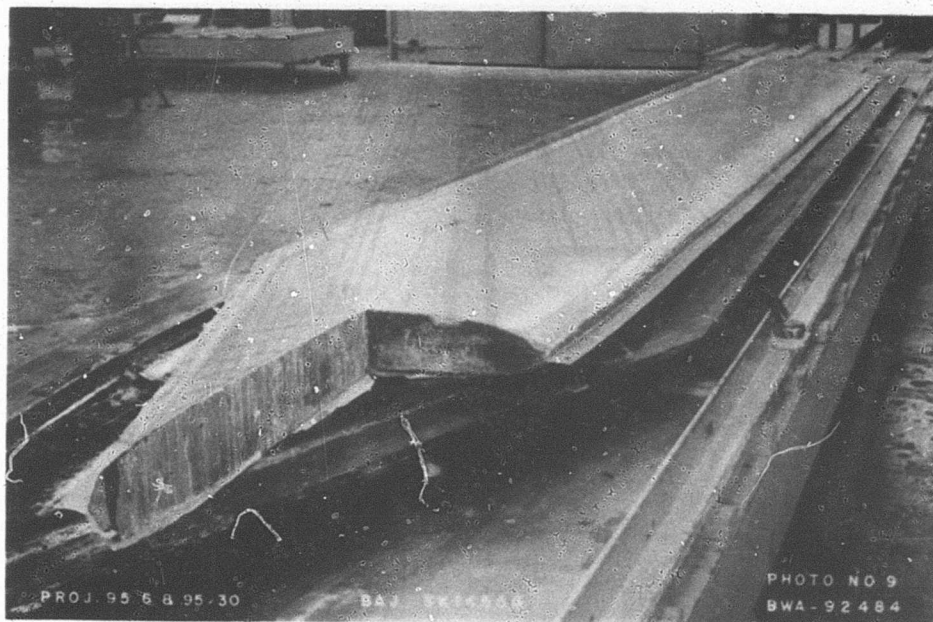


Figure 47. Core-Skin Assembly Bonding Jig.

of the stabilizing skins. It was subsequently necessary to decrease the tool pin spacing to 4-inch intervals and, in addition, to provide tool pinholes along the entire leading edge of the tool at 4-inch spacing in order to adequately restrain fore and aft core movement during the cure of the skins.

A flexible, laminated, fiberglass-reinforced-plastic caul plate molded to match the lower core surface contour was used with this bonding tool. Mold contour was obtained by transfer splashes taken from the lower surface core machining pattern tool. This caul plate overlies the core-skin assembly while secured along its trailing edge by the tool pins. The caul plate transfers autoclave pressures smoothly and evenly to the lower skin surface while the upper skin surface receives its surface smoothness control from the bonding jig.

Spar Molding Jig (Figure 48)

The function and tool concept for this molding jig have been defined previously. The tool, partially disassembled to expose the as-molded spar, is shown in the top photograph.

The base structure was assembled of welded and bolted aluminum channels, beams, plates, and other parts.

A simulated socket was located at the inboard end of the tool on a pedestal in such a manner as to properly lock and hold the root-end fitting in its relative twist alignment around the pitch axis of the blade. The simulated socket allowed the root-end fitting to be pinned to permit inboard or outboard movement (expansion or contraction) while at the same time holding twist alignment. It was also possible to positively restrain inboard or outboard movement during layup and compression operations by securing the simulated socket with a tool pin.

The outboard end was constructed to align and hold the tip anchor fitting at the required blade twist angle. Alignment bolts were fitted with compression springs to provide supplemental outboard tension to the anchor fitting during the cure operation.

The inside mold line surface of the spar was controlled by use of a 2-section, inflatable, room-temperature-vulcanizing, cast silicone-rubber mandrel which was joined to the root-end fitting and the tip anchor fitting to provide the full-length mandrel (Figure 48, middle and bottom left photographs).

Inner caul plates fabricated of glass-fabric-reinforced epoxy-resin laminate were provided to overlie the rubber mandrel between stations 94 and 356.75. During layup of the spar, the caul plates were held in place with bolts along the tool base. After layup was complete, the bolts were removed to allow the caul plates to float, or move toward the laminate, as it compressed during cure.

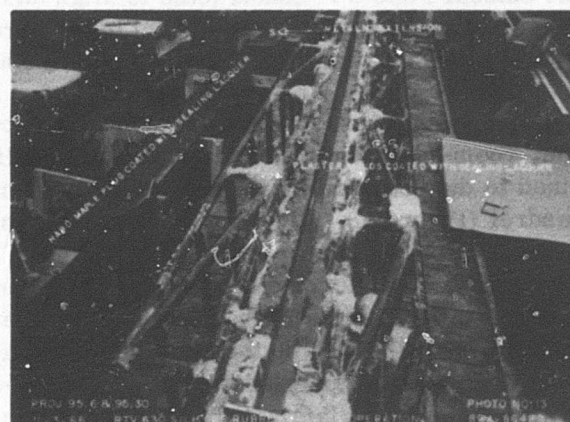
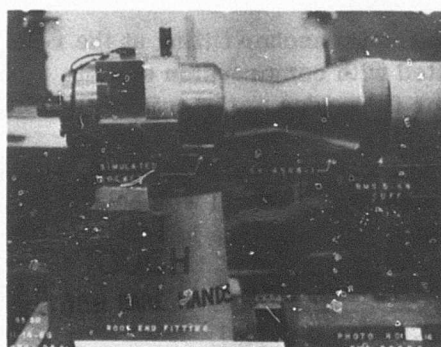
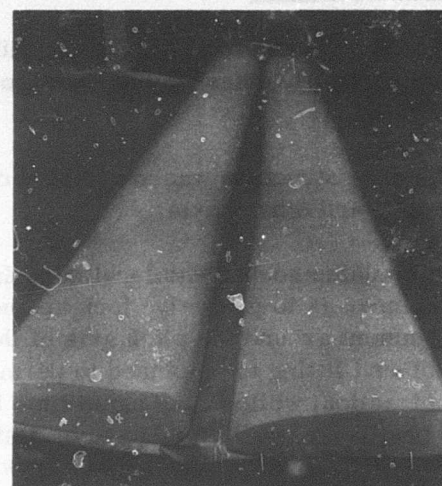
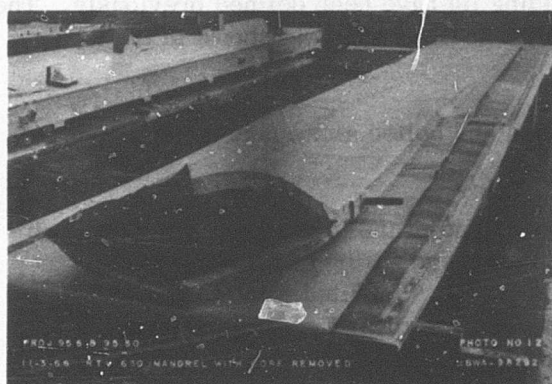
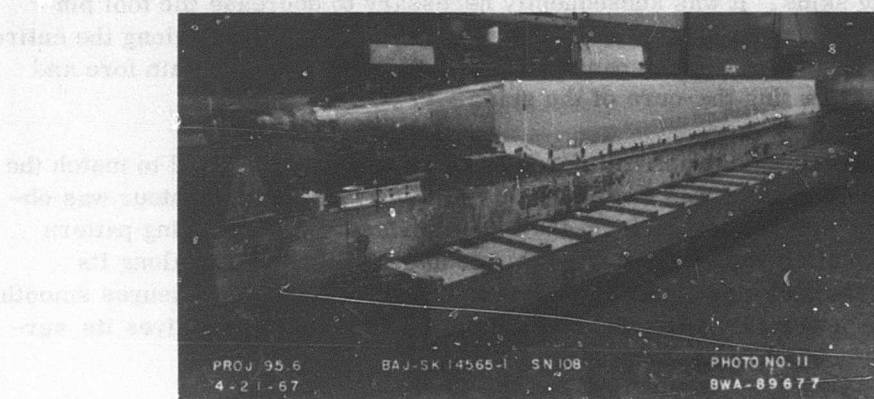


Figure 48. Spar Molding Jig.

The outside mold line surface of the spar was controlled by a 2-piece, glass-fabric-reinforced, epoxy-resin laminate shell, so constructed as to enclose and size the spar during the autoclave cure cycle. Positive enclosure with the laminated tooling was constant outboard of station 44.80.

Tool contours for the inner caul plate and the outer restraining shell laminates were obtained by transfers from the applicable inner and outer spar mold line plaster masters.

Spar laminate pressure over the root-end fitting was applied with autoclave bag pressure supplemented by a cylindrical wrap of glass-fiber roving. The glass-fiber roving was used to restrain and entrap the natural flow or movement of material in the inboard direction under the pressurized outer shell during heating.

Fabrication of the inflatable mandrels proved to be one of the more difficult developments in the tool program. Variations in material quality, incompatibility of silicone-rubber materials with other tooling materials, contamination and temperature control requirements, air entrapped in the mix, and gassing problems during cure were the major processing difficulties encountered. Investigation, development, and implementation of corrective processing measures resulted in sound cast inflatable bladders.

Plaster molds coated with sealing lacquer were used to cast the silicone-rubber outboard mandrel. A pattern consisting of hard maple, where thickness allowed, and thin metal sheet at the outboard end (Figure 48, bottom right photograph) was suspended within the mold cavity. The pattern was positioned and restrained by threaded bolts through the molds on each side, thus providing for adjustment of distance between the mold and pattern. With the mold canted, the silicone-rubber mix was poured at the higher end and allowed to flow slowly toward the lower end, washing the air ahead of it to prevent entrapment. After casting, the material was allowed to cure at room temperature for approximately 14 hours (overnight), after which it was finish-cured in an air-circulating oven. After removal of the pattern by cutting an opening at the inboard end, the inboard end was closed with a pre-cured, adhesive-bonded, silicone-rubber plug.

The smaller inboard mandrel was cast in much the same manner except that it was cast in a vertical position with the inboard end down.

Blade Assembly Bonding Jig

This tool was designed to permit the following multipurpose progressive operations:

1. Spar-to-core assembly bonding
2. Noseblock assembly-to-spar-core assembly bonding
3. Final skin application to spar-core-noseblock assembly

The tool was fabricated by molding a female fiberglass-reinforced-plastic laminate conforming to the outside mold line contour of the upper surface of the final blade. Appropriate splashes and transfers from the outside mold line plaster master were used to provide the control surface upon which this laminate was molded. A honey-comb sandwich-board box support structure was adhesive-bonded to the underside of the laminate for reinforcement.

For spar-to-core assembly and noseblock assembly operations, a simulation of the final skin thicknesses, as well as the erosion strip thickness, was required upon the surface of the blade assembly bonding jig. This was accomplished by using adhesive-backed aluminum tape laminated to the jig surface to provide a simulated tooling surface of the appropriate thickness.

Multipurpose Use A (Figure 49)

For this operation a leading-edge adapter was used to hold the spar in its proper position in the jig. The leading edge of the spar was secured to the adapter by tooling buttons attached to the spar with EPON 934 room-temperature-cure adhesive. The core assembly was positioned and restrained by trailing-edge tool pins. A small caul plate was fabricated and used to create a bridge over the foam bond joint between the spar and the abutting core-skin assembly in-board of station 94.

To prevent collapse in the unsupported root-end region of the spar from the in-board end of the stabilizing core to the root-end fitting (station 48 to station 94), a removable internal rigidized beanbag mandrel was used to provide support during the autoclave cure phase of all three A, B, and C operations. The mandrel bag was made of silicone rubber shaped to conform to the internal spar cavity. When installed in the spar cavity and filled with glass beads, it is rigidized by the application of a vacuum. Upon release of the vacuum, the glass beads can be poured out and the bag collapses for removal through the root-end fitting.

Multipurpose Use B

During noseblock assembly bonding, the blade assembly bonding jig was used in the same manner as for the spar-to-core assembly bonding operation except that the leading-edge adapter and the caul plate were not used.

Multipurpose Use C (Figure 50)

For the application of the final skins, a fiberglass-reinforced-plastic flexible caul plate was fabricated to duplicate the outside mold line of the lower blade surface. This caul plate overlaps the lower skin layup to transfer autoclave pressure smoothly and evenly to the lower skin surface.

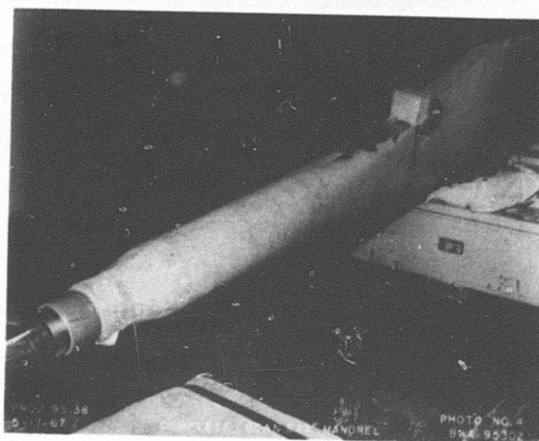
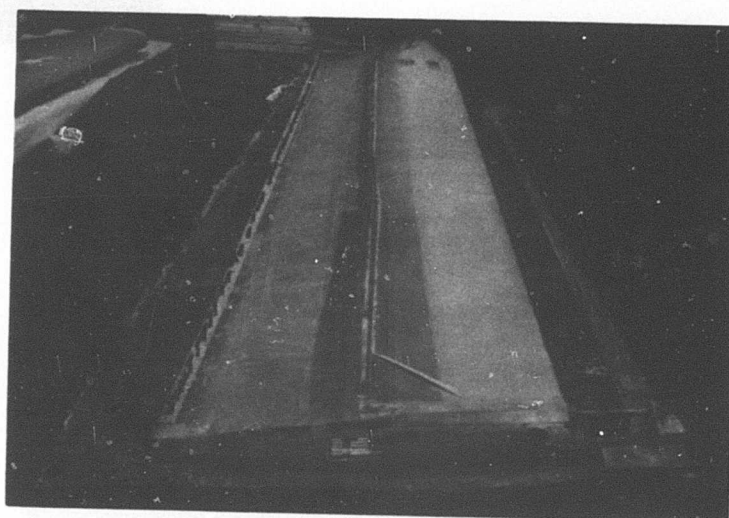
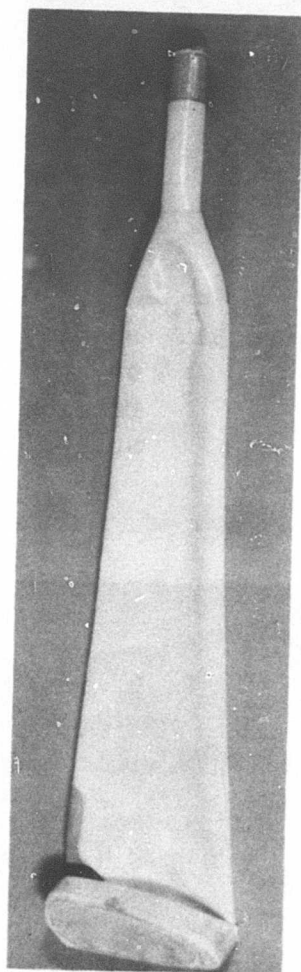
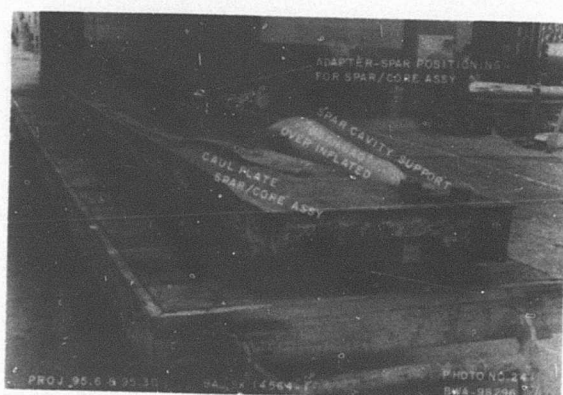


Figure 49. Blade Assembly Bonding Jig - Multipurpose Use A.

Figure 50. Blade Assembly
Bonding Jig -
Multipurpose
Use C.

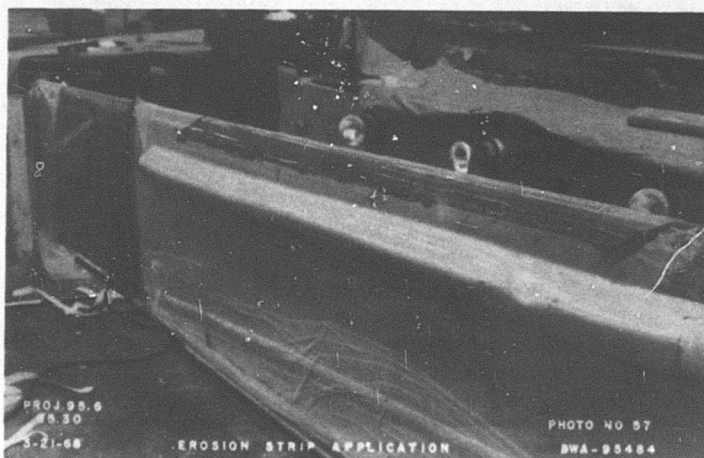
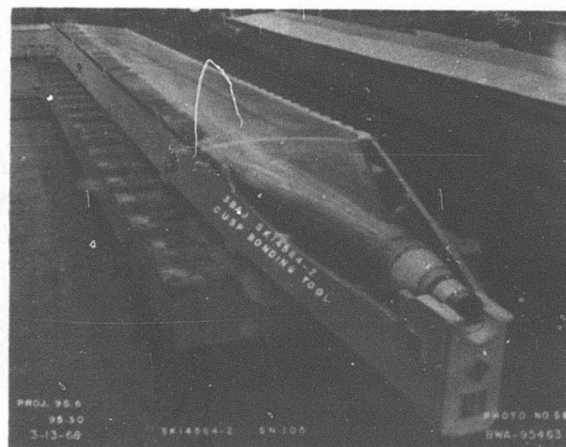


Figure 51. Bonding
of
Erosion
Strip.

Figure 52. Bonding of
Trailing-
Edge Cusp.



Erosion Strip Bond (Figure 51)

Bonding of the erosion strips to the leading edge of the blade did not require any special tooling. Conventional vacuum-bag bonding techniques were used in conjunction with spreader blocks to control the manner in which vacuum pressure is initially applied to the part.

Trailing-Edge Cusp Bonding (Figure 52)

A skeleton, reinforced-plastic, box-type structure was fabricated to support and align the blade assembly relative to a hard trailing-edge-clamping tool plate. The tool plate incorporated provisions for dimensional and angular orientation of the trailing-edge cusp laminates relative to the trailing edge of the blade as well as mechanical clamping of the parts for adhesive bonding.

These tools were the largest high-temperature-resistant, laminated-plastic tools fabricated at that time. Construction of these tools was complicated by their configuration, involving a high length-to-width ratio, which made them ideally suited for warpage. Cross-sectional areas were such that internal bracing was not practical. Many problems were encountered during fabrication of the first tooling components.

Considerable development effort was required before warpage and leakage were reduced to a minimum. The solution of these problems came about only after several unsuccessful attempts at fabricating such large components.

BLADE FABRICATION METHODS AND PROCEDURES

This section describes the principal methods used in the fabrication of the rotor blades. The writeup reflects the final procedures established and in use at the conclusion of the fabrication program. See the preceding section for the description and use of the major fabrication tools.

Procedural steps included specific requirements to weigh and record the weight of all details and materials used in the fabrication of each blade. Because of the routine nature of this procedure, the weight recording steps are not included in this description.

Titanium Detail Parts

The rotor blade socket was hogged out and finish-machined from a forged, annealed block of 6A14V titanium in accordance with specification MIL-T-9047. Machining was done by conventional tracer-machining methods (see Figure 53). The finish process on the sockets included shotpeening and bearingizing.

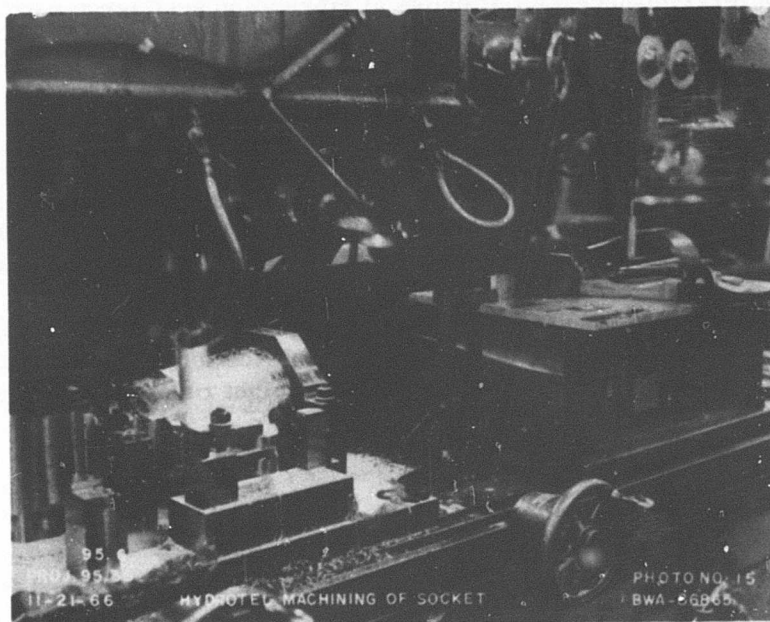
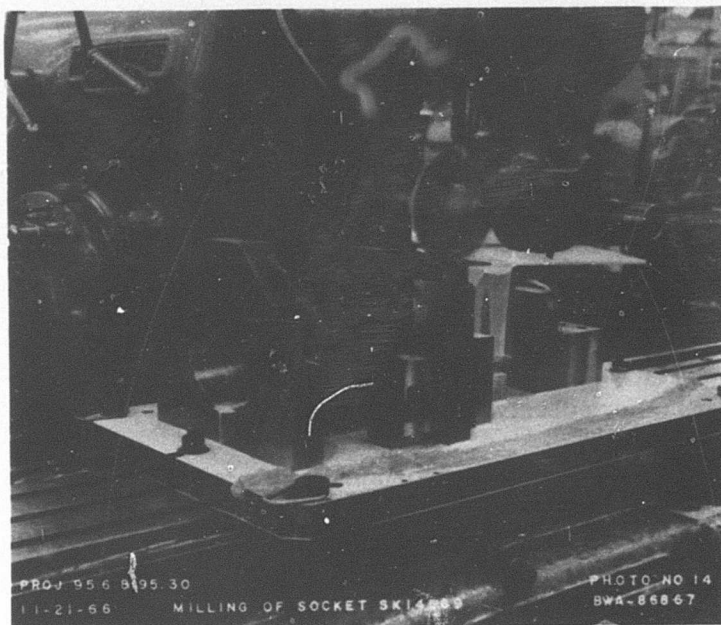


Figure 53. Machining of Rotor Blade Sockets.

The root-end fitting (see Figure 48) was hogged out and finish-machined from annealed titanium rod. Finishing of the root-end fittings included shotpeening and silver-plating on the threads. The blade tip anchor fitting was tracer-machined from annealed titanium.

The formed sheet-metal erosion strips were made from annealed titanium sheet measuring 36 by 96 by 0.016 inch thick. Final fabrication was performed by a hot stretch-forming technique.

Reinforced-Plastic Detail Parts

The rotor blade tip channel, tip cover, overbalance fitting, tip rib assembly, and trailing-edge wedges were fabricated from preimpregnated fiberglass BP907-143S material laminated over high-temperature-resistant epoxy tooling. These parts were bagged and cured at 325° to 350°F at 65-psig pressure.

The trailing-edge cusp laminates were fabricated of alternating plies of 134-150 glass fabric and a thermoplastic resin. The layup was bagged and cured in the autoclave at 345° to 355°F and 100-psig pressure for 25 minutes. The resultant laminate was capable of being thermoplastically formed on assembly.

The 12 noseblock shells were molded of crossply XP251S material over an inflatable mandrel and were cured in a mold at 325° to 350°F and 65-psig pressure.

Spar Assembly

The titanium root and tip anchor fittings were cleaned chemically and then treated with a conversion coating. The faying surfaces were primed, air-dried, and baked. A layer of film adhesive was then applied to the primed faying surfaces. The prepared fittings were attached and pinned to the bonding assembly jig. The inboard silicone-rubber mandrel, overlaid with a Teflon mold-release tape, was positioned on the tool and joined to the outboard end of the root-end fitting. The outboard mandrel section was then positioned between the tip anchor fitting and the inboard mandrel.

The inner caul plates, overlaid with Teflon tape, were positioned over the silicone-rubber mandrel in the area between station 94 and the tip anchor fitting and bolted to the tool base. Preformed metal strips to bridge the top butt joint of the two caul plates were positioned and taped in place. The inner caul plates and the inboard rubber mandrel were covered with one ply of Miltex peel-ply material and taped down tight. The inboard mandrel was then inflated to the prescribed dimensions. The tool was then ready for layup of the laminate (see Figure 54).

A spar laminate layout diagram was used to control the specific termination locations, both spanwise and chordwise, for each ply of the laminate to attain the tapered wall thickness of the spar.

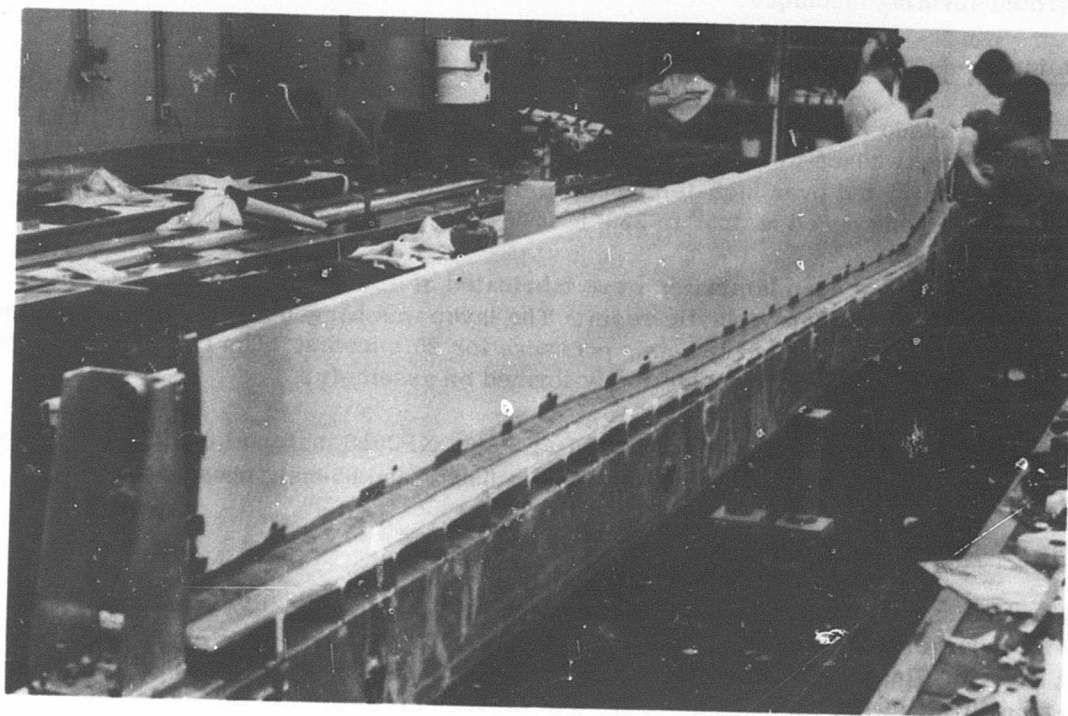


Figure 54. Spar Fabrication Tool Ready for Layup.

The first ply of the inner torsional liner, XP251S preimpregnated fiberglass tape, was laid up on the mandrel with the unidirectional fibers oriented at a 45 ± 5 -degree angle to the pitch axis of the blade. The layup inboard of station 71 resulted in a spiral wrap around the closed inboard end of the spar. The shape of the blade dictated the use of 1/4-inch-wide tape material in this region, with the ends extending out to station 94 (see Figure 55). Outboard of station 94, 12-inch-wide material was used. The fiber orientation on each ply in sequence was oriented 90 degrees to that of the previous ply (alternated ± 45 degrees relative to the pitch axis) to attain a balanced crossply liner.

The longitudinal unidirectional core plies, 1002S preimpregnated material, were laid over the inner torsional liner in continuous-length, 2-inch-wide tapes. Some of these plies were wrapped around the tip anchor fitting in a continuous length from root end to tip end to root end. The outer torsional liner plies were laid over the core layup in the same manner as for the inner torsional liner.

At the completion of each 10-ply application of preimpregnated material, except for the last set, the layup was vacuum-bagged and cold-compacted under pressure and vacuum in an autoclave (see Figure 56).

The completed layup was covered with one layer of peel-ply material, and pre-formed metal caul strips were positioned over the leading and trailing edges of the layup between stations 48 and 94 and taped in place. Thermocouples were then installed at designated locations, and the bolts attaching the inner caul plates to the tool base were removed.

The outer caul plates were lined with Teflon tape, positioned to enclose the layup, and bolted to the tool base. A split clamping-ring adapter encompassed the layup at station 48 and was bolted to the inboard ends of the two outer caul plates. The layup adjacent to the adapter was wrapped with fiberglass roving. The root and tip anchor fittings were freed to allow for spar expansion.

The entire tool was covered with fiberglass bleeder cloth, vacuum-bagged with nylon film, sealed with tape, and tested for leaks. The layup was cold-compacted under vacuum and pressure in an autoclave prior to the start of the heat cure cycle. The vacuum was vented to atmosphere, and the cure was accomplished at 100 psig and 325° to 350°F for 1 hour.

The cured spar was subsequently inspected by X-ray and ultrasonic methods. A molded spar is shown in Figures 57 and 58.

Core-Skin Assembly

The aluminum honeycomb core block sections of differing densities were sawed to template size. These core sections and a prefabricated trailing-edge wedge, with an extended integral tool tab, were prefitted in the milling fixture and then bonded

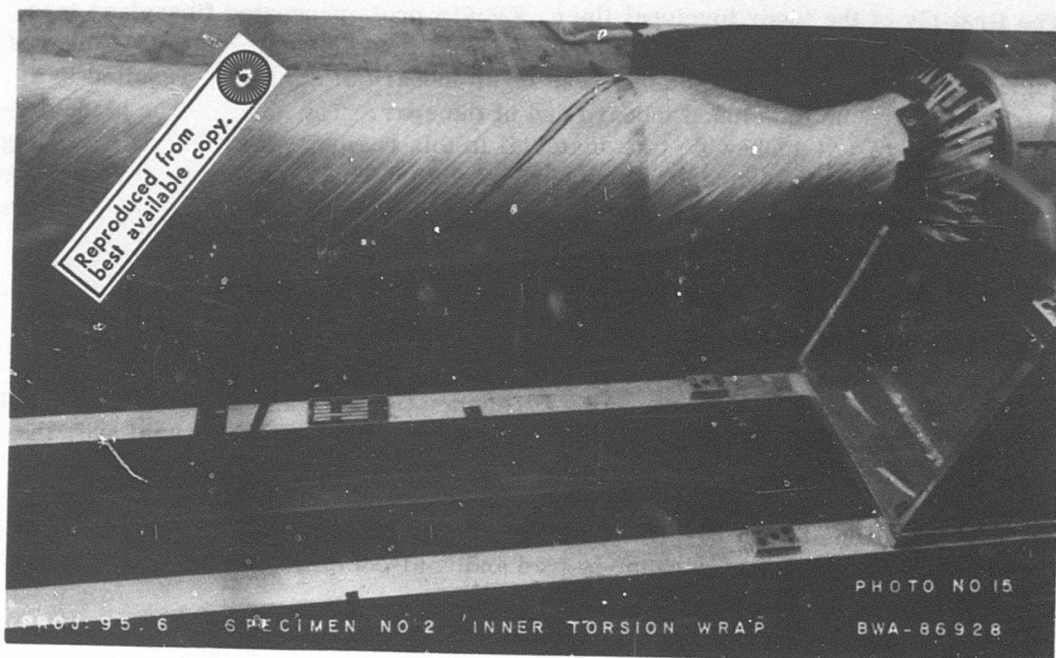


Figure 55. Inner Torsion Wrap of No. 2 Root-End Specimen.

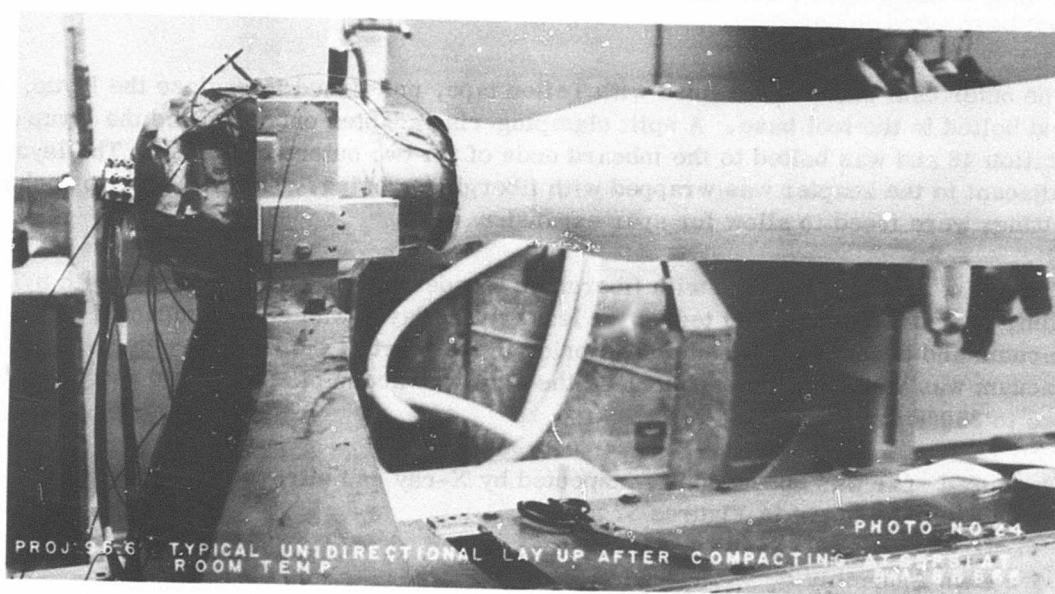


Figure 56. Unidirectional Tape Layup of No. 2 Root-End Specimen After Cold-Compacting.

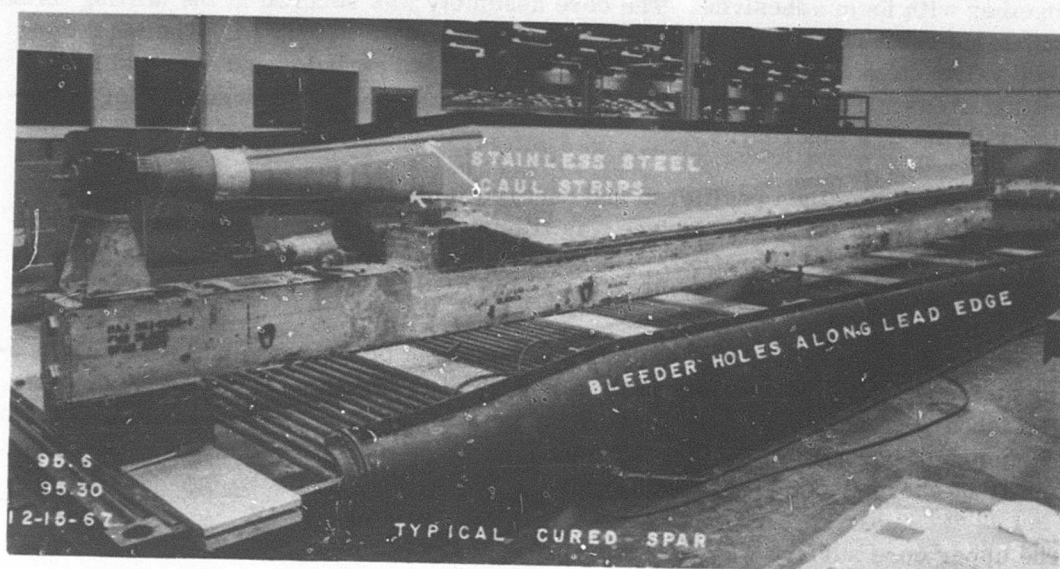


Figure 57. Cured Spar Before Removal From Mold.

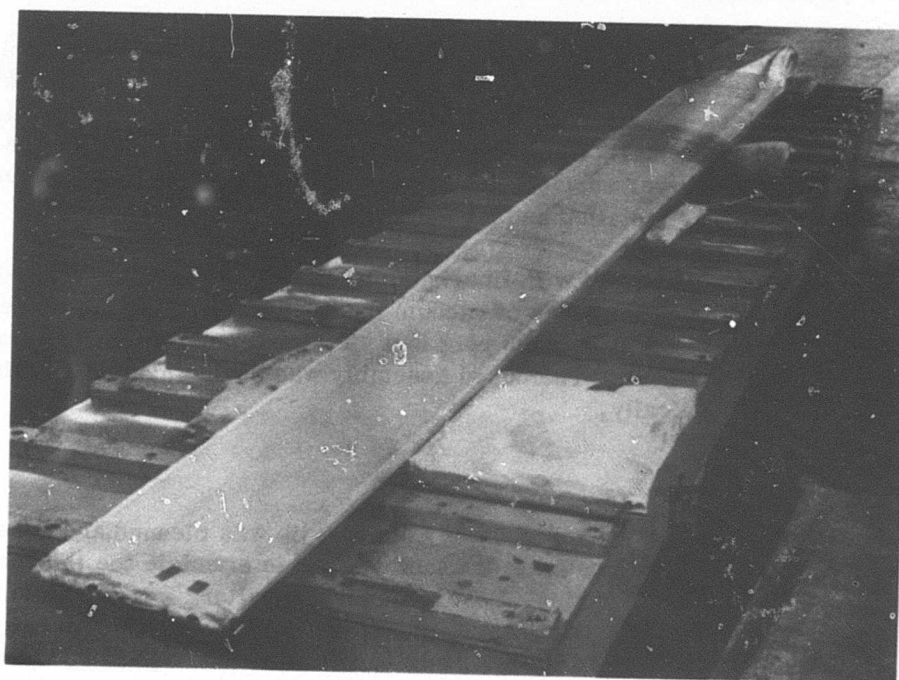


Figure 58. Cured Spar After Removal From Mold.

together with foam adhesives. The core assembly was secured in the milling fixture with a hot-melt resin, and the upper surface was tracer-machined. The machining used valve-stem and shaped-type cutters having both carboloy and diamond grit cutting areas. The assembly was released from the tool in an oven-heating operation with the tool inverted.

The assembly was then positioned and secured in the second milling fixture, in a like manner, and the lower surface was tracer-machined, followed by a second oven-heating release operation. The core assembly was then solvent-cleaned, vapor-degreased, and oven-dried.

A full-length tool tab was bonded to the leading edge of the core, and metal reinforcing strips were bonded to the extended tool tab of the trailing edge (see Figure 47). The inboard transition section of the core assembly was stiffened by potting selected groupings of core cells, top and bottom, with a syntactic foam material to form a family of chordwise supporting rib caps (see Figure 59).

The upper core surface was covered with a layer of American Cyanamid BP907U adhesive resin film followed by a layer of BP907-143S preimpregnated glass-fiber skin material. The skin material was installed with the warp fiber oriented 45 degrees to the pitch axis. One ply of Miltex peel ply was applied to the tool surface of the core-skin assembly bonding jig; an inboard tool support block was installed (see Figure 60), and the upper surface thermocouples were located.

The core assembly, with upper skin in place, was positioned in the tool and pinned at all locations. The lower core surface was covered with adhesive film and skin material in the same manner as for the upper surface. Fiber orientation on both skins must be identical. One ply of Miltex peel ply was applied over the lower skin material, and the lower surface thermocouples were installed. The lower surface tool caul plate was installed and pinned in place.

The tool was then covered with fiberglass tooling cloth, vacuum-bagged and sealed, and vacuum-checked (5 inches of vacuum maximum). The core-skin assembly was cured in an autoclave at 18 to 20 psig in a stepped-temperature cure finalized at 325° to 350°F for 1 hour. The cured assembly was sealed against moisture and then inspected ultrasonically.

Spar-Core Assembly

The tool surface of the final assembly bonding jib was cleaned, and adhesive-backed aluminum tape was laminated to the tool surface to simulate the thickness of the final skins and erosion strips. Several prefit operations were conducted to check and record the interface fits between the spar, core-skin assembly, overbalance fitting, and premolded foam filler part used at the inboard joint between the spar trailing edge and the transition section of the core-skin assembly. Contour adjustments were made on the lower surface of the core-skin assemblies forward of



Figure 59. Chordwise Potting of Selected Cells of Honeycomb Core.

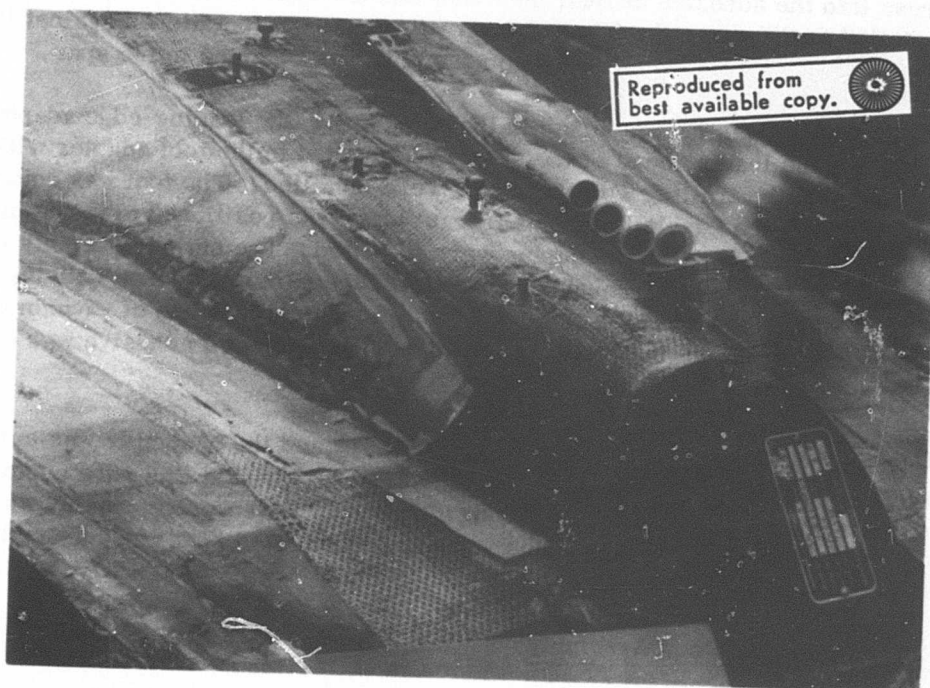


Figure 60. Installation of Inboard Tool Support Block.

the pitch axis as part of these prefit operations to correct an undersize thickness condition detected on earlier spar-core assemblies (see Figure 61).

A beanbag mandrel was installed inside the spar cavity inboard of station 94, vacuum was applied to rigidize the bag, and parting film was applied to all exposed surfaces. The peel ply was removed from the inboard end of the spar molding inboard of station 48, a layer of adhesive film was applied to the laminate, and the laminate was wrapped circumferentially with 1002S preimpregnated tape material to attain a sufficient buildup of material for the subsequent tapered cone machining operation.

The peel ply was removed from the inside surfaces of the spar, externally from the spar trailing-edge area where the foam filler part was to be bonded, and both surfaces of the core-skin assembly that interface with the inside spar surfaces at assembly. All faying surfaces of the spar, core-skin assembly, and overbalance fitting were primed and air-dried. One layer of adhesive film was then applied to the faying surface of the core-skin assembly and overbalance fitting. All edges of the overbalance fitting, all interface surfaces of the inboard foam filler part, and core-to-tip-anchor-fitting interfaces were covered with foam adhesive tape.

Continuous spanwise beads of EPON 934 epoxy adhesive were next applied along the inside upper and lower surfaces of the spar so that the core-skin assembly would press into the adhesive at final insertion into the spar. The overbalance fitting was installed in the spar, the inboard foam filler part was positioned against the trailing edge of the spar, and the core-skin assembly was inserted in the spar.

The assembly was next mounted in the bonding jig; the leading-edge adapter tool was installed; the leading edge of the spar was fastened to the tool adapter with tool buttons; and the trailing-edge tool pins were installed. The tool was covered with glass fabric bleeder cloth, the small caul plate was positioned over the inboard foam filler area, and the thermocouples were installed. The entire assembly was then wrapped in nylon film to form a vacuum bag, the film was sealed with tape, and vacuum was drawn to check the tightness of the seal (5 inches of vacuum maximum). Full vacuum was retained on the beanbag. The EPON 934 adhesive was cured at room temperature.

The tool vacuum was then vented to atmosphere, and the assembly was cured in the autoclave at 23 to 25 psig and 270° to 290°F for 18 hours; this cure cycle included time for postcure of the spar molding. The cured spar-core assembly was subjected to X-ray and ultrasonic inspection. A finished, bonded spar-core assembly is shown in Figures 62 and 63.

Spar-Core-Noseblock Assembly

The 12 noseblock shells were filled with an elastomeric compound weighted with tungsten powder to the proper density and total weight requirements and cured. The bonding tool was again prepared to simulate the thickness of the final skins and

Figure 61.
Core-Skin Assembly
Showing Buildup
of Thickness.

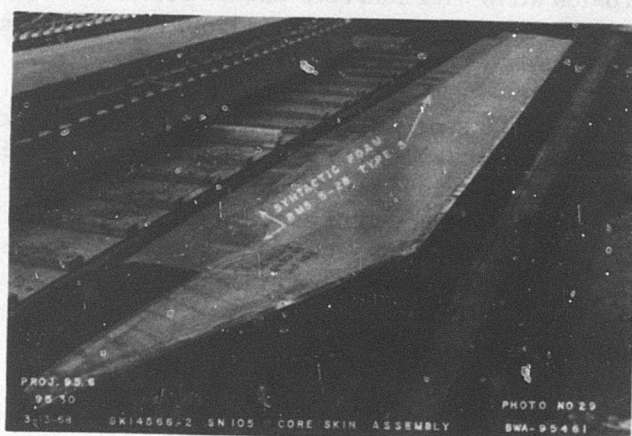


Figure 62.
Tip-End View of Finished
Spar-Core Assembly.

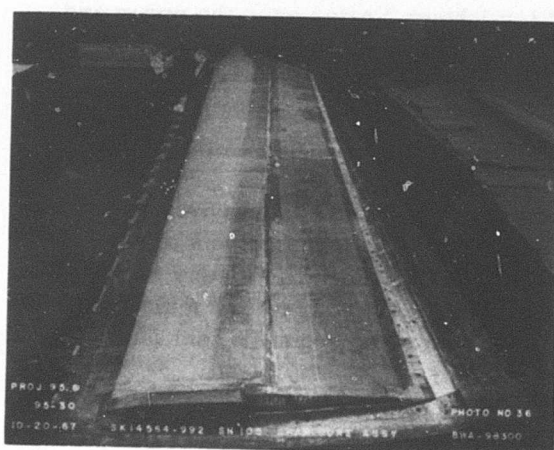
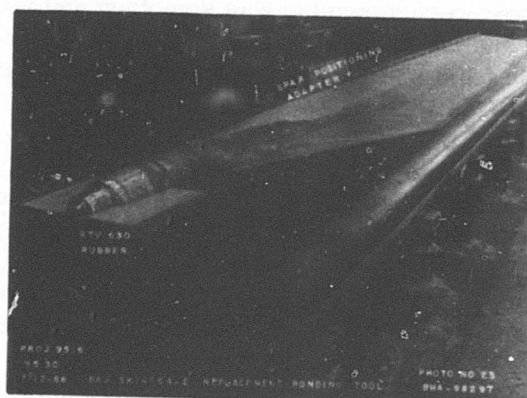


Figure 63.
Root-End View of Finished
Spar-Core Assembly.



erosion strip with adhesive-backed aluminum tape. The peel ply was removed from the spar-nose bonding area and from the bond area of each of the 12 noseblock weights.

The fit of the spar-core assembly and the noseblocks was checked in the tool. All bonding surfaces were primed and air-dried, and the required thickness of adhesive film material was applied to the primed surfaces. A thin layer of adhesive sealant was applied to one end of each noseblock weight. The nose weights were then installed in the tool, in sequence, against the leading edge of the spar-core assembly. Weights were applied to hold the noseblocks in position for cure of the sealant adhesive at room temperature. The tool was covered with glass fabric bleeder cloth, and the thermocouples were installed.

The assembly was vacuum-bagged with nylon film, sealed with tape, and checked for leakage (5 inches of vacuum maximum). Full vacuum was retained on the bean-bag. The tool vacuum was vented to atmosphere, and the assembly was cured in an autoclave at 23 to 25 psig and 225° to 250°F for 1 hour. After cure, the upper and lower corners at the bond line interface were filled and faired to the adjacent surfaces with an elastomeric sealant material.

Application of the Final Blade Skins

The tool surface of the final assembly bonding jig was cleaned and covered with a layer of Teflon tape. A 0.026-inch-thick sheet of silicone rubber was applied to the tool surface from station 117 to the tip. Inboard of station 117, silicone rubber was cast in place, using the actual spar-core-noseblock assembly as the male mold element, and cured. The latter assembly was then removed from the tool (see Figure 64).

An upper-surface half of a shop-aid metal erosion strip was fitted and installed on the leading-edge area of the tool. The inboard foam bonding area, stations 55 to 94, of the spar-core assembly was smoothed and faired; the tip rib assembly was installed; and the fillet gap between the tip anchor fitting and the tip rib was filled with syntactic foam material. The foam was then cured and faired flush to the adjacent surfaces (see Figures 65 and 66).

The peel ply was removed from all areas of the spar-core-noseblock assembly to be bonded and from the tip channel and tip rib details. One layer of BP907-143S preimpregnated glass-fiber skin material was applied over the tip anchor fitting bonding surfaces, to the upper and lower faying surfaces of the core-skin assembly and tip channel, and to the upper and lower inboard foam bonding areas between stations 55 and 94. The tip channel was assembled to the core-skin assembly.

The upper-surface final skins of BP907-143S preimpregnated material were laid up on the assembly. Two skin doublers were applied to the tip end of the assembly with the warp fibers oriented 90 degrees to the pitch axis. An inner skin ply, extending

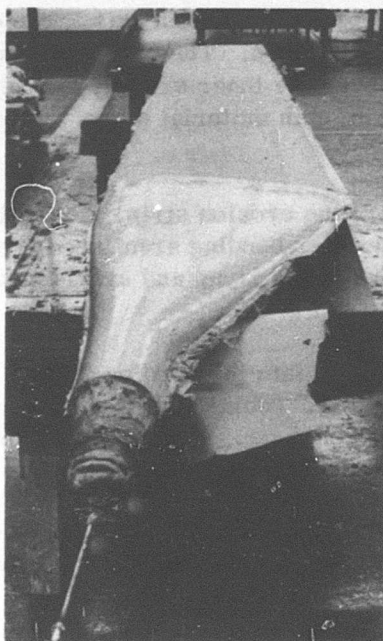


Figure 64.
Blade Assembly With Tooling
Silicone Rubber in Place.

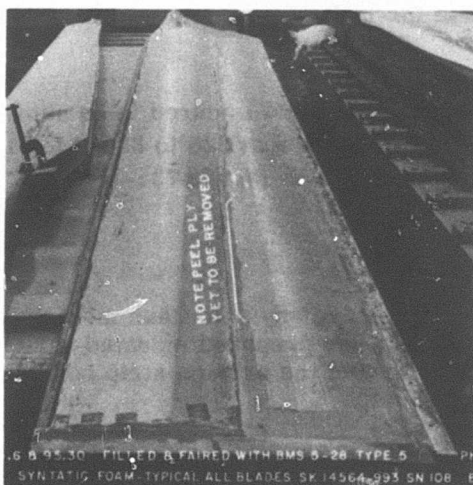


Figure 65. Blade Assembly
Filled and Faired
With Syntactic
Foam.

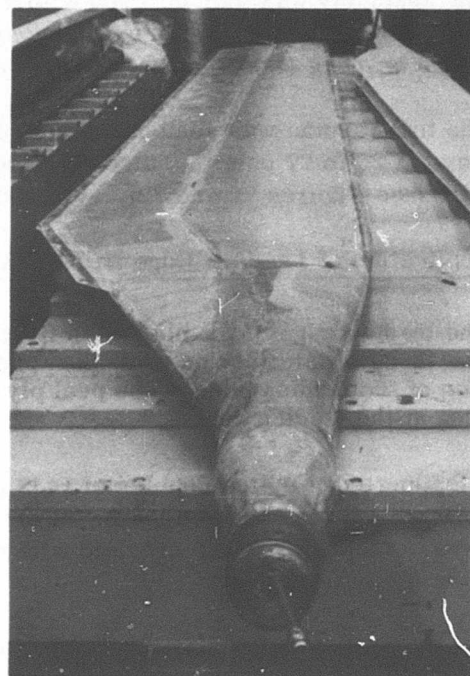


Figure 66. Blade Assembly
Ready for Application
of Final Skins.

from the leading edge to 70 percent of chord and from station 48 to the tip, was applied with the warp fiber oriented 45 degrees to the pitch axis. The edges of the skin material were overlapped from 1/2 to 3/4 inch. The outer skin, with 100 percent chord coverage, was applied over the inner skin ply with the warp fiber oriented 90 degrees to that of the inner skin; skin material edges were again overlapped.

Miltex peel ply was installed in the areas of the erosion strip, the trailing-edge cusp bonding area, and the leading-edge doubler bonding area inboard of station 117. A layer of bondable Tedlar film was applied to the layup and overlapped onto the peel ply areas.

The spar-core-noseblock assembly was placed into the bonding jig, and the lower-surface skin doublers, skin plies, peel ply, and Tedlar film were applied in the same manner and sequence as for the upper surface. Warp fiber orientation was parallel to that of the corresponding ply on the opposite surface.

The thermocouples were installed, Teflon tape was applied to the lower-surface tool caul plate, and the caul plate was installed and pinned to the tool (see Figures 67 and 68).

The assembly was then covered with glass-fabric bleeder cloth and enclosed in nylon film. The film was sealed with tape and checked for leakage; vacuum was retained on the beanbag (see Figures 69 and 70).

The tool vacuum was vented to atmosphere, and the assembly was cured in an autoclave at 25 to 27 psig in a stepped-temperature cure finalized at 325° to 330°F for 1 hour (see Figures 71 and 72). A cured assembly is shown in Figure 73.

Application of Leading-Edge Erosion Strips

The leading edge of the blade was first trimmed to remove any skin flash material. The three erosion strips were then prefitted to nest in the prepared indented surface of the leading edge. The peel ply was removed from the erosion strip bonding area at the leading edge.

A leading-edge splice doubler of 143S glass fabric impregnated with EC2216 adhesive resin was prepared and applied, covering the noseblock area under the erosion strip. The doubler was overlaid with the erosion strips and vacuum-bag-cured at room temperature.

The erosion strip bonding surfaces were chemically cleaned followed by a conversion coating treatment. They were then rinsed, oven-dried, primed, air-dried, and oven-cured.

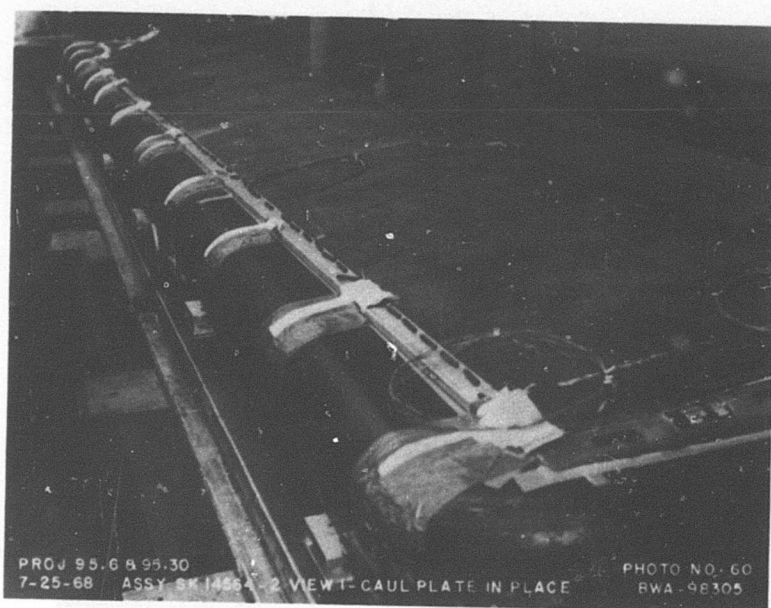


Figure 67. Tip-End View of Blade in Final Assembly With Caul Plate in Place.

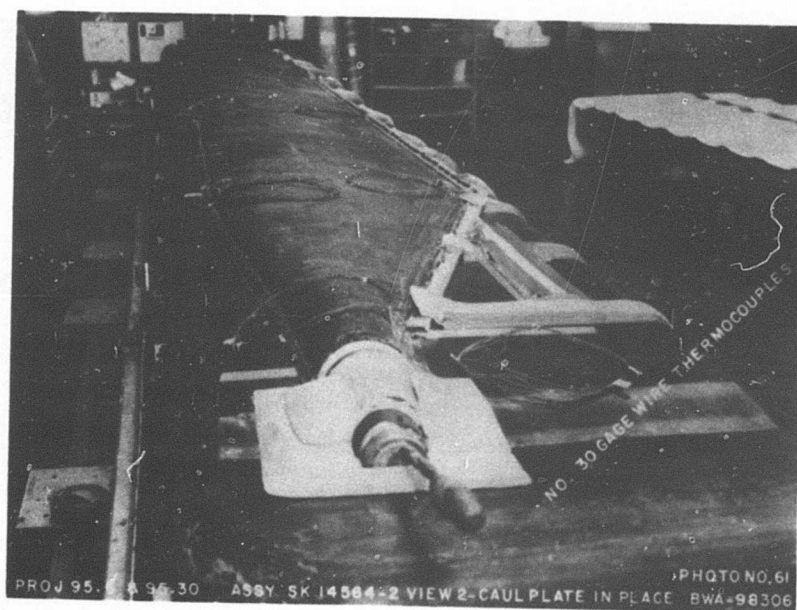


Figure 68. Root-End View of Blade in Final Assembly With Caul Plate in Place.

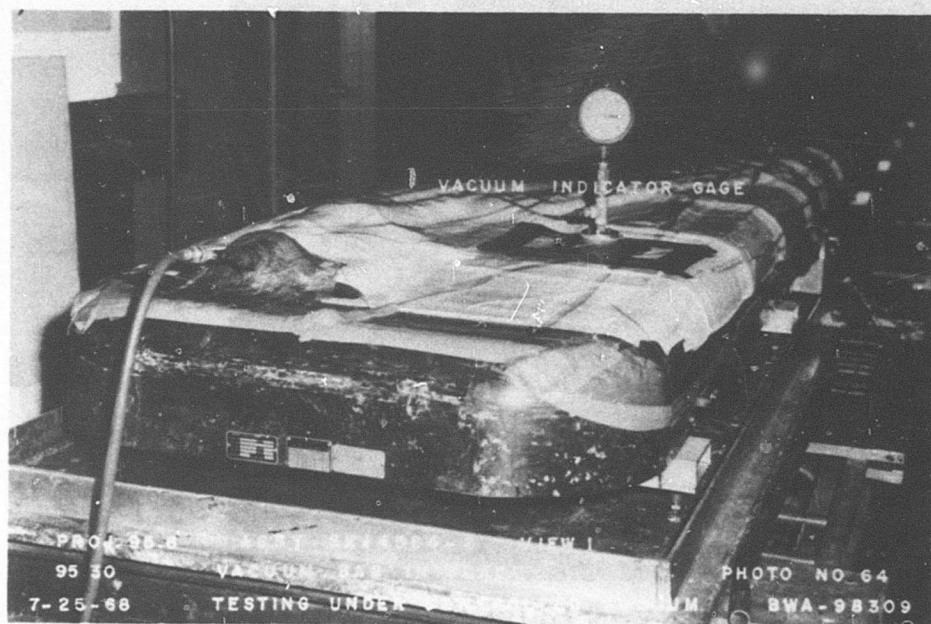


Figure 69. Blade Assembly in Vacuum Bag for Cure of Outer Skins.

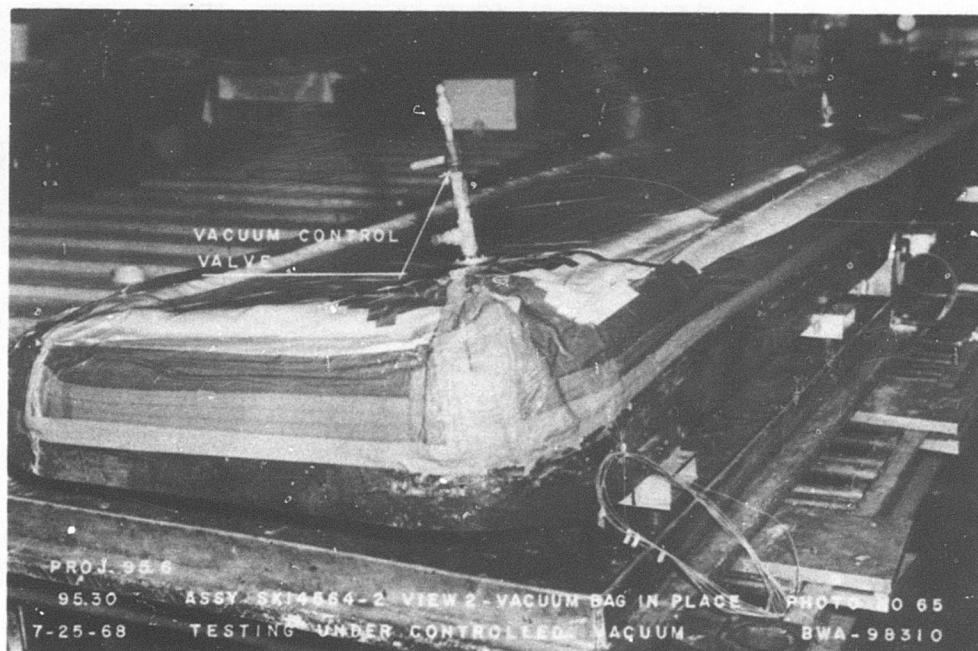


Figure 70. Tip-End View of Blade Assembly in Vacuum Bag for Cure of Outer Skins.

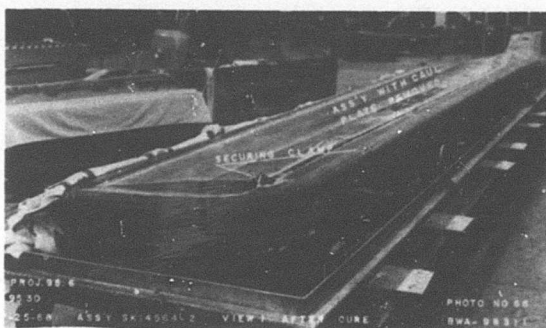


Figure 71. Tip-End View of Blade After Cure of Skins.

Figure 72. Root-End View of Blade After Cure of Skins.

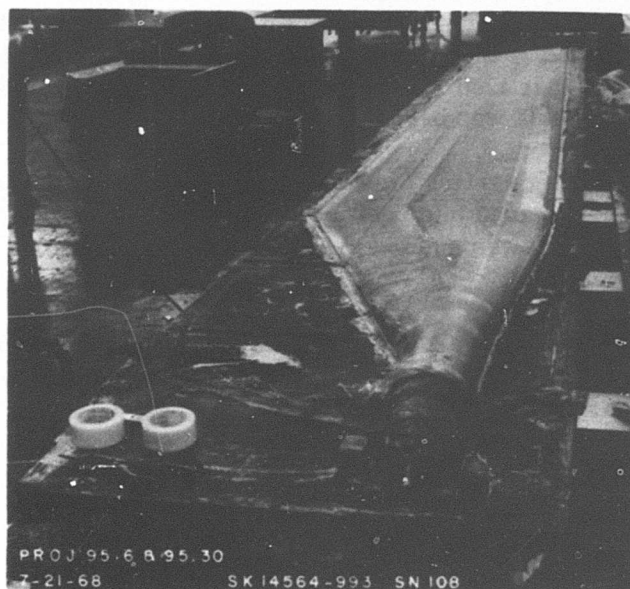
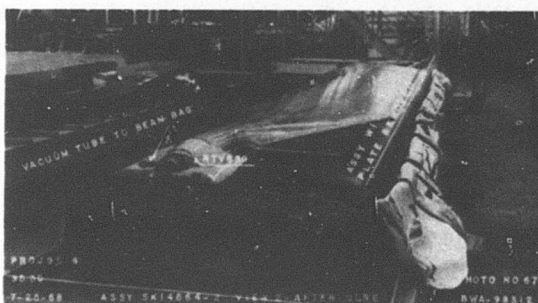


Figure 73. Cured Blade Assembly Before Installation of Final Detail Parts.

The blade bonding area was coated with EC2216 adhesive resin, scrim cloth was applied, the erosion strips were installed, and pressure was applied with the vacuum bag. The assembly was then cured at room temperature under vacuum pressure (see Figure 74).

Application of the Trailing-Edge Cusp

The trailing-edge tool tab was removed and the edge was trimmed to template size. The upper-and lower-surface cusp laminate details were prefitted to the blade in the cusp bonding jig.

The peel ply was removed from the bonding areas of the cusp and the blade. The blade bonding areas were coated with EC2216 adhesive resin, and scrim cloth was applied; the cusp laminates were positioned; and the assembly was clamped mechanically in the bonding jig. The cure was accomplished at room temperature.

Final Assembly Operations

The inboard leading-edge and trailing-edge skin splice doublers of 143S glass fabric impregnated with EC2216 adhesive resin were prepared and applied between stations 48 and 117. The doubler layups were vacuum-bagged and cured at room temperature under vacuum pressure (see Figure 75).

The root-end taper on the blade was machined on a boring mill. The tool fixtures used for blade support and alignment are shown in Figure 76. The blade socket was then installed and indexed at the designated incidence angle. The blade was set up in a similar manner to that used for the taper-machining operation, and a close-tolerance incidence pin hole was bored through the root-end adapter.

The socket-to-blade faying surfaces were cleaned and coated with EC2216 adhesive resin, the socket was threaded into position, and the incidence pin was installed. A fillet of sealant material was applied circumferentially at the outboard end of the socket-to-blade juncture.

The installation of the tip hardware and tip cover completed the blade assembly, after which the finished blade (Figure 77) was checked by dimensional, X-ray, and ultrasonic inspection.

FABRICATION PROBLEMS AND SOLUTIONS

A summary discussion of the major blade tooling and processing problem areas and their solutions is presented below.

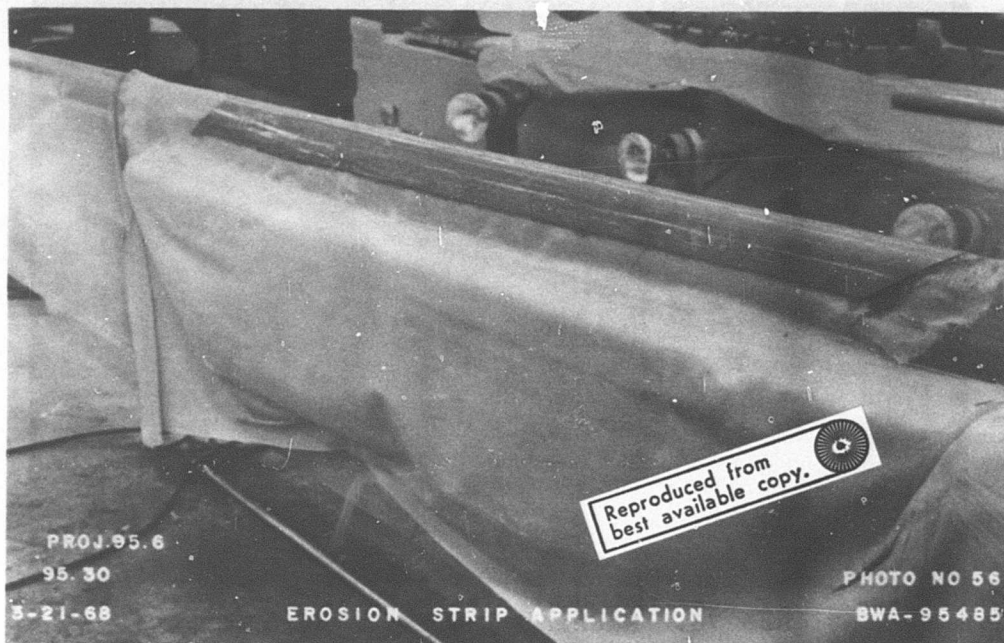


Figure 74. Installation of the Erosion Strip.

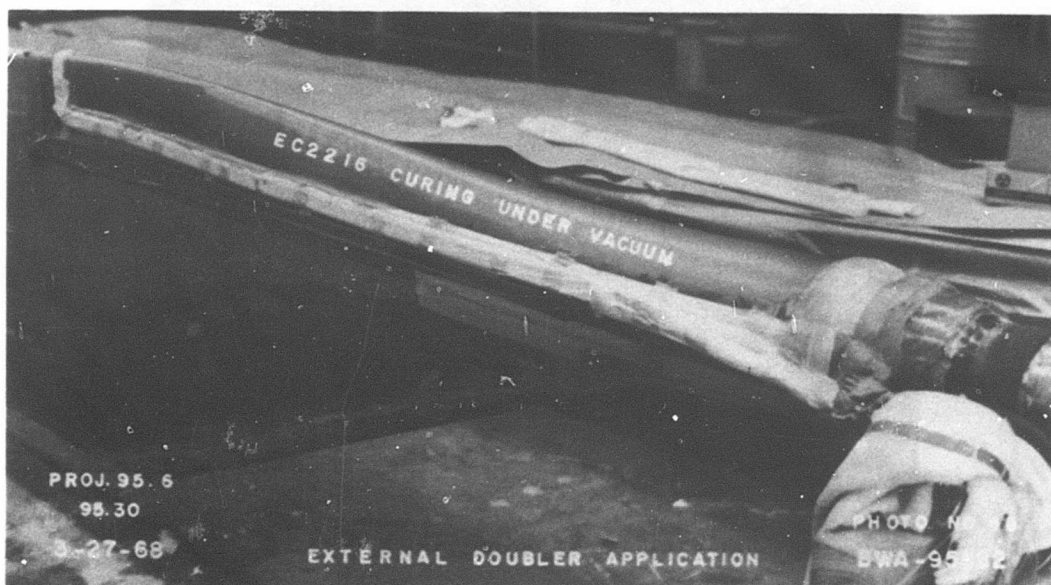


Figure 75. Installation of the Leading- and Trailing-Edge Doublers.

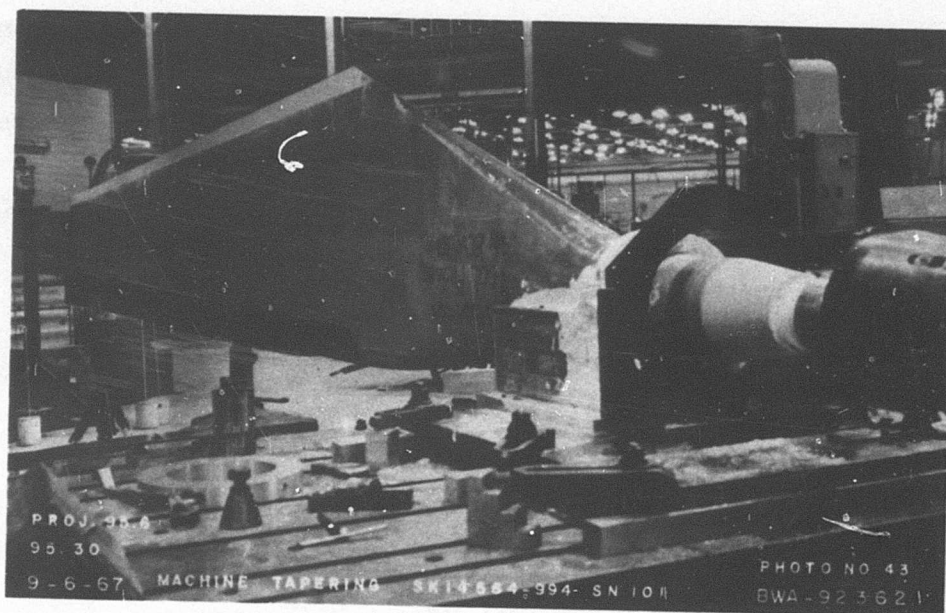


Figure 76. Machining the Root-End Taper.

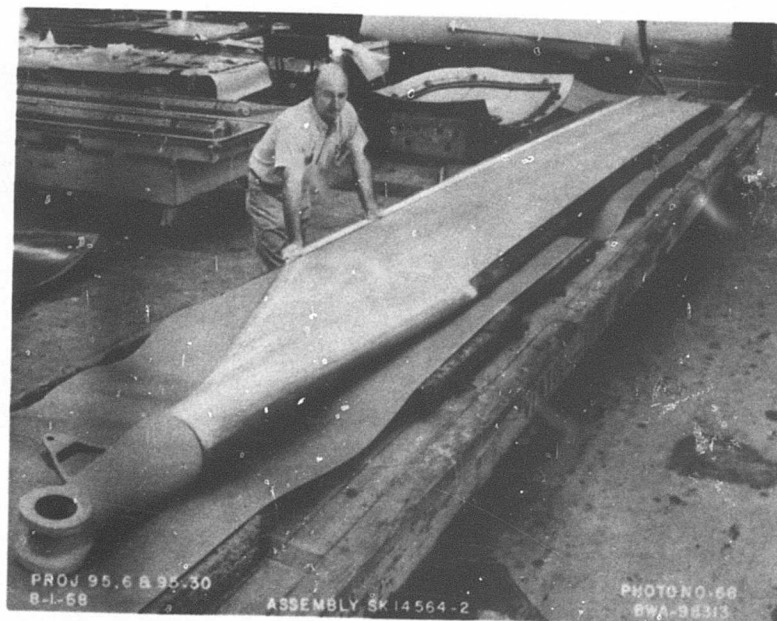


Figure 77. The Finished Advanced-Geometry Rotor Blade.

Spar Fabrication

Many sequential changes in processing occurred during the evolution of spar fabrication between the initial attempt and the procedures and techniques used to control the fabrication of later spars. Initial spar molding deficiencies of consequence included wrinkles, voids, and delaminations, particularly in the closed section of the spar inboard of station 71; resin rich accumulation in the laminate along the leading edge; and waviness and moderate kinking of lead tracer strands (fiber orientation indicators) evident in radiographic (X-ray) inspections and evidence of expansion and contraction problems (see Figure 78).

Low cure pressures due to tool, expandable mandrel, and/or vacuum bag leaks, as well as restraints on the movement of the laminate to become fully pressurized and sized, caused substandard laminate quality. Insufficient allowances for expansion and contraction of tooling elements were contributing factors.

The corrective measures discussed below were implemented by progressive tooling and process alterations until the desired improvements and quality levels were attained on a repeatable basis.

Corrective Tooling Measures

1. Correction of an undersize condition of the outboard expandable tool mandrel for better conformance with the tool cavity to eliminate leak problems from this source. Also, resizing of the inboard mandrel.
2. Use of a double vacuum bag system for increased reliability.
3. Resealing of the tool base to eliminate tool leaks.
4. Provision for free axial movement of the root end fitting, simulated socket, and outer mold shells, relative to the tool base, during heating and cooling to counteract expansion and contraction problems.
5. Replacement of the hard tool insert at the apex of the Vee opening in the trail edge of the spar at station 71 with a rubber plug to provide payoff for expansion and contraction (see Figure 79).
6. Addition of spring-loaded tension provision for the tip anchor fitting during cure.
7. Addition of a collar type extension adapter to the inboard end of the outer mold shells to eliminate a laminate bulge problem over the outboard cylindrical end of the root end fitting (see Figure 57).

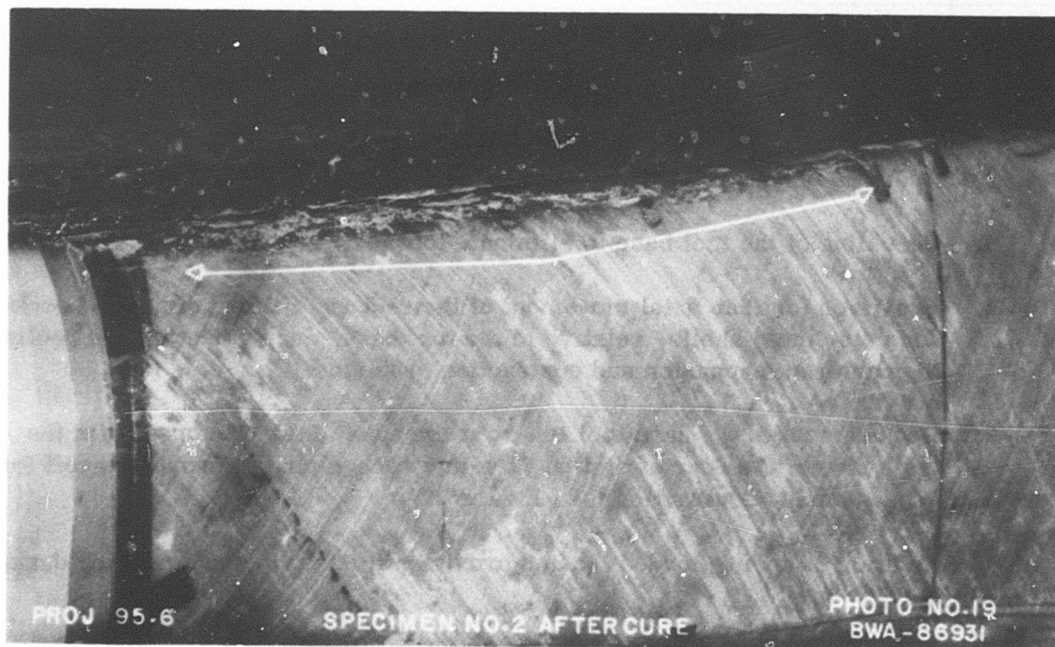
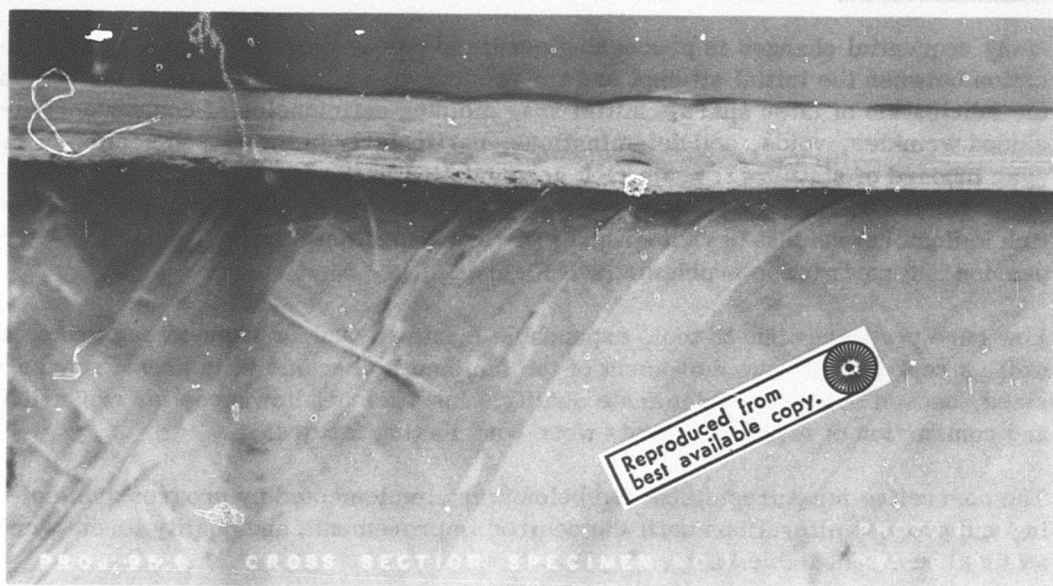


Figure 78. Initial Spar Molding Deficiencies.

8. Provision for leading-edge radii buildup to the inner spar surface caul plates to prevent mark-off and resin-rich areas. Also, drilling of bleeder holes in both outer mold shells along the lead edge to reduce resin and air entrapment.
9. Addition of formed stainless-steel caul strips from stations 48 to 94 at leading and trailing edges (see Figure 57).

Corrective Processing Measures

1. Periodic cold compaction of the laminate layup at 80-psig pressure and full vacuum for 30 minutes after each 10-ply application of prepreg material. This overcame the bulk factor and assisted in the removal of entrapped air in the layup.
2. Inflation of the inboard mandrel with air to preselected dimensions during the laminate layup. This served not only to stiffen the mandrel, but to cause the innermost fibers to be layed up more nearly to the final cured diameter. This sizing eliminated some of the restraints which prevent the curing laminate from "bottoming out" against the outer mold shell and becoming fully pressurized and sized.
3. Adding supplemental external wrapping around the laminate over the root end fitting prior to cure.
4. Compaction of the completed layup at 100 psig and full vacuum for 3 hours at the beginning of the cure cycle and prior to the application of heat.
5. Raising final cure temperature from 270°-290°F to 325°-350°F.
6. Increasing the number of thermocouples to improve monitoring and control during cure cycle.

Core-Skin Assembly Bonding

The first attempts at bonding core skin assemblies made use of the 2MF core machining tool which had been originally designed for both core machining and core skin bonding operations. Tool leakage, local pressure problems, and tool failures resulted in the loss of several assemblies. The use of the 2MF tool for this bonding operation was dropped, and new core skin bonding assembly tools (BAJ's) and caul plates were fabricated.

These early trials also indicated that the stability of the thicker core section, in the region between station 60 and 115, in resisting designated cure pressure was marginal. This section was stiffened by the addition of a number of chordal syntactic foam support ribs (Figure 59) as a design corrective measure.

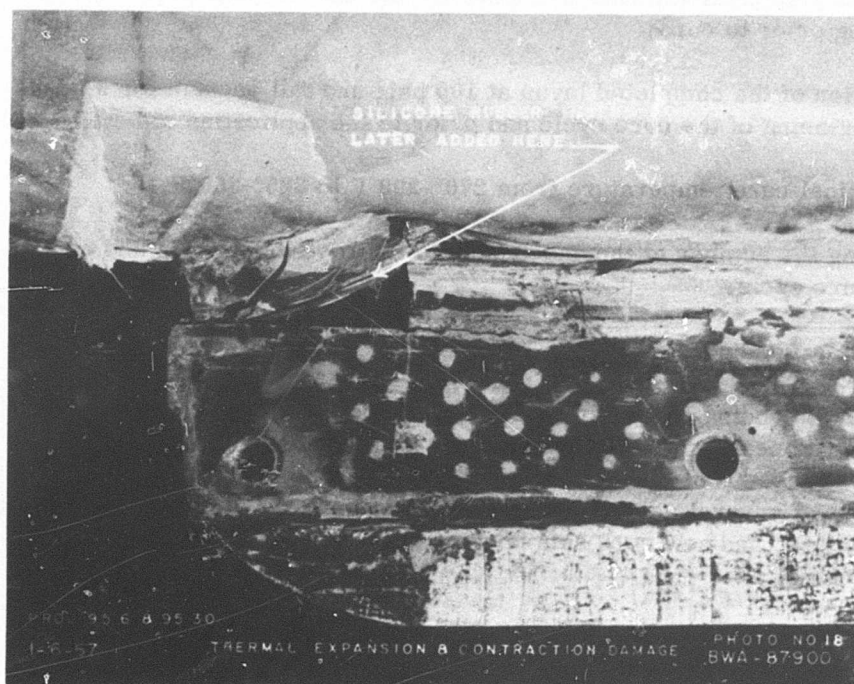


Figure 79. Spar Damage From Thermal Expansion and Contraction.

Additional core hold-down and restraining provisions had to be incorporated with the new BAJ and core details to resist chordal movement which caused core distortion, skin wrinkling and bag leaks during cure. These included strengthening the trailing-edge tool tab, increasing the number of trailing-edge tool pins (decreased spacing), and adding a similar tool tab and pinning arrangement along the entire leading-edge length of the core (see Figure 47).

The caul plate was reworked and made thinner to provide increased flexibility and better conformability to the part, to eliminate local unpressurized areas on the lower surface of the assembly.

The above corrective measures resulted in a satisfactory appearing assembly. However, coupon tests of core-to-skin bond strength were below specification requirements. Investigation indicated a deficiency in the resin fillet size at core edge-to-skin interface. This deficiency was corrected by a process change to provide additional resin in the form of an unsupported film of BP907U resin applied to the core side of the prepreg skins at the time of assembly. Acceptable bond strength values were attained by this fix. Core skin assemblies exhibiting this deficiency were reworked by removing the original skins and replacing with new skins plus the added resin film material.

Spar-to-Core Assembly Bonding

Evidence of distortion and chordal movement of the core skin assembly relative to the spar molding was found after cure of the initial assembly (see Figure 80). Additional trailing-edge hold-down and restraining provisions were incorporated in the blade assembly bonding jig (BAJ) similar to that accomplished on the core skin assembly bonding jig.

A caul plate was added to bridge and size the free-foam bond joint between the spar trailing edge and the abutting transition core section (STA 54-94). The flexible nylon film pressure bag did not provide the necessary constraint in this area.

Three 1/16-inch-diameter holes were drilled in the vertical leading-edge wall of the spar molding to facilitate removal of air from within the assembly during cure.

A concave contour deviation of the lower assembly surface forward of the pitch axis occurred on several assemblies. This was initially attributed to chordal movement of the core skin assembly during cure. Further investigation and analysis, including the cross sectioning of a blade, indicated that the honeycomb core section was undersize relative to the inside mold line of the spar in this area. This condition exhibited lack of bond between the core skin assembly and the spar in the affected area, as well as the contour deviation. Syntactic foam contour adjustments were made on subsequent core skin assemblies to correct the undersize condition (see Figure 81), and a heavier grade of adhesive film was used in the spar core skin assembly bond line. As radiographic inspection did not reveal this condition, an

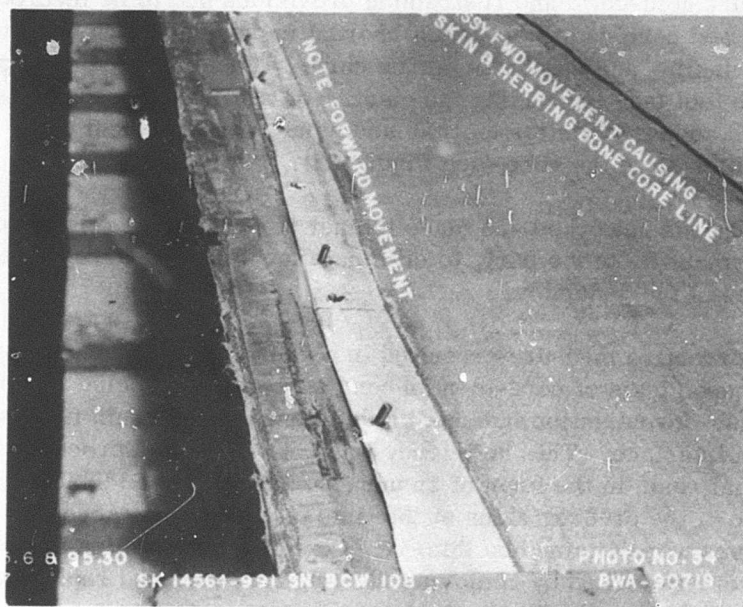


Figure 80. Evidence of Distortion and Chordal Movement of the Core-Skin Assembly Relative to the Spar.

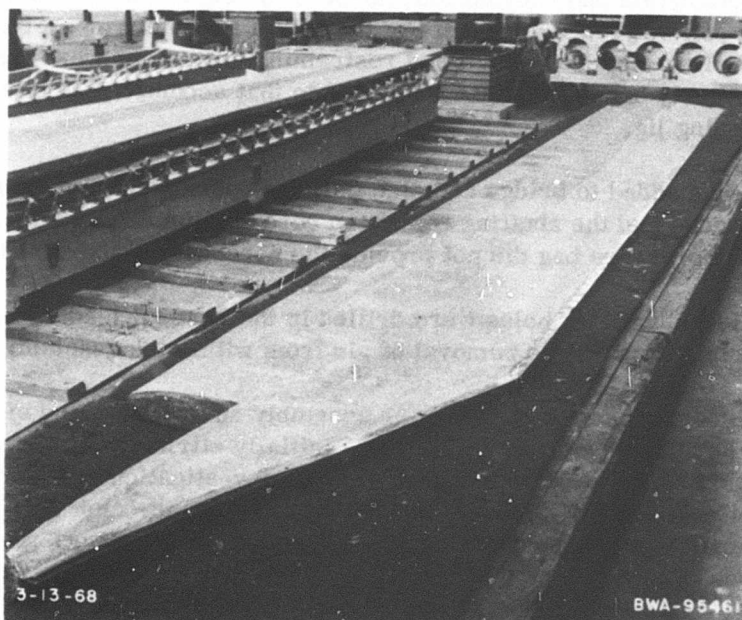


Figure 81. Blade Contour Adjustments With Syntactic Foam.

ultrasonic bond line inspection technique was defined and implemented on subsequent spar/core assemblies. Refer to NDT inspection methods in the quality control section of this report.

Noseblock Assembly

Adhesion of the weighted compound to the internal surface of the noseblock fiberglass shells was found to be inadequate on the three initial assemblies bonded. This deficiency was corrected by changing the matrix of the weighted compound from a silicone rubber to a polysulfide elastomeric material.

The structural adequacy of the modified noseblock weight configuration was demonstrated in whirl testing of sample test specimens on a whirling arm rig to a 1128 "G" load level without evidence of specimen deterioration or damage.

Final Skin Assembly

Original processing plans called for a 17-hour post-cure operation, after the final skin cure, to fully polymerize the 1002S and XP251S material of the spar molding. Results of the first post-cured assembly showed damage to the skin-to-core bond as evidenced by visual detectable fillet stress-induced whiteness and minor skin damage over the inboard foam filler area. These problems were attributed to honeycomb core cell-entrapped air expansion and foam adhesive shrinkage under post cure. Processing changes were made to reschedule the post-cure operation, and the application of the 1002S hoop wrap over the root end fitting zone of the spar, to be done concurrent with the spar-to-core adhesive bond cure cycle, thereby removing the barrier effects of the final skin material. A change in foam adhesive material was also implemented to overcome the shrinkage problem.

Proper pressurization of the two-ply final skins during cure required provisions to overcome any mismatch between the BAJ bonding tool surface contour and the corresponding actual upper surface contour of the cured spar/core/noseblock assembly. These provisions included the use of a thin silicone rubber sheet placed over the entire BAJ tool surface outboard of station 117, and a cast-in-place RTV silicone rubber filler molded onto the tool surface inboard of station 117. For the latter operation, the RTV rubber was poured onto the tool surface, and the actual spar/core/noseblock assembly was then seated in the poured rubber. Following cure, the assembly was removed from the tool and the final skin layup operations were initiated. Entrapped air pockets in the cast-in-place silicone rubber filler resulted in local unbond areas on initial final skin cures. On the next RTV cast operation, the seated assembly was sealed to the tool in a vacuum bag and vacuum was maintained during cure to remove entrapped air. After subsequent final skin cure, some local core damage in this area was detected in X-ray and NDT inspection checks. Controlled slow release of vacuum pressure, at the end of the cast rubber cure cycle, and return to atmospheric pressure, was implemented prior to the application of positive

pressure. No further core damage conditions were experienced in later skin cure operations.

MANUFACTURING EVALUATION

An evaluation of the manufacturing experience and problems encountered during the blade fabrication program is presented below. Included are general guidelines and recommendations for improved producibility and efficiency in manufacturing practices.

1. The major problem areas experienced in the fabrication and usage of the original reinforced plastic tools employed were low heatup rates, porosity (tool leaks), and warp control on large tools with such a high aspect ratio (length to width). However, the replacement aft (BAJ) blade assembly bonding tool (the original tool was destroyed in an autoclave fire in April 1968), built with the benefits of prior tool fabrication and usage experience, performed very satisfactorily. No tool leaks occurred during the eight cure cycles that this tool was used for to complete the AGB fabrication program. Further, this same plastic tool was subsequently used at Boeing-Vertol for an additional 12 similar heat cure cycles in the boron rotor blade fabrication program with no leakage and no evidence of distortion or deterioration. Blade twist angle variations on the four boron rotor blades were minimal, exhibiting a total variation of $0^{\circ}36'$ at station 117 and $0^{\circ}25'$ at station 360. This suggests that factors other than tool design may have been responsible for the higher blade-to-blade twist angle variations experienced on the AGB fabrication program. Significant differences in the autoclave heating systems of the two facilities comprise one such factor. This tool is still serviceable and its life cycle limit is indeterminate. Program experience indicates that the use of properly designed and fabricated reinforced plastic tooling provides a practical and successful means of fabricating a limited quantity of blades.
2. Nonporous metallic tooling offers the benefits of faster heating rates, no leakage problems, ease of attachment of mechanical accessories, and probably some greater dimensional stability over long production runs. For short runs, the cost factors associated with the complex machining of large compound curvature contours to the accuracy and smoothness standards required may be prohibitive, particularly if multiple tools are required as they were in this program. Thermal expansion and contraction compatibility factors can be more significant in the use of metallic tooling versus plastic tooling.
3. Vacuum bagging of the tools with conventional plastic film materials and manually applied sealing tapes was a time-consuming operation and subject to repetitive cases of leaks occurring during cure cycles. Custom-

designed silicone or butyl rubber blankets with integral snap-on vacuum-sealed peripheral joints are recommended. They provide reliability: the vacuum seal joint can be checked independently, can be quickly installed, and is reusable. Care in usage is required to adequately protect the blanket when draping over sharp corners, tool protrusions, etc., and/or avoidance of sharp reentry corners to avoid excessive elongation of the blanket material when full vacuum and pressures are applied.

4. Improved methods of honeycomb core machined thickness gaging are necessary for better dimensional control.
5. Honeycomb core densities must support the vertical and horizontal curing pressures required. Vertical cell walls should be oriented to reduce the angle deviation from 90° to the skin surface to a minimum. Adequate support and chordal restraining provisions of airfoil-shaped core or stabilized core skin parts are necessary during bonding operations
6. The multiple sequential assembly operations used in this development program were pre-planned so that step-by-step process and quality control assessments and evaluations could be made in a timely and effective manner, thereby assuring the structural integrity of the finished product. For further programs, more efficient manufacturing practices and producibility concepts need to be explored. Suggested items include:
 - a. Automation of the spar molding layup. An automated tape-laying machine is currently being developed for this application.
 - b. Redesign of the spar to adapt it for automation of the layup.
 - c. Reduction in multiplicity of assembly operations. Including the nose-blocks in the spar molding is an example.
 - d. Purchase of materials manufactured for the operation, as opposed to adaptation of materials for the general industry. For example, bias-woven wide glass cloth epoxy-impregnated skin material instead of narrow material widths that must be pieced together to form the final laminate.
 - e. Use of compression or injection molded composite materials in lieu of laminated materials for details such as overbalance fitting, tip rib, and tip cover.
 - f. Use of custom-designed forgings for metal components.
 - g. Reduction in use of free-foaming adhesives.

QUALITY CONTROL

INTRODUCTION

Engineering design drawings and an engineering fabrication document⁸ established the engineering requirements for the manufacture of the advanced-geometry blades. The engineering fabrication document defined in detail the material, facilities, manufacturing, fabrication and assembly process, and quality control requirements for the fabrication program.

An inspection plan document⁹ was implemented by the Quality Control Department to identify the inspection characteristics and procedures to be used for the inspection of all details, subassemblies, and finished products. In addition, a blade process control log and records documentation procedures were implemented to record the day-by-day processing of each blade in order to permit full traceability and configuration identification of each blade.

To assure the structural integrity of critical components, nondestructive test methods (NDT) were prescribed for the inspection of spar moldings, core-skin assembly bonding, spar-to-core bonding, and final assembly bonding¹⁰. Both ultrasonic and X-ray techniques were used to determine the presence of voids, delaminates, honeycomb core defects, and unbond areas. Lead-base glass tracer strands were incorporated in the preimpregnated fiberglass materials used in the spar molding to determine, by X-ray, the conformance of the unidirectional fiber orientation in the finished spar molding.

NONDESTRUCTIVE ULTRASONIC INSPECTION METHODS

Core-Skin Assembly Bonding

The initial inspection efforts were made with a Sperry Mini-Wheel mounted in a framework and supported by an Electro-Circuits wand and manipulator. Due to the airfoil configuration of the part, the Mini-Wheel had a tendency to track to one side when running lengthwise on the part. An attempt was made to eliminate the cocking action by building a gimbal framework for the Mini-Wheel and by adding a 3-point roller system to track on the part surface. This modification failed to eliminate the tendency for the Mini-Wheel to mistrack, and the rollers would score the surface when the wheel rocked up on one side.

At this point a bubbler-type, water-column inspection method was initiated. The original design was machined from a brass bar with a Teflon insert through which water flowed and provided a water cushion between the bubbler and the part surface. Unfortunately, water flowing through the bubbler with sufficient pressure to produce a cushion between the bubbler and the part caused an excessively high hash level on the scope.

Various modifications were made to the bubbler system, including a larger volume of water with lower pressure; however, any time that water was flowing past the transducer face, the high hash level was present.

To eliminate the water flow across the transducer face, a static or standing water column was devised.

The initial model was constructed from an aluminum tube. The tube held the transducer and water column and was equipped with a water inlet tube, an air outlet hole above the transducer face, and a felt shoe at the bottom for sliding on the part and sealing the water inside the tube.

The aluminum tubing caused many spurious signals from reflected sound waves, and the felt shoe allowed excessive water seepage; therefore, a tube of polyethylene was used in place of the aluminum, and a closed-cell, sponge-rubber shoe replaced the felt shoe.

This system produced the best results, and the final water-column housing was constructed from phenolic tubing having a 1/8-inch wall thickness. The sponge-rubber shoe had a tendency to drag on the part surface sufficiently to tilt the tube to one side, causing loss of the entrapped water. This problem was remedied by replacing the sponge rubber with a latex rubber prophylactic. Water flow was regulated so that a minimum amount was allowed to overflow from the air bleed hole. This water traveled down the tube and acted as a couplant between the rubber and the part surface.

The parts being inspected were sealed so the water would not enter the honeycomb cells. Care had to be exercised when bringing the rubber into contact with the part, as the contour of the rubber would produce an erroneous signal. The rubber had to be depressed sufficiently on the part surface to produce a flattened area for the passage of the sound waves. This could be seen on the scope as the erroneous signal moved toward the front surface signal when the rubber was depressed.

When inspecting with this system, the scope presentation will be only the initial pulse and front surface signals as long as the bond line is acceptable. Any signal indication noted at a distance equal to the thickness of the part being inspected indicates an unbond or a very weak bond. The test is conducted on the bond line opposite the face upon which the bubbler is in contact.

Figure 82 shows the following components which were developed sequentially for this program: the Sperry Mini-Wheel, prototype bubbler, prototype aluminum tube static water column, polyethylene tube static water column, and two phenolic tube static water columns. All water columns shown have the sponge-rubber contact shoe.

Figures 83 and 84 show the final configuration of the static water column as used throughout the rotor blade inspection program. The core-skin sample upon which the fixture rests in Figure 83 was fabricated with 3/8-, 1/2-, and 1-inch squares of Teflon between the core and skin on the side opposite and directly beneath the X's marked on the surface. These simulated unbonds are readily detectable and can be recorded during automatic scanning with this system. Minimum water flow is regulated by means of the clamp which is visible on the polyethylene tubing leading from the phenolic tube.

Spar Molding

Pulse-echo ultrasonic techniques were used for the nondestructive inspection of the spar. A manual-contact method with a compatible couplant was used for scanning between blade stations 45 and 99, the transition region of the spar. An immersion method employing an adjustable reflector plate positioned inside the C-spar was used between blade stations 99 and 355 (see Figure 85). Automatic scanning and recording were obtained in the latter method by adaptation of the basic equipment shown in Figure 84.

Spar-to-Core Assembly Bonding

A through-transmission ultrasonic technique was used for this inspection. The search units were positioned opposite one another as shown in Figure 86. A glycerine couplant was applied to both sides of the inspection area. In order to verify the side, upper, or lower surface from which any unbond indication occurred, a secondary pulse-echo evaluation was performed from the lower surface. Hand scanning was used, and any areas indicating unbond were mapped for record purposes.

Final Assembly Bonding

A pulse-echo ultrasonic method was used for this inspection on both upper and lower surfaces. Manual contact and scanning methods using a glycerine couplant were used. All ultrasonic indications were physically mapped on each blade as a baseline reference for subsequent ultrasonic inspections performed after the whirl test and flight test phases of the program. Duplicate paper maps were also made for record purposes.

Posttest Inspections

Both ultrasonic and penetrating radiation (X-ray) inspections were performed on the blades at the conclusion of the 50-hour whirl test of the forward blades; after the whirl tower track investigations of both sets of blades, following removal of the titanium erosion strips and replacement with urethane shoes; and after the completion of the flight test program. No significant changes in the ultrasonic maps or other signs of degradation of the blades were found when compared with the pretest baseline inspection findings. Records were kept of all inspections.

DIMENSIONAL INSPECTIONS

The dimensional inspection of all finished blades (less socket) was accomplished in a combination checking fixture and locating jig (see Figure 87). The blade was cradled in a leading-edge-down position by supports located at station 270 and at the root-end fitting. A set of blade-section contour inspection templates, machined 0.25 inch oversize and incorporating optical alignment and pivoting provisions, was located and aligned on the fixture after the blade was in place. Individual templates were then centered relative to the actual blade section by appropriate angular pivoting of the template and selective use of 0.25-inch spacer dowel pins.

Tables V through VIII tabulate the inspection findings on the eight flight blades for twist-angle distribution, trailing-edge cusp angle, and blade-section contours. Section contours were checked with wire gages over discrete chordal zones A, B, and C, as shown in Figure 88.

A spanwise contour deviation was found on the three aft blades, serial Nos. 102-2, 103-2, and 104-2, fabricated in the replacement aft bonding tool. These blades had a concave bow on the upper surface and a corresponding convex bow on the lower surface at station 288, as shown in Figure 89. It was determined that this deviation was due to a similar deviation in the plastic pattern used in fabricating the replacement bonding tool and was ultimately traced to a process error in the transfer splash taken from the plaster master.

BLADE WEIGHT

Table IX shows a weight summary breakdown for the eight flight blades. Actual weights of the major details and subassemblies of each blade as well as the total blade weight are shown and can be compared to the nominal design calculated weight. Calculated weights include all of the process changes adopted in the fabrication development program and accordingly reflect the actual configuration of the as-fabricated blades. Average weights, total weight variation, and the percentage of weight variation from the average weight are shown to indicate the levels of weight variability experienced.

The average as-manufactured blade weight exceeded the calculated blade weight by approximately 5.5 percent. This increase can be attributed to the cumulative effects of small differences between actual and calculated fiberglass laminate densities; a higher average core-skin assembly weight due to additional skin resin in core cells from reskinning operations; higher resin content in final skin material; greater variability in adhesive foam bond and core splice joints; and compensating increase in variable noseblock weights.

The approximately 2-percent variation in the as-manufactured blade weights and span moments exhibits a low variability level and shows that good repeatability is

attainable in composite blade construction. These results were attained without any selectivity of component weights used in a particular blade. The higher blade weight variation (2.32 percent) on the as-flown blades can be attributed to the instrumentation weight on blades Nos. 105-1 and 103-2.

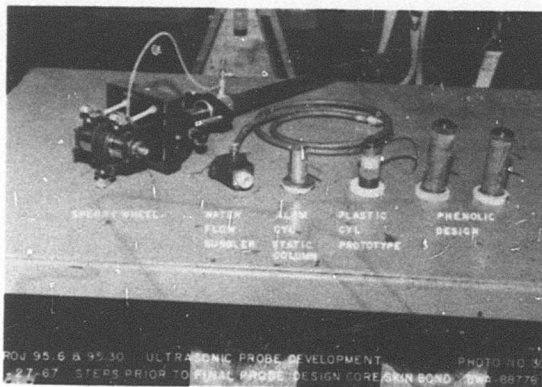


Figure 82. Components Developed for Ultrasonic Inspection.

Figure 83. Final Ultrasonic Probe With Phenolic Static Water Column.

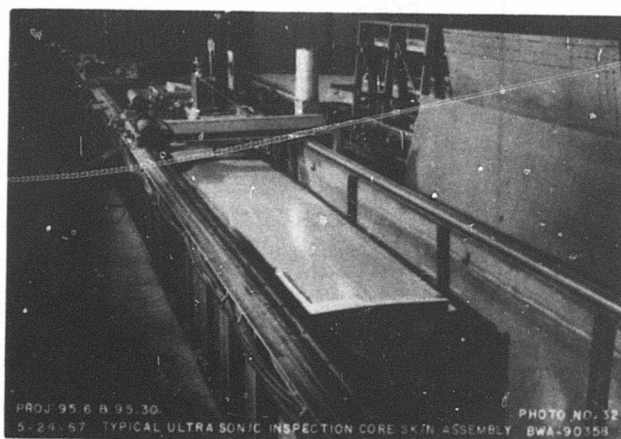
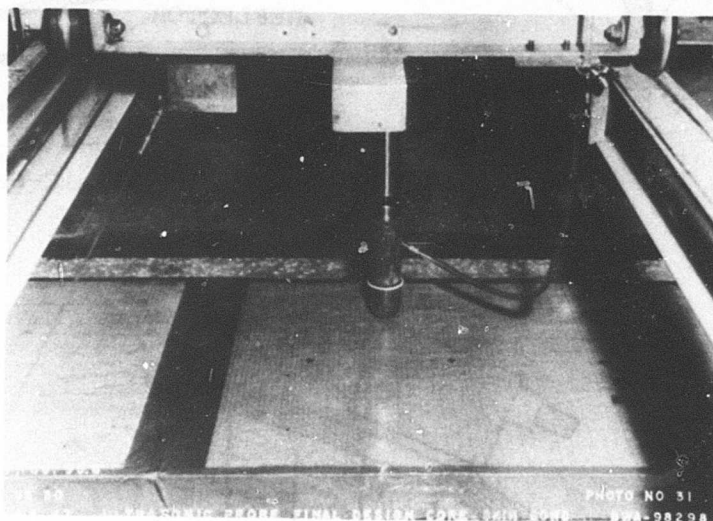


Figure 84. Ultrasonic Inspection of Blade Core-Skin Assembly.

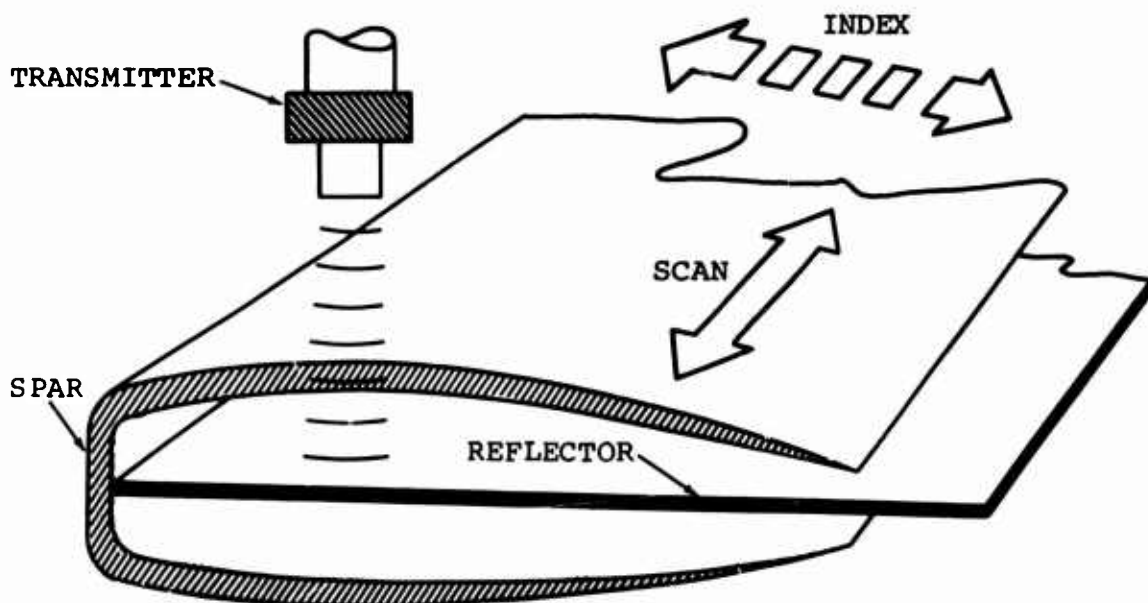


Figure 85. Inspection of the C-Shaped Spar.

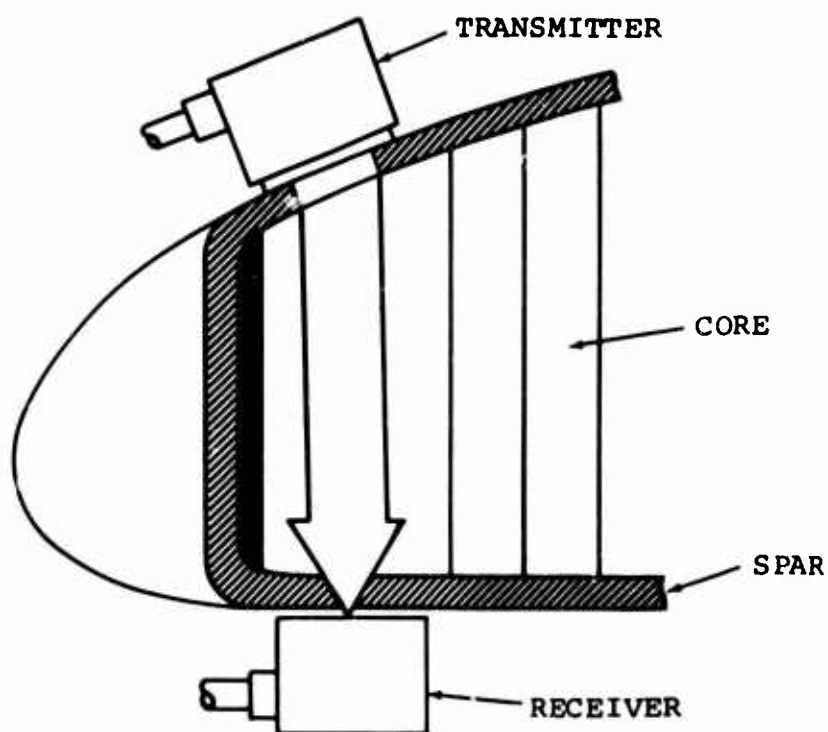


Figure 86. Inspection of the Spar-Core Assembly.

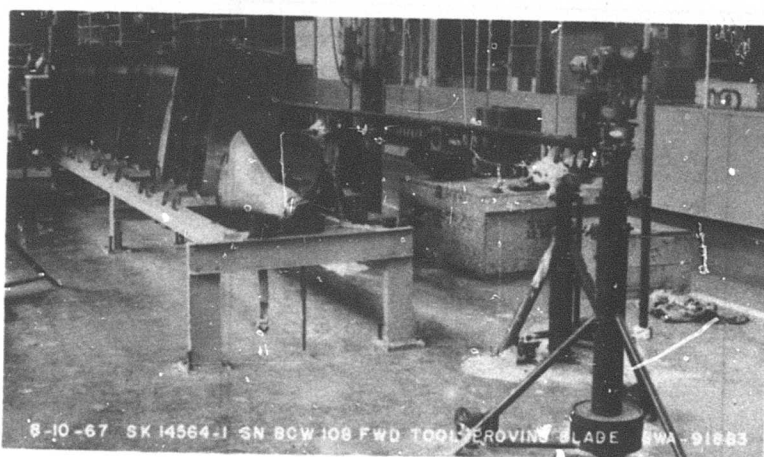


Figure 87. Dimensional Inspection of the Finished Blade.

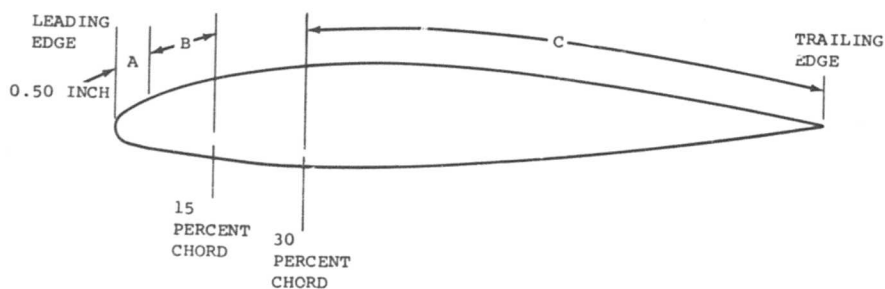


Figure 88. Blade Measurements for Section Contour Check.

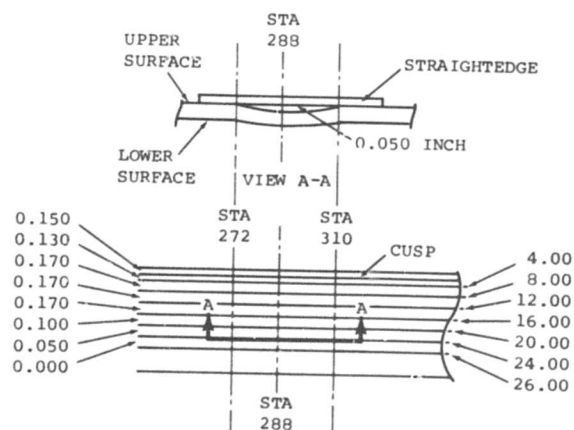


Figure 89. Contour Variation of the Aft Blades.

TABLE V. TWIST-ANGLE DISTRIBUTION OF THE ADVANCED-GEOMETRY BLADES									
Blade Station	Design Twist ± 0 deg, 10 min (deg, min)	Actual Twist (deg, min) Forward Blades Serial Nos.				Actual Twist (deg, min) Aft Blades Serial Nos.			
		102-1	104-1	105-1	106-1	102-2	103-2	104-2	105-2
117	13 03	13 33	12 51	14 00	13 15	13 42	13 02	12 55	13 05
144	12 36	13 05	12 31	13 26	12 45	13 18	12 47	12 40	12 55
160	12 20	12 38	12 14	13 01	12 28	13 01	12 34	12 30	12 03
175	12 05	12 24	12 10	12 50	12 20	12 41	12 30	12 18	12 27
200	11 40	11 53	11 45	12 17	11 56	12 25	12 08	12 04	12 00
216	11 24	11 28	11 20	11 48	11 33	11 46	11 53	11 38	11 24
225	11 15	11 20	11 12	11 36	11 23	11 31	11 41	11 25	11 17
246	10 54	10 48	10 54	11 05	11 04	10 58	11 33	11 01	11 21
264	10 36	10 23	10 36	10 44	10 43	10 32	10 57	10 41	10 46
276	10 24	10 18	10 30	10 16	10 33	10 23	10 52	10 34	10 46
288	10 12	10 04	10 26	10 26	10 24	10 22	10 55	10 43	10 13
300	10 00	9 44	10 17	10 11	10 18	10 02	10 48	10 32	10 38
312	9 48	9 25	10 18	9 58	10 20	9 31	10 35	10 15	10 20
324	9 36	9 10	10 09	9 41	10 15	9 06	10 26	10 02	9 39
360	9 00	8 11	10 05	8 44	10 06	8 22	10 27	10 09	9 14

TABLE VI. TRAILING-EDGE CUSP ANGLE OF THE ADVANCED-GEOMETRY BLADES									
Blade Station	Design Cusp Angle ± 0 deg, 15 min (deg, min)	Actual Cusp Angle (deg, min) Forward Blades Serial Nos.				Actual Cusp Angle (deg, min) Aft Blades Serial Nos.			
		102-1	104-1	105-1	106-1	102-2	103-2	104-2	105-2
117	3 00	-	-	4 10	2 45	3 05	3 58	3 10	-
144	3 00	3 14	3 50	5 03	3 50	3 06	5 41	3 09	3 54
160	3 00	3 00	3 55	5 00	3 51	3 40	4 05	3 40	2 59
175	3 00	2 50	4 31	5 20	3 45	3 50	4 08	3 30	2 49
200	3 00	2 43	3 30	6 05	3 06	3 30	3 27	3 45	3 06
216	3 00	3 51	4 39	4 50	3 30	3 36	3 23	3 10	3 20
225	3 00	2 45	3 15	4 45	2 55	3 34	3 23	3 00	3 06
246	3 00	2 20	3 40	5 30	3 45	3 10	4 08	3 05	2 59
264	3 00	2 25	3 30	4 46	3 10	2 58	4 49	3 10	3 20
276	3 00	3 03	3 50	4 45	3 30	2 56	-	2 55	4 29
288	3 00	3 20	3 25	5 20	3 00	3 00	4 32	3 32	3 51
300	3 00	2 52	3 15	3 20	3 45	2 56	3 20	3 30	3 25
312	3 00	2 40	3 12	3 50	3 15	3 05	3 39	3 15	3 20
324	3 00	3 00	3 30	3 40	3 10	3 00	3 54	3 30	3 17
360	3 00	2 55	3 45	5 45	3 06	3 09	2 21	3 20	3 17

TABLE VII. SECTION: CONTOUR DATA ON THE FORWARD ADVANCED-GEOMETRY BLADES																			
Blade Station	Contour Surface	A -0.005				B +0.015				C +0.03									
		102-1	104-1	105-1	106-1	Lower	Upper	102-1	104-1	105-1	106-1	Lower	Upper	102-1	104-1	105-1	106-1	Lower	Upper
117		+0.001	0	-0.064	-0.027	-0.021	+0.030	-0.041	0	-0.056	-0.017	+0.011	+0.029	-0.079	-0.028	-0.019	+0.029	+0.009	+0.018
144		+0.001	0	-0.025	-0.008	+0.048	+0.017	-0.041	-0.016	-0.098	-0.048	-0.001	-0.004	-0.051	-0.042	-0.051	-0.042	-0.041	-0.032
160		-0.001	0	-0.020	+0.004	+0.024	+0.007	-0.031	0	-0.027	-0.020	+0.042	-0.008	-0.063	-0.035	-0.042	-0.054	-0.043	-0.063
175		0	0	-0.017	-0.007	+0.040	-0.001	+0.001	+0.018	-0.007	+0.013	+0.013	+0.013	-0.036	-0.013	+0.018	+0.023	+0.035	+0.023
200		-0.001	0	-0.008	-0.002	+0.030	+0.005	-0.017	+0.003	-0.016	-0.003	+0.042	-0.008	-0.012	-0.013	-0.013	-0.047	-0.043	-0.055
216		+0.001	0	-0.021	+0.009	0	+0.003	-0.015	+0.024	-0.04	-0.042	+0.075	+0.033	-0.025	-0.005	+0.012	+0.017	-0.028	-0.041
225		+0.001	0	-0.021	+0.005	+0.016	+0.006	-0.030	-0.011	-0.002	+0.029	+0.017	-0.018	-0.029	-0.005	-0.002	+0.036	-0.011	-0.041
246		-0.001	0	+0.027	+0.021	-0.002	+0.020	-0.030	-0.015	-0.043	-0.006	-0.045	-0.043	-0.050	-0.025	-0.024	+0.007	+0.017	+0.005
264		0	0	+0.006	+0.005	-0.038	-0.020	-0.014	+0.009	+0.001	+0.015	+0.045	-0.038	-0.053	-0.022	-0.024	+0.001	0	-0.016
276		0	0	+0.024	+0.010	-0.018	+0.010	-0.012	+0.018	+0.043	+0.015	-0.051	-0.023	-0.047	-0.012	-0.007	0	+0.009	+0.010
288		0	0	+0.015	+0.010	-0.024	+0.025	-0.003	+0.005	+0.046	+0.020	+0.013	-0.015	-0.032	+0.005	+0.002	+0.003	+0.021	+0.011
300		+0.001	0	+0.050	+0.013	-0.035	+0.025	-0.015	0	+0.036	+0.045	-0.029	-0.035	-0.029	+0.003	-0.002	+0.023	+0.013	-0.010
312		-0.001	0	+0.004	+0.013	-0.035	+0.035	-0.015	-0.003	+0.058	+0.037	-0.056	-0.021	-0.043	+0.001	-0.003	+0.008	-0.022	+0.032
324		0	0	-0.003	+0.011	-0.021	+0.017	-0.004	+0.023	-0.034	-0.006	+0.017	+0.002	-0.025	-0.021	-0.010	-0.043	-0.032	-0.024
360		0	0	-0.118	-0.039	-0.066	0	-0.005	-0.020	+0.002	+0.033	+0.060	+0.009	0	+0.016	+0.009	+0.004	+0.001	+0.019
										-0.035	-0.002	-0.015	-0.013	0	+0.011	+0.016	+0.008	+0.023	-0.025
										-0.075	-0.065	+0.132	+0.134			-0.035	-0.038	-0.036	+0.085

Notes: 1. All dimensions in inches

2. + value = oversize from nominal, - value = undersize from nominal

3. When 2 values are given, they indicate the maximum and minimum variation over the designated length.

4. Lower surface measurements not obtained on blades serial Nos. 102-1 and 104-1

- Notes: 1. All dimensions in inches
2. + value = oversize from nominal, - value = undersize from nominal
3. When 2 values are given, they indicate the maximum and minimum variation over the designated length.
4. Lower surface measurements not obtained on blades serial Nos. 102-1 and 104-1

TABLE VIII. SECTION CONTOUR DATA ON THE AFT ADVANCED-GEOMETRY BLADES																			
Blade Station	Co. Sur Surface Serial No.	A -0.005			B +0.015			C +0.03											
		Upper 102-2	Upper 103-2	Upper 104-2	Lower 102-2	Lower 103-2	Lower 104-2	Upper 102-2	Upper 103-2	Upper 104-2	Lower 102-2	Lower 103-2	Lower 104-2						
117		+0.015	+0.023	+0.009	+0.003	-0.032	+0.010	+0.005	+0.018	+0.013	-0.042	-0.032	-0.007	-0.060	+0.005	+0.014	+0.046	+0.030	+0.032
144		+0.020	+0.010	-0.005	-0.029	-0.015	+0.025	-0.018	+0.010	+0.007	-0.044	-0.018	-0.006	-0.009	-0.005	-0.005	-0.001	-0.055	0
160		-0.007	-0.003	-0.008	+0.005	+0.002	+0.050	-0.010	0	-0.037	-0.037	0	+0.025	-0.018	-0.024	-0.012	-0.018	-0.005	-0.007
175		+0.007	-0.012	+0.004	+0.005	-0.010	+0.006	-0.017	0	-0.027	-0.043	+0.010	-0.060	-0.008	-0.044	-0.028	-0.020	-0.075	+0.014
200		+0.011	+0.001	-0.022	-0.005	+0.018	-0.007	-0.008	-0.003	-0.015	-0.035	-0.027	-0.010	-0.010	-0.002	-0.003	-0.008	-0.037	+0.004
216		-0.001	-0.015	-0.024	+0.001	+0.012	-0.026	-0.065	-0.010	-0.036	-0.024	-0.014	-0.005	-0.033	-0.002	0	-0.027	-0.005	-0.007
225		+0.008	+0.007	+0.030	+0.001	-0.006	-0.017	-0.052	-0.005	-0.017	-0.027	+0.022	-0.010	-0.005	-0.007	0	-0.010	-0.020	+0.002
246		+0.017	+0.022	+0.022	-0.020	-0.015	-0.050	-0.015	-0.009	-0.017	-0.027	+0.011	-0.016	-0.015	-0.007	+0.015	+0.028	-0.035	+0.004
264		+0.035	+0.064	+0.035	-0.019	-0.023	-0.057	+0.001	+0.003	+0.020	-0.015	+0.001	-0.060	-0.033	-0.016	+0.005	+0.013	-0.055	-0.016
276		+0.035	+0.037	+0.018	-0.005	-0.043	-0.057	+0.103	+0.149	+0.099	-0.014	+0.043	+0.010	-0.050	-0.028	-0.016	+0.010	+0.009	+0.005
288		+0.025	+0.035	+0.018	-0.003	-0.025	-0.035	+0.019	+0.006	+0.033	-0.003	-0.017	-0.073	-0.011	-0.006	-0.003	-0.010	-0.023	-0.025
300		+0.004	+0.001	+0.018	+0.005	-0.038	-0.025	+0.132	+0.145	+0.099	-0.003	+0.018	+0.015	+0.017	0	-0.009	+0.033	-0.020	0
312		+0.004	-0.011	+0.017	-0.001	-0.008	-0.007	+0.042	+0.007	+0.039	-0.015	-0.043	-0.095	+0.001	-0.010	-0.001	+0.001	-0.002	-0.019
324		+0.004	+0.007	+0.009	+0.005	-0.022	-0.031	+0.091	+0.072	+0.098	-0.015	-0.025	+0.018	-0.050	+0.020	+0.005	+0.009	+0.041	+0.045
360		-0.087	-0.079	-0.082	-	0	+0.044	+0.022	+0.008	+0.030	-0.028	-0.024	-0.020	-0.010	-0.014	+0.032	+0.002	+0.004	+0.014
								+0.067	+0.063	+0.079	-0.028	-0.055	-0.097	+0.004	+0.010	-0.028	+0.047	+0.060	+0.060
								+0.025	0	+0.030	-0.025	-0.045	-0.050	-0.002	-0.018	-0.010	+0.005	-0.006	+0.011
								+0.037	+0.030	+0.032	-0.025	+0.014	+0.035	+0.029	+0.005	+0.019	+0.033	+0.008	-0.011
								-0.017	-0.022	-0.016	+0.007	+0.010	+0.019	-0.012	-0.004	-0.020	+0.015	-0.015	-0.001
								-0.043	+0.035	+0.091	+0.007	-0.036	+0.002	+0.040	+0.001	+0.027	+0.035	+0.033	+0.019
								-0.004	0	-0.004	-0.007	-0.025	+0.002	-0.003	-0.010	+0.003	+0.025	-0.033	-0.011
								-0.045	+0.006	-0.059	-0.037	+0.021	+0.190	+0.034	+0.010	+0.030	-0.035	+0.043	+0.008
								-0.033	-0.064	-0.032		-	+0.025	-0.012	-0.002	-0.027	-0.018	-0.021	-0.019

Notes:

- All dimensions in inches
- + value = oversize from nominal; - value = undersize from nominal
- When 2 values are given, they indicate the maximum and minimum variation over the designated length.
- Lower surface measurements not obtained on blades serial Nos. 103-2 and 105-2

- Notes:
1. All dimensions in inches
 2. + value = oversize from nominal; - value = undersize from nominal
 3. When 2 values are given, they indicate the maximum and minimum variation over the designated length.
 4. Lower surface measurements not obtained on blades serial Nos. 103-2 and 105-2

Major Details and Subassemblies	Nominal Calculated Weight (lb)	Actual Weight (lb)				Actual Weight (lb)				Average Weight (8 Blades) (lb)	Total Variation (lb)	Spread From Average Weight (percent)
		102-1	104-1	105-1	106-1	102-2	103-2	104-2	105-2			
Root-End Fitting	12.50	13.02	13.15	13.12	13.24	13.03	13.13	13.12	13.17	13.12	0.22	1.68
Tip Anchor Fitting	1.45	1.56	1.53	1.58	1.53	1.45	1.45	1.48	1.48	1.51	0.13	8.61
Spar Molding	139.66	137.45	142.14	142.11	144.46	143.14	141.44	142.94	137.86	141.44	7.01	4.96
Spar Assembly	153.61	155.51	160.11	160.23	162.17	160.79	159.35	160.85	155.77	159.35	6.66	4.17
Honeycomb Core (With Tool Tab)	42.50	42.97	44.43	44.19	43.83	41.98	45.27	44.91	43.85	43.93	3.29	7.49
Core-Skin Assembly	56.87	61.73	62.54	60.85	59.98	61.05	60.28	61.58	60.59	61.08	2.56	4.19
Overbalance Fitting	4.63	3.97	3.94	3.99	4.15	3.97	3.93	4.05	4.07	4.01	0.22	5.49
Spar-Core Assembly	226.48	233.19	238.57	237.44	241.48	237.12	236.67	239.02	238.63	237.77	8.29	3.49
Fixed Nose Weights	10.15	10.08	10.05	10.10	10.18	9.92	10.06	10.05	10.20	10.08	0.28	2.78
Variable Nose Weights	32.45	36.09	34.90	35.11	33.75	34.96	34.18	35.62	34.40	34.87	2.34	6.71
Final Skins	26.06	28.83	28.99	28.92	27.78	30.02	29.14	29.29	28.40	28.92	2.24	7.75
Erosion Strips	6.83	6.70	6.08	5.87	5.99	5.75	6.33	5.69	6.70	6.14	1.01	16.45
Trailing-Edge Cusp Laminates	1.65	1.83	1.78	1.84	1.71	1.69	1.65	1.68	1.69	1.73	0.19	10.98
Blade Socket	39.40*	39.10	39.40	39.55	39.45	39.31	39.40	39.64	39.34	39.40	0.54	1.37
Blade Weight As Manufactured**	361.43	375.96	380.39	382.30	380.14	381.62	382.25	383.14	383.02	381.10	7.18	1.88
Blade Span Moment As Manu- factured	62,264	64,941	65,257	65,635	65,167	65,838	65,916	66,284	66,294	65,667	1,353	2.06
Blade Weight As Flown***	-	370.72	374.02	379.44	373.97	373.37	378.50	374.66	374.32	374.88	8.72	2.32
Blade Span Moment As Flown	-	63,532	63,532	63,532	63,532	63,734	63,734	63,734	63,734	-	-	-

* Actual average value used

** Includes full complement of balance weights

*** Urethane leading-edge shoes installed in lieu of titanium erosion strips

Note: Weight of blades serial Nos. 105-1 and 103-2 as flown includes 6.5 lb of instrumentation.

STRUCTURAL TESTING

The structural testing program was conducted to substantiate the structural integrity of the fiberglass advanced-geometry blade and to establish safety of flight. The program consisted of static and fatigue tests of full-scale blades and blade components.

STATIC TESTS

Static testing consisted of (1) an ultimate test of a blade root end section, (2) blade natural frequency determination, (3) blade section moduli determination, (4) trailing-edge buckling test, and (5) static proof load test.

Root End Ultimate Test

The purpose of this test was to confirm the ultimate strength of the root end retention system, the strength of the fiberglass spar, and the strength of the blade tip construction. The preliminary design strength was 100,000 pounds, which simulated centrifugal force at 230 rpm. The limit load was 156,700 pounds and the ultimate load was 235,000 pounds.

The test specimen was a spar tool proving* root end consisting of the socket, root end fitting and spar. The fitting and socket were fabricated per drawings SK14568 and SK14569, respectively, but the parts were not shot-peened and a layer of adhesive was missing at the spar-root end fitting interface. The spar was identical to the full-scale spar with inner and outer torsion wraps except for its length. The unidirectional plies of the spar were stepped down in the spanwise sense, and seven plies were carried over an outboard draw block which was designed and installed to simulate the tip anchor fitting of the full-scale spar. Honeycomb core, core stabilizer, and blade skins were not included in this test specimen.

The specimen was mounted vertically in a Baldwin test machine with the root end attachment at the bottom and the draw block at the top (see Figure 90). A line was scribed on the spar at the end of the socket at blade station 48. Relative motion between the metal socket and the composite spar could be noted by a change of position of the scribed line. Initially the load was run up to 190,000 pounds incrementally and returned to 10,000 pounds. Then the load was increased incrementally until failure. At each load level the specimen was visually examined.

The results of the test are the following:

1. At 232,000 pounds, there was a loud report. The probable explanation was separation of the spar from the root end fitting (98.8 percent of ultimate load).

*This root end section was made to validate the fabrication procedures and to prove the dimensional accuracy of the spar tool.

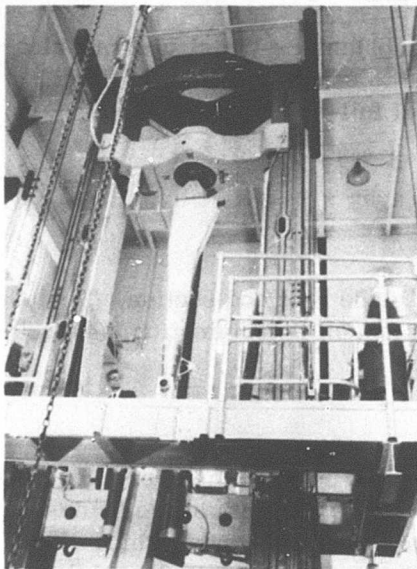


Figure 90. Ultimate Test of Root-End Section of the Advanced-Geometry Blade.

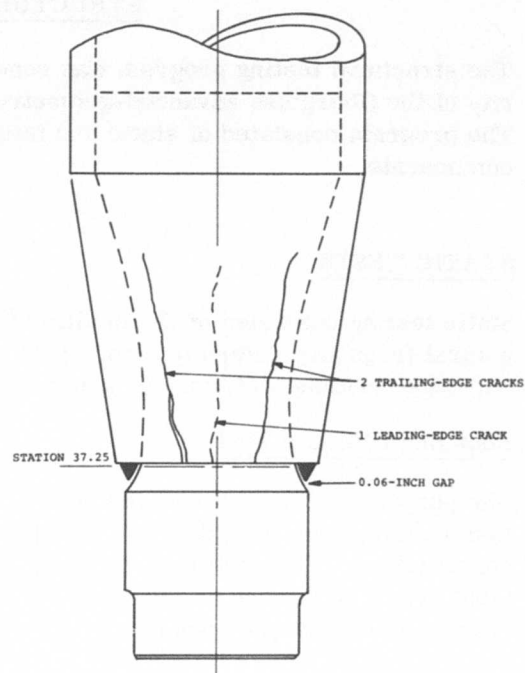


Figure 91. Spanwise Crack System in Test Root-End Section.

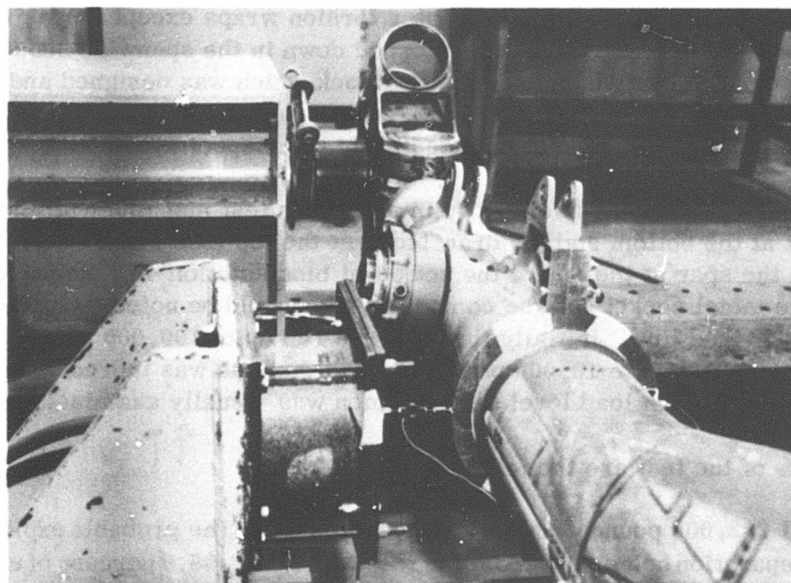


Figure 92. Shaker Setup for Vibration of Blade in Flapwise Direction.

2. At 240,000 pounds, inspection showed an outboard movement of the spar of approximately 0.100 inch (102 percent of ultimate load).
3. At 320,000 pounds, the movement of the spar was measured as 0.130 inch (136 percent of ultimate load).
4. At 330,000 pounds, the movement measured 0.16 inch (140 percent of ultimate load).
5. At 335,000 pounds, the nuts attaching the outboard draw block of the test apparatus failed and the test was halted (143 percent of ultimate load).

After removal of the socket, inspection of the tapered portion of the spar disclosed a crack system traveling in the spanwise direction. There were two trailing-edge cracks and one leading-edge crack, as shown in Figure 91. The inspection also showed a 0.06-inch translation of the pretest root end fitting position relative to the spar and a bond area of only 10-15 percent of the specified bond area between the socket and spar.

For a design limit centrifugal force of 156,700 pounds, the test article withstood 148 percent of limit load without any type of failure and was capable of carrying 143 percent of ultimate load. This strength was developed despite omission of adhesive at the spar-root end fitting interface (see Figure 91). Thus, the limit and ultimate strengths of the root end section were demonstrated under simulated loading. In addition, the simulated blade tip-anchor fitting did not fail at 335,000 pounds, and its potential strength capability was demonstrated.

Blade Nonrotating Natural Frequency Test

This test was performed to determine the nonrotating natural frequencies of the advanced-geometry blade in the flapwise, chordwise, and torsional directions.

An advanced-geometry forward blade, P/N SK14564-1, S/N 107-1, was used as the test specimen. It was attached to a modified CH-47 rotor hub assembly, which was rigidly mounted to support structure as shown in Figure 92. The blade was oriented with the trailing edge upward throughout the test. A bungee chord was used to support the blade in the flapwise and chordwise tests, and tip clamps and cables were used in the torsional tests.

For the flapwise test, the input force was oriented in the horizontal direction and was applied at blade station 46.5. The shaker frequency was scanned from 5 cps to 60 cps, while maintaining a constant input force. The resonant frequencies were determined and recorded.

The shaker was oriented vertically for an input force at blade station 46.5 for the chordwise test and was positioned near the trailing edge at the blade tip for the torsional test. The same test procedures as mentioned above were used.

The test results are shown in Figures 93, 94 and 95 for the flapwise, chordwise and torsional natural frequencies, respectively. A comparison is made in the above figures with the analytical natural frequencies of two blade designs, 42E and 43. Design 42E refers to prefabrication design, and design 43 is the final "as fabricated" blade design.

In Figure 93 the analytical first and second flapwise natural frequencies of designs 42E and 43 agree with the results of the natural frequency test. In the chordwise direction the first-mode natural frequency of the shake test falls between the two designs, while the second-mode frequency is greater than the predicted frequencies in both designs (Figure 94). In Figure 95 the first-mode torsional frequency obtained by testing slightly exceeds designs 43 and 42E. The predicted second torsional mode of design 43 is greater than the corresponding test result.

The test results confirm the predicted first and second nonrotating flapwise frequencies and indicate that design 43 is probably the best representation of the blade flapwise frequency distribution. The blade's first chordwise frequency is probably between design 42E and design 43. The chordwise stiffness distributions shown in the next section support this statement. The nonrotating first-mode torsional frequency approximates the design 43 prediction and indicates that design 43 is the better representation of the blade torsional frequency distribution.

Blade Section Moduli Test

The section moduli test was performed to determine the flapwise and chordwise stiffness distribution of the AGB and to verify the analytical stiffness calculations.

Blade S/N 106-1 was used as the test specimen and was instrumented at locations around the cross section at blade stations 50, 71, 94, 117, 180, 252, 288 and 324. After instrumentation, the blade was mounted as a cantilever beam in the test fixture. The blade was supported at the root end by a modified CH-47 pitch housing and vertical pin. Motion of the vertical pin was prevented by an adjustable link between the lag damper attachment points. The test setup is shown in Figure 96.

For the chordwise stiffness test, the chord reference line at each blade station mentioned above was set in a vertical position. A static load of 200 pounds was applied at station 355, and the gage outputs were monitored and recorded. This procedure was repeated with small changes in chord reference line position ($<2^\circ$) because the data from the first test indicated that this parameter could substantially influence the test results.

In the flapwise stiffness test, the chord reference line was set horizontally at each blade station to be evaluated. Two hundred pounds of static load was applied at station 355, and the gage output was monitored and recorded. The data indicated that the chordline position was not critical. For verification, the flapwise stiffness measurement at

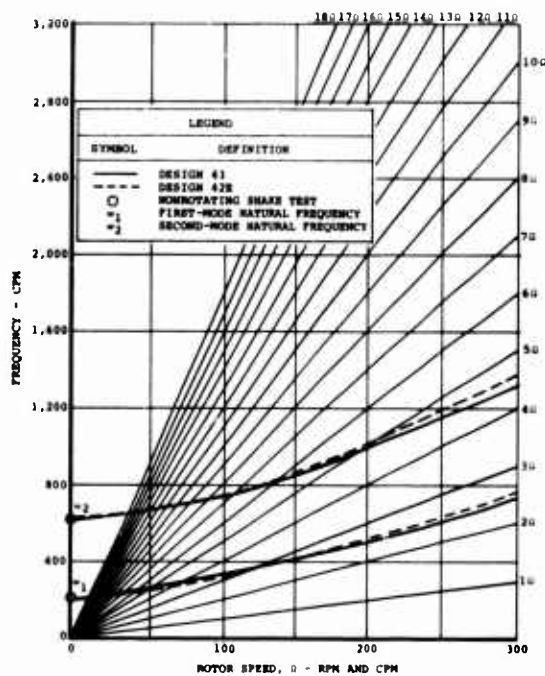


Figure 93. Flapwise Natural Frequency Spectrum of the Advanced-Geometry Blade.

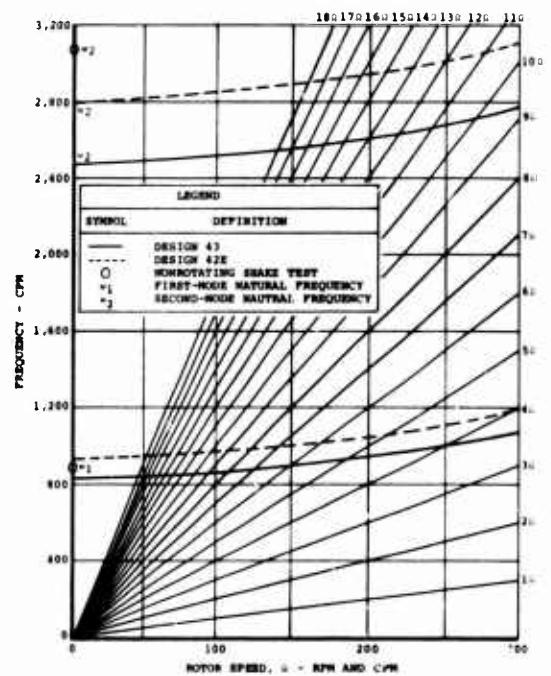


Figure 94. Chordwise Natural Frequency Spectrum of the Advanced-Geometry Blade.

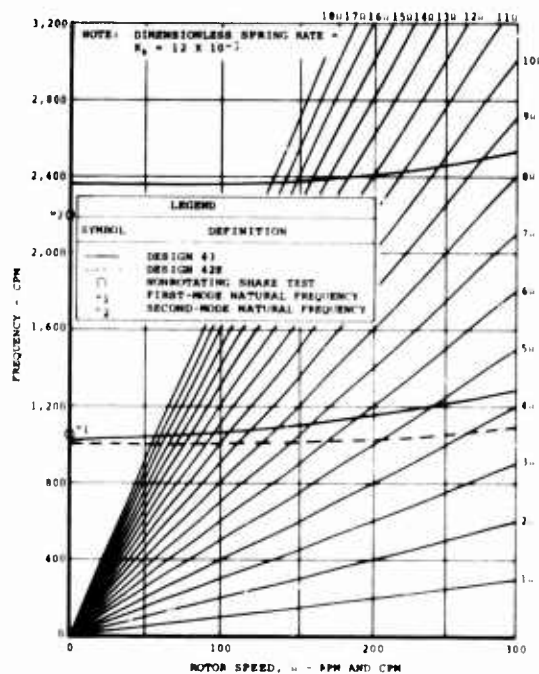


Figure 95. Torsional Natural Frequency Spectrum of the Advanced-Geometry Blade.

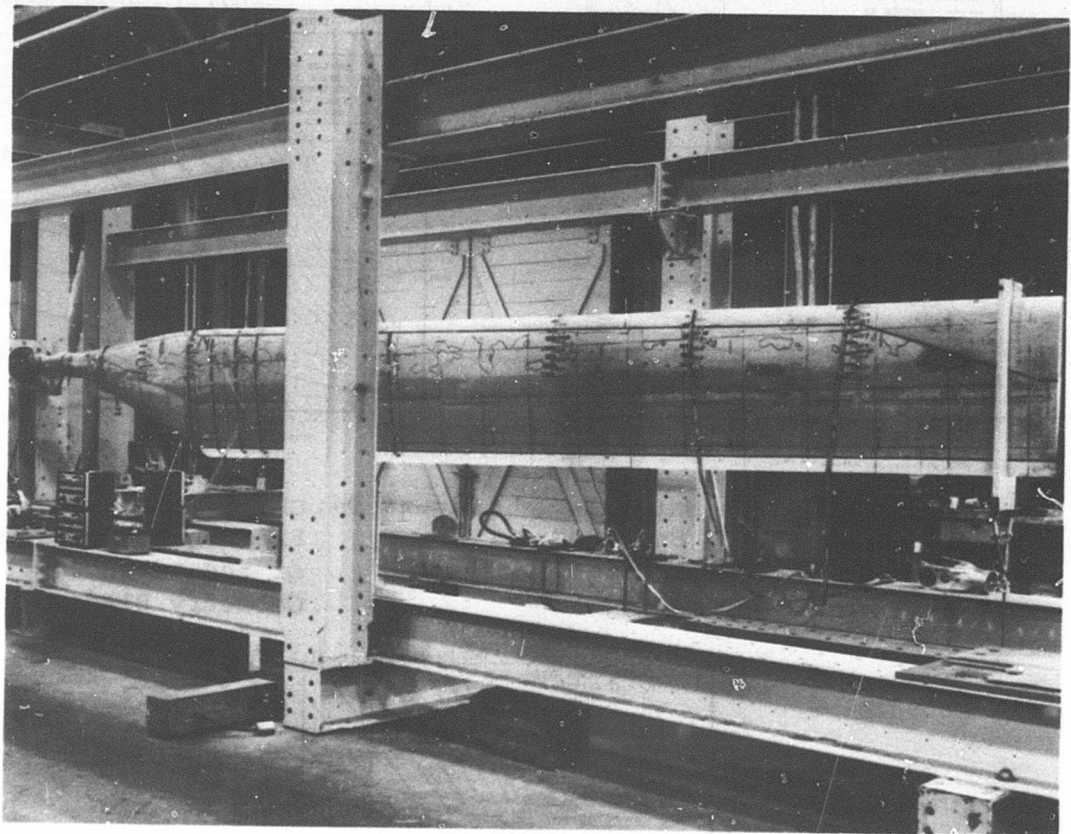


Figure 96. Setup for Test of Blade Section Moduli.

blade station 180 was repeated with a rotation of approximately 2° in chordline position. The change in flapwise stiffness was 1.2 percent, which confirmed the initial observations.

The test results of flapwise stiffness are compared with the flapwise stiffness predictions of design 43 in Figure 97. There is a good agreement between the two distributions. In Figure 98 the chordwise test results are compared with the analytical stiffness of designs 42E and 43. The experimental chordwise stiffness showed a wide range of values from station 117 to 324. This was caused by varying the angle between the chord reference line and the load, which was acting vertically. Analytically, the magnitude of such variations would not be expected because the angles were very small. As a result, it was difficult to determine an accurate predicted stiffness distribution. For design 42E, the calculated distribution from station 117 to 324 approaches the maximum test values, while the design 43 distribution is generally lower than the minimum test values. This discrepancy in chordwise stiffness is reflected in the nonrotating natural frequency test described previously. The test point falls between the frequencies predicted by the two designs.

In conclusion, the section modulus test for the flapwise stiffness showed good agreement with analytical prediction. For the chordwise test, the stiffness distribution was apparently the average between the values calculated for design 42E and 43.

Trailing-Edge Buckling Test

The objective of this test was to evaluate the buckling stability of the trailing edge under rotor starting conditions.

The trailing-edge buckling test consisted of supporting the blade, S/N 107-1, as a cantilever beam with the leading edge upward and applying loads at blade station 351 until a maximum load of 200 pounds was reached. No indications of buckling were observed throughout the above loading.

The chordwise moment due to the above loading conditions (200 pounds plus the weight of the blade) is plotted and compared with the calculated ultimate chordwise moment on the blade due to the starting condition (Figure 99). The curves show that the chordwise moment which resulted from the buckling test is significantly greater than the calculated starting chordwise moments.

The test results indicated that the blade trailing edge would withstand the starting chordwise moment without buckling.

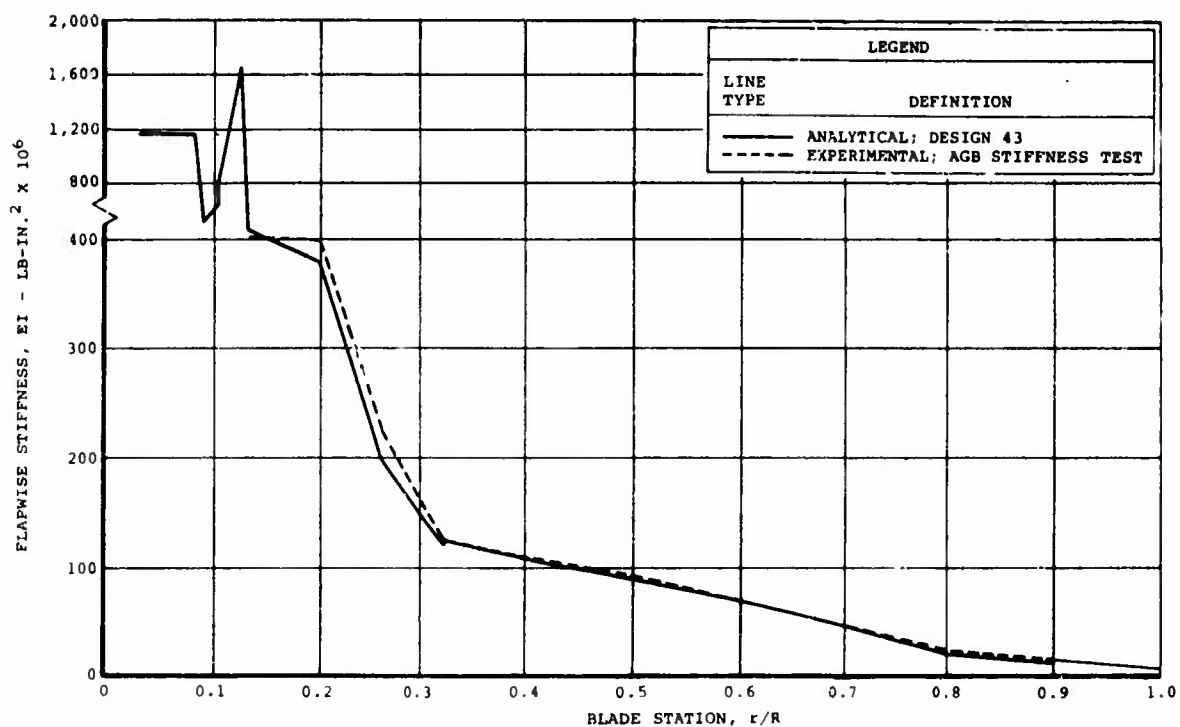


Figure 97. Radial Variation of Flapwise Stiffness of the Advanced-Geometry Blade.

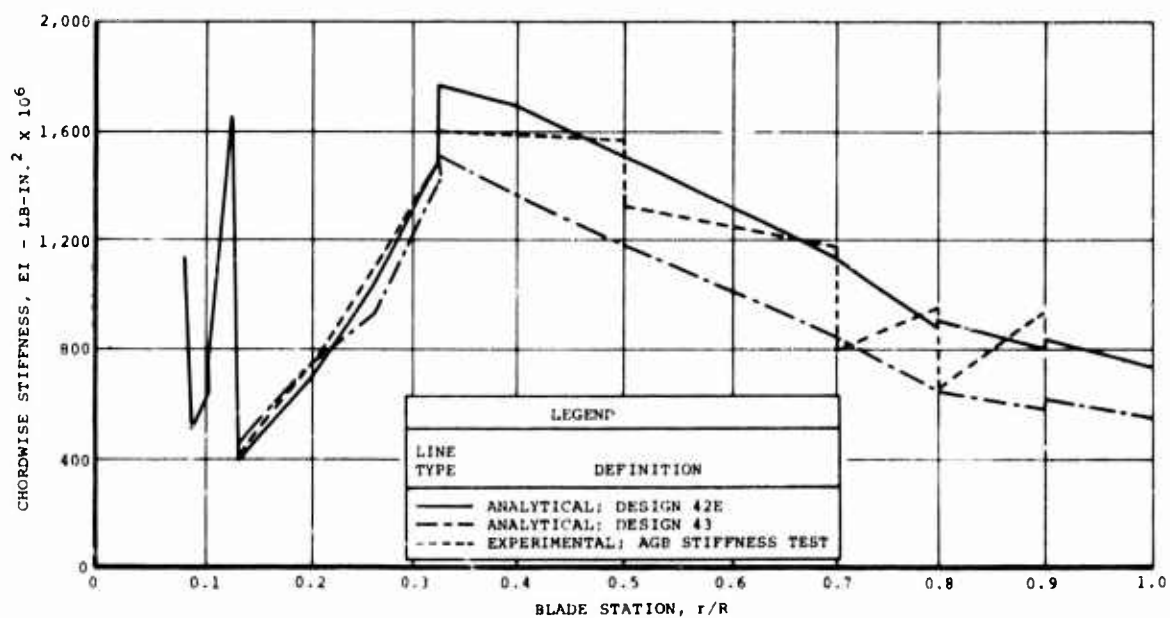


Figure 98. Radial Variation of Chordwise Stiffness of the Advanced-Geometry Blade.

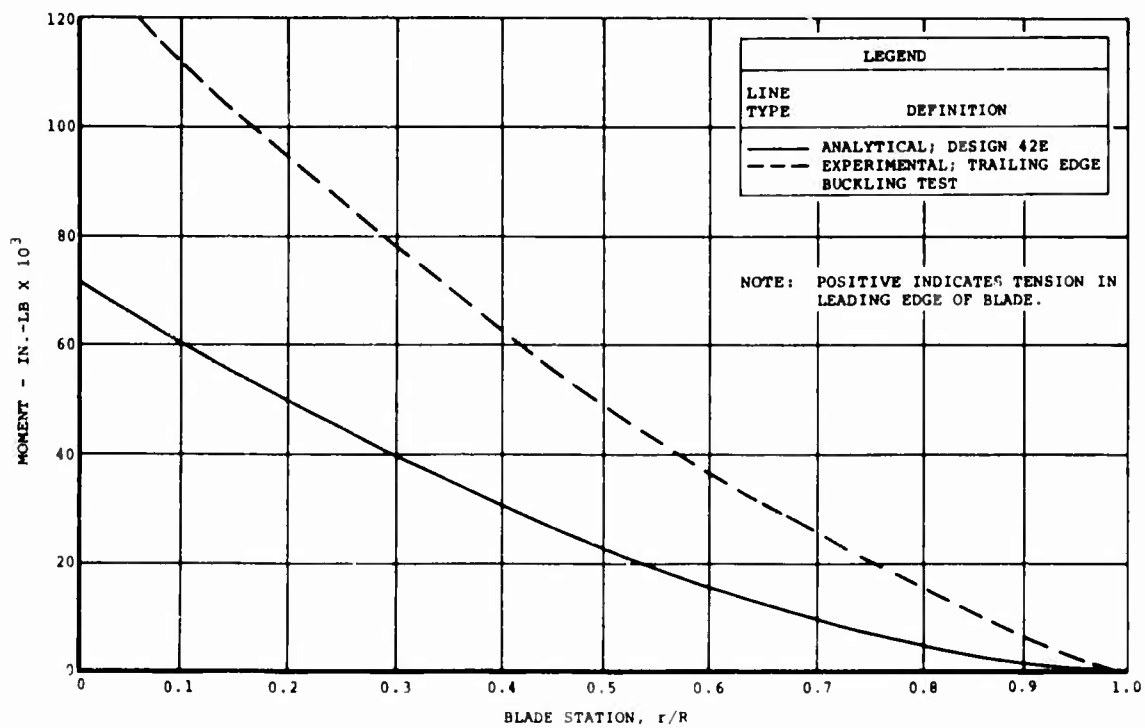


Figure 99. Ultimate Chordwise Moment During Start of the Advanced-Geometry Blade.

Static Proof Load Test

A static proof loading test was conducted on blades S/N 105-2 and S/N 102R-1 to verify their acceptability as flight test spares.

During the fabrication of these blades, a dimensional error had caused inadequate fiberglass-to-core bonding in some areas. The static proof test was performed to determine the extent to which the unbond areas had adversely affected the blades' structural integrity. The reasoning was that if the blades did not buckle under a 4g static loading without centrifugal relief, they could be considered as acceptable spares. Prior to their use as flight test spares, they were subjected to whirl tower testing. The known damaged areas were inspected after whirl tower testing by nondestructive test methods (NDT) and compared with NDT data taken after static testing. No appreciable growth of voids was noted. If a spare blade was flown, these areas were to be monitored during flight test to identify any changes or propagation of the damaged areas. For the record, there was no need to use these spare blades in the flight test program.

The subject blades were jig mounted as cantilevered beams with the vertical pin normal to the floor. The g loads above the 1g dead-weight distribution were obtained by the placement of weights at blade stations 180, 252, and 350 (Figures 100 and 101). Figure 102 shows the comparison of predicted 4g static moment versus the proof load application of sequence 5, Figure 103. The results of this test showed that under the 4g static bending moment, there was no visible buckling of the spar on either blade.

The deflection of the blades was measured at blade stations 180, 252, and 360 as the incremental loads were applied. A plot of g loads versus deflection is shown on Figure 103.

The actual deflection of the blade tip, station 360, due to a 3g load (deflections were measured from the 1g static position) was 26.938 inches. The predicted deflection of the tip due to the dead weight (1g) of the blade was 8.3193 inches (design 43, computer program S-07). For a 3g static load, the predicted deflection was 24.9579 inches (3×8.3193). There is approximately a 2-inch discrepancy which could be attributed to the following:

1. The modulus of the spare blades may differ from that of coupon test specimens.
2. The blade mass distribution may not agree with calculated section properties.
3. The unbond area may have caused decreased shear stiffness.
4. The proof moment distribution does not equal the predicted 4g moment distribution.

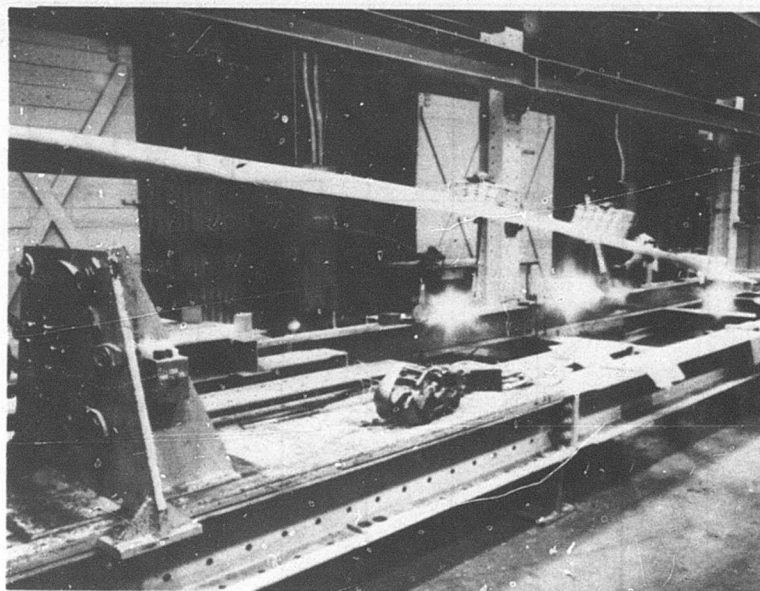


Figure 100. Placement of Weights on the Advanced-Geometry Blade at Stations 180, 252, and 350.

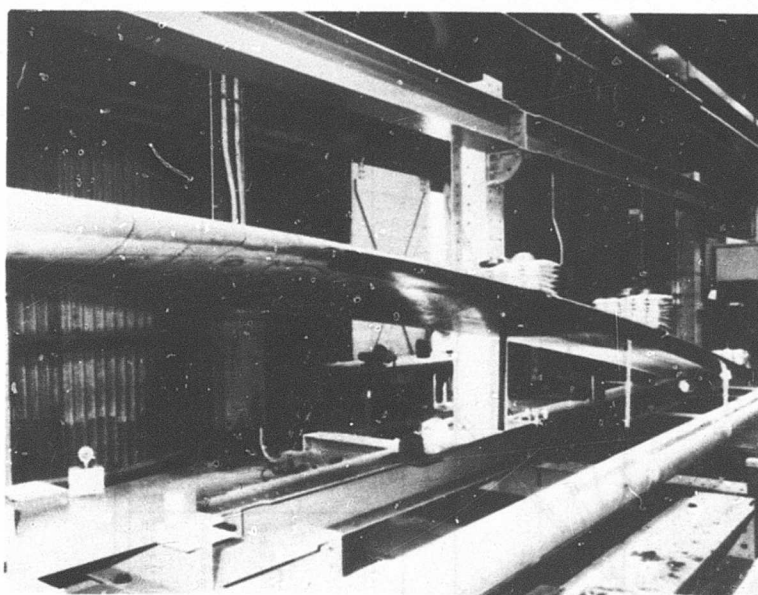


Figure 101. Placement of Weights on the Advanced-Geometry Blade at Stations 180, 252, and 350.

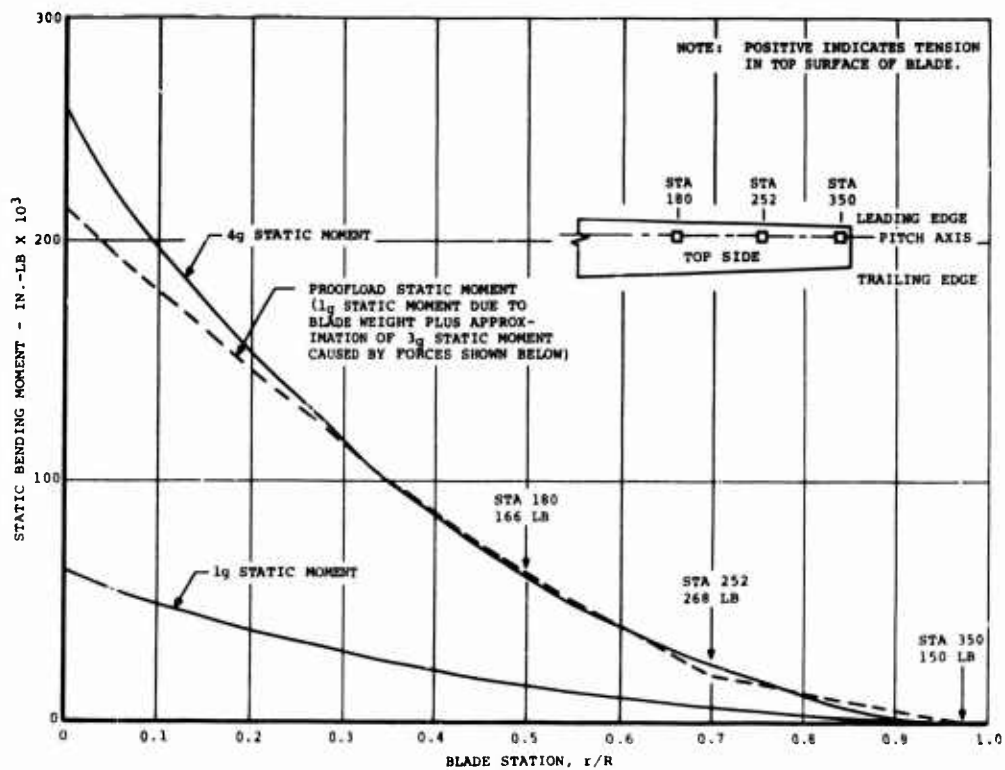


Figure 102. Radial Variation of Static Bending Moment in Analytical Design 42E.

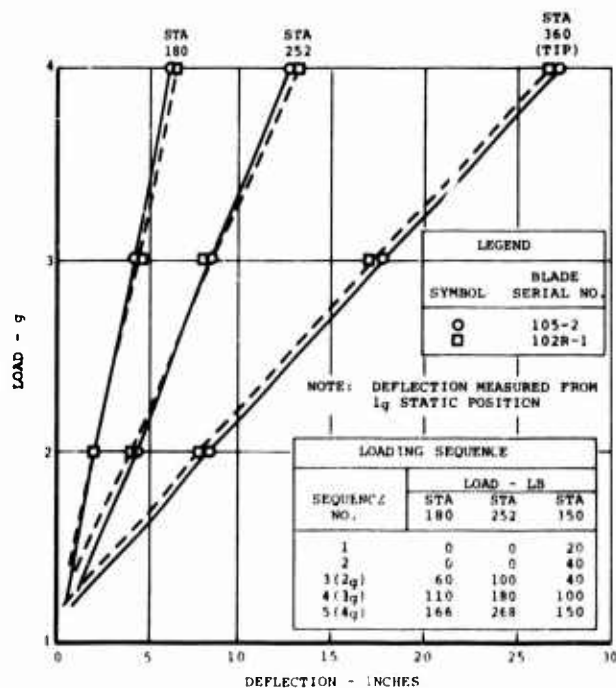


Figure 103. Static Proof Load Test of the Advanced-Geometry Blade.

From the results of the proof load test, blades S/N 105-2 and S/N 102R-1 have fulfilled the static requirements to qualify them as flight test spares.

FATIGUE TESTS

Fatigue testing consisted of (1) a chordwise airload test of two outboard blade sections, (2) a tip hardware test of two blade tip sections, and (3) two root end sections, two intermediate blade sections and two outboard blade sections subjected to centrifugal force and blade bending moments.

Chordwise Airload Test

The purpose of this test was to demonstrate the structural integrity of the blade section under chordwise airloads and to evaluate the bending strength of the trailing-edge structure.

The chordwise airload fatigue specimens consisted of an outboard section (stations 330 to 342) of blades S/N 103-1 and S/N 107-1. These specimens were jig mounted as cantilever beams with the bottom of the blade facing upward. The simulated chordwise airload was applied by a wiffle tree arrangement as shown in Figure 104.

The predicted airload distribution was calculated by a computer program as a variation of net aerodynamic pressure across the chord length at blade stations 216, 252, 288, and 324 using a nondimensional pressure profile and local blade shear. An envelope of these pressure distributions is shown on Figure 105. The steady and alternating shear forces caused by the envelope of the net pressure distributions are shown in Figures 106 and 107 along with the shear forces on the test sections due to the test loading. The actual test loads and their locations on the specimen are shown in Figures 108 and 109, plus the moment distribution caused by the test loading.

The steady and alternating chordwise bending stresses on the skin for the three runs for both blade test sections are tabulated in Table X. The maximum stresses occur at 22 inches from the leading edge (70 percent of the chord length). The maximum stress for run 1, which ran 10 million cycles, is 1330 psi \pm 665 psi with a stress ratio (R) of + 0.333. Runs 2 and 3 give stresses at the 70 percent chord length of 1330 psi \pm 950 psi with R equal to + 0.166 and 1520 psi \pm 1235 psi with R equal to + 0.104 respectively. Both test specimens ran for 5 million cycles at load level 2 (Table XI). The test section of blade S/N 103-1 failed after 1.126 million cycles at load level 3, while the test specimen of blade S/N 107-1 ran for 0.271 million cycle at load level 3 before failure.

Typical failures in the two test sections are shown in Figures 110 and 111. Figure 110 is the inboard end of test section S/N 107-1. The erosion strip on the top side of the blade has debonded from the fiberglass, while the honeycomb core has debonded from the fiberglass on the bottom side of the blade. Figure 111 is the

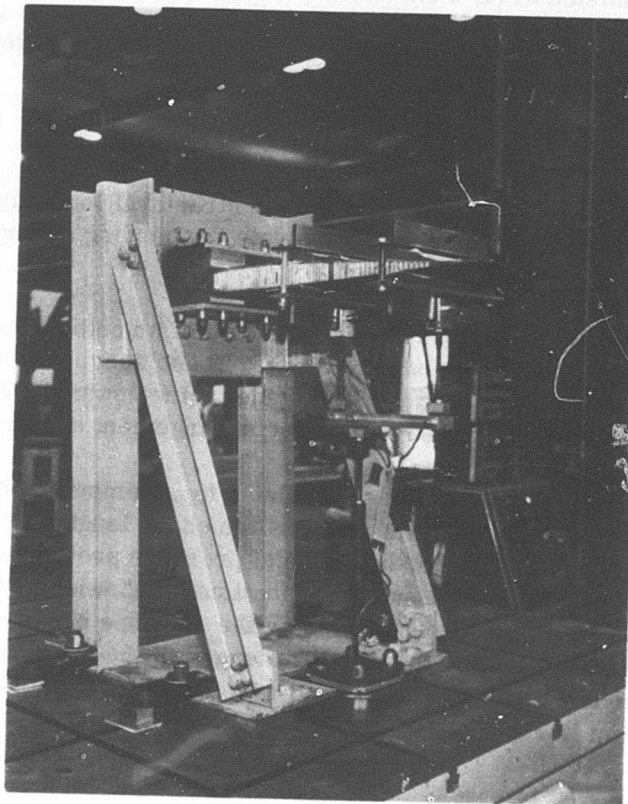


Figure 104. Setup for Chordwise Airload Fatigue Test.

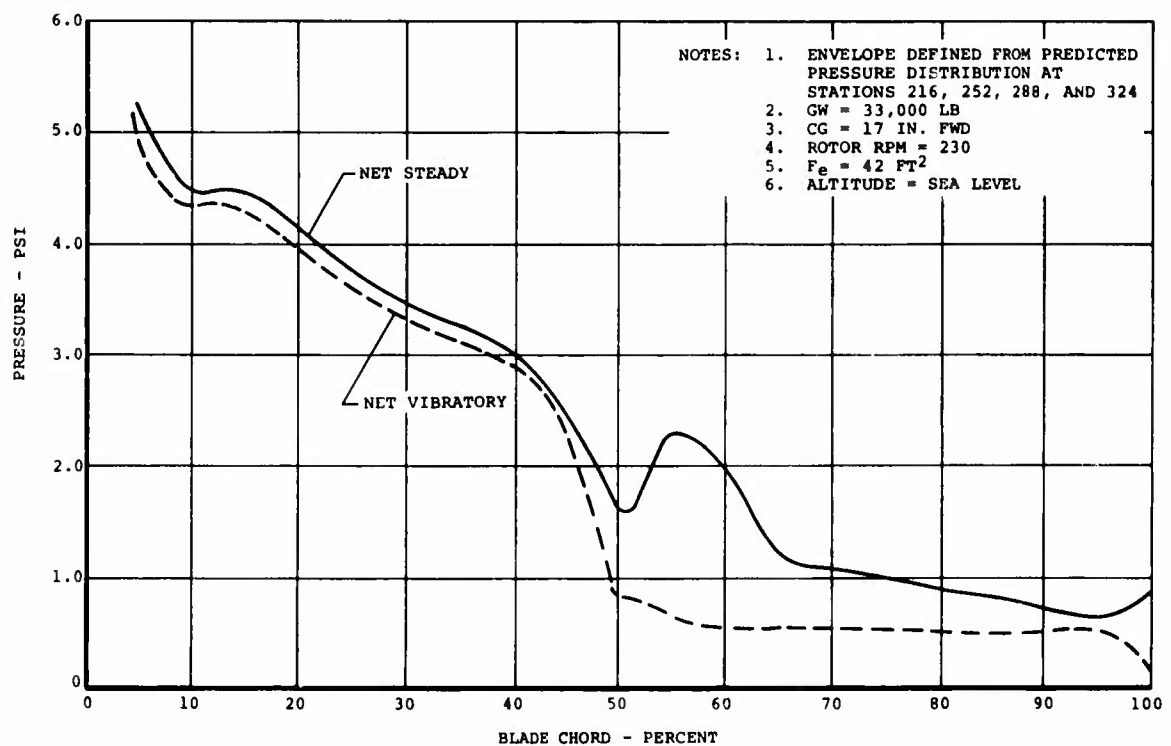


Figure 105. Envelope of Chordwise Variation of Aerodynamic Pressure on the Aft Rotor.

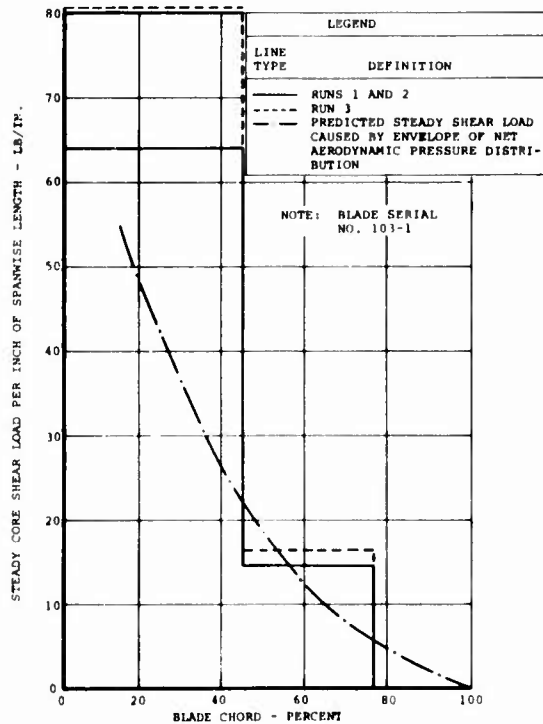


Figure 106. Steady Shear Loads of the Advanced-Geometry Blade.

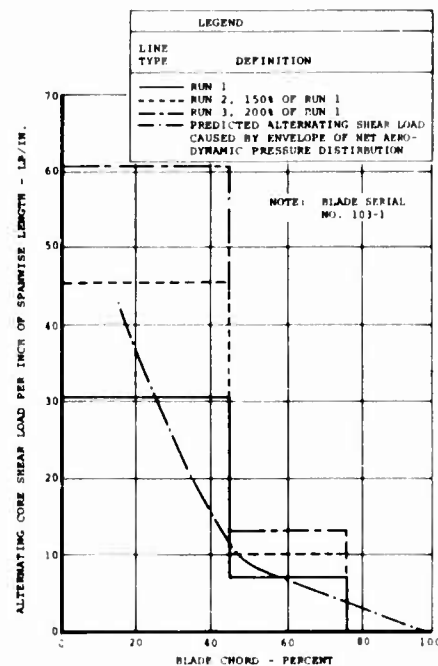


Figure 107. Alternating Shear Loads of the Advanced-Geometry Blade.

Figure 108. Steady Bending Moment of the Advanced-Geometry Blade.

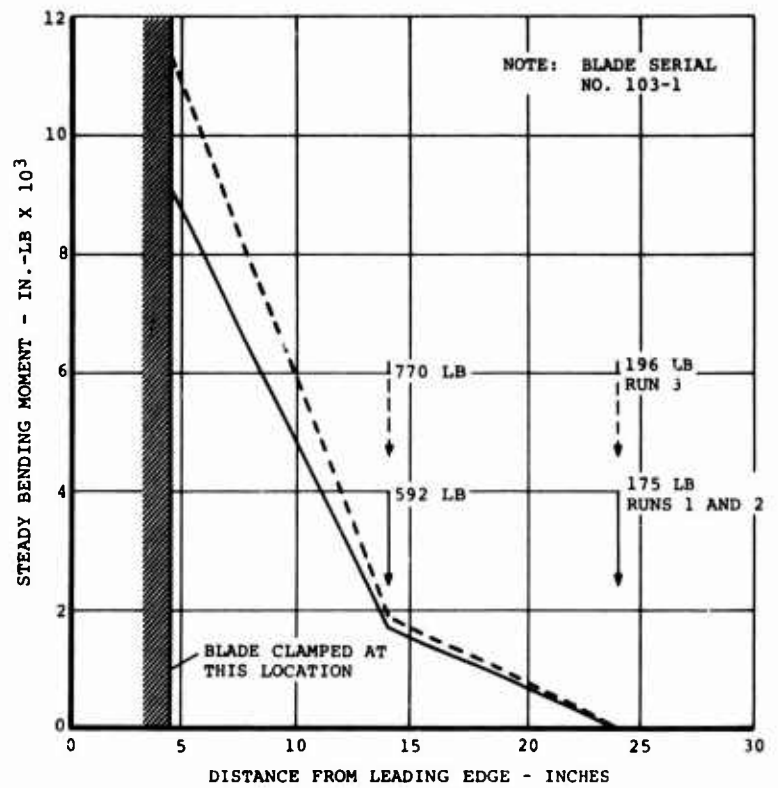
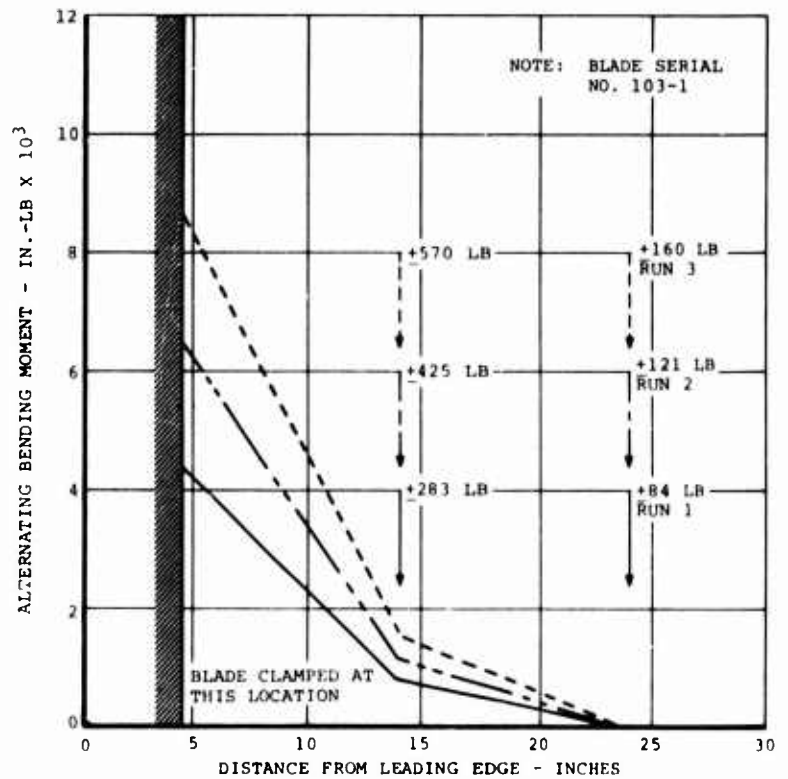


Figure 109. Alternating Bending Moment of the Advanced-Geometry Blade.



**TABLE X. DETAILS AND RESULTS OF CHORDWISE
AIRLOAD FATIGUE TEST OF THE
ADVANCED-GEOMETRY BLADE**

Load Location (in. from leading edge)	Run No.	Blade Serial No. 103-1			Blade Serial No. 107-1		
		Steady (psi)	Alter- nating (psi)	R	Steady (psi)	Alter- nating (psi)	R
6	1	585	281	0.351	555	289	0.315
	2	585	411	0.174	555	415	0.144
	3	722	550	0.135	722	561	0.125
9.5	1	750	360	0.351	721	374	0.317
	2	750	535	0.168	721	541	0.142
	3	931	721	0.127	931	735	0.118
15.75	1	915	458	0.333	817	441	0.299
	2	915	654	0.230	817	637	0.124
	3	1,045	865	0.094	1,045	850	0.103
18	1	766	365	0.354	657	365	0.286
	2	766	529	0.183	657	529	0.108
	3	875	711	0.103	875	673	0.131
22	1	1,330	665	0.333	1,140	665	0.263
	2	1,330	950	0.166	1,140	950	0.091
	3	1,520	1,140	0.142	1,520	1,235	0.104

Note: $R = \text{stress ratio} = \frac{\text{Steady} - \text{Alternating}}{\text{Steady} + \text{Alternating}}$

**TABLE XI. CYCLE HISTORY OF CHORDWISE AIRLOAD FATIGUE
TEST OF THE ADVANCED-GEOMETRY BLADE**

Run No.	No. of Cycles		Remarks
	Blade Serial No. 103-1	Blade Serial No. 107-1	
1	10.002×10^6	10.007×10^6	Runout
2	5.010×10^6	5.000×10^6	Runout
3	1.126×10^6	0.271×10^6	Component failure

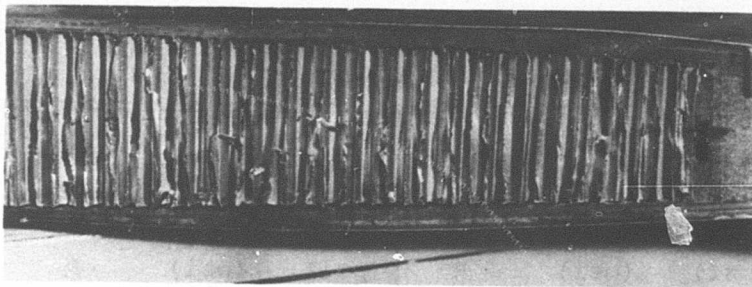


Figure 110. Inboard Failure of Advanced-Geometry Blade Serial No. 107-1 During Chordwise Airload Fatigue Test.

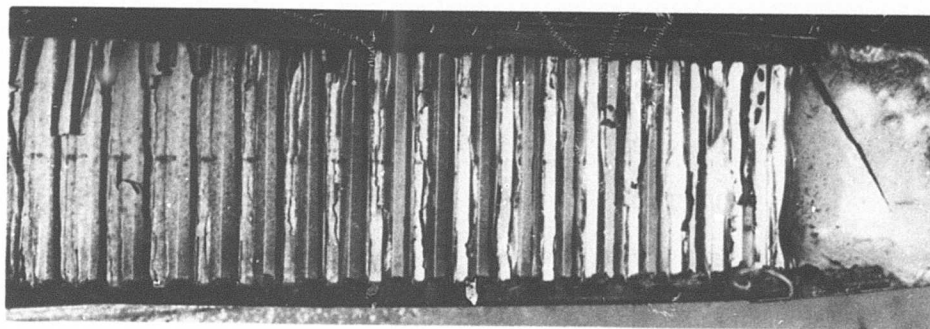


Figure 111. Outboard Failure of Advanced-Geometry Blade Serial No. 107-1 During Chordwise Airload Fatigue Test.

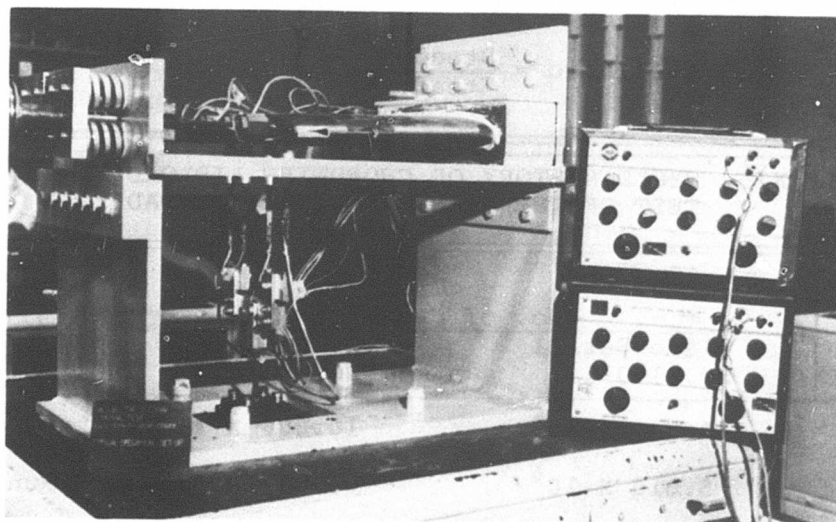


Figure 112. Setup for Fatigue Test of Tip Hardware.

outboard end of test section S/N 107-1. The core has debonded from the fiberglass on the bottom side of the blade.

The chordwise airload fatigue test has proven the structural integrity of the test section when subjected to the predicted net aerodynamic pressure distribution and 1.5 times the net pressure distribution. The skin stresses were not large enough to obtain a good comparison with the design allowable of the skin, but the skin did not fail during the test.

Tip Hardware Test

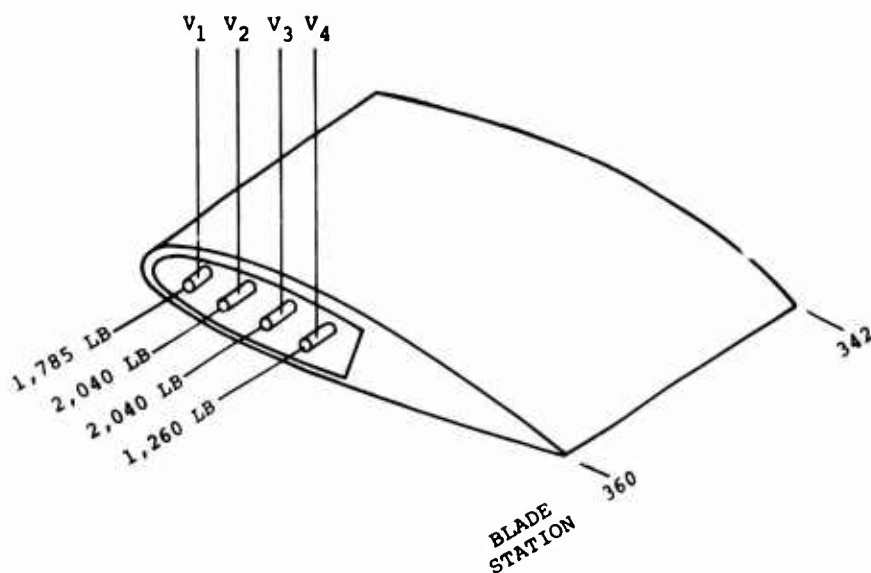
The objective of the tip hardware test was to evaluate the tip weights and retention hardware under fatigue loading conditions.

The tip hardware test specimens consisted of two 12-inch sections (stations 342 to 360) of blades S/N 103-1 and S/N 107-1. The two sections were mounted and the loads were applied as shown in Figure 112. The springbank applied the steady axial loads to the four tip studs. These loads simulated the centrifugal force generated by the nominal design weights of the studs and their associated tip weights whirling at 230 rpm. The actuator under the specimen (Figure 112) applied a steady plus alternating shear force with a stress ratio of +.10 on the studs. This shear load was the result of a predicted 40g vibratory force on the tip weights and studs from a computer program.

The load sequence on each blade section and the number of cycles run are shown in Figure 113. For run 1 the total centrifugal force was 7125 pounds and the total shear force was +330 pounds \pm 270 pounds. The centrifugal force remained constant for runs 1, 2 and 3, while the steady and alternating shear force was increased by 150 percent for run 2 and 200 percent for run 3.

The results of the tip hardware fatigue test showed that the tip assembly of blade S/N 103-1 ran for 10 million cycles at design loads plus .658 million at 150 percent of design loads before failure. A stud failed in the threaded portion where the stud is screwed into the tip anchor fitting. The tip assembly of blade S/N 107-1 ran for 10 million cycles at design loads, 7.373 million cycles at 150 percent of design loads, and 5.006 million cycles at twice the design loads without failure of the studs or retention system.

This test demonstrated that the tip hardware and retention assembly can support the design loads for 10 million cycles.



SERIAL NO.	STUD	SHEAR LOAD - LB								
		RUN 1			RUN 2			RUN 3		
		STEADY	ALTER-NATING	NO. OF CYCLES	STEADY	ALTER-NATING	NO. OF CYCLES	STEADY	ALTER-NATING	NO. OF CYCLES
103-1	V ₁	83	68	10 X 10 ⁶	124	102	0.658 X 10 ⁶ *	-	-	-
	V ₂	94	77		141	115		-	-	-
	V ₃	94	77		141	115		-	-	-
	V ₄	59	48		89	72		-	-	-
107-1	V ₁	83	68	10 X 10 ⁶	124	102	7.373 X 10 ⁶	166	136	5.006 X 10 ⁶
	V ₂	94	77		141	115		188	154	
	V ₃	94	77		141	115		188	154	
	V ₄	59	78		89	72		118	96	
*STUD V ₃ FAILURE AT ANCHOR FITTING										

Figure 113. Details and Results of Fatigue Test of Tip Hardware.

Root-End Test

The root-end sections were tested in order to evaluate the fatigue capability of the fiberglass transition area and the structural components of the titanium root-end fitting and socket.

A typical root-end fatigue test specimen is shown in Figure 114. The specimen consisted of the section inboard of blade station 117 and included the titanium attachment socket. The three root-end sections tested were from the No. 1 tool-proving blade and blades S/N 103-1 and S/N 107-1. The tool-proving blade specimen was used for developmental testing to determine the fatigue critical items of the root end.

Load level 1 for the tool-proving root-end test consisted of theoretical design loads for configuration No. 42E at blade station 52. The applied loads were an axial load of 90,000 pounds, which simulated centrifugal force at 230 rpm for a calculated blade weight of 343 pounds, a flapwise moment of $\pm 71,000$ inch-pounds, and a chordwise moment of $+24,000$ inch-pounds. At load level 2, the axial load was increased to 106,000 pounds. This represented the centrifugal force at 230 rpm and the final production weight of the fabricated blades (average of 3 blades, 380 pounds). The flapwise moment was increased to approximately 150% of the design loads ($\pm 110,000$ inch-pounds), while the chordwise moment was increased to $\pm 32,000$ inch-pounds. For load level 3, the axial load was the same as load level 2. The flapwise moment was increased to approximately 225 percent of design loads ($\pm 171,000$ inch-pounds) and the chordwise moment was increased to $\pm 46,000$ inch-pounds.

The tool-proving root-end section ran for 10 million cycles at load level 1 and 5 million cycles at load level 2 without blade or metal component failure. After 1,325 million cycles at load level 3, the attachment socket failed through the vertical pin bore. Figure 115 shows this failure of the socket.

From the results of the tool-proving root-end test, it was decided to obtain additional bending moment data at the vertical pin joint on the subsequent root-end sections of blades S/N 103-1 and S/N 107-1.

For these two test sections, the axial loading was 106,000 pounds and the flapwise moment at the center line of the vertical pin bore (blade station 29.5) was $\pm 75,000$ inch-pounds for S/N 103-1 and $\pm 55,000$ inch-pounds for S/N 107-1.

The alternating moment on the S/N 107-1 socket has been changed from $\pm 75,000$ inch-pounds. An investigation of the AGB root end testing in conjunction with another program raised a question about the calibration of the S/N 107-1 section. Reevaluation of the calibration data showed that $\pm 55,000$ inch-pounds was the more conservative interpretation.

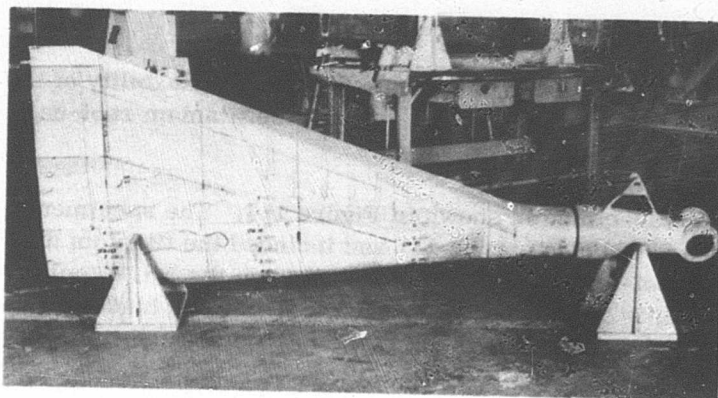


Figure 114. No. 1 Tool-Proving Root-End Test Section.

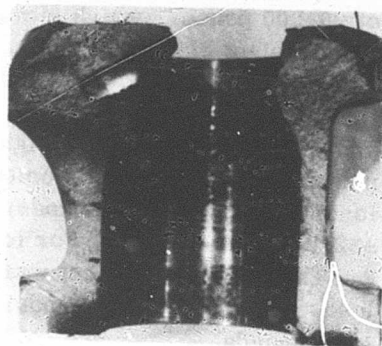


Figure 115.
Fatigue Failure
of Root-End Socket.

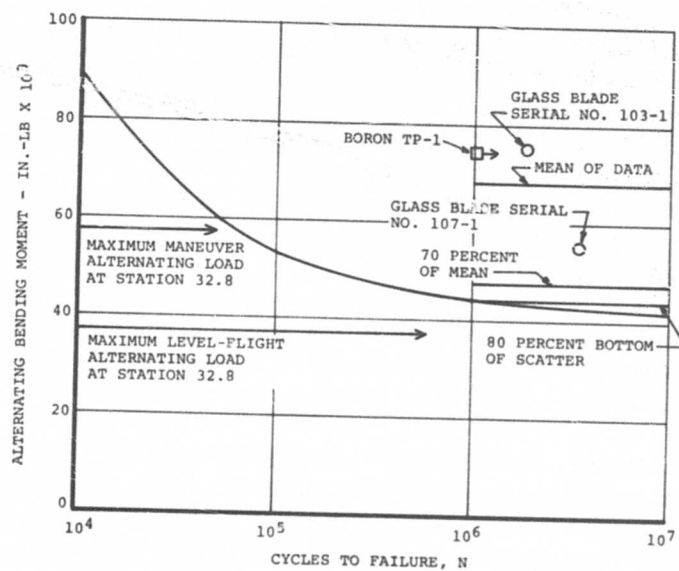


Figure 116. Fatigue-Life Curve for the Vertical Pin Joint.

The root-end section of S/N 103-1 ran for 1.87 million cycles before failure at the vertical pin bore, while the section of S/N 107-1 ran for 3.51 million cycles before failure at the vertical pin bore. These two failures were similar with regard to type and location to the failure of the tool-proving socket shown in Figure 115.

Figure 116 shows the results of the two tests on a moment-versus-cycle diagram. In addition, a data point from the boron blade structural testing program (Contract AF33(615)-5275) is shown. The boron blade has the same vertical pin joint as the AGB; therefore, its inclusion as a data point is valid. The load level on the boron blade vertical pin was $\pm 74,000$ inch-pounds, and the specimen ran for 1.041 million cycles. Although the specimen did not fail at the vertical pin, this point is considered a failure in this data analysis.

The data analysis consisted of establishing the mean of the three test points, 70 percent of mean and 80 percent of the lowest strength value as shown in Figure 116. The lowest of the above three strengths was selected, and a typical titanium curve shape was passed through this point at one million cycles. Also indicated on Figure 116 are the maximum level flight and maneuver flight alternating loads obtained during the flight test program.

The results of the root-end fatigue tests have shown that the titanium attachment socket is the fatigue critical component. A fatigue life M-N curve has been constructed which indicates that the attachment socket was satisfactory for initial level-flight operations and was acceptable for limited maneuver flight.

Outboard Blade Section Test

The 100-inch outboard blade section was tested under various loading conditions to evaluate the fatigue strength capability of the spar, skin, torsion wrap, erosion strip, honeycomb core and trailing-edge cusp.

The outboard fatigue test specimen consisted of the blade section between station 227 and station 327. The two outboard sections tested were cut from blades S/N 103-1 and S/N 107-1. The blade section of S/N 103-1 was tested under simulated centrifugal force and flapwise and torsional moments, while the blade section S/N 107-1 was tested under simulated centrifugal force and flapwise and chordwise bending moments. The test setups of the S/N 107-1 section and the S/N 103-1 section are shown in Figure 117.

The test requirements stated that the initial loading on the section of S/N 103-1 would consist of a steady axial load of 45,000 pounds, an alternating flapwise moment of $\pm 30,000$ inch-pounds at blade station 277, and a steady and alternating torsional moment of $11,400 \pm 10,950$ inch-pounds at blade station 288. The axial load simulated the centrifugal force at blade station 277 for 230 rpm and a calculated blade weight of 373 pounds. The alternating flapwise moment at blade

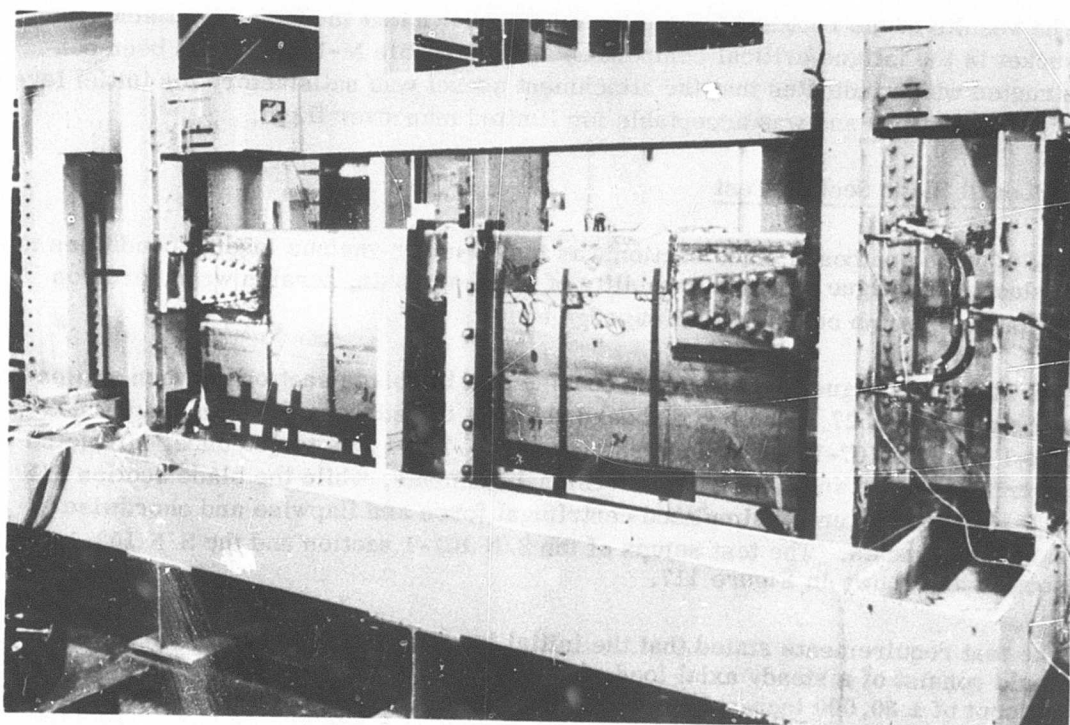
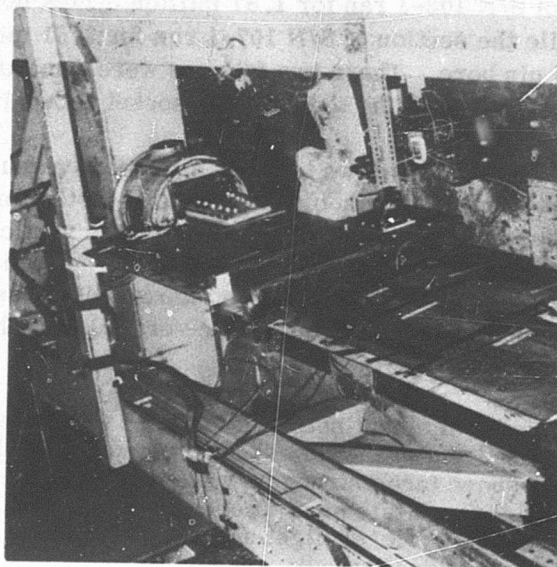


Figure 117. Setup for Fatigue Test of Outboard Blade Sections Serial Nos. 103-1 and 107-1.

station 277 was the predicted top of envelope moment for the design 43 configuration corrected by a Goodman diagram to account for the absence of a steady flapwise moment. The steady and alternating torsional moments at blade station 288 were the predicted top of envelope moments for the design 43 configuration.

The actual loads on the S/N 103-1 test section are shown in Table XII. The simulated centrifugal force was 43,500 pounds. The flapwise moment was $\pm 27,700$ inch-pounds and the average torsional moment was $11,400 \pm 10,500$ inch-pounds. With this loading, the test specimen ran for 0.211 million cycles, at which time the titanium erosion strip became partially debonded from the fiberglass. The debonded area was located on the bottom side of the blade between blade station 272 and 292. After 1.065 million cycles, an inadvertent static torsional overload damaged the fiberglass and core on the outboard end of the section. This overload resulted from failure of a microswitch. Testing was continued at the same loading to 1.69 million cycles. The test was terminated at this point due to propagation of the damaged area. Figure 118 shows the failures on the top and bottom of the blade section at the outboard end. The top side of the blade indicates debonding of the blade skins from the core at a 45° angle from the edge of the attachment to the blade trailing edge. The bottom side has a large debonded area around the attachment towards the trailing edge and localized area of resin failures.

On the fatigue test of S/N 107-1, the test requirements stated that the loads would consist of a steady axial force of 43,500 pounds, an alternating flapwise moment of $\pm 23,000$ inch-pounds at blade station 277, and an alternating chordwise moment of $\pm 12,000$ inch-pounds at blade station 277. The axial load simulated the same centrifugal force as the S/N 103-1 test specimen. The flapwise moments were the predicted maximum level-flight loads for the design 43 configuration. The applied predicted chordwise moments were divided by a factor of 3 to account for load phasing.

The actual loads on the S/N 107-1 test specimen are shown in Table XII. For load level 1, the steady axial load was 43,500 pounds. The alternating flapwise moment was $\pm 23,000$ inch-pounds and the chordwise moment was $\pm 10,300$ inch-pounds at blade station 277. With this loading, the specimen ran for 10 million cycles without failure, except for some debonding of the erosion strip and localized void growth.

At load level 2, the axial load remained constant, while the alternating flapwise moment was increased to 150 percent of the moment load level 1 ($\pm 34,000$ inch-pounds). The alternating chordwise moment was increased to $\pm 19,200$ inch-pounds. The test section ran for 5 million cycles at this loading without major failures, although further debonding occurred. For load level 3, the axial load remained constant. The alternating flapwise moment was increased to $\pm 46,000$ inch-pounds or 200 percent of the initial flapwise moment. The chordwise moment was increased to $\pm 25,600$ inch-pounds. The blade section ran for 3.36 million cycles before accumulated damage (debonding and core shear failures, but no primary structural failures) forced termination of the test.

TABLE XII. LOADS SUMMARY OF FATIGUE TEST OF OUTBOARD BLADE SECTIONS							
Blade Serial No.	Run No.	Predicted Top-of- Envelope Load (percent)	Centrif- ugal Force (lb)	Flap Moment at Sta- tion 277 (in.-lb)	Chord Moment at Sta- tion 277 (in.-lb)	Torsional Moments (in.-lb)	No. of Cycles
103-1	1	100	43,500	<u>+27,700</u>	-	11,400 <u>+10,500</u>	1.69 X 10 ⁶
	1	100	43,500	<u>+23,000</u>	<u>+10,300</u>	-	10 X 10 ⁶
107-1	2	150	43,500	<u>+34,000</u>	<u>+19,200</u>	-	5 X 10 ⁶
	3	200	43,500	<u>+46,000</u>	<u>+25,600</u>	-	3.36 X 10 ⁶

Figure 119 shows the ultrasonic mappings of the bottom side of the S/N 107-1 test section. The coding used is the following: ① indicates voids present before testing started; ② indicates voids after load level 1; ③ indicates voids after load level 2; and ④ indicates voids after load level 3. Referring to Figure 119, voids were present before testing in the bonding of the titanium erosion strip to the fiberglass and probably in the bond between the honeycomb core and the fiberglass (① areas marked adjacent to the erosion strip). At the end of load level 1, voids (② markings) encompassed the area around the end fittings and showed a growth in the debonding of the erosion strip. The initiation of debonding around the erosion strip splice was also evident. After load level 2, additional localized voids (③ markings) were present on the erosion strip and additional debonding occurred around the splice. At load level 3 and after 0.5187 million cycles, core damage was found under both tuning weight channels approximately 1 foot from the trailing edge. This core deterioration progressed forward toward the spar and was noted after 2.05 million cycles. At 3 million cycles, the damage area had propagated to the trailing edge of the spar. Testing was stopped after 3.36 million cycles, and ultrasonic mapping and inspection showed that the core had failed from the trailing edge to the leading edge in the mid-section of the test specimen (Figure 119, areas marked ④).

It was theorized that the core damage was caused by out-of-plane forces generated by the action of the tuning weight and channels on the blade section. Relative motion between the tuning weights and test section was thought to have caused impacting. The origin of the voids between the skins and the core was located at points near the trailing edge where the contour of the channels deviated from the shape of the blade. These points were stress raisers which concentrated the impacting force and failed the core in shear. The shear failure then propagated toward the leading and trailing edges.

The calculated steady and alternating stresses on each type of fiberglass are tabulated in Table XIII for each load level. The analysis considered the stresses caused by centrifugal force and alternating flapwise bending moments at blade station 277 and at the maximum distance from the flapwise neutral axis. Figures 120 through 122 show a comparison between calculated stresses in the test section at the three load levels and the design allowable fatigue stress obtained from coupon testing. In addition, the predicted alternating stresses at blade station 277 for the maximum level and maneuvering flight conditions at 33,000 pounds gross weight and 230 rpm are indicated in these figures.

Figure 120 makes the comparison for the spar material, unidirectional 1002S glass. Stress level 1, which is the stress for maximum predicted alternating flapwise loads occurring at sea level and 140 knots TAS, is below the design allowable stress at 10 million cycles. Stress levels 2 and 3 are greater than the allowable stresses at the same number of cycles. The predicted stress level for maneuvering flight is between stress levels 1 and 2. Figure 121 compares XP251S glass ($\pm 45^\circ$ cross-ply) design allowable stresses with the stresses on the outer torsion wrap of the

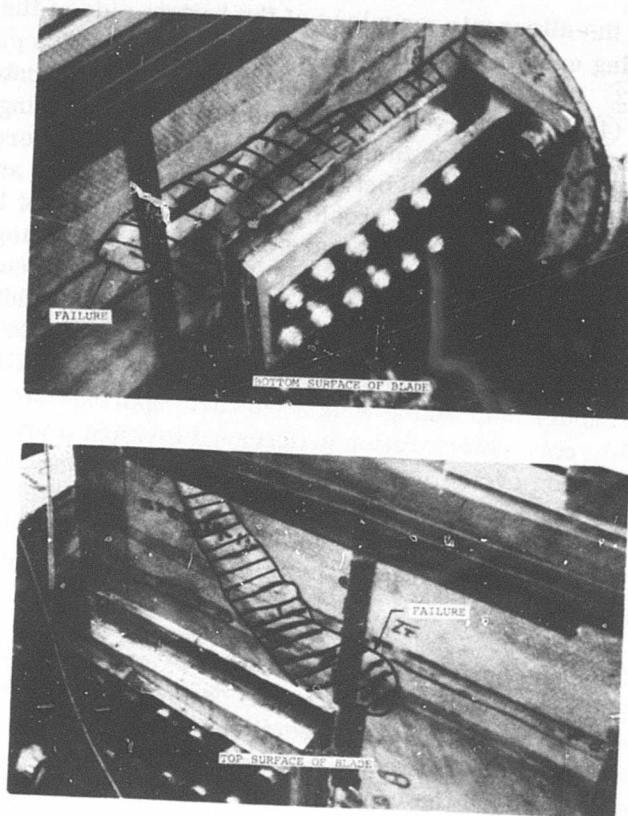


Figure 118. Failure of Outboard End of Outboard Blade
Section Serial No. 103-1.

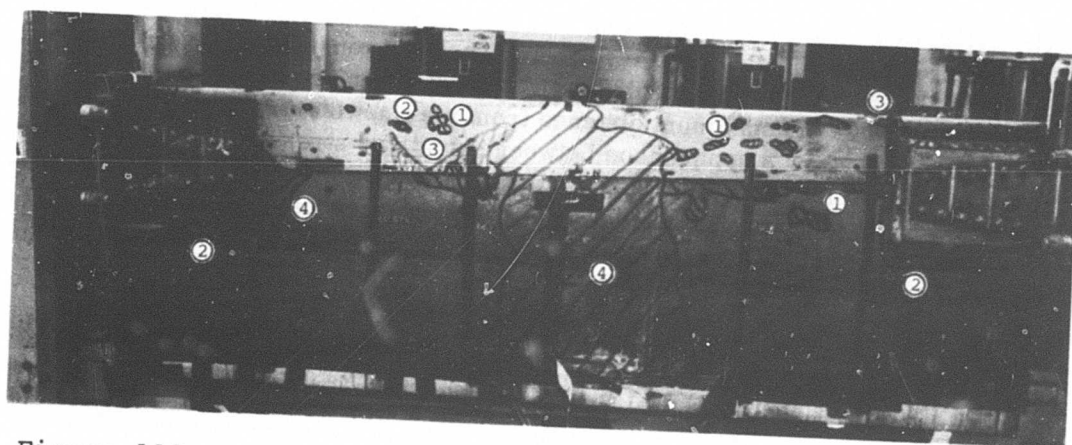


Figure 119. Ultrasonic Mapping of Bottom Surface of Outboard
Blade Section Serial No. 107-1, End of Load
Level 3.

TABLE XIII. STRESS SUMMARY OF FATIGUE TEST OF OUTBOARD BLADE SECTION SERIAL NO. 107-1, STATION 277										
Blade Element	Glass Material	Load Level 1			Load Level 2			Load Level 3		
		Steady (psi)	Alter- nating (psi)	R	Steady (psi)	Alter- nating (psi)	R	Steady (psi)	Alter- nating (psi)	R
Skin	BP907- 143S +45°	3,798	+2,223	0.262	3,798	+3,286	0.073	3,798	+4,446	-0.079
Torsion Wrap	XP251S +45°	5,060	+2,935	0.266	5,060	+4,340	0.077	5,060	+5,870	-0.074
Spar	1002S 0°	13,300	+7,600	0.273	13,300	+11,230	0.085	13,300	+15,200	-0.067
Note: R = stress ratio = $\frac{\text{Steady} - \text{Alternating}}{\text{Steady} + \text{Alternating}}$										

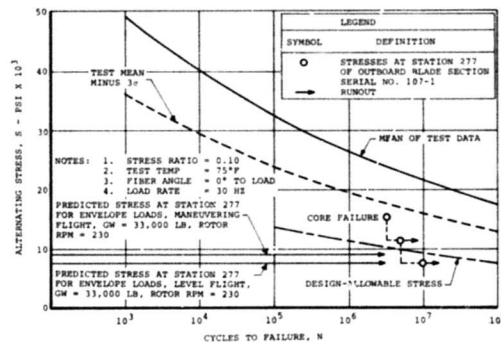


Figure 120. Stress Curve for Analytical and Test Results of Unidirectional 1002S Epoxy-Resin Laminates Loaded in Tension-Tension Fatigue.

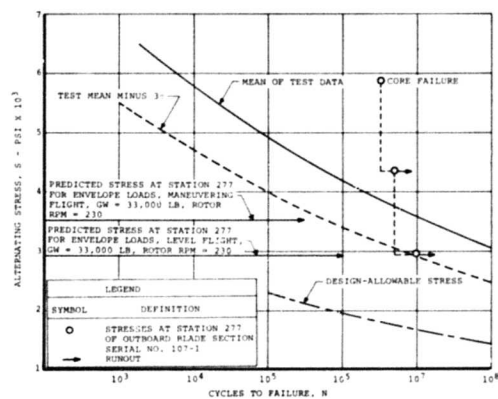


Figure 121. Stress Curve for Analytical and Test Results of XP251S +45-Degree Crossply Epoxy-Resin Laminates Loaded in Tension-Tension Fatigue.

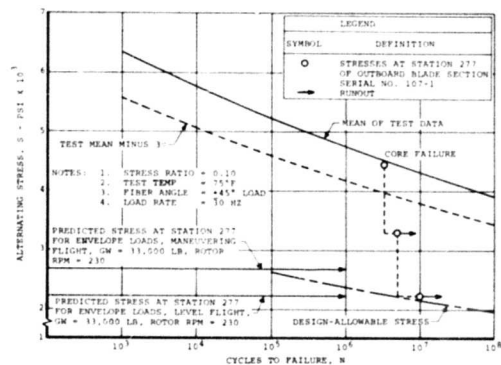


Figure 122. Stress Curve for Analytical and Test Results of BP907-143S +45-Degree Crossply Epoxy-Resin Laminates Loaded in Tension-Tension Fatigue.

spar. The calculated stresses in this material exceed the coupon strength and fall into the data scatter. However, there were no visible resin shear failures at 45° to the load axis, which is the expected failure mode of XP251 $\pm 45^\circ$ crossply. Based on coupon experience, the crossply will not fail at these high stress levels if the XP251S crossply and the unidirectional spar material behaved like the uni-crossply test coupons. In the test coupons the crossply strains with the uni, which carries most of the load and is the fatigue critical material in this combination. In this case, the structural test loads were not high enough to fail the uni-crossply combination of the blade. Figure 122 shows the three stress levels and the design allowable stresses for BP907-143S glass ($\pm 45^\circ$ crossply). Stress level 1 is slightly greater than the design allowable at 10 million cycles. Stress levels 2 and 3 are greater than the allowable stresses at the same number of cycles. The predicted stress level for maneuvering flight is between stress levels 1 and 2.

The fatigue testing of the 100-inch outboard section of S/N 103-1 has shown that the spar, torsion wraps, skin, honeycomb core, and trailing-edge cusp can withstand predicted design loads of centrifugal force and torsional and flapwise moments for over a million cycles. The adhesive bond or the bonding procedures between the erosion strip and the fiberglass were shown to be inadequate under fatigue loading.

The results of the S/N 107-1 outboard fatigue test have proved the structural integrity of the spar, torsion wraps, skin, and trailing-edge cusp when subjected to the predicted load spectrum. The erosion strip bonding was found to be unacceptable under fatigue loading. The honeycomb core was shown to be satisfactory at 1.5 times the predicted fatigue loads for 5 million cycles. The core failure, which was probably induced by the test setup, might suggest that the core is the fatigue critical component. This test indicated that each fiberglass material would be satisfactory for initial flight operations.

Inboard Blade Section Test

The 100-inch inboard blade structure was tested under centrifugal force and flapwise and chordwise bending to evaluate the spar, torsion wraps, skin, erosion strip, honeycomb core, and trailing-edge cusp fatigue strength.

The inboard fatigue test specimens consisted of two 100-inch sections (blade station 127 to 227) of blades S/N 103-1 and S/N 107-1. The sections were jig mounted as pinned-pinned beams in the test fixture as shown in Figure 123.

The steady and alternating loads on the two test sections are tabulated in Table XIV. The steady axial load of 70,000 pounds simulated the centrifugal force at blade station 177 for 230 rpm and a calculated blade weight of 373 pounds. The alternating flapwise moment of $\pm 36,000$ inch-pounds at blade station 177 was the maximum predicted alternating moment for design 43. The alternating chordwise moment was $\pm 23,500$ inch-pounds at blade station 177, which corresponded to one-third of the maximum

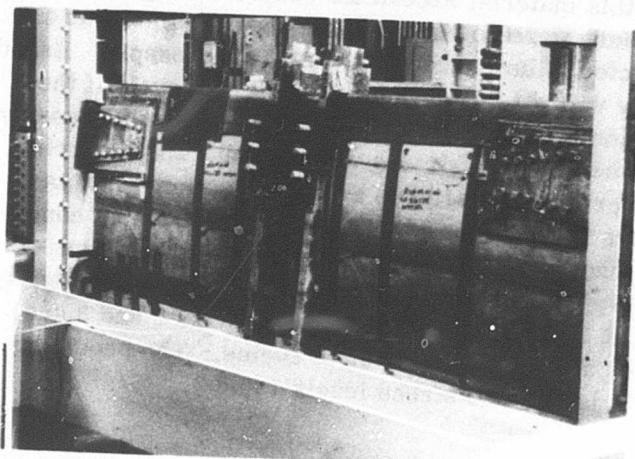


Figure 123.
Setup for Fatigue Test
of Inboard Blade Section
Serial No. 103-1.

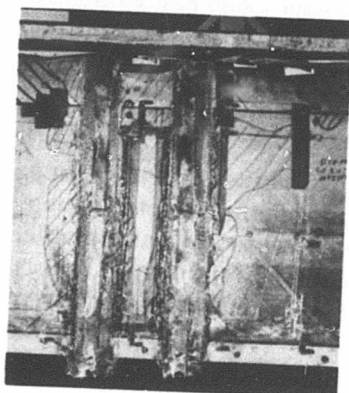


Figure 124.
Skin Failures
on Bottom Surface
of Inboard Blade
Section Serial
No. 103-1,
End of Load Level 3.

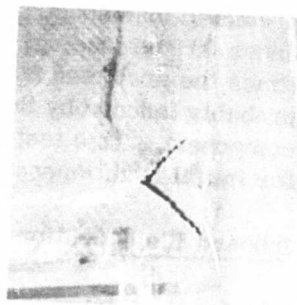


Figure 125.
Closeup of Skin Failure on Top
Surface at Inboard End of Inboard Blade
Section Serial No. 103-1.

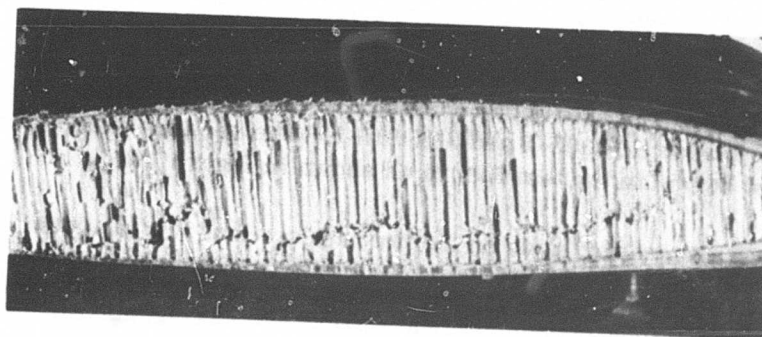


Figure 126. Core Failure at Outboard End of Inboard Blade
Section Serial No. 103-1.

TABLE XIV. LOADS SUMMARY OF FATIGUE TEST OF INBOARD BLADE SECTIONS						
Blade Serial No.	Run No.	Predicted Top-of- Envelope Load (percent)	Centri- fugal Force (lb)	Flap Moment at Sta- tion 177 (in.-lb)	Chord Moment at Sta- tion 177 (in.-lb)	No. of Cycles
103-1	1	100	70,000	<u>+36,000</u>	<u>+23,500</u>	10 X 10 ⁶
	2	150	70,000	<u>+54,000</u>	<u>+30,350</u>	5.62 X 10 ⁶
	3	200	70,000	<u>+72,000</u>	<u>+40,470</u>	0.0275 X 10 ⁶
	4	100	70,000	<u>+36,000</u>	<u>+20,000</u>	0.1725 X 10 ⁶
107-1	1	100	70,000	<u>+36,700</u>	<u>+20,700</u>	10 X 10 ⁶
	2	150	70,000	<u>+54,000</u>	<u>+30,350</u>	3.23 X 10 ⁶

level-flight moment of design 43. At this loading, both test sections ran 10 million cycles without failure. Load level 2 for the two test specimens consisted of increasing the flapwise moment to 150 percent of the initial flapwise moment ($\pm 54,000$ inch-pounds), while the axial load remained constant. The chordwise alternating load was increased to $\pm 30,350$ inch-pounds. The S/N 103-1 test section ran for 5.62 million cycles at this load level, and the S/N 107-1 test section ran for 3.23 million cycles before termination. (Load levels 3 and 4 pertained only to the S/N 103-1 test section.) Load level 3 consisted of increasing the flapwise moment to $\pm 72,000$ inch-pounds, which was 200 percent of the flapwise moment at load level 1. The axial load remained constant, but the chordwise moment was increased to $\pm 40,470$ inch-pounds. The test section ran for 0.0275 million cycles at this load level. At load level 4, the flapwise moment was reduced to the value at load level 1 ($\pm 36,000$ inch-pounds) and the chordwise moment was decreased to $\pm 20,000$ inch-pounds and ran for 0.1725×10^6 cycles.

During load level 1 at 0.353 million cycles, the titanium erosion strip debonded at the splice (blade station 197) on the top and bottom sides of the S/N 103-1 test section. The bond failure was attributed to poor initial bond resulting from either deficiencies in the bonding materials or cleaning procedures.

After 1.25 million cycles at load level 2, core damage resulted from the action of the tuning weights and channels upon the middle of the test section. The damage originated on both sides of the blade section at approximately 75 percent chord and 10 inches either side of the mid-section. The ultrasonic mappings in Figure 124 show the damaged areas. Fiberglass doublers were added in an attempt to redistribute the active loading, and the contour of the tuning weight channels was changed to relieve the damaged areas at mid-section. Figure 124 shows the fiberglass doubler modification. Despite this attempt to stop the core failure, it propagated forward to the spar and aft to the trailing edge during the remainder of Run 2.

The S/N 103-1 test section sustained breaks in the skins at the trailing edge after 0.0275 million cycles at load level 3. Figure 124 shows two cracks on the bottom side of the section. Figure 125 shows a break in the skins on the top side of the test section.

As mentioned previously, load level 4 consisted of reducing the flapwise moment to that of load level 1. This was done to test the structure's capability of carrying 100 percent of design loads after accumulating damage. At this load level, the section ran 0.1725 million cycles with no loss of load-carrying capability. Testing was terminated because of accumulated damage to the section. The primary load-carrying structure, the spar, remained undamaged.

At the end of the test, the end fittings were cut from the test section. Figure 126 shows the outboard cutout viewed from the outboard end of the section. The crack propagation of the core from the trailing edge to the leading edge (left to right) is evident.

The calculated steady and alternating stresses on each fiberglass material are tabulated in Table XV for the three load levels. The analysis considered the stresses caused by centrifugal force and alternating flapwise bending moments at blade station 177 and at the maximum distance from the flapwise neutral axis. Figures 127 through 129 show a comparison between the three calculated stresses obtained from coupon testing. Also indicated on these figures are the predicted alternating stresses at blade station 177 for the maximum steady level and maneuvering flight conditions at 33,000 pounds gross weight and 230 rpm.

Figure 127 compares structural test data with coupon data for spar material, unidirectional 1002S glass. Stress level 1, which is the stress for maximum predicted alternating moments is less than the design allowable stress at 10 million cycles. Stress levels 2 and 3 are also less than their respective design allowable stresses at the same number of cycles. The predicted stress level for maneuvering flight is between stress levels 1 and 2. Figure 128 compares the design allowable stresses of XP251S glass ($\pm 45^\circ$ crossply) with the stresses on the outer torsion wrap of the spar. Stress levels 1, 2 and 3 are greater than the respective design allowable stresses at the same number of cycles. The predicted stress level for maneuvering flight is between stress level 1 and 2. Figure 129 shows the three stress levels and the design allowable stress for BP907-143S ($\pm 45^\circ$ crossply), which is the material of the blade skins. Stress levels 1 and 2 are less than the design allowable stresses at 10 million and 5 million cycles, respectively. Stress level 3 is greater than the design allowable stress at 0.0275 million cycles. The predicted stress level for maneuvering flight is between stress levels 1 and 2.

The S/N 107-1 test section completed 10 million cycles at load level 1 without major damage. The titanium erosion strip did not debond at the splice. After 0.898 million cycles at load level 2, core deterioration was found in approximately the same locations as the S/N 103-1 test section. The core failure had propagated forward to 50 percent chord by 1.168 million cycles. After 3.23 million cycles, the core failure encompassed the area from the trailing edge to the leading edge at the middle of the test section. (It should be noted that fiberglass doublers were used to try to eliminate the impacting of the tuning weights on the blade section. Although this system was installed at the beginning of the test, apparently this modification was not effective.) Figure 130 shows the S/N 107-1 test section with the trailing edge removed aft of approximately 60 percent chord. The core shear failure is evident under one tuning weight channel, and debonding between the core and fiberglass on the bottom side is also present.

The calculated steady and alternating stresses on the S/N 107-1 test section are tabulated on Table XV for each fiberglass material at the two load levels. The analysis considered the stresses caused by centrifugal force and alternating flapwise bending moments at blade station 177 and the maximum distance from the flapwise neutral axis. The stresses on each fiberglass material are plotted on Figures 127, 128, and 129. The comments made on the S/N 103-1 stress levels pertain to the S/N 107-1 stress levels.

TABLE XV. STRESS SUMMARY OF FATIGUE TEST OF INBOARD BLADE SECTIONS, STATION 177											
Blade Serial No.	Blade Element	Glass Material	Load Level 1		Load Level 2		Load Level 3		R	Steady (psi)	Alter- nating (psi)
			Steady (psi)	Alter- nating (psi)	Steady (psi)	Alter- nating (psi)	Steady (psi)	Alter- nating (psi)			
103-1	Skin	BP907- 143S +45°	3,706	±1,437	0.441	3,706	±2,156	0.264	3,706	±2,874	0.126
	Tor- sion wrap	XP251S +45°	4,940	±1,900	0.445	4,940	±2,850	0.268	4,940	±3,800	0.131
	Spar	1002S 0°	13,000	±4,890	0.454	13,000	±7,340	0.279	13,000	±13,000	0.142
107-1	Skin	BP907- 143S +45°	3,706	±1,465	0.433	3,706	±2,156	0.264	-	-	-
	Tor- sion Wrap	XP251S +45°	4,940	±1,940	0.436	4,940	±2,850	0.268	-	-	-
	Spar	1002S 0°	13,000	±4,990	0.445	13,000	±7,340	0.279	-	-	-

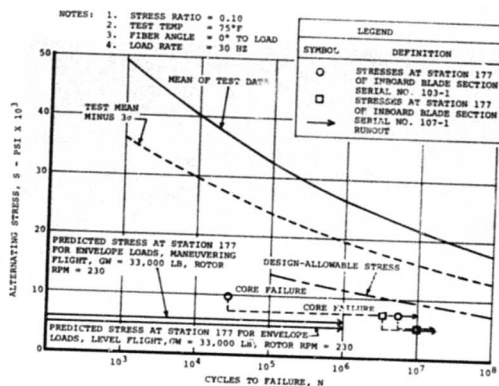


Figure 127.

Stress Curve for Analytical and Test Results of Unidirectional 1002S Epoxy-Resin Laminates Loaded in Tension-Tension Fatigue.

Figure 128.
Stress Curve for Analytical and Test Results of XP251S +45-Degree Crossply Epoxy-Resin Laminates Loaded in Tension-Tension Fatigue.

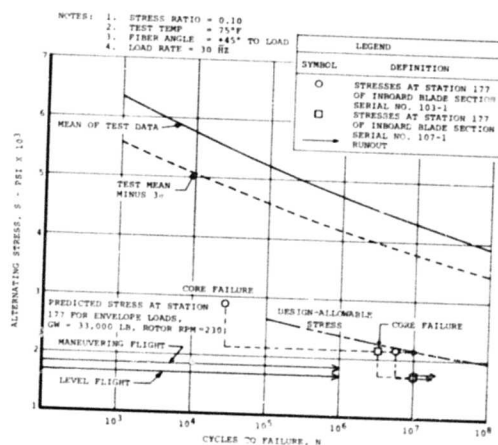
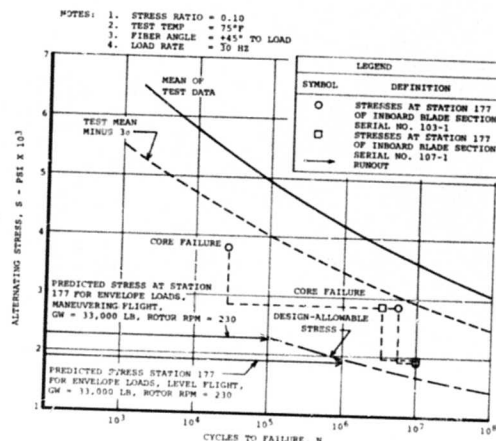


Figure 129. Stress Curve for Analytical and Test Results of BP907-143S +45-Degree Crossply Epoxy-Resin Laminates Loaded in Tension-Tension Fatigue.

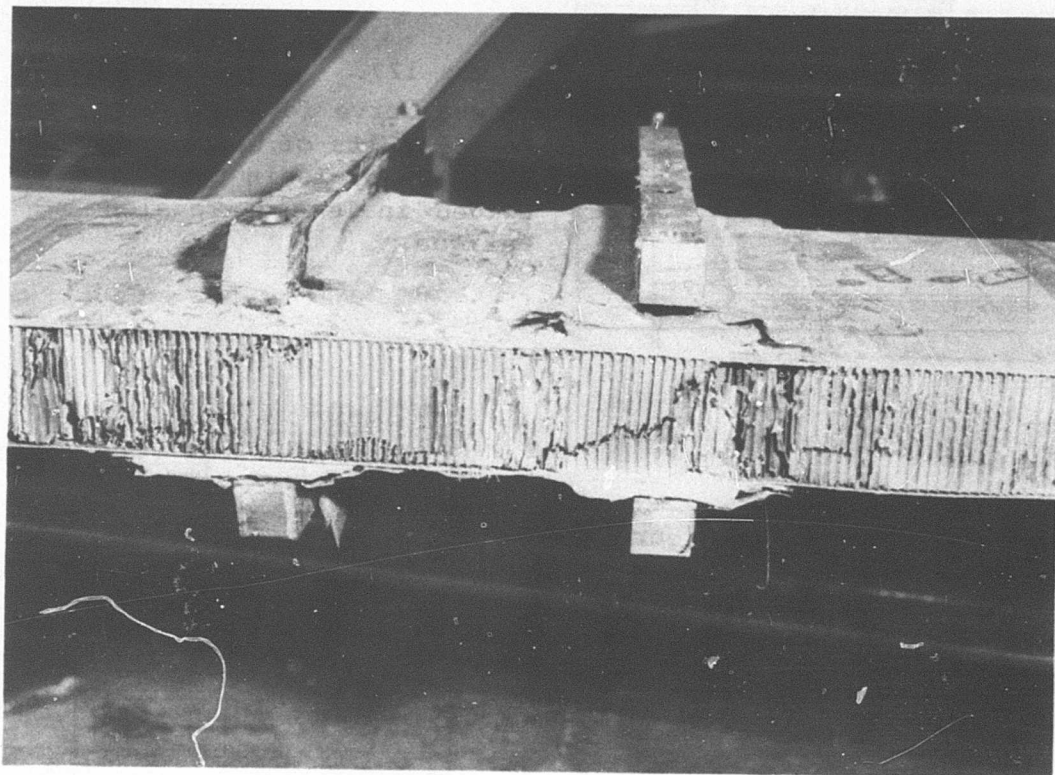


Figure 130. Core Failure in Middle of Inboard Blade
Serial No. 107-1.

Additional testing was performed on the S/N 107-1 test section, and failure of the spar was the objective. The failed core was removed from the cut-up section and the resulting cavities were filled with foam. Instrumentation was added and the reworked section was calibrated.

The alternating load at which the specimen could be expected to fail was determined from the mean curve of the 1002S glass test laminates at 1 million cycles (Figure 131). This load level consisted of a steady strain of 5120 microinches per inch and an alternating strain of ± 4650 microinches per inch. The alternating strain had to be adjusted to account for the difference between the test applied steady strain due to the 70,000 pounds axial load and the steady strain applied to the test laminates. This adjusted alternating strain was ± 5060 microinches per inch.

Because of limitations of the test equipment, the alternating strain obtained was only $\pm 22,000$ microinches per inch, but this strain corresponded to a moment of $\pm 133,000$ inch-pounds, which was 3.14 times the alternating moment at load level 1. At the maximum attainable alternating strain, the reworked section ran for 0.985 million cycles before the foam started to disintegrate and the remaining core failed in shear. These failures forced the termination of the test.

Figures 131 through 133 compare the strain level on each fiberglass material with the design allowable strain. Figure 131 makes the comparison for the spar material, unidirectional 1002S glass. The strain on the reworked section is greater than the design allowable strain at 1 million cycles, but the strain level is not in the failure region of the test laminates. Figure 132 compares the XP251S glass ($\pm 45^\circ$ crossply) design allowable strains with the strain on the reworked section. The strain on the specimen exceeds mean $+3\sigma$ of the test coupons, with only minor damage (45° resin failures shown in Figure 134). The behavior of the crossply in this section supports the conclusion for the coupon testing that the crossply, when fatigue tested with unidirectional material, operates at the strain level of the unidirectional material. Figure 133 shows the strain level on the skins for the design allowable strain. As indicated in the diagram, the strain level is greater than the design allowable strain, but it is not in the failure region of the laminates.

The results of the S/N 103-1 and S/N 107-1 inboard fatigue test demonstrated that the spar, torsion wraps, skin, and trailing edge can withstand 10 million cycles at the predicted design loads. The structure's capability to carry the design loads with massive core damage and trailing-edge skin failures was shown. The spar, torsion wraps and skin of the forward part of the section withstood more than three times the predicted design loads for approximately a million cycles. The erosion strip bonding was found to be unacceptable on one section, but satisfactory on the other section. The honeycomb core was shown to be satisfactory for 10 million cycles at the predicted fatigue loads. The core failure, which was probably induced by the test setup, might suggest that the core is the fatigue critical component. These tests indicated that each fiberglass material would be satisfactory for initial flight operations.

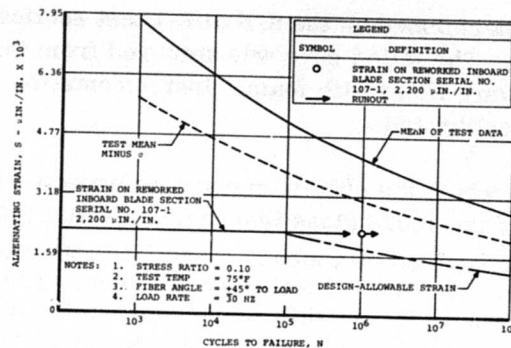


Figure 131. Stress Curve for Analytical and Test Results of Unidirectional 1002S Epoxy-Resin Laminates Loaded in Tension-Tension Fatigue After Rework.

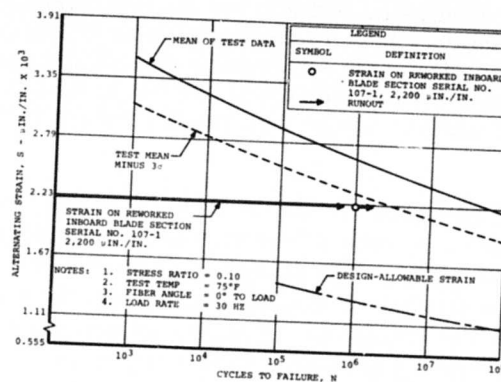


Figure 132. Stress Curve for Analytical and Test Results of XP251S +45-Degree Crossply Epoxy-Resin Laminates Loaded in Tension-Tension Fatigue After Rework.

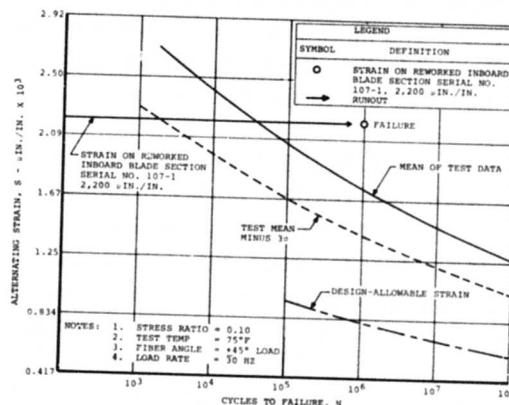


Figure 133. Stress Curve for Analytical and Test Results of BP907-143S +45-Degree Crossply Epoxy-Resin Laminates Loaded in Tension-Tension Fatigue After Rework.

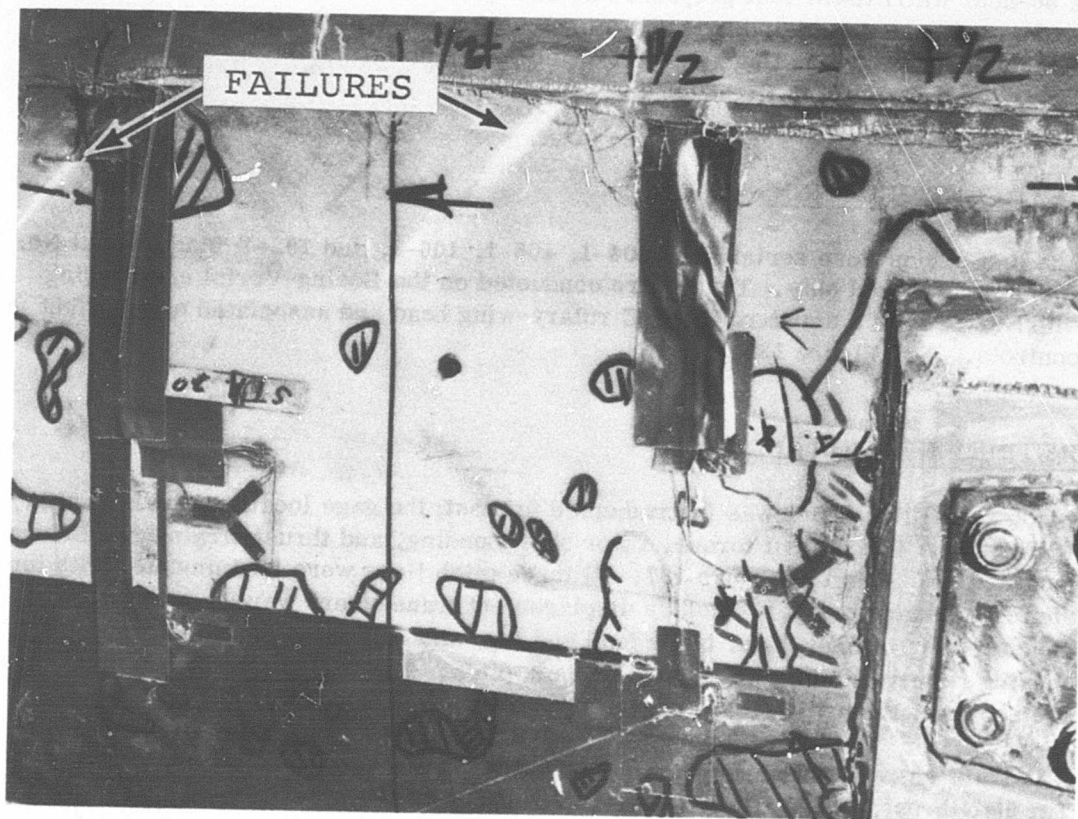


Figure 134. Failures of Inboard Blade Section Serial No. 107-1 After Rework.

WHIRL TEST PROGRAM

INTRODUCTION

A 50-hour whirl tower test program was conducted on the forward set of advanced-geometry blades to obtain blade strain and motion data, static thrust performance data, and endurance testing as a part of the preflight substantiation data requirements for the safety-of-flight review.

TEST CONFIGURATION

The test blades were serial Nos. 104-1, 105-1, 106-1, and 102-1; blade serial No. 102-1 was tracked only. Tests were conducted on the Boeing-Vertol engineering whirl tower with a standard CH-47C rotary-wing head and associated upper flight controls. (See Figure 135.)

INSTRUMENTATION AND DATA

Blade serial No. 105-1 was instrumented for test; the gage locations are shown in Figure 136. Rotor shaft torque, rotor shaft bending, and thrust strain-gage bridge locations are shown in Figure 137. All three pitch links were instrumented with tension strain-gage bridges. Rotary displacement transducers were mounted for the measurement of blade flap, blade lead and lag, and rotational motion of the pitch housing relative to the pitch shaft for blade pitch. The transducer installations are shown in Figure 138.

All strain-gage outputs except torque and thrust were recorded on oscillographs. Torque, thrust, and input collective and cyclic pitch were read on meters. Rotor shaft rpm was observed on an electronic counter. All strain gages were load-calibrated and shunt-calibrated. The lead-lag transducer was calibrated in terms of lag damper displacement. The pitch and flap transducers and the collective- and cyclic-pitch input meters were all calibrated relative to an inclinometer at the blade vertical pin attachment. It should be noted that pitch inputs are measurements of swashplate displacement, while the pitch transducer measures pitch housing rotation relative to the pitch shaft. Blade strain-gage zeros were read with the instrumented blade hanging against the droop stop and in the full-lead position (i.e., blade static position).

LIMITATIONS

Cyclic-pitch input angle was restricted to avoid droop-stop pounding, and rotor shaft power was limited to a maximum of 3,750 horsepower.

BLADE TRACKING

Satisfactory blade track was attained by conventional pitch-link and tip-tracking-weight adjustments, plus adjustments in the reflex angle of the trailing-edge cusp.

STRESS AND MOTION SURVEY

Stress and motion data were obtained for the test conditions shown in Table XVI.

TABLE XVI. STRESS AND MOTION SURVEY CONDITIONS		
Rotor Speed (rpm)	Collective-Pitch Input Angle (deg)	Cyclic-Pitch Input Angle (deg)
230	2, 5, 8, 11	1
245	2, 5, 8, 10.1	1
250	2, 5, 8, 9.8	1
230	11	2, 4, 6, 8, 9
245	9.8	2, 4, 6, 7, 8

Data for blade flap and chord bending moments, rotor shaft bending moments, pitch link loads, and blade flap, pitch, and lag motions are shown in Figures 139 through 162.

STATIC THRUST PERFORMANCE

Torque and thrust were recorded for stabilized rotor speeds of 225, 235, 245, and 250 rpm, while collective pitch varied from 2 degrees to 11.75 degrees, in 1-degree increments, with an upper limit of 3,750 horsepower. Thrust-versus-collective pitch and horsepower-versus-collective pitch plots for the four rpm settings are shown in Figures 163 and 164.

ENDURANCE TEST

The 50-hour endurance test consisted of the 5 test hours accumulated during the stress and motion survey plus 45 hours of endurance conducted per the schedule

shown in Table XVII. The schedule was repeated until the total of 50 hours was obtained. Collective input angle was adjusted to obtain the specified power.

TABLE XVII. ENDURANCE TEST WHIRL SCHEDULE				
Time (hr)	Rotor Speed (rpm)	Horsepower	Nominal Collective Input Angle (deg)	Cyclic Input Angle (deg)
2	250	3,250	9.0	4
3	245	3,420	9.5	4
5	230	3,420	10.5	4

TEST OBSERVATIONS

The Tedlar protective film on the upper surfaces of the blades became debonded locally and peeled off early in the test program. This peeling progressed throughout the test program, but only on the upper surface. The loss of this film was not detrimental to the blade structure or to the conduct of the test program.

Partial debonding of the outboard titanium erosion strips also occurred early in the program on blades serial Nos. 104-1 and 106-1. Local repairs were made at the tower, but they were only partially effective. Pressure-sensitive aluminum tape was also applied in an attempt to retain the strips. Testing was stopped after approximately 27 hours of endurance running due to an abnormal noise. Inspection of blade serial No. 106-1 showed an almost complete debonding of the upper surface of the outboard erosion strip and partial failure of the metal strip due to wind buffeting (see Figure 165).

This erosion strip was removed and replaced with laminated pressure-sensitive aluminum tape of equivalent weight. The remainder of the endurance test was completed in this configuration.

POSTTEST REMARKS

Examination of the erosion strip removed from blade serial No. 106-1 indicated that the failure mode was an adhesive failure of the primer to the metal. After further checks of erosion-strip bonds on all the blades and consideration of potential safety hazards, the titanium erosion strips were removed from all blades and replaced with polyurethane erosion-resistant shoes for the flight test program. Subsequent company-sponsored investigations and tests showed that satisfactory

adhesion of the primer was attained by applying the primer immediately after the metal conversion coating treatment, air-drying the primer for 30 minutes, followed by a cure-bake cycle at 300°F minimum for 30 minutes. The effectiveness of these revised processing procedures has been demonstrated on the boron rotor blade structural fatigue tests and the 50-hour whirl tower endurance test programs.

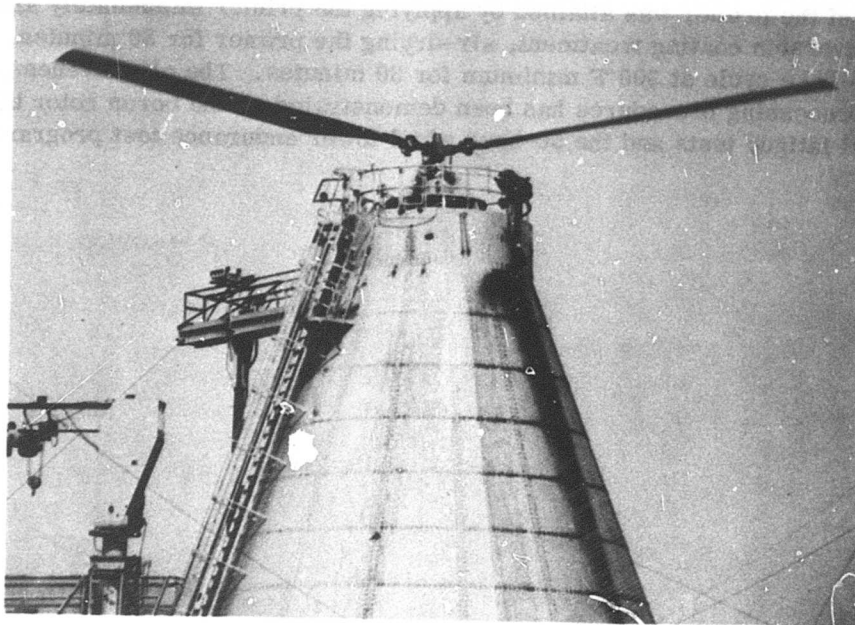


Figure 135. Whirl Tower With Advanced-Geometry Blades.

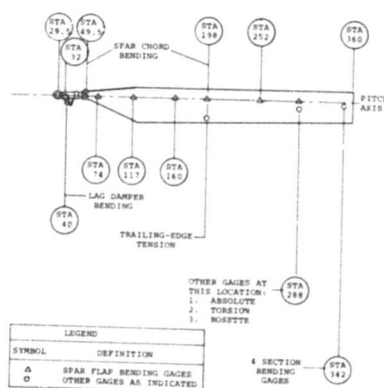


Figure 136. Locations and Types of Strain Gages Installed on Advanced-Geometry Blade Serial No. 105-1.

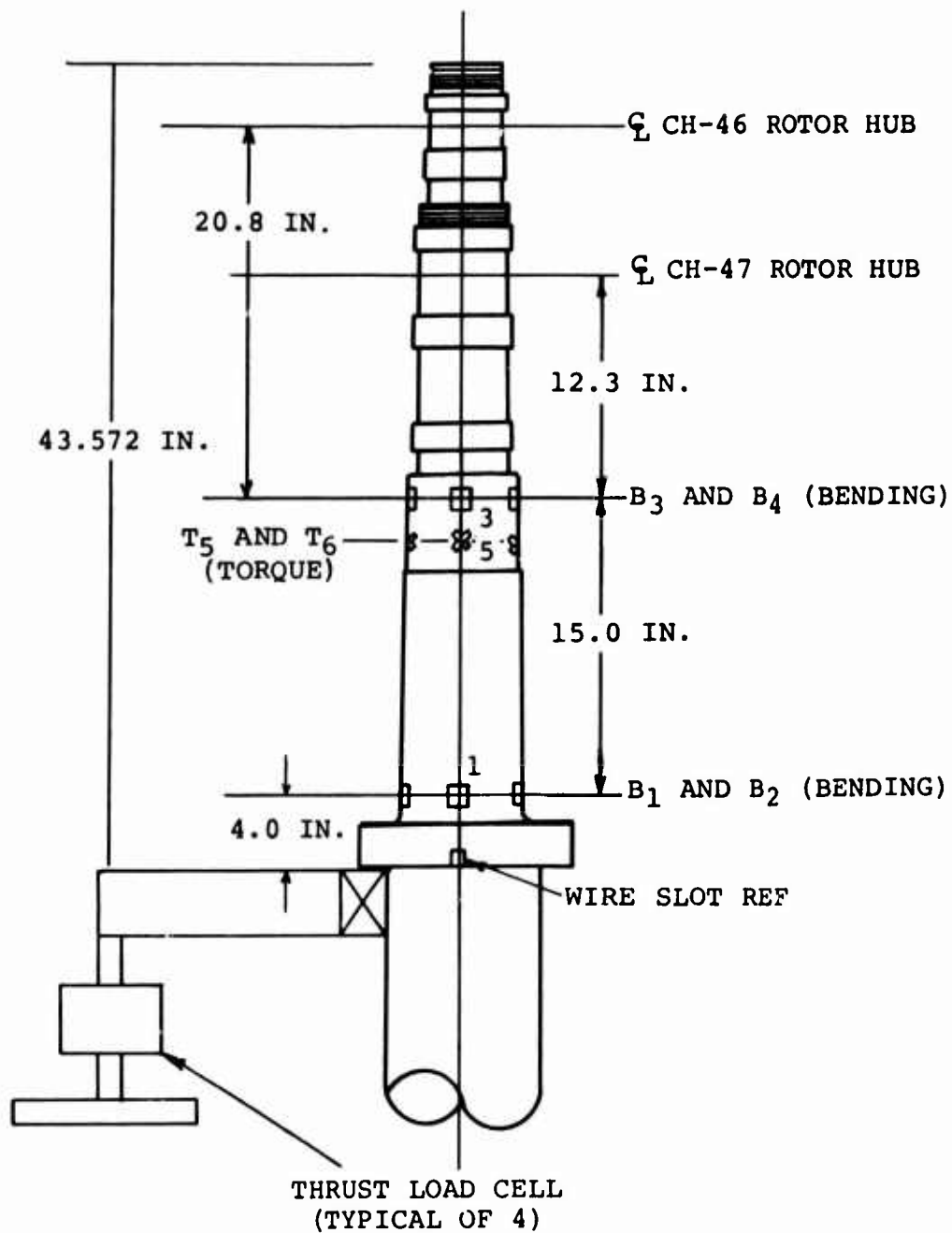


Figure 137. Locations of Gages on Whirl Tower Rotor Shaft.

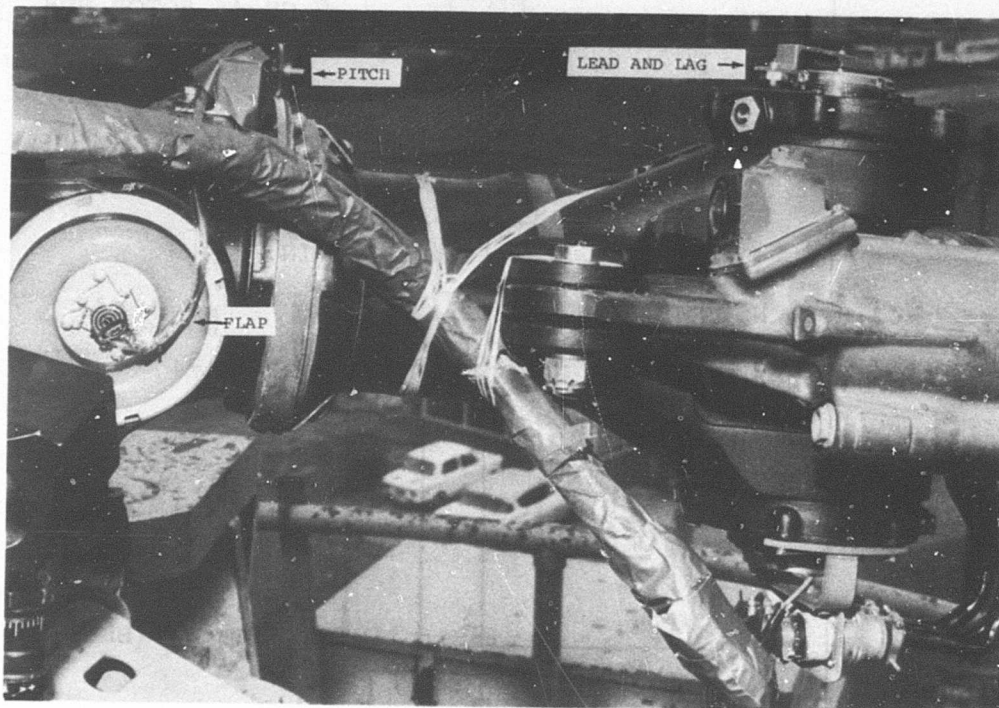


Figure 138. Installation of Blade Motion Transducers.

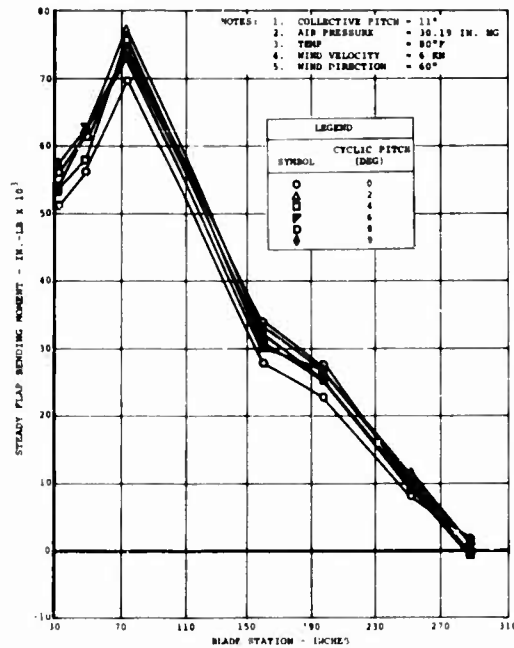


Figure 139. Steady Flap Bending Moment in Whirl Test at 230 Rotor RPM.

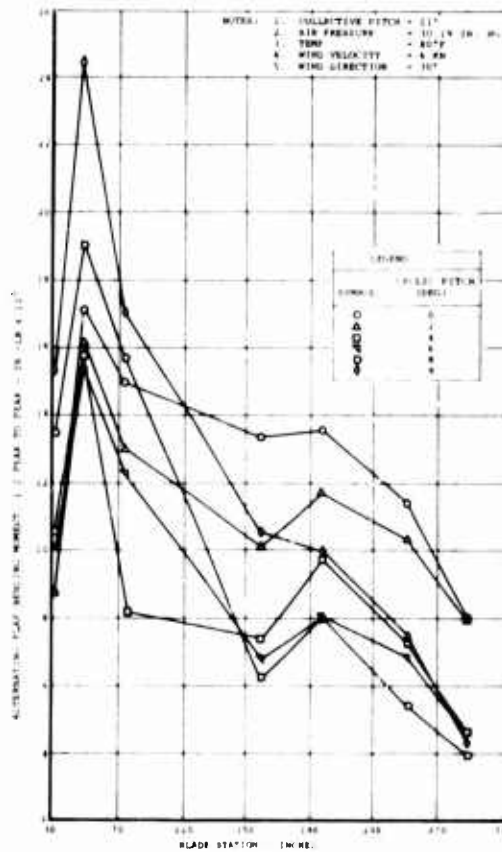


Figure 140. Alternating Flap Bending Moment in Whirl Test at 230 Rotor RPM.

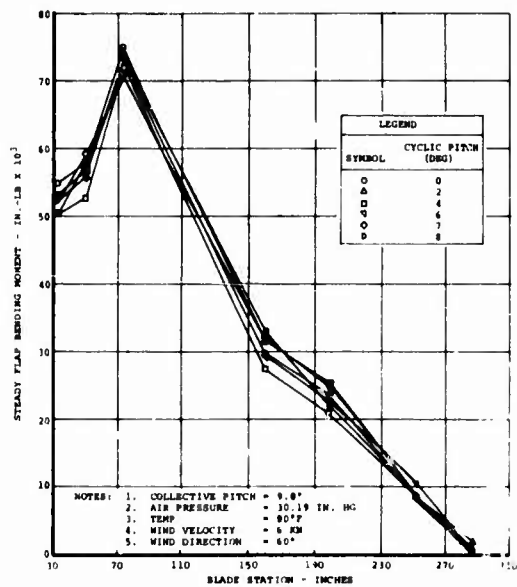


Figure 141. Steady Flap Bending Moment in Whirl Test at 245 Rotor RPM.

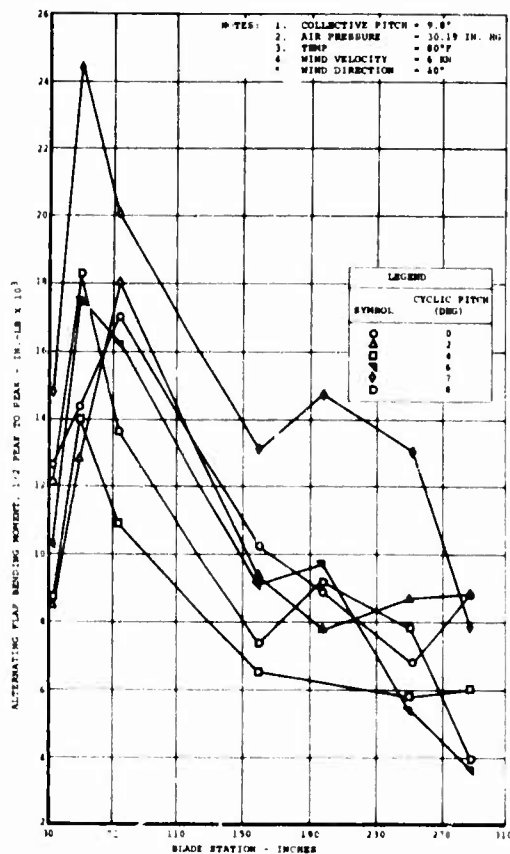


Figure 142. Alternating Flap Bending Moment in Whirl Test at 245 Rotor RPM.

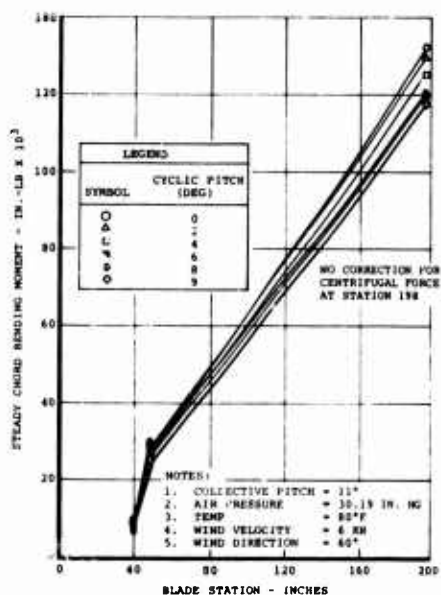


Figure 143.
Steady Chord Bending Moment
in Whirl Test at 230 Rotor
RPM.

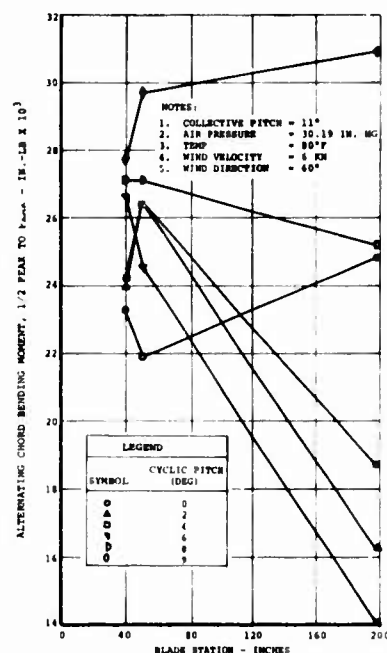


Figure 144.
Alternating Chord Bending
Moment in Whirl Test at
230 Rotor RPM.

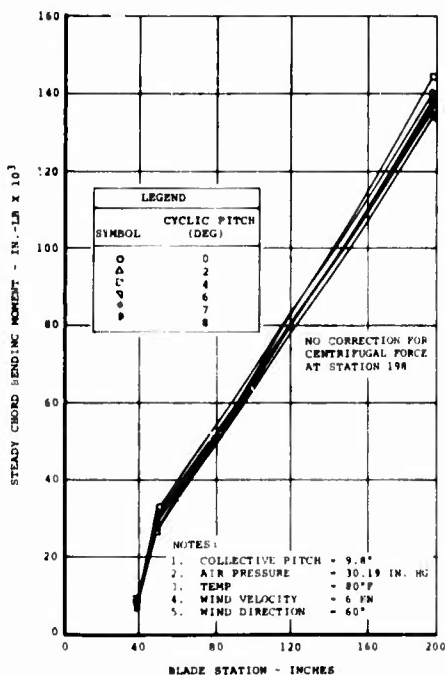


Figure 145.
Steady Chord Bending
Moment in Whirl Test
at 245 Rotor RPM.

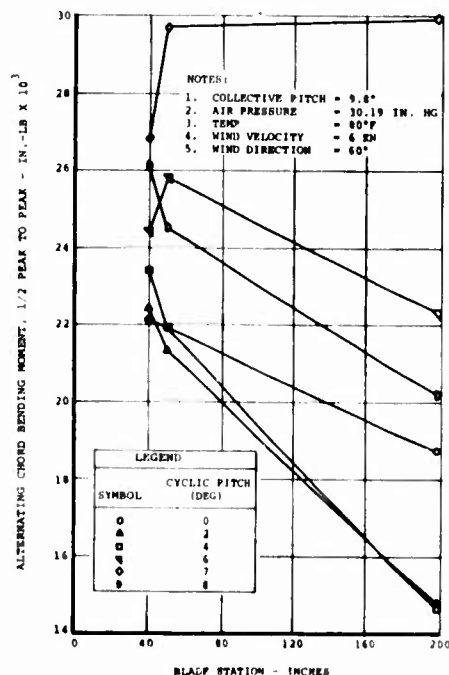


Figure 146.
Alternating Chord Bending
Moment in Whirl Test at
245 Rotor RPM.

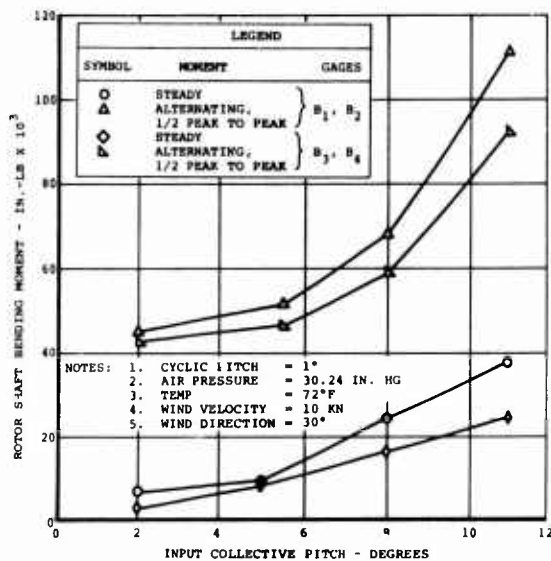


Figure 147. Rotor Shaft Bending Moment Versus Collective Pitch in Whirl Test at 230 Rotor RPM.

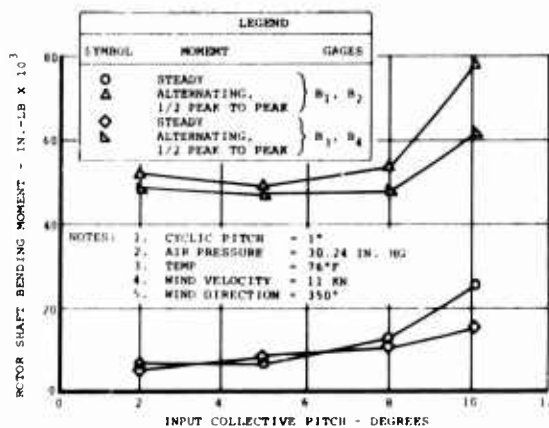


Figure 148. Rotor Shaft Bending Moment Versus Collective Pitch in Whirl Test at 245 Rotor RPM.

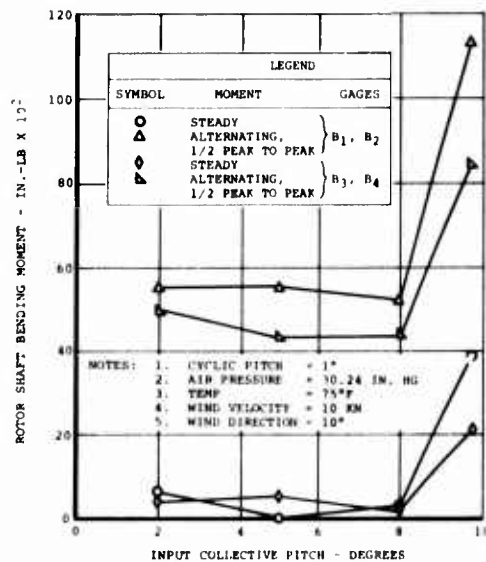


Figure 149. Rotor Shaft Bending Moment Versus Collective Pitch in Whirl Test at 250 Rotor RPM.

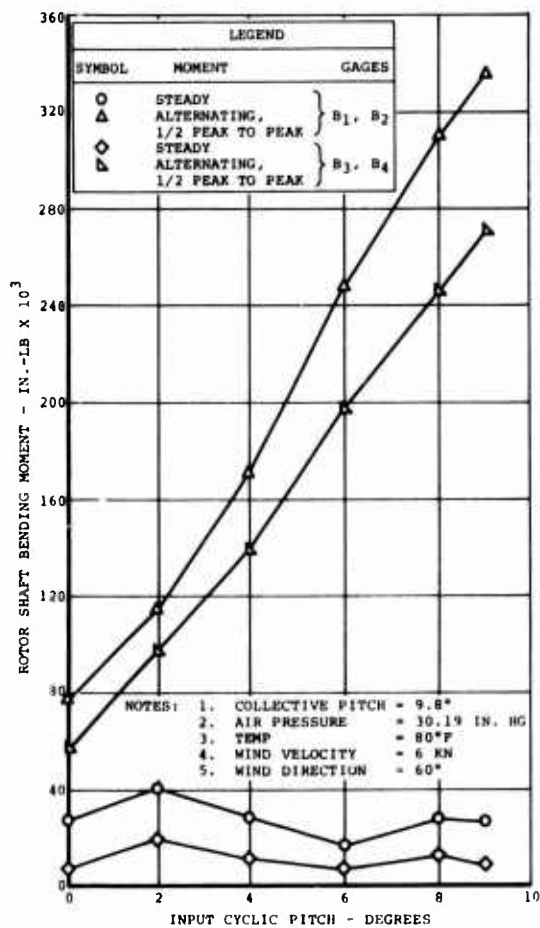
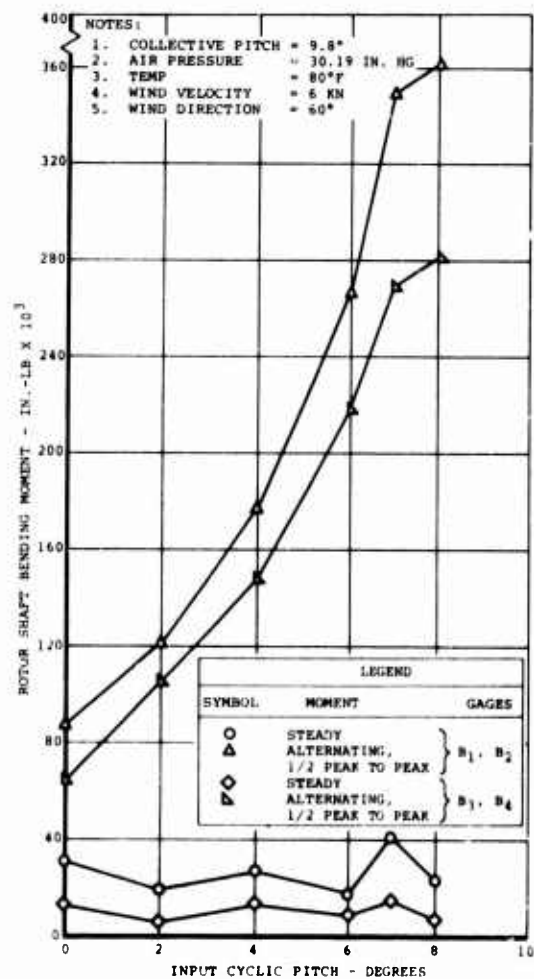


Figure 150. Rotor Shaft Bending Versus Cyclic Pitch in Whirl Test at 230 Rotor RPM.

Figure 151. Rotor Shaft Bending Moment Versus Cyclic Pitch in Whirl Test at 245 Rotor RPM.



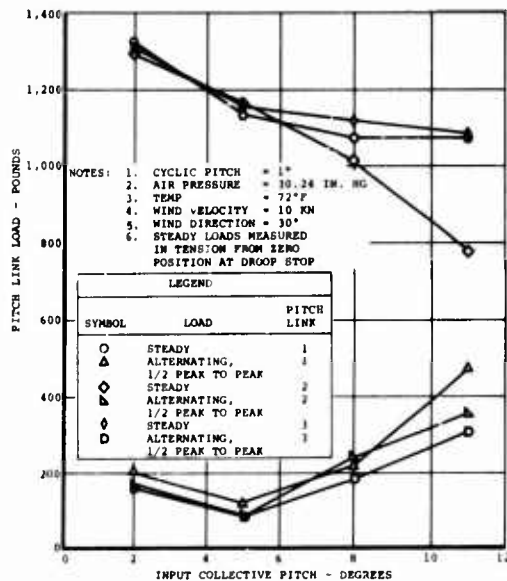


Figure 152.
Pitch Link Loads Versus
Collective Pitch in Whirl Test
at 230 Rotor RPM.

Figure 153.
Pitch Link Loads Versus
Collective Pitch in Whirl Test
at 245 Rotor RPM.

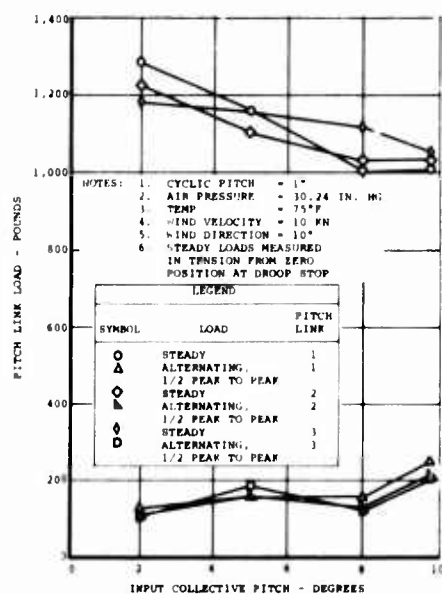
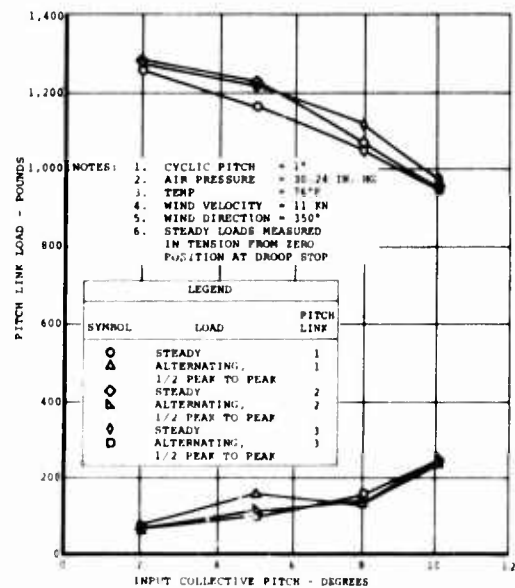


Figure 154.
Pitch Link Loads Versus
Collective Pitch in Whirl Test
at 250 Rotor RPM.

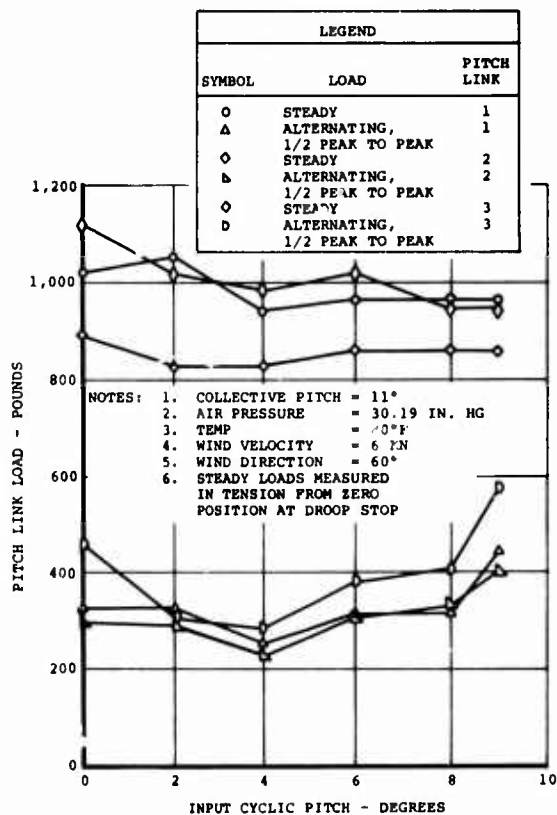
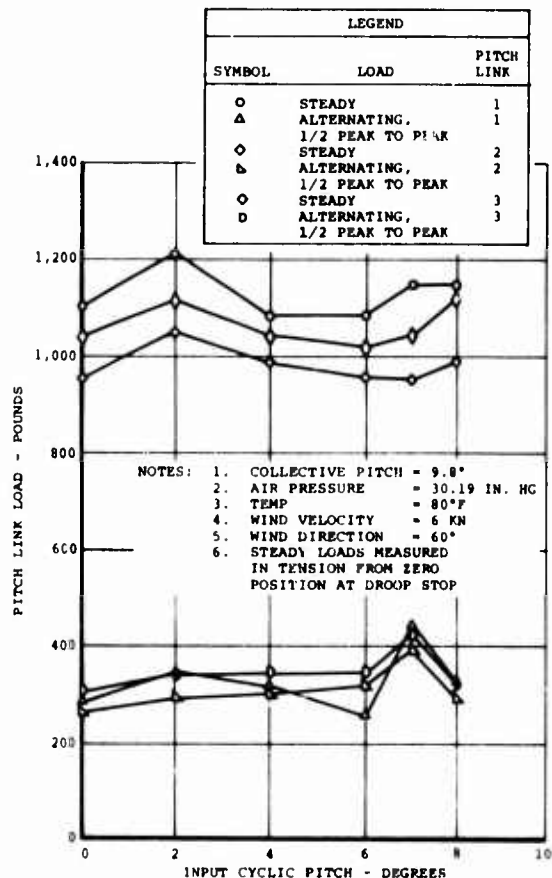


Figure 155. Pitch Link Loads Versus Cyclic Pitch in Whirl Test at 230 Rotor RPM.

Figure 156. Pitch Link Loads Versus Cyclic Pitch in Whirl Test at 245 Rotor RPM.



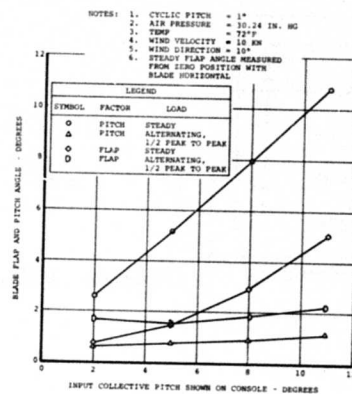


Figure 157. Blade Flap and Pitch Angle Versus Collective Pitch in Whirl Test at 230 Rotor RPM.

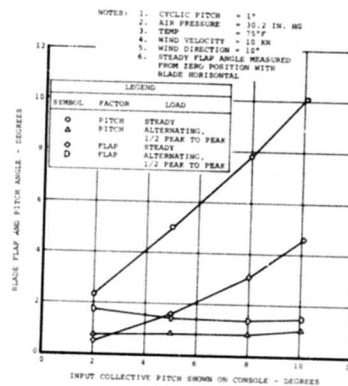


Figure 158. Blade Flap and Pitch Angle Versus Collective Pitch in Whirl Test at 245 Rotor RPM.

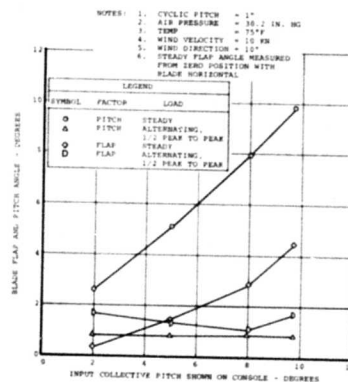


Figure 159. Blade Flap and Pitch Angle Versus Collective Pitch in Whirl Test at 250 Rotor RPM.

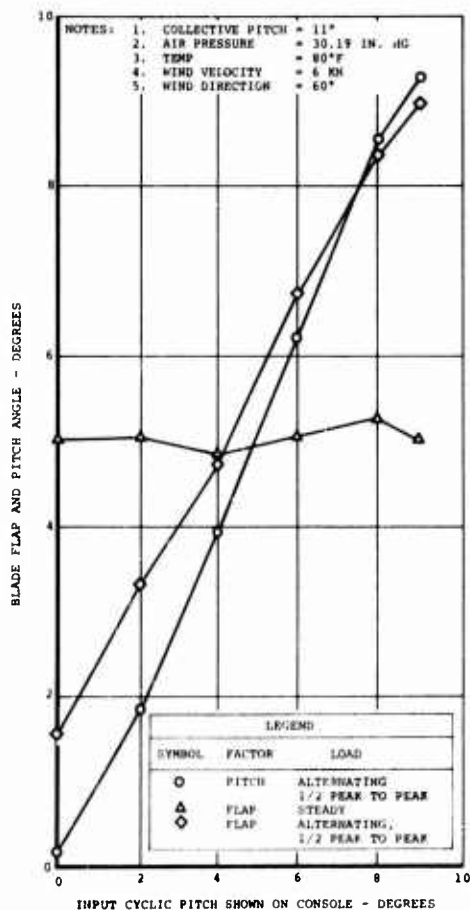


Figure 160. Blade Flap and Pitch Angle Versus Cyclic Pitch in Whirl Test at 230 Rotor RPM.

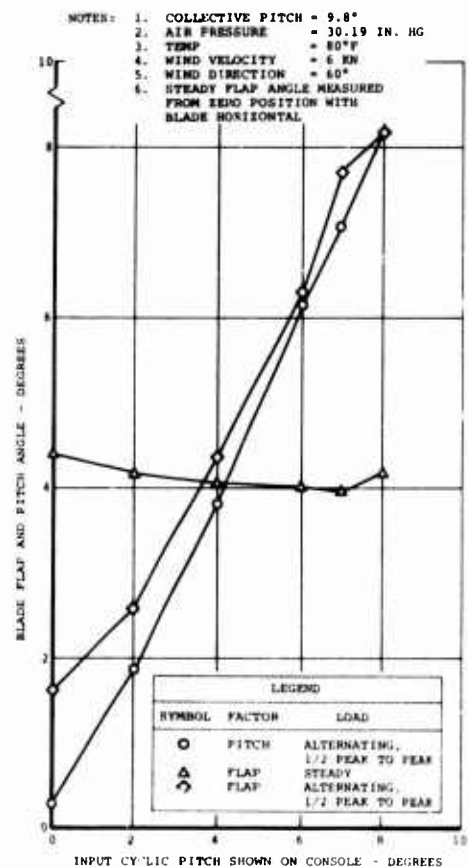


Figure 161. Blade Flap and Pitch Angle Versus Cyclic Pitch Angle in Whirl Test at 245 Rotor RPM.

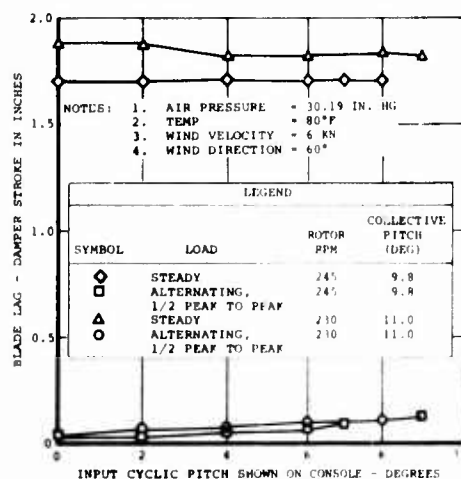


Figure 162. Blade Lag Versus Cyclic Pitch in Whirl Test.

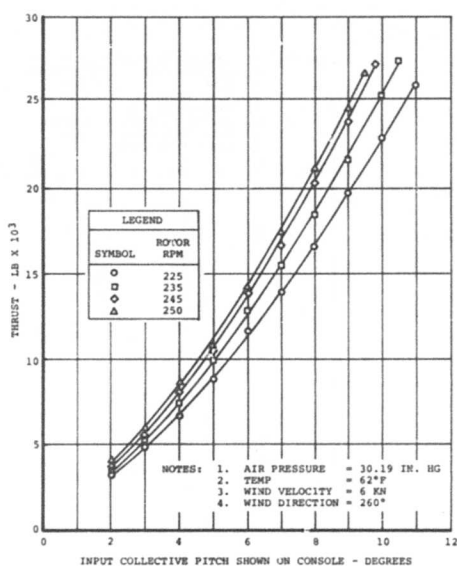


Figure 163. Blade Thrust Versus Collective Pitch in Whirl Test.

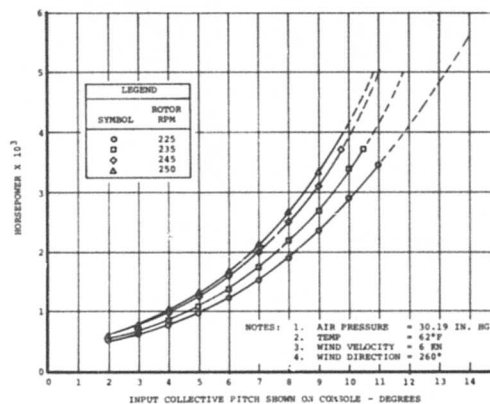
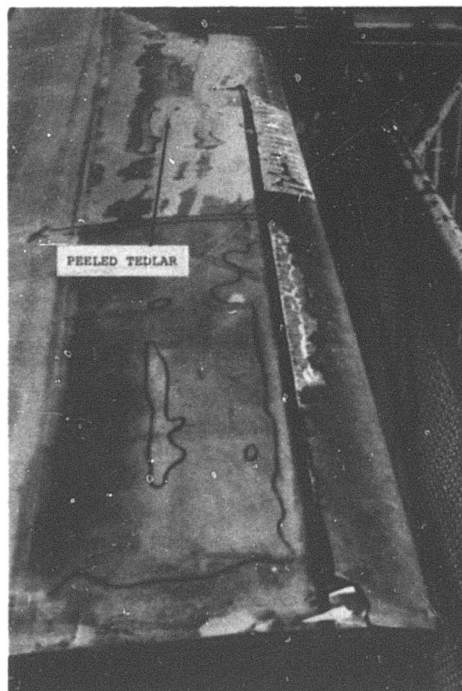


Figure 164. Horsepower Versus Collective Pitch in Whirl Test.

Figure 165. Advanced-Geometry Blade Serial No. 106-1 Showing Peeled Tedlar, Bond Failure, and Missing Pieces.



FLIGHT TEST PROGRAM

INTRODUCTION

Flight test of the advanced-geometry rotor blades was conducted on a CH-47C helicopter, Army S/N 66-19103.

The primary objectives of the flight test program were as follows:

- Flight demonstration of the advanced-geometry fiberglass rotor blades
- Acquisition of rotor system stress and motion data for comparison with data from CH-47C production blades
- Identification of control load rotor limits
- Establishment of performance envelope

The detailed flight test requirements for the program are contained in Reference 11. The methods and procedures for conducting stress and motion and performance tests are contained in Reference 12. Table XVIII is a summary of the flight test conditions and associated data flight runs conducted to comply with the requirements of Reference 11. The summary shown in Table XIX also indicates other sources of supplementary data recorded in the performance of the flight test program.

The program encompassed a broad spectrum of test conditions and configurations across the gross weight envelope of the aircraft. Because previous stress and motion data on the CH-47 have shown that maximum loads occur for an aft-center-of-gravity configuration, stress and motion tests were concentrated on this maximum rearward cg configuration.

In addition to the stress and motion tests, performance, flying qualities, vibration, and acoustic data were obtained to round out the program. Evaluation of mechanical instability and rotor blade tracking were accomplished to assure safe operation with the experimental rotor blade system and to provide a satisfactory operational testbed.

The flight test program on the advanced-geometry blade accumulated 40 hours 10 minutes of flight time versus a minimum contractual time of 26 hours. An additional 6 hours 25 minutes of flight was accumulated for the CH-47C engine inlet pressure survey program for a total flight time of 46 hours 35 minutes. Flight test data for the blade was recorded concurrently with the engine inlet pressure survey program whenever appropriate test conditions existed; this accounts for the specific remarks in Tables XVIII and XIX.

TABLE XVIII. PROGRAM DATA FLIGHT SUMMARY						
Data Category	Gross Weight (lb)	CG Location	Rotor Speed (rpm)	Altitude, H _D (ft)	Flight No.	Remarks
Stress and motion	33,000	7 in. aft	235	3,000	243	-
Stress and motion	33,000	7 in. aft	235	3,000	244	-
Stress and motion	33,000	7 in. aft	235	3,000	246	-
Stress and motion	33,000	7 in. aft	235,245	3,000	254	-
Stress and motion	40,000	6 in. aft	235	IGE, 3,000	251	-
Stress and motion	40,000	6 in. aft	235	3,000	252	-
Stress and motion	40,000	6 in. aft	235	3,000, 6,000	253	-
Stress and motion	40,000	6 in. aft	235	3,000, 6,000, 8,000	255	-
Stress and motion	46,000	4 in. aft	245	IGE, 3,000	267	-
Stress and motion	46,000	4 in. aft	235	3,000	269	-
Stress and motion	46,000	4 in. aft	235	1,000, 3,000	270	-
Stress and motion	46,000	4 in. aft	245	Service ceiling,	271	-
				service ceiling-1,000		
Stress and motion	46,000	4 in. aft	245	6,000	272	-
Stress and motion	46,000	11 in. fwd	245	IGE, 3,000, 6,000	287	-
Stress and motion	50,000	mid	245	IGE, 2,000	285	-
Stress and motion	50,000	mid	245	Service ceiling,	286	-
				service ceiling-1,000		
Performance						
Hover, OGE	40,000	mid	225,245	300	280	10,500-lb external wt
Hover, OGE	46,000	mid	225,245	200	280	16,000-lb external wt
Speed polar	33,000/6	mid	235/6	1,000	258	Screens off
Speed polar	33,000/6	mid	235/6	1,000	276	Screens on
Speed polar	60,000/6	mid	235/6	1,000	279	Screens on
Speed polar	60,000/6	mid	245/6	10,000	274	Screens on
Flying qualities	40,000	6 in. aft	235	3,000	253	-
Flying qualities	40,000	6 in. aft	235	6,000, 8,000	255	-
Flying qualities	40,000	6 in. aft	230	10,000	281	-
Flying qualities	40,000	6 in. aft	230	5,500	282	-
Flying qualities	40,000	6 in. aft	230	8,500, 9,000	283	-
Flying qualities	46,000	4 in. aft	245	5,000	270	-
Flying qualities	46,000	4 in. aft	245	Service ceiling-1,000	271	-
Flying qualities	46,000	4 in. aft	245	6,000	272	-
Flying qualities	46,000	4 in. aft	235	1,000	272	-

TABLE XIX. SUPPLEMENTARY DATA FLIGHT SUMMARY				
Data Category	Gross Weight (lb)	CG Location	Source	Flight
Stress and motion	33,000	4 in. fwd-2 in. aft	Initial hover	
	33,000		Engine inlet pressure survey	256-258-259
	33,000		Engine inlet pressure survey	261-262-276
	33,000	4 in. fwd	Auterotatation investigation	263
	40,000	6 in. aft	Mechanical instability tests	248
	40,000	6 in. aft	Flying qualities	
	40,000	1-3 in. fwd	OGE hover performance	281-282-283
	40,000	3 in. fwd	Speed polar performance	280
	46,000	4 in. aft	Flying qualities	288
	46,000		Mechanical instability tests	284
Performance Flying qualities Acoustics	46,000	0.5-2 in. fwd	Speed polar performance	249
	46,000	mid	OGE hover performance	274-279
	50,000/6	3 in. fwd	Speed polar performance	280
	33,000	mid	Stress and motion	288
	46,000	mid	Speed polar performance	263
	40,000	4 in. aft	Speed polar performance	279
	40,000	4 in. aft	Acoustic dive	282
	40,000	4 in. aft	Acoustic dive	283
	33,000	7 in. aft	Qualitative tests performed	243
	40,000	6 in. aft	prior to start of program tests.	248
Vibration	46,000	4 in. aft		249
Data obtained on all scheduled data flight tests; partial complement of sensors used on Flights 281 through 288				

AIRCRAFT CONFIGURATION

The aircraft used for the flight test was a CH-47C helicopter, Boeing manufacturing Tab No. B-361, with the following changes:

- Fiberglass-reinforced plastic rotor blades
- Forward No. 104-1 - green
- Forward No. 105-1 - yellow (instrumented)
- Forward No. 106-1 - red
- Aft No. 102-2 - green
- Aft No. 103-2 - yellow (instrumented)
- Aft No. 104-2 - red

See Figure 166 for the installed orientation of the blades. For safety considerations, the leading-edge titanium erosion strips were removed from the 8 flight blades, due to debonding problems experienced in whirl test, and replaced with polyurethane erosion-resistant shoes made from Y9265A tape material. Planform coverage and thickness (0.015 inch) were the same as the original titanium strips. The modified blades were rebalanced, the instrumented blades were recalibrated, both forward and aft sets of blades were retracked on the whirl tower, and posttrack NDT inspections were performed.

- Modification to control kinematics to maintain similarity of longitudinal and pitch SAS control system sensitivities with production, cambered-airfoil, steel-spar rotor blades
- Standard production self-tuning vibration absorbers with friction damping installed in nose and cockpit, tuned for 232 to 251 rotor rpm
- Transmissions uprated to 6,800 shp for a maximum flight time at maximum power of 4 hours beginning with Flight 254
- Standard production lag dampers (high rate, cold weather), part No. 114H6800-3

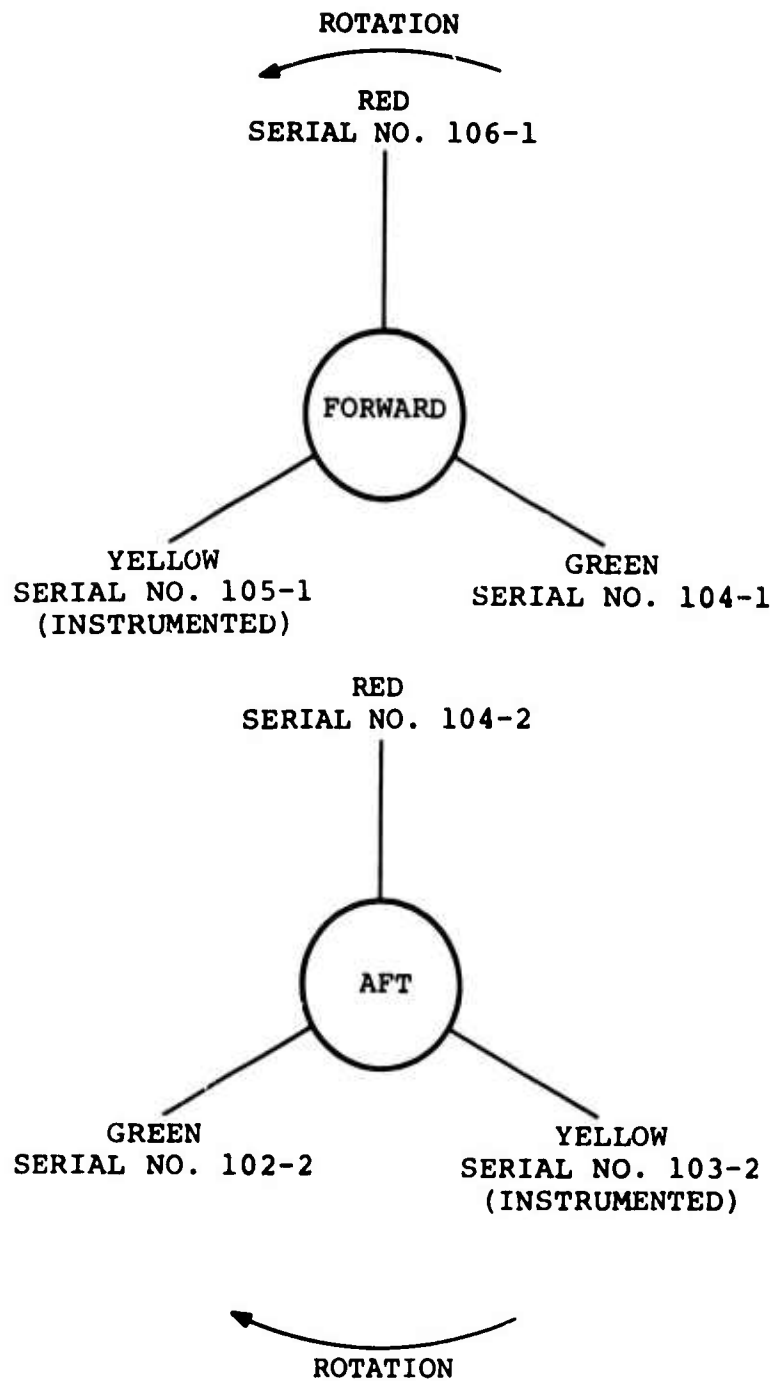


Figure 166. Orientation of Advanced-Geometry Blades on CH-47C Helicopter.

EQUIPMENT

Special equipment required during the program was as follows:

- SAS pulser box and oscillator installed to apply lateral and directional oscillations to determine critical frequency during 40,000-pound and 46,000-pound gross weight mechanical stability evaluation
- SAS pulser box installed to apply longitudinal control pulses for assessment of pitch control kinematic changes and investigation of control load rotor limits (stall flutter) during flying qualities evaluation
- External cargo dead weights of approximately 12,000 and 16,000 pounds for hover performance requirements
- Strobex blade tracker for in-flight blade tracking

INSTRUMENTATION

All data were recorded on a narrowband frequency modulation (NBFM) 14-track Ampex tape recorder, Model AR-200, fitted with 250-kilocycle recording heads.

Table XX lists all parameters which were recorded during the program. NBFM data signals from each of the 14 banks of limited-frequency range oscillators were mixed into a composite signal and recorded on tape, with the exception of the acoustic signal. Data were recovered by passing the composite signal through a bank of frequency discriminators to obtain the individual analog signals.

Acoustic data were recorded over a full frequency band, or wideband FM (WBFM), on a track from which data were not required for the test.

Prior to each flight, all data parameters were monitored and their electrical signals were adjusted to a standard baseline of zero or other predetermined constant. Because of static preloads on certain dynamic components, the rotor blades were positioned at the same azimuth for each preflight calibration.

Preflight requirements were:

- Lag damper blocks installed so that the rotor blades were maintained in the full-lead position throughout the calibration sequence
- Forward yellow (instrumented) blade pitch arm 90 degrees to the fuselage centerline on the right side

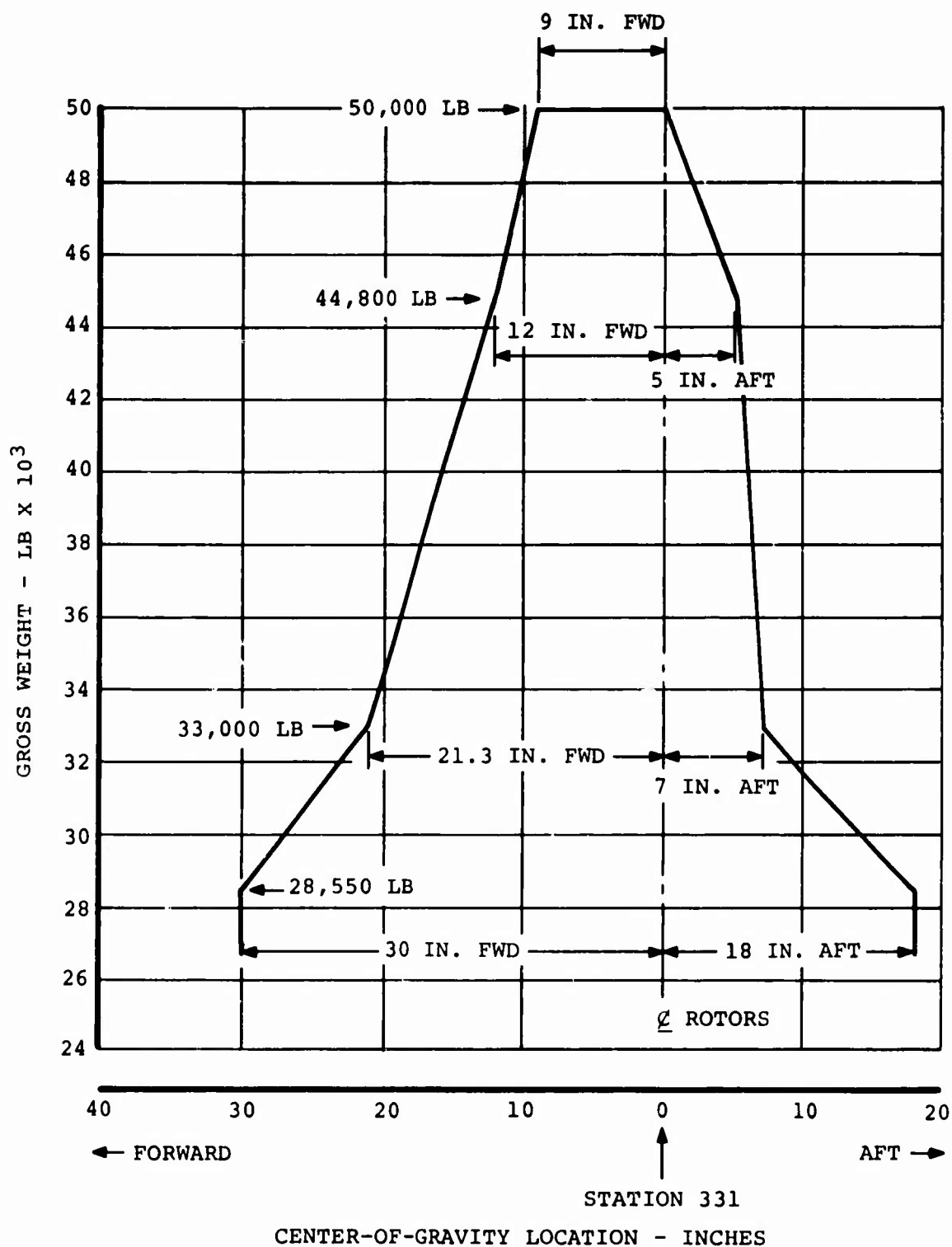


Figure 167. Center-of Gravity Envelope for the CH-47C Helicopter.

TABLE XX. AVAILABILITY OF INSTRUMENTATION AND DATA RECORDING

TABLE XX. AVAILABILITY OF INSTRUMENTATION AND DATA RECORDING					
Code No.	Parameter	Location	Unit		Flight
ACCOUNTS					
Acc001	Rotor Blade Noise	Fus Sta 270, Left BL 85, WL#7			
Aircraft and Engine					
1501	Rotor Speed - Analog		rpm		
1503	Engine N ₁ Speed	No. 1 (left)	rpm		
1504	Engine N ₂ Speed	No. 2 (right)	rpm		
1601	Pitch Rate		deg/sec		
1602	Roll Rate		deg/sec		
1603	Yaw Rate		deg/sec		
1609	Ldg Gear Oleo Position	Aft left	in.		
2102	Ldg Gear Oleo Position	Forward left	in.		
2103	Ldg Gear Oleo Position	Aft right	in.		
2104	Ldg Gear Oleo Position	Forward right	in.		
2107	Longitudinal Stick Position		in.		
2108	Lateral Stick Position		in.		
2109	Directional Pedal Position		in.		
2112	SAS Pitch Actuator Position	No. 1	in.		
2113	SAS Pitch Actuator Position	No. 2	in.		
2114	SAS Roll Actuator Position	No. 1	in.		
2115	SAS Roll Actuator Position	No. 2	in.		
2116	SAS Yaw Actuator Position	No. 1	in.		
2117	SAS Yaw Actuator Position	No. 2	in.		
2124	Long. Cyc Trim Act. Pos	Forward	deg		
2125	Side Slip Angle	Att	deg		
2208	Collective Pitch Lever Pos	Forward head	deg		
2250	Pitch Attitude		deg		
2251	Roll Attitude		deg		
3601	Rotor Speed	Forward	pct		
3606	Engine Shaft Torque	No. 1 (left)	pct		
3607	Engine Shaft Torque	No. 2 (right)	pct		
3608	Event Marker		pct		
6130	Altitude (Analog)		in./H ₂ O		
6130	Altitude (Freq)		Ship(prod.) system in./H ₂ O		
6240	Airspeed		Ship(prod.) system in./H ₂ O		
7201	Fuel Temperature	Boom system	°C		
7203	Fuel Temperature	No.1 (left) engine	°C		
7301	Fuel Temperature	No.2(right) engine	°C		
8201	Fuel Flow Rate	Rosemont	gal/min		
8202	Fuel Totalizer	No. 1 engine	gal		
8203	Fuel Flow Rate	No. 1 engine	gal/min		
8204	Fuel Totalizer	No. 2 engine	gal		

TABLE XX. Continued

TABLE XX. Continued																																																																																																																																																																																																																																																																																																																																																																																																																																																																																																																																																																																																																																																																																																																																																																																																																																																																																																																																																																																																																																																																																																																																																																																																																																																																																																																	
Code No.	Parameter	Location	Unit	Flight																																																																																																																																																																																																																																																																																																																																																																																																																																																																																																																																																																																																																																																																																																																																																																																																																																																																																																																																																																																																																																																																																																																																																																																																																																																																																																													
				GR22	GR23	GR24	242	243	244	245	246	247	248	249	250	251	252	253	254	255	256	257	258	259	260	261	262	263	264	265	266	267	268	269	270	271	272	273	274	275	276	277	278	279	280	281	282	283	284	285	286	287	288																																																																																																																																																																																																																																																																																																																																																																																																																																																																																																																																																																																																																																																																																																																																																																																																																																																																																																																																																																																																																																																																																																																																																																																																																																																												
Airframe Loads																																																																																																																																																																																																																																																																																																																																																																																																																																																																																																																																																																																																																																																																																																																																																																																																																																																																																																																																																																																																																																																																																																																																																																																																																																																																																																																	
582a	Aft Thrust Deck Supt Fty	Aft left aft	psi																																																																																																																																																																																																																																																																																																																																																																																																																																																																																																																																																																																																																																																																																																																																																																																																																																																																																																																																																																																																																																																																																																																																																																																																																																																																																																														</

TABLE XX. Continued

TABLE XX. Continued																								
Code No.		Parameter	Location	Unit	Flight																			
Rotor Blades and Hubs																								
Forward																								
4113		Chord Bend Moment	Sta 49.5	in.-lb	0	0	0	0	0	0	0	0	0	0	0	0	0	0	0	0	0	0	0	0
4117		Flap Bend Moment	Sta 74.0	in.-lb	0	0	0	0	0	0	0	0	0	0	0	0	0	0	0	0	0	0	0	0
4121		Flap Bend Moment	Sta 117.0	in.-lb	0	0	0	0	0	0	0	0	0	0	0	0	0	0	0	0	0	0	0	0
4123		Flap Bend Moment	Sta 160.0	in.-lb	0	0	0	0	0	0	0	0	0	0	0	0	0	0	0	0	0	0	0	0
4125		Flap Bend Moment	Sta 198.0	in.-lb	0	0	0	0	0	0	0	0	0	0	0	0	0	0	0	0	0	0	0	0
4127		Flap Bend Moment	Sta 252.0	in.-lb	0	0	0	0	0	0	0	0	0	0	0	0	0	0	0	0	0	0	0	0
4129		Flap Bend Moment	Sta 288.0	in.-lb	0	0	0	0	0	0	0	0	0	0	0	0	0	0	0	0	0	0	0	0
4133		Section Bend Moment	Sta 26.95	in.-lb	0	0	0	0	0	0	0	0	0	0	0	0	0	0	0	0	0	0	0	0
4135		Section Bend Moment	Sta 21.9	in.-lb	0	0	0	0	0	0	0	0	0	0	0	0	0	0	0	0	0	0	0	0
4137		Section Bend Moment	Sta 16.86	in.-lb	0	0	0	0	0	0	0	0	0	0	0	0	0	0	0	0	0	0	0	0
4139		Section Bend Moment	Sta 11.82	in.-lb	0	0	0	0	0	0	0	0	0	0	0	0	0	0	0	0	0	0	0	0
4141		Chord Bend Moment	Sta 198.0	in.-lb	0	0	0	0	0	0	0	0	0	0	0	0	0	0	0	0	0	0	0	0
4145		Spar Torsion	Sta 285.6	in.-lb	0	0	0	0	0	0	0	0	0	0	0	0	0	0	0	0	0	0	0	0
4149		Absolute Stress	Sta 288 up 90°	min/in.	0	0	0	0	0	0	0	0	0	0	0	0	0	0	0	0	0	0	0	0
4151		Absolute Stress	Sta 288 low 0°	min/in.	0	0	0	0	0	0	0	0	0	0	0	0	0	0	0	0	0	0	0	0
4153		Absolute Stress	Sta 288 up 255°	min/in.	0	0	0	0	0	0	0	0	0	0	0	0	0	0	0	0	0	0	0	0
4155		Absolute Stress	Sta 288 up 315°	min/in.	0	0	0	0	0	0	0	0	0	0	0	0	0	0	0	0	0	0	0	0
Rotor Shaft																								
Aft																								
5251		Bending Moment 0-180	Sta 23.1	in.-lb	0	0	0	0	0	0	0	0	0	0	0	0	0	0	0	0	0	0	0	0
5259		Bending Moment 0-180	Sta 37.0	in.-lb	0	0	0	0	0	0	0	0	0	0	0	0	0	0	0	0	0	0	0	0
5261		Bending Moment 0-180	Sta 37.0	in.-lb	0	0	0	0	0	0	0	0	0	0	0	0	0	0	0	0	0	0	0	0
5267		Bending Moment 0-180	Sta 62.94	in.-lb	0	0	0	0	0	0	0	0	0	0	0	0	0	0	0	0	0	0	0	0
5505		Torque	Sta 66.2	in.-lb	0	0	0	0	0	0	0	0	0	0	0	0	0	0	0	0	0	0	0	0
5507		Torque	Sta 66.0	in.-lb	0	0	0	0	0	0	0	0	0	0	0	0	0	0	0	0	0	0	0	0
5509		Torque	Sta 66.0	in.-lb	0	0	0	0	0	0	0	0	0	0	0	0	0	0	0	0	0	0	0	0
Rotor Shaft																								
Forward																								
5260		Bending Moment 0-180	Sta 23.47	in.-lb	0	0	0	0	0	0	0	0	0	0	0	0	0	0	0	0	0	0	0	0
5268		Bending Moment 0-180	Sta 32.82	in.-lb	0	0	0	0	0	0	0	0	0	0	0	0	0	0	0	0	0	0	0	0
5276		Bending Moment 0-180	Sta 18.4	in.-lb	0	0	0	0	0	0	0	0	0	0	0	0	0	0	0	0	0	0	0	0
5504		Torque	Sta 22.4	in.-lb	0	0	0	0	0	0	0	0	0	0	0	0	0	0	0	0	0	0	0	0
5506		Torque	Sta 22.4	in.-lb	0	0	0	0	0	0	0	0	0	0	0	0	0	0	0	0	0	0	0	0
5510		Torque	Sta 23.5	in.-lb	0	0	0	0	0	0	0	0	0	0	0	0	0	0	0	0	0	0	0	0
5612		Shear	Sta 31.6	lb	0	0	0	0	0	0	0	0	0	0	0	0	0	0	0	0	0	0	0	0
Upper Control System																								
Aft																								
2121		Swiveling Actuator Pos		in.	0	0	0	0	0	0	0	0	0	0	0	0	0	0	0	0	0	0	0	0
2123		Pivoting Actuator Pos		in.	0	0	0	0	0	0	0	0	0	0	0	0	0	0	0	0	0	0	0	0
2431		Pitch Link Load	Yellow	lb	0	0	0	0	0	0	0	0	0	0	0	0	0	0	0	0	0	0	0	0
2443		Pitch Link Load	Red	lb	0	0	0	0	0	0	0	0	0	0	0	0	0	0	0	0	0	0	0	0
2451		Pitch Link Load	Green	lb	0	0	0	0	0	0	0	0	0	0	0	0	0	0	0	0	0	0	0	0

TABLE XX. Continued									
Code No.	Parameter	Location	Unit	GR22	GR24	GR25	GR26	GR27	Flight
<u>Upper Control System</u>									
<u>Aft</u>									
5481	Fixed Link Load			0	0	0	0	0	0
5927	Swivelling Actuator Load	Axial	lb	0	0	0	0	0	0
5931	Pivoting Actuator Load	Tension	lb	0	0	0	0	0	0
5939	Lower Drive Arm Load		lb	0	0	0	0	0	0
<u>Forward</u>									
<u>Upper Control System</u>									
2120	Swivelling Actuator Pos		in.	0	0	0	0	0	0
2122	Pivoting Actuator Pos		in.	0	0	0	0	0	0
5434	Pitch Link Load	Yellow	lb	0	0	0	0	0	0
5442	Pitch Link Load	Red	lb	0	0	0	0	0	0
5452	Pitch Link Load	Green	lb	0	0	0	0	0	0
5482	Fixed Link Load		lb	0	0	0	0	0	0
5904	Lower Drive Arm Load		lb	0	0	0	0	0	0
5906	Swivelling Actuator Load	Axial	lb	0	0	0	0	0	0
5910	Pivoting Actuator Load	Tension	lb	0	0	0	0	0	0
<u>Vibration - Dynamics</u>									
<u>Airframe</u>									
1318	Vertical Acceleration	Pilot Seat	g	0	0	0	0	0	0
1319	Longitudinal Acceleration	Sta 95	g	0	0	0	0	0	0
1320	Vertical Acceleration	Pilot Seat	g	0	0	0	0	0	0
1328	Vertical Acceleration	Sta 95	g	0	0	0	0	0	0
1329	Lateral Acceleration	Sta 95	g	0	0	0	0	0	0
1330	Longitudinal Acceleration	Sta 95	g	0	0	0	0	0	0
1350	Vertical Acceleration	Sta 320	g	0	0	0	0	0	0
1351	Lateral Acceleration	Sta 320	g	0	0	0	0	0	0
1353	Vertical Acceleration	Sta 320	g	0	0	0	0	0	0
1357	Vertical Acceleration	Sta 320	g	0	0	0	0	0	0
1358	Lateral Acceleration	Sta 350	g	0	0	0	0	0	0
1359	Longitudinal Acceleration	Sta 350	g	0	0	0	0	0	0
1360	Vertical Acceleration	Sta 350	g	0	0	0	0	0	0
1361	Vertical Acceleration	Sta 482	g	0	0	0	0	0	0
1363	Lateral Acceleration	Sta 482	g	0	0	0	0	0	0
1373	Vertical Acceleration	Sta 50 left	g	0	0	0	0	0	0
1375	Vertical Acceleration	Sta 50 right	g	0	0	0	0	0	0

Notes: 1. Blank space - Data intentionally not recorded
2. 0 - Operational throughout
3. N - Operational on Preflight calibration
4. S - Operational on Preflight calibration; data trace showed occasions to frequent spikes
5. B - Operational on Preflight calibration; data trace drifted or went to blank edge
6. I - Operational on Preflight calibration; data trace became intermittent during flight
7. X - Gauge inoperative during preflight calibration or disconnected
8. N.S.B. and I malfunctions can be attributed to gauge failure, broken wire, loose connection, or tape recorder malfunction

FLIGHT ENVELOPE AND LIMITATIONS

The gross-weight, center-of-gravity envelope for the CH-47C helicopter is shown in Figure 167. The estimated flight envelopes for 33,000-, 40,000-, and 46,000-pound gross weights are shown in Figures 168, 169, and 170, respectively.

Level-flight speeds were to be terminated in flight when load levels on any telemetry parameter reached 150 percent of endurance limit values; maneuvers were to be terminated when these load levels reached 200 percent of endurance limit values. The aircraft fuselage q-limit airspeed of 201 knots EAS was to be observed. All maneuvers were limited to 1.5g.

The maximum rotor speed was restricted to 247 rpm (power on or power off) due to the heavier weight of the advanced-geometry blade versus the standard metal blade. The test program was to be conducted using the CH-47C programmed cyclic trim on the forward and aft rotor heads.

MECHANICAL INSTABILITY TESTS

Qualitative mechanical instability tests were performed before the testing described in Table XVIII at 33,000 pounds gross weight, 235 rotor rpm; 41,000 pounds gross weight, 235 rotor rpm; and 46,000 pounds gross weight, 235 and 245 rotor rpm.

At each gross weight and associated rotor speed setting, testing consisted of a hover in ground effect and hover-to-landing tests encompassing touchdown collective positions of 1 degree to 5 degrees in 1-degree increments, with the landing gear swivels both locked and unlocked. At each gross weight, rpm, and touchdown collective pitch setting, the pilot excited the aircraft with the lateral stick and directional pedals at a medium and fast frequency with a minimum of 25 percent of control travel and 5 cycles of input. All tests were performed with SAS off.

A qualitative evaluation of the stability characteristics of the helicopter was performed by the test pilot. Stability assessments were made at each test point using the standard pilot numerical rating of aircraft response shown below:

1. Unable to induce oscillation
2. Oscillation damps rapidly
3. Oscillation damps slowly
4. Neutral oscillation
5. Oscillation slowly divergent
6. Oscillation rapidly divergent

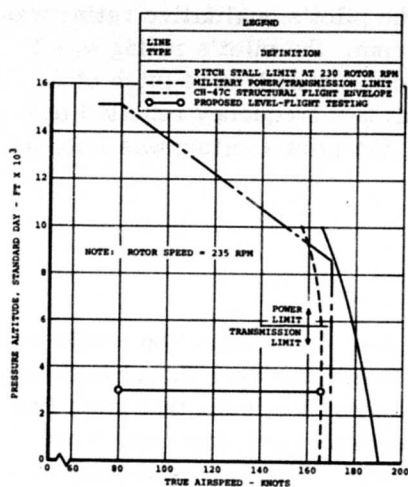


Figure 168.
Predicted Airspeed Capability for the
CH-47C Helicopter With Advanced-
Geometry Blades at 33,000 Pounds
Gross Weight.

Figure 169.
Predicted Airspeed Capability for
the CH-47C Helicopter With
Advanced-Geometry Blades at
40,000 Pounds Gross Weight.

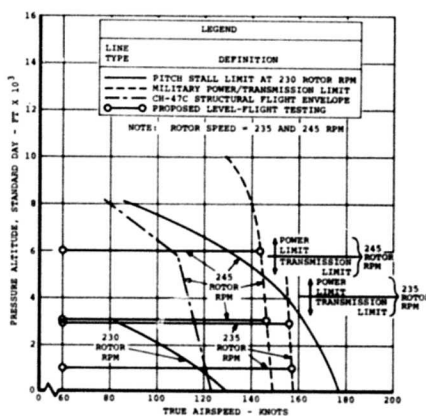
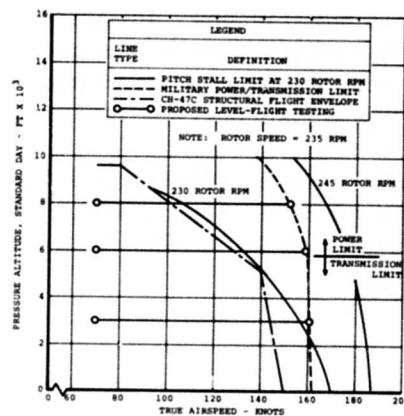


Figure 170.
Predicted Airspeed Capability
for the CH-47C Helicopter With
Advanced-Geometry Blades at
46,000 Pounds Gross Weight.

At 33,000 pounds gross weight and 235 rotor rpm, the pilot's qualitative rating was 1 for all test conditions. At 41,000 pounds and 235 rpm, the pilot's rating was 1 for all test conditions with one exception. At a touchdown collective pitch of 2 degrees with swivels unlocked, a yaw control input at fast frequency resulted in a rating of 2. At 46,000 pounds and 235 and 245 rpm, the pilot's rating was 1 for all test conditions.

BLADE TRACKING

Significant out-of-track conditions and associated higher 1/rev vibration levels were encountered in forward flight early in the flight test program, even though both sets of blades had been pretracked on the whirl tower. It was also found that pitch link adjustments based on in-flight Strobex track investigations were generally more effective than those based on ground track investigations. The advanced-geometry blades exhibited greater sensitivity to pitch link adjustments as compared to standard metal blades. Progressive blade track investigations and corresponding pitch link adjustments were made throughout the flight test program to alleviate the 1/rev constraints as much as possible. Blade tracking results and corresponding pitch link adjustments are summarized in Appendix I.

An analysis of the effects of twist angle variations between blades and adjusted trailing-edge cusp angle settings on the 1/rev vibration levels experienced in flight is presented in the section of this report entitled Flight Test Data Analysis - Vibration.

FLIGHT TEST DATA ANALYSIS

ROTOR MOMENT STALL CHARACTERISTICS

Introduction

This section presents studies of the flight loads of the CH-47C, equipped with advanced-geometry blades, for the purpose of establishing the rotor blade moment stall characteristics. Primary emphasis is placed upon analysis and comparison of pitch link waveforms as they best identify the moment stall condition.

The information given in this section may be categorized as follows:

1. Definition of moment stall for the AGB (versus the CH-47C metal blade).
2. Display of CH-47C/AGB flights encountering moment stall including percent occurrence.
3. Illustration of pitch link load growth rate in stall.
4. Effect of RPM on moment stall.
5. Effect of altitude on moment stall including growth rate with altitude.
6. Effect of sideslip on moment stall.
7. Comparison of CH-47C/AGB and CH-47C pitch link loads and waveforms for similar flight conditions and equivalent C_T/σ .
8. Comparison of CH-47C/AGB and CH-47C data on the basis of a flutter parameter.
9. Effect of structural and aerodynamic damping.

Definition of Moment Stall

Moment stall in its simplest terms is merely a recognition of the fact that a portion of the blade has stalled sufficiently to cause sudden increases in blade alternating pitching moments. The growth of these moments (occurring at the blade's torsional natural frequency) depends on the severity and duration of the stall and the amount of negative aerodynamic damping present.

The real concern to most designers, of course, is the magnitude of the cyclic loads felt by the control system. Moment stall in itself would not be significant if the magnitude of peak-to-peak pitch link loads were not affected. Recognition was given to this situation when the criterion for moment stall was originally established for

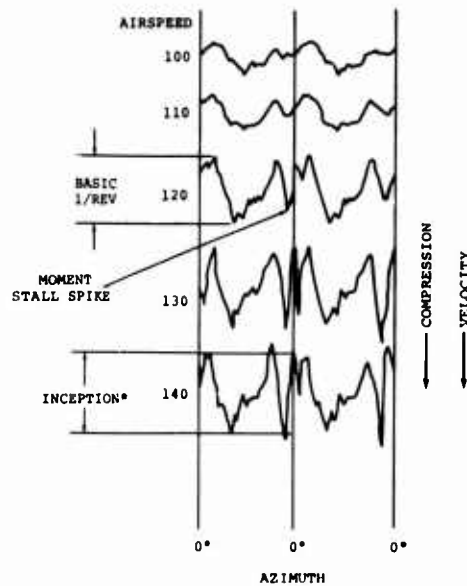
use on the CH-47C metal blade. By definition, moment stall inception was established as that point at which the peak-to-peak load occurring during the moment stall cycle equals the peak-to-peak loading of the basic pitch link waveform and occurs in at least 50 percent of the rotational cycles in a flight run. Figure 171 shows the type of moment stall waveform for the CH-47C metal spar blades, where at 120 knots (for this particular gross weight/altitude condition) moment stall can be seen, but not until 140 knots does the amplitude of the stall load spike exceed otherwise occurring peak-to-peak alternating loads; hence, moment stall inception for this sample case would be 140 knots.

It became evident early in the analyses of the AGB pitch link waveforms that it might be necessary to modify this original definition of moment stall. The peak-to-peak value of the moment stall "spike" on the AGB data, with few exceptions, does not exceed peak-to-peak amplitude of the basic pitch link waveform. However, it was evident that moment stall was occurring and that the peak-to-peak pitch link loads were affected by the compression portion of the stall cycle.

Figure 172 illustrates the definition of the inception of moment stall used in the AGB analysis. Inception is defined as the point at which the first full cycle of moment stall is discernible. This is evidenced by the second break in the pitch link load trace toward a compression load (a nose down) in the pitch link. It will be further understood that this characteristic must occur in at least 50 percent of the cycles during a level-flight run. See waveform 4 of Figure 172. Note that the growth of the basic 1/rev load is much more evident on the AGB than it is for the CH-47C blade.

Load Growth Rate

Another method used in the past to approximate the point of moment stall inception (especially if waveforms were not available for analysis) was to locate the intersection of two lines drawn tangent to control load data plotted versus airspeed; one line drawn through loads below stall, and another drawn through the loads obviously above stall. Referring to Figure 173, the "sudden" load growth rate upon reaching moment stall is apparent for the CH-47C blades. Similarly, Figure 174 illustrates the load growth characteristics of the AGB data. Although, upon first examination, there is an apparent break in the load trend, examination of the load waveforms reveals that moment stall has not occurred; however, there is obvious evidence of an increasing compression pulse between rotor azimuth angles (ψ) of 270 and 360 degrees, with a slight influence on load excursion. It is concluded, therefore, that the determination of moment stall inception for the AGB can only be accomplished by evaluation of the pitch link load waveforms. Figure 174 indicates that the load growth rate for the AGB follows a V^2 trend line while the CH-47C growth rate is much more abrupt. Taking an average of the measured load growth rates for all AGB flights encountering moment stall, we find a 23 pounds/knot rate of increase. This rate contrasts to an approximate rate of 55 pounds/knot measured on the CH-47C metal blade.



*MOMENT STALL SPIKE EXCEEDS BASIC 1/REV

Figure 171. Illustration of a Typical CH-47C Metal Blade Pitch Link Waveform During Moment Stall.

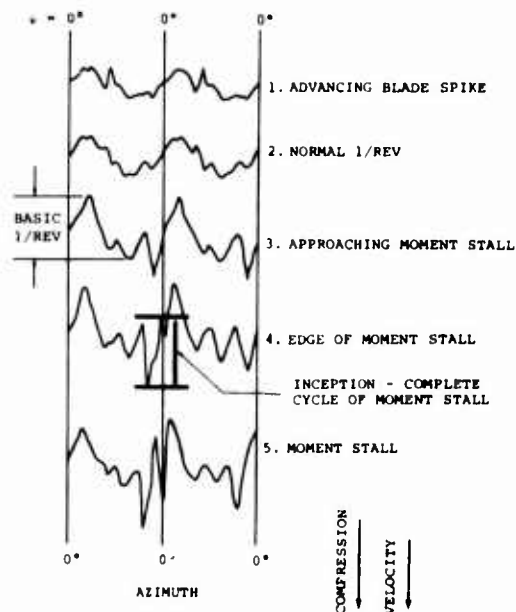


Figure 172. Illustrations of Typical CH-47C/AGB Pitch Link Waveforms.

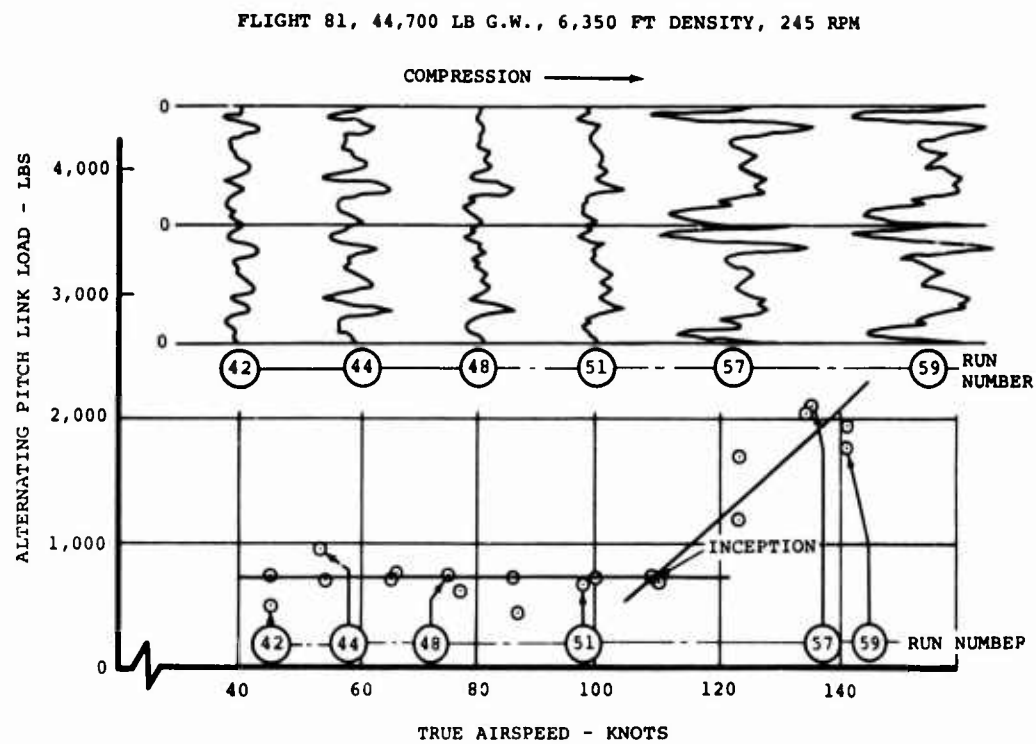


Figure 173. CH-47C Pitch Link Load Growth With Airspeed.

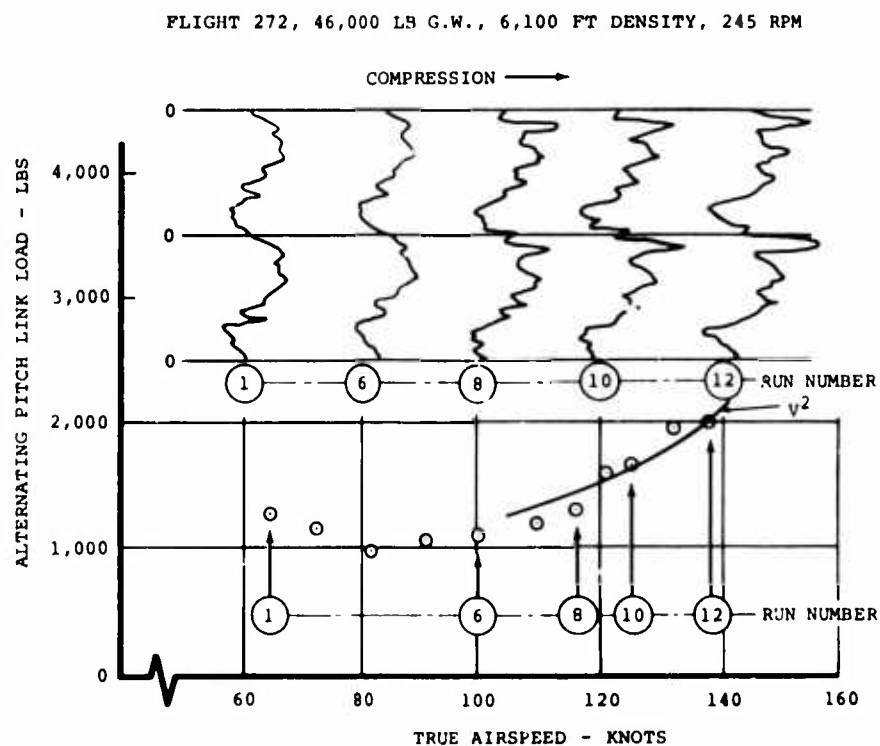


Figure 174. CH-47C/AGB Pitch Link Load Growth With Airspeed.

An explanation for the difference in load growth rates between the two blades was not determined. Structural damping may be the significant factor, although the analysis has not quantified the difference. Further discussion of the effect of damping is contained in a later paragraph.

Summary of Flight Conditions Analyzed

Table XXIV of this report summarizes the flight conditions tested during the AGB program. However, since this section of the report is concerned primarily with moment stall, the flights that show some evidence of moment stall were identified and have been tabulated in Table XXI. Figure 175 presents the same information on an airspeed/altitude plot to obtain a better perspective of the test conditions wherein moment stall was encountered. The percentage of occurrence of the moment stall waveform is also displayed by varying the cross hatching of the bars used to outline the airspeed range covered in the testing. Figure 175 also illustrates how the analysis was hampered by a lack of flight data covering a transition from unstalled to stalled flight to enable a positive determination of moment stall inception. Either no appreciable stall was encountered throughout the speed sweep or the entire sweep was in stall. The clearest example of a transition from unstalled to stalled flight was obtained in the military power climb as shown in Figure 176.

Effect of RPM on Moment Stall

The effect of RPM is illustrated in Figure 177 and is similar to that seen on the CH-47C blade. As the RPM increases, the stall spike progressively becomes smaller until it disappears altogether.

Effect of Altitude on Moment Stall

Figure 175 displays the effect of altitude on the pitch link load waveforms, all other parameters being the same. It shows the increase in the retreating blade moment stall spike with altitude (increasing C_T/σ). The test data was obtained by stabilizing the aircraft in a military power climb at 75 knots airspeed and recording data at various altitudes.

Effect of Sideslip Angle on Moment Stall

The effect of sideslip angle on pitch link waveforms displayed in Figure 178 evidences maximum interference and therefore moment stall in the waveforms at a 0° sideslip angle. Sideslip angles to the left show a marked reduction in the moment stall spike, but sideslip angles to the right indicate no such trends. CH-47C metal blade load trends are similar to that seen in the AGB data with the exception that sideslip angles to both right and left showed a reduction in pitch link loads. As yet there is no explanation for the difference between the two blades. (Note: A left sideslip angle is defined as a nose-right condition of the aircraft with respect to the relative wind.)

TABLE XXI. SUMMARY OF FLIGHTS HAVING MOMENT STALL
BASED UPON WAVEFORM ANALYSIS

Flight and Run No.	Gross Weight (lb)	Altitude (ft)	RPM	Velocity (kt)
X-255, 10-13	40,000	6,000	235	145-158
X-255, 31-33	40,000	7,500	235	149-156
X-270, 33-35	46,000	3,000	235	146-155
X-271, 13-23	46,000	10,400	245	60-126
X-272, 8-12	46,000	6,000	245	68-136
X-272, 15-18	46,000	6,000	235	108-139
X-284, 5-9	46,000	5,600	235	101-144
X-284, 10-18	46,000	7,500	235	63-137
X-284, 19-27	46,000	9,400	235	64-129
X-284, 28-35	46,000	11,000	235	66-111
X-285, 14-15	50,000	2,500	245	132-138
X-286, 17-28	50,000	10,000	245	66-125

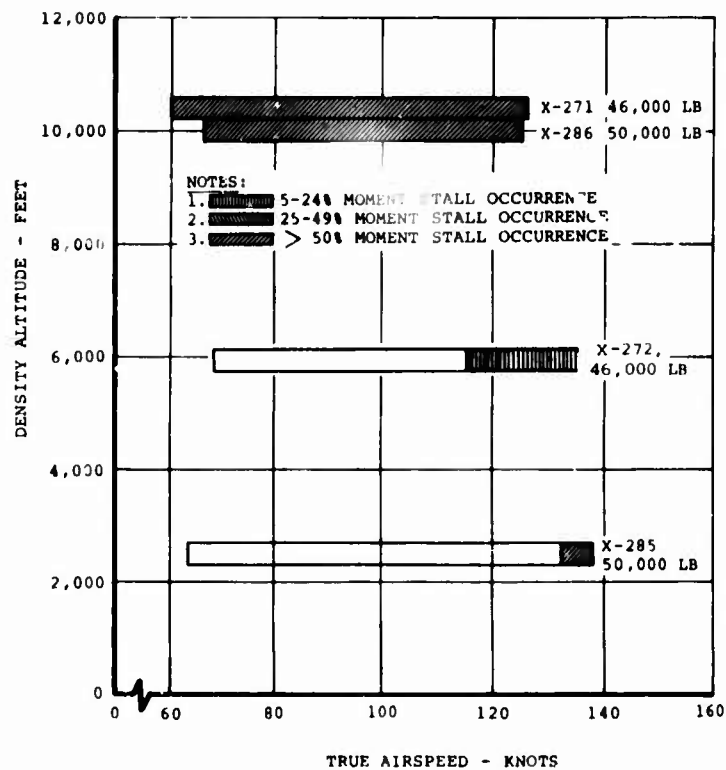
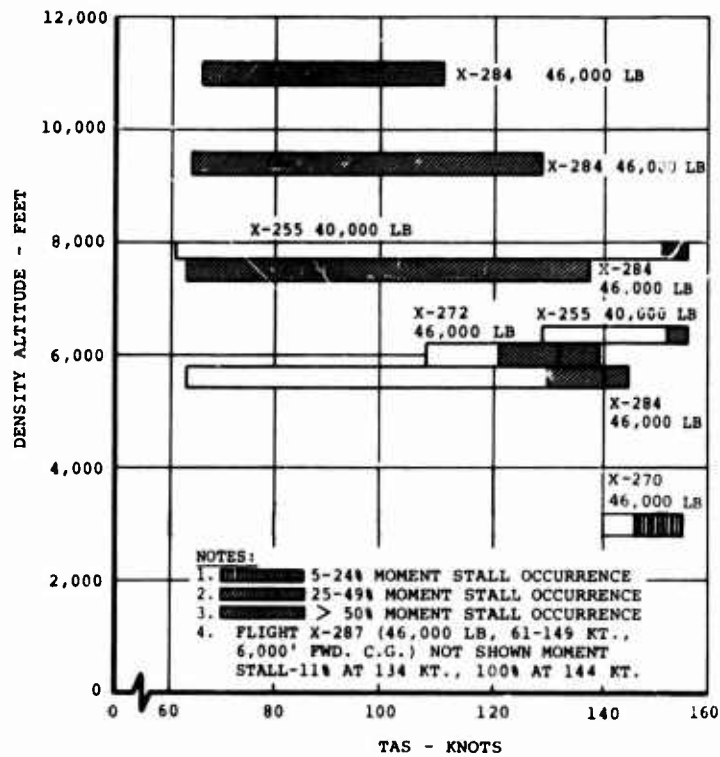


Figure 175. Summary of Flights Having Moment Stall.

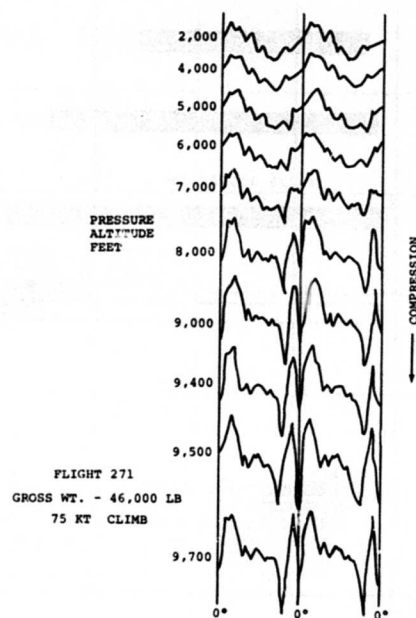


Figure 176. Illustration of the Effect of Altitude on Pitch Link Load Waveforms.

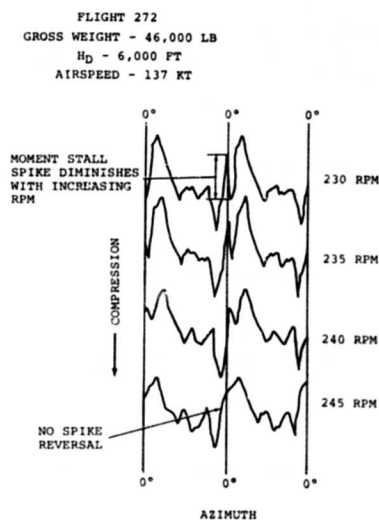


Figure 177. Illustration of the Effect of RPM on Pitch Link Waveform.

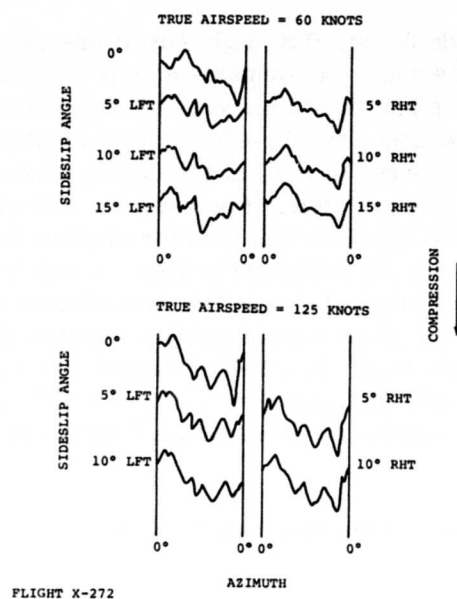


Figure 178. Effect of Sideslip on Pitch Link Waveforms.

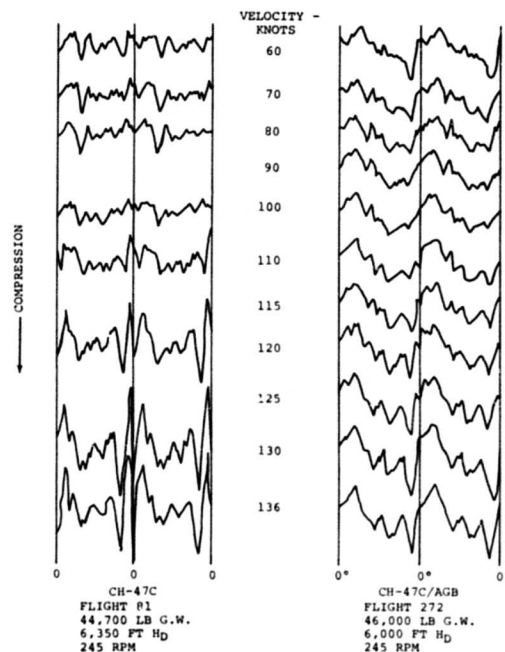


Figure 179. Comparison of CH-47C and CH-47C/AGB Pitch Link Load Waveforms - Similar Flight Conditions.

Pitch Link Load Comparison of CH-47C and CH-47C/AGB

Comparisons may be made for similar flight conditions (equal thrust) or equivalent C_T/σ (equal unit blade loading). A comparison of pitch link load waveforms for similar flight conditions is shown in Figure 179 at a gross weight of 46,000 pounds. As one would intuitively expect, the CH-47C with its smaller blade area (lower solidity) shows distinct evidence of stall at the higher airspeeds while the AGB barely indicates the beginning of stall. Figures 180, 181 and 182 present airspeed comparisons of the critical aft pitch link load for similar flight conditions over the gross weight range from 33,000 to 50,000 pounds. It can be seen from these plots that the load relationship changes between the so-called unstalled and stalled flight regimes. At 33,000 pounds gross weight and low altitude (Figure 180) where the CH-47C is operating below stall, the CH-47C data is lower than the AGB data. As the gross weight and altitude increase (increasing C_T/σ), the CH-47C begins to experience moment stall and the pitch link loads first approach and then exceed those of the AGB.

The following relationship is normally used by Boeing-Vertol to compare pitching moment data:

$$P. L. L. = K \frac{C^2}{R\bar{b}} \left(\frac{T}{b} \right) \quad (1)$$

where P. L. L. = pitch link load, lb

K = pitch link load coefficient (nondimensional)

C = chord, ft

\bar{b} = pitch arm, ft (pitch link to pitch axis distance)

R = radius, ft

T = thrust, lb

b = number of blades

V_T = tip velocity, ft/sec

Since

$$T = \frac{C_T}{\sigma} b \rho C R (V_T)^2 \quad (2)$$

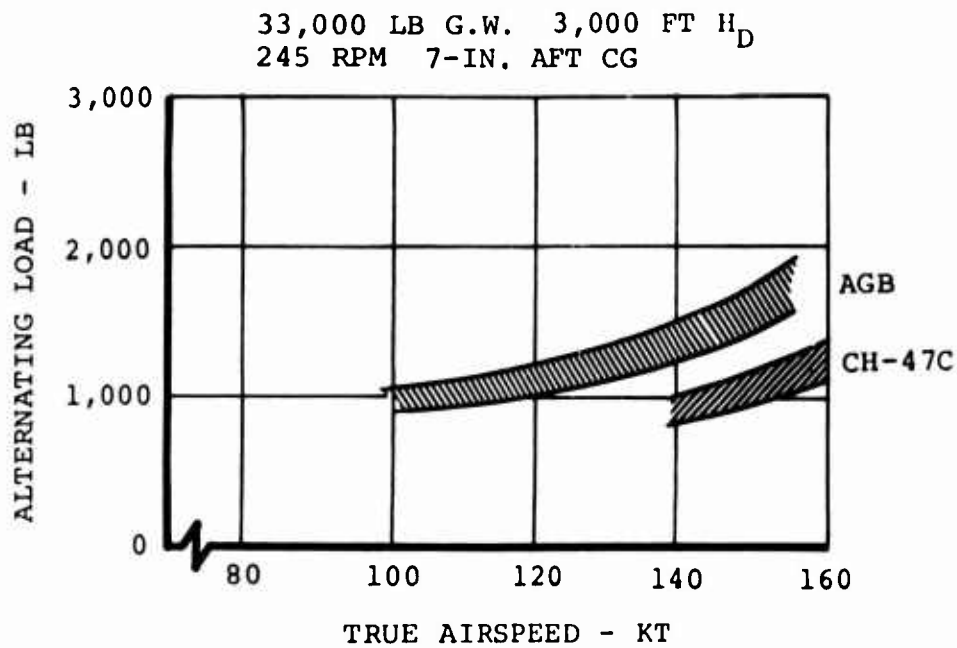
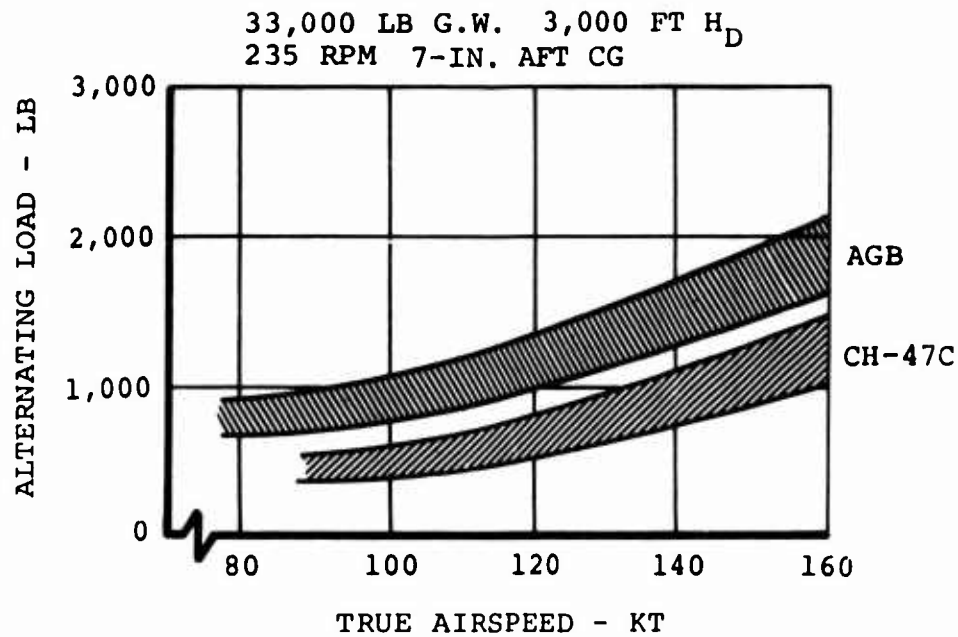


Figure 180. Comparison of CH-47C and CH-47C/AGB Aft Pitch Link Loads for Similar Flight Conditions.

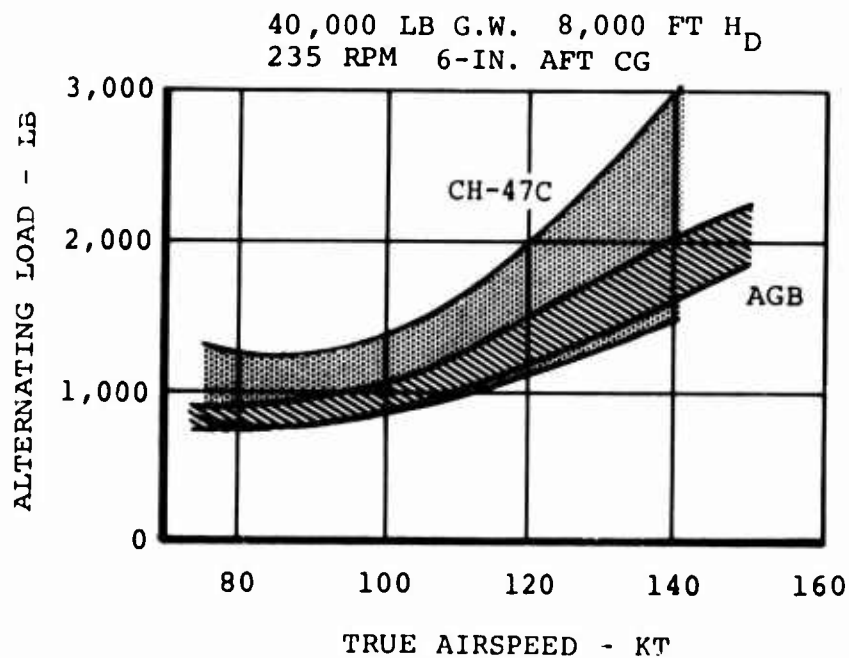
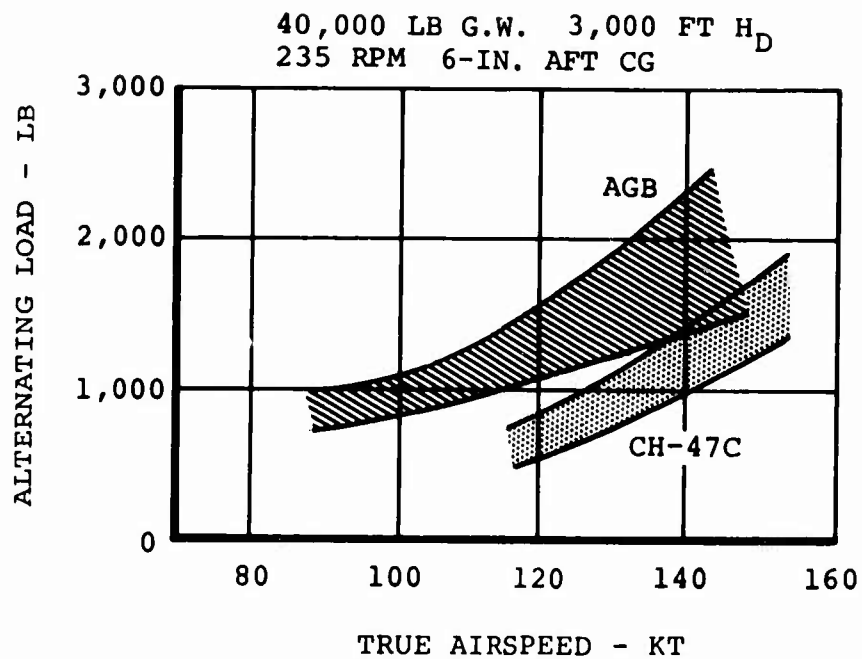


Figure 181. Comparison of CH-47C and CH-47C/AGB Aft Pitch Link Loads for Similar Flight Conditions.

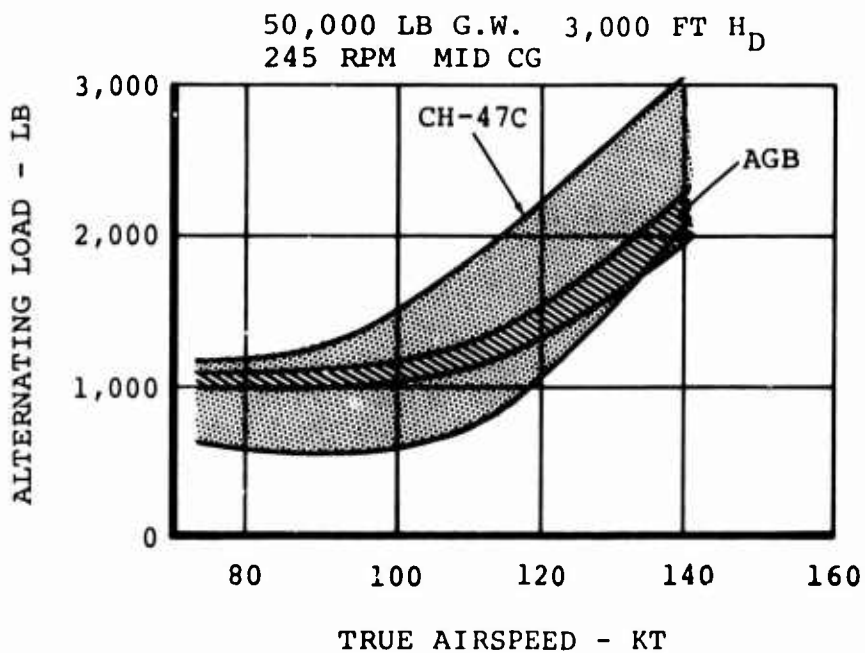
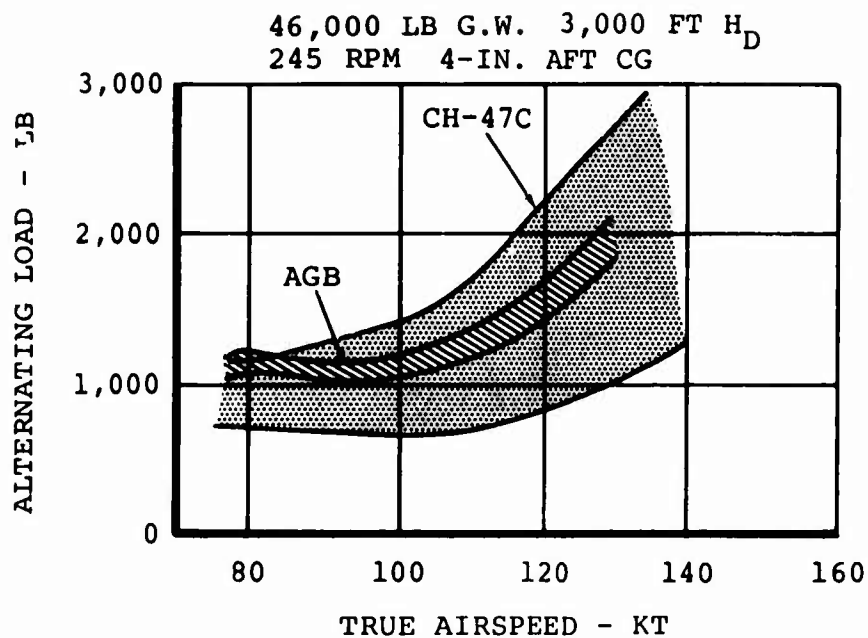


Figure 182. Comparison of CH-47C and CH-47C/AGB Aft Pitch Link Loads for Similar Flight Conditions.

$$P.L.L. = K C^3 \frac{C_T}{\sigma} \frac{\rho}{b} V_T^2 \quad (3)$$

Noting that $(P.L.L.) \times \bar{b}$ is the pitching moment (M_θ),

$$K = \frac{M_\theta}{\rho C^3 \frac{C_T}{\sigma} V_T^2} \quad (4)$$

Detailed examination of the preceding data for similar flight conditions shows that, in the unstalled region (such as Figure 180), the load relationship between the two blades appears to follow the relationship of equation (1); i.e., a $(\text{chord})^2 \times (\text{thrust})$ relationship. Since the thrust is the same for similar flight conditions, this simply means that the higher pitch link loads of the AGB in the unstalled condition are due to the wider chord.

The preceding observations relating to the unstalled pitch link loads were generally confirmed by a subsequent analytical study. Pitch link loads were computed at a constant thrust level for:

1. Standard CH-47C blades (pitch axis at 19.5 percent).
2. Standard blade with increase (AGB) chord.
3. Standard blade with AGB chord and pitch axis (25 percent).
4. AGB

Unstalled steady and alternating pitch link loads with the larger AGB chord increased almost exactly with the square of chord ratio. Shifting the pitch axis to the AGB 25 percent location reduced the steady pitch link loads up to 65 percent and the alternating loads up to 20 percent. Alternating load magnitude and waveform with the increased chord and pitch axis shift compared favorably with the calculated AGB results. It is concluded from this analysis that the AGB loads show an increase over the CH-47C primarily due to the increased chord. As a result of the more favorable pitch axis location, the increase is somewhat less (20 percent) than that indicated by a chord squared relationship.

Waveforms for an equivalent C_T/σ condition are displayed in Figure 183. The AGB shows the beginning of a moment stall spike with little evidence of stall in the CH-47C waveform. It would appear that the thin tip section (6 percent) on the AGB may be stalling earlier than the 10 percent section on the CH-47C blade. Unfortunately, there were very few flights made which allow a comparison of the pitch link loads for equivalent C_T/σ , and the data of Figure 184 represent the highest value of C_T/σ

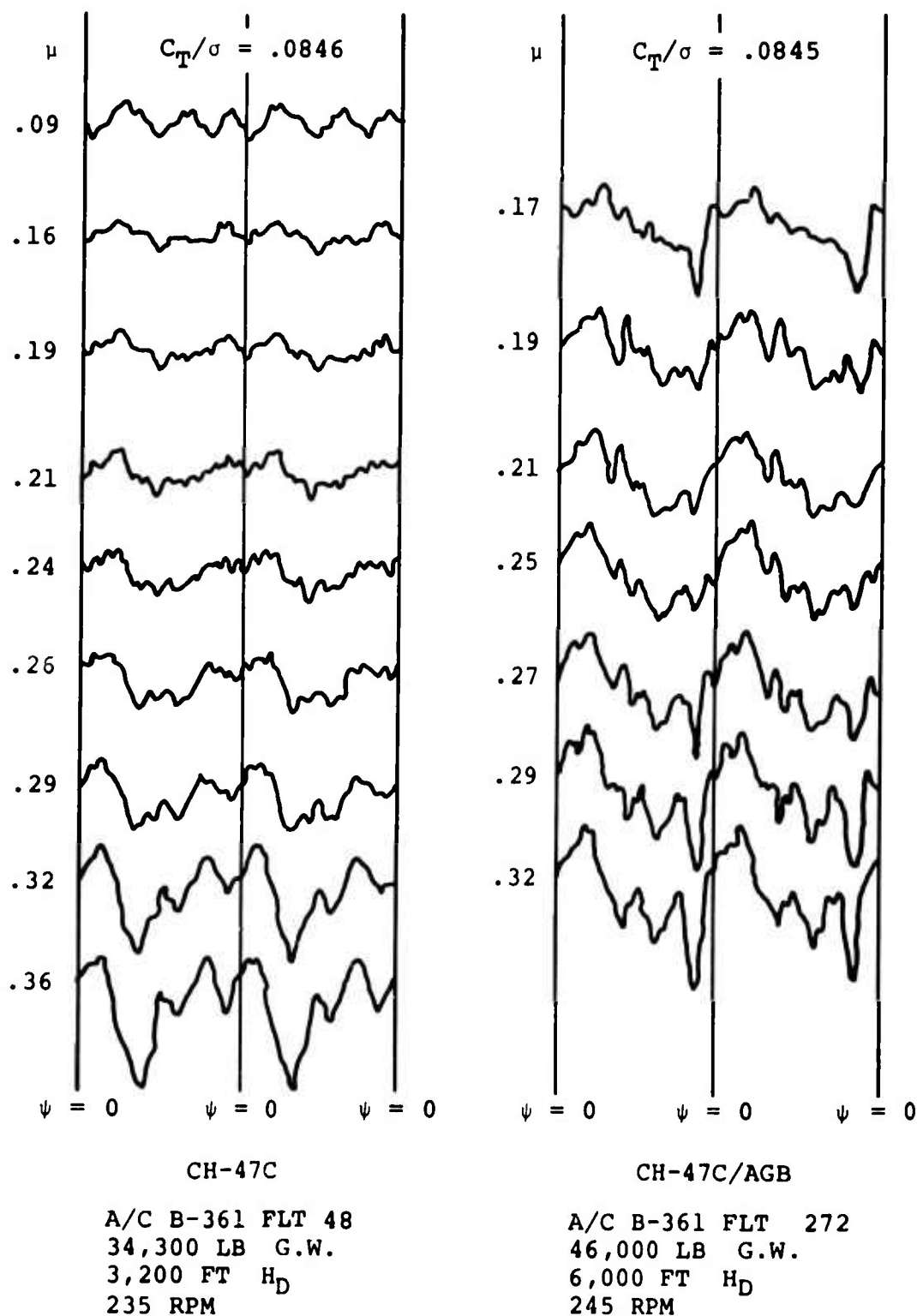


Figure 183. Comparison of CH-47C and CH-47C/AGB Pitch Link Load Waveforms - Equivalent C_T/σ .

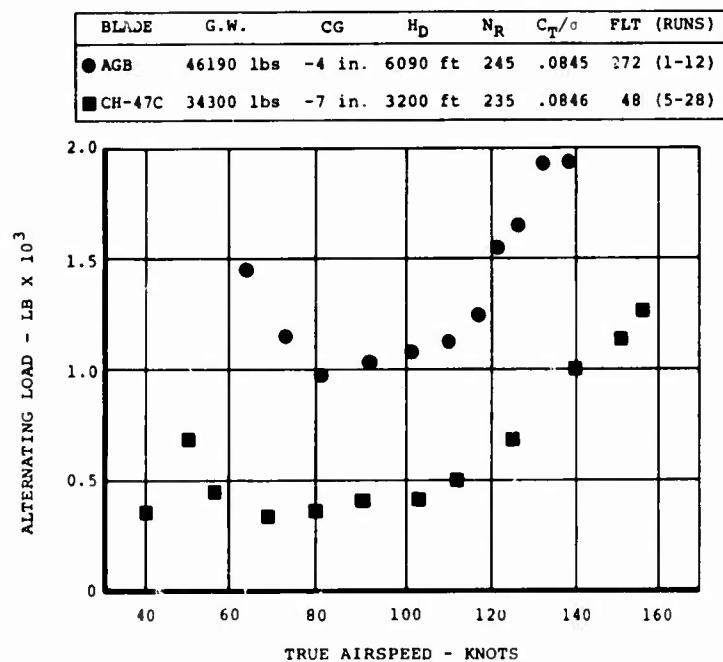


Figure 184. Comparison of CH-47C and CH-47C/AGB Aft Pitch Link Loads at Equivalent C_T/σ .

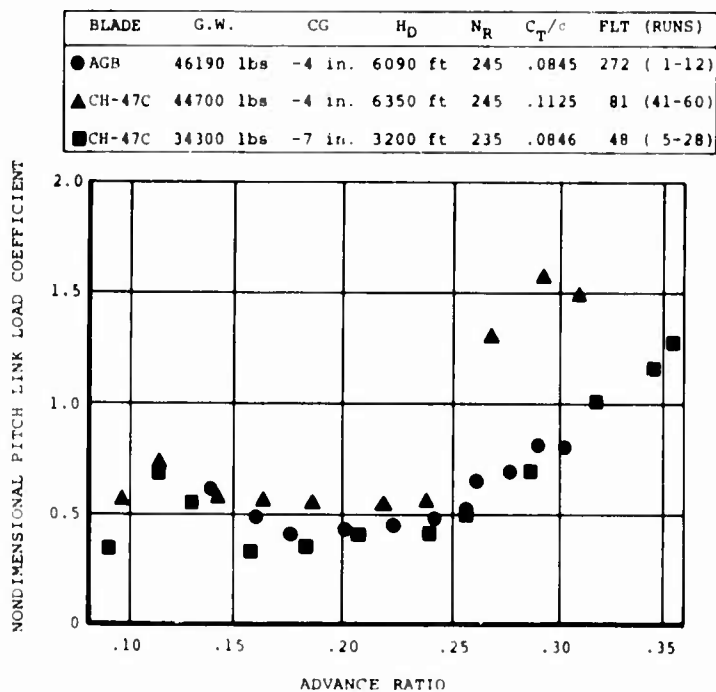


Figure 185. Nondimensional Comparison of CH-47C and CH-47C/AGB Aft Pitch Link Loads for Similar Flight Conditions and Equivalent C_T/σ .

for which there is significant CH-47C data at comparable airspeeds. The data shown is for an unstalled condition, and the load relationship between the two blades is approximated by the $(\text{chord})^3 \times (C_T/\sigma)$ relationship of equation (2). Figure 185 presents a nondimensional comparison, equation (3), of the same equivalent C_T/σ data together with CH-47C data at the same thrust level as the AGB. The plot indicates that for the unstalled condition, the pitch link load coefficient is approximately the same for both blades. When the lower solidity CH-47C is operated at the same thrust level as the AGB (Flight 81), the CH-47C blade stalls at a lower advance ratio, resulting in a rapid increase in the pitch link load coefficient.

Comparison Based on Moment Stall Parameters

In order to evaluate the two blades on a common basis, the flight data was reduced to a nondimensional form using a moment stall inception parameter developed by Boeing-Vertol involving the following:

$$\begin{aligned} \rho/\rho_o &= \text{density altitude ratio} \\ V_T &= \text{tip speed, ft/sec} \\ \mu &= \text{advance ratio } (V/V_T) \\ C &= \text{chord} \\ R &= \text{radius} \\ \omega_\theta \sqrt{I_\theta} &= \text{effective torsional stiffness} \end{aligned}$$

Figure 186 compares the AGB moment stall inception points with those of the CH-47C. The points for the AGB generally fall to the left of the CH-47C metal blade scatterband, indicating poorer moment stall qualities. It appears that the 6 percent tip section on the AGB triggers blade stall at lower angles of attack than the 10 percent airfoil on the metal blade. Looking back at the pitch link waveform comparison presented in Figure 183, there is clear evidence that moment stall does indeed occur earlier on the AGB.

It is recognized that the criterion for moment stall inception differs for the two blades. However, if the metal blade inception criterion - point where peak-to-peak pitch link loads are first affected by the moment stall spike - were used instead of the AGB criterion defined above - point where the moment stall spike develops a

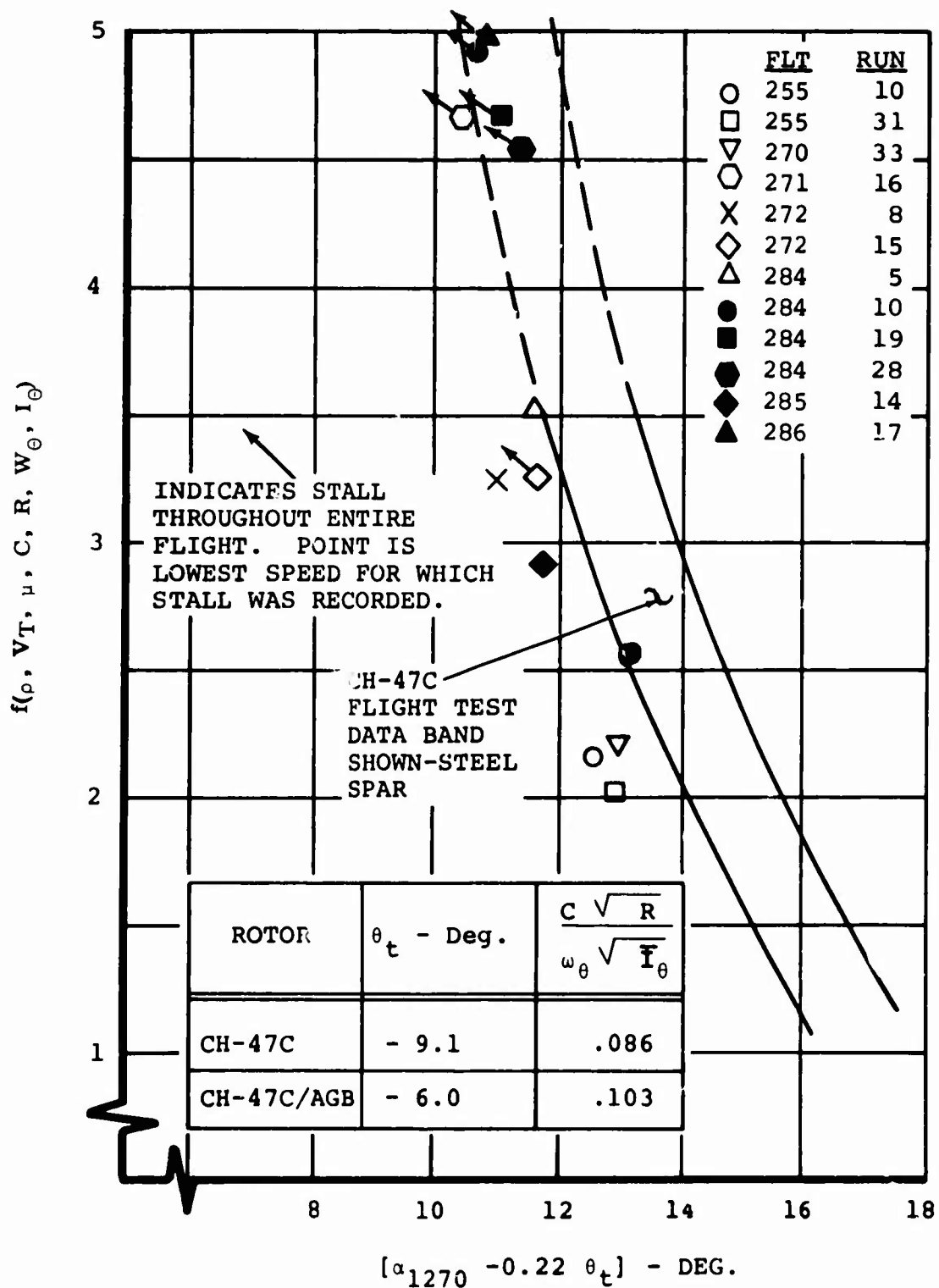


Figure 186. Moment Stall Inception Summary of Vertol Experience.

full reversal - then the AGB points would move even further left and within the spread between the two blades. In view of the more gradual growth rate of the pitch link loads for the AGB blade, it is felt that the criterion used in this report to define the moment stall boundary establishes the proper relationship between the two blades.

Those symbols in Figure 186 with arrows attached pointing upward and to the left indicate that stall occurred during the entire flight for that altitude and gross weight. The data point represents the lowest speed for which stall was recorded. Note that there were only five flights in which there was data to define moment stall inception. The other six flights encountered moment stall throughout the flight.

Summary of Pitch Link Waveforms

Appendix II contains a display of many of the pitch link waveforms examined in the process of establishing waveform characteristics and moment stall inception for the AGB flight program. Waveforms have been included for flights 255, 270, 271, 272, 284, 285, 286.

Effect of Structural and Aerodynamic Damping

Torsion "twang" tests were made of the CH-47C metal and AGB fiberglass rotor blades on the CH-47C aircraft during ground tests with the rotors stationary. The purpose of the tests was to determine the difference in the structural damping characteristics between the two rotor blades in their first torsional natural modes. The tests were accomplished by depressing the directional pedal control, recording the resulting pitch link load waveform, and analyzing its time decay to determine the damping. Results of a typical test, as illustrated in Figure 187, show that the metal blade has a structural damping ratio of 0.017 or 1.7 percent, whereas the AGB has a corresponding value of 0.022 or 2.2 percent. The average from a number of such tests indicates the first torsional natural mode critical structural damping ratios to be approximately 1-1/2 percent and 2-1/2 percent for the metal and AGB respectively.

Theoretical calculations were made to determine the critical damping ratios for the first torsional natural modes of the CH-47C metal and AGB blades in the normal rotating condition at 230 RPM. These calculations are based upon the linear incompressible two-dimensional flat-plate oscillating airfoil theory derived by Theodorsen for bending-torsion classical flutter vibration of fixed and rotating wings. The results of these calculations show that the metal blade has a critical aerodynamic damping ratio of 24 percent, whereas the AGB has a corresponding value of 29 percent, in the first torsional natural modes. This difference in damping is readily attributed to the fact that the AGB has a wider chord than the metal blade and hence generates more air damping.

In comparing the structural and aerodynamic critical damping ratios for the first torsional natural mode of either rotor blade, it seems reasonable to conclude that

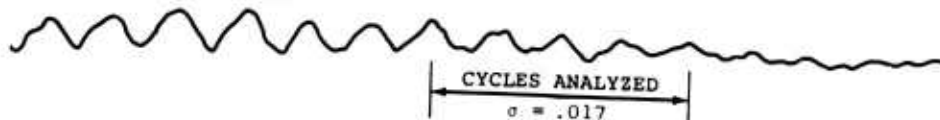
aerodynamic damping is far more important than structural damping in its effects on the torsional response, as well as loads and vibrations, of the rotor blade. This is true so long as the blade sections are operating in an unstalled environment governed by linear aerodynamic theory. However, when the blade sections are operating in momentarily stalled regimes, wherein the aerodynamic damping in torsion is at a minimum, or even negative, then the structural damping becomes of greater importance in suppressing the torsional response in these regimes. Since the AGB generates more structural and aerodynamic damping in torsion than the CH-47C metal rotor blade, then it seems reasonable to conclude that the AGB will generate lower torsional loads and vibrations than the metal blade for both the unstalled and stalled regimes of the rotor cycle.

Tables XXII and XXIII summarize the natural frequencies and critical aerodynamic damping ratios for the two rotor blades in flap bending, chord bending and torsion natural modes, as well as their fundamental design parameters.

Principal Results and Observations

1. In the unstalled condition, the AGB pitch link loads are higher than the CH-47C loads due to the increased chord of the AGB. There is a $(\text{chord})^2 \times (\text{thrust})$ relationship in pitch link loads for blades of different chords with the same pitch axis location. This relationship may be expressed alternatively as $(\text{chord})^3 \times (CT/\sigma)$. Compared to the CH-47C, the AGB loads are approximately 20 percent lower than those predicted by the chord squared relationship due to the more favorable pitch axis location of the AGB.
2. For the same gross weight, stall inception is delayed by the increased solidity (chord) of the AGB rotor.
3. On an equal chord basis, the thin tip section (6 percent) of the AGB appears to bring about the inception of moment stall at lower angles of attack (lower CT/σ) than on the CH-47C metal blade, which has a 10 percent section.
4. The large improvement in stall inception provided by the increased solidity is sufficient to overcome the thin tip stall degradation and still provide a net improvement.
5. Above the stall inception boundary, the pitch link waveforms of the AGB have a different stall spike characteristic than those of CH-47C metal blades.
6. Once into stall, the pitch link load growth rates of the AGB are substantially lower than for the CH-47C metal blade. The reason for this is not clear, but may be due to a combination of higher aerodynamic pitch damping due to the wider chord and higher structural damping due to the fiberglass reinforced plastic construction.

CH-47C METAL BLADE
B-361 X-295 RUN 4
FWD. GREEN PITCH LINK



CH-47C/AGB BLADE
B-361 G.R.23, RUN 12
AFT. RED PITCH LINK LOAD

$$\sigma = \text{DAMPING RATIO} = \frac{1}{8\pi} \left(\frac{x_1 - x_5}{x_1} \right)$$

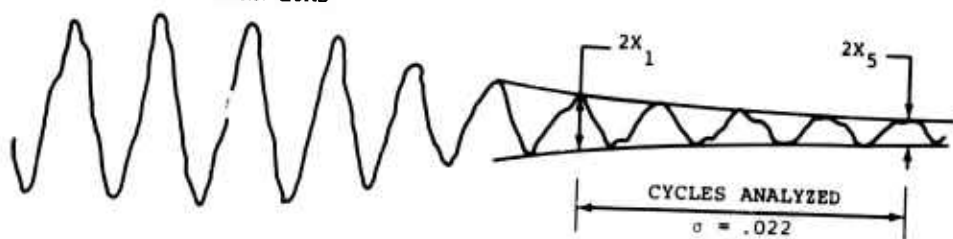


Figure 187. A Comparison of Typical Pitch Link Load Decay Waveforms for the CH-47C Metal and CH-47C/AGB Blades.

**TABLE XXII. CH-47B/C METAL AND ADVANCED-GEOMETRY
FIBERGLASS ROTOR BLADES, UNCOUPLED
NATURAL FREQUENCIES AND CRITICAL
DAMPING RATIOS**

Flap Modes		CH-47B/C	AGB Glass
Zero	ω_0	1.018	1.018
	ζ_0	0.5439	0.6449
First	ω_1	2.569	2.479
	ζ_1	0.1531	0.1883
Second	ω_2	4.748	4.685
	ζ_2	0.07559	0.09711
Third	ω_3	7.899	7.863
	ζ_3	0.04495	0.06651
Fourth	ω_4	12.19	11.88
	ζ_4	0.03047	0.04129
Chord Modes		CH-47B/C	AGB Glass
Zero	ω_0	0.3656	0.3719
First	ω_1	5.225	4.256
Second	ω_2	14.70	11.51
Torsion Modes		CH-47B/C	AGB Glass
First	ω_1	6.416	5.449
	ζ_1	0.2421	0.2903
Second	ω_2	14.74	10.88
	ζ_2	0.07140	0.1314
ω_n : n^{th} mode natural frequency ζ_n : n^{th} mode critical damping ratio NOTE: Damping in chord modes based on lag damper only			

**TABLE XXIII. CH-47B/C METAL AND ADVANCED-GEOMETRY
FIBERGLASS ROTOR BLADES, DESIGN
PARAMETERS**

Item	CH-47B/C	AGB Glass
Rotor Radius, ft	30.0	30.0
Blade Chord 75 percent R, in.	25.25	33.38
Number of Blades/Rotor	3	3
Rotor Solidity Ratio	0.0669	0.0848
Rotor RPM	230	230
Rotor Tip Speed, fps	723	723
Flapping Weight*, lb	491.7	492.7
Flapping Weight Moment, in.-lb	5.527×10^4	6.125×10^4
Flapping Inertia, lb in. ²	1.239×10^7	1.351×10^7
Lagging Weight**, lb	331.8	371.4
Lagging Weight Moment, in.-lb	4.635×10^4	5.207×10^4
Lagging Inertia, lb in. ²	1.021×10^7	1.108×10^7
Pitching Inertia, lb in. ²	1.109×10^4	2.105×10^4
Pitch Axis, Percent Chord	19.53	25.00
Shear Center, Percent Chord	19.53	21.15
Static CG, Percent Chord	22.24	23.39
Dynamic CG, Chord	24.88	24.86
CF at Hor. Pin., lb	88,963	97,955

*Flapping weight is all weight that rotates around the horizontal hinge.
 **Lagging weight is all weight that rotates around the vertical hinge.

7. Increasing RPM delays moment stall by effectively decreasing blade angles of attack.
8. Increases in altitude require increases in blade angles of attack, thereby bringing about the inception of moment stall.

CONTROL SYSTEM AND ROTOR SHAFT LOADS

Introduction

Control system and rotor shaft loads for level flight and maneuver conditions used to determine the structural flight envelope of the CH-47C/AGB configuration are discussed. Restrictions imposed by the test-bed limitations are examined, and the validity of the test data is established. Feasibility of a cruise guide indicator (CGI) and its effect on the flight envelope are also reviewed. Finally, steady upper control system loads are investigated to determine the adequacy of the CH-47C upper boost actuators on the CH-47C/AGB configuration.

Level-Flight Data

The summary of Table XXIV identifies the level-flight test conditions for the 31 stress and motion airspeed sweeps conducted in the CH-47C/AGB configuration. Scattergrams of load versus airspeed for these 31 test conditions are presented in Appendix III for the most critical fatigue-loaded components (exclusive of rotor blades), namely, the aft pitch links, aft rotor shaft and aft fixed link. Blade loads are examined in a later section of the report and are shown to be noncritical.

The development of the AGB control and drive system structurally limited level flight speed envelope depends, in essence, on the determination of the forward speed at which limit loads were reached in each load scattergram for the 31 test conditions. Statistically, the data sample is not large considering that 4 gross weights, 2 rotor rpm's and several altitudes from 3,000 to 10,000 feet are represented in the 31 test flights. The envelope developed here is for demonstration purposes using the methodology corresponding to that of the CH-47C. Because of the limited sample, however, it is not considered adequate as a full qualification.

Typical level-flight airspeed sweep data for the aft pitch links and rotor shaft at approximately 46,000 pounds gross weight are shown in Figures 188 and 189 for 235 and 245 rpm respectively. At 235 rpm (Figure 188), the aft pitch link loads are slightly above the endurance limit, while at 245 rpm, the pitch link loads are just below the endurance limit. In both cases the rotor shaft bending moment is below the endurance limit. By extrapolating along a velocity squared line, the pitch link loads are found to intercept the endurance limit at 133 knots for 235 rpm, and 147 knots for 245 rpm. Since it was established previously that the pitch link load growth rate in the stall region follows a velocity squared curve, this method of extrapolation appears satisfactory.

TABLE XXIV. ADVANCED-GEOMETRY BLADE STRESS AND MOTION
LEVEL FLIGHT SUMMARY

NOMINAL GROSS WEIGHT (LB)	CENTER OF GRAVITY (IN.)	ROTOR RPM	NOMINAL DENSITY ALTITUDE (FT)	ACTUAL GROSS WEIGHT (LB)	ACTUAL DENSITY ALTITUDE (FT)	FLIGHT - RUN	V _{NE} (KTAS)	AIRSPEED ATTAINED (KTAS)	LOAD LIMITED AIRSPEED (KTAS)	CRITICAL PARAMETER AFT CONTROLS	LOAD-LIMITED AIRSPEED NORMALIZED TO NOMINAL GROSS WEIGHT ②																	
33,000	-7	245	3000	32,800	2740	243 (50-59)	180	165	181	Pitch Link	181																	
				33,500	3570	244 (1-6)																						
				33,400	3160	246 (2-10)																						
				33,350	3350	254 (1-9)																						
				31,550	2960	254 (24-29)																						
40,000	-6	235	3000	39,400	3120	251 (9-18)	158	141	170	Pitch Link	167																	
				40,600	3300	252 (2-5)						151	137	153	Pitch Link	156												
				39,850	3070	253 (1-8)											155	152	175	Pitch Link	174							
				40,150	3060	255 (2-6)																154	155	163	Pitch Link	164		
				38,550	6150	253 (20-33)																					154	151
		39,600	6200	255 (7-13)	149	155	162	Pitch Link	160																			
		38,700	7600	255 (17-33)						149	155	160	Pitch Link	154														
		38,860	5400	282 (6)											155	192	171	Pitch Link	166									
		38,500	9000	283 (11)																185	165	Pitch Link	166					
		38,880	8640	283 (10)																				170	166	Fixed Link	166	
		46,000	+10	235	3000	46,600	3300	287 (5-14)	125																			152
						46,100	6600	287 (15-24)		107	148	136	Fixed Link	137														
						44,800	6600	287 (16-48)							146	155	135	Fixed Link	149									
						46,500	2030	270 (1-6,13-17)												129	133	138	Pitch Link					
						45,850	3330	269 (2-15)																129	119	135	Pitch Link	
44,070	3220			270 (27-33)	136	146	155	Pitch Link	146																			
45,500	5970			272 (15-18)						122	138	133	Pitch Link	127														
47,000	5500			284 (1-9)											112	140	130	Pitch Link	135									
46,200	7400			284 (10-18)																95	128	117	Pitch Link					119
45,300	9600			284 (19-27)																				135	135	95	Pitch Link	
245	10000	44,800	11000	284 (28-35)	110	110	70	Fixed Link	58																			
		45,940	3110	267 (6-14)						149	127	165	Pitch Link	165														
		46,190	6090	271 (1-12)											140	137	147	Fixed Link	148									
		45,940	10470	271 (13-23)																99	125	109	Pitch Link					109
		50,000	0	245																				2000	50,500	2600	285 (6-15)	
10000	50,000	10000			286 (18-26)	121	No	Pitch Link	No																			
NOTE: ① No Capability																												
② Load-limited airspeed adjusted to account for the difference between the actual gross weight and the nominal gross weight. Based on structural																												

G.W.	CG	H _D	N _r	C _T /o	FLT. (RUNS)
45,500 LB	-4 IN.	5,970 FT.	235 RPM	.0915	272 (15-18)

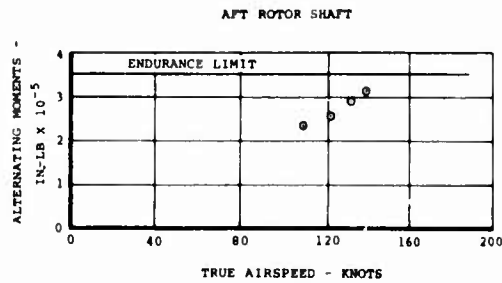
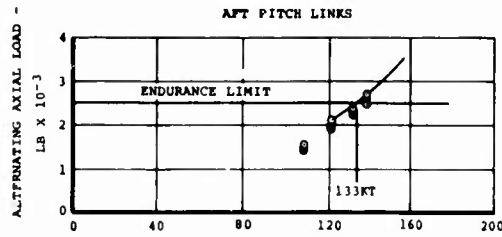


Figure 188. Typical Aft Pitch Link and Rotor Shaft Loads at 45,500 Pounds Gross Weight and 235 RPM.

G.W.	CG	H _D	N _r	C _T /o	FLT. (RUNS)
46,190 LB	-4 IN.	6,090 FT.	245 RPM	.0845	272 (1-12)

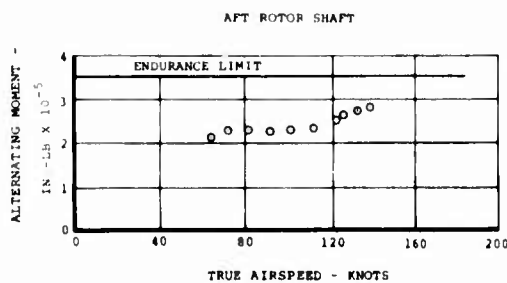
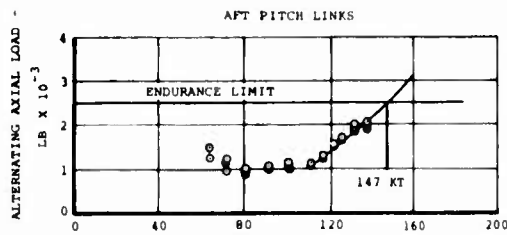


Figure 189. Typical Aft Pitch Link and Rotor Shaft Loads at 46,190 Pounds Gross Weight and 245 RPM.

For a comparison of CH-47C and CH-47C/AGB pitch link loads, the reader is referred to the discussion of this subject under the Rotor Moment Stall Characteristics section. Since the aft pitch link load is the critical item in level flight, a similar examination of the rotor shaft loads and other control components does not appear worthwhile.

Maneuver Data

A summary of all maneuvers conducted during the CH-47C/AGB stress and motion program is contained in Appendix IV. An investigation of the loads incurred and a comparison with the CH-47C maneuver experience at all gross weights is contained in Figures 190 and 191. Again, the parameters investigated are the aft pitch links for the control system and the aft rotor shaft for the drive system. These figures present a comparison of the range of maximum alternating loads (moments) experienced during the defined maneuvers.

Figure 190 shows the range of pitch link loads to be lower for the CH-47C/AGB, except for the transition and partial power descent maneuvers, which show a higher load for the CH-47C/AGB aircraft. For the two exceptions, the loads are less than the endurance limit of 2500 pounds and therefore do not affect the component life.

Figure 191 shows the range of rotor shaft bending moment to be generally higher for the CH-47C/AGB than the production CH-47C. This increase is attributed to the higher centrifugal force with the heavier fiberglass blades.

The scope of the CH-47C/AGB testing was not as extensive as the CH-47C qualification program. However, at endurance limits of 2500 pounds for the aft pitch link and 353,000 inch-pounds for the aft rotor shaft, the load comparisons suggest that fatigue damage in maneuvers for the CH-47C/AGB is equal to or less than for the CH-47C. This is encouraging for two reasons:

1. The CH-47C has been shown to meet component fatigue life guarantees.
2. The CH-47C/AGB airspeed and bank angle capability exceed those of the basic CH-47C, as will be shown in subsequent paragraphs.

Test-Bed Limitations

The complete Advanced Geometry Blade flight test program was conducted on CH-47C Helicopter, Tab B-361. Due to its configuration, this vehicle imposed certain limitations on the blade investigation. These limitations were as follows:

1. The investigation was restricted to operation within the CH-47C strength and power limits. Blade and control fatigue loads were monitored via

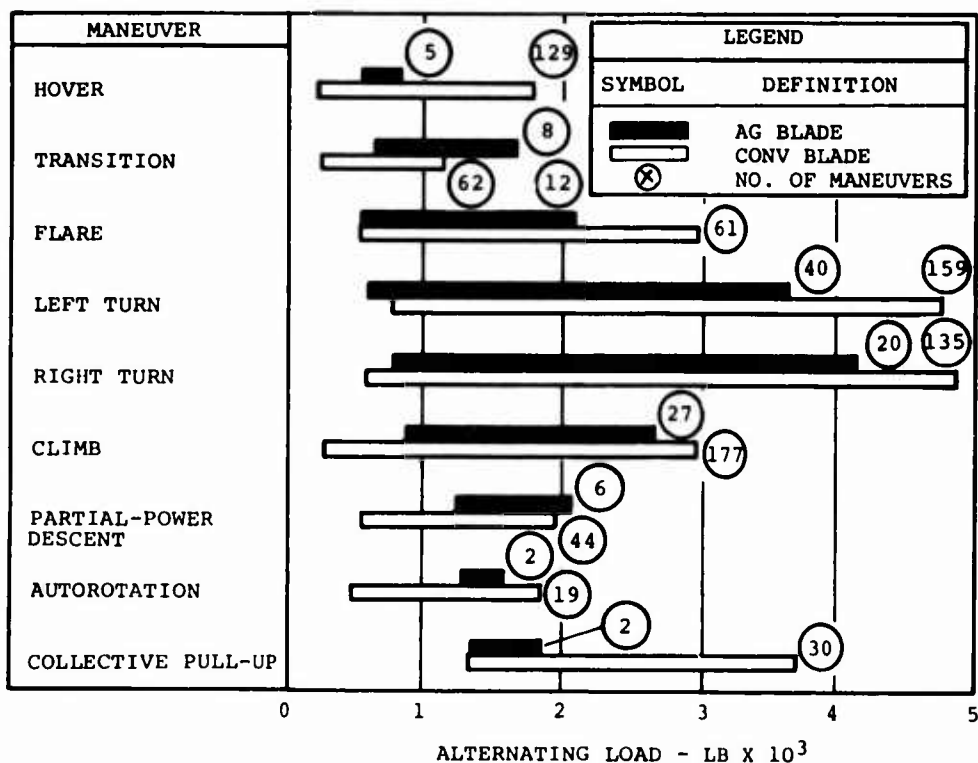


Figure 190. Comparison of Conventional and Advanced-Geometry Blades Through Maneuver Loads at Aft Pitch Links.

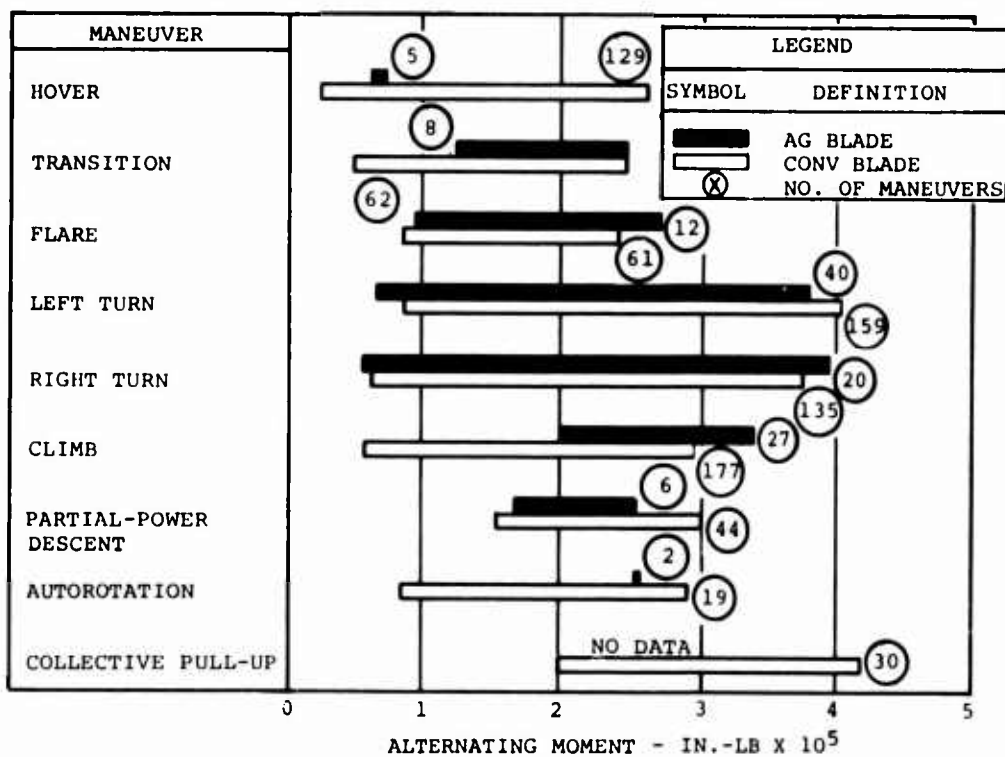


Figure 191. Comparison of Conventional and Advanced-Geometry Blades Through Maneuver Loads on Aft Rotor Shaft.

telemetry during all flights. The proposed initial safe flight limits with this system were 150 percent of endurance limit for level flight testing and 200 percent for maneuvering flight. These cutoffs were never attained during the program.

The testing was frequently restricted by available power of the T55-L-11 engines as well as the transmission limit. The aircraft was initially restricted to the CH-47C transmission limit of 6000 hp at 243 rotor rpm. This limit was later increased to 6800 hp at 243 rotor rpm for testing purposes.

The operation of the aircraft was limited to 247 maximum rotor rpm due to the additional centrifugal force of the heavier AGB blades.

2. The most frequently limiting factor in level flight was "once per rev" vibration as discussed in the Vibration Section. Most of the speed sweeps which were initially limited to "once per rev" were eventually extended to some other limit.
3. On Flight Number 252, a 0.4 "g" gust occurred which produced high control loads. The probability of the occurrence of a gust-induced load factor of this magnitude (1.4) is relatively low for a CH-47 helicopter. Reference 13 documents only approximately 25 occurrences per 1000 hours of flight on the CH-47A helicopter. This load exposure is insignificant compared to the four pull-ups per hour to a load factor of 1.5 as considered in the CH-47C fatigue life calculations. Therefore, this particular gust condition was deleted from the level-flight envelope analysis.
4. The aircraft was restricted to operation within the limitations of the systems installed. For example, the aircraft was equipped with the production CH-47C cyclic trim, which is programmed as a function of altitude and airspeed. The effect on loads of changes to the cyclic trim program was not evaluated, consistent with the interest of reducing program costs.
5. Analysis of the control and drive system loads revealed several level-flight sweeps which unduly limited the flight envelope. For example, Figure 192 displays the airspeed capability at 46,000 pounds, wherein the load-limited airspeed is plotted for each speed sweep. This data shows that one unusual limit of 97 knots at 3100 feet density altitude occurred on Flight Number 269. Such an unusual load occurrence was evaluated as follows:
 - a. Figure 193 presents the alternating pitch link loads versus forward speed for Flight Number 269.

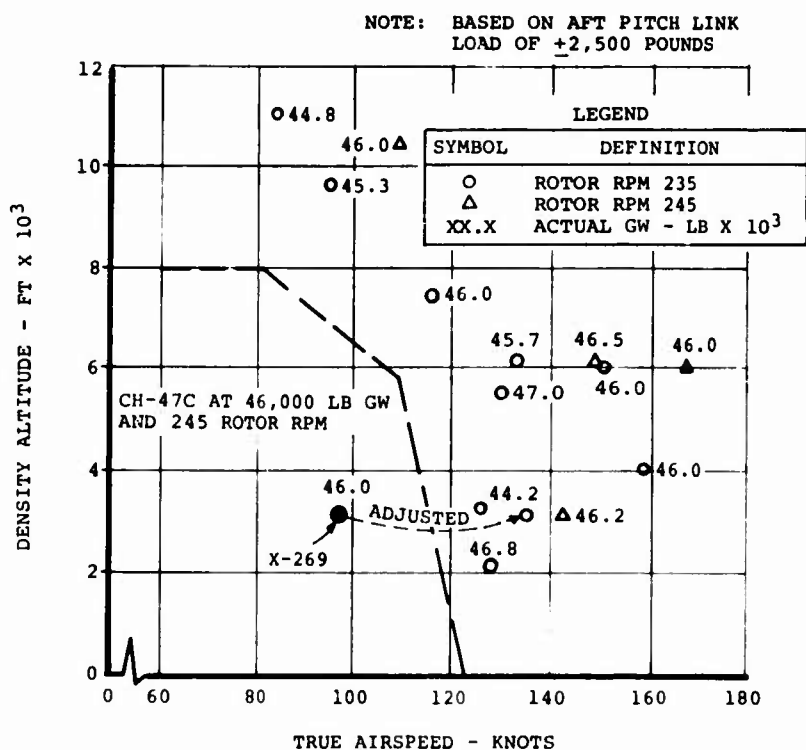


Figure 192. Speed Capability of CH-47C Helicopter With Advanced-Geometry Blades at 46,000 Pounds Gross Weight.

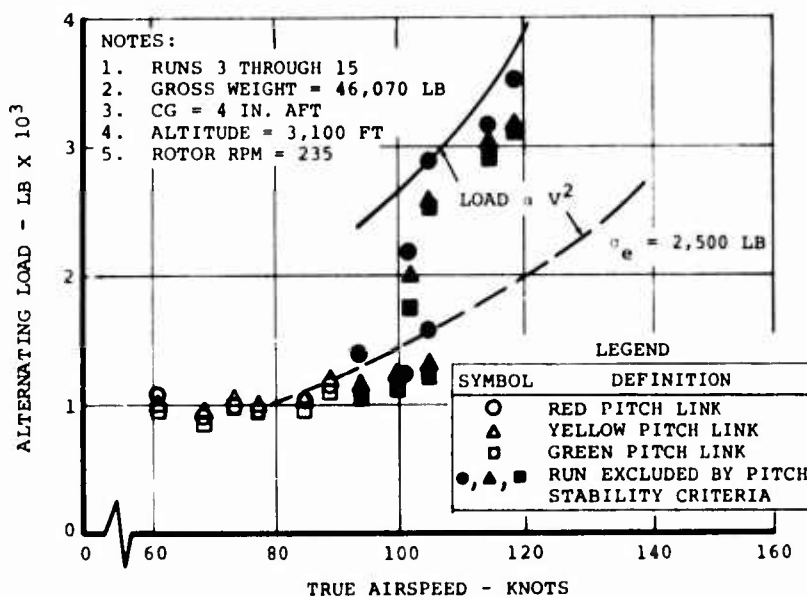


Figure 193. Aft Pitch Link Loads for Flight 269 of CH-47C Helicopter Equipped With Advanced-Geometry Blades.

**TABLE XXV. CH-47/AGB HELICOPTER PITCH STABILITY
INVESTIGATION**

Aircraft: B-361	Rotor RPM: 235
Flight: 269	Density Altitude: 3,000 ft
Gross Weight: 46,000 lb	

Run No.	Aft Pitch Link Alternating Loads (lb)			Variation Within Run		
	Red	Yellow	Green	Long. Stick Position* (in.)	Pitch Attitude (deg)	Pitch Rate (deg/sec)
9	1292	1139	1073	1.23	5.08	5.26
10	1174	1188	1063	1.14	1.90	2.96
11	1529	1405	1360	1.21	7.31	6.90
12	2090	2123	1752	1.36	3.72	5.35
13	2790	2596	2580	1.52	5.30	6.93
14	3060	3090	2940	1.44	3.28	7.50
15	3450	3237	3318	1.05	3.32	8.74

*The criteria established during the CH-47C Stress and Motion Program provided for the deletion of any data point which displayed a pitch axis oscillation of approximately 6 to 8 seconds and a longitudinal stick motion in excess of 1 inch.

- b. Pilots reported that the whole program was flown with the Pitch Stability Augmentation (PSA) system off.
- c. In the analysis of CH-47C load data obtained prior to the installation of the PSA system, the criterion was established to delete all level-flight data which exhibited more than 1 inch of longitudinal stick motion within one data record.
- d. An investigation of the aircraft motion and control characteristics during the time interval of the peak alternating load is contained in Figure 194. This investigation indicated that the pilot was required to use an exceptional amount of longitudinal control stick motion to maintain a stabilized attitude. This control motion resulted in higher dynamic component loads than normally encountered.
- e. Table XXV presents other data points in Flight Number 269 where high loads occurred and tabulates the associated control motions and attitudes.

In accordance with the criterion in item c above, runs 9 through 15 of Flight Number 269 (Figure 193) have been deleted from the analysis. Using the same load versus control variation, other data points in the CH-47C/AGB test program were evaluated and the test points of Table XXVI invalidated from the load analysis.

TABLE XXVI. INVALID TEST POINTS BASED ON PITCH STABILITY CRITERIA		
Flight	Run	Delta Longitudinal Stick (in.)
244	4	1.333
246	8	1.025
267	13	1.360
267	14	1.135
269	9-15	1.05 to 1.52
270	3	1.084
270	4	1.330
270	5	1.048
270	6	1.048
270	28	1.048
270	29	1.000
270	31	1.000

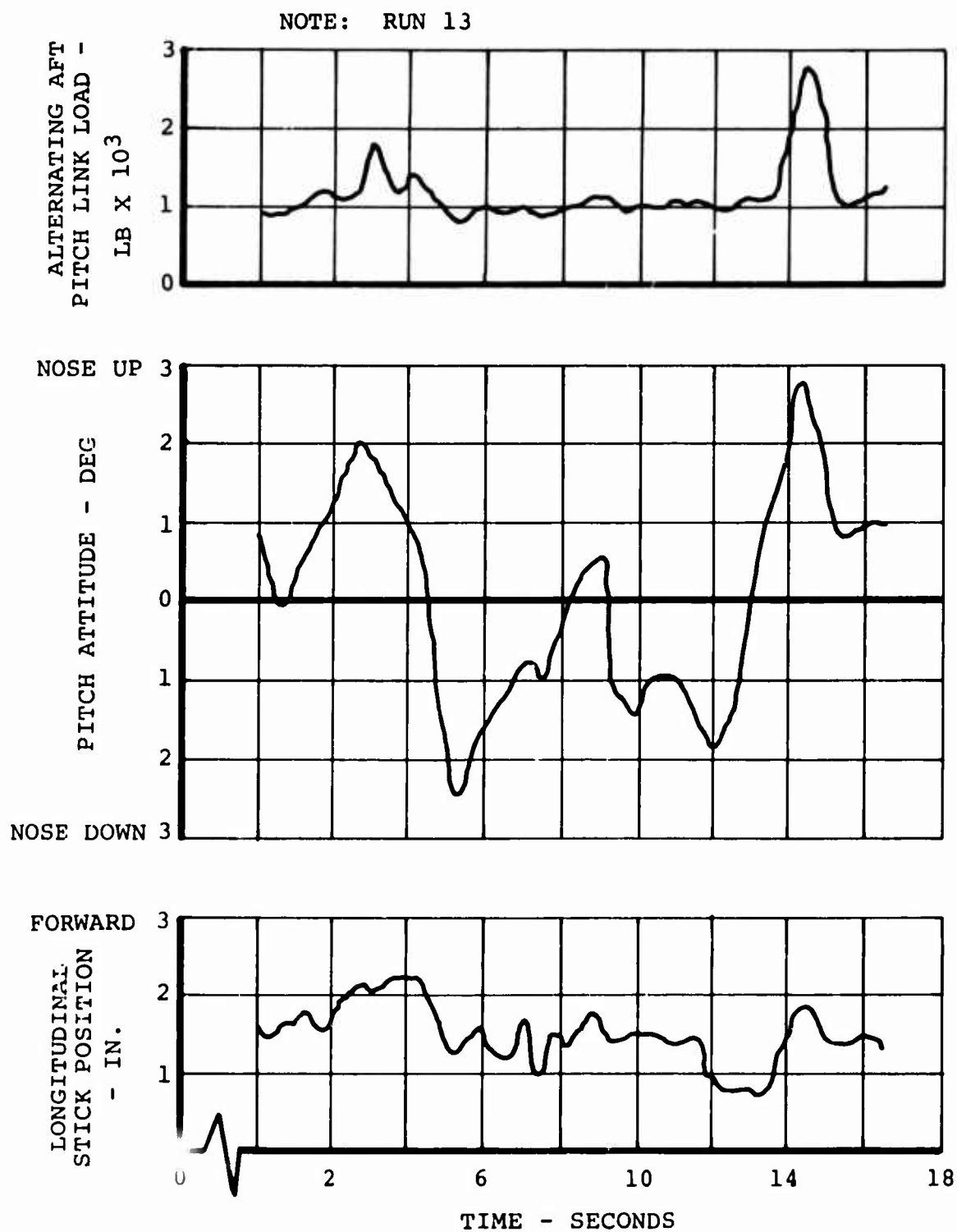


Figure 194. Time History of Flight 269 Showing Effect of Negative, Long-Period Pitch Stability With Pitch Stability Augmentation System Off.

It should be pointed out, then, that the structural flight envelopes constructed for the CH-47C/AGB aircraft assume long-period pitch stability (and resultant lessened control motions) as should occur with the PSA system "on".

Although this has been validated for the CH-47C, it has not yet been accomplished for the CH-47C/AGB (that is, the AGB blades have not been flown with the PSA system "on").

Structural Flight Envelope - Level Flight

Figures 195 and 196 present the CH-47C/AGB structural airspeed limits. These limits have been obtained using the same criteria and endurance limits as used in the construction of the CH-47C structural flight limits. The figures also display the maximum demonstrated blade tip Mach number and equivalent airspeed (EAS) during the AGB program.

Figures 197 and 198 show the relationship of the CH-47C/AGB airspeed capability to the test data and to the CH-47C limits. This data shows the envelopes to be conservative throughout the entire gross weight/density altitude range experienced. Also, this data displays the considerable increase in capability afforded the CH-47C helicopter equipped with advanced-geometry rotor blades.

The level-flight summary of Table XXIV lists all the speed sweeps performed during the AGB stress and motion survey. It also shows the relationship of the loads incurred to the structural airspeed limits. The load-limited airspeeds were determined from the scattergrams in Appendix III. The most critical parameters and corresponding endurance limits were:

<u>PARAMETER</u>	<u>ENDURANCE LIMIT</u>
<u>Aft Controls</u>	
Pitch Links	±2500 pounds
Fixed Link	±2500 pounds
Pivoting Actuator	±2500 pounds
Swiveling Actuator	±1790 pounds
Rotor Shaft Bending, Sta. 37	±353000 inch-pounds
<u>Aft Blades</u>	<u>ENDURANCE LIMIT @ 10⁷ CYCLES</u>
Flapwise Bending, Sta. 32.8	±41900 inch-pounds
Flapwise Bending, Sta. 288	±17037 inch-pounds
Trailing Edge Tension, Sta. 198	±62985 inch-pounds

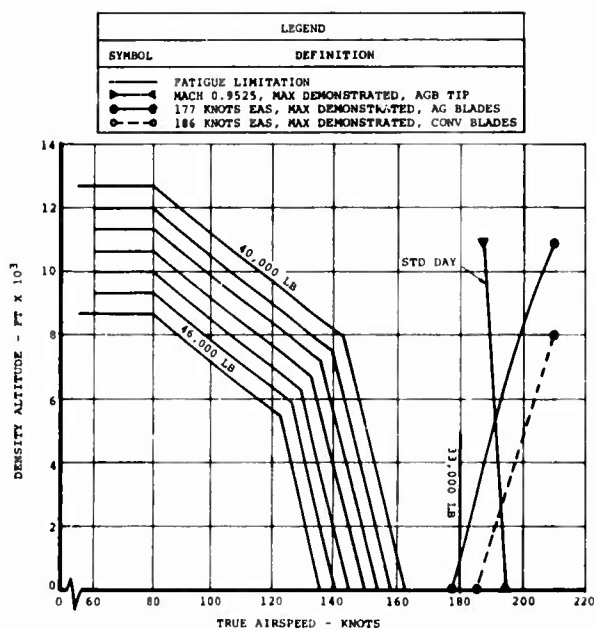


Figure 195. Structural Airspeed Limits of CH-47C Helicopter Equipped With Advanced-Geometry Blades at 235 Rotor RPM.

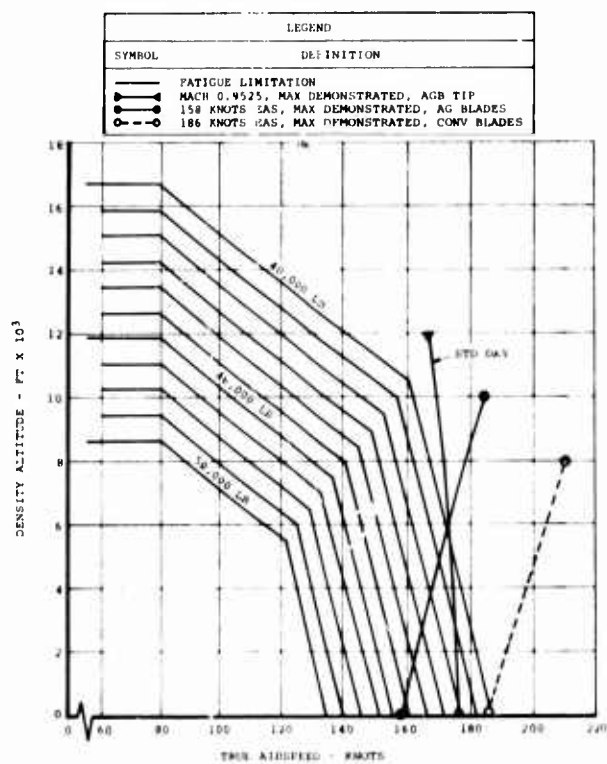


Figure 196. Structural Airspeed Limits of CH-47C Helicopter Equipped With Advanced-Geometry Blades at 245 Rotor RPM.

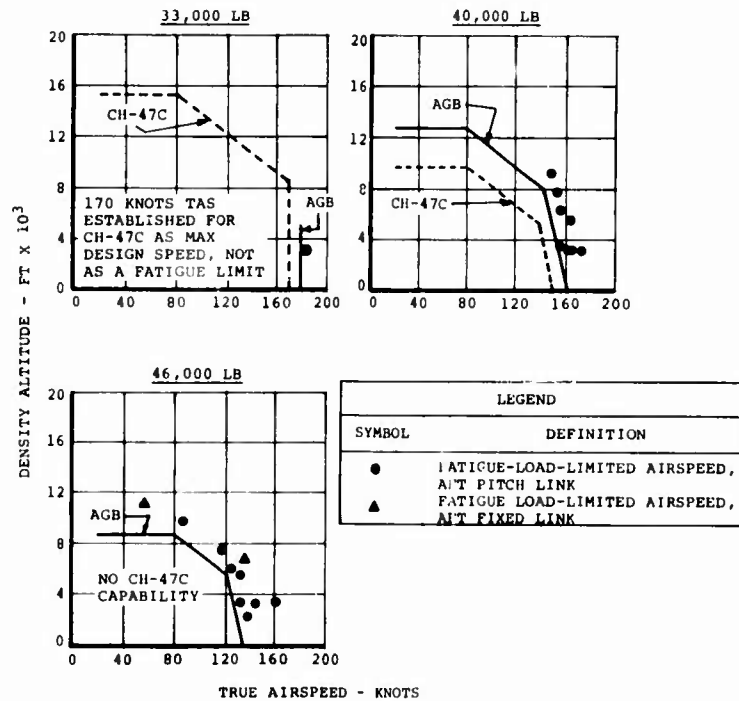


Figure 197. Evaluation of Flight Envelope of CH-47C Helicopter Equipped With Advanced-Geometry Blades at 235 Rotor RPM.

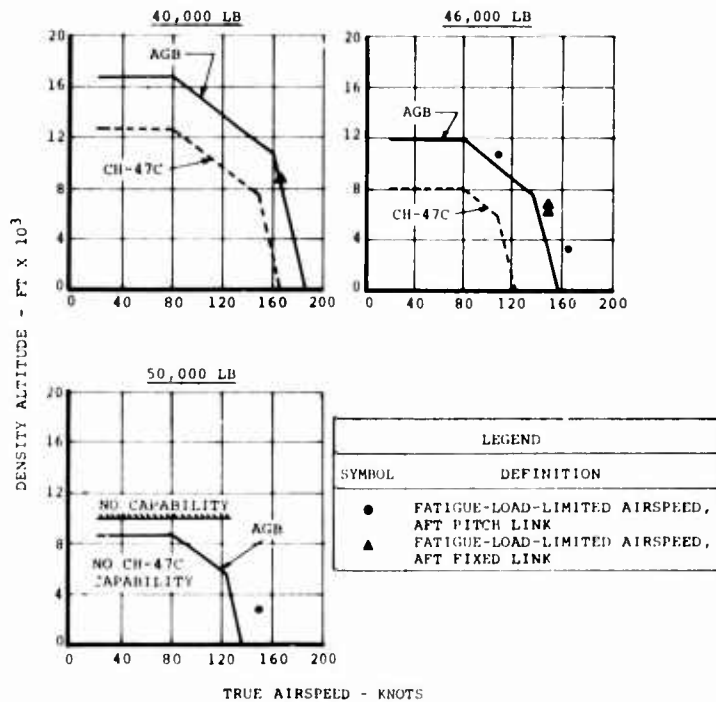


Figure 198. Evaluation of Flight Envelope of CH-47C Helicopter Equipped With Advanced-Geometry Blades at 245 Rotor RPM.

An advancing blade tip Mach number of 0.9525 was attained during a dive on Flight 283, Run 11. Figure 195 shows that, for standard atmosphere, this experience exceeds the fatigue envelopes for 235 rpm rotor speed. At 245 rpm, however, a small portion of the fatigue envelope is not substantiated even for standard day conditions, as shown in Figure 196. Since the effect of transonic tip Mach numbers on fatigue loads is relatively unknown, it is advisable to restrict airspeeds until test experience at higher tip Mach numbers is obtained.

A maximum dynamic pressure at 177 knots EAS was experienced on Flight 282, Run 6, in the CH-47C/AGB configuration. The CH-47C had attained 186 knots EAS during structural demonstration. The dynamic pressure at the AGB tip has been adequately demonstrated for 235 rpm, Figure 195, but is more critical than the projected fatigue limit at 245 rpm, Figure 196. It is recommended that airspeeds be restricted to the maximum demonstrated dynamic pressure on the AGB tip.

The blade tip Mach number and dynamic pressure experience do not impose serious restrictions to operation in the CH-47C/AGB configuration. The 245 rpm envelope could be limited to gross weights above 46,000 pounds, for instance, using 235 rpm for lighter weights. A variation of this would be to leave rotor speed optional (235-245 rpm) at airspeeds up to 158 knots EAS (but within fatigue limits) using only 235 rpm for higher airspeeds.

Bank Angle Envelope

Figure 199 presents the AGB bank angle envelope. This envelope was constructed using all turn maneuvers performed during the test program. In comparison to the CH-47C envelope, a significant improvement in capability is afforded the AGB equipped helicopter at the higher gross weights.

The test points are displayed in Figure 200 to demonstrate the extent to which the envelope was investigated.

The tabulation of Table XXVII summarizes the maximum alternating loads measured on the critical parameters within the bank angle envelope.

This summary demonstrates that the AGB-equipped aircraft will incur fatigue loads equal to or less than the production CH-47C while operating to an expanded envelope.

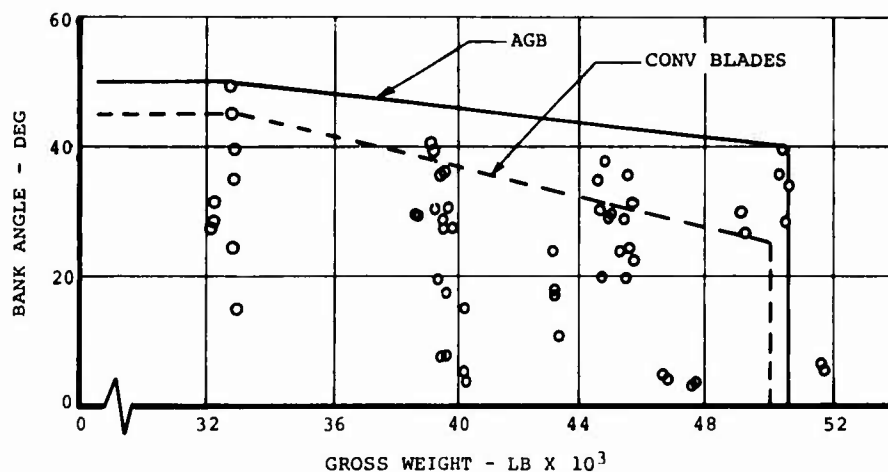


Figure 199. Comparison of Conventional and Advanced-Geometry Blades Through Bank-Angle Envelope and Demonstrated Points.

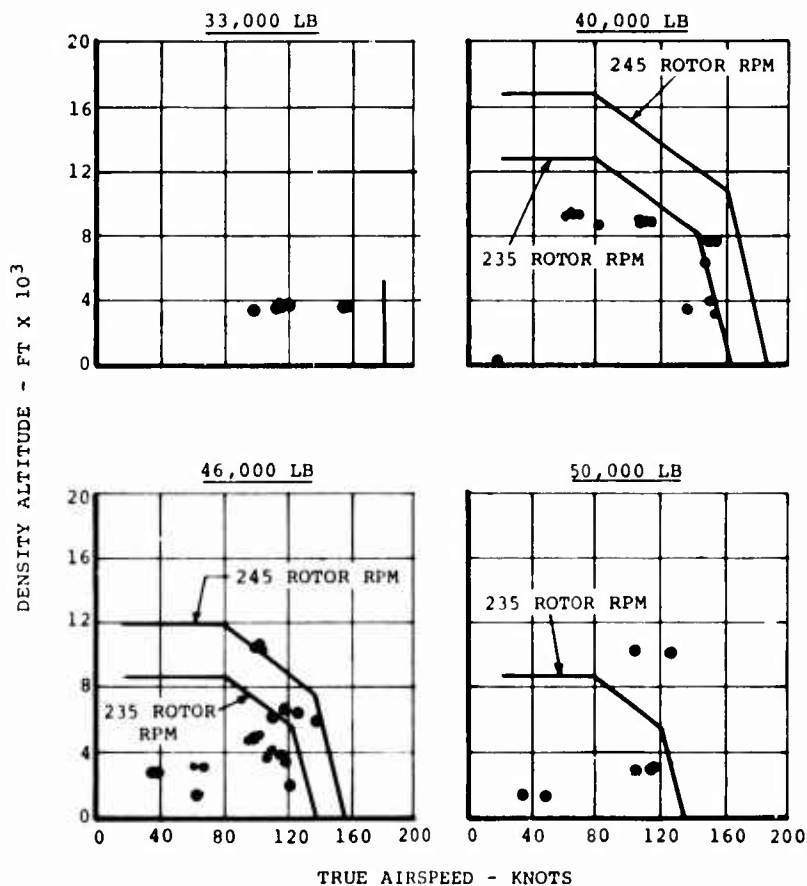


Figure 200. Flight Test Turn Experience of CH-47C Helicopter Equipped With Advanced-Geometry Blades.

TABLE XXVII. MAXIMUM ALTERNATING LOADS DURING TURN MANEUVERS		
Parameter	CH-47C	CH-47/AGB
Aft Pitch Links, lb	5,037	4,134
Aft Fixed Link, lb	4,199	3,565
Aft Pivoting Actuator, lb	5,314	3,399
Aft Swiveling Actuator, lb	3,572	2,245
Aft Rotor Shaft Bending, Sta. 37, in. -lb	405,000	396,100
Aft Blade Flap Bending, Sta. 32.8, in. -lb	43,920 (Sta. 47)	45,350
Aft Blade Flap Bending, Sta. 288, in. -lb	31,670	24,220
Aft Blade Trailing Edge Tension, Sta. 198, in. -lb	90,870	87,398

CGI Feasibility

An analysis of CH-47C/AGB stress and motion test data was conducted to determine the feasibility of installing a cruise guide indicator (CGI) for airspeed and maneuver control. The analysis consisted of the following steps:

1. Selection of the critical control components and their fatigue loads to be monitored for fatigue damage.
2. Determination of the proper monitor load values to assure fatigue protection.
3. Assessment of the effect of the proposed CGI system on aircraft operations.

The feasibility of using the CH-47C CGI was considered. This system uses the aft fixed link (2400 pounds) and aft pivoting actuator (2300 pounds) as monitor loads.

Tables XXVIII and XXIX were compiled to identify the critical fatigue loads. Load values are presented in percentage of endurance limit for convenience. The summary was generated by finding the maximum load measured on each parameter and then entering the values of the other measurements for the same flight condition. Evaluation of parameters progressed from left to right in Table XXVIII, followed by the same sequence in Table XXIX. For each parameter, flight conditions previously listed in the tables were excluded from those available for

TABLE XXVIII. MAXIMUM FATIGUE LOAD SUMMARY, CH-47C/AGB CONFIGURATION, AFT ROTOR									
Parameter	Fixed Link	Pivot Act.	Pitch Link	Swivel Act.	Drive Arm	R/Shaft Bend	Bld/TE Tension	Bld/Flp Bend 50	Bld/Flp Bend 288
Endurance Limit Units	2400* (lb)	2300* (lb)	2500 (lb)	1790 (lb)	1410 (lb)	353,000 (in.-lb)	84,200 (in.-lb)	55,100 (in.-lb)	22,200 (in.-lb)
Flt-Run	Percent Endurance Limit								
MANEUVER									
285-19	149	113	164	94	28	78	61	117	72
282-6	112	168	169	143	32	122	143	136	86
270-36	70	148	164	115	43	115	131	94	95
283-11	115	141	147	128	31	98	107	138	75
286-31	51	33	42	51	34	88	91	94	67
284-35	106	119	122	88	18	108	41	53	51
282-5	105	119	164	118	31	107	148	116	77
269-16	84	66	71	62	28	88	113	116	97
282-8	38	42	51	50	24	37	80	97	95
287-25	116	115	133	104	31	108	84	89	65
286-30	130	137	146	94	25	97	57	75	72
284-18	103	76	107	71	19	94	54	55	53
286-37	89	61	92	71	20	76	48	61	70
254-19	26	25	36	32	7	-	33	31	36
286-4	110	98	105	62	19	96	63	90	84
271-48	79	46	66	52	30	67	78	86	85
272-43	91	56	83	61	26	61	77	74	80
267-22	70	47	55	68	33	76	106	115	84
* Current monitor limit for CH-47C Cruise Guide Indicator									

TABLE XXIX. MAXIMUM FATIGUE LOAD SUMMARY, CH-47C/AGB CONFIGURATION, FORWARD ROTOR										
Parameter	Fixed Link	Pivot Act.	Pitch Link	Swivel Act.	Drive Arm	R/Shaft Bend	Bld/TE Tension	Bld/Flp Bend 50	Bld/Flp Bend 288	
Endurance Limit Units	1860 (lb)	1094 (lb)	2500 (lb)	910 (lb)	1410 (lb)	368,000 (in.-lb)	84,200 (in.-lb)	55,100 (in.-lb)	22,200 (in.-lb)	
Flt-Run	Maneuver	Percent Endurance Limit								
285-19	Rt. Turn	67	68	47	63	8	60	47	51	36
282-6	Dive	126	<u>256</u>	100	162	31	78	83	56	42
270-36	SAS Pulse (Pull-up)	90	159	77	58	26	69	72	43	60
283-11	Dive	120	<u>258</u>	110	181	34	81	89	54	48
286-31	Left S/S	56	88	47	72	5	58	48	59	30
284-35	Level Flt	50	47	32	36	6	51	31	34	24
282-5	Left Turn	80	110	58	34	15	60	56	44	31
269-16	Flare	51	85	52	95	16	64	103	114	75
282-8	Flare	48	93	43	95	10	56	60	75	34
287-25	Left Turn	130	<u>135</u>	77	69	27	66	55	47	41
286-30	Left Turn	76	145	62	87	8	63	46	51	35
284-18	Level Flt	66	97	92	49	12	54	34	29	27
286-37	PPD	68	66	52	91	9	50	40	40	30
254-19	Climb	31	32	25	-	20	30	28	29	30
286-4	Climb	52	75	45	65	7	65	54	62	36
271-48	Flare	50	77	41	86	19	58	89	<u>92</u>	74
272-43	Flare	40	95	51	88	16	60	83	<u>99</u>	66
267-22	Flare	50	83	65	86	11	54	87	99	80

selection of the maximum load. The rows of the combined tables can be used to identify the most critical fatigue measurements as well as to display the fatigue load relationship of parameters. The following parameters are identified as critical in fatigue:

1. Aft fixed link (climb)
2. Aft pitch link (turn, pull-up, level flight, PPD, climb)
3. Aft blade flapwise bending, Sta. 50 (sideslip, flare)
4. Forward pivoting actuator (dive, turn)
5. Forward blade flapwise bending, Sta. 50 (flare)

Flight evaluation of the CH-47C/AGB configuration was primarily conducted at an aft center of gravity. Therefore, selection of a forward rotor parameter for CGI monitor cannot logically be made. The high loads in diving flight conditions on the forward pivoting actuator occur well beyond the level-flight performance capability of the configuration and could easily be avoided by imposing an airspeed limitation. The critical turn maneuver on the forward pivoting actuator is equally as critical on the aft pitch link within reasonable data accuracy.

Both the forward and aft rotor blades experienced relatively high loads during flare maneuvers. Transient maneuvers in the low airspeed regimes are generally not suitable for CGI control, primarily because there is no readily available method for the pilot to avoid these loadings. Retirement of components in accordance with current fatigue methodology is a preferable solution to this fatigue problem.

Aft rotor blade flapwise bending was critical in a 5° left sideslip on Flight 286. The maneuver summary in Appendix IV shows that this load occurred at heavy gross weight, high altitude, and low airspeed. Figure 201 displays the sensitivity of this load to both rotor thrust (gross weight) and sideslip angle and also shows that the fatigue strength was not exceeded. Since the measured moment does not exceed the endurance limit, there is no need for CGI protection. The data does point out a need for additional investigation of the low airspeed flight regime for gross weights greater than 50,000 pounds.

Table XXVIII clearly shows that the aft pitch link is the most critical fatigue component. However, CGI monitoring of a rotating measurement imposes the additional design problem of reliably transposing the recorded signal to the fixed system. Because of the design complications, it is reasonable in this case to assess the suitability of fixed control measurements to provide pitch link fatigue protection. An evaluation of the CH-47B/C CGI monitors is logical, i.e., the aft fixed link and aft pivoting actuator loads.

The relationships of the aft fixed link and pivoting actuator loads to the pitch link are shown in Figure 202. It is obvious from the figure that the CH-47C monitor levels of 2400 pounds on the fixed link and 2300 pounds on the pivoting actuator do not adequately protect the pitch link at a 2500-pound endurance limit. Of the various possible choices to select a CGI monitor, two alternatives merit further consideration:

1. Incorporate CH-47C/ECP 630, which increases the aft pitch link endurance limit to approximately 3250 pounds. The CH-47C CGI system provides adequate protection of the aft pitch link at this strength level, with an improved airspeed potential of 5-10 knots at 40,000 pounds gross weight and 10-20 knots at 46,000 pounds gross weight. ECP 630 is approved for CH-47C models, and qualification bench testing is in progress.
2. Monitor the aft fixed link at 1800 pounds alternating load. Observe from Figure 202 that this level of monitoring on the fixed link protects both the pitch link and the pivoting actuator. The maximum airspeed capability will be reduced from 180 to 170 knots (TAS) with this system, but the heavy gross weight capability will approximate the flight envelopes of Figures 195 and 196. While this approach does not provide airspeed benefits, it has the advantage of being able to monitor a forward component, if required, without redesign of the CGI instrument. The loss of 10 knots maximum airspeed capability is not significant since recommended cruise speed will still be attainable at all gross weights.

Control System Steady Loads

Level-flight steady pitch link loads in the CH-47C/AGB configuration were noticeably more tensile than those measured during the CH-47C qualification, as shown in Figure 203. The resulting lower loads were well within the design limit strength of the control system as indicated by Figures 204 through 206. Figures 204 and 205 show that the peak alternating loads exceed the single boost static design capacity of the dual upper boost actuators. Note, however, that the mean or steady loads are within the single boost static capacity. In order to assess the importance of these facts, a study was conducted to determine the adequacy of the CH-47C upper boost actuators for the CH-47C/AGB configuration.

Separate plots of steady versus alternating load for level flight, turns, and other maneuvers were generated for the following forward and aft measurements:

1. Pitch link
2. Fixed link

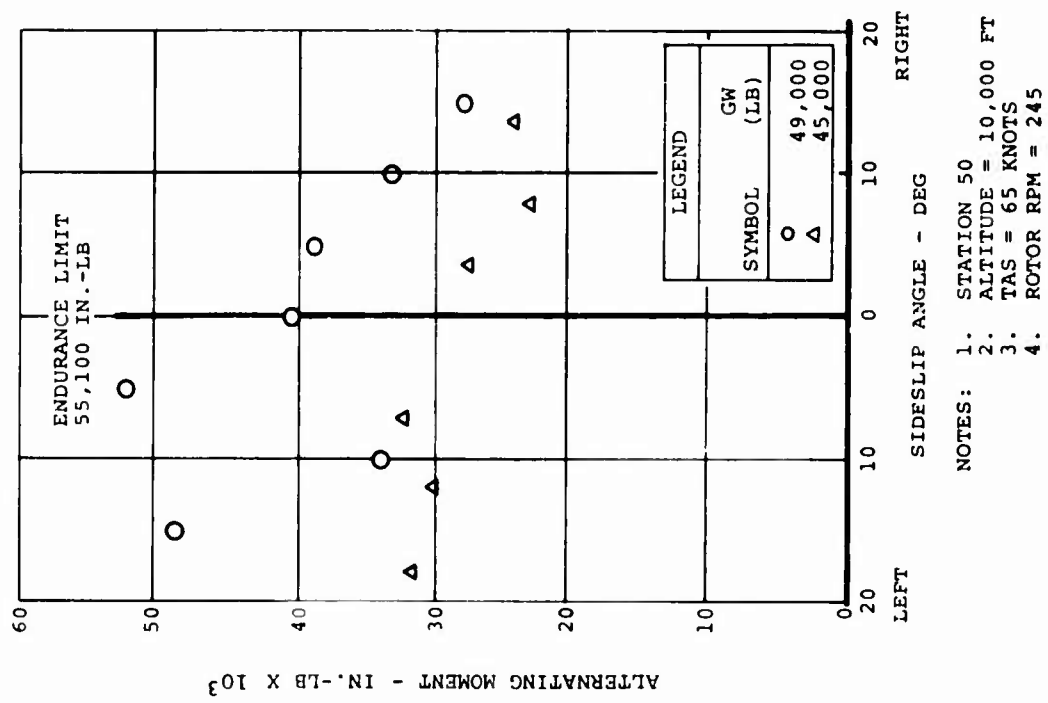


Figure 201. Flapwise Bending Moment of Aft Advanced-Geometry Blade.

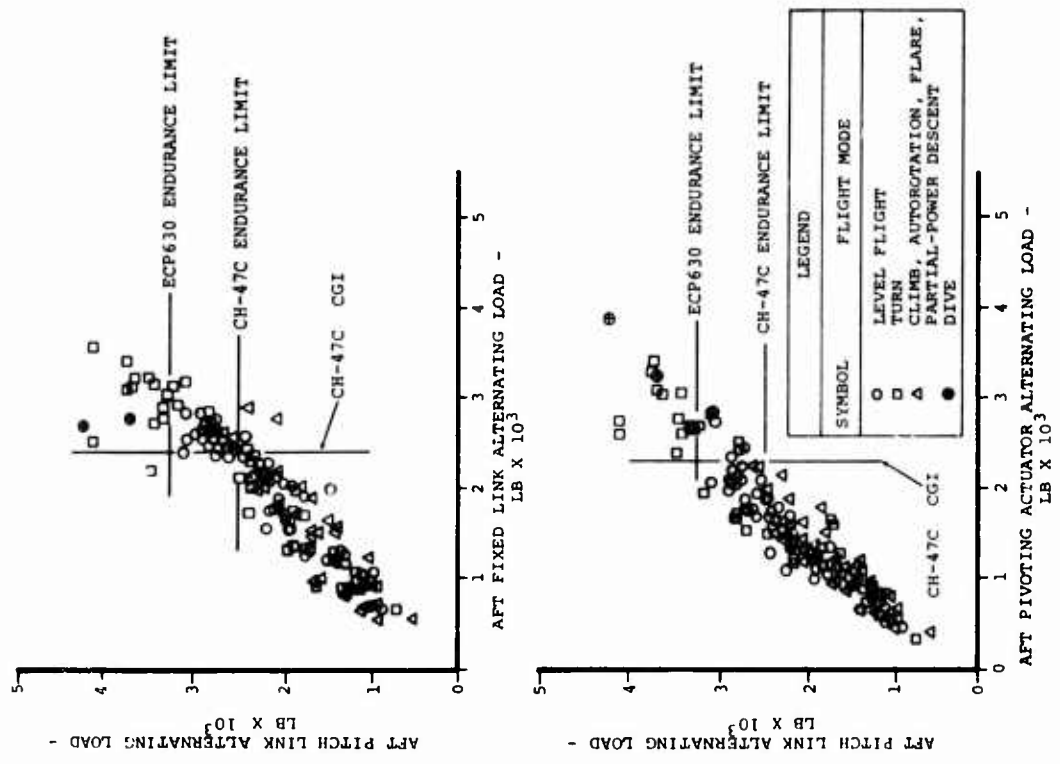


Figure 202. Feasibility of Cruise Guide Indicator With Advanced-Geometry Blades.

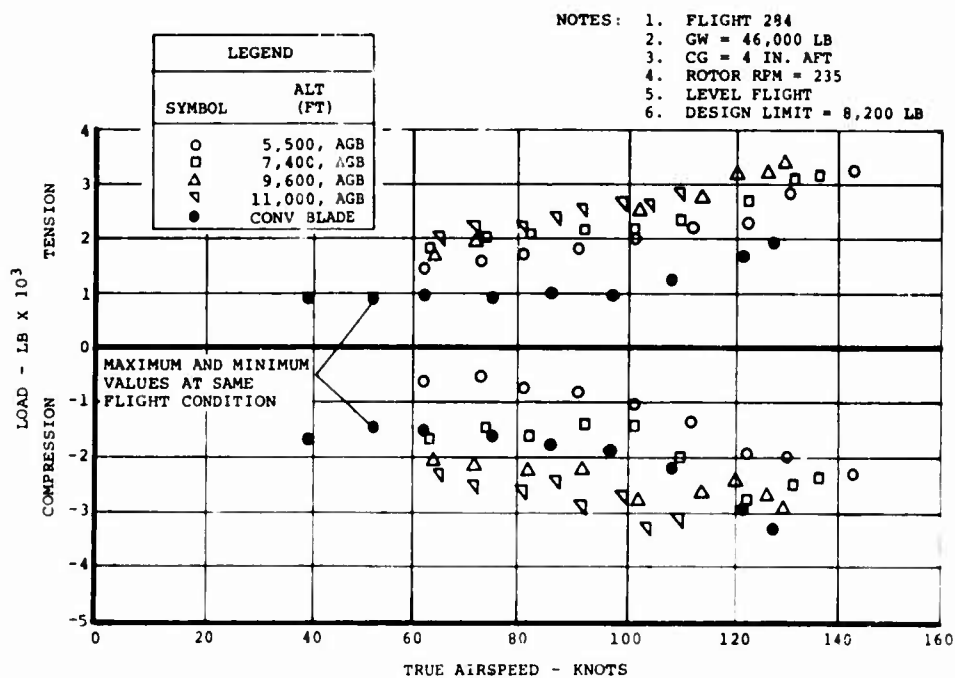


Figure 203. Comparison of Aft Pitch Link Steady Loads Conventional and Advanced-Geometry Blades.

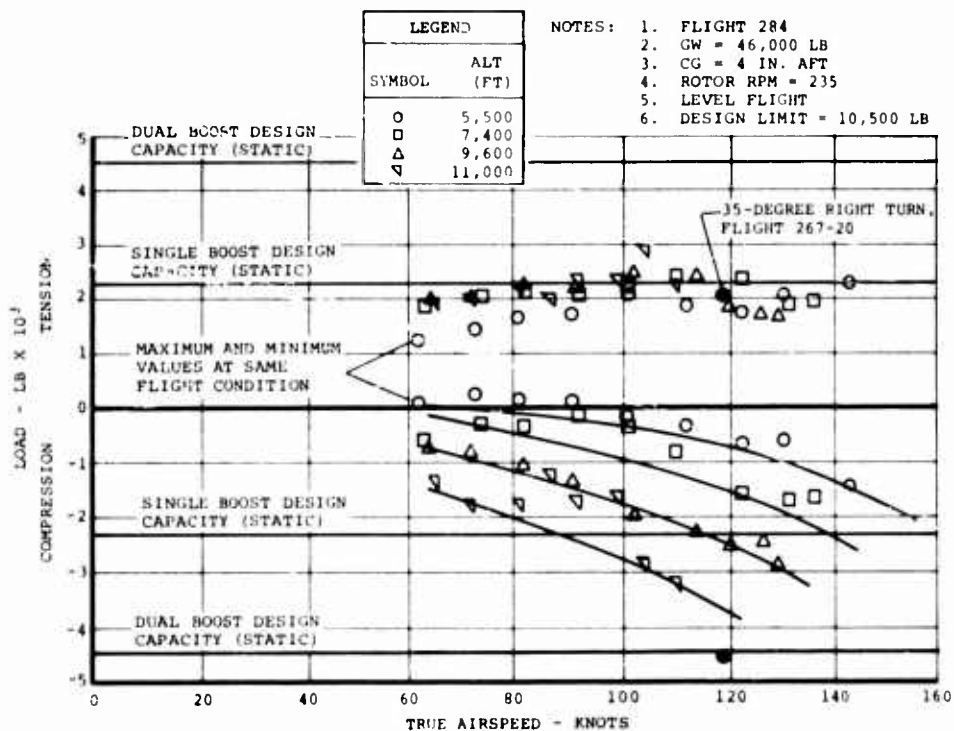


Figure 204. Aft Pivoting Actuator Loads on CH-47C Helicopter Equipped With Advanced-Geometry Blades.

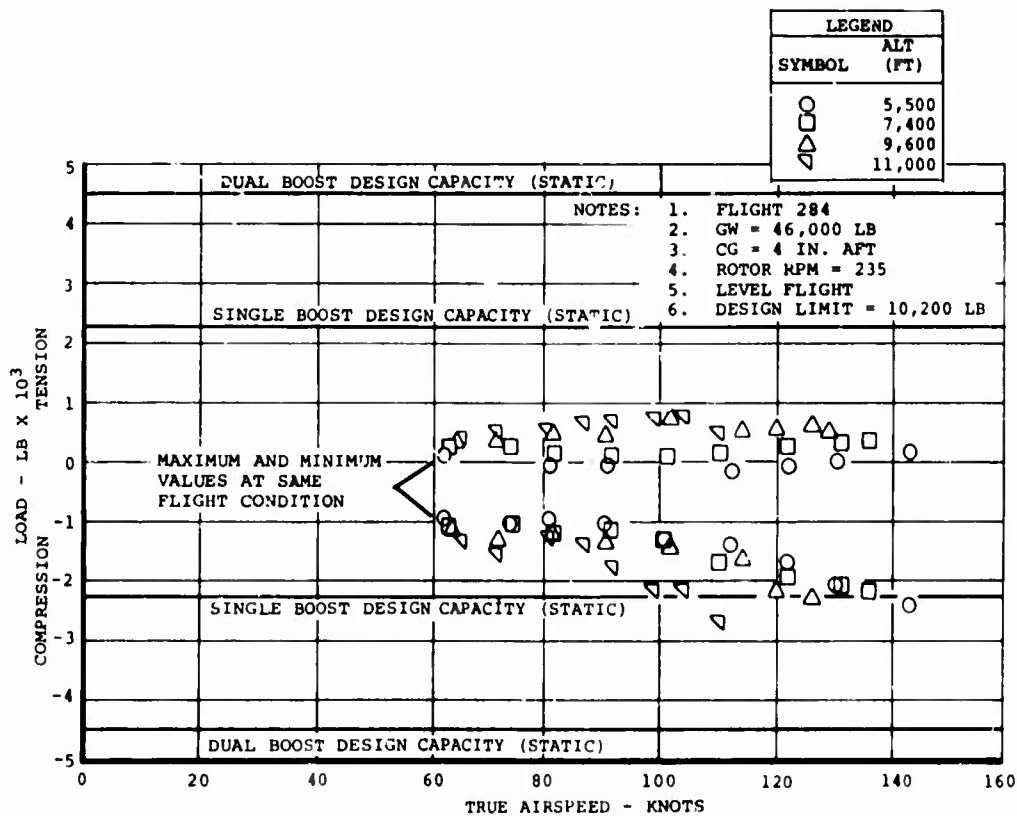


Figure 205. Aft Swiveling Actuator Loads on CH-47C Helicopter Equipped With Advanced-Geometry Blades.

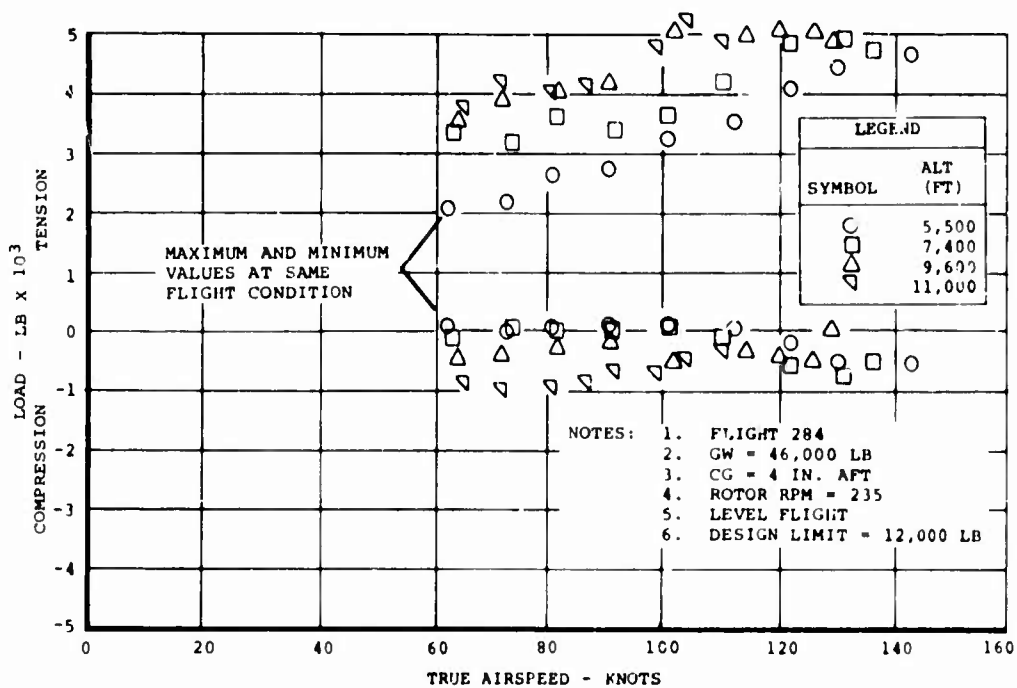


Figure 206. Aft Fixed Link Loads on CH-47C Helicopter Equipped With Advanced-Geometry Blades.

3. Pivoting actuator

4. Swiveling actuator

These plots led to the following conclusions:

1. A large ultimate margin of safety exists for all measured loads.
2. The aft pivoting actuator is the most critical with respect to control boost power.

The aft pivoting actuator steady-alternating load plots are reproduced in Figure 207 for convenience. The chevron lines on this figure are the boundaries of the static design capacity of the upper boost actuators for both dual and single boost operation. Observe that the dual boost static capacity of the system is slightly exceeded only during turns in the CH-47C/AGB testing, but the load values are considerably less than those experienced during the CH-47C structural demonstration. It is concluded, in view of the successful demonstration of the CH-47C, that the CH-47C boost actuators are adequate on the CH-47C/AGB for dual boost operations.

Typical level-flight load waveforms, Figure 208, display a predominant 3/rev alternating load, the peak of which exceeds the single boost capacity. This momentary exceedance of the static load capacity of the actuator does not compromise flight safety, since the actuators are of irreversible design which prevents actuator displacement due to external load. The consequence of exceeding the actuator static capacity, then, is a reduction in control response rate, since displacement can take place only during the portion of the load cycle within the actuator static capacity.

Loss of control response in stabilized flight conditions is generally undesirable. For the CH-47C/AGB configuration, however, this occurs only during single boost operation, which is in itself an emergency condition requiring a precautionary landing. Figures 207 and 208 suggest that adequate control response is available to perform the precautionary landing; however, flight demonstration of this capability is advisable prior to extensive operations in the CH-47C/AGB configuration.

BLADE LOADS

Introduction

This section contains comparisons between measured blade bending moments for level and maneuvering flight and predicted maximum moment distributions. Variation of alternating moments with airspeed is presented for selected blade

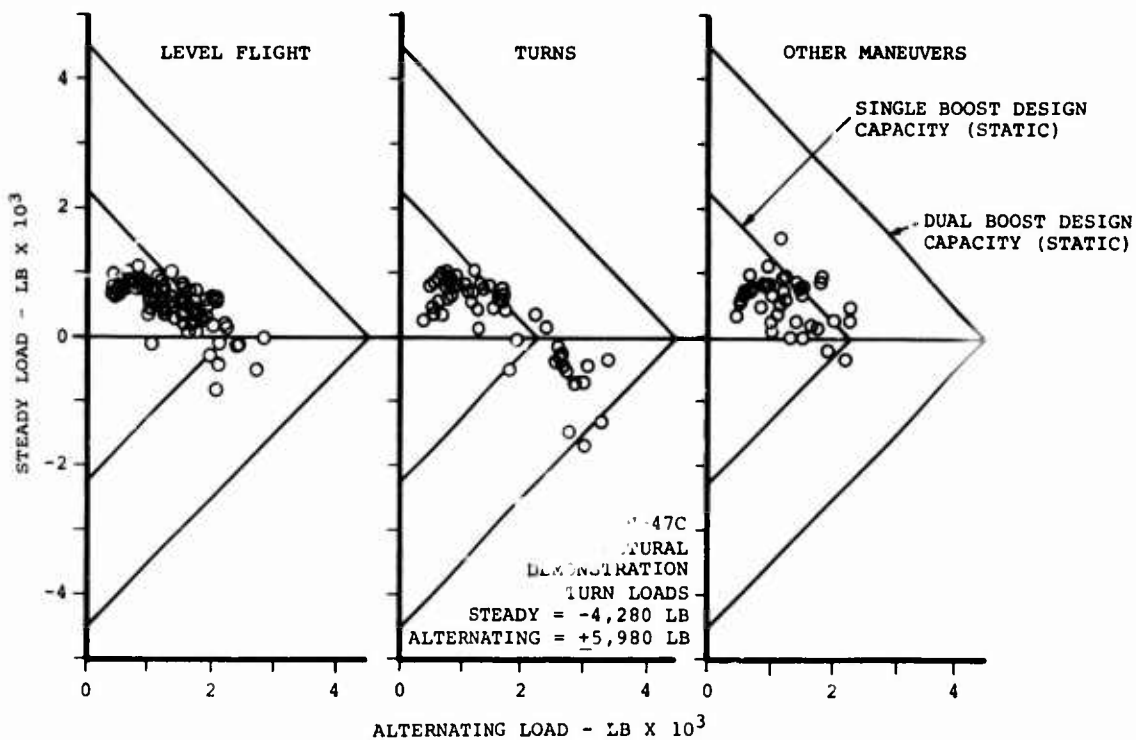


Figure 207. Steady and Alternating Loads on Aft Pivoting Actuator of CH-47C Helicopter Equipped With Advanced-Geometry Blades.

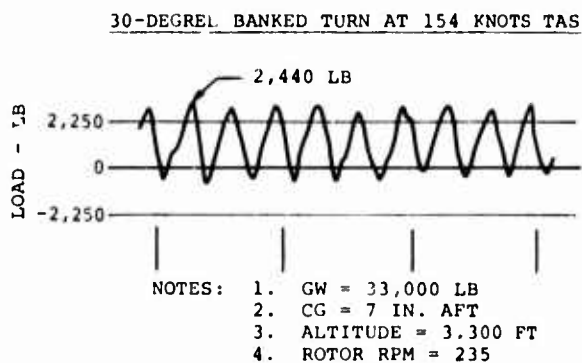
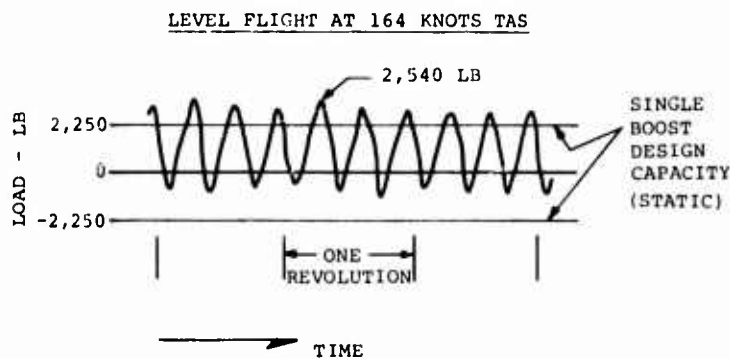


Figure 208. Waveform of Loads on Aft Pivoting Actuator of CH-47C Helicopter Equipped With Advanced-Geometry Blades.

parameters. CH-47C and AGB moment comparisons are made at various blade stations for equivalent C_T/σ and similar flight conditions. In addition, load phasing between blade parameters is established for different gross weights and airspeeds.

Component life is estimated for the socket, spar, and trailing-edge skin based on an assumed AGB mission profile, and comparisons are made between the allowable alternating stress and the stress due to the maximum flight test loads for the primary blade materials. Flight test strain levels are compared to the strains on the structural test articles to establish the validity of these tests. Possible changes of the fiberglass material characteristics due to fatigue loading are explored. Finally, the trailing-edge cracks which developed on three blades during flight testing are described and their repair is discussed.

Spanwise Moment Distributions

The purpose of this section is to compare the predicted loads used in the fatigue stress analysis with the loads recorded during flight testing.

The spanwise steady and alternating moment distributions determined by flight testing are shown in Figures 209 through 216. The maximum bending moments measured for various flight conditions throughout the program are presented as a data band. Loading on both the forward and aft instrumented blades is included. The flight moments are divided into loads recorded during level-flight conditions and loads recorded during maneuvering flight. A further subdivision is made according to gross weight (33,000, 40,000, 46,000 and 50,000 pounds).

Review of Methods of Predicting Blade Loads

The predicted level-flight moment distributions for the aft blade were determined from computer programs and consisted of an envelope determined by five airspeeds (60, 80, 100, 140 and 180 knots). The flight conditions for these calculations were:

<u>Gross Weight</u>	<u>RPM</u>	<u>Altitude</u>	<u>Center of Gravity</u>
33,000	230	S/L	17 inches fwd
44,000	243	S/L	17 inches fwd

The trim schedule used for these calculations is shown in Figure 34. The computer output for the predicted alternating chordwise moments has been adjusted upward to correlate with flight test data based on past experience. The increased level-flight moment distribution is indicated in the appropriate figures.

Comparison of Test and Predicted Steady Flapwise Moment Distribution

Referring to Figure 209, the level-flight steady flapwise moments generally exceed the predicted envelope loads at the inboard end of the blade ($r/R = 0.082$ to 0.205). From station 117 ($r/R = 0.325$) to 198 ($r/R = 0.55$), the flight test moments are less than the predicted loads. Outboard of station 198, the flight test moments are generally greater than the predicted moments.

Comparison of Test and Predicted Alternating Flapwise Moment Distribution

The flight test alternating flapwise moments presented in Figure 210 show good agreement with the envelope of predicted moments at all gross weights. At 46,000 pounds gross weight, minor deviations occur at station 198, 252 and 288 ($r/R = 0.55$; 0.70 and 0.80 respectively).

Comparison of Test and Predicted Steady Chordwise Moment Distribution

Figure 211 presents the level-flight steady chordwise moment comparison. Variations occur at station 198 ($r/R = 0.55$) between the analyzed flight test data and the predicted moments.

In analyzing the flight test data to obtain steady chordwise moments, the effect of centrifugal force was subtracted from the steady output of the trailing-edge tension gage. The factor for centrifugal force was calculated analytically and was dependent upon rpm, axial stiffness, chordwise stiffness and the distance from the gage location to the chordwise neutral axis. The difficulty of predicting chordwise stiffness has been discussed in the Structural Test section, and the neutral axis location is related to the stiffness predictions. Because of the variability of these two blade properties, the analytical conversion from trailing-edge tension to steady chordwise moment could partially account for the discrepancies between the predicted and flight test results.

Just as the actual chordwise stiffness and neutral axis location affect the flight test data, they also influence the predicted steady chordwise moments. The offset between the neutral axis and the center of gravity is an important parameter influencing trailing-edge tension or compression. If the center of gravity is aft of the neutral axis, a moment results which gives tension in the trailing edge. For the center of gravity forward of the neutral axis, the moment produces compression in the trailing edge. Steady drag force and the moment it creates is the other factor and results in compression of the trailing edge. The chordwise stiffness and neutral axis location affect the magnitude of this moment distribution. The addition of these two moments gives the steady chordwise moment. Incorrect prediction of these blade properties could explain the difference between the analytical and flight moments.

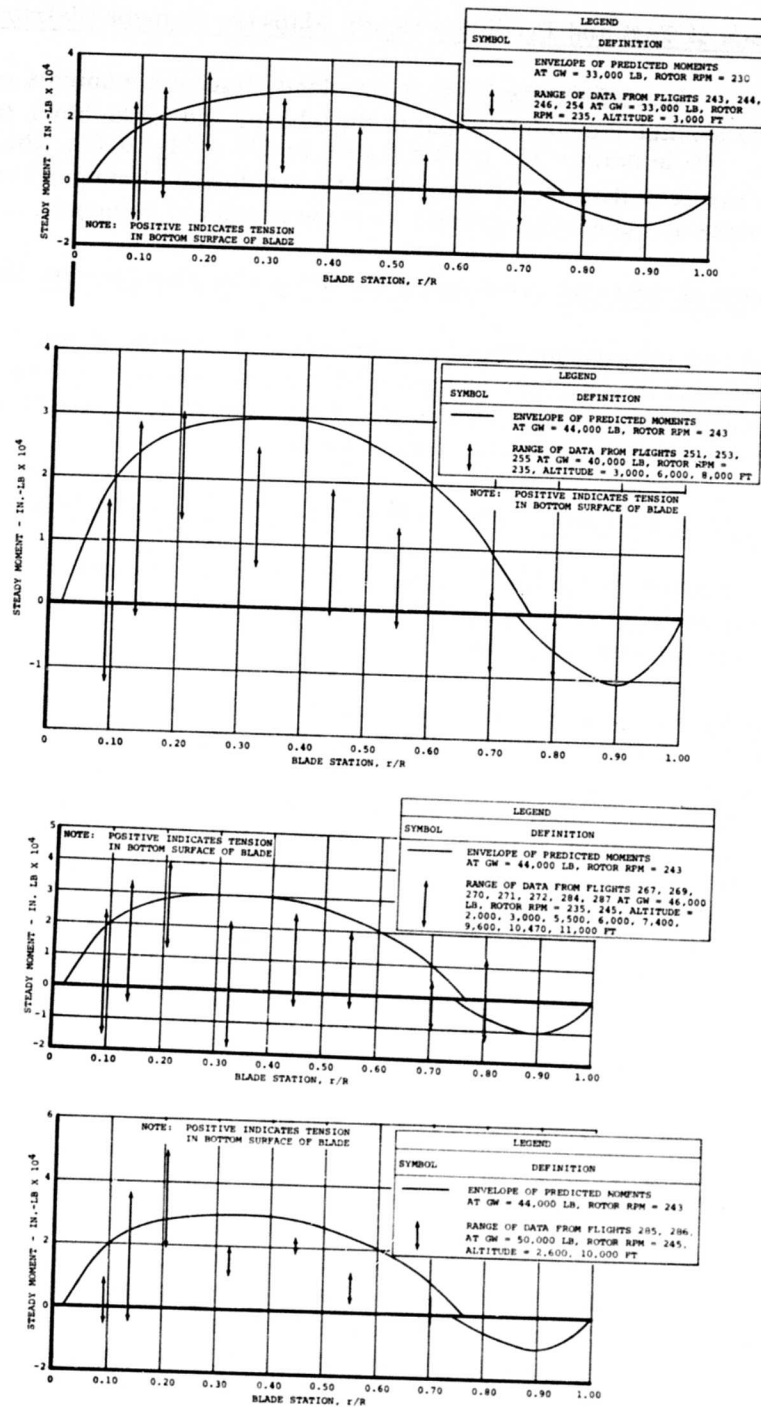


Figure 209. Comparison of Predicted and Flight Test Steady Flapwise Bending Moments in Level Flight.

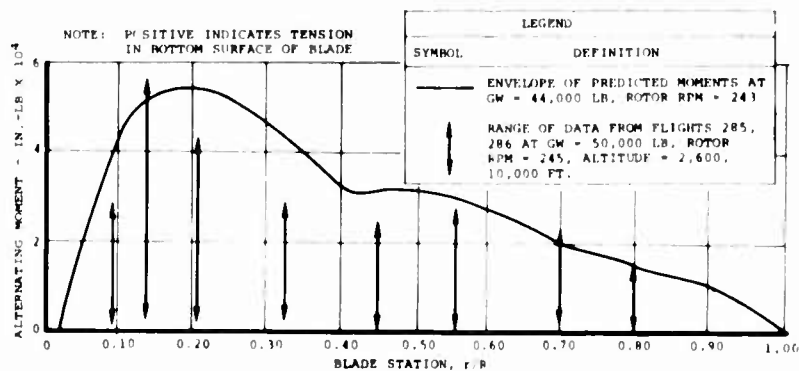
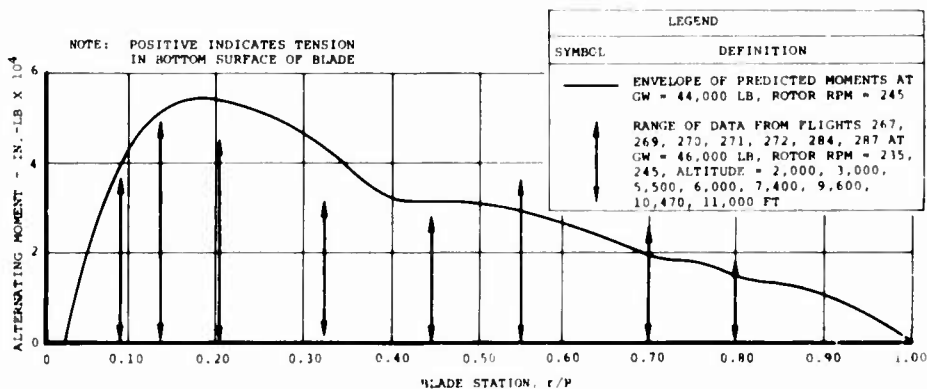
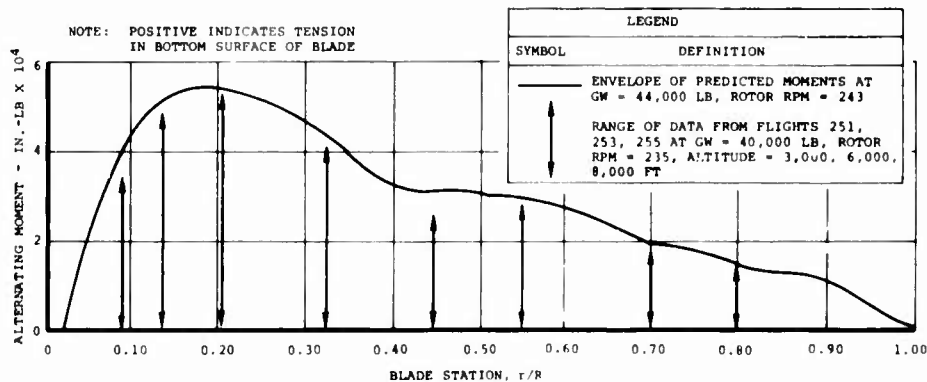
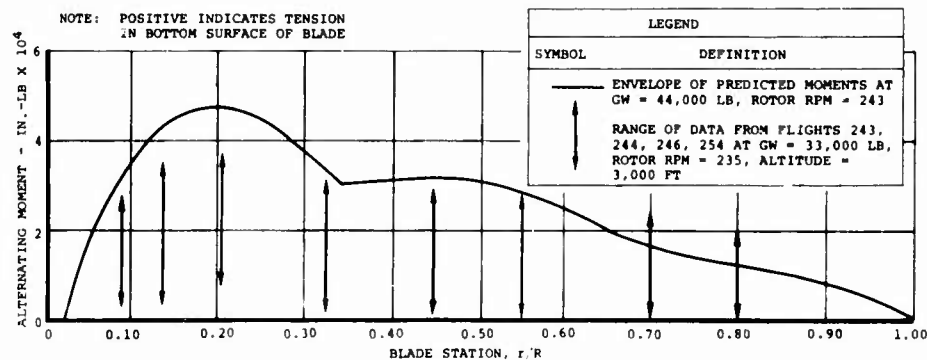


Figure 10. Comparison of Predicted and Flight Test Alternating Flapwise Bending Moments in Level Flight.

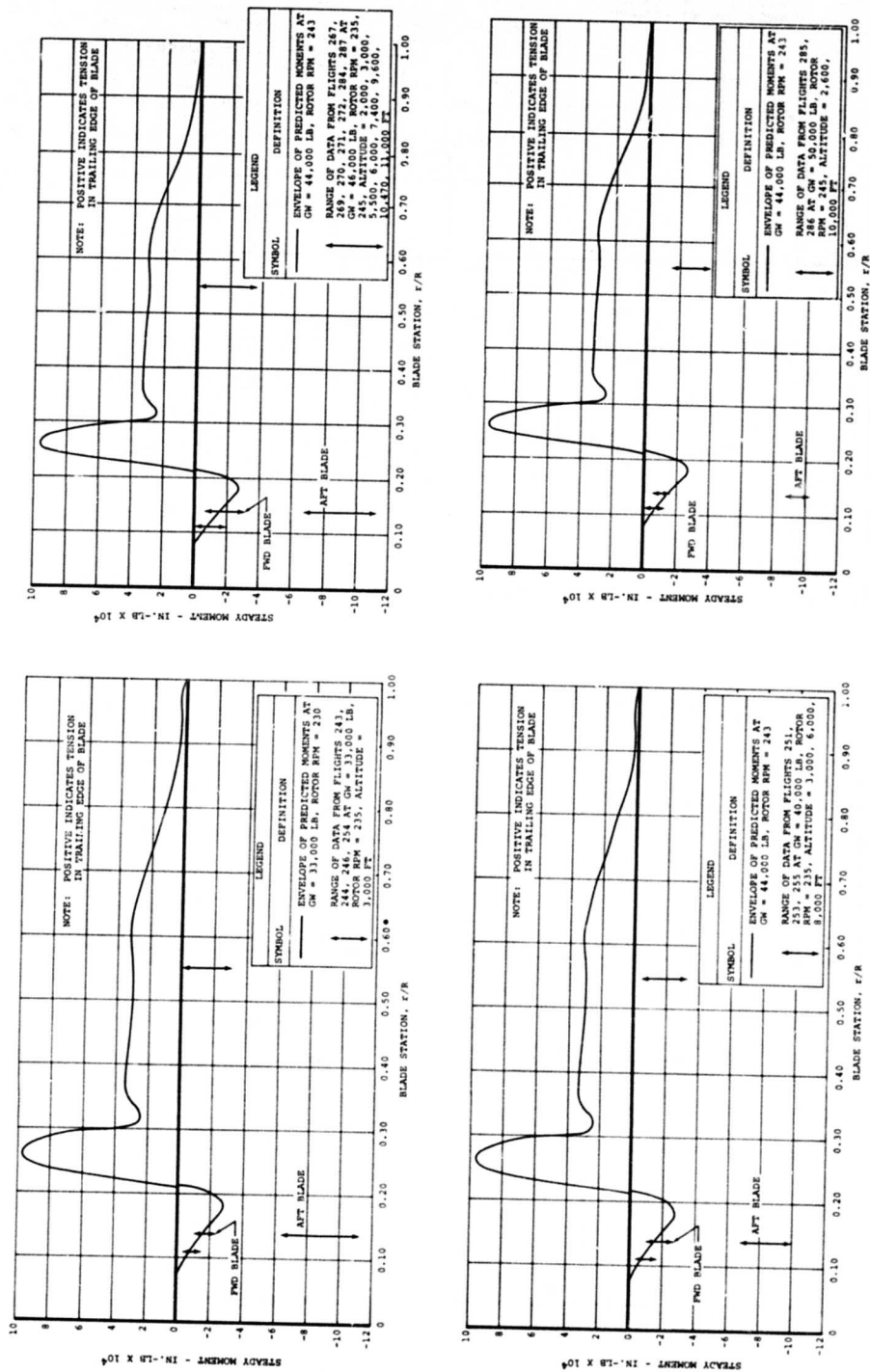


Figure 211. Comparison of Predicted and Flight Test Steady Chordwise Bending Moments in Level Flight.

Figure 211 shows a major deviation between test data and predictions at station 49.5 ($r/R = 0.1375$). The steady chordwise moments on the forward blade follow the trend of the prediction at each gross weight, but the aft blade moments are significantly greater than both the prediction and the forward blade data. The spare chordwise bending bridge was used for a period of time and, in general, gave the same results as the active bridge. An investigation of the blade bridge calibration data and procedures failed to provide an explanation.

At this time, no firm reason can be given to adequately explain the magnitude of this chordwise moment. General areas for further study concern the blade structure and instrumentation. For the blade, a chordwise neutral axis shift in the aft direction would produce a moment due to centrifugal force. Only a relatively small shift would be needed because the centrifugal force is approximately 100,000 pounds. A neutral axis shift might be caused by a nonuniform wall thickness in the section, an elliptical cross section instead of a circular one, a localized reduction of the fiberglass modulus, or local debonding of the titanium adapter and/or socket from the spar. Concerning the area of instrumentation, the blade calibration might be thoroughly checked. The location of the bending bridge on the blade might be verified and the recording and analysis of the bridge output in the flight test data system might be examined for possible errors.

Comparison of Test and Predicted Alternating Chordwise Moment Distributions

Figure 212 presents the level-flight alternating chordwise moments and the distribution of maximum predicted alternating chordwise moments. The comparisons show that the flight moments are less than or equal to the predicted moments at each gross weight.

Maneuver Loads

The maneuver loads for the steady flapwise moments, the alternating flapwise moments, the steady chordwise moments and the alternating chordwise moments are presented in Figures 213, 214, 215, and 216, respectively. The appropriate level-flight predicted moments are shown for reference. The steady flapwise and chordwise moments and the alternating flapwise moments are generally greater than the level-flight data, which is expected. The problem with the steady chordwise data for the aft blade is also shown in the maneuver moments. The alternating chordwise moments at station 198 were greater than anticipated. These high alternating loads ($\pm 125,000$ inch-pounds maximum) were recorded during landing flares. Their adverse effect on the life of the trailing-edge skin is evaluated in a later discussion of blade life.

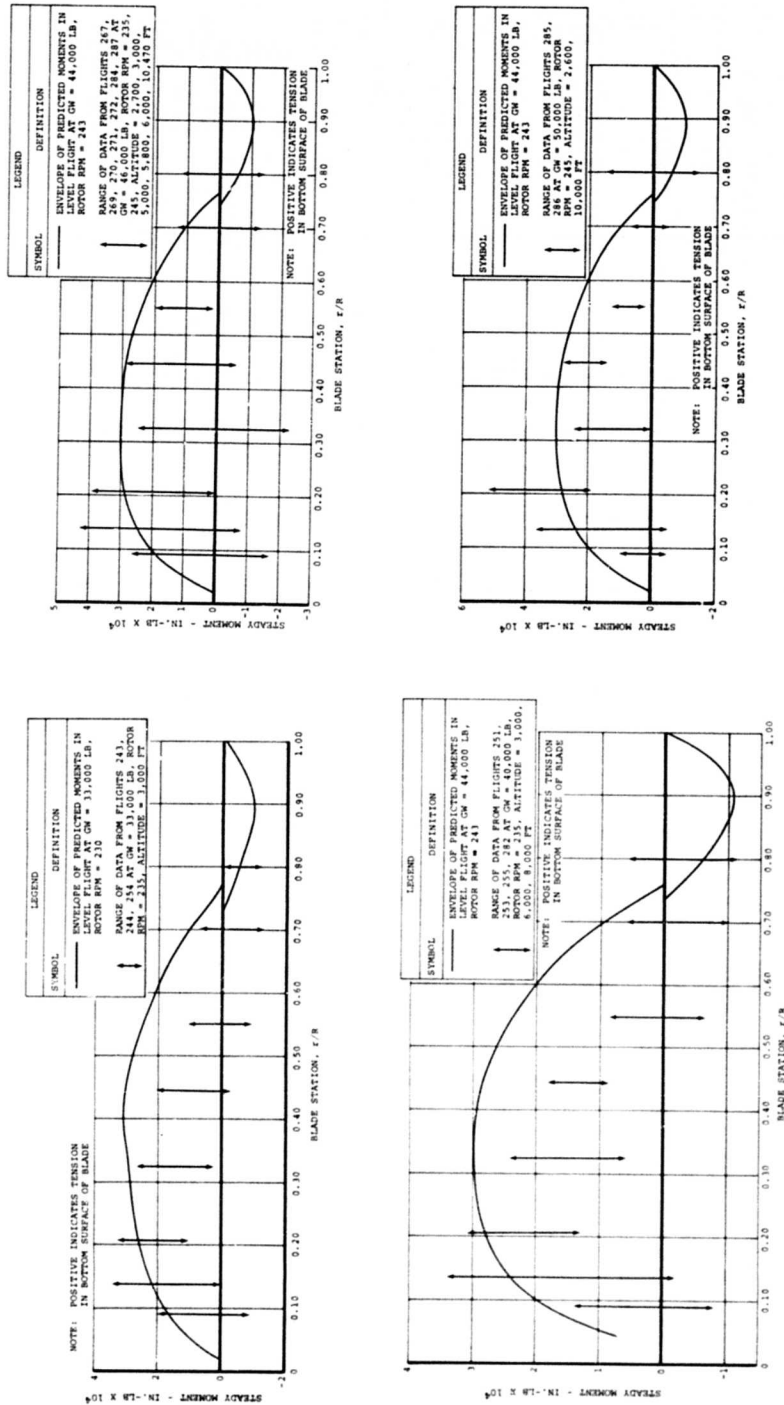


Figure 213. Comparison of Predicted and Flight Test Steady Flapwise Bending Moments in Maneuvering Flight.

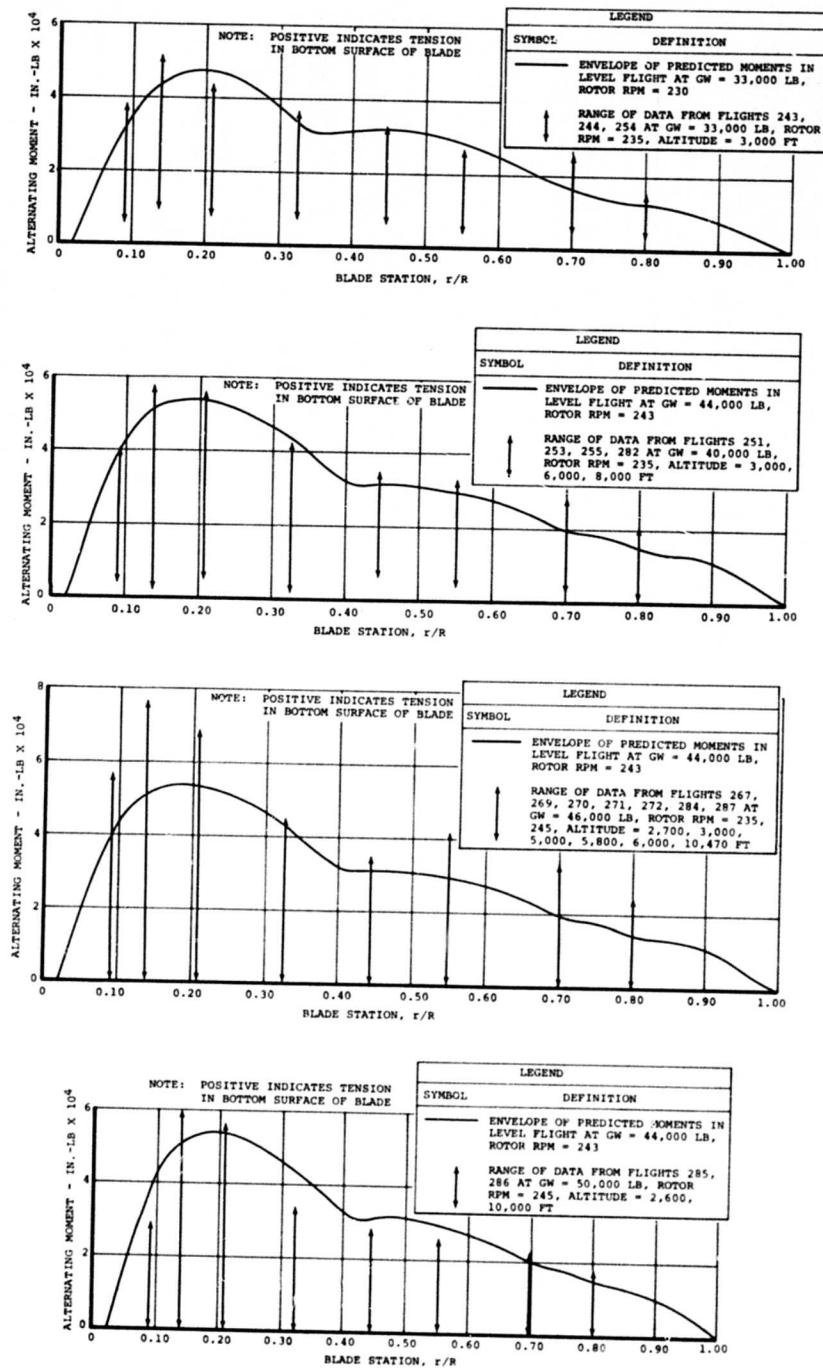


Figure 214. Comparison of Predicted and Flight Test Alternating Flapwise Bending Moments in Maneuvering Flight.

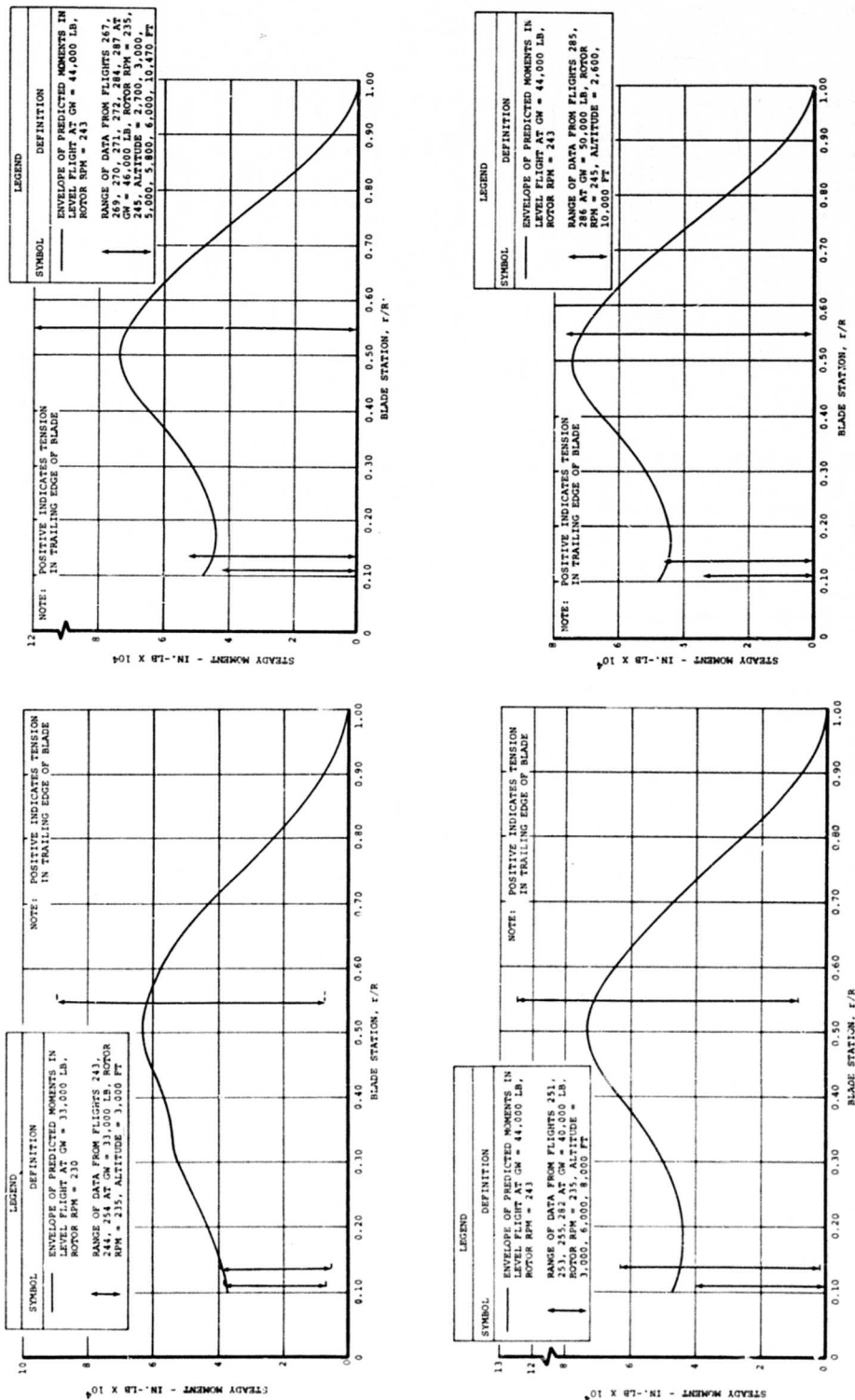


Figure 216. Comparison of Predicted and Flight Test Alternating Chordwise Bending Moments in Maneuvering Flight.

Discussion - Blade Moment Distribution Results

The level-flight alternating flapwise and chordwise moments were in agreement with the maximum predicted alternating flapwise and chordwise moments. The level-flight steady flapwise moments showed minor deviations from the predicted loads. The aft blade steady chordwise moments at station 49.5 indicated discrepancies for level and maneuvering flight. The magnitudes of all maneuver loads were as expected, except alternating chordwise moments at station 198 during landing flares.

Scattergrams of Blade Parameters

This section compares the fatigue strength of potentially fatigue critical blade components to the level-flight alternating moments recorded during flight testing. The blade components were: (1) aft blade socket at blade station 32.8, (2) aft blade spar at station 288, and (3) aft blade trailing-edge skin at station 198. The alternating moments for the above parameters were the top of scatter loads measured at the flight conditions indicated in each figure.

The fatigue strength of the socket was determined by structural testing of root-end blade sections. This is discussed in the Structural Test section. The socket fatigue strength at 10^6 cycles is $\pm 44,300$ inch-pounds, as shown in Figure 116.

The allowable alternating stresses for the spar and skin were established from coupon testing described in the Materials Testing and Analysis section. Based on the stress ratio of the coupon tests, the steady stress associated with the allowable alternating stress at 10^6 cycles was calculated. Knowing this steady and alternating stress and a curve shape, the variation of allowable alternating stress with steady stress at 10^6 cycles was determined. To establish the fatigue strength at 10^6 cycles for the two materials, the steady stress was calculated using centrifugal force and the appropriate maximum level-flight steady moment measured at each gross weight rpm condition. At this calculated steady stress, the allowable alternating stress at 10^6 cycles was determined and converted to allowable alternating moment.

Figure 217 shows the scattergrams for the aft blade socket. All the data falls below the allowable fatigue strength. The alternating moments are the highest at low airspeeds (60-100 knots) and show a gradual decline through the mid (100-140 knots) and high (> 140 knots) airspeed ranges. The loads do not seem to rise at the highest airspeeds, which is contrary to expected trends. Data for this parameter is shown only up to flight number 271 because the instrumentation for this bending bridge became inoperative and was not easily repairable.

The alternating flapwise moments at station 288 are presented in Figures 218 and 219 for 235 and 245 rpm. In general, the moments are high at low airspeeds and reach a minimum in the 100-130 knot airspeed range. A definite increase is noted at the higher airspeeds (> 130 knots), but the rate of increase seems to be moderate. Like the socket data, no loads exceed the fatigue strength of the spar.

Figures 220 and 221 present the 235 and 245 rpm loads data for the aft blade trailing edge tension at station 198. At low airspeeds (< 100 knots), the alternating moments at 33,000 and 40,000 pounds gross weight are significantly lower than the alternating moments at 46,000 pounds gross weight. The minimum loads are obtained at 100-120 knots. The highest moments, in general, occur at the higher airspeeds (> 120 knots), with the rate of increase apparently greater with this parameter than the other two. The 40,000- and 46,000-pound gross weight data of Figure 221 seem to indicate an almost vertical load buildup which is characteristic of blade stall. The 46,000-pound, 235-rpm data of Figure 221 also shows that the loads at 68 and 152 knots are nearly equal to the fatigue strength.

If the limiting effects of the test bed, such as transmission limit, power availability, vibration levels and rotor control loads were eliminated, a structural envelope based on blade loads could be constructed. This envelope would be significantly greater than the present AGB structural envelope because of the margin between the maximum load and the fatigue strength of each component. The trailing-edge skin might require structural modifications to increase its strength, but the socket and spar fatigue strengths seem more than adequate.

In summary, this section shows: (1) that no level-flight alternating moments exceed the fatigue strength of any critical blade component, and (2) that the alternating moments are generally low compared to the fatigue strength of each critical blade component.

Comparison of CH-47C and CH-47C/AGB Blade Loads for Equivalent C_T/σ

The purpose of this section is to compare blade loads of the CH-47C and the AGB at equivalent C_T/σ conditions. Blade moments for the CH-47C are also compared to the AGB blade loads at similar flight conditions.

The AGB and CH-47C moments in this comparison are top-of-scatter alternating loads recorded during level-flight airspeed sweeps. The following AGB parameters are used: (1) forward blade flapwise bending moments at station 49.5, (2) aft blade flapwise bending moments at station 49.5, (3) aft blade flapwise bending moments at station 288, and (4) aft blade trailing-edge tension at station 198. The

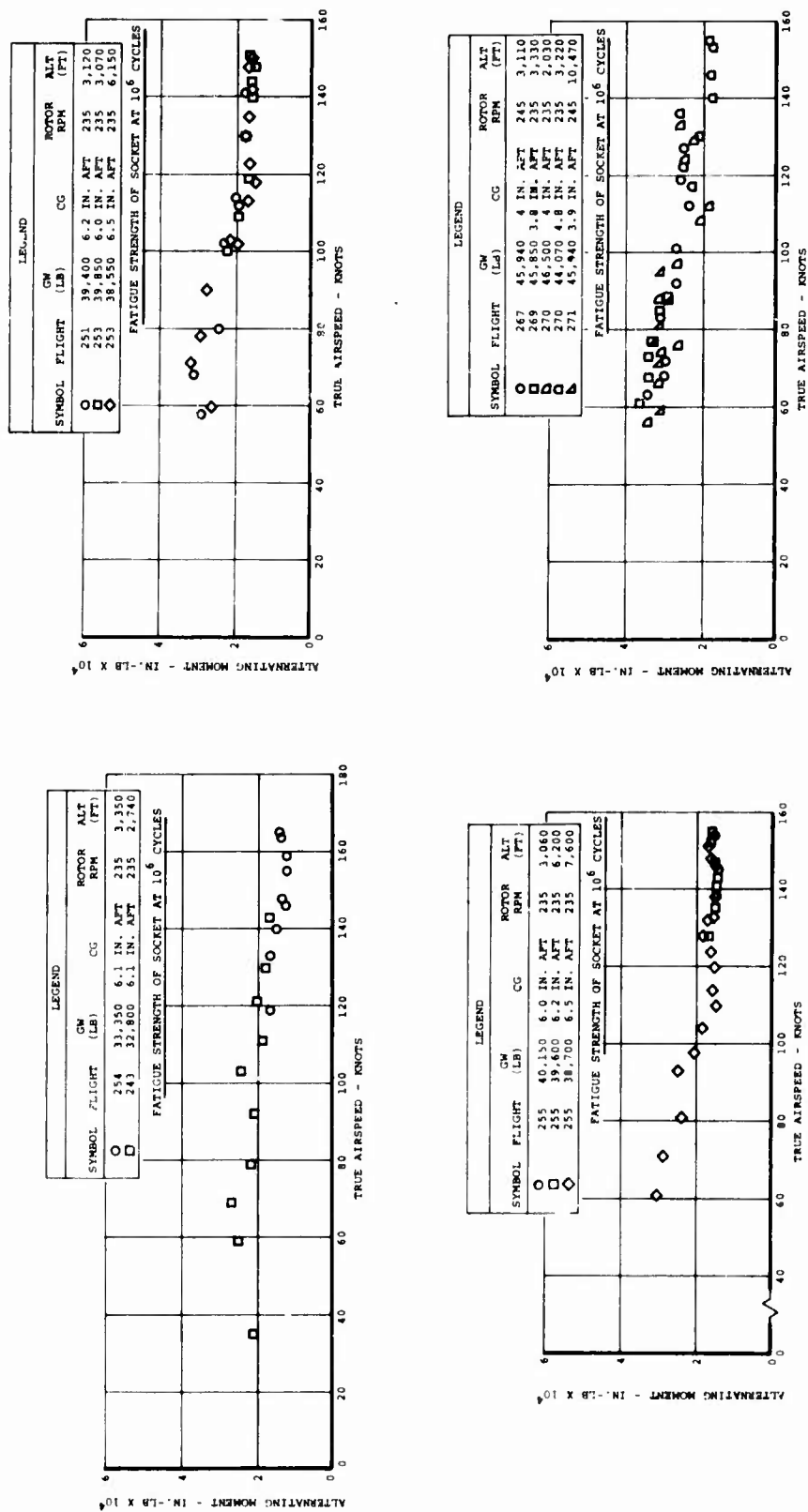


Figure 217. Flap Bending at Station 32.8 of Aft Blade Socket on CH-47C Helicopter Equipped With Advanced-Geometry Blades.

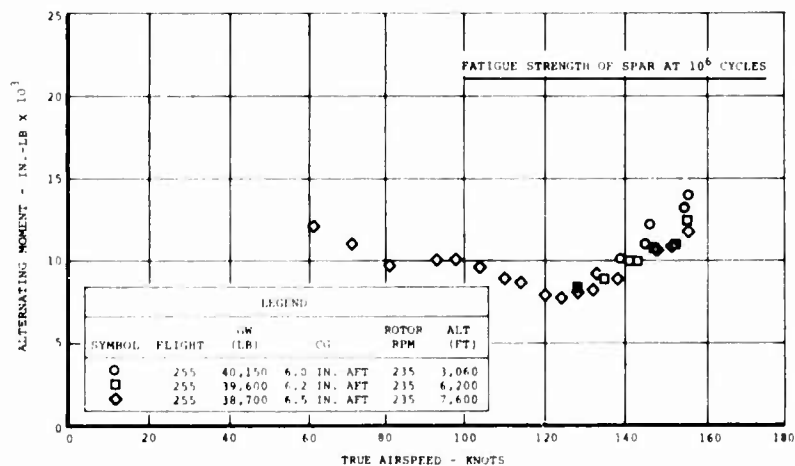
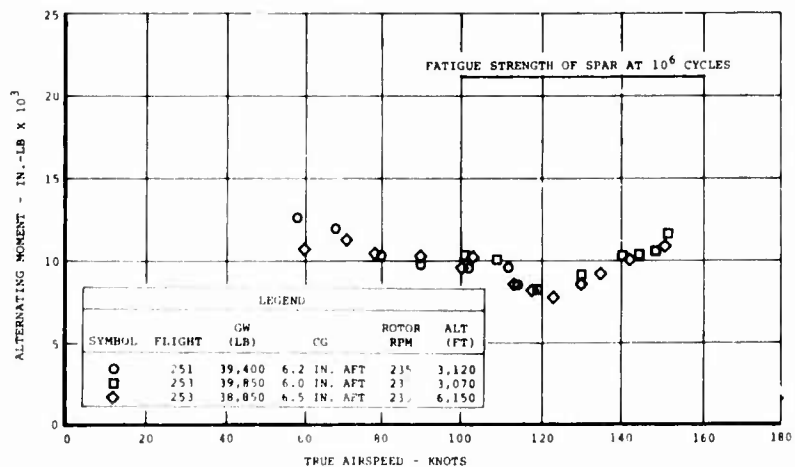
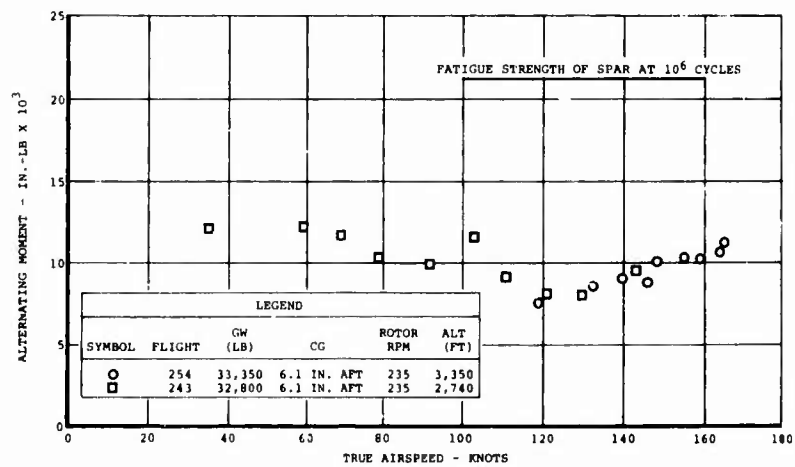


Figure 218. Flap Bending at Station 288 of Aft Blade Spar on CH-47C Helicopter Equipped With Advanced-Geometry Blades.

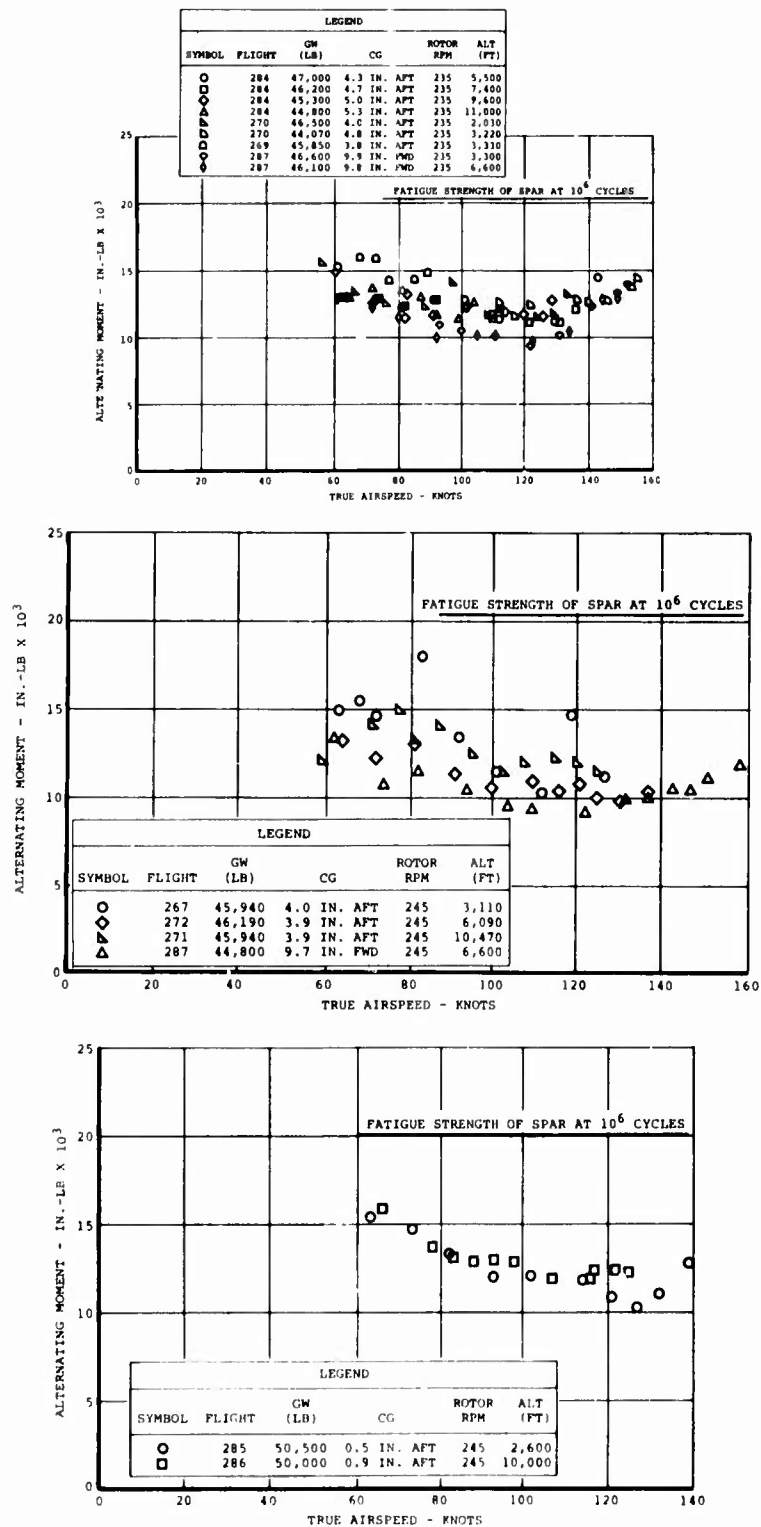


Figure 219. Flap Bending at Station 288 of Aft Blade Spar on CH-47C Helicopter Equipped With Advanced-Geometry Blades.

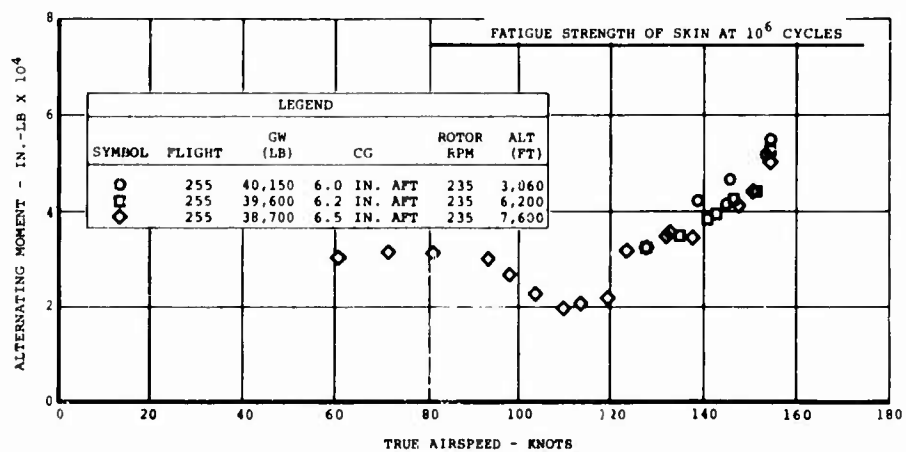
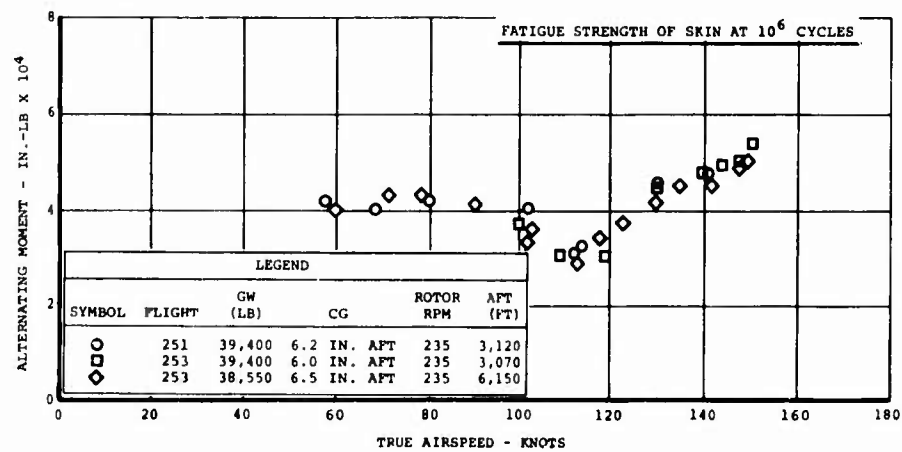
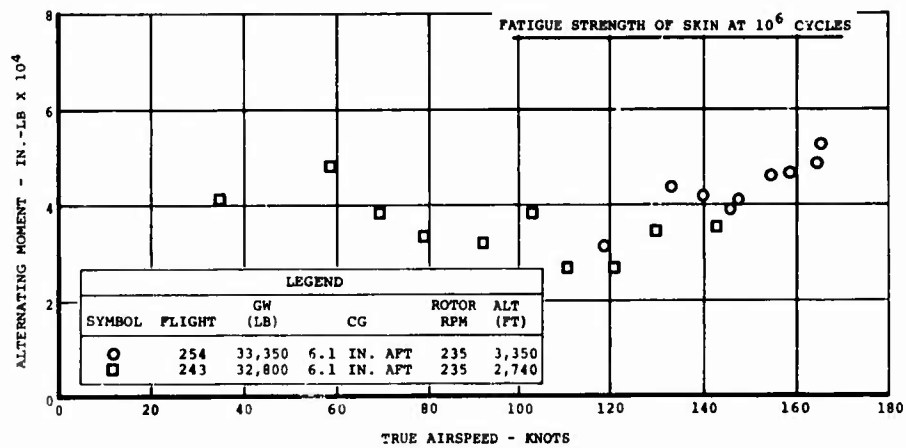


Figure 220. Trailing-Edge Tension at Station 198 of Aft Blade on CH-47C Helicopter Equipped With Advanced-Geometry Blades.

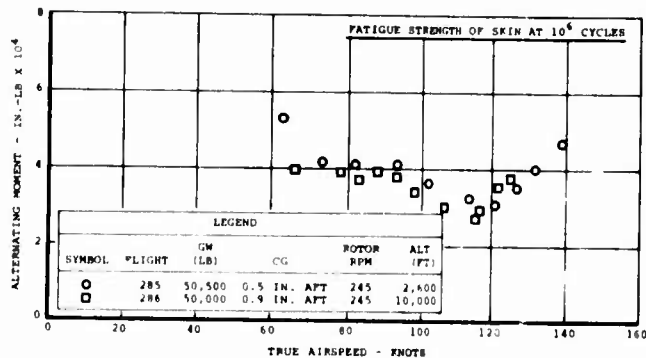
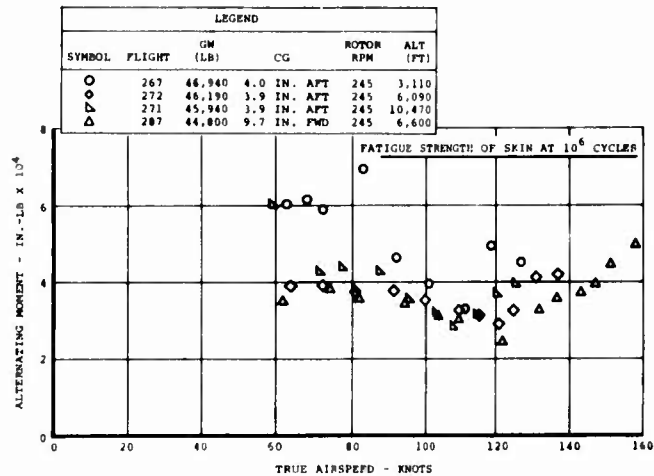
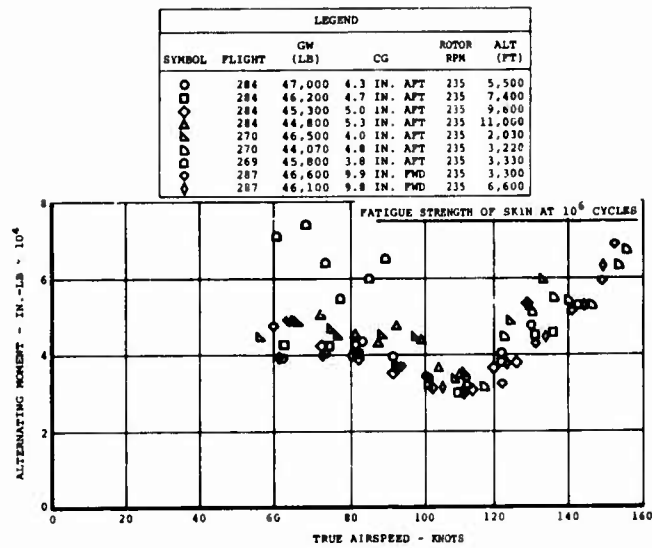


Figure 221. Trailing-Edge Tension at Station 198 of Aft Blade on CH-47C Helicopter Equipped With Advanced-Geometry Blades.

corresponding CH-47C loads are the following: (1) forward blade flapwise bending moments at station 47, (2) aft blade flapwise bending moments at station 47, (3) aft blade flapwise bending moments at station 285, and (4) aft blade trailing-edge tension at stations 144 and 200.

Figure 222 shows the flapwise moments for the root end of the forward blade. The AGB loads are higher than the "C" loads for equivalent C_T/σ and similar flight conditions. The comparison of Figure 223 for the aft blade moments at the root end indicates the same results as above. At the outboard end of the blades, the equivalent C_T/σ data for the two blades are approximately equal, as shown in Figure 224. The AGB moments are less than the "C" moments for similar flight conditions. The trailing-edge tension comparison, Figure 225, shows the AGB moments are greater than the "C" loads for equivalent C_T/σ conditions, but are equal to the "C" loads for similar flight conditions.

Based on the results of the above comparison, it is concluded that the AGB loads tend to be greater than the CH-47C at the same C_T/σ . This is a subject for additional analytical investigation since the observed differences are probably due to a number of different factors.

Load Phasing

This section presents the phase relationship in terms of the percentage of alternating moment between certain blade parameters. The load parameters were: (1) aft blade alternating flapwise and chordwise moments at station 49.5, (2) aft blade alternating flapwise and chordwise moments at station 198, (3) aft blade flapwise and torsional moments at station 288, and (4) aft blade torsional moments at station 288 and aft blade pitch link loads. These parameters were compared at 34,500, 41,000, and 47,500 pounds gross weight. At each gross weight, a low, mid, and high airspeed condition was selected.

Five consecutive rotor cycles were extracted from the data records of each parameter at each flight condition. At 5-degree increments around the azimuth, numerical values of these load waveforms were converted into percentages of the alternating load of that rotor cycle. For the first rotor cycle of a control parameter, such as flapwise bending at station 49.5, the point of 100 percent alternating moment and its azimuthal location were determined. For the same azimuthal location, the percentage of alternating moment was noted at the first rotor cycle for a variable parameter such as chordwise bending at station 49.5. This procedure was repeated for the remaining four rotor cycles of the variable parameter. The second, third, fourth and fifth rotor cycles of the control parameter were then analyzed like the first cycle and compared with the five cycles of the variable parameter. At the end of this operation, there were 25 percentages of alternating load for the variable parameter and one percentage, 100 percent, of the alternating moment for the control parameter. Of these 25 percentages, the maximum one appears in the results for the designated variable parameter.

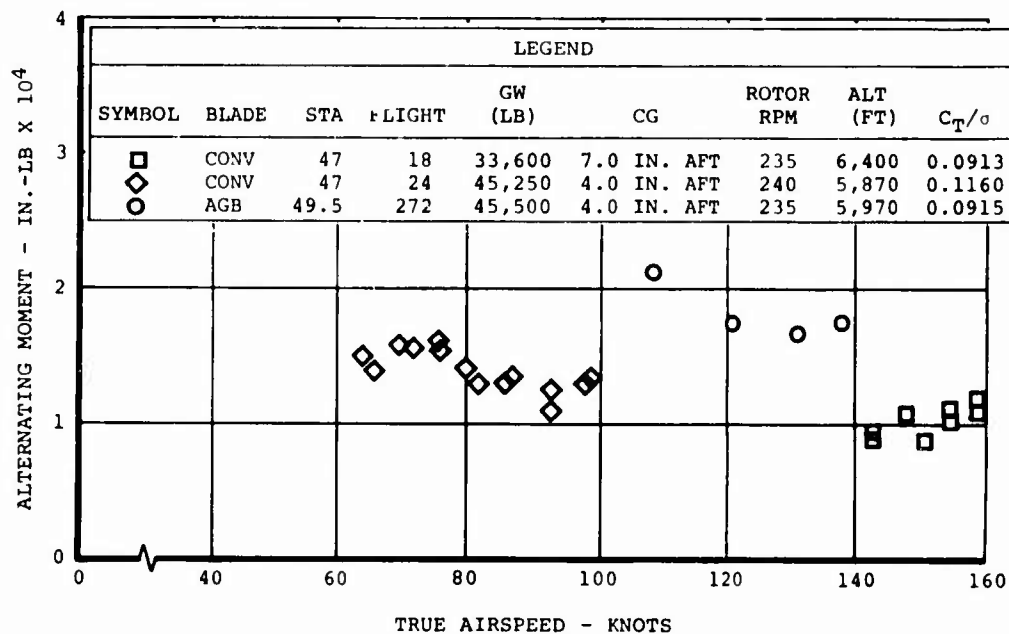
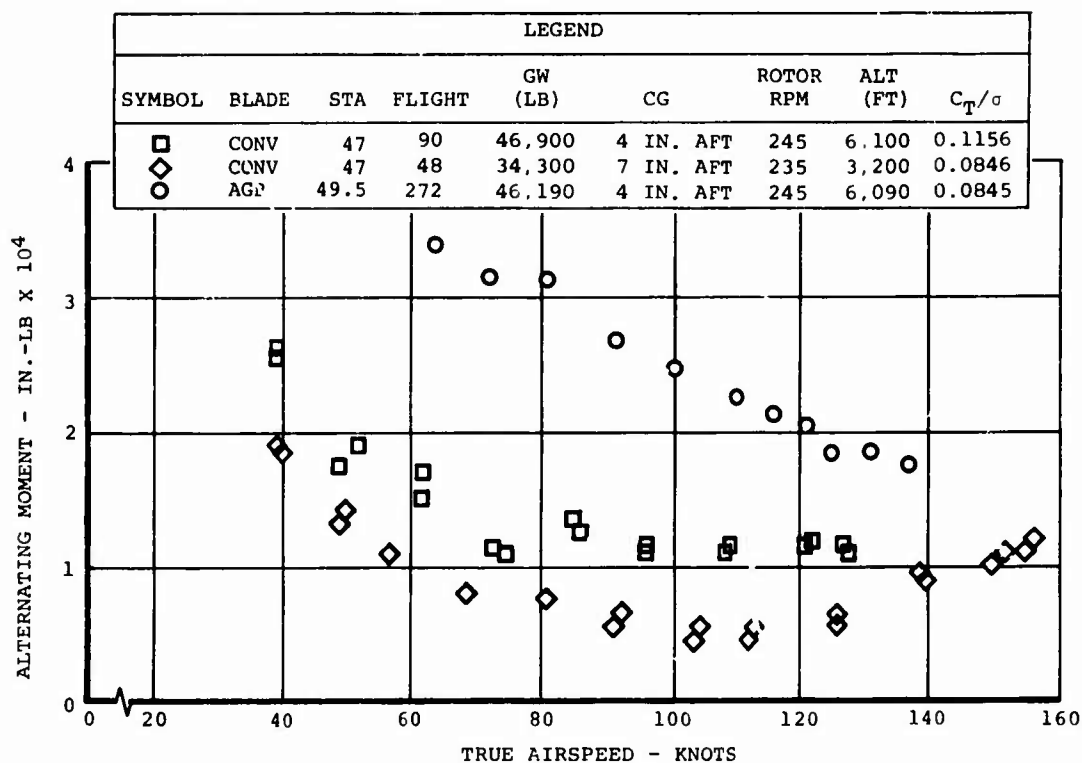


Figure 222. Comparison of CH-47C and CH-47C/AGB at Equivalent C_T/σ and Similar Flight Conditions, Forward Blade Flap Bending at Station 47.

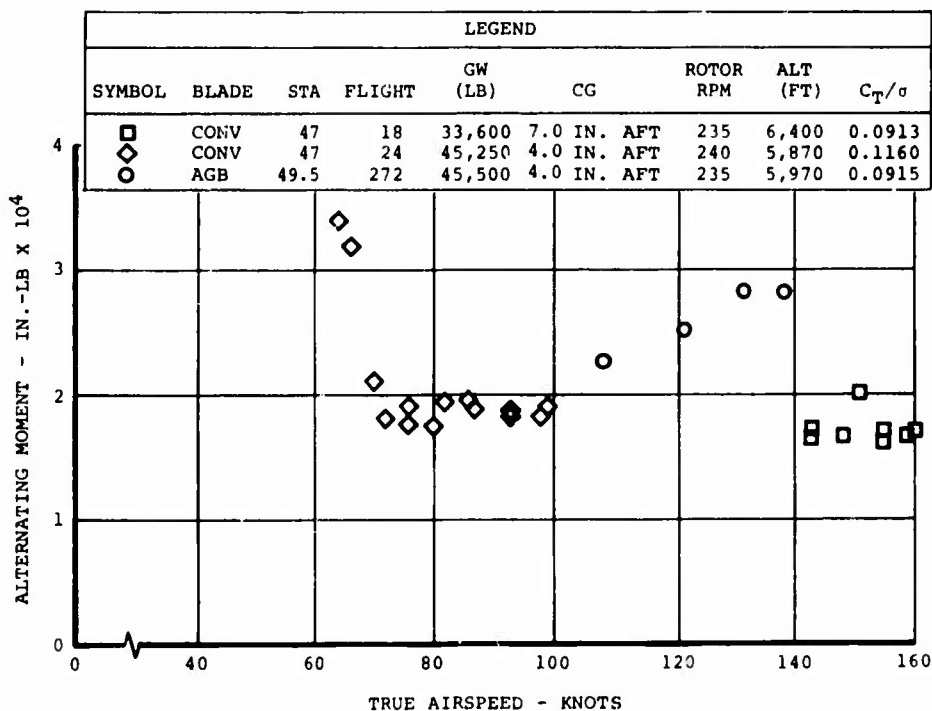
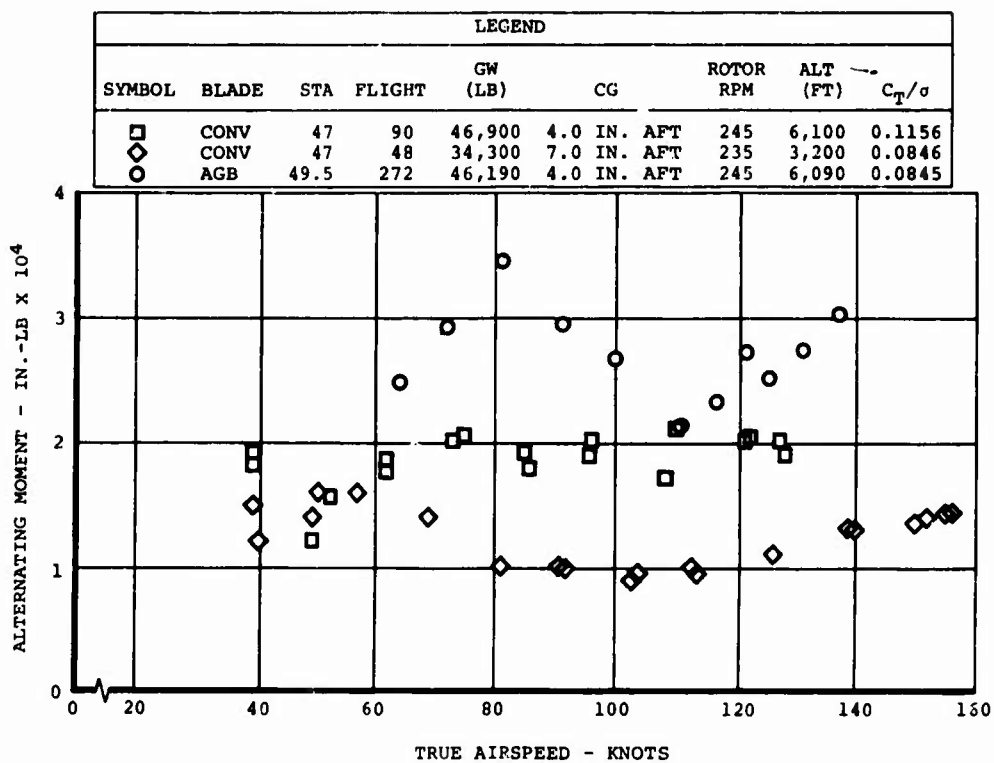


Figure 223. Comparison of CH-47C and CH-47C/AGB at Equivalent C_T/σ and Similar Flight Conditions, Aft Blade Flap Bending at Station 47.

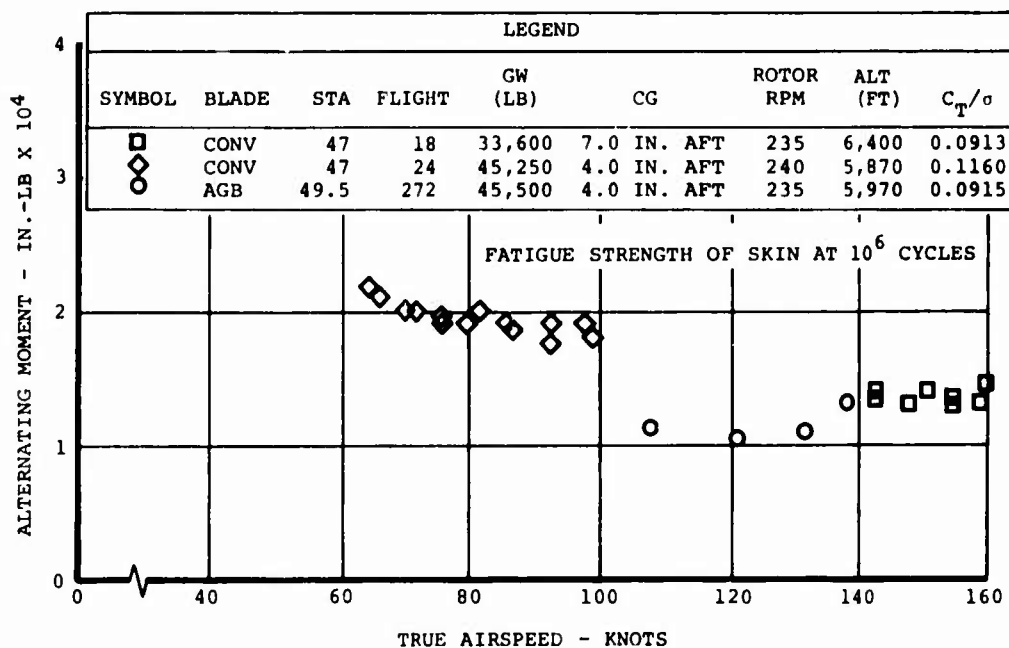
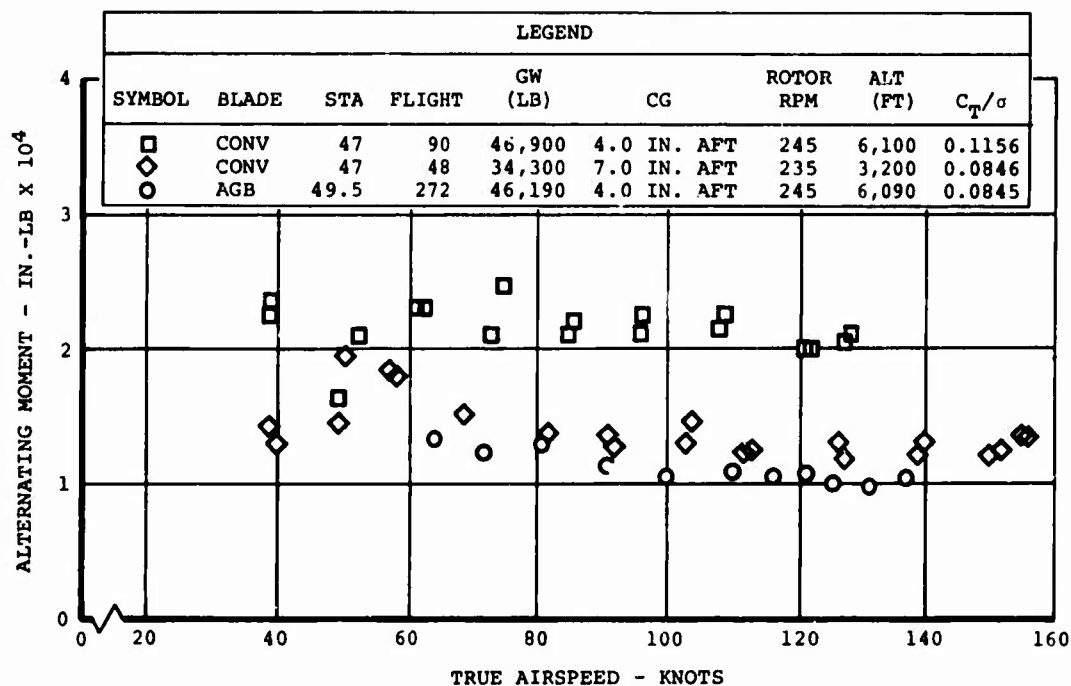


Figure 224. Comparison of CH-47C and CH-47C/AGB at Equivalent C_T/σ and Similar Flight Conditions, Aft Blade Flap Bending at Station 285.

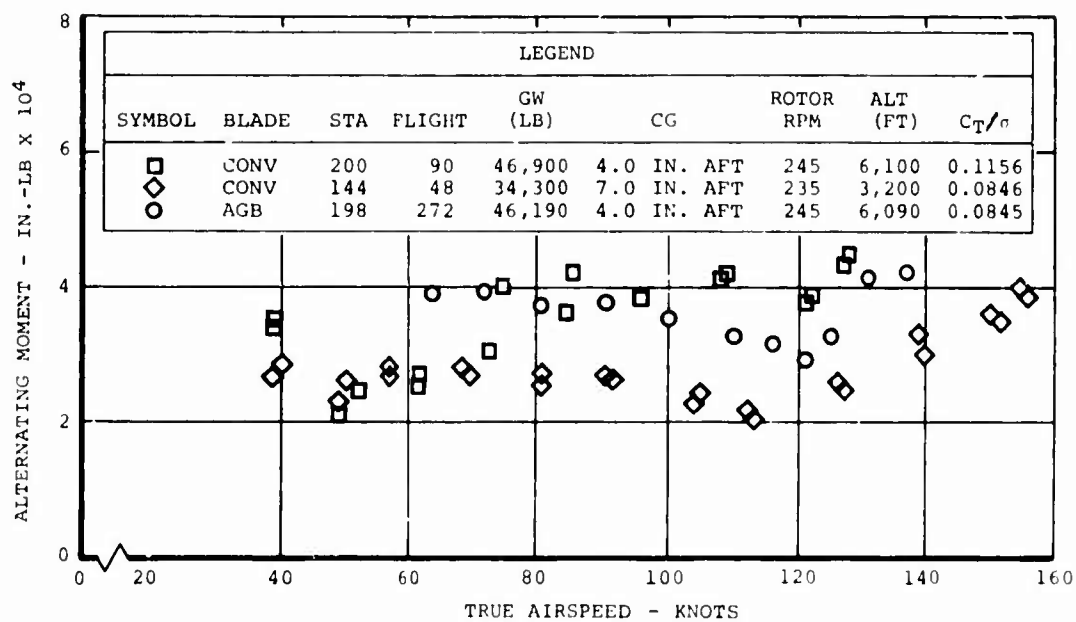


Figure 225. Comparison of CH-47C and CH-47C/AGB at Equivalent C_T/σ and Similar Flight Conditions, Aft Blade Trailing-Edge Tension at Station 198.

Figures 226 through 229 present the results of this analysis for the comparisons listed above. To help the reader understand the graphs, an example is given in the upper plot of Figure 226. At 41,000 pounds gross weight and 80-knot airspeed (point 1), proceed vertically until the second gross weight line is intersected (point 2). From this point, go horizontally to point 3. This gives a value of 89 percent of alternating flapwise bending moment at station 49.5 (variable parameter) for 100 percent of alternating chordwise bending moment at station 49.5 (control parameter).

Table XXX summarizes the results of this analysis. It shows that at some flight condition: (1) the flapwise and chordwise alternating moments at station 49.5 and 198 are in phase, (2) the torsional and flapwise alternating moments at station 288 are in phase, and (3) the alternating pitch link load and alternating torsional moments at station 288 are in phase.

The results also indicate that some revisions to the combined loading relationships used in the original structural analysis are in order, to reflect the in-phase relationship noted above.

Blade Life

The fatigue life of potentially critical components of the aft blade is calculated based on "Miner's Hypothesis". The hypothesis states that fatigue damage equals the number of cycles applied to the part (n) divided by the number of cycles that the part can withstand at that alternating stress or load level (N). According to the hypothesis, failure is said to occur when the term n/N or $\sum n/N$ equals 1.00. The life in hours equals $1/(\sum n/N)$ when (n) is expressed in cycles per hour. This theory assumes that applied alternating loads or stresses lower than the endurance limit do not affect fatigue life.

The potentially fatigue critical components of the blade are the socket at blade station 32.8, the spar at station 288, and the trailing-edge skins at station 198. The parts were subjected to a mission profile in the above calculations. The mission profile for the AGB was developed from the CH-47C mission profile of Table XXXI.

A modified CH-47C profile for the AGB is presented in Table XXXII. The 33,000-pound and 40,000-pound gross weight portions of the flight program were combined because data gathered at 33,000 pounds was very limited. The amount of time assigned to this part of the profile is 70 percent. There is no forward center of gravity split, because forward center of gravity was not flown at these weights. The altitude ranges are the same as the "C" profile, but the number of splits are determined by the level-flight data available. The level-flight conditions are the same as those for the CH-47C, but the maneuver conditions are modified. Because the AGB program did not include pull-ups and reversals,

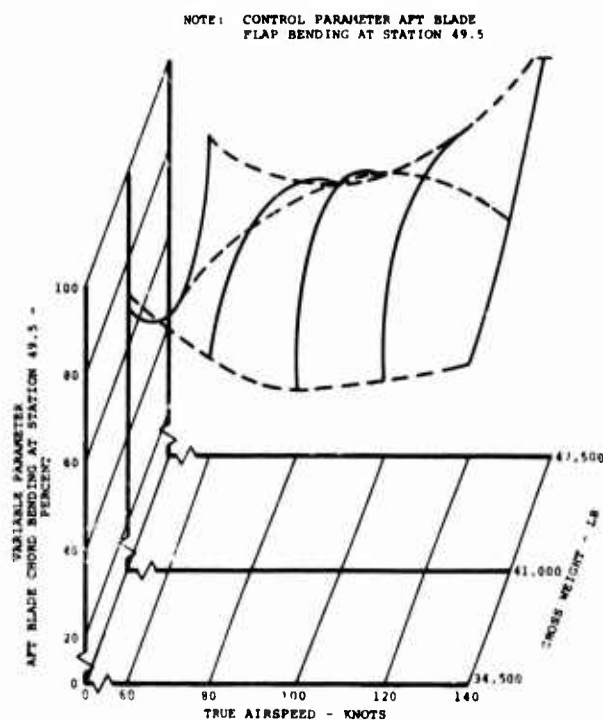
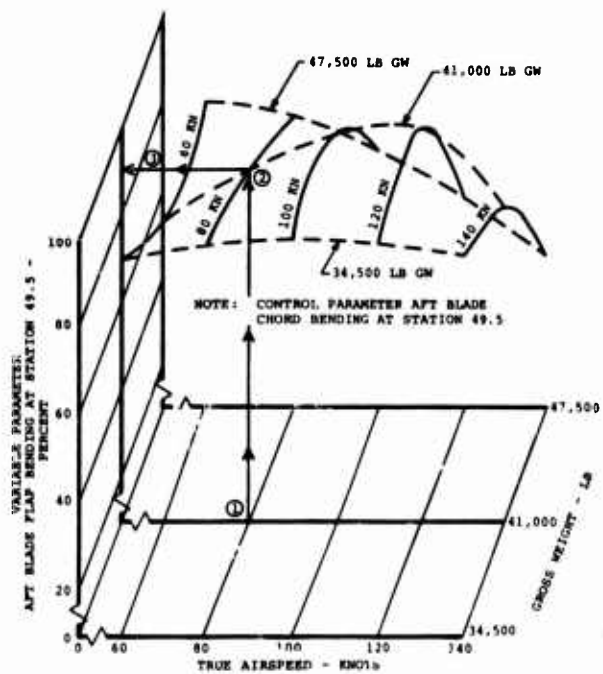


Figure 226. Alternating Load Phasing, Aft Blade Flap/Chord at Station 49.5.

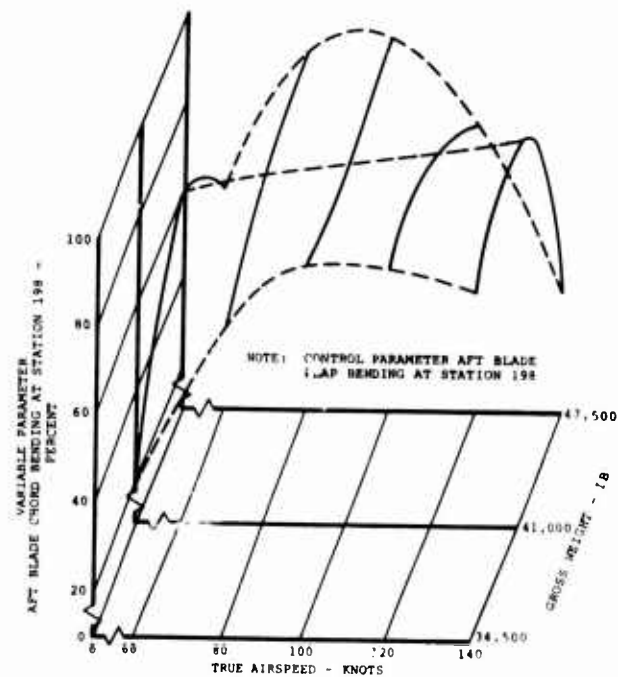
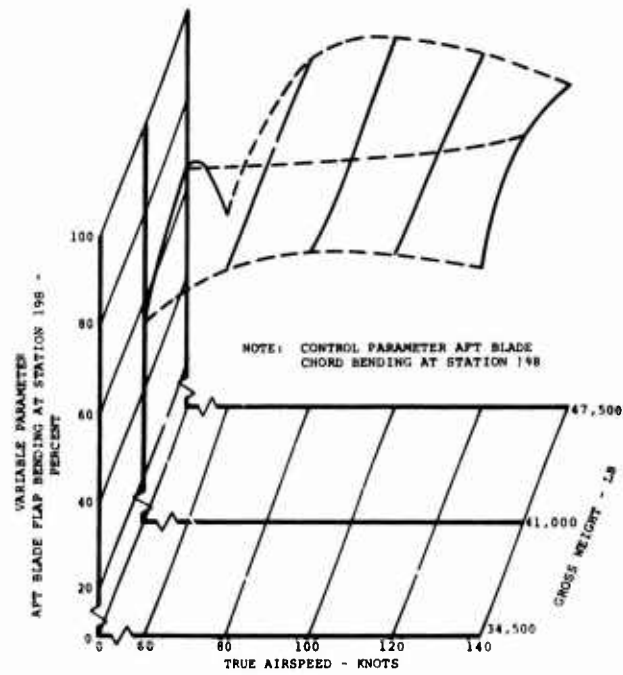


Figure 227. Alternating Load Phasing, Aft Blade Flap/Chord at Station 198.

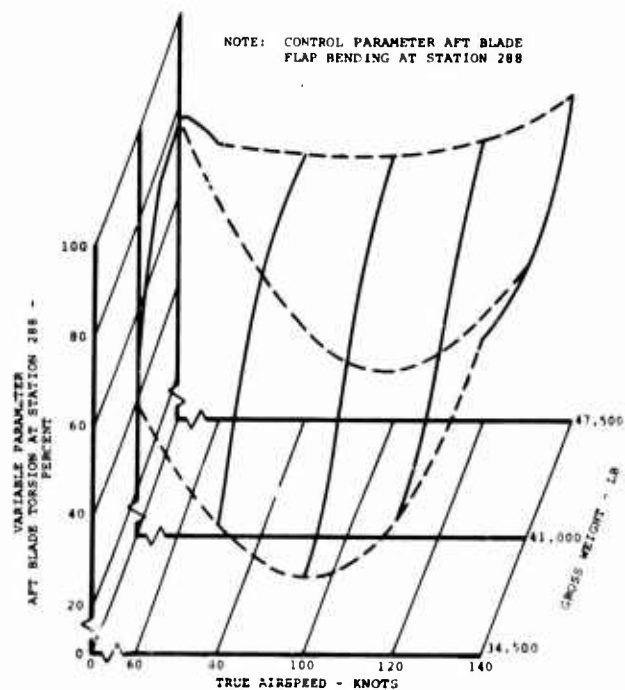
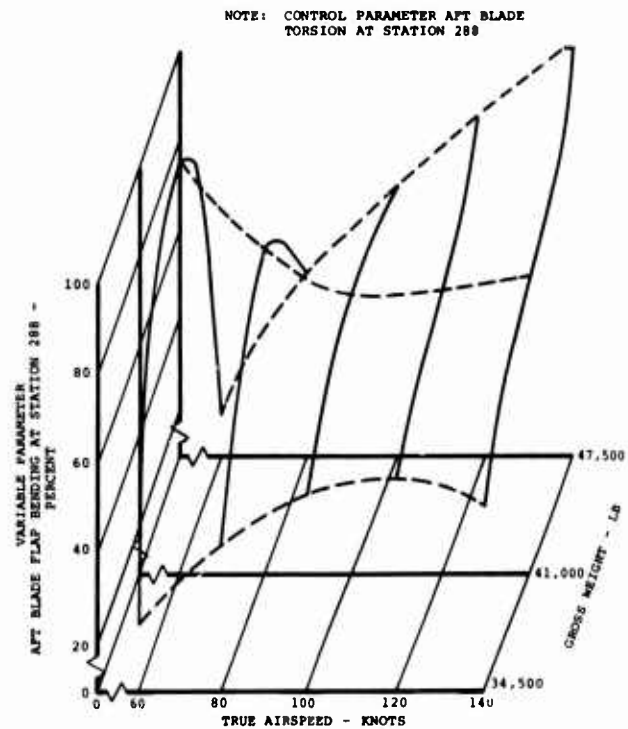
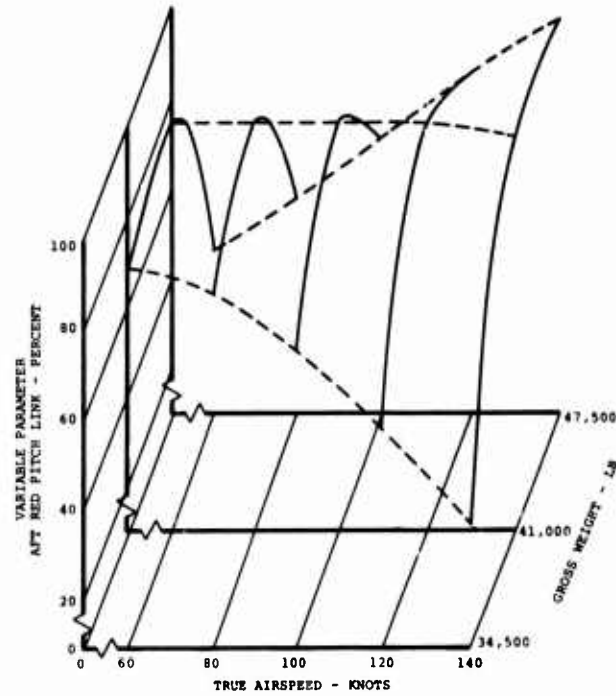


Figure 228. Alternating Load Phasing, Aft Blade Flap/Torsion at Station 288.

NOTE: CONTROL PARAMETER AFT BLADE
TORSION AT STATION 288



NOTE: CONTROL PARAMETER AFT
RED PITCH LINK

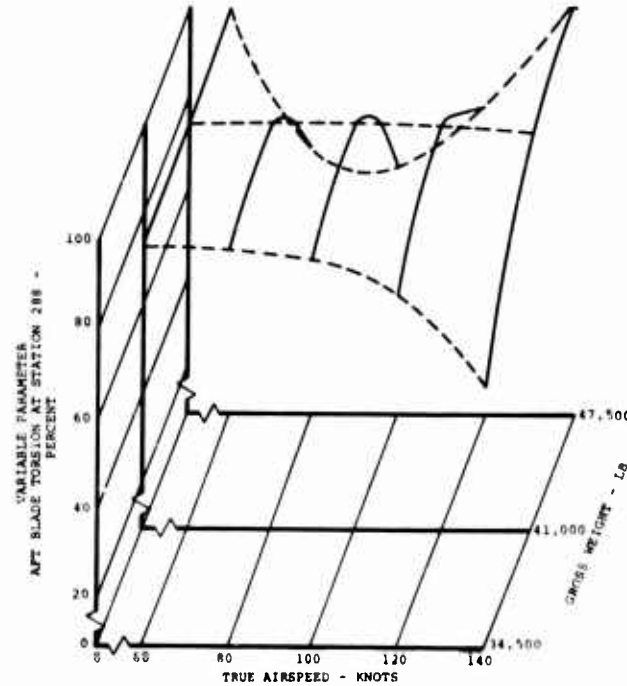


Figure 229. Alternating Load Phasing, Aft Blade Torsion/Pitch Link at Station 288.

TABLE XXX. SUMMARY OF ALTERNATING LOAD PHASING					
Parameter	Sta.	Type of Load	Max %	Flight Conditions	
				Gross Weight (lb)	Airspeed (kt)
Control	49.5	Chordwise Bending	100	1) 34,500	1) 100
Variable	49.5	Flapwise Bending	100	2) 41,000	2) 110
Control	49.5	Flapwise Bending	100	1) 41,000	1) 112
Variable	49.5	Chordwise Bending	100	2) 47,500	2) 140
Control	198	Chordwise Bending	100	41,000	140
Variable	198	Flapwise Bending	97.5		
Control	198	Flapwise Bending	100	41,000	140
Variable	198	Chordwise Bending	97.5		
Control	288	Torsion	100	1) 41,000	1) 60
Variable	288	Flapwise Bending	100	2) 47,500	2) 140
Control	288	Flapwise Bending	100	41,000	60
Variable	238	Torsion	100		
Control	288	Torsion	100	41,000	60-120
Variable	-	Pitch Link	100		
Control	-	Pitch Link	100	1) 41,000	60-120
Variable	288	Torsion	100	2) 47,500	60&140

TABLE XXXI. CH-47C MISSION PROFILE, BASIC FATIGUE LOADING SCHEDULE					
Gross Wt: 27,000 Lb Percent Time: 50%		Gross Wt: 33,000 Lb Percent Time: 25%		Gross Wt: 46,000 Lb Percent Time: 25%	
Flight Condition	Occurrence	Flight Condition	Occurrence	Flight Condition	Occurrence
<u>Level Flight</u>		<u>Level Flight</u>		<u>Level Flight</u>	
Hover	10 percent	Hover	10 percent	Hover	10 percent
Transition	15 percent	Transition	15 percent	Transition	15 percent
60% V _{ne}	25 percent	60% V _{ne}	25 percent	70% V _{ne}	25 percent
90% V _{ne}	20 percent	90% V _{ne}	20 percent	90% V _{ne}	20 percent
100% V _{ne}	20 percent	100% V _{ne}	20 percent	100% V _{ne}	20 percent
110% V _{ne}		110% V _{ne} or		110% V _{ne} or	
or V _{mil}		V _{mil} Power	10 percent	V _{mil} Power	10 percent
Power	10 percent				
<u>Maneuvers</u>		<u>Maneuvers</u>		<u>Maneuvers</u>	
Landing Flare	4 per hour	Landing Flare	4 per hour	Landing Flare	4 per hour
Turn	10 per hour	Turn	10 per hour	Turn	10 per hour
Pull-up	4 per hour	Pull-up	4 per hour	Pull-up	4 per hour
Lateral Reversal	4 per hour	Lateral Reversal	4 per hour	Lateral Reversal	4 per hour
Longitudinal Reversal	4 per hour	Longitudinal "	4 per hour	Longitudinal Reversal	4 per hour
Directional Reversal	4 per hour	Directional "	4 per hour	Directional Reversal	4 per hour
<u>RPM Split</u>		<u>RPM Split</u>		<u>RPM Split</u>	
Nominal 235-245 rpm	100 percent	Nominal 235-245 rpm	100 percent	Nominal 245 rpm	100 percent
<u>CG Split</u>		<u>CG Split</u>		<u>Cargo Split</u>	
Normal CG	100 percent	Fwd CG	50 percent	External Cargo	
		Aft CG	50 percent	at Aft CG,	75 percent
				6000 ft and below	
<u>Altitude Split</u>		<u>Altitude Split</u>		Internal Cargo	25 percent
6000 ft and below	50 percent	6000 ft and below	50 percent	50% at Fwd CG	
6000 ft -10000 ft	40 percent	6000 ft -10000 ft	40 percent	50% at Aft CG	
Above 10000	10 percent	Above 10000	10 percent	<u>Altitude Split (Int. Cargo)</u>	
				6000 ft and below	50 percent
				6000 ft and above	50 percent

TABLE XXXII. GLASS AGE MISSION PROFILE					
Gross Weight: 33,000 & 40,000 Lb Percent Time: 70%		Gross Weight: 46,000 Lb Percent Time: 25%		Gross Weight: 50,000 Lb Percent Time: 5%	
Flight Condition	Occurrence	Flight Condition	Occurrence	Flight Condition	Occurrence
<u>Level Flight</u>		<u>Level Flight</u>		<u>Level Flight</u>	
Hover	10 percent	Hover	10 percent	Hover	10 percent
Transition	15 percent	Transition	15 percent	Transition	15 percent
60% VNE	25 percent	70% VNE	25 percent	70% VNE	25 percent
90% VNE	20 percent	90% VNE	20 percent	90% VNE	20 percent
100% VNE	20 percent	100% VNE	20 percent	100% VNE	20 percent
110% VNE or VMIL power	10 percent	110% VNE or VMIL power	10 percent	110% VNE or VMIL power	10 percent
<u>Maneuvers</u>		<u>Maneuvers</u>		<u>Maneuvers</u>	
Landing Flare	4 per hour	Same as 33,000 lb schedule		Same as 33,000 lb schedule	
Maneuver	26 per hour				
<u>RPM Split</u>		<u>RPM Split</u>		<u>RPM Split</u>	
Nominal 235-245rpm	100 percent	Nominal 235-245 rpm	100 percent	Nominal 245 rpm	100 percent
<u>CG Split</u>		<u>CG Split</u>		<u>CG Split</u>	
Aft CG	100 percent	Fwd CG	12.5 percent	Aft CG	100 percent
		Aft CG	87.5 percent		
<u>Altitude Split</u>		<u>Altitude Split</u>		<u>Altitude Split</u>	
6,000 ft and below	50 percent	Fwd CG:		6,000 ft and below	100 percent
6,000 ft and above	50 percent	6,000 ft and below	50 percent		
		6,000 ft and above	50 percent		
		Aft CG:			
		6,000 ft and below	50 percent		
		6,000 ft to 10,000 ft	50 percent		
		10,000 ft and above	10 percent		

TABLE XXXIII. FATIGUE DAMAGE SUMMARY - SPAR AT STA. 288								
Flight Condition	Gross Weight (pounds)						Totals	
	33,000 to 44,000		46,000		50,000			
	70.0 Percent Time		25.0 Percent Time		5.0 Percent Time		Max Load	Percent Damage
	Max Load	Percent Damage	Max Load	Percent Damage	Max Load	Percent Damage		
Level Flight								
Within Envelope	13300	0.0	17980	0.0	15462	0.0	17980	0.0
Exceed Envelope	14500	0.0	17000	0.0	13100	0.0	17000	0.0
Maneuvers								
Landing Flare	21114	0.0	24587	81.2	24587	9.8	24587	100.0
Other	17052	0.0	18510	0.0	17561	0.0	18510	0.0
Totals	0.0		81.2		9.8		100.0	
Material: Fiberglass, Unidirectional 1002S								
Total Damage = 52.2 x 10 ⁻⁶ /hr								
Endurance Limit: ±22114 Inch-Pounds at 10 ⁶ Cyc.								
Life = 19,157 hr								
(All Loads are Inch-Pounds)								

all of the maneuvers and the associated occurrences in the "C" profile, except landing flares, are grouped together for the AGB profile. This modification is considered conservative and should be noted when the results are presented.

The amount of time assigned to the 46,000-pound gross weight split is the same in both profiles, 25 percent. External cargo flights were not part of the AGB program; therefore, this was eliminated from the profile. Forward center of gravity is assigned to the CH-47C at this gross weight for 12.5 percent of the flight time. This figure is used for the AGB profile at forward center of gravity. The remaining 87.5 percent is spent at aft center of gravity. The criterion for the altitude splits is the same as above, and the maneuver condition occurrences are the same.

Although the "C" profile does not contain any gross weight split for 50,000 pounds, two flights at this weight with an aft center of gravity were flown in the AGB program. Consequently a 50,000-pound gross weight split is presented in the AGB profile with a 5 percent time allocation. Only one altitude split is shown in the profile because the high altitude airspeed sweep was eliminated from the structural envelope due to excessive control loads.

The loads used for the life calculations are the maximum moments experienced during flight testing for each gross weight, center of gravity and altitude split. In this analysis, the top of scatter loads are assumed to act at all times in the level-flight conditions. The socket and trailing-edge skin experience one load cycle per revolution, and the spar at station 288 is loaded twice per revolution. This two-load cycle is assumed to be equal in magnitude for these calculations. In maneuvers, ten load cycles are assumed to occur for each maneuver performed.

The strain gage on the socket at station 32.8 became inactive after flight 271. Consequently, load data for the socket at 46,000 pounds gross weight, aft center of gravity was incomplete, and no data was available at 46,000 pounds gross weight, forward center of gravity and 50,000 pounds gross weight. The life of the socket was calculated with the aft socket data available, and loads data of the forward blade socket was used to replace the missing aft socket loads.

During the flight test data operations, load records of hover and landing flare at 50,000 pounds gross weight were inadvertently excluded from the computer output. The maximum load on each component that occurred during any hover and flare condition regardless of gross weight was used for the hover and flare loads at 50,000 pounds gross weight.

The load at each split for the maneuver conditions, except landing flares, is the maximum moment which occurred during any maneuver applicable to the particular split. Bank turns or sideslips produced the maximum loads in all splits.

The profile states that 10 percent of each altitude split is spent outside the structural envelope. The limit airspeed at this condition is determined by selecting the lowest of 110 percent V_{ne} , the airspeed at the maximum power of the engines, or the airspeed at 88 percent of the transmission torque limit. Load data was not available in all cases at this limiting airspeed. Based on top of scatter, loads were projected linearly to this limit airspeed.

The moment versus cycles curves for the fiberglass material were derived from the S-N curves presented in the Material Testing and Analysis section. The alternating stresses of the allowable curve for 1002S and BP907-143S were converted into a modified Goodman diagram. The steady stress due to centrifugal force was calculated at 245 rpm and added to the stresses due to the steady flap or chord moment. The maximum steady flap or chord moment recorded during flight testing was used. Based on this steady stress and Goodman diagram, the allowable stresses were determined and converted into allowable alternating moments.

The moment versus cycles curve presented in the Structural Test section was used for the titanium socket. No corrections for steady stresses were made because the curve was derived from components which failed under predicted loading.

The fatigue damage summaries for the three components are shown in Tables XXXIII through XXXVII. The total fatigue damage and component life are given and the maximum loads and percentage of damage per hour for the flight conditions are presented in each table. The spar at station 288 has a life of 4024 hours based on a fatigue strength of ± 17037 inch-pounds at 10^7 cycles. If the fatigue strength is changed to 10^6 cycles and ± 22114 inch-pounds, the component life increases to 19,157 hours. This indicates that relatively minor changes in the S-N curve or increases in the alternating loads have a very significant effect on the life of the spar at this station. Tables XXXIII and XXXIV summarize the above results.

Table XXXV shows that the titanium socket has a life of 5850 hours with an endurance limit of ± 41900 inch-pounds at 10^7 cycles. An inactive strain gage limited the amount of data for this parameter. Aft socket loads were available for only three out of eight altitude splits. Forward socket loads were used for the remaining altitude splits.

The trailing-edge skin at station 198 has the lowest life--567.0 hours based on a fatigue strength of ± 62985 inch-pounds at 10^7 cycles. Table XXXVI gives the damage summary. It is interesting to note that 85.7 percent of the damage is due to landing flares. This fact lead to a reevaluation of the M-N curve used in the analysis. The chord moments were found to be -17743 ± 89370 inch-pounds, -18599 ± 120237 inch-pounds, and -22335 ± 104431 inch-pounds; the rpm during these flares was 235. Therefore, the compressive steady chord moment reduces the steady stress due to centrifugal force, which is also reduced (235 versus 245 rpm). Using a steady chord moment of -17743 inch-pounds, the same procedure mentioned earlier was used to establish an M-N curve for flares. When this curve

TABLE XXXIV. FATIGUE DAMAGE SUMMARY - SPAR AT STA. 288								
Flight Condition	Gross Weight (pounds)						Totals	
	33,000 to 44,000		46,000		50,000			
	70.0 Percent Time		25.0 Percent Time		5.0 Percent Time			
	Max Load	Percent Damage	Max Load	Percent Damage	Max Load	Percent Damage	Max Load	Percent Damage
Level Flight								
Within Envelope	13,300	0.0	17,980	49.9	15,462	0.0	17,980	49.9
Exceed Envelope	14,500	0.0	17,000	0.0	13,100	0.0	17,000	0.0
Maneuvers								
Landing Flare	21,114	15.0	24,587	17.6	24,587	3.9	24,587	36.4
Other	17,052	7.4	18,510	4.9	17,561	1.4	18,510	13.7
Totals	22.4		72.3		5.3		100.0	
Material: Fiberglass, Unidirectional 1002S								
Endurance Limit: ± 17037 Inch-Pounds at 10^7 Cyc. (All Loads are Inch-Pounds)					Total Damage: $248.5 \times 10^{-6}/\text{hr}$ Life: 4024 hr			

TABLE XXXV. FATIGUE DAMAGE SUMMARY - BLADE SOCKET								
Flight Condition	Gross Weight (pounds)						Totals	
	33,000 to 44,000		46,000		50,000			
	70.0 Percent Time		25.0 Percent Time		5.0 Percent Time			
	Max Load	Percent Damage	Max Load	Percent Damage	Max Load	Percent Damage	Max Load	Percent Damage
Level Flight								
Within Envelope	31,870	0.0	35,404	0.0	28,956	0.0	35,404	0.0
Exceed Envelope	20,400	0.0	27,000	0.0	16,758	0.0	27,000	0.0
Maneuvers								
Landing Flare	40,670	0.0	57,405	31.8	57,405	18.7	57,405	50.5
Other	32,020	0.0	45,354	49.5	29,388	0.0	45,354	49.5
Totals	0.0		81.3		18.7		100.0	
Material: Ti - 6Al - 4V								
Total Damage: 170.9 x 10 ⁻⁶ /hr								
Endurance Limit: ±1900 Inch-Pounds at 10 ⁷ Cyc.								
Life: 5850 hr								
(All Loads are Inch-Pounds)								

TABLE XXXVI. FATIGUE DAMAGE SUMMARY - TRAILING-EDGE SKIN AT STA. 198								
Flight Condition	Gross Weight (pounds)						Totals	
	33,000 to 44,000		46,000		50,000			
	70.0 Percent Time		25.0 Percent Time		5.0 Percent Time			
	Max Load	Percent Damage	Max Load	Percent Damage	Max Load	Percent Damage	Max Load	Percent Damage
Level Flight								
Within Envelope	58,870	0.0	74,096	5.5	52,968	0.0	74,096	5.5
Exceed Envelope	62,000	0.0	53,886	0.0	47,600	0.0	62,000	0.0
Maneuvers								
Landing Flare	89,370	30.2	120,237	39.1	120,237	16.4	120,237	85.7
Other	59,010	0.0	79,059	7.6	71,939	1.2	79,059	8.8
Totals	30.2		52.2		17.6		100.0	
Material: Fiberglass; BP907-143S ±45°					Total Damage: 1762.4 x 10 ⁻⁶ /hr			
Endurance Limit: ±62985 Inch-Pounds at 10 ⁷ cyc. (All Loads are Inch-Pounds)					Life: 567.4 hr			

TABLE XXXVII. FATIGUE DAMAGE SUMMARY - TRAILING-EDGE SKIN AT STA. 198								
Flight Condition	Gross Weight (pounds)						Totals	
	33,000 to 44,000		46,000		50,000			
	70.0 Percent Time		25.0 Percent Time		5.0 Percent Time			
	Max Load	Percent Damage	Max Load	Percent Damage	Max Load	Percent Damage	Max Load	Percent Damage
Level Flight								
Within Envelope	58,870	0.0	74,096	9.0	52,968	0.0	74,096	9.0
Exceed Envelope	62,000	0.0	53,886	0.0	47,600	0.0	62,000	0.0
Maneuvers								
Landing Flare	89,370	28.8	120,237	39.3	120,237	8.3	120,237	76.4
Other	59,010	0.0	79,059	12.6	71,939	2.0	79,059	14.6
Totals	28.8		60.9		10.3		100.0	
Material: Fiberglass; BP907-143S ± 45°					Total Damage: 1066.7 x 10 ⁻⁶ /hr			
Endurance Limit: ±77618 Inch-Pounds at 10 ⁷ Cyc. for Flares; ±62985 Inch-Pounds at 10 ⁷ Cyc. for all other conditions (all loads are Inch-Pounds)					Life: 937.5 hr			

is used for flares and the original one is used for the remaining conditions, the life of the skins is increased from 567 hours to 938 hours as shown in Table XXXVII.

The above analysis shows that the spar has a very good life (4024 hours) at the only critical station for this component. The socket life of 5850 hours is unconservative, but it is the best estimate available at the present time. The life of the trailing-edge skins is low (938 hours). As a result, it may be necessary to increase the trailing-edge structure of the blade.

Comparison of Design Allowables and Flight Stresses

This section compares the maximum flight stresses on the spar, outer torsion wrap, and skin of the blade to the fatigue design allowables of the material used in these parts of the blade structure.

Referring to Figure 230, a comparison is made between the unidirectional 1002S coupon testing results and the stresses on the spar which resulted from flight loading. The alternating stresses on the spar at blade station 288 were calculated at the maximum distance from the flapwise neutral axis. The loads were the maximum level flight and maneuver flight alternating flapwise bending moments at station 288 recorded during the flight test program. The flight conditions for this level-flight moment of ± 17980 inch-pounds were: flight number 267, 46,000 pounds gross weight, 4 inches aft center of gravity, 245 rpm, 3110 feet density altitude, and 83 knots true airspeed. The maximum maneuver load of ± 24600 inch-pounds occurred during a landing flare on flight number 284 at 46,000 pounds gross weight, 4 inches aft center of gravity, and 235 rpm. The steady stresses on the spar at the above conditions were calculated from the steady flapwise moments and the centrifugal forces. Based on the steady stress, the design allowable alternating stresses were determined from a modified Goodman diagram. The allowable curve between 10^5 and 10^8 cycles is shown in the above figure. The alternating level-flight stress intersects the allowable curve at just over 10^7 cycles. The alternating stress at the maximum maneuver load shows a fatigue life of approximately 1.07×10^6 cycles.

Figure 231 illustrates the same comparison for the $\pm 45^\circ$ XP251S composite (outer torsion wraps). The maximum alternating stresses at station 288 were calculated. The steady and alternating loads were the same as mentioned above and occurred at the same flight conditions. The comparison shows that the level flight and maneuver flight stresses significantly exceed the allowable stresses in the high cycle area (10^5 to 10^8). Although the stresses are well above the design allowables, no resin failures or delaminations of the torsion wraps were observed during the flight test program. High stress levels on the XP251S $\pm 45^\circ$ composite were also encountered in the structural testing program without failures. In this case the stress on the outer torsion wrap not only exceeded the allowable but was greater than the mean $+3\sigma$ of the coupon data (Reference Figure 121). The reason for the above phenomenon was deducted from fatigue testing mixtures of the

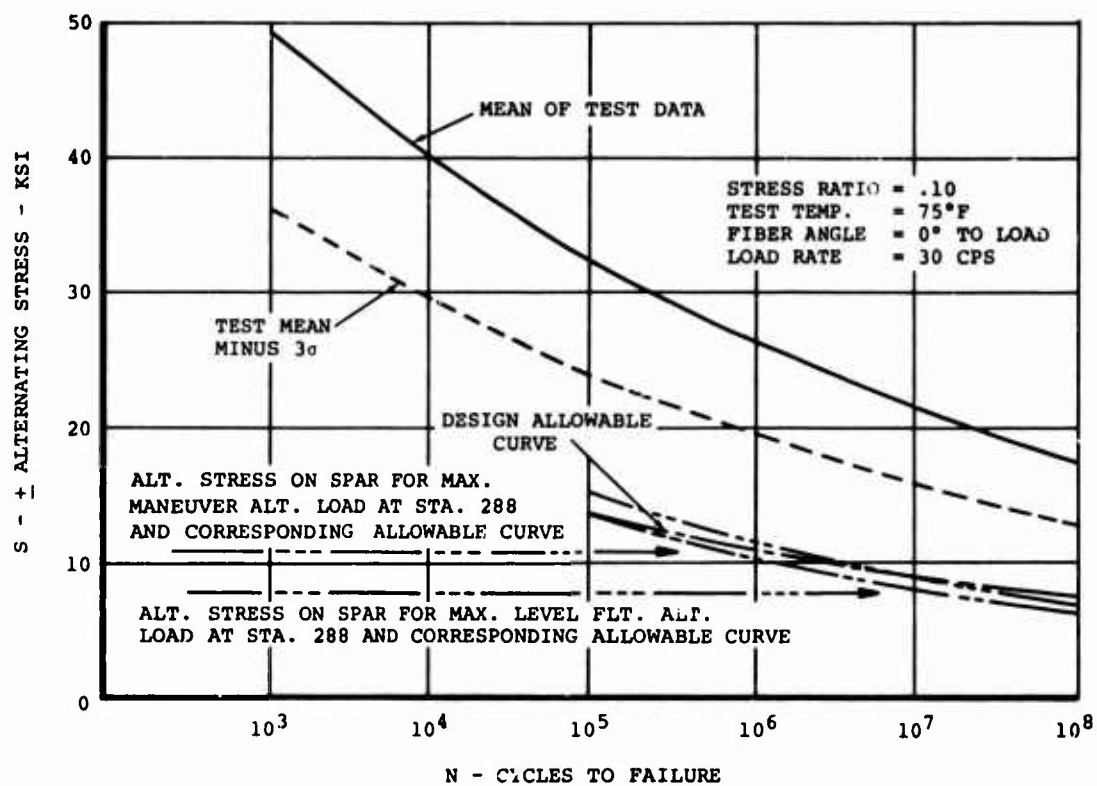


Figure 230. S-N Curve for Unidirectional 1002S Epoxy Resin Laminates Loaded in Tension-Tension Fatigue.

unidirectional and crossply (+45°) S-glass as explained in the Material Testing and Analysis section. The results indicate that the unidirectional material is the fatigue-critical element in these combinations, and as a result, the crossply can be designed to the fatigue strain limit of the unidirectional material. These conclusions would explain why the torsion wrap gave no indication of failure during the structural or flight testing.

The same type of comparison is made for the blade skins at the trailing edge of blade station 198. Figure 232 shows this comparison. The alternating stresses on the skin were calculated at the maximum distance from the chordwise neutral axis. The loads were the maximum level flight and maneuver flight alternating chordwise moments at station 198. These moments were ± 74100 inch-pounds for level flight and $\pm 120,238$ inch-pounds for maneuvering flight. The level-flight load occurred during flight number 269 at 46,000 pounds gross weight, 4 inches aft center of gravity, 235 rpm, 3330 feet density altitude, and 68 knots true airspeed. The maneuver load occurred during a landing flare on flight number 269 at 46,000 pounds gross weight, 4 inch aft center of gravity, and 235 rpm. The steady stresses were calculated from the respective steady chordwise moments and centrifugal forces. Based on the steady stresses, the allowable alternating stress distribution is shown. The level flight stress intersects the design allowable curve at 4×10^6 cycles, while the maneuver flight alternating stress intersects at 3.2×10^4 cycles.

The comparison of allowable and flight stresses demonstrated that level-flight stresses on the spar and skins are low compared to the design allowables. The stress on the spar due to maneuver loads shows adequate life, while the stress on the blade skins during maneuver flight is critical.

Comparison of Structural Test Strain Levels and Flight Strains

The strain distributions experienced in flight testing at 33,000, 40,000, 46,000, and 50,000 pounds gross weight are compared with the strain levels attained during fatigue testing of the 100-inch inboard and outboard blade sections (Figures 233 and 234). The alternating flight strain distributions were calculated at the maximum distance from the flapwise neutral axis. The loads were the maximum alternating flapwise moments measured during the level flight and maneuver portions of the flight test program at the instrumented blade stations. The strains due to centrifugal force were calculated analytically and added to the steady strains due to the maximum steady flapwise moments measured during flight testing. The centrifugal force at a blade weight of 373 pounds was calculated at 235 rpm for 33,000 and 40,000 pounds gross weight and at 245 rpm for 46,000 and 50,000 pounds gross weight. The maximum alternating strains on the structural test specimens were calculated at the maximum distance from the flapwise neutral axis using the maximum alternating flapwise moments, which occurred at station 177 for the inboard section and at station 277 for the outboard section. The steady strains at the same blade stations mentioned above were calculated analytically from the simulated centrifugal force.

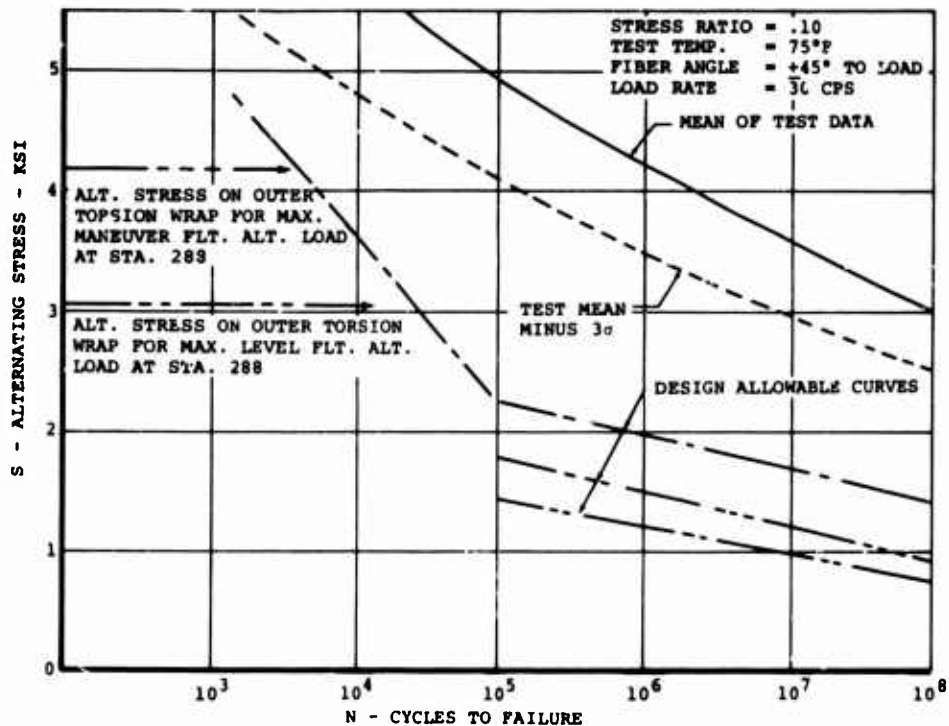


Figure 231. S-N Curve for XP251S+45° Crossply Epoxy Resin Laminates Loaded in Tension-Tension Fatigue.

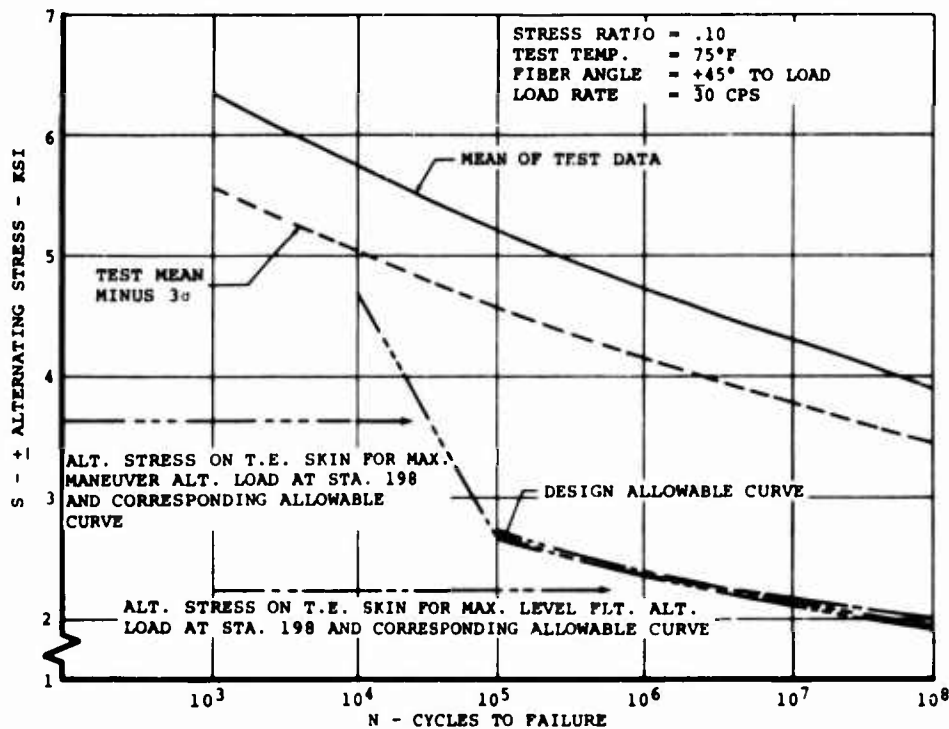


Figure 232. S-N Curve for BP907-143S+45° Crossply Epoxy Resin Laminates Loaded in Tension-Tension Fatigue.

Referring to Figures 233 and 234, the steady strain on the two structural test sections are less than the steady flight strains. The absence of steady flapwise moments in the structural test specimens and the minor variations of rotor rpm in the centrifugal force calculations account for the differences. The alternating strains experienced in level and maneuvering flight at all gross weights for blade stations 160 ($r/R = 0.445$), 198 ($r/R = 0.55$), 252 ($r/R = 0.70$) and 288 ($r/R = 0.80$) are in the range or in excess of the lowest structural test alternating strain level. The intermediate and highest structural test alternating strain levels exceed the above alternating level and maneuvering flight strains at the same stations.

The test sections of the structural test specimens were subjected to alternating strains which equalled or exceeded those encountered during the flight test program. In order to qualify the blade structure for an extended flight program, it would be necessary to perform additional structural testing to establish a statistically broader data base. However, the structural testing which was performed was sufficient to qualify the blades for the limited flight test program which was conducted under this contract.

Material Characteristic Changes Due to Fatigue Loading

The purpose of this section is to present and discuss the variation of material properties and characteristics due to fatigue loading which have been observed during the AGB program.

An apparent change in blade stiffness resulting from fatigue loading has been observed during the structural testing program. Blade sections were tested under predicted flapwise and chordwise alternating moments using natural frequency vibration as the loading mechanism. Since the natural frequency is directly proportional to the square root of the stiffness, measurements of the natural frequency might be a method of detecting stiffness or modulus changes of the test section.

During the testing of the 100-inch inboard section of blade S/N 103-1, natural frequency readings were taken during the four load increments. The readings in cycles per second were 15.7-16.1, 14.6-15.3, 12.0-12.7 and 12.0 for load levels one through four, respectively. These changes in frequency could be attributed to the following:

1. Modulus degradation of the fiberglass material.
2. Decrease in the blade moment of inertia as areas become damaged and fail to carry load.
3. Change in the stiffness of the system as a whole, since the frequency in this test is that of the blade section, the grips attaching the section to the fixture, and the fixture itself.

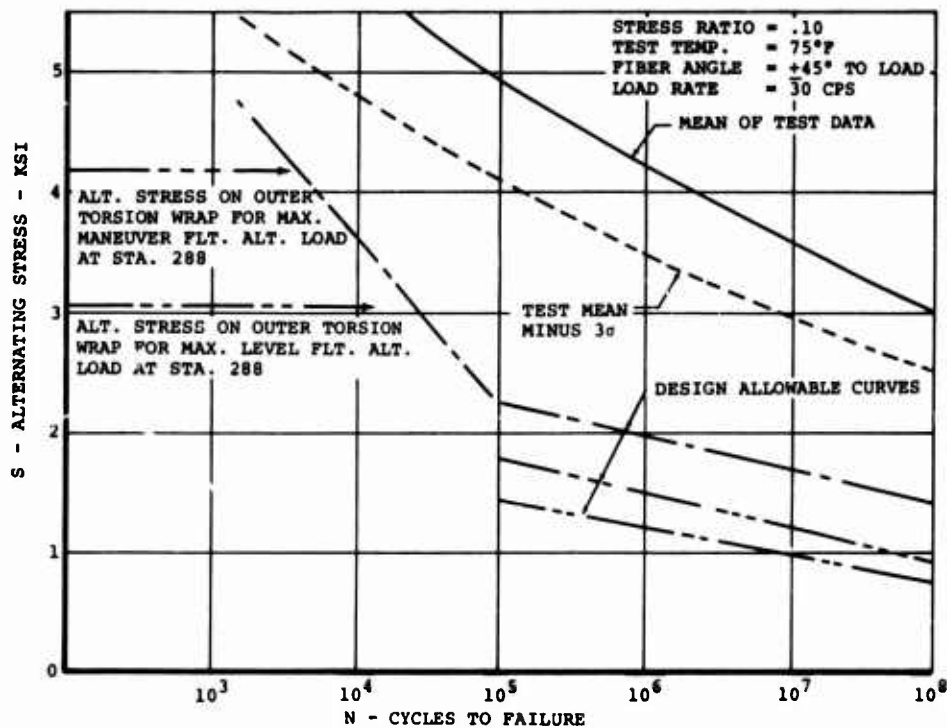


Figure 231. S-N Curve for XP251S+45° Crossply Epoxy Resin Laminates Loaded in Tension-Tension Fatigue.

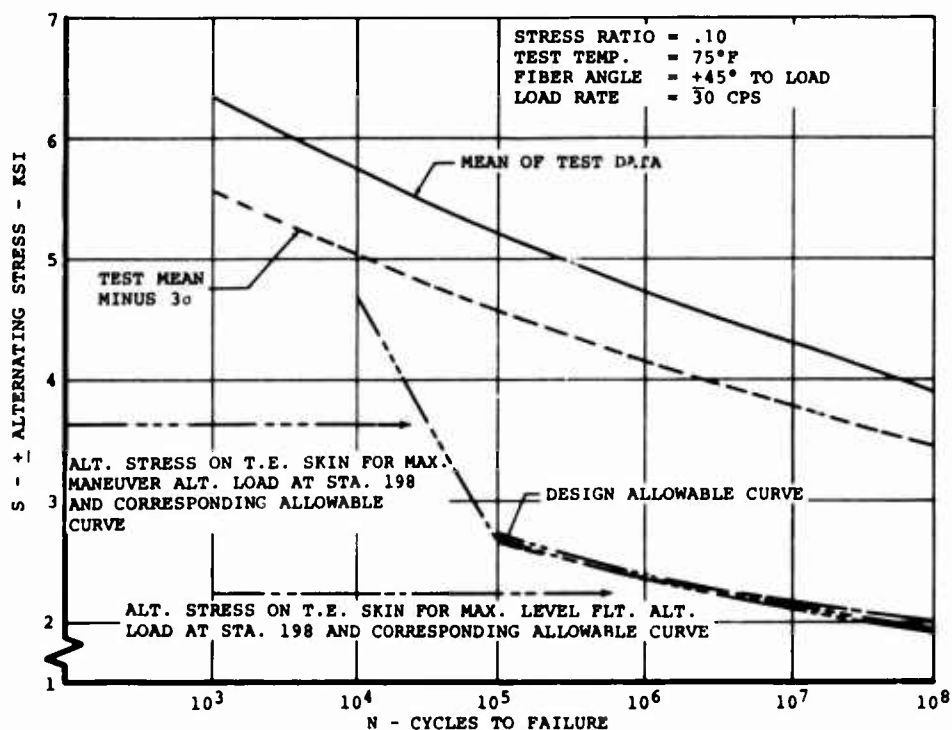


Figure 232. S-N Curve for BP907-143S+45° Crossply Epoxy Resin Laminates Loaded in Tension-Tension Fatigue.

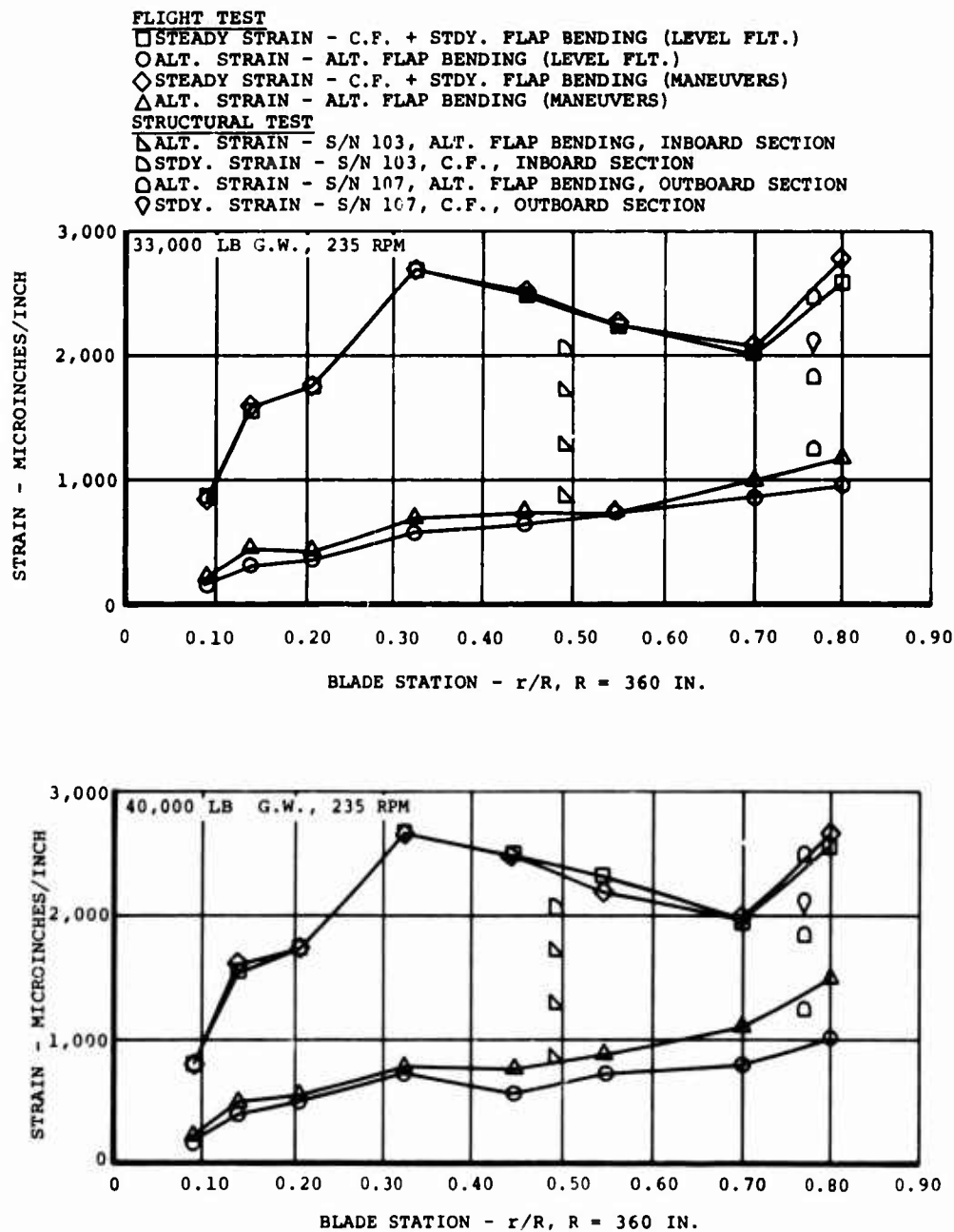


Figure 233. Comparison of Flight Test and Structural Test Measured Strain - 33,000 and 40,000 Pounds Gross Weight.

If the contributions of the fixture and grips to the total change in frequency could be minimized and if sufficient data is recorded before areas of the structure become ineffective, this method could be a means of determining modulus reductions resulting from fatigue loading.

Further changes in material characteristics due to fatigue loading have also been noted during structural testing. Two inboard and one outboard blade section were tested, and the behavior of the materials in each section was similar. Resin crazing was the first visual observation. Microscopic cracks that developed in the resin appeared collectively as faint white areas on the blade. Because of fixture-induced impact loads, delaminations between plies of fiberglass and debonding between fiberglass and core occurred aft of the spar near the trailing edge. The delaminated areas could be depressed by hand pressure. Cracks developed in the skins at 45° to the trailing edge and are shown in Figure 125. Although the material was not failed by the type of loading expected in flight, at least its behavior under impacted loading was observed and recorded.

During the flight test program no modulus degradation was noted. Blade static droop was qualitatively measured during the program and indicated no stiffness changes. Ultrasonic inspection after flight testing showed no new ultrasonic indications in the blade structure or growth of existing ultrasonic indications. These measurements support the conclusion that the stiffness of the blades was unchanged.

Trailing-Edge Cracks in the Blade Transition Area

This discussion concerns the trailing-edge cracks which developed in the transition area of three blades during flight testing. The location of these cracks is shown and the subsequent repair is presented.

After flight number 271, cracks were discovered in the trailing-edge fiberglass doublers of two forward blades (S/N 104-1 and S/N 106-1) and one aft blade (S/N 102-2). The cracks were in the transition area of the blade; their location is shown in Figure 235 for blades S/N 104-1, S/N 106-1, and S/N 102-2. After the cracks were measured and their location was documented, flight number 272 was flown for a duration of two hours. Following this flight, the cracks were re-inspected, and only one showed evidence of propagation. The crack in the aft blade grew 3/8 inch on the lower surface and 1/4 inch on the upper surface. Prior to repair, the outer trailing-edge doubler cap was sanded down to the skin surface and photographs were taken of every crack, as shown in Figures 236 through 238.

The cracks in blade S/N 104-1 are shown in Figure 236 for crack "B" and "C". Crack "A" was a hairline fracture, and it disappeared after the outer doubler cap was removed. Crack "B" initiated at a small hole or void in the trailing-edge wedge. The area around crack "C" showed a discontinuity in the trailing-edge wedge. This looked like a possible butt joint of the wedge at the core splice, although the wedge

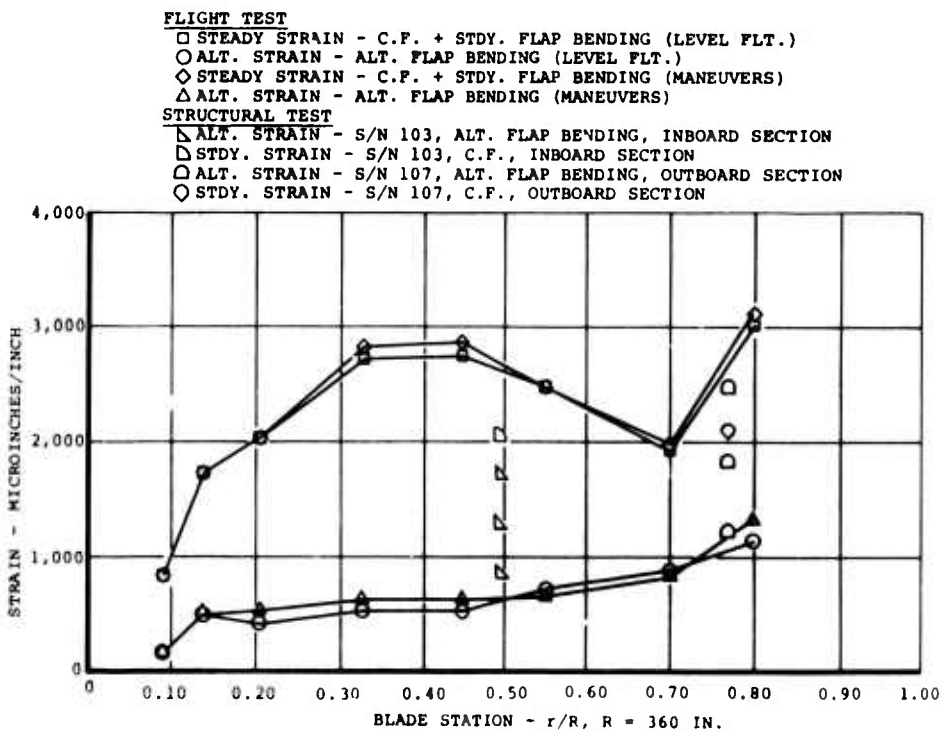
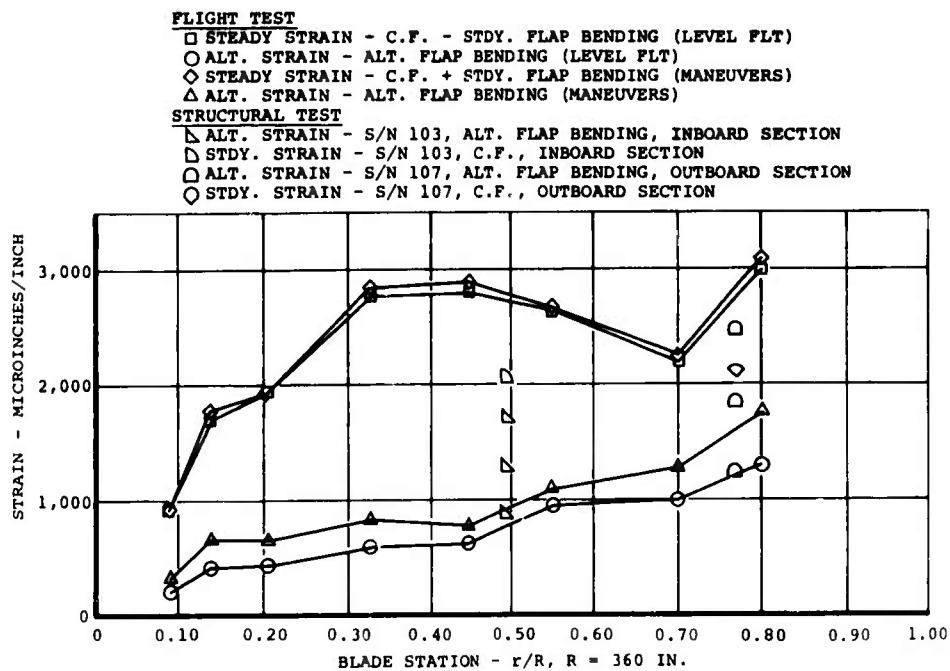


Figure 234. Comparison of Flight Test and Structural Test Measured Strain.

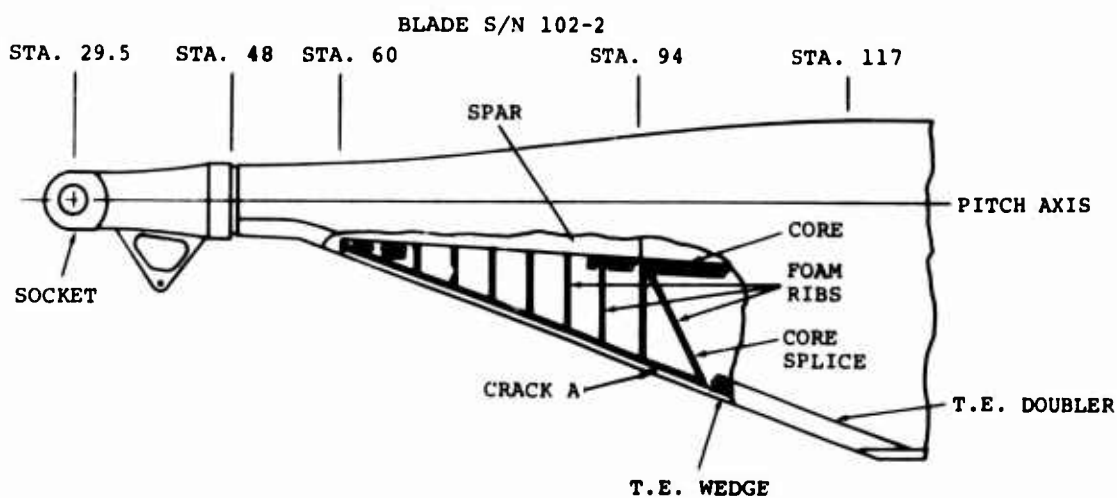
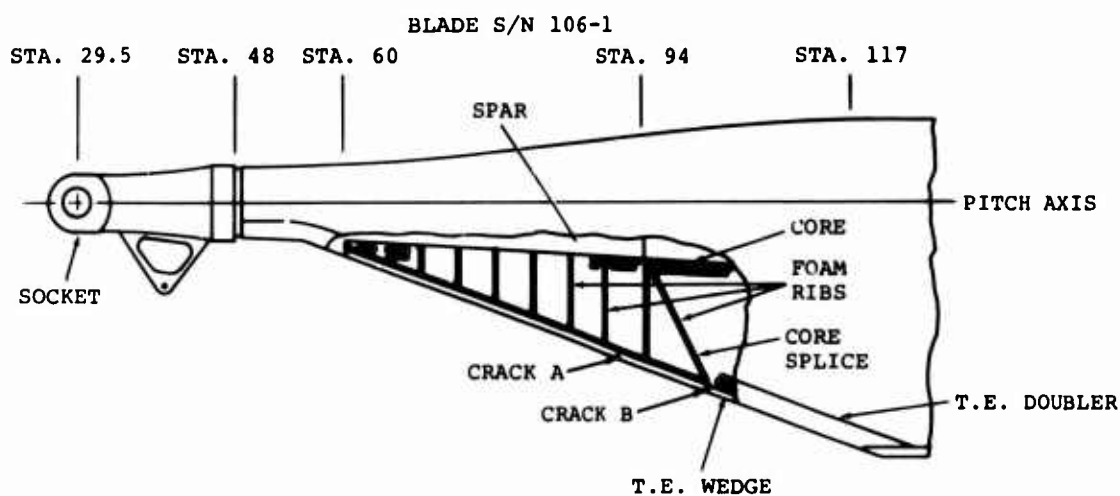
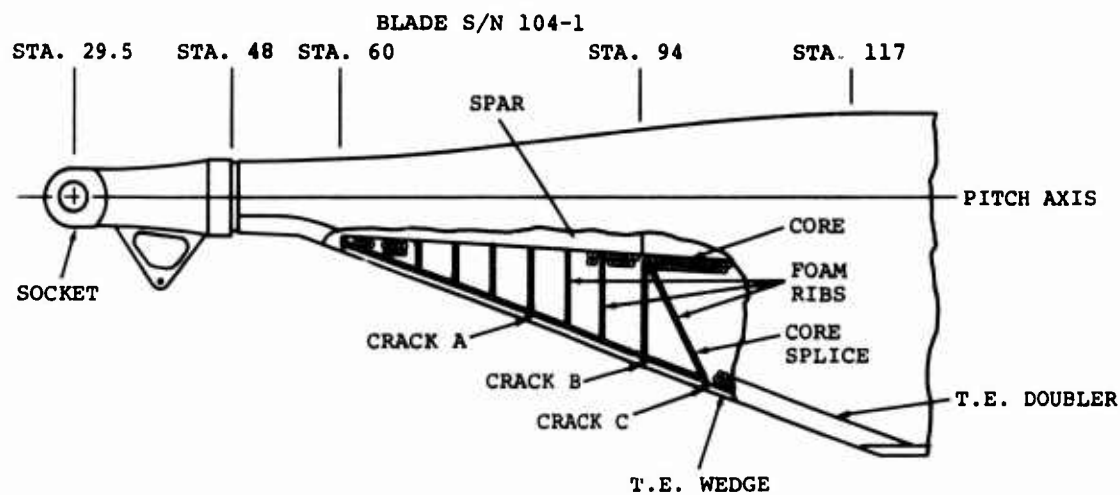


Figure 235. Location of Blade Trailing-Edge Cracks.

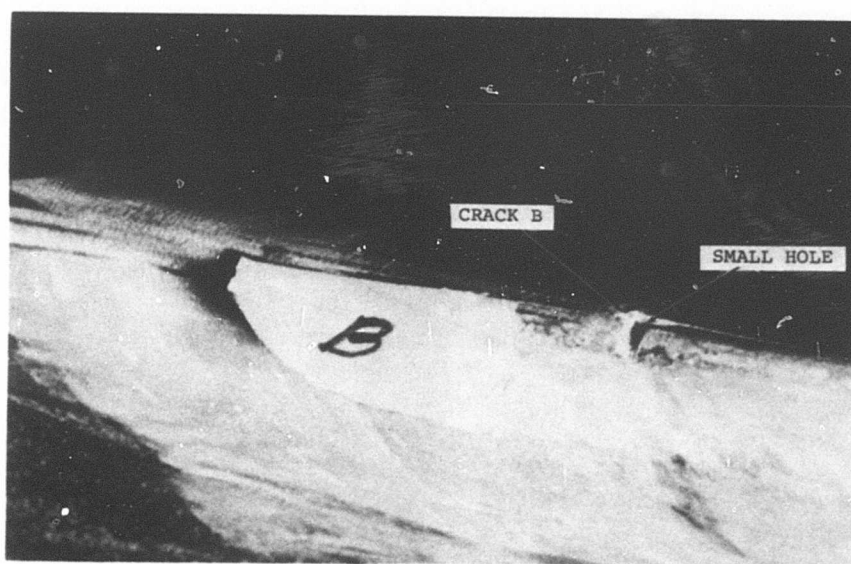
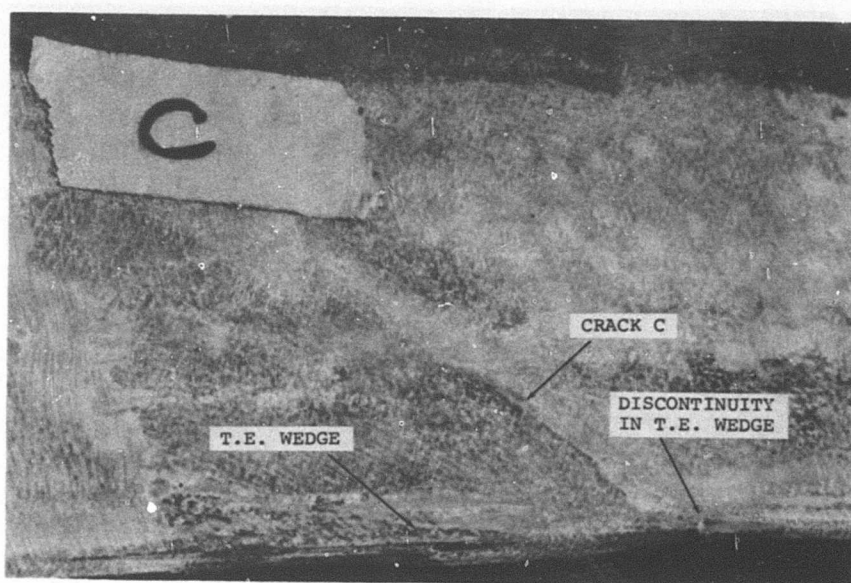


Figure 236. Trailing-Edge Cracks, Blade S/N 104-1.

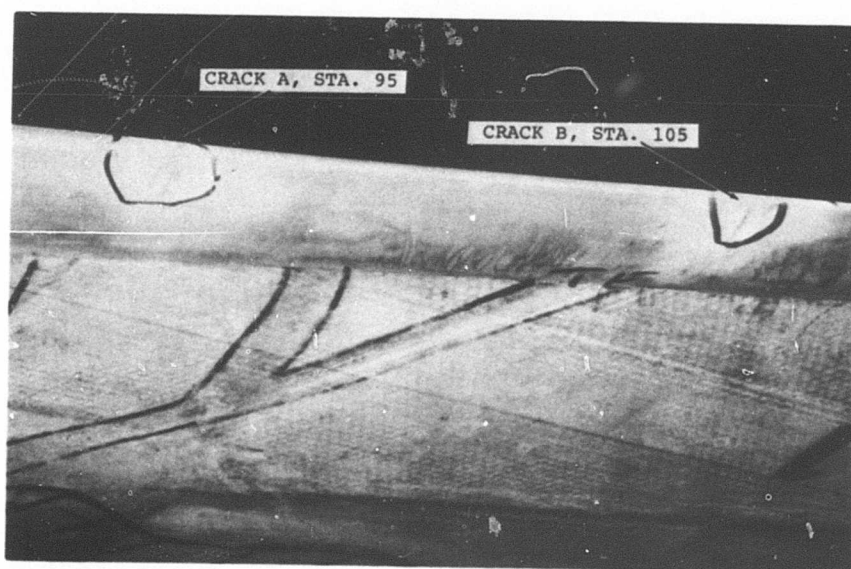
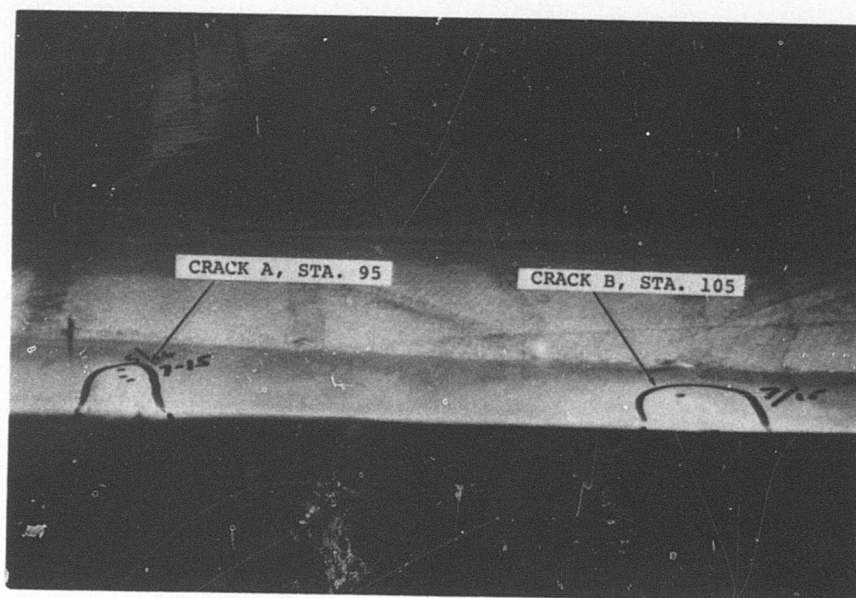


Figure 237. Trailing-Edge Cracks, Blade S/N 106-1.

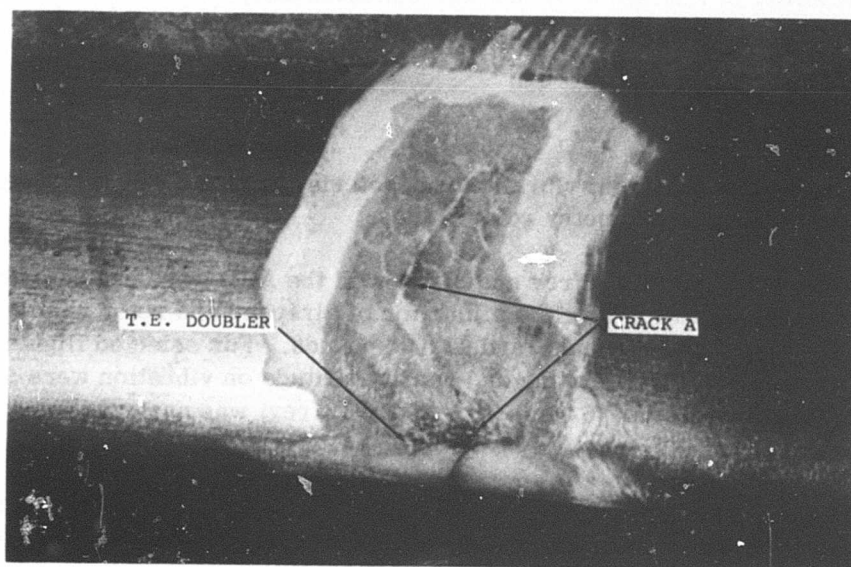
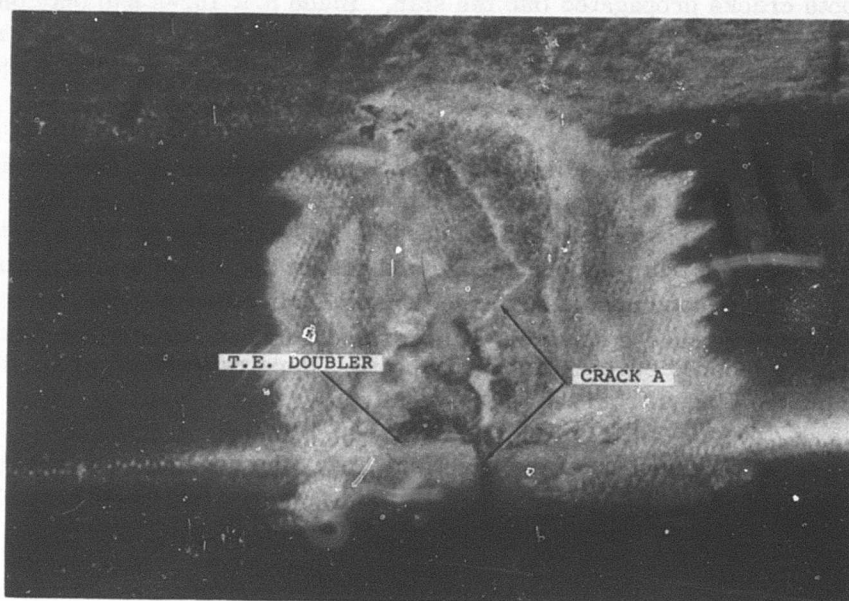


Figure 238. Trailing-Edge Cracks, Blade S/N 102-2.

should have been continuous. Propagation of this crack into the blade skins is evident. Figure 237 shows the cracks in blades S/N 106-1 for the upper and lower blade surfaces. The trailing-edge wedge was not continuous at either crack location and both cracks propagated into the skin. Blade S/N 102-2 had only one crack at station 97. Figure 238 shows the upper and lower blade surfaces. A discontinuity in the trailing-edge wedge initiated the crack, and it travelled forward through the blade skins on both surfaces.

Local repair patches were applied to the crack areas, consisting of a three-ply fiberglass cloth laminate impregnated and bonded to the blade with EC2216 room temperature-curing epoxy resin. The inner ply was extended spanwise 3 inches inboard and outboard from the crack edge and chordwise 1 inch forward from the crack edge. The second ply was extended spanwise 4 inches and chordwise 2 inches respectively and the outer ply 5 inches and 3 inches respectively, so as to provide a tapered edge to the repair patch. Repairs were accomplished without removing the blades from the test aircraft.

During the remaining portion of the flight program, the repairs were checked after each flight. No propagation of the original cracks was detected, and no discrepancies were found in the repair patches.

The cracks described above were not critical to the blade structure. The crack rate was slow enough to allow detection and then repair after 2 hours of flight. The reparability of fiberglass blades was demonstrated.

VIBRATION

Introduction

This section studies the flight vibration characteristics of the CH-47C aircraft equipped with advanced-geometry rotor blades.

Vibration characteristics at 1/rev and 3/rev with the AGB were evaluated by investigation of the vibration level as a function of airspeed and rotor rpm for TOGW of 34,500 pounds, 41,000 pounds, and 47,500 pounds. For selected flights, the effects of maneuvers, cyclic trim, and density altitude on vibration were studied. Higher harmonics vibration (6/rev, 9/rev, and 12/rev) was analyzed for a limited number of conditions.

Vibration levels occurring with the AGB are compared to vibration of the CH-47C production configuration. In addition, a qualitative comparison with the CH-47C vibration specification is made.

An additional analysis of the cause of the severe 1/rev vibration characteristics reported for the AGB was undertaken. Geometric twist and trailing-edge reflex of each blade were measured, and the results were used to analytically study their influence on blade track.

Vibration Test Conditions

Absorber Configuration

Three CH-47C production self-tuning vibration absorbers were used in the cockpit and tuned for a range from 232 to 251 rotor rpm. Two standard production configuration 90-pound mass aft pylon absorbers tuned to 243 rotor rpm were installed at Station 575 in the upper aft pylon.

Vibration Flights

A summary of the vibration flights and the critical parameters is shown in Table XXXVIII.

AGB Ballast Arrangement

For the AGB flight program, the helicopter was ballasted to the required weight using water ballast along the fuselage in conjunction with palletized lead ballast forward and aft. Ballast diagrams showing the ballast location and the amount are shown in Figure 239 for the primary flight configurations: 34,500 pounds takeoff gross weight, 6.1-inch aft center of gravity; 41,000 pounds takeoff gross weight, 5.6-inch aft center of gravity; and 47,500 pounds takeoff gross weight, 3.5-inch aft center of gravity. The instrumentation package weighing 1040 pounds is also shown on Figure 239.

CH-47C Ballast Arrangement

Vibration comparisons were made with the CH-47C aircraft, using vibration data for similar configurations recorded during APE IV (Army Preliminary Evaluation, CH-47C Compliance Program). Ballast diagrams for 34,000 pounds and 47,000 pounds takeoff gross weight, corresponding to A/C B570 x 20 and A/C B570 x 22, respectively, are shown in Figure 240. Lead was used for CH-47C troop and alternate gross weight ballast, unlike the AGB Program, which was partially ballasted using water.

Vibration Measurement Locations

Vibration transducer locations for each flight are summarized in Table XXXIX.

TABLE XXXVIII. CH-47C, B361, ADVANCED GEOMETRY BLADES

Flight No.	Flight Date	TOGW (lb) & TOCG (in.)	Density Altitude (ft)	Vibration Measurements			
				Airspeed Sweep		RPM Sweep	
				At 235 rpm * (kt)	V _{Max} Fuel (lb)	Airspeed (kt)	Fuel (lb)
243	5-2-69	34,500 6.1 Aft	2,000	61-133	5,300		
244	5-5-69	34,500 6.1 Aft	3,000	98-157	2,900	11b	2,900
246	5-6-69	34,500 6.1 Aft	3,000	97-133	4,150		
253	5-16-69	41,000 5.6 Aft	3,000 6,000	101-152 61-102	5,650 4,350		
254	5-21-69	34,500 6.1 Aft	3,000	119-164	4,150	157	3,150
255	5-22-69	41,000 5.6 Aft	3,000 6,000 8,000	131-144 119-145 51-144	5,800 5,250 4,350		
261	6-16-69	34,315 3.7 Fwd	3,000	60-157	5,200		
262	6-20-69	34,300 3.7 Fwd	3,000 3,000	91-161 51-160	4,500 3,400		
263	6-26-69	34,300 3.7 Fwd	3,000	92-164	4,300		
267	7-2-69	47,500 3.5 Aft	3,000	63-128 (245 rpm)	4,700		
269	7-9-69	47,500 3.5 Aft	3,000	63-113	5,100		
271	7-14-69	48,000 3.4 Aft	10,000	72-120 (245 rpm)	4,650	100	3,300
272	7-15-69	48,000 3.4 Aft	6,000	63-138 (245 rpm)	5,000		
274	7-31-69	45,800 1.7 Fwd	9,000	60-95 (245 rpm)	5,200		
276	8-7-69	33,494 0.9 Fwd		20-153	5,300		
279	8-11-69	45,003 0.6 Fwd	9,000 5,000	50-109 77-129 (245 rpm)	3,600 1,550		
281	8-13-69	40,122 5.8 Aft	10,000		4,750		
283	8-18-69	40,122 5.8 Aft	9,000 8,500 6,500		5,800		
284	8-19-69	48,142 4.0 Aft	5,000 7,000 9,000 10,500	60-140 60-135 60-128 60-110	4,750 4,000 3,300 2,750		
285	8-20-69	52,055 0.2 Aft	2,000	60-136 (245 rpm)	4,650		
286	8-20-69	52,055 0.2 Aft	5,000 to 8,000 7,300	75-121 (245 rpm)	3,300		
287	8-21-69	48,036 10.0 Fwd	3,000 6,000 6,000	60-152 60-148 60-155	4,500 3,950 2,750		
288	8-21-69	39,990 3.1 Fwd	7,000	40-127	3,550		

*Unless otherwise noted

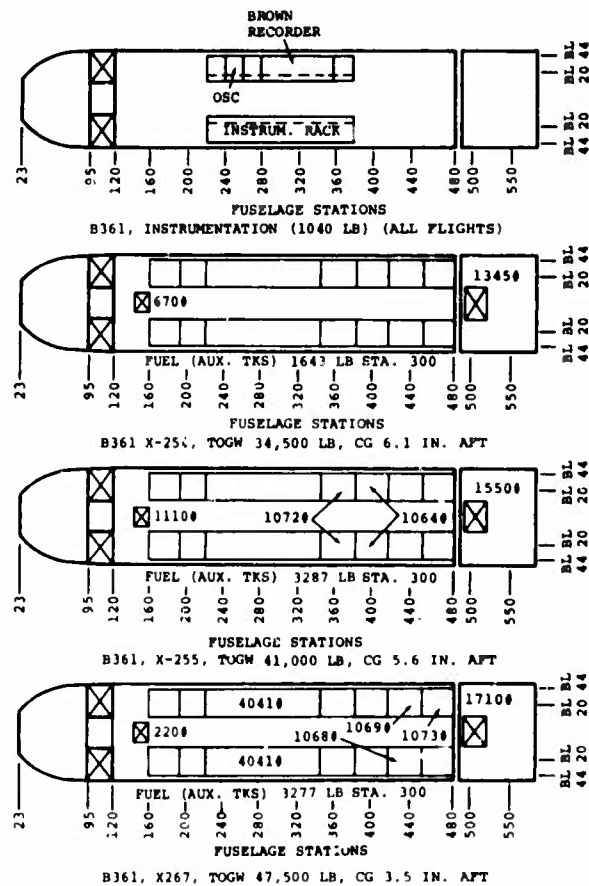


Figure 239. Ballast Diagrams - Advanced-Geometry Blades.

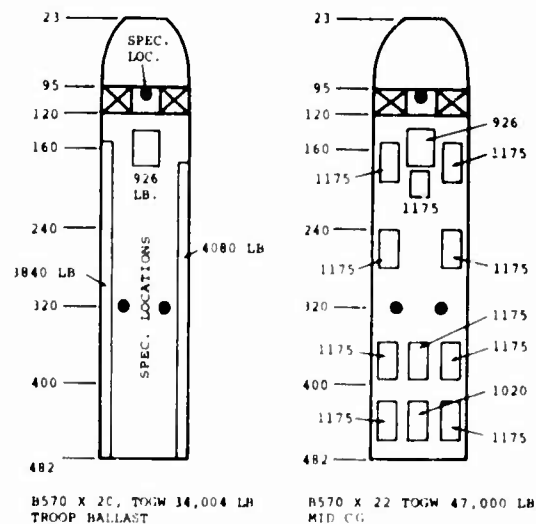


Figure 240. Ballast Diagrams - CH-47C Vibration Compliance Program.

TABLE XXXIX. VIBRATION INSTRUMENTATION

Code No.	Data Param-eter	Location	Flight No.																							
			X243	X244	X246	X253	X254	X255	X261	X262	X263	X267	X269	X271	X272	X274	X276	X279	X281	X283	X284	X285	X286	X287	X288	
1375	Vertical Accel.	Sta. 50 Right	O	O	O	O	O	O	O	O	O	O	O	O	O	O	O	O	O	O	O	O	O	O	O	
1373	Vertical Accel.	Sta. 50 Left	O	O	O	O	O	O	O	O	O	O	O	O	O	O	O	O	O	O	O	O	O	O	O	
1318	Vertical Accel.	Pilot Seat	O	O	O	O	O	O	O	O	O	O	O	O	O	O	O	O	O	O	O	O	O	O	O	
1328	Vertical Accel.	Sta. 95	O	O	O	O	O	O	O	O	O	O	O	O	O	O	O	O	O	O	O	O	O	O	O	
1330	Longitud. Accel.	Sta. 95	O	O	O	O	O	O	O	O	O	O	O	O	O	O	O	O	O	O	O	O	O	O	O	
1351	Lateral Accel.	Sta. 320 RBL 44	O	O	O	O	O	O	O	O	O	O	O	O	O	O	O	O	O	O	O	O	O	O	O	
1353	Vertical Accel.	Sta. 320 RBL 44	O	O	O	O	O	O	O	O	O	O	O	O	O	O	O	O	O	O	O	O	O	O	O	
1357	Vertical Accel.	Sta. 350 LBL 25			O	O	O								O	O	O	O	O	O	O	O	O	O	O	
1358	Lateral Accel.	Sta. 350 LBL 25			O	O	O	O	O	O	O	O	O	O	O	O	O	O	O	O	O	O	O	O	O	
1359	Longitud. Accel.	Sta. 350 LBL 25			O	O	O	O	O	O	O	O	O	O	O	O	O	O	O	O	O	O	O	O	O	
1360	Vertical Accel.	Sta. 482 LBL 44	O	O	O	O	O	O	O	O	O	O	O	O	O	O	O	O	O	O	O	O	O	O	O	
1361	Vertical Accel.	Sta. 482 RBL 44	O	O	O	O	O	O	O	O	O	O	O	O	O	O	O	O	O	O	O	O	O	O	O	
1363	Lateral Accel.	Sta. 482 LBL 44	O	O	O	O	O	O	O	O	O	O	O	O	O	O	O	O	O	O	O	O	O	O	O	

Test Results

Flight vibration data is presented herein, using the 85 percent level for all stabilized flight conditions. This approach simplifies the data presentation by elimination of the data scatter, but still provides an adequate technique for assessment of the vibration characteristics. Vibration for maneuvers is plotted at the 100 percent "g" level, which corresponds to the maximum vibratory "g" experienced within a maneuver. Figure 241 illustrates the CH-47C specification requirement for vibration comparison.

Airframe vibration of the CH-47C equipped with advanced-geometry fiberglass blades is presented in the following sections followed by comparison with vibration of the CH-47C equipped with standard blades, as measured during compliance testing on A/C B570.

CH-47C/AGB, Airspeed Sweep at 34,500 Pounds

Cockpit, cabin, and aft pylon vibration of the CH-47C equipped with AGB is presented in Figures 242 and 243 for a 235-rpm airspeed sweep at a 34,500-pound takeoff gross weight. Aircraft ballast for this condition is given in Figure 239.

Vibration at 1/rev shows an increasing trend with airspeed, with the highest measured vertical vibration in the cockpit area. Lateral vibration is generally lower than the vertical. The CH-47C specification vibration of 0.065, as shown in Figure 241, is exceeded at station 95.

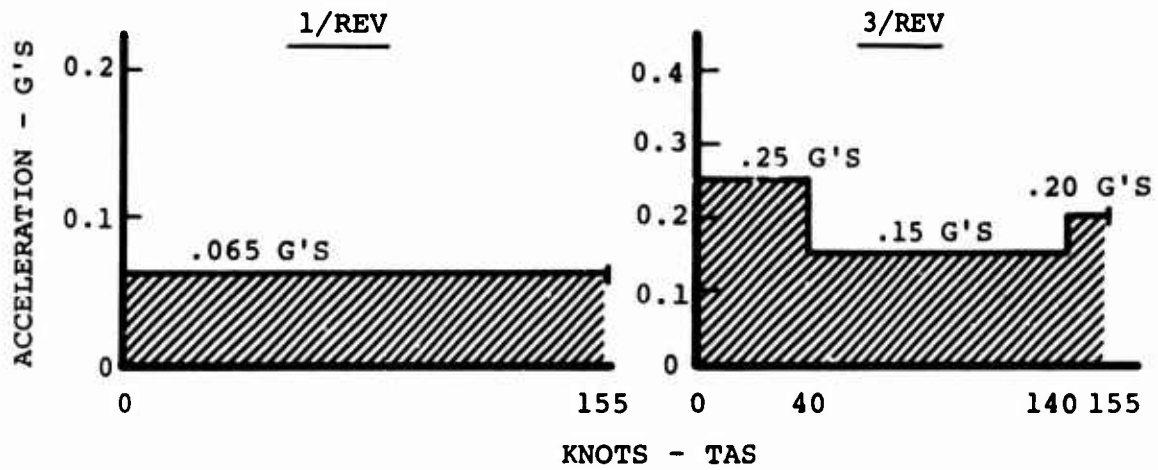
Three/rev vibration shows a moderate increase with airspeed for all stations, except Station 320 vertical, which shows no trend with airspeed. Station 95 longitudinal has the most significant trend with airspeed, increasing from 0.3 "g" at 120 knots to 1.7 "g" at 162 knots. Three/rev vibration does not exceed the specification limits.

Six/rev and nine/rev vibration decreases with airspeed, with the higher measured cockpit levels in the vertical direction. Station 50 R/H and L/H vertical vibration shows a rapid buildup with airspeed at 12/rev, whereas pilot seat vertical, Station 95 lateral and vertical, shows only a moderate airspeed trend.

CH-47C/AGB, RPM Sweep at 34,500 Pounds

Vibration during an rpm sweep at 157 knots at 34,500 pounds takeoff gross weight is shown in Figures 244 and 245 for the AGB configuration. One/rev vertical vibration in the cockpit area shows a moderate increasing trend with rpm. Lateral 1/rev vibration shows only a slight increase with rpm, similar to the vertical cabin and Station 95 longitudinal vibration.

UNACCELERATED LEVEL FLIGHT - 235 RPM
STA. 95 & 320, VERTICAL & LATERAL



ACCELERATION & DECELERATION - 235 RPM
STA. 95 & 320, VERTICAL & LATERAL

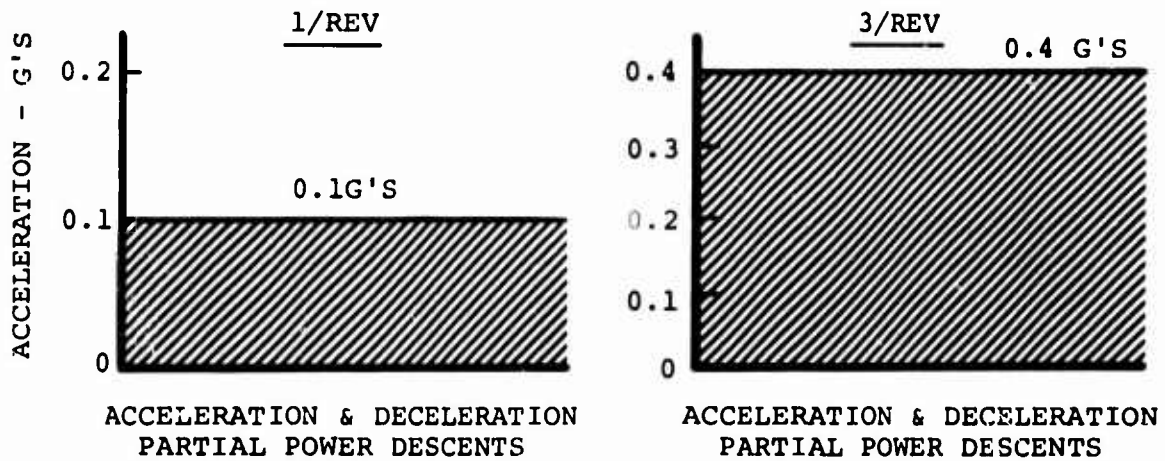


Figure 241. CH-47C Detail Specification Limits.

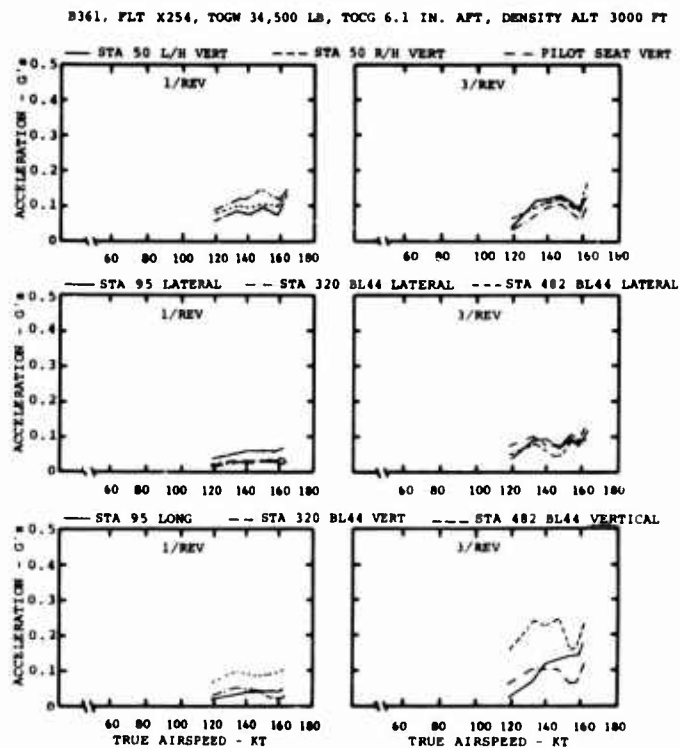


Figure 242. CH-47C Airframe Vibration With AGB Airspeed Sweep at 235 RPM.

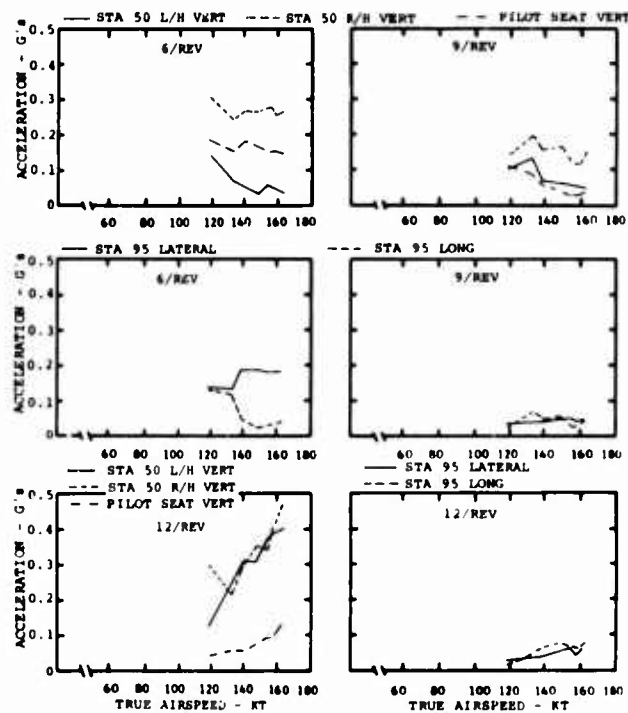
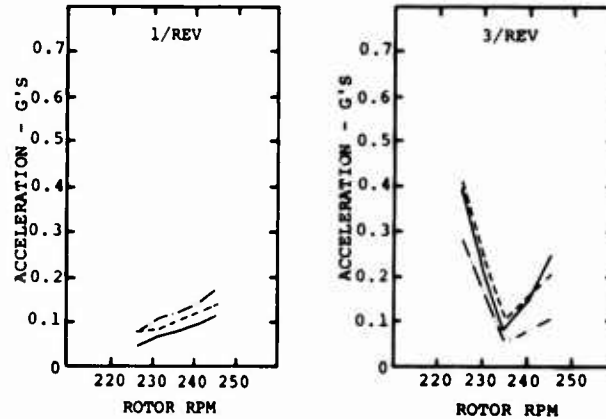


Figure 243. CH-47C Airframe Vibration With AGB Airspeed Sweep at 235 RPM.

B361, FLT X254, TOGW 34,500 LB, TOCG 6.1 IN. AFT, DENSITY ALT 3000 FT

— STA 50 L/H VERT --- STA 50 R/H VERT --- PILOT SEAT VERT



— STA 95 LATERAL --- STA 320 LATERAL --- STA 482 LATERAL

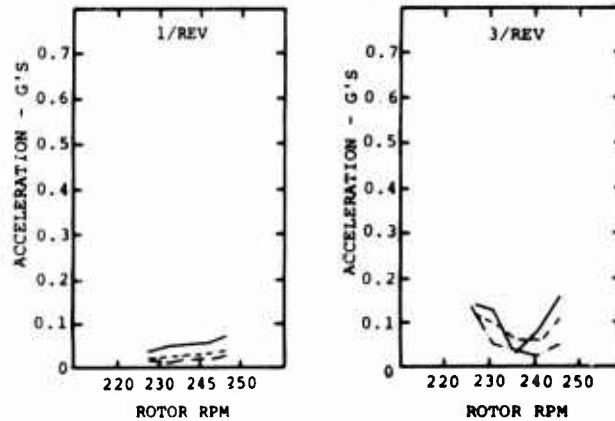


Figure 244. CH-47C Airframe Vibration With AGB RPM Sweep at 157 Knots (34,500 Pounds).

— STA 95 LONG --- STA 320 BL44 VERTICAL --- STA 482 BL44 VERTICAL

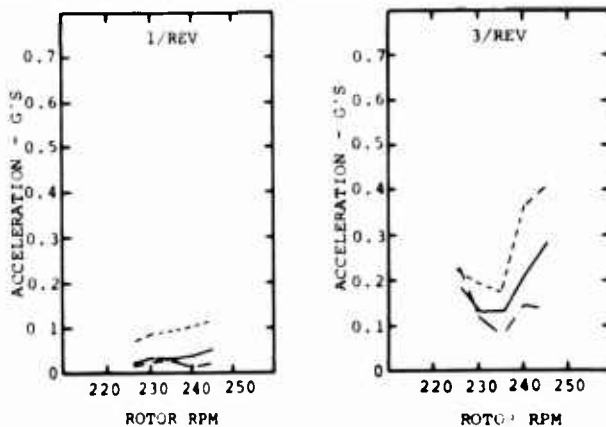


Figure 245. CH-47C Airframe Vibration With AGB RPM Sweep at 157 Knots (34,500 Pounds).

Vertical vibration in the cockpit shows a minimum level at 235 rpm. This characteristic results from a 3/rev vibration increase with RPM as a result of increased rotor excitation and the lower rpm being extended from the tuning limitation of the self-tuning vibration absorber. Cabin vertical and lateral vibrations show similar trends.

CH-47C/AGC, Effect of Gross Weight

Figures 246, 247, and 248 compare the effect of gross weight on aircraft vibration for the CH-47C equipped with AGB. Vertical vibrations at the 41,000- and 47,500-pound ballast configurations generally show an increased 1/rev vibration of approximately 20 percent through the airspeed sweep. Vertical vibration at 3/rev in the cockpit area increases with the aircraft gross weight. No clearly defined trend of cabin 3/rev vertical and lateral vibration is apparent from the data. Three/rev Station 95 longitudinal vibration at the higher gross weights does not show the increasing trend with airspeed which is apparent for the 34,500-pound configuration.

CH-47C/AGB, Effect of Altitude

The effect of density altitude on CH-47C vibration levels with AGB at 47,500 pounds takeoff gross weight is examined in Figures 249 through 252. One/rev vibration levels show no significant difference between altitude except for Station 50 vertical and pilot seat vertical. For Station 50 L/H vertical, 1/rev vibration is lower at the 9000-foot density altitude.

Lateral 3/rev vibration levels are relatively unchanged with altitude. Mid and aft cabin vertical 3/rev vibration levels are lower at Station 320 R/H and Station 482 L/H for the 6000 and 9000 foot density altitude. Cockpit 3/rev levels show some difference, but no definite trend. Forward cockpit (Station 50) levels are higher at the higher altitude, while pilot seat and Station 95 vertical levels are higher at the lower altitudes.

CH-47C/AGB, Effect of Rotor Speed

Figures 253 through 256 examine the influence of rpm on vibration with AGB at 47,500 pounds takeoff gross weight. One/rev vibration levels are generally slightly lower at the cockpit, mid and aft cabin for the 235 rpm. Forward cockpit (Station 50) shows lower 3/rev vibration at the higher 245 rpm; Station 95, mid and aft cabin 3/rev vibration are higher for the 245 rpm. Vibration trends (3/rev) with airspeed show similarity for both the 235 and 245 rpm.

CH-47C/AGB Cyclic Trim Effect

The influence of cyclic trim on vibration with AGB is examined in Figures 257 and 258. Cockpit vibration levels at 1/rev show no change with cyclic trim.

_____ FLT X253, TOGW 41,000 LB, TOCG 5.6 IN. AFT, 3,000 FT HD
 - - - - - FLT X254, TOGW 34,500 LB, TOCG 6.1 IN. AFT, 3,000 FT HD
 FLT X269, TOGW 47,500 LB, TOCG 3.5 IN. AFT, 3,000 FT HD

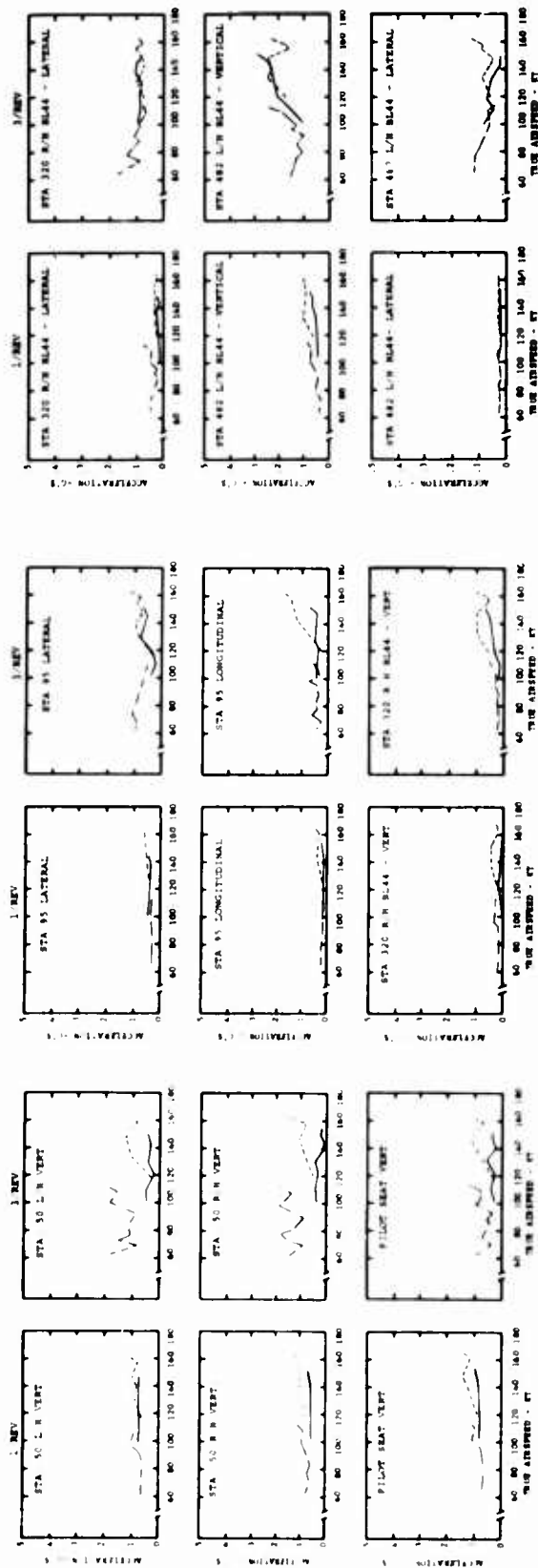


Figure 246. CH-47C Airframe Vibration With AGB Effect of Gross Weight at 235 RPM.

Figure 247. CH-47C Airframe Vibration With AGB Effect of Gross Weight at 235 RPM.

Figure 248. CH-47C Airframe Vibration With AGB Effect of Gross Weight at 235 RPM.

— B361, FLT X267, 3,000 FT H_D , 47,500 LB TOGW, 3.5 IN. AFT TOCG
 ---- B361, FLT X272, 6,000 FT H_D , 48,000 LB TOGW, 3.4 IN. AFT TOCG
 - - - B361, FLT X271, 9,000 FT H_D , 48,000 LB TOGW, 3.4 IN. AFT TOCG

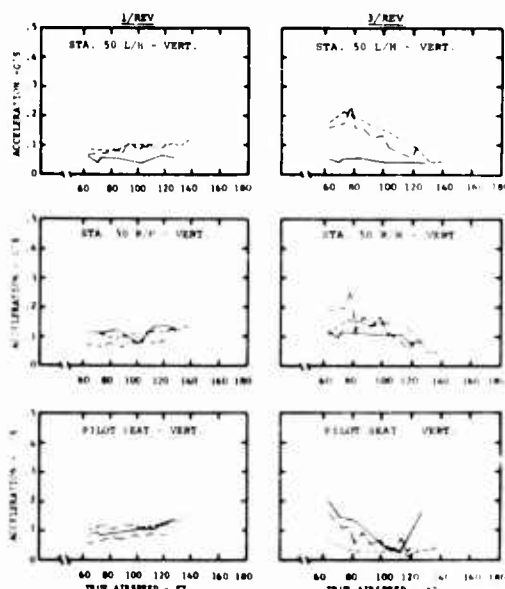


Figure 249. CH-47C Airframe Vibration With AGB Effect of Altitude at 245 RPM.

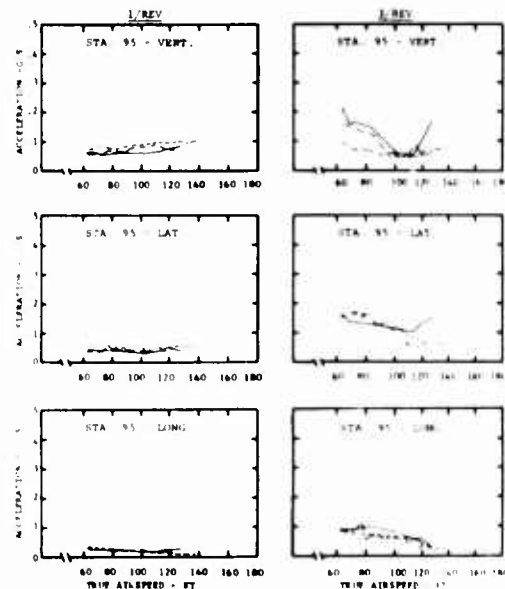


Figure 250. CH-47C Airframe Vibration With AGB Effect of Altitude at 245 RPM.

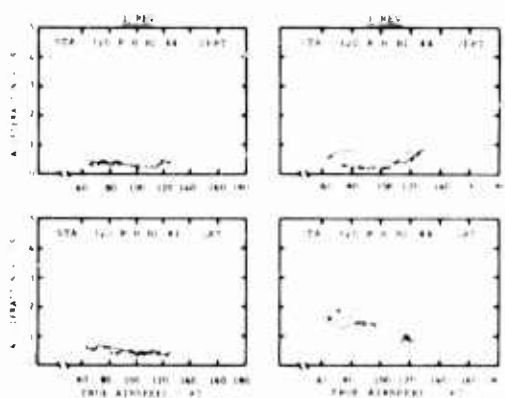


Figure 251. CH-47C Airframe Vibration With AGB Effect of Altitude at 245 RPM.

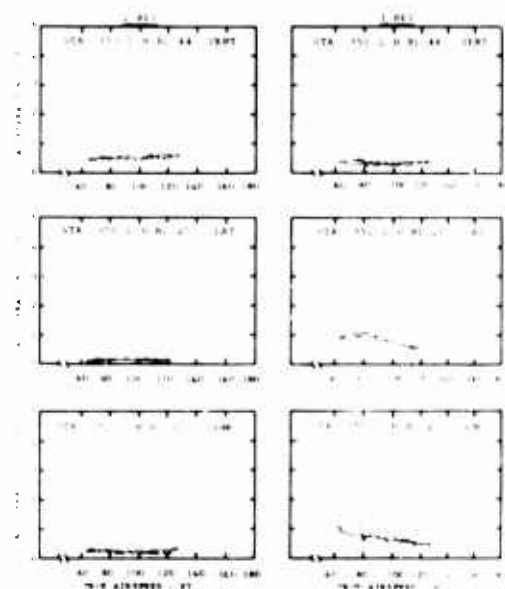


Figure 252. CH-47C Airframe Vibration With AGB Effect of Altitude at 245 RPM.

—B361,FLT X269, 3,000 FT H_D, TOCG 3.5 IN. AFT, 235 RPM
 - -B361,FLT X267, 3,000 FT H_D, TOCG 3.5 IN. AFT, 245 RPM
 —.B361,FLT X271, 9,000 FT H_D, 48,000 LB TOGW, 3.4 IN. AFT TOCG

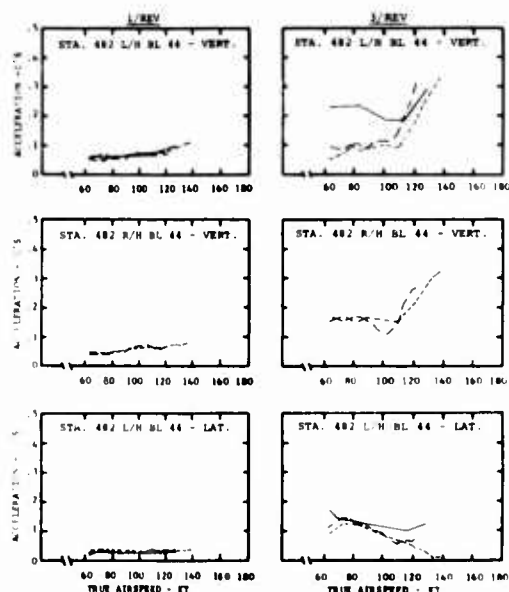


Figure 253. CH-47C Airframe Vibration With AGB Effect of Altitude at 245 RPM.

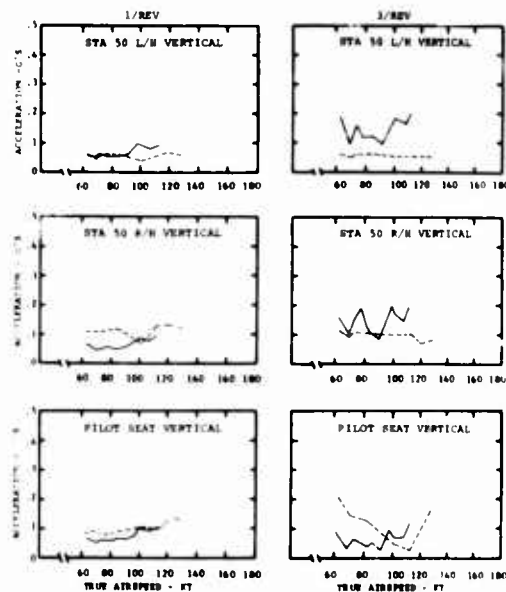


Figure 254. Airframe Vibration With AGB Effect of RPM at 47,500 Pounds TOGW.

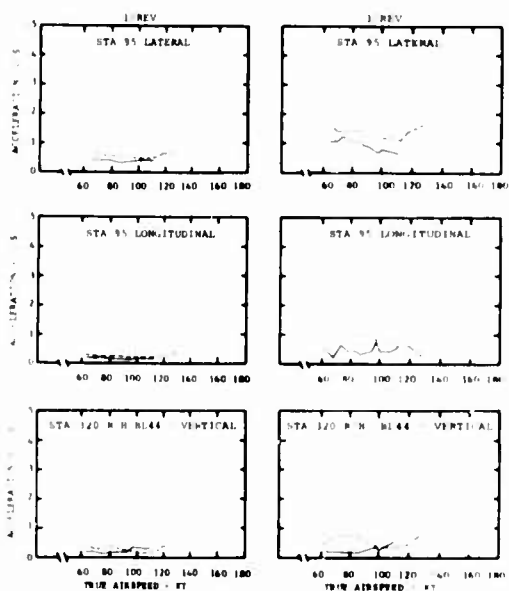


Figure 255. Airframe Vibration With AGB Effect of RPM at 47,500 Pounds TOGW.

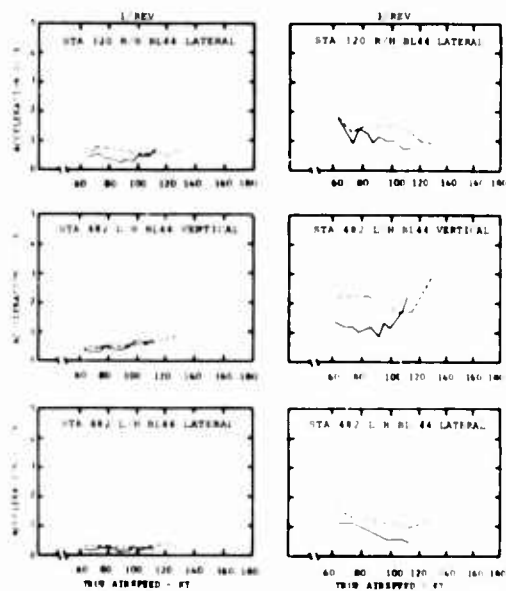


Figure 256. Airframe Vibration With AGB Effect of RPM at 47,500 Pounds TOGW.

B-361 FLT X244, 3,000 FT H_D, 34,500 LB TOGW, CG 6.1 IN. AFT 235 RPM.
100 KNOTS

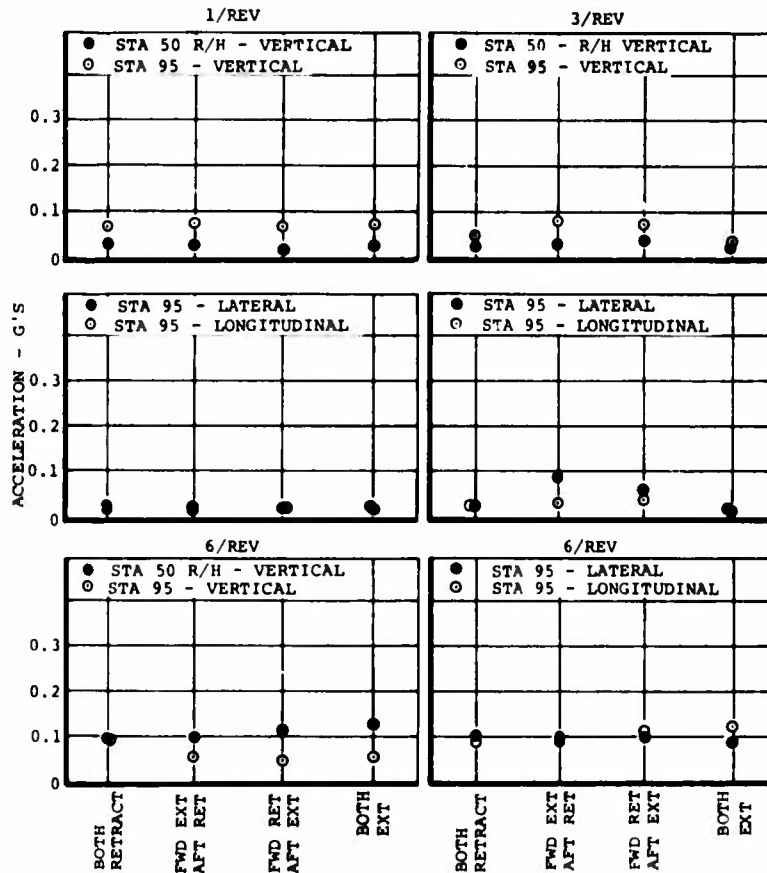


Figure 257. Airframe Vibration With AGB Effect of Cyclic Trim.

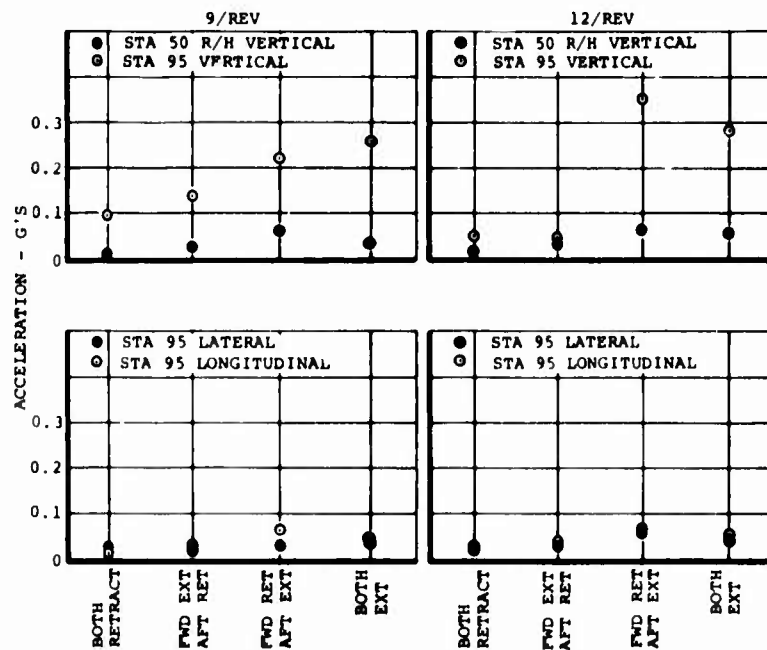


Figure 258. Airframe Vibration With AGB Effect of Cyclic Trim.

Three/rev vibration in the cockpit has a trend toward lower levels for the extended and retracted cyclic at both rotors. For 6/rev vibration, no significant trends were measured.

Station 50 R/H vertical, lateral and longitudinal cockpit vibration at 9/rev and 12/rev show no influence from cyclic trim. Large changes in both 9/rev and 12/rev vibration with cyclic trim variation occur at Station 95 vertical. Nine/rev vibration of 0.1 "g" with retracted cyclic increases to a maximum of 0.25 "g" with extended cyclic forward and aft. Vibration at 12/rev for Station 95 vertical varies from a minimum of 0.05 "g" to 0.35 "g" with aft cyclic extended and forward cyclic retracted.

Vibration time histories of the cockpit accelerations are given in Figures 259, 260, and 261. An examination of the traces shows that for vertical cockpit response, the high-frequency acceleration levels are very significant with two cyclic settings: forward retracted and aft extended, and forward and aft extended.

CH-47C/AGB Maneuver Vibration

Figures 262 and 263 present a comparison of maneuver vibration with AGB blades for three gross weights at selected cockpit and mid-cabin stations. In general, maneuver vibration levels are well below the 0.3 "g" specification limit (Figure 241) established for the CH-47C helicopter. No identifiable trends are apparent from the available vibration measurements during maneuvers.

Comparison of CH-47C and CH-47C/AGB Vibration

Airframe vibration of the CH-47C equipped with advanced-geometry fiberglass blades is compared to vibration data obtained with the standard production blades. CH-47C vibration levels used for comparison were measured on A/C B-570 during compliance testing. Gross weight of the aircraft for comparison was identical, but center of gravity differences existed between aircraft due to different ballast distributions. In the AGB test, water ballast provided a portion of ballast, whereas for the CH-47C compliance testing, only lead was used to establish a troop ballast configuration. Considering these differences, vibration levels of these aircraft are compared at the same gross weight.

Airspeed Sweep Comparison at 34,500 Pounds

Vibration comparisons of the AGB and production blades for an airspeed sweep at 34,500 pounds TOGW are shown in Figures 264 and 265. One/rev vibration with production blades was acceptable to the pilot throughout the speed range; however, no data was available for specific airspeeds. For the AGB, the pilot considered 1/rev vibration acceptable for airspeed below 130 knots.

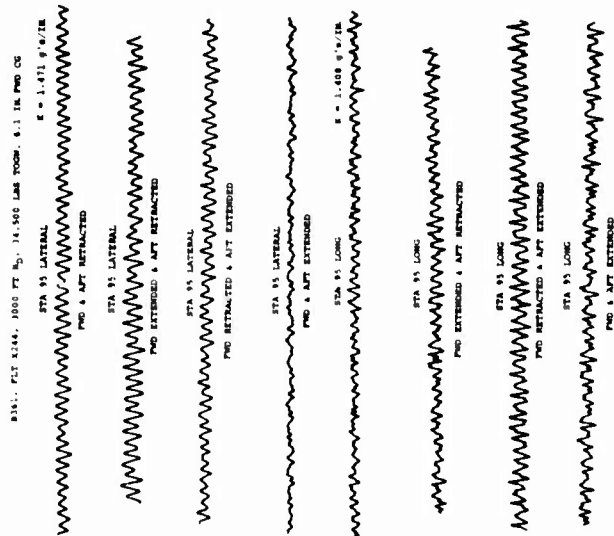


Figure 261. Vibration Time History, Sta 95 Lateral and Longitudinal Effect of Cyclic Trim, 100 Knots, 235 RPM.

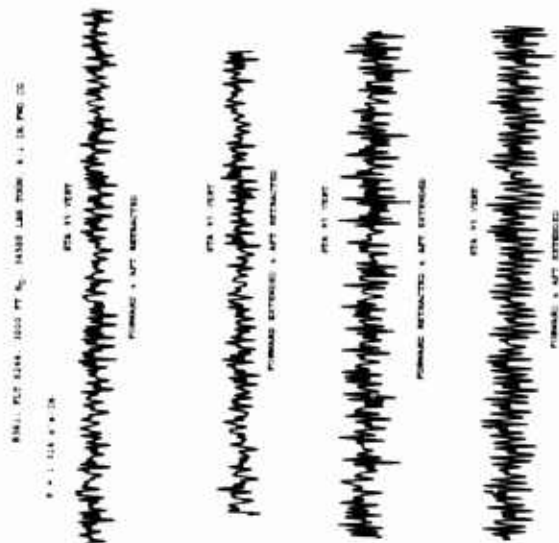


Figure 260. Vibration Time History, Sta 95 Vertical Effect of Cyclic Trim, 100 Knots, 235 RPM.

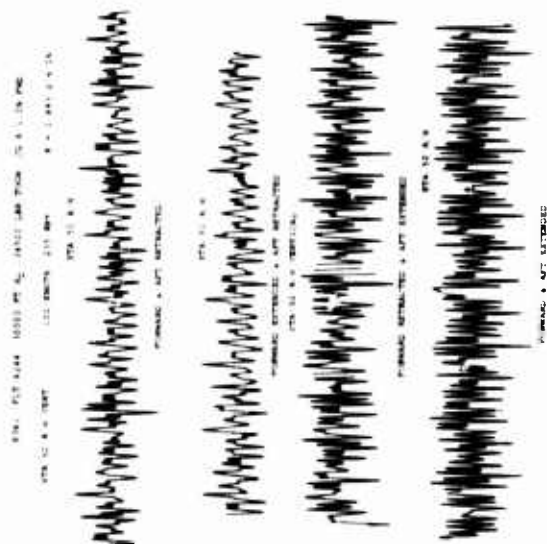


Figure 259. Vibration Time History Effect of Cyclic Trim.

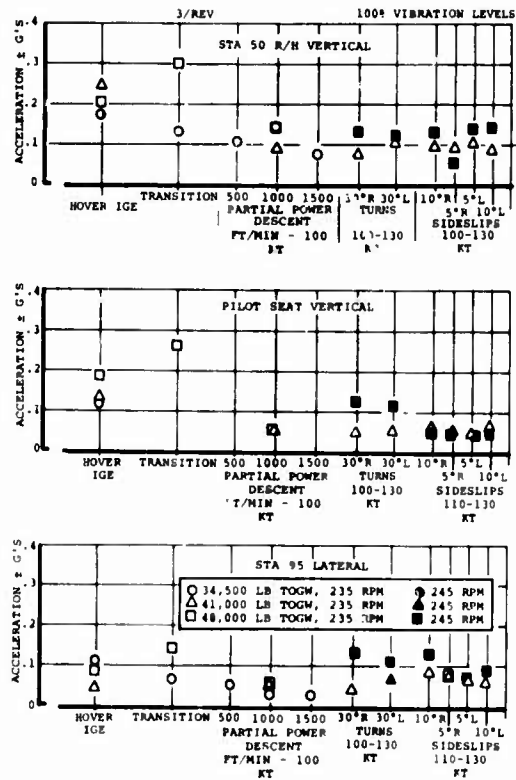


Figure 262. Maneuver Vibration With AGB Effect of Gross Weight.

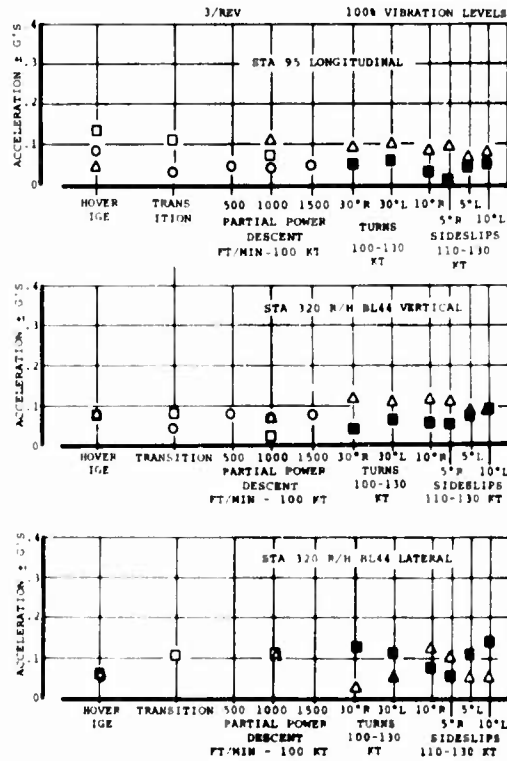


Figure 263. Maneuver Vibration With AGB Effect of Gross Weight.

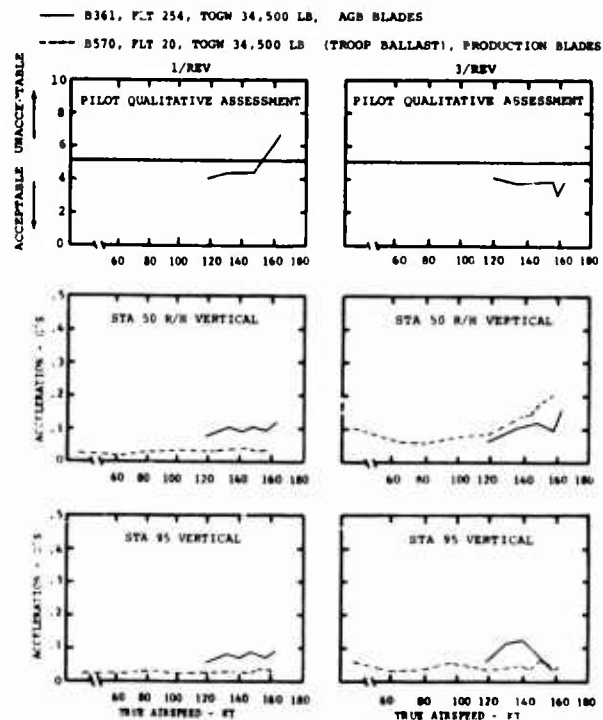


Figure 264. CH-47C Airframe Vibration, Advanced Geometry Blades vs CH-47C Production Blades.

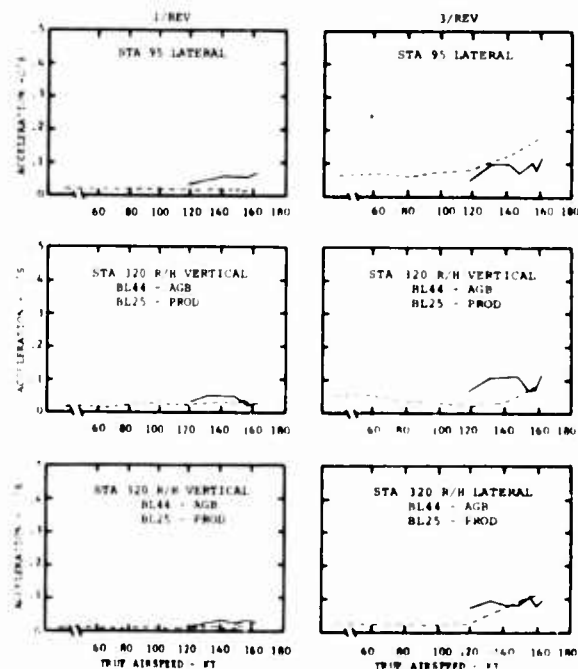


Figure 265. CH-47C Airframe Vibration, Advanced Geometry Blades vs CH-47C Production Blades.

One/rev measured vibrations in the cockpit for the AGB are above specification and approximately two times the production blade vibration. Mid-cabin 1/rev levels are below 0.05 for both configurations.

Three/rev vibration with AGB shows no significant trends. AGB vibration is acceptable to the pilot. Cockpit levels are slightly lower at Station 50 vertical, higher at Station 95 vertical for several airspeeds, and lower laterally at Station 95.

Airspeed Sweep Comparison at 47,000 Pounds

Vibration of the CH-47C equipped with AGB and production blades is examined in Figures 266 and 267. AGB 1/rev vibration was rated as unacceptable by the pilot throughout the airspeed sweep. The production blades vibration (flight X22) was rated acceptable at all airspeeds. Station 95 vertical and lateral 1/rev vibration with the AGB was at least twice that for production blades. The vibration specification as shown in Figure 241 was exceeded for 1/rev.

Vibration at 3/rev in the cockpit for AGB was above the level recorded with the production blade. AGB vibration shows a downward trend with airspeed similar to the vertical vibration with production blades. Station 320 vertical vibration is below the production configuration; Station 320 lateral is above the production configuration. Pilot rating with AGB showed an unacceptable level to 115 knots and marginal upward to 135.

RPM Sweep Comparison at 34,500 Pounds

Figures 268 and 269 compare the influence of blades on 3/rev vibration during an rpm sweep at 157 knots, 34,500 pounds takeoff gross weight. Three/rev cockpit vibration shows no definite trends: at 245 rpm, Station 50 levels for the AGB are lower; Station 95 remains the same. For the higher rpm at mid-cabin, vertical vibration is higher and the lateral vibration is lower with the AGB.

Pilot Qualitative Comparison

Figures 270 and 271 examine the pilot qualitative assessment of 1/rev and 3/rev compared to the harmonically analyzed data measured in the cockpit for both AGB and production blades. It is noted that the 1/rev and 3/rev vibrations for flight X22 (production blades) were judged acceptable by pilot comment throughout the airspeed envelope, but relative assessment at the airspeed points was not recorded. One/rev vibration with the AGB was judged unacceptable at all airspeeds, with the condition worsening as the speed increased. Cockpit and pilot's heel vertical vibration at 1/rev was higher for the AGB, but the "g" level increase, as shown in Figure 270, does not appear to substantiate the pilot's relative assessment between configurations. It is noted that at the 1/rev frequency, the pilot would be more susceptible to amplitude

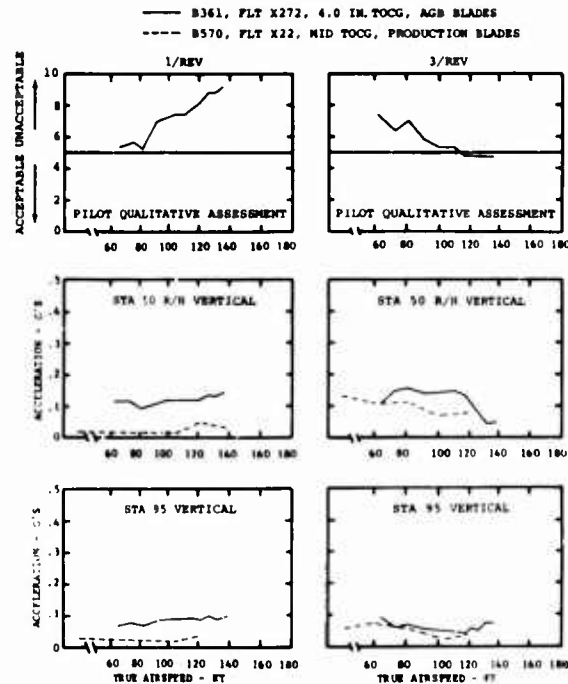


Figure 266. CH-47C Airframe Vibration, Advanced-Geometry Blades vs CH-47C Production Blades at 245 RPM Airspeed Sweep at 47,000 Pounds TOGW.

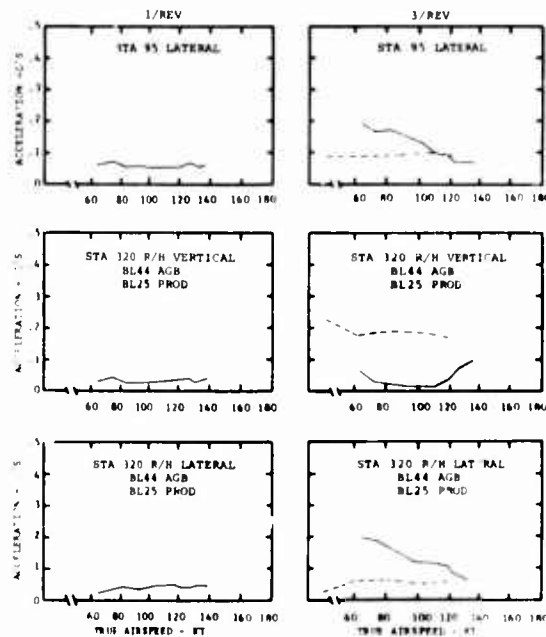


Figure 267. CH-47C Airframe Vibration, Advanced-Geometry Blades vs CH-47C Production Blades at 245 RPM Airspeed Sweep at 47,000 Pounds TOGW.

— B361, FLT X254, 34,500 LB TOGW, AGB BLADES
 ---- B570, FLT X20, 34,500 LB TOGW, CH-47C PRODUCTION BLADES

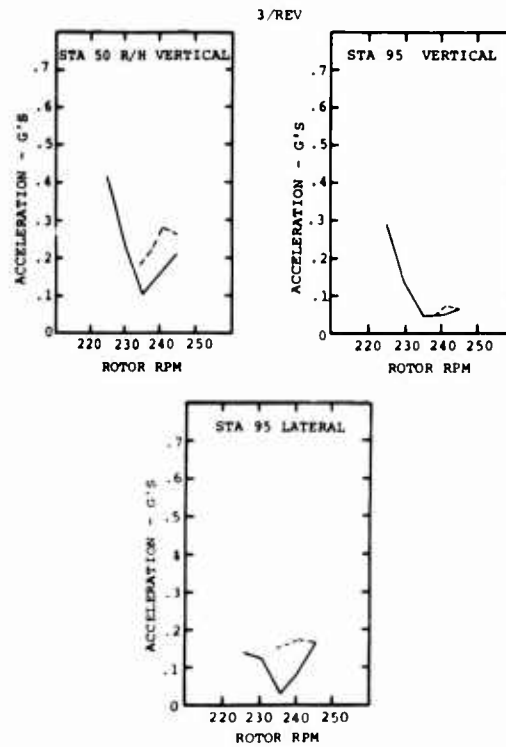


Figure 268. CH-47C Airframe Vibration, Advanced-Geometry Blades vs CH-47C Production Blades, RPM Sweep at 157 Knots, 34,500 Pounds TOGW.

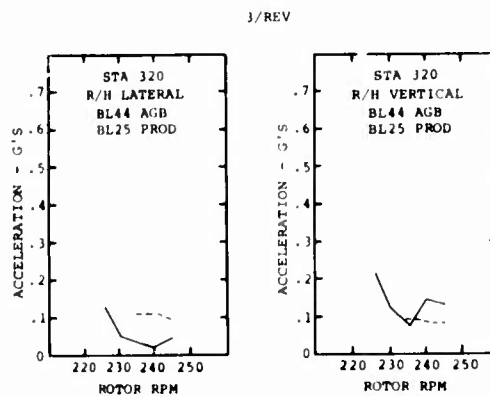


Figure 269. CH-47C Airframe Vibration, Advanced-Geometry Blades vs CH-47C Production Blades, RPM Sweep at 157 Knots, 34,500 Pounds TOGW.

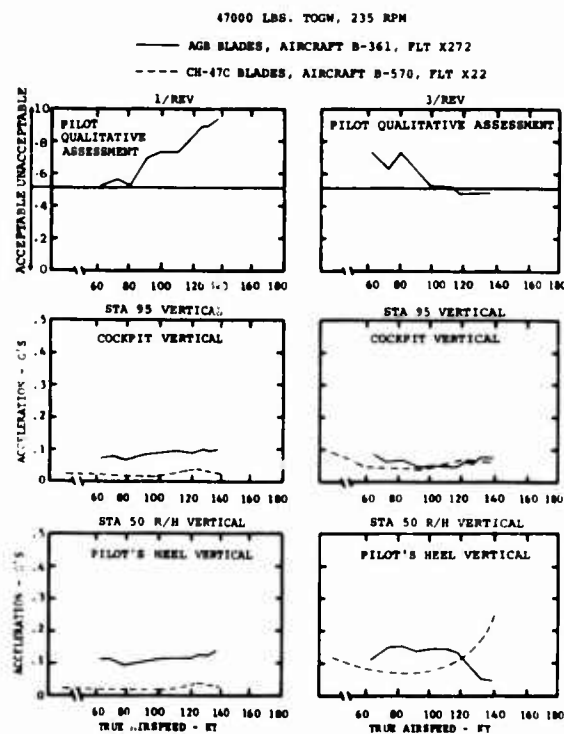


Figure 270. Cockpit Accelerations, Advanced-Geometry Blades vs CH-47C Production Blades.

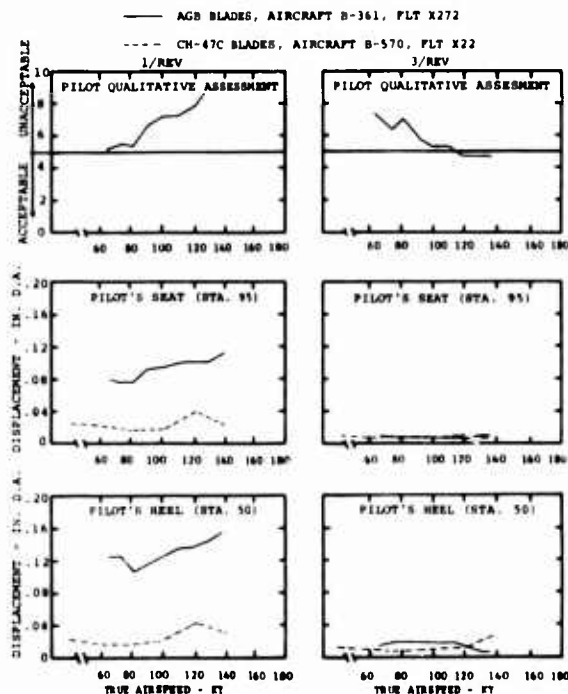


Figure 271. Cockpit Vibration Displacements, Advanced-Geometry Blades vs CH-47C Production Blades, 47,000 Pounds TOGW, 235 RPM.

of motion than "g" level. Referring to Figure 271, it is noted that the cockpit displacement with AGB is between 0.10 and 0.15 inch double amplitude compared to less than 0.05 inch for production blades. This amplitude increase of 2 to 3 times would provide a very poor ride quality and would, without question, be judged unacceptable by the pilot.

Three/rev vibration was judged unacceptable by the pilot for the AGB, disagreeing with the measured data which show vibration levels similar to those of the production blades. The opinion is that the qualitative assessment of 3/rev vibration by the pilot is adversely influenced by the presence of the large displacement at 1/rev. The assessment shows an improvement with airspeed, following the trend of the vertical vibration at the pilot's heel.

Maneuver Vibration Comparison

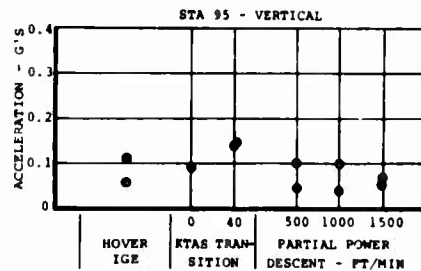
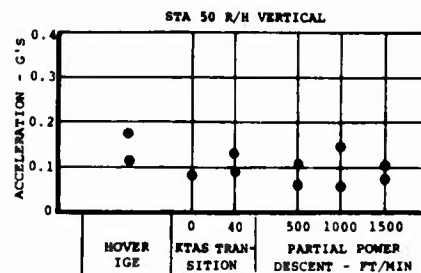
Maneuver vibration in the cockpit at 3/rev with AGB is compared to the CH-47C production configuration in Figures 272 and 273. In the vertical direction at both Station 50 RH and Station 95 during partial-power descents, the vibration with AGB is higher than the production configuration but within the vibration specification; lateral and longitudinal levels in the cockpit are slightly lower. Transition vibration levels are approximately the same. For IGE hover, the comparison shows no trends.

One/Rev Vibration Investigation

During the Flight Test Program, objectionable 1/rev vertical vibration was encountered with the AGB. Flat pitch ground tracking was unusually sensitive to pitch link adjustments, and such ground-established tracks generally proved inadequate in flight. As a consequence, it became necessary to make track adjustments based on inflight observations in order to continue the flight program. Continuous pitch link adjustments were necessary as the airspeed gross weight envelope was expanded, and the procedure was only moderately successful. The trailing-edge tabs on all blades, which were adjusted during tracking on the whirl tower, were not readjusted during the flight program. Ground tracking records indicate that the odd blades were S/N 105-1 in the forward set and S/N 102-2 in the aft set.

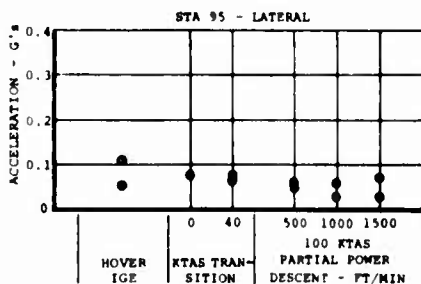
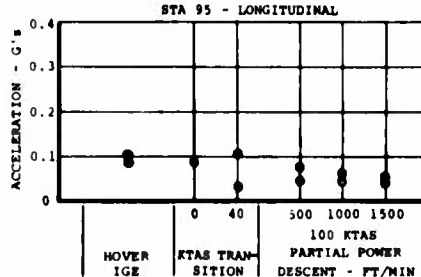
Analytical Investigation

Following the Flight Test Program, an analytical investigation was undertaken to determine the source of the 1/rev vibration encountered during flight test. Figures 274 and 275 show the twist distribution measured on the forward and aft blade sets, respectively. Figures 276 and 277 show the effective blade twist, which is the measured twist after the angle-of-attack shift due to trailing-edge tab variations is included.



● CH-47C PRODUCTION BLADES, AIRCRAFT B-570
 ○ AGB, AIRCRAFT B-361

Figure 272. Maneuver Vibration, Cockpit Vertical Advanced-Geometry Blades vs CH-47C Production Blades, 34,500 Pounds TOGW, 235 RPM.



● CH-47C PRODUCTION BLADES, AIRCRAFT B570
 ○ AGB, AIRCRAFT B361

Figure 273. Maneuver Vibration, Cockpit Lateral and Longitudinal Advanced-Geometry Blades vs CH-47C Production Blades, 34,500 Pounds TOGW, 235 RPM.

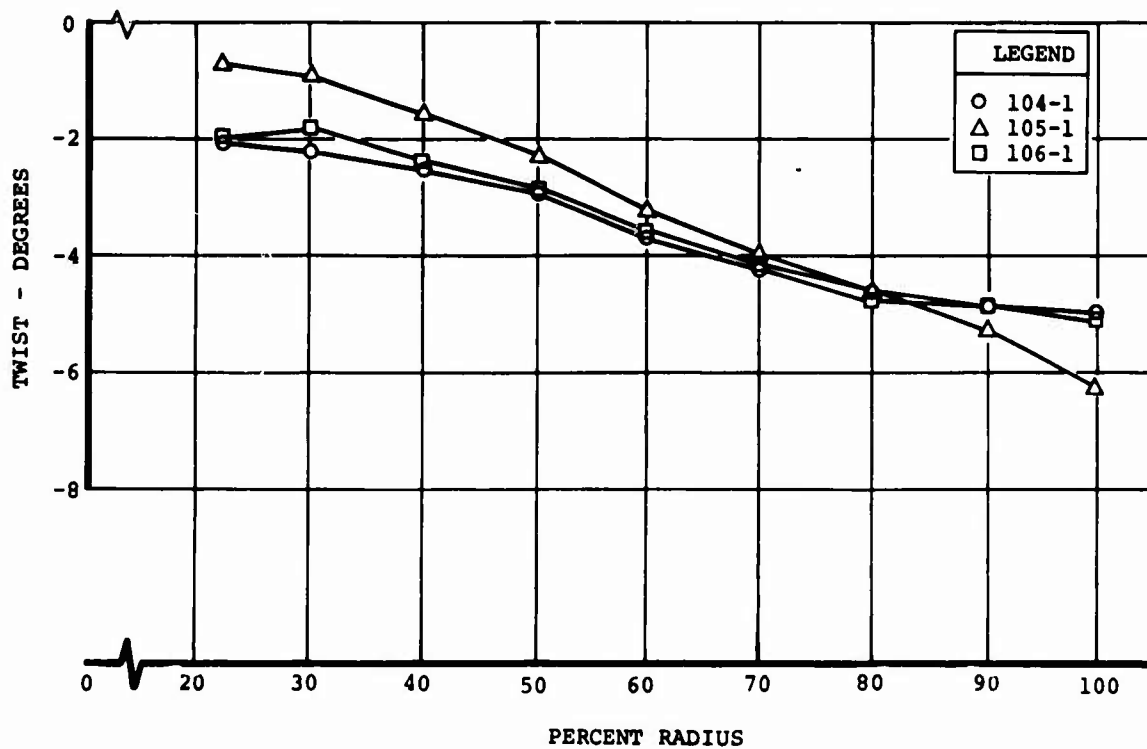


Figure 274. Measured Twist, AGB Forward Rotor Blades.

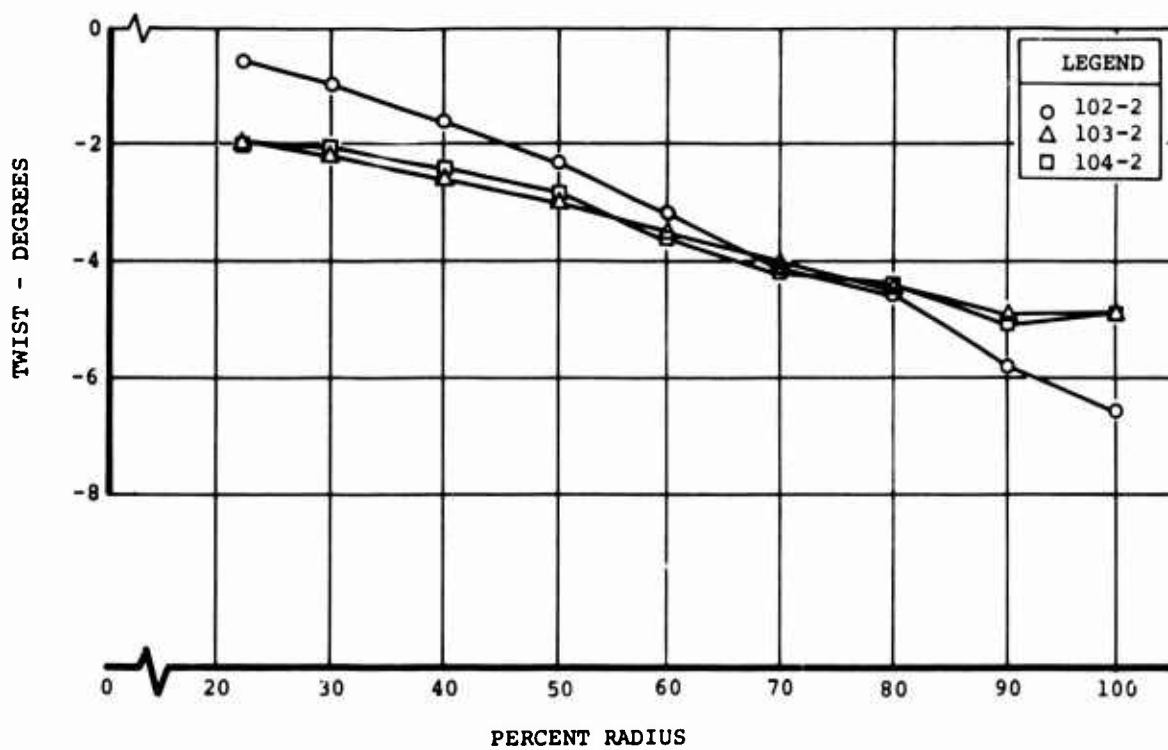


Figure 275. Measured Twist, AGB Aft Rotor Blades.

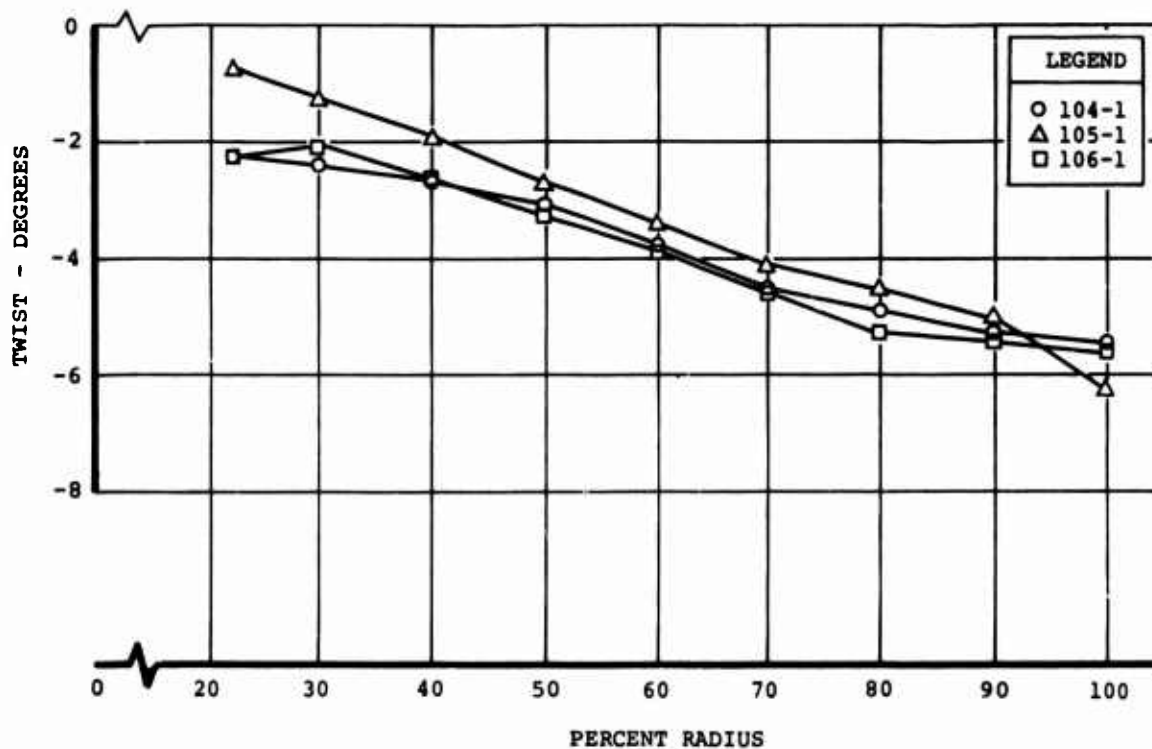


Figure 276. Effective Twist, AGB Forward Rotor Blades.

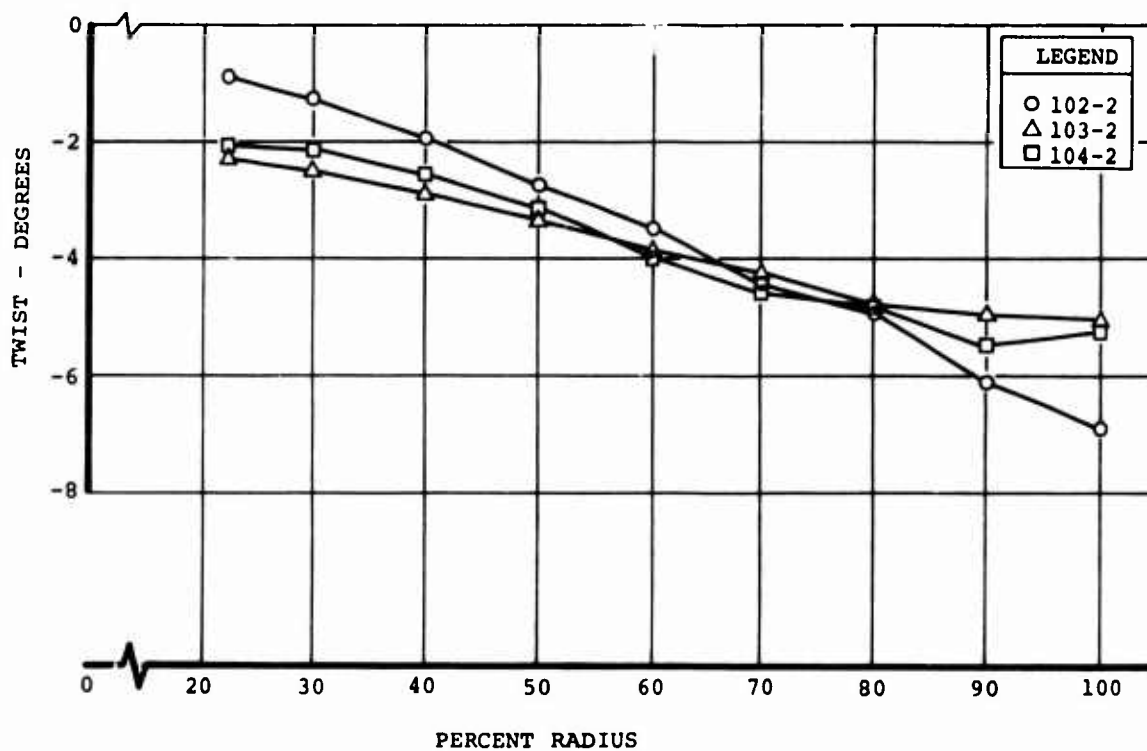


Figure 277. Effective Twist, AGB Aft Rotor Blades.

As can be observed, the influence of the trailing-edge tab deviation from the nominal value is not large, and both the measured and effective twist exhibit the same general pattern; i.e., forward blade S/N 105-1 and aft blade S/N 102-2 appear to have significant twist defects relative to the other blades in the set. However, the effect of whirl tower trailing-edge tab adjustments was significant enough to allow the blades to be tracked on the whirl tower. The blades could not be tracked adequately on the whirl tower by weights and pitch link adjustments alone.

The effect of the measured trailing-edge tab angle on the local pitching moment coefficient is shown in Figures 278 and 279. Forward blade S/N 105-1 appears to be particularly mismatched in local pitching moment level. Significantly enough, blade S/N 105-1 is also the blade most seriously mismatched in twist, and therefore the blade which required the largest trailing-edge tab adjustment during whirl tower tracking. In the case of the aft rotor, the mismatch is less pronounced, but still far from negligible.

Using the effective twist values together with the spanwise variation in pitching moment coefficient due to trailing-edge reflex, calculations were performed to determine the tip track at 140 knots. The results shown in Figure 280 indicate that the best track with pitch link adjustment is 2.8 inches for the forward rotor and 1.1 inches for the aft rotor. In the case of the forward rotor, the out-of-track condition is due primarily to blade S/N 105-1 with the mismatch in both twist and pitching moment. On the aft rotor, blade S/N 102-2, which is mismatched in twist, is low, but the mean track is parallel and can be somewhat compensated for by a pitch link adjustment.

Historically, there is little question that a 2.8-inch, out-of-track condition can lead to a substantial 1/rev vertical vibration. General CH-47 flight test experience indicates that an aircraft which is 1.0 inch out-of-track generally has a total 1/rev vertical vibration approaching 0.065 "g". On this basis, a 2.8-inch out-of-track would lead to 1/rev levels of approximately 0.18 "g".

It is still not clear which one, the twist variation or the pitching moment deviations, was the main cause of 1/rev vibrations in flight. However, an investigation of 1/rev problems conducted on CH-47B blades in 1967 and 1968 showed that the most significant cause of 1/rev vibrations was the variation from blade to blade of the local pitching moment coefficient. This variation was due to manufacturing inaccuracies in blade contour and trailing-edge angle accuracy (significant twist deviations did not exist); and after the pitching moment deviations were corrected locally by means of an aerodynamic correction (trailing-edge wedges), the 1/rev vibration level was very significantly reduced.

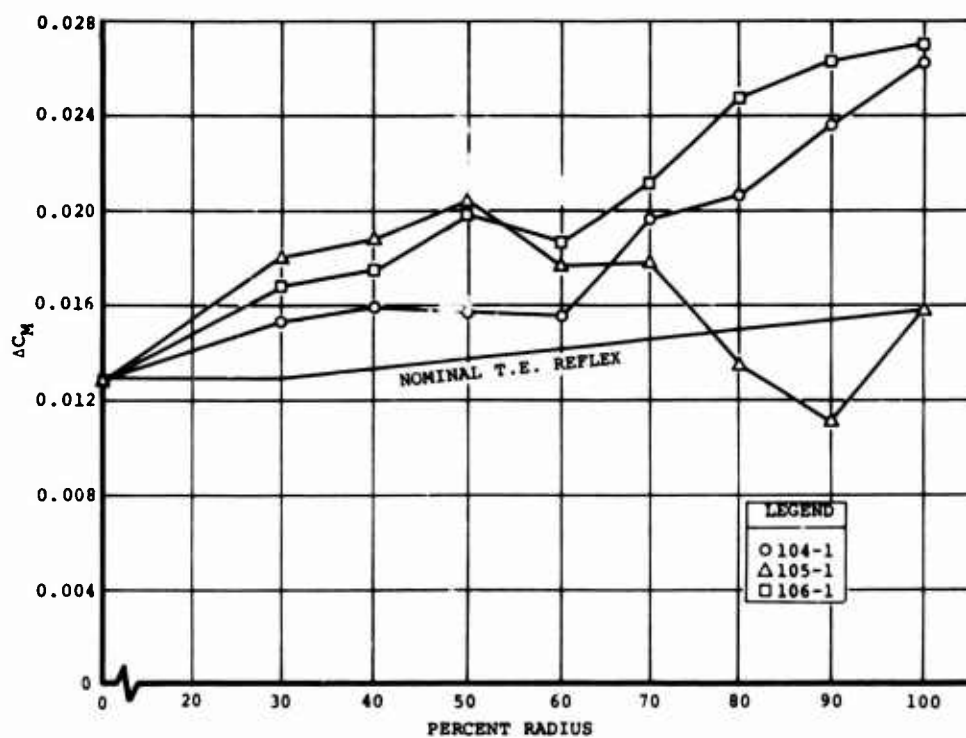


Figure 278. Pitching Moment Variation, AGB Forward Rotor Blades.

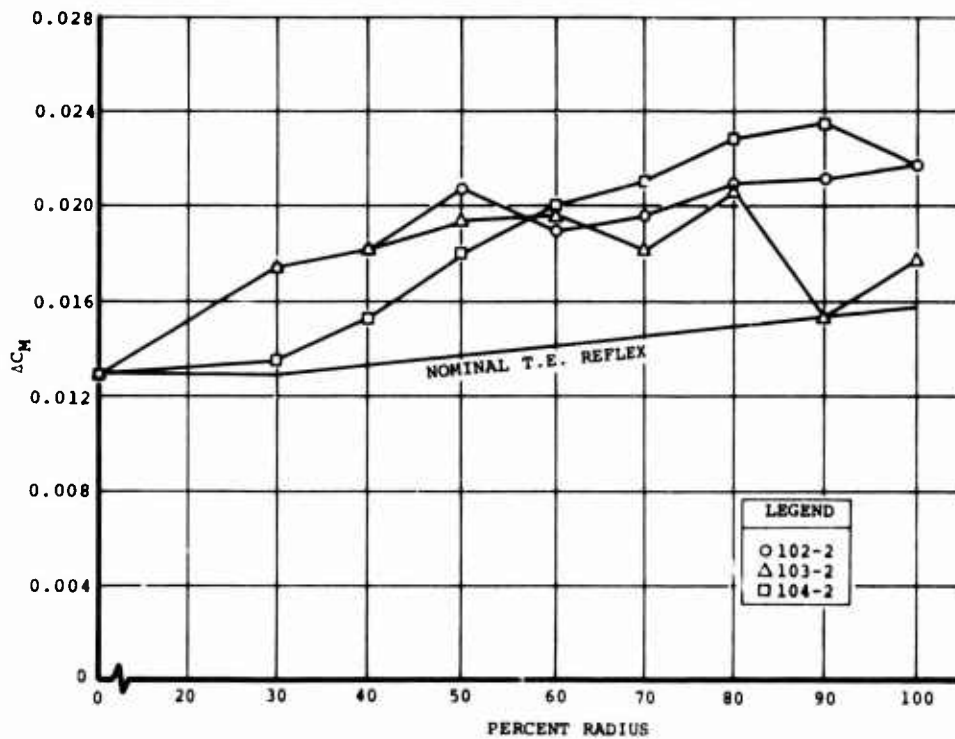


Figure 279. Pitching Moment Variation, AGB Aft Rotor Blades.

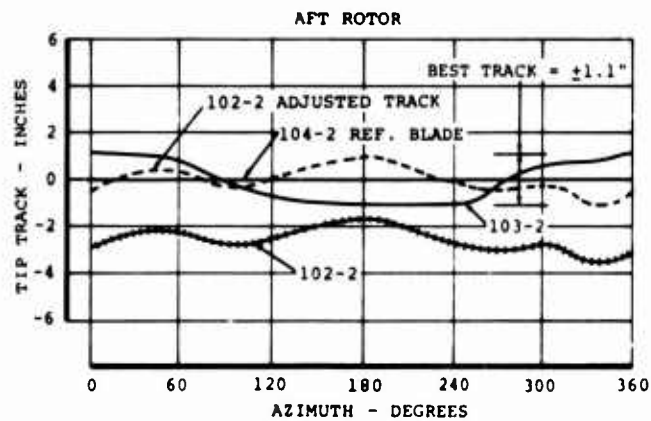
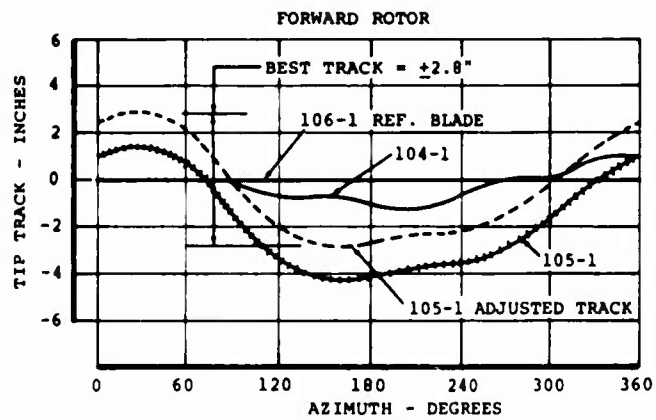


Figure 280. AGB Calculated Track at 140 Knots.

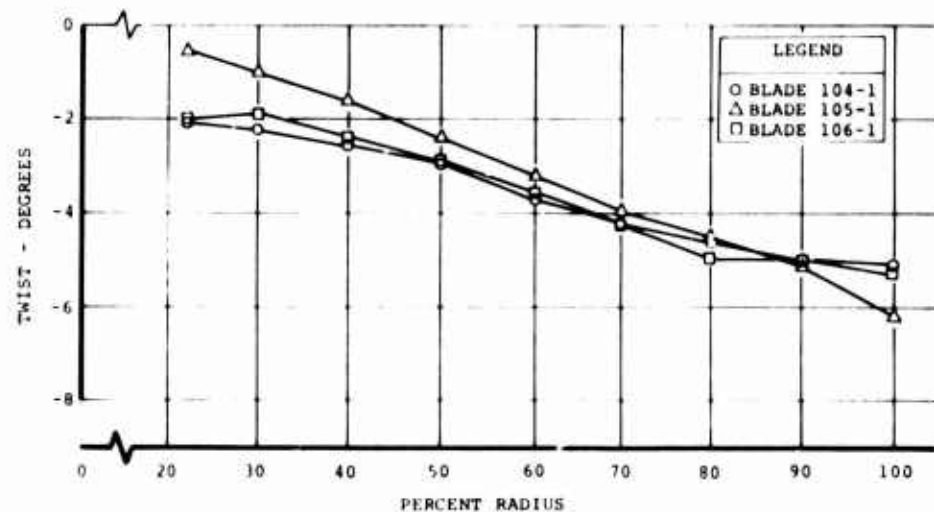
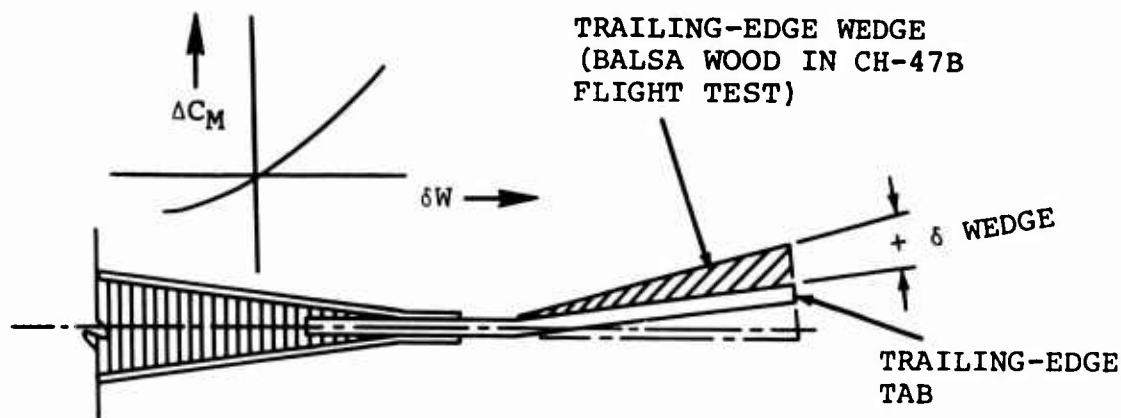


Figure 281. Effective Twist With T.E. Wedges, AGB Forward Rotor Blades.

In order to isolate analytically the effect of twist variations on the 1/rev vibration level, the local pitching moment deviations were ideally eliminated by means of the aerodynamic correction used in the CH-47B program (trailing-edge wedges), as shown below.



The effect of trailing-edge wedges on the effective twist is shown in Figures 281 and 282. Tip track with the wedges was calculated and is presented in Figure 283.

On the forward rotor, where blade S/N 105-1 exhibited a calculated out-of-track condition of ± 2.8 inches and displayed a considerable nonparallel tip path, the effects of pitching moment correction (via wedges) was quite significant; i.e., Figure 280 shows S/N 105-1 can be made to fly "more parallel", and the out-of-track condition could then be analytically "pitch link adjusted" for an out-of-track reduction from ± 2.8 inches to ± 1.0 inch.

On the aft rotor, Figure 280 showed blade S/N 102-2 out-of-track by ± 1.1 inches, but with a more parallel tip path than S/N 105-1 on the forward rotor. Pitching moment correction (via wedges) for aft blade S/N 102-2, although reshaping the tip path somewhat, does not provide (when analytically "pitch link adjusted") an improvement on the aft rotor track. Figure 283 shows that ± 1.1 inches out-of-track would still occur.

For either rotor, ± 1 inch out-of-track historically would suggest a condition which would still have excessive 1/rev vibration levels. Further improvement could only be obtained by closer matching of blade twist.

Aircraft Investigation

Pitch link bearing clearances were investigated as a possible source of 1/rev vibration; however, the tabulated results of Table XL show no clearances considered sufficient to constitute a problem at 1/rev.

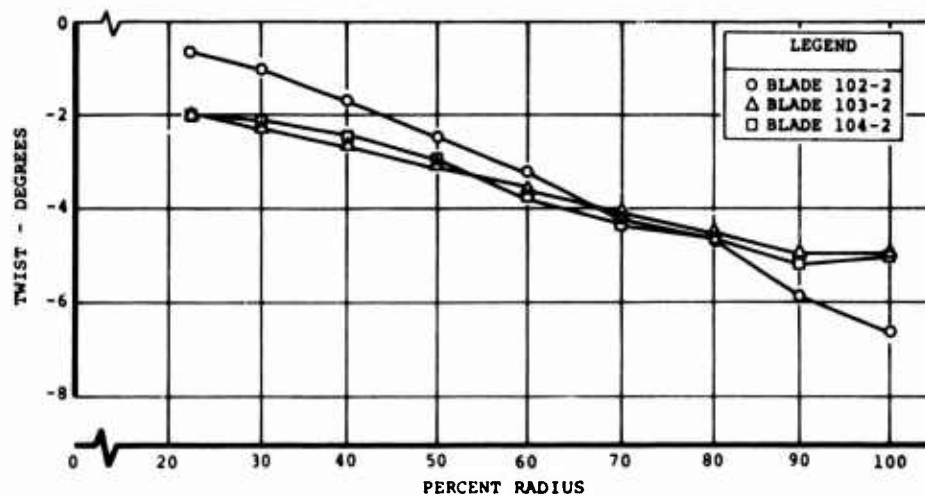


Figure 282. Effective Twist With T.E. Wedges, AGB Aft Rotor Blades.

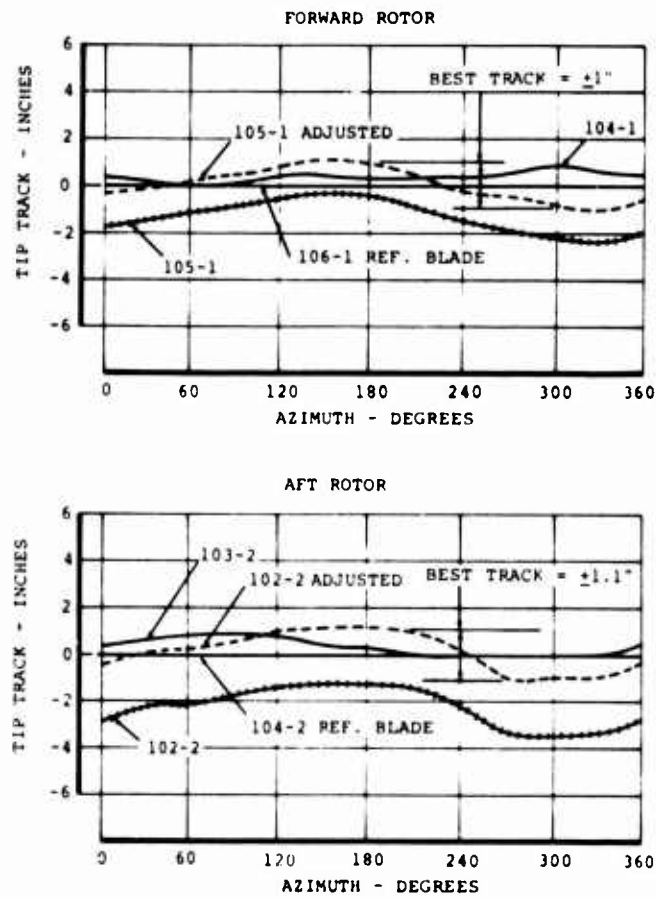


Figure 283. AGB Calculated Track at 140 Knots With T.E. Wedges.

TABLE XL. PITCH LINK ROD END BEARING CLEARANCE MEASUREMENTS		
Pitch Link Assembly	Total Radial Play (in.)	
	Rod End No. 1	Rod End No. 2
1	0.0030	0.0050
2	0.0015	0.0040
3	0.0025	0.0030
4	0.0040	0.0050
5	0.0025	0.0050
6	0.0055	0.0053
NOTE: Pitch links were inspected at conclusion of the AGB Flight Test Program.		

To determine the extent to which 1/rev vibration was being influenced by rotor-to-rotor aerodynamic interference, representative 1/rev vertical data was obtained in yawed flight. Results plotted in Figure 284 for 60 and 120 knots show no significant variation in the 1/rev levels with side-slip angle. It is concluded, therefore, that the 1/rev with AGB is not usually sensitive to rotor interference effects.

Principal Results and Observations

1. One/rev vibration levels were generally unacceptable throughout the flight program and were consistent with out-of-track blades. Analysis indicates that tracking of the blades to an acceptable tolerance can not be accomplished without correcting the twist differences between blades. With correction of this fabrication tolerance problem, the 1/rev vibration levels with AGB should fall within the requirements of the CH-47C specification.
2. In general, vibration at 3/rev for the CH-47C equipped with AGB was similar to the production configuration. For 47,000 pounds takeoff gross weight, lateral vibration was higher at speeds below 120 knots; vertical vibration was much lower at mid-cabin station 320. High-speed 3/rev vibration (160 knots) for 34,500 pounds takeoff gross weight appeared slightly lower with the AGB. Ballast arrangement between aircraft is a logical explanation of local variations in vibration level. Equipped with AGB, the 3/rev vibration is within the CH-47C specification.
3. Cyclic trim variations at 100 knots have no significant influence on 1/rev and 6/rev vibration. However, large changes are experienced for 9/rev and 12/rev vibration at station 95 vertical; no other stations show the effect. For this station, with aft cyclic extended and forward retracted, and forward and aft extended, the vibration increases from 0.10 "g" to 0.25 "g" at 9/rev, and from 0.05 "g" to 0.3 "g" at 12/rev.
4. Maneuver vibration of the CH-47C equipped with AGB is within the CH-47C production specification.
5. Qualitative assessment of vibration by the pilot shows poor agreement with the measured data. The high 0.1 "g" 1/rev vibration produced double amplitudes of 0.10 inch, which result in poor ride quality. Pilot assessment of 1/rev vibration as very unacceptable reflects the large amplitude, and the 3/rev assessment is adversely influenced by the presence of the large 1/rev displacements.

B-361, FLT X222, 48,000 LB TOGW, 3.4 IN. AFT TOCG

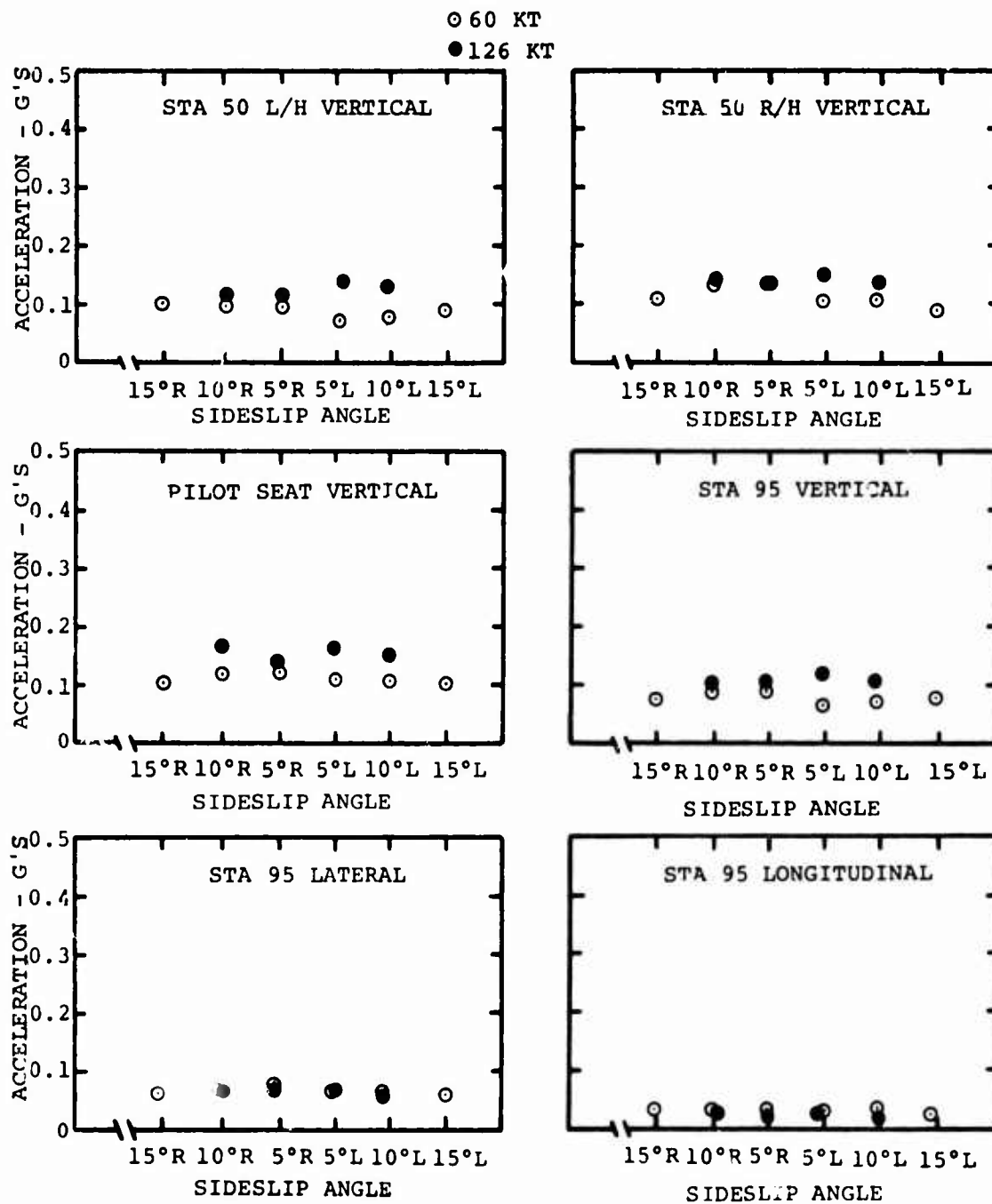


Figure 284. CH-47C 1/Rev Vibration With AGB Yawed Flight at 245 RPM.

PERFORMANCE

Performance Capabilities of the AGB Rotor Compared to the CH-47C Rotor

This section presents the performance analysis and results of the AGB flight program and compares the capabilities of the CH-47C with AGB rotors to those of the production CH-47C. The areas of investigation in this phase of the program include hover out of ground effect, and level-flight power required. Out-of-ground-effect (OGE) hover data were obtained on one flight utilizing external loads. Level-flight power-required polars were gathered during five performance flights and during three strain survey flights. Test conditions are shown in Table XLI.

The dimensional characteristics of the CH-47C production rotor, the AGB rotor, and the wind tunnel model AGB rotor are compared in Table XLII, and plan views of the rotor blades are shown in Figure 285. The rotor solidity difference between the production CH-47C rotor and the AGB rotor is of particular significance in the discussion which follows. Because of the difference in solidity, the test results presented in this report cannot be compared directly. To show a meaningful comparison, in addition to showing the production CH-47C test results, a theoretical correction has been added to a few selected hover and forward flight charts to illustrate the effect of the difference; the benefits derived from the difference in blade twist, planform, thickness and airfoils can then be assessed.

Hover Out-of-Ground-Effect (HOGE) Performance Summary

A comparison of the AGB rotor and production CH-47C rotor figure of merit is shown in Figure 286. The figure of merit shown for the CH-47C tandem-rotor configuration includes the power required for transmission losses, accessory power, rotor overlap induced power, and airframe down-load based on flight test data. The isolated rotor figure of merit was obtained by subtracting power and thrust (download) increments noted above. The figure of merit of the total configuration is shown to be equal for the AGB rotor ($\sigma = 0.0845$) and the production rotor ($\sigma = 0.067$) at a thrust coefficient of 0.0070 (figure of merit is 0.573). However, when the production rotor power is incrementally adjusted for the solidity difference, the AGB rotor at a thrust coefficient of 0.0070 would have a 0.07 figure of merit advantage over the production rotor. The 0.07 increase in figure of merit is equivalent to a 1.5 percent reduction in power required. This is a small advantage and is within the range of measurement accuracy. Of more significance is the trend of the figure of merit with increasing thrust coefficient. The trend suggests that the AGB rotor would widen its advantage over the production rotor at higher thrust coefficients and higher tip speeds than those demonstrated.

TABLE XLI. AGB ROTOR TEST CONDITIONS

Flight Condition	Nominal Gross Weight (lb)	CT/o	True Airspeed (kt)	Pressure Altitude (ft)	Rotor Tipspeed (fps)	Advancing Blade Tip Mach Number	μ
Hover out of ground effect	41,000 to 47,000	0.0640 to 0.0815	Ground speed zero. Wind speed less than 5 knots	Sea level	707 to 773	0.622 to 0.686	0
Forward level flight	33,000 to 52,000	0.0535 to 0.1015	50 to 165	2,000 to 10,000	729 to 773	0.736 to 0.92	0.114 to 0.375

**TABLE XLII. COMPARISON OF THE PRODUCTION CH-47C
ROTOR AND AGB ROTOR**

Characteristic	1/7.377 Model AGB*	Production CH-47C	AGB
Rotor Radius	48.8 in.	30 ft	30 ft
Blades Per Rotor	3	3	3
Blade Chord (at .75R including trailing-edge tab)	4.28 in.	25.25 in.	33.3 in.
Rotor Solidity		0.067	0.0845
Blade Thickness	AGB Taper	Constant	Tapered
Blade Planform	1.31 taper ratio	Constant chord (rectangular)	1.31 taper ratio
Blade Twist	-6.1°	-9.1°	-6°
Blade Root Cutout	16% radius	10% radius	Inverse taper from 16% radius to 32% radius
*See Reference 14 for further details and performance characteristics.			

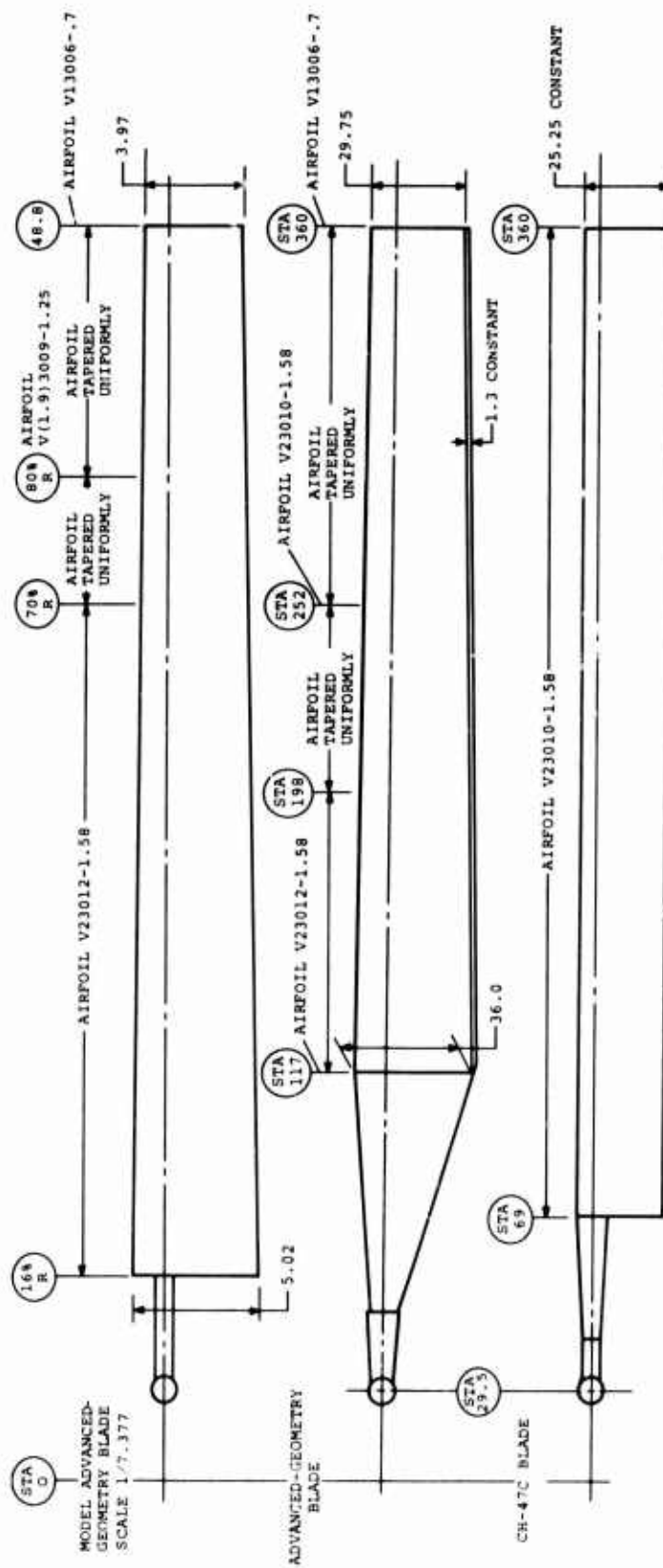
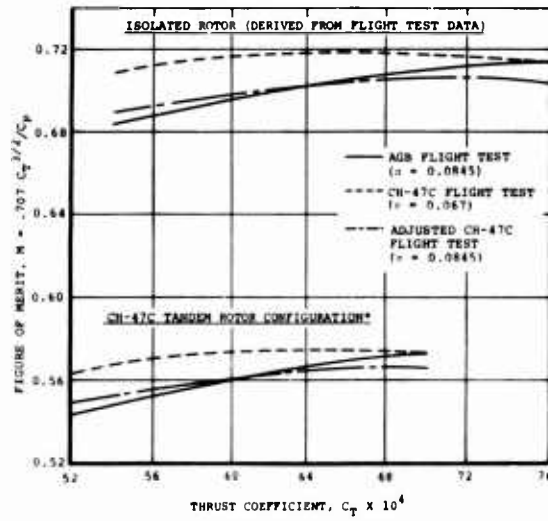


Figure 285. Rotor Blade Geometric Characteristics.



*INCLUDES TRANSMISSION LOSSES, AUXILIARY POWER, ROTOR OVERLAP INDUCED POWER AND AIRFRAME DOWNLOAD BASED ON FLIGHT TEST DATA. C_T BASED ON AIRCRAFT GROSS WEIGHT.

Figure 286. CH-47C/AGB Rotor Figure of Merit - Hover Out of Ground Effect at 235 Rotor RPM.

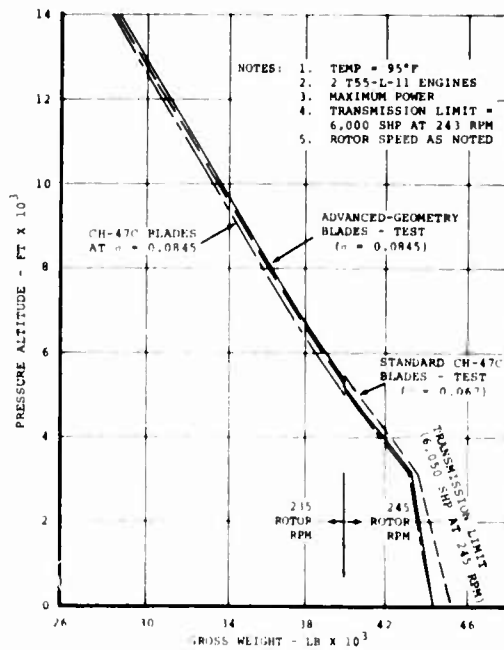


Figure 287. Comparison of Hover Capability Out of Ground Effect for Conventional and Advanced-Geometry Blades.

Effects of twist and taper on hover power required were examined theoretically. AGB rotor twist is approximately -6° compared with -9.1° for the CH-47C; taper ratio is 1.31 compared with 1. The reduction in twist results in an estimated increase in power required of 1.3 percent, while the increased taper decreases power required by a similar amount.

Using the flight test power required measured for the rotors, the hover ceiling capability chart presented in Figure 287 was derived. Hover OGE ceiling at 90°F temperature is shown for the production CH-47C ($\sigma = 0.067$), the CH-47C with the AGB rotor, and the CH-47C with the production rotor corrected to a solidity equal to the AGB ($\sigma = 0.0845$). At the 6000 feet, 90°F condition, the AGB rotor displays about a 200-pound advantage over the production rotor ($\sigma = 0.067$) and about a 600-pound advantage over the production rotor at equal solidity ($\sigma = 0.0845$). The advantage of the AGB rotor would be further exploited when operating at higher power, higher thrust, higher tip speeds, and lower ambient temperatures to take advantage of the better compressibility characteristics of the thin blade tips of the AGB.

Forward-Flight Performance Summary

A comparison between the AGB rotor (model and full scale) and the production CH-47 rotor nondimensional power requirements at an advance ratio of 0.35 is shown in Figure 288. The increased power requirements of the full-scale AGB rotor at higher thrust coefficients can be attributed to the stall characteristics of the thin airfoils near the tip and to the difference in root cutout. Comparison of the model AGB rotor at high lift levels suggests that a difference in root cutout may penalize the AGB more than expected. The model AGB rotor, which compared very favorably with the CH-47C production rotor, had a root cutout of only 16 percent without the reverse taper of the full-scale AGB (see Figure 285).

At low lift levels ($C_T/\sigma = 0.06$), the benefits of the thin (V13006-1.58) tip airfoil section of the AGB are manifested in significantly reduced compressibility power at Mach number up to 0.93 - 0.95. Unfortunately the maximum level-flight advance ratio attained during the AGB flight program was $\mu = 0.375$ due to transmission torque limitations on the test aircraft.

Power required versus true airspeed at 3000 feet, standard temperature conditions is shown in Figure 289 for the CH-47C with AGB blades ($\sigma = 0.0845$), CH-47C production blades ($\sigma = 0.067$), and the estimate for increased solidity production blades ($\sigma = 0.0845$). Also shown is the estimated power required of the AGB system with the airframe drag (D/q) of the CH-47C reduced to 36

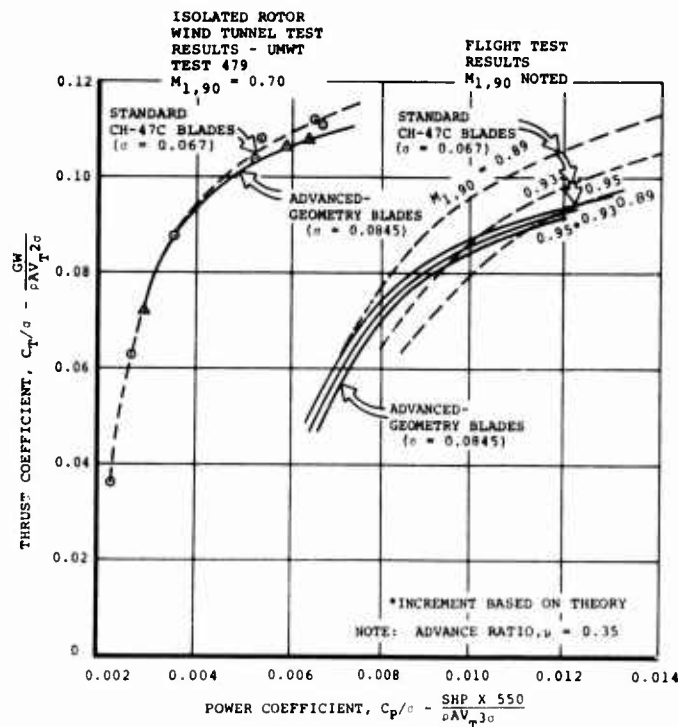


Figure 288. Comparison of Nondimensional Power Requirements of Conventional and Advanced-Geometry Blades.

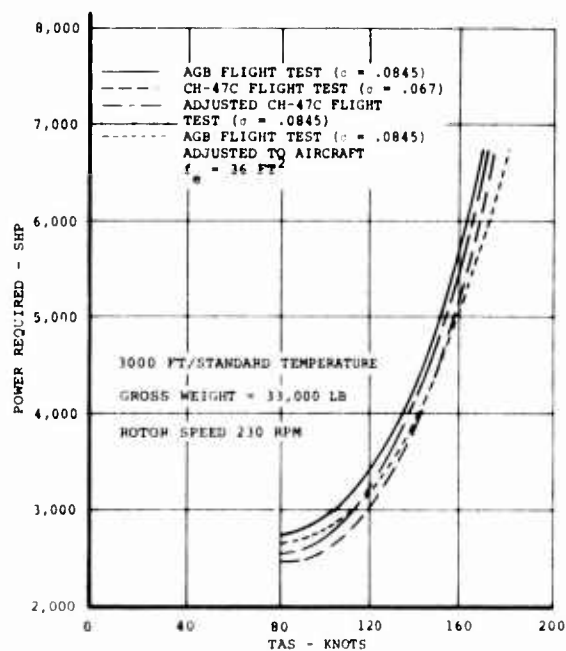


Figure 289. Comparison of Power Required With Conventional and Advanced-Geometry Blades at 3,000 Feet and Standard Temperature.

square feet (baseline drag at zero angle of attack). Table XLIII shows the power required for each configuration at 165 knots:

TABLE XLIII. POWER REQUIRED AT 165 KNOTS			
Configuration	Source of Data	Power Required (shp)	Trim Airframe and Hub Drag at 165 kt, D/q (sq ft)
AGB Rotor ($\sigma = .0845$)	Flight test	6,230	53
Adjusted Production CH-47C Rotor ($\sigma = .0845$)	Corrected flight test	6,000	53
Production CH-47C Rotor ($\sigma = .067$)	Flight test	5,670	51
AGB Rotor With Reduced Drag ($\sigma = .0845$)	Corrected flight test	5,250	37

The conditions at 165 knots in Figure 289 are not the optimum for exploiting the advantages of the AGB rotor; at 165 knots, $\mu = 0.38$, $C_T/\sigma = 0.0597$ and the advancing tip Mach number is only 0.905. The maximum lift to drag ratio would occur at C_T/σ of about 0.075, and the AGB rotor does not have a significant compressibility advantage over the production rotor when the advancing tip Mach number is below 0.93 (see Figure 288). To exploit the speed advantages of the AGB rotor, more installed power and reduced airframe drag would be required.

Figure 290 presents a comparison of adjusted AGB flight test power requirements with current prediction methodology and the 1965 AGB proposal level of performance at an aircraft flatplate area of 36 square feet ($\alpha_f = 0$). The reasons for the overly optimistic prediction made in 1965 for the AGB rotor proposal are attributed to underestimating the profile power and overestimating the propulsive efficiency capabilities of rotors at advance ratios above 0.4. Evidence of the optimistic estimate of the profile power is shown in Figure 290 at 100 knots, where the power requirement of the configuration is very low when compared to the levels measured in the flight test program. This estimate was based on theory and model rotor test data available at that time. Regarding propulsive efficiency of rotors, model rotor tests and full-scale rotor tests indicate a rapid deterioration in propulsive efficiency at advance ratios greater than 0.35 (Reference 15).

The optimistic propulsive efficiency used in 1965 to estimate the AGB rotor capability for a "cleaned up" CH-47 airframe ($f_e = 36$ square feet) accounts for most of the difference between that estimate and the estimate based on the flight test data collected in this program. The basic profile power difference accounts for the remainder of the difference in total power required.

The current prediction methodology is based on a longitudinal trim and power analysis (Reference 16) which employs extended lift tabular airfoil characteristics (extended to $20^\circ \alpha$ without stall) and nonuniform downwash corrections, and assumes a rigid blade. This methodology is currently being revised to include unsteady aerodynamic effects on blade lift and angle of attack, aeroelastic effects on blade torsional and flapwise bending, and spanwise (radial) flow considerations. These modifications will improve the prediction capability at high airspeeds.

Performance Test Program

Aircraft Configuration

The test aircraft was basically a FY 68, CH-47C with two T55-L-11 engines. For the AGB rotor test program, the current 6000-shp transmission limitation was increased to 6800 shp at 243 rpm to provide increased performance margins at high gross weight and airspeed. The external configuration of the test aircraft (S/N 66-19103) is presented in Table XLIV. Primary differences between the CH-47C aircraft described in the detail specification, Reference 17, and the test aircraft are the addition of instrumentation "satellites" to each rotor head, the airspeed nose boom, and the deletion of two external antennas (AS-1922 and AN/ARC-102). These external changes result in an additional 3.05 square feet of equivalent flatplate drag area for the test aircraft as compared to the specification CH-47C. The power required derived from measured test data was decrementally adjusted to negate the drag of these additional items. The performance shown throughout this report is representative of a specification CH-47C aircraft equipped with AGB rotors.

The longitudinal cyclic trim schedule employed during the acquisition of performance data for the AGB rotor is presented in Figure 291. This schedule represents the standard trim for the CH-47C aircraft.

Performance Test Instrumentation

During the AGB rotor performance testing, data parameters were recorded on magnetic tape and by an observer in the cockpit. The following parameters were recorded.

AMPEX MAGNETIC TAPE RECORDER

1. Airspeed - Boom System
2. Airspeed - Ship System

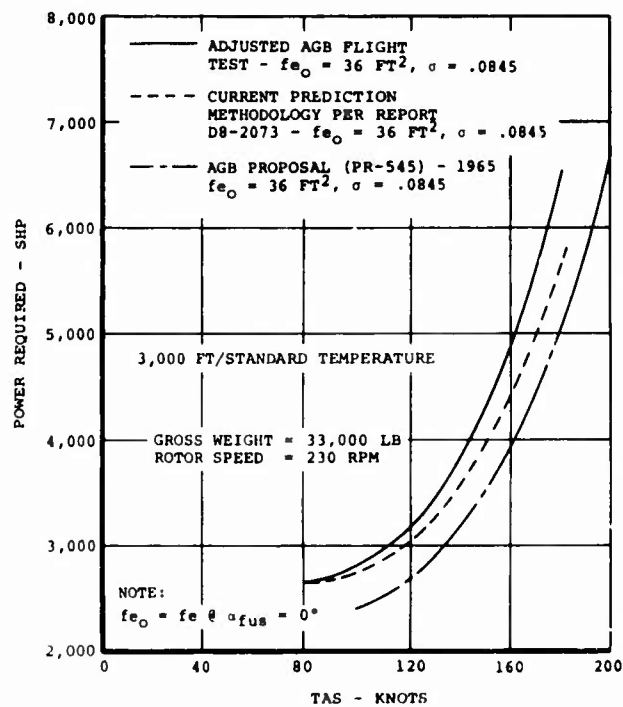


Figure 290. CH-47C/AGB Rotor Comparison of Flight Test and Predicted Power Required at 33,000 Pounds and 230 RPM.

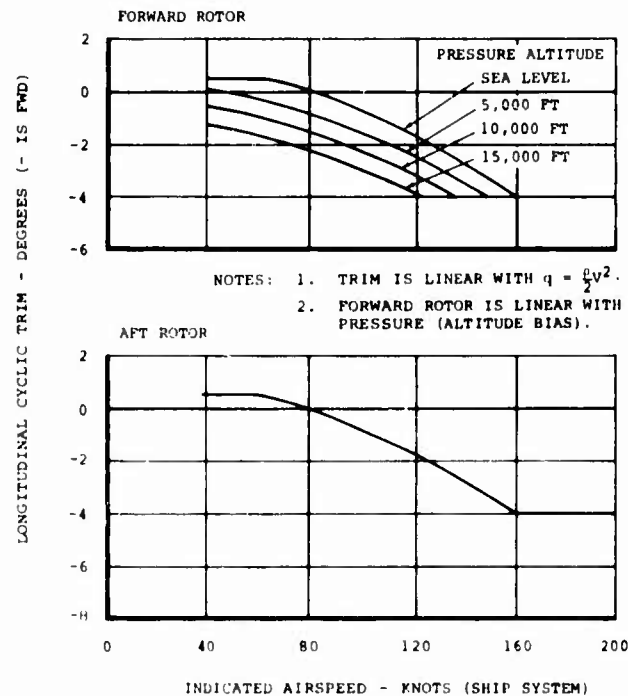


Figure 291. Longitudinal Cyclic Trim Schedules for CH-47C Helicopter Equipped With Advanced-Geometry Blades.

TABLE XLIV. EXTERNAL CONFIGURATION CH-47/AGB ROTOR
FLIGHT TEST AIRCRAFT S/N 66-19103

Item	Included in Configuration Per EV Report 114-PJ-803	Increase in Test Airframe Drag (sq ft) *
1. Instrumentation "satellites", one mounted vertically on each rotor shaft	No	3.0
2. Airspeed nose boom with swiveling pitot-static tube extending forward from fuselage nose. (Length = 132 in., diameter = 3.5 in.)	No	0.32
3. Cover plate mounting flanges (adjacent to sync-shaft tunnel cover)	No	0.19
4. Antennas (underside of fuselage)		
a. AN/ARC-54 (Whip Antenna-on C_L at STA 55)	Yes	-
b. APX-44/72 (IFF Small Blade Antenna on C_L at STA 90)	Yes	-
c. AS-1922 (FM Loop Antenna - C_L at STA 130)	Yes	0.04
d. AT-1108/ARC (VHF/UHF Large Blade Antenna - on C_L at STA 150)	Yes	-
e. AN/ARN-83 (Sense and Loop Antennas in boat fairing - on C_L at STA 190)	Yes	-
f. AT-640 A/ARN (Small Blade Antenna - on C_L at STA 230)	Yes	-
5. Antennas (side of fuselage)		
a. DM4-4 (Split Loop Antennas - one on each side of fuselage at STA 330 and WL8)	Yes	-
b. AN/ARC-102 (HF Long Wire Antenna - mounted on left side of fuselage in the area bounded by STA 100 and 485 and WL (-)15 and 45)	Yes	0.42
*Drag increase relative to specification aircraft.	Total Airframe Drag Difference	3.05

3. Pressure Altitude - Ship System
4. Outside Air Temperature
5. Rotor Speed - 1/Rev Frequency
6. Rotor Cyclic Trim - Forward and Aft Rotors
7. Angle of Sideslip - Mounted on Forward Shaft
'Satellite'
8. Rotor Shaft Torque - Six Torque Bridges:
Three Forward and Three Aft
9. Fuel Flow - Potter Volume Flowmeter; #1 and #2 Engines
10. Total Fuel Burned Per Engine - Potter Fuel Totalizers
11. Fuel Temperature at Flow Meter; #1 and #2 Engines
12. Engine Gas Generator Speed: #1 and #2 Engines
13. Engine Shaft Torque; #1 and #2 Engines
14. Record Coder
15. Time Code Generator - Dubbed Onto Tape
16. Airborne Time Code Generator - Elapsed Time During Flight

COCKPIT OBSERVER

1. Airspeed - Boom System
2. Pressure Altitude - Ship System
3. Outside Air Temperature
4. Rotor Speed
5. Engine Torque; #1 and #2 Engines
6. Potter Fuel Totalizers; #1 and #2 Engines

7. Aircraft Fuel Quantity Remaining

8. Record Number

9. Time Stopwatch

The information recorded in the cockpit was used to check the basic aircraft parameters as recorded on tape. Tape data systems were used as the final data source for all parameters except for total fuel burned and engine shaft torque. As regards the fuel burned, the automatic data reduction program incorporates a fixed fuel specific weight; performance data was derived using the cockpit observed fuel totalizers and actual fuel specific weights. Cockpit engine torque was utilized since engine torque as recorded on tape requires a nonlinear calibration to allow for the nonlinearity of the Lycoming torque-meter system.

Performance Test Conditions

Free-flight hover data was obtained utilizing an external load suspended from the cargo hook. Table XLV is a list of the pertinent hover test conditions.

TABLE XLV. OUT-OF-GROUND-EFFECT TEST CONDITIONS (150-FOOT WHEEL HEIGHT)					
Flt No.	Takeoff Gross Weight (lb)	Takeoff CG (in.)	Avg. Test Weight (lb)	Rotor Speed (rpm)	$\frac{N_R}{\sqrt{\theta}}$ (rpm)
X-280	33697	0.9 Fwd	42164 (1)	227-246	225-244
			46083 (2)	225-246	224-244
(1) High-density external load: Weight = 10,964 lb					
(2) High-density external load: Weight = 16,986 lb					

Level-flight speed-power polars were obtained at the nominal test conditions presented in Table XLVI.

TABLE XLVI. LEVEL-FLIGHT TEST CONDITIONS						
Flt No.	Takeoff Gross Weight (lb)	Takeoff CG (in.)	Rotor Speed (rpm)	Test Conditions W/δ (lb)	$N/\sqrt{\theta}$ (rpm)	Type of Flight
X-254	34835	6 Aft	236	37500	235	S&M ⁽¹⁾
			246	35700	245	
X-258	32662	2.0 Aft	236	33000	235	P ⁽²⁾
X-274	45756	1.7 Fwd	242	63000	235	P
X-276	33643	0.9 Fwd	237	33000	235	P
X-279	45065	0.6 Fwd	232	60000	235	P
			242	60000	245	
X-286	52282	0.2 Aft	245	68000	245	S&M
X-287	48148	10 Fwd	235	56000	235	S&M
			245	54600	245	
X-288	40080	3.1 Fwd	233	50000	235	P
(1) Stress and motion - rotor strain survey - level-flight speed sweep						
(2) Performance flight - level-flight power polars						

Performance Hover-OGE Test Procedure

Hover tests were conducted in free flight using internal ballast and high-density external loads. The height of the aft wheel was held constant at 150 feet using a weighted rope of known length and an observer. Wind speed and direction were monitored during the testing to insure that local winds did not exceed 5 knots. Two external loads of 10,964 pounds and 16,986 pounds, respectively, were used. The high values of thrust coefficient were obtained at the start of testing (high gross weight - low rotor speed). A 75-second data record was taken at each rotor speed with each external load. Rotor speed was successively increased in 5-rpm increments from minimum allowable to maximum allowable speed. Test conditions were repeated by successively decreasing rotor speed in 5-rpm decrements from maximum to minimum with each external load. Four data bits were obtained from each 75-second data record.

Performance Level-Flight Test Procedure

During performance flights, each speed-power polar was conducted at a constant generalized weight (W/δ) and generalized rotor speed ($N/\sqrt{\theta}$). Pressure altitude was increased to allow for fuel burnoff after each speed to decrease the ambient pressure ratio, δ , and thus maintain a constant value

of generalized weight. Rotor speed was adjusted as outside air temperature varied to maintain constant generalized rotor speed. The relationship between nondimensional and generalized parameters is developed in Appendix V. Stabilized test points were flown in 10-knot increments at speeds from approximately 40-knot boom IAS to maximum attainable airspeed as limited by engine power available, transmission limit, or telemetered rotor strain data. Test data was recorded at stabilized conditions with a test record length of 90 seconds. Four data bits at 30-second intervals were reduced from the test data. Rate of climb during each stabilized data record was monitored. The test point was repeated if a rate of climb exceeding ± 100 feet per minute was observed.

During rotor strain survey flights, performance parameters were recorded over a shorter period of time than on performance flights. Level-flight speed sweeps from approximately 50-knot boom IAS to maximum allowable airspeed were flown with one 10-second data record at each speed. Adjustments for fuel burnoff and generalized rotor speed were not made during the flight. Rate of climb and acceleration were not recorded.

Performance Data Acquisition and Reduction Methods

The test data was recorded on magnetic tape and reduced to engineering values using automatic analog-digital conversion and digital frequency counters. The pre-flight calibration on each parameter was used as the basis for all data; post-flight calibrations were used only as a check. Analog data such as airspeed, temperature, and rotor torque were derived for mean and alternating values. Digital data such as fuel flow, rotor speed, and altitude were compared to a known frequency over a time base and calibrated into engineering values. The data reduction handbook, Reference 18, details the flight test data processing system and the various programs available. The subsequent paragraphs detail the data acquisition procedures for the pertinent performance parameters.

Power required measured during the AGB flight test program was determined from two independent sources:

1. Rotor shaft torque and rotor speed
2. Measured engine fuel flow

Strain-gaged rotor torque was considered the primary data source, as the installed engines were calibrated only during production checkout and did not possess the wide-range power turbine speed calibrations required to obtain accurate performance data. The following lists the engines and effective flights during performance testing of the AGB rotor.

<u>Engine</u> <u>Ser No.</u>	<u>Calibration</u> <u>Date</u>	<u>Position</u>	<u>Effective</u> <u>Flights</u>
LE-19105	-	#2	X-242 - X-272
LE-19131	1-2-69	#1	X-247 - X-288
LE-19240	5-30-69	#2	X-275 - X-288
LE-19268	6-6-69	#2	X-273 - X-274

Since power derived from engine fuel flow did not exhibit a consistent trend with either engine torque or rotor shaft torque, the performance presented in this report is based on rotor torque measured power. In all cases the rotor torque measured power was higher than that recorded utilizing fuel flow. The torque measurements were obtained from three separate torque-strain bridges on each rotor shaft and averaged to obtain the shaft torque for each rotor. A transmission power loss of 180 shp was applied to the measured rotor horsepower. This loss is substantiated in the CH-47C performance flight test report (Reference 1').

Aircraft gross weight on performance flights was calculated for each data record using takeoff gross weight adjusted for actual fuel and flight crew weights and fuel burned as measured by fuel flow totalizers and fuel specific weight. On strain survey flights the aircraft system fuel quantity indicators were used with the adjusted takeoff gross weight to determine the run gross weight.

Boom and ship airspeed systems were calibrated to determine position error on Flight X-276. The calibration was conducted using the measured ground course method at speeds from 32 knots to 156 knots calibrated airspeed. Reciprocal headings were flown to negate the effect of wind. Winds of less than 6 knots were encountered during the calibration. Figures 292 and 293 present results of this calibration for the boom and ship systems, respectively. Since these calibrations are for the magnetic tape airspeed recording system, the indicated airspeed value accounts for any error associated with the airspeed transducer. These specific calibrations were used throughout the AGB testing and are considered valid for the magnetic tape system only.

Ship pressure altitude was recorded on magnetic tape from static pressure transducers. The transducer output is converted to a high-frequency digital signal prior to recording on tape. Transducer altitude was compared to cockpit indicated altitude, and a consistent trend was derived. Tape altitude for the data points was calibrated to cockpit altitude using the above trend and the resultant value used in the performance calculations.

Outside air temperature was recorded on tape from a sensitive Rosemount probe located under the fuselage at Station 250.

Performance Determination of Power Required

The output of the flight test data analysis was used as input to the aerodynamics power reduction program, Reference 20. This program is used to determine the test measured power and significant aircraft parameters in generalized and nondimensional form. Pertinent performance parameters in the form of output from the power reduction program, are listed in Appendix V. The generalized method of data reduction (W/δ ; $shp/\delta\sqrt{\theta}$; $V/\sqrt{\theta}$; $N/\sqrt{\theta}$) is used for level-flight performance; nondimensional parameters and blade tip Mach number (C_T , C_P , M_T or $N/\sqrt{\theta}$) are used to present hover performance. The equivalence of these methods for presenting rotorcraft performances is presented in Appendix V.

Time histories of generalized power ($SHP/\delta\sqrt{\theta}$), generalized true airspeed ($V/\sqrt{\theta}$), and pressure altitude were obtained for each data record and an average power and airspeed determined. The time histories of airspeed and altitude were also used to calculate the corrections for acceleration and rate of climb.

Generalized gross weight (W/δ) was corrected to either the target W/δ or the average W/δ . Gross weight corrections were developed by fairing preliminary power polars at the average test generalized weight and determining the slope of the power/weight curve at constant $V/\sqrt{\theta}$.

Test rotor speeds were corrected to target $N/\sqrt{\theta}$ (235 and 245 rpm). These speed corrections were based on test-measured performance of the AGB at 235 and 245 rpm ($N/\sqrt{\theta}$) and trends established during performance testing of the CH-47C.

As previously mentioned, the external drag differences between the test aircraft and the specification CH-47C were accounted for in the final power polars. A power increment corresponding to 3.05 ft² of equivalent flatplate area was subtracted from test-measured power at each airspeed.

Performance data reduced from rotor strain survey flights was based upon one 10-second data record at each airspeed. Power required was calculated from rotor shaft torque, and no power corrections for acceleration or climb were obtainable. Adjusted takeoff gross weight and aircraft cockpit fuel quantity indicators were used to determine run gross weights. These flights are included in the Appendix V data listings.

During hover performance testing with the external loads, four data bits were reduced from the 75-second data record at each stabilized rotor speed. Each of these data bits is presented in the hover summary and listed in the tables of Appendix V. The nondimensional performance parameters of power

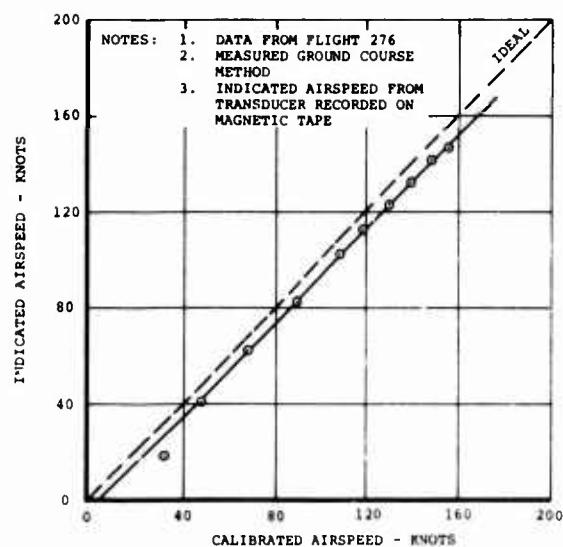


Figure 292. Airspeed Position Error From Boom System Magnetic Tape on CH-47C Helicopter Equipped With Advanced-Geometry Blades.

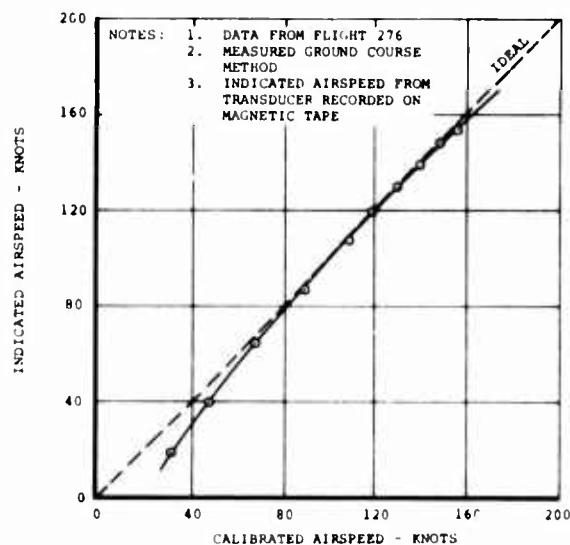


Figure 293. Airspeed Position Error From Ship System Magnetic Tape on CH-47C Helicopter Equipped With Advanced-Geometry Blades.

coefficient (C_P), thrust coefficient (C_T), and generalized rotor speed ($N/\sqrt{\sigma}$) were calculated with the aid of the power reduction program (Reference 20).

Discussion of Performance Test Results

Hover Power Required - Out of Ground Effect

Figure 294 presents a summary of the hover data collected during the AGB flight test program. The range of thrust coefficients tested is sufficient to calculate hover capability only at low rotor speed (low tip Mach numbers). Rotor speed restrictions on the test AGB rotor (247 rpm maximum) and ambient test conditions (sea level/22°C) precluded testing of high thrust coefficients (C_T) at high tip Mach numbers (generalized rotor speed above 245 rpm). Therefore, the test data fairing of Figure 294 represents generalized rotor speeds of 235 rpm (tip Mach numbers of 0.661) and below.

The performance capabilities measured during the AGB test program are presented in nondimensional terms (C_P , C_T) and generalized rotor speed ($N/\sqrt{\sigma}$) for hover OGE, and in generalized forms $\text{shp}/\delta\sqrt{\sigma}$, GW/δ , $V/\sqrt{\sigma}$, and $N/\sqrt{\sigma}$ for forward flight. These terms were chosen to allow direct comparison of AGB performance to standard CH-47C performance. The relationships between nondimensional and generalized performance parameters are presented in Appendix V.

Figure 294 includes a comparison of test data with the current method of hover power required prediction. This method is based on the calculated power required for an isolated rotor, using explicit vortex influence techniques (Reference 21), with induced power corrections for rotor overlap and fuselage down-load based on recent powered model testing of a 34 percent overlap tandem helicopter (Reference 22). A comparison of hover ceiling capability calculated using the power requirements of Figure 294 is presented in Figure 295 for standard day temperatures at rotor speeds of 230 and 245 rpm. As noted, the incremental performance between the test data and the current prediction methodology is less than 1.5 percent.

The effect of compressibility on hover capability cannot be determined for the operating range of the CH-47C from the limited data obtained during the tests. However, the data of Figure 294 does not indicate any compressibility effects between $N/\sqrt{\sigma}$ of 230 and $N/\sqrt{\sigma}$ of 245 up to a thrust coefficient of 0.006.

Tests of the standard CH-47C rotor indicate that compressibility effects occur at thrust coefficients above 0.0048. Figure 296 compares AGB hover power requirements ($\sigma = 0.0845$) to CH-47C hover power ($\sigma = 0.067$) as defined by CH-47C flight testing documented in Reference 19. As noted, the power required is lower for the AGB system for thrust coefficients of 0.007 and higher.

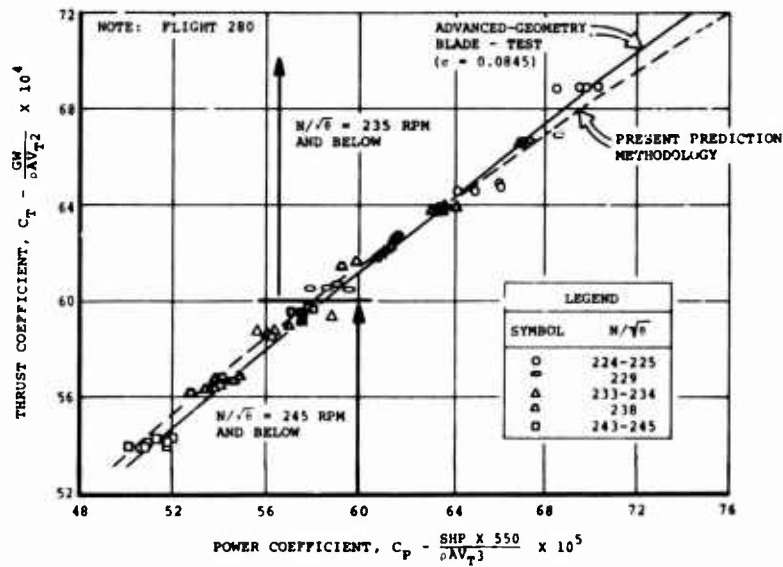


Figure 294. Comparison of Predicted and Test Hover Power Required With Advanced-Geometry Blades.

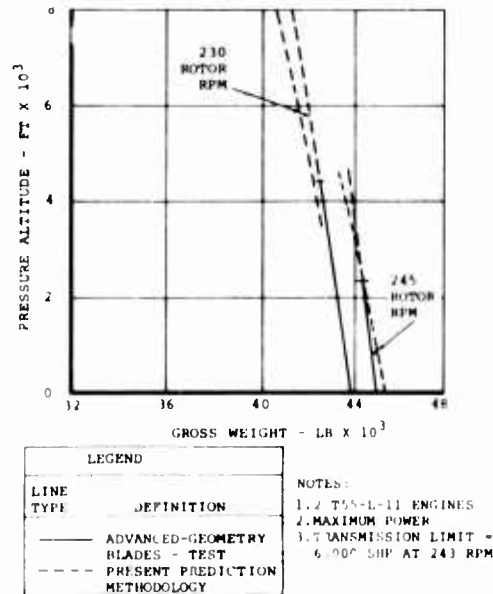


Figure 295. Comparison of Predicted and Test Hover Capability Out of Ground Effect With Advanced-Geometry Blades.

Hover power requirements for the AGB rotor system have been compared with requirements for the CH-47C rotor in order to determine the influence of increased blade area (solidity), twist, taper, and airfoil section. The effect of increased blade area is illustrated in Figure 297 for hover OGE at a generalized rotor speed of 235 rpm. CH-47C test results were adjusted by increasing profile power by the ratio of AGB to CH-47C rotor solidity (0.067 to 0.0845). As shown, the CH-47C/AGB rotor possesses greater lifting capability than the CH-47C at equal solidity at thrust coefficients (C_T) above 0.006.

The comparison of adjusted CH-47C data and the AGB level of performance at equal solidity indicated that both rotors at equal solidity have approximately the same hover performance. Therefore, the increased hover power required with the AGB at low thrust coefficients results from increased solidity. The improvement in hover capability with the AGB rotor at the high thrust coefficients is attributed primarily to the thin airfoil section at the tip, which provides improved lifting capability at the tip Mach numbers associated with hover. It is anticipated that at higher tip Mach numbers not covered by this test program, a larger benefit would be gained by the AGB tip. As noted in the previous section, the performance effects of decreased twist (-6° AGB vs. -9.1° CH-47C) and increased taper ratio (1.3 AGB vs. 1.0 CH-47C) are estimated to have equal resultant effects for the hover condition.

Level-Flight Power Required

Level-flight power required test data is shown in generalized terms of W/δ , $V/\sqrt{\theta}$, $\text{shp}/\delta \sqrt{\theta}$ for $N/\sqrt{\theta}$ of 235 (Figure 298), and $N/\sqrt{\theta}$ of 245 rpm (Figure 299). The final fairings of the results, which include weight, climb, acceleration, and rotor speed corrections, are based on all of the data shown -- strain survey flights as well as performance flights. Performance shown in these figures is representative of a specification CH-47C aircraft (Reference 17) equipped with an AGB rotor system; external differences between the test aircraft and specification aircraft are presented in the Aircraft Configuration section.

Power required for a CH-47C with AGB rotor system ($\sigma = 0.0845$) is compared to a standard rotor CH-47C ($\sigma = 0.067$) in Figures 300 and 301 for generalized rotor speeds of 235 and 245 rpm, respectively. The AGB rotor system provides increased speed capability at generalized gross weights (W/δ) above 55,000 pounds at $N/\sqrt{\theta} = 235$ rpm, and above 50,000 pounds at $N/\sqrt{\theta} = 245$ rpm. Figure 302 presents a comparison of standard CH-47C and AGB rotor power requirements at the AGB solidity (0.0845) and $N/\sqrt{\theta} = 245$ rpm. An increase in speed capability of 3 to 4 knots is realized with the AGB rotor as compared to the CH-47C rotor at equal solidity. This increase in speed capability is attributed to the decreased compressibility power required with the thin tips.

Speed capability based on Normal Power for the AGB rotor system is shown in Figures 303 and 304 for rotor speeds of 235 and 245 rpm, respectively. Both figures indicate an improvement in speed capability with the AGB rotor system

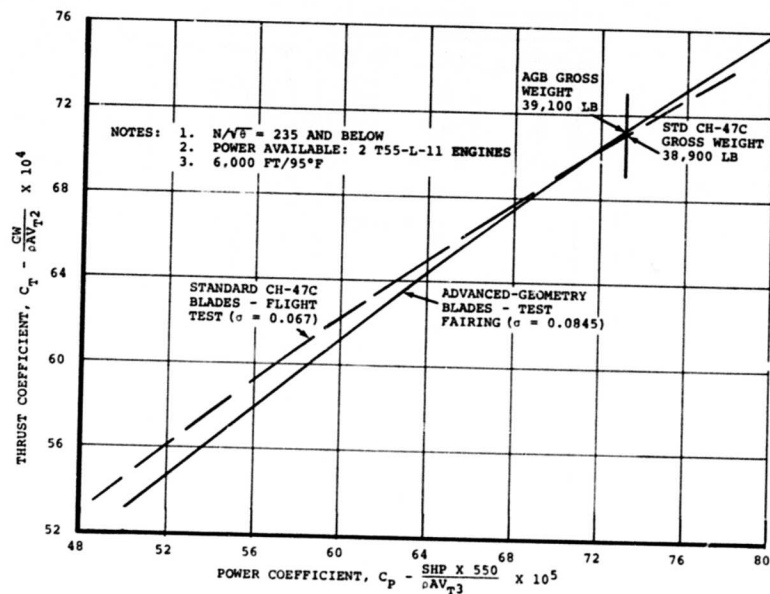


Figure 296. Comparison of Hover Power Required Out of Ground Effect for Conventional and Advanced-Geometry Blades.

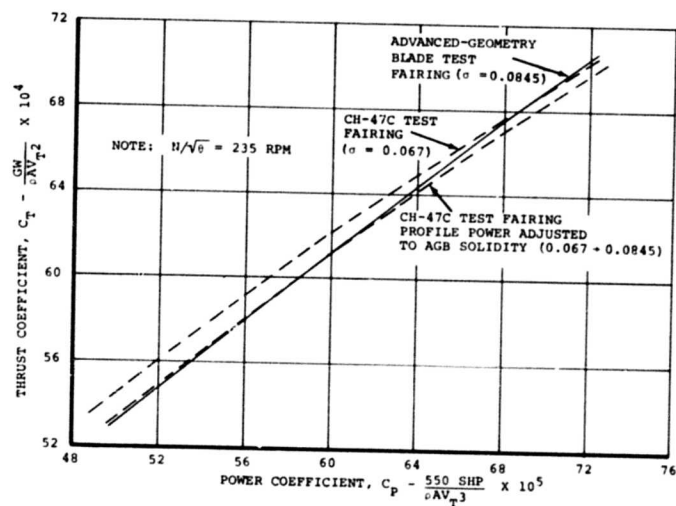


Figure 297. Comparison of Hover Power Required Out of Ground Effect for Adjusted Conventional and Advanced-Geometry Blades.

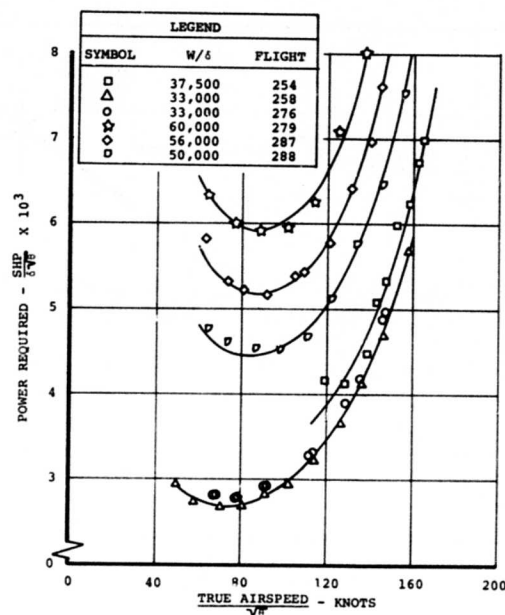


Figure 298. Test Results for Level-Flight Power Required With the Advanced-Geometry Blades at 235 Rotor RPM.

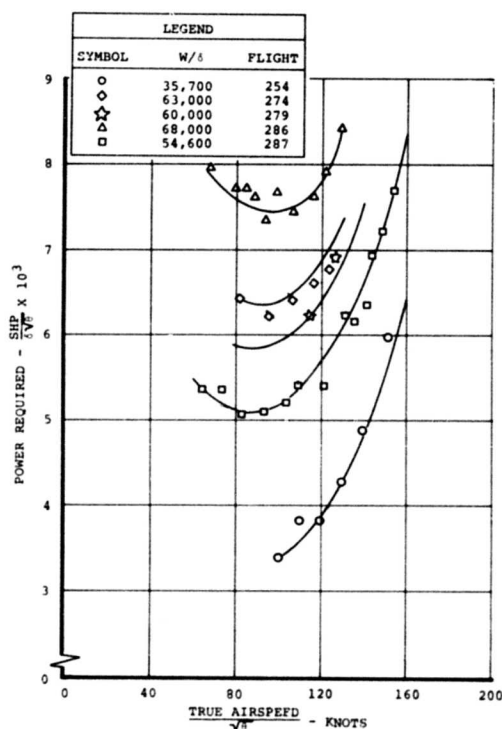


Figure 299. Test Results for Level-Flight Power Required With the Advanced-Geometry Blades at 245 Rotor RPM.

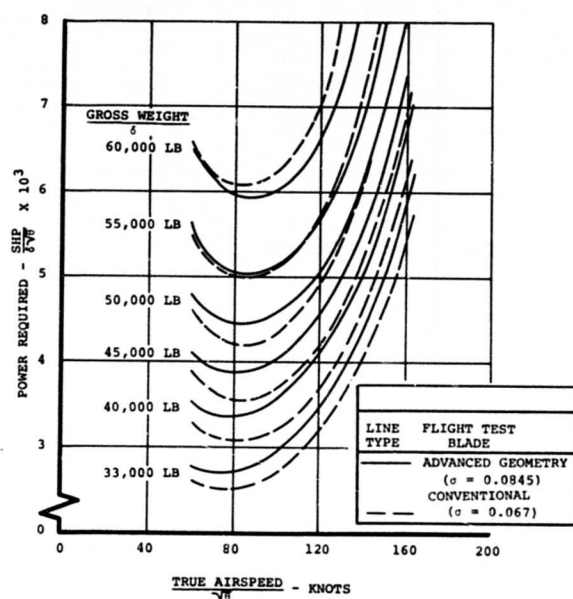


Figure 300. Comparison of Level-Flight Power Required for Conventional and Advanced-Geometry Blades at 235 Rotor RPM.

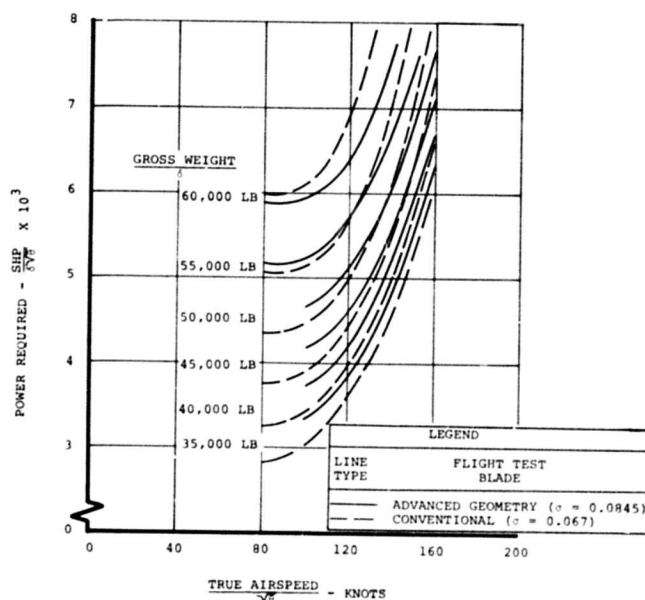


Figure 301. Comparison of Level-Flight Power Required for Conventional and Advanced-Geometry Blades at 245 Rotor RPM.

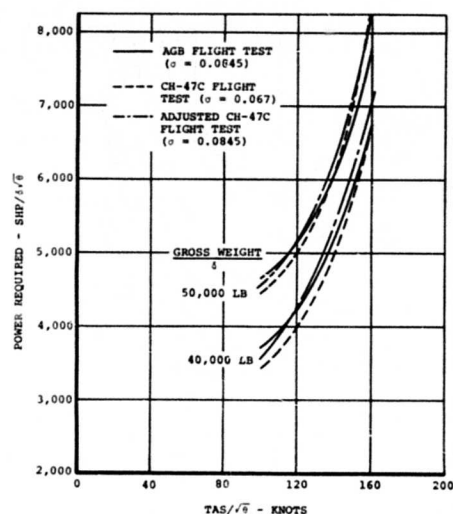


Figure 302. CH-47C/AGB Rotor Comparison of Level Flight Power Required at Constant Solidity (0.0845) - $N/\sqrt{\theta} = 245$ Rotor RPM.

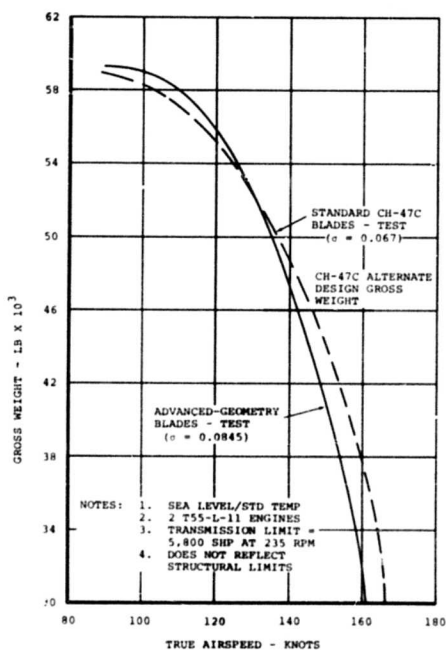


Figure 303. Comparison of Speed Capability With Conventional and Advanced-Geometry Blades at 235 Rotor RPM.

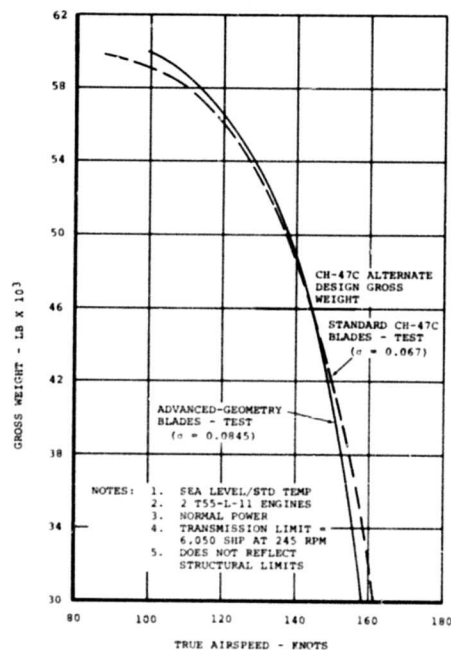


Figure 304. Comparison of Speed Capability With Conventional and Advanced-Geometry Blades at 245 Rotor RPM.

at weights above 46,000 pounds at sea level/standard day conditions. At higher altitudes, this benefit is seen at lower weights, as shown in Figure 305 for an ambient condition of 5000 feet/standard +10°C.

Because level-flight power required for only two tip Mach numbers (two values of $N/\sqrt{\theta}$) was obtained during this test program, it is not possible to determine the exact variation of power required with generalized rotor speed. Figure 306 presents a comparison of level-flight power required at an advance ratio of 0.3 for the two advancing tip Mach numbers flown during the test. This figure illustrates the relationship of both total power and compressibility power between the standard CH-47C rotor ($\sigma = 0.067$) and the AGB rotor ($\sigma = 0.0845$) and shows the advantage of the AGB thin-tip airfoil section. The AGB rotor shows less of a rise in compressibility power in the RPM ($N/\sqrt{\theta}$) range from 235 to 245 but higher total power requirements at thrust coefficients up to 0.007. This reduction in drag rise with increased rotor speed is attributable to the 6 percent thick tip of the AGB rotor system. This benefit is offset somewhat by the increase in profile power resulting from the higher solidity of the AGB test rotor.

Comparison With Predictions - Forward Flight

Comparisons of AGB forward-flight power required derived from flight test and current prediction methodology are presented in Figures 307 and 308. The prediction methodology is based on a longitudinal trim analysis which employs tabular airfoil characteristics and nonuniform downwash corrections (Reference 16). The figures indicate the level of agreement to be good over the entire range of comparison for both generalized rotor speeds tested.

Figures 309 and 310 present a comparison of test and theoretical speed capability at sea level/standard for rotor speeds of 235 and 245 rpm, respectively. Over the range of gross weight shown (up to the CH-47C alternate design gross weight), theory is seen to be somewhat optimistic with regard to the actual performance.

Forward Climb Capability

Level-flight power required at the airspeed associated with minimum power is presented in Figure 311 for the AGB rotor and the standard CH-47C rotor at a generalized rotor speed of 235 rpm. AGB minimum power required was derived from the forward-flight power polars previously presented.

Single-engine climb capability at Military Rated Power and dual-engine climb capability at Normal Rated Power for the AGB rotor system ($\sigma = 0.0845$) are presented in Figure 312 at sea level/standard conditions. Climb capability was derived using potential energy relationships and a climb efficiency factor ($K_p = 0.87$) previously measured on the standard CH-47C (Reference 19). This figure

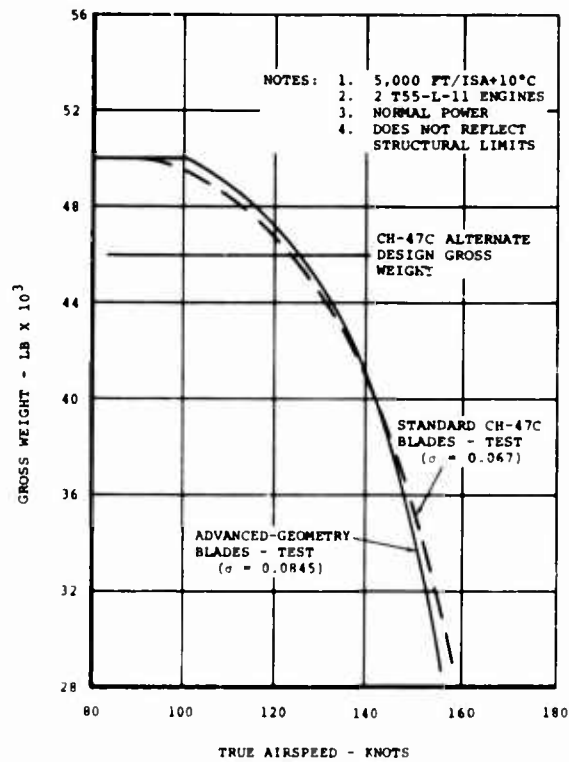


Figure 305. Comparison of Speed Capability With Conventional and Advanced-Geometry Blades at 245 Rotor RPM at Higher Altitude.

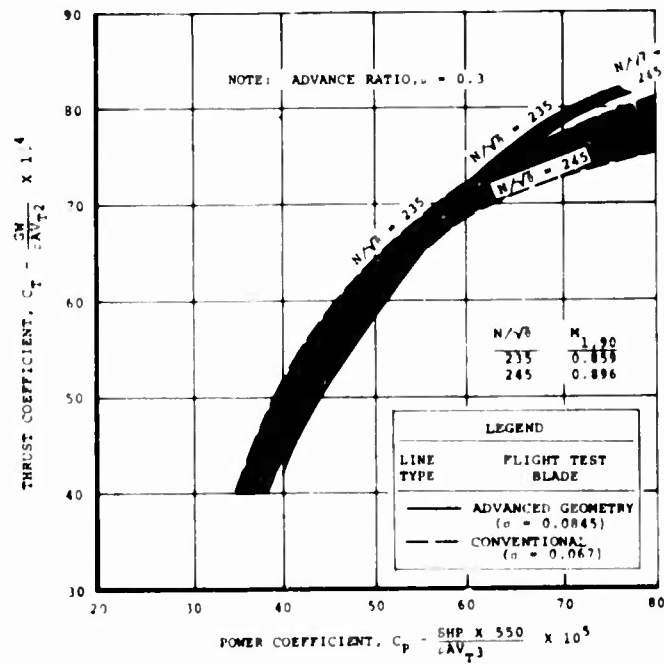


Figure 306. Comparison of Compressibility With Conventional and Advanced-Geometry Blades.

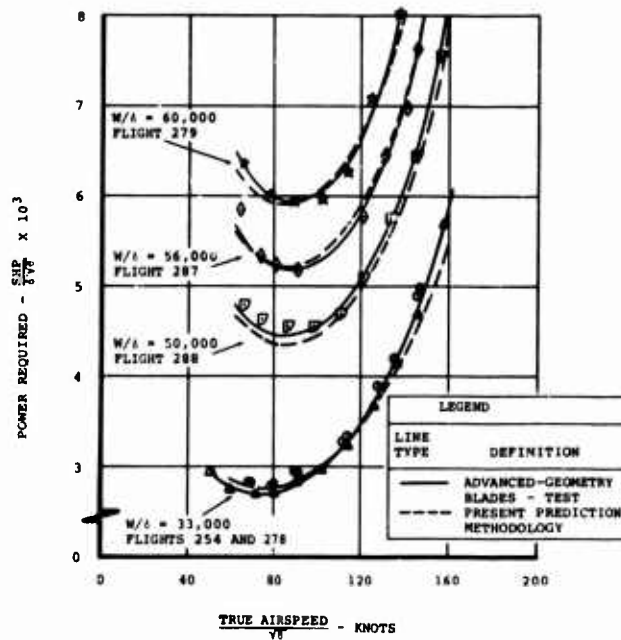


Figure 307. Comparison of Predicted and Test Level-Flight Power Required With Advanced-Geometry Blades at 235 Rotor RPM.

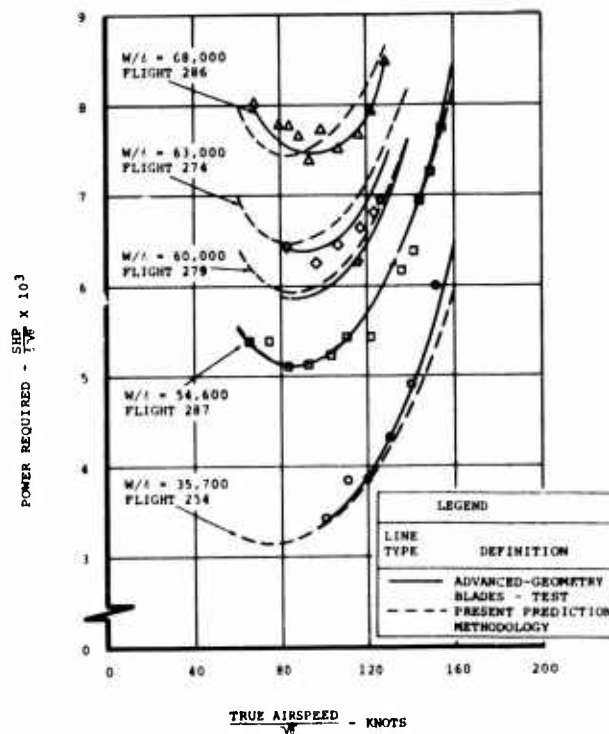


Figure 308. Comparison of Predicted and Test Level-Flight Power Required With Advanced-Geometry Blades at 245 Rotor RPM.

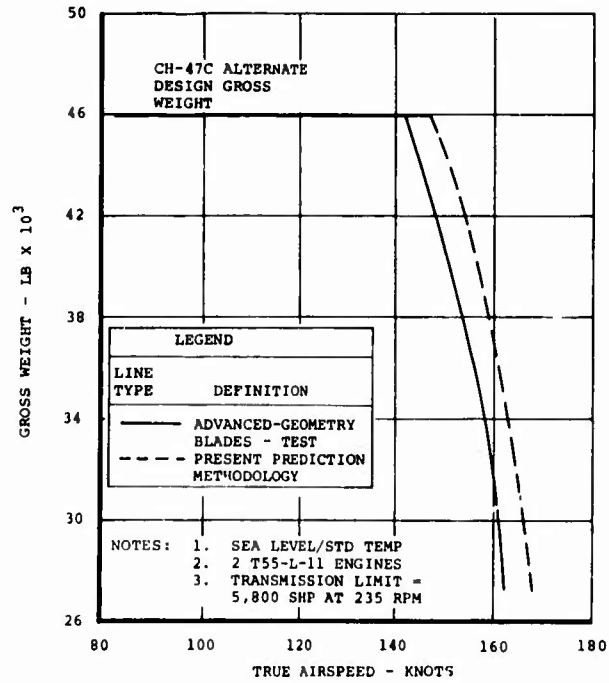


Figure 309. Comparison of Predicted and Test Speed Capability With Advanced-Geometry Blades at 235 Rotor RPM.

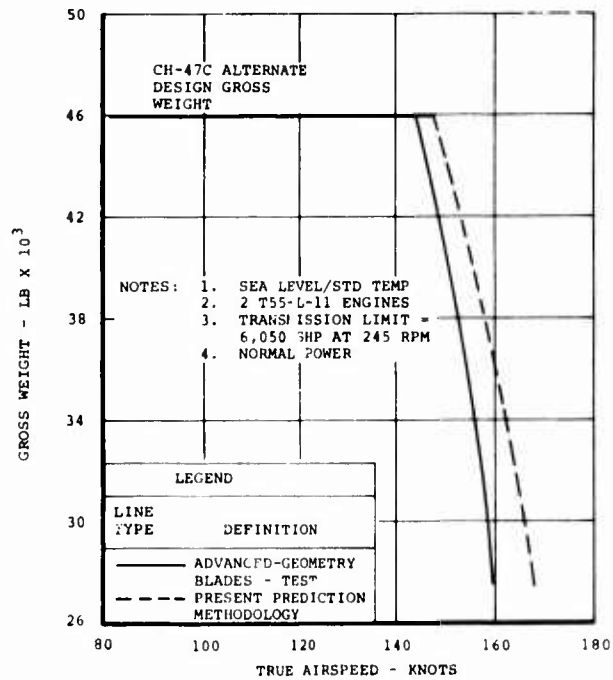


Figure 310. Comparison of Predicted and Test Speed Capability With Advanced-Geometry Blades at 245 Rotor RPM.

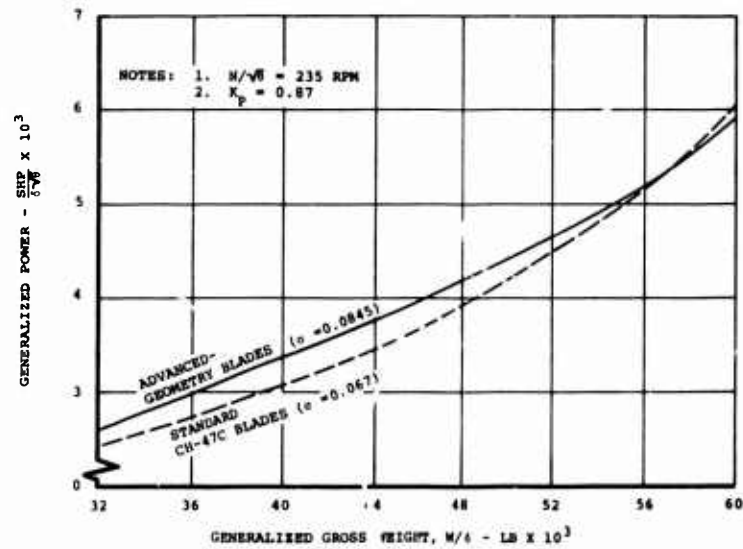


Figure 311. Comparison of Minimum Power Required With Conventional and Advanced-Geometry Blades.

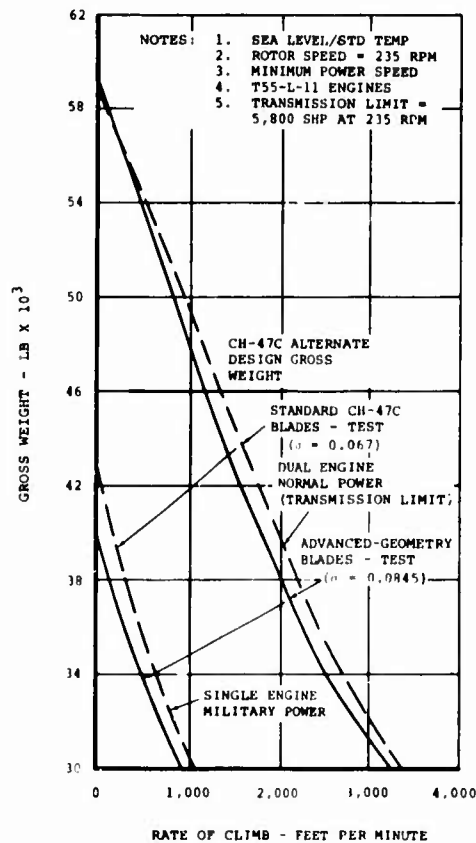


Figure 312. Comparison of Single- and Dual-Engine Forward Climb Capability With Conventional and Advanced-Geometry Blades.

shows that rate of climb with the AGB rotor is approximately 200 fpm less than with the CH-47C ($\sigma = 0.067$), which is indicative of the higher power required with the AGB over the CH-47C gross weight envelope due to its increased solidity.

FLYING QUALITIES

The basic objective of the tests reported in this section was to assess pitch axis handling qualities of the CH-47C helicopter equipped with advanced-geometry rotor blades (AGB). The tests were evaluated on the basis of a comparison of the longitudinal control sensitivity characteristics of the AGB rotor with that of the standard "C" model blades, when operating under high rotor loading conditions. In order to compensate for the increased solidity ($\sigma = 0.085$) of the AGB compared to ($\sigma = 0.067$) of the "C" blades, the pitch kinematics (gearing ratio - degree blade/inch stick) were reduced on the AGB aircraft to provide similar longitudinal control sensitivity when operating in the linear C_{L_α} range.

The tests were conducted at gross weights nominally within 38,000 to 45,000 pounds with attendant rotor thrust levels to 56,500 pounds, produced by trim banked turns. The parameter of primary interest, being longitudinal control sensitivity, was assessed in two ways. First, qualitatively, the pilot attempted to identify at what point a deterioration in control sensitivity occurred. A noticeable increase in effort required to maintain trim control at high rotor thrust levels attained during banked turns at density altitudes of nominally 8,000 to 10,000 feet was the criterion. Admittedly, the high rate turn method of loading the rotors produces some side effects which hinder the pilot's ability to isolate pitch characteristics. These include load factor, lateral trim required, and the roll attitude itself.

However, it is an effective thrust buildup technique and provides the test environment necessary to conduct the maneuvers resulting in the quantitative evaluation of control sensitivity. These maneuvers consist of applying pitch control step inputs from trim and measuring the resultant initial angular acceleration as the trim rotor thrust is increased. Figures 313 and 314 contain the data in plotted format presented as pitch control sensitivity (M δ foot-pounds per inch of stick) vs thrust coefficient/solidity (C_T/σ) and total thrust coefficient (C_T) respectively.

Comparing pitch sensitivities on the basis of thrust coefficient to solidity ratio does not clearly indicate any significant difference between the two blades. The trends are similar through the maximum AGB rotor loading of $C_T/\sigma = 0.0936$. For the AGB this represents a total thrust of approximately 56,500 pounds and maximum power available, but only 43,500 pounds for the "C" blade. It is not apparent that if a higher C_T/σ were attainable, the AGB would deviate from the trend established by the "C" blades. If, however, a comparison is made on the basis of thrust coefficient alone, the test data shown on Figure 314 indicates that the "C" blade control sensitivity deteriorates more quickly than the advanced-geometry blade.

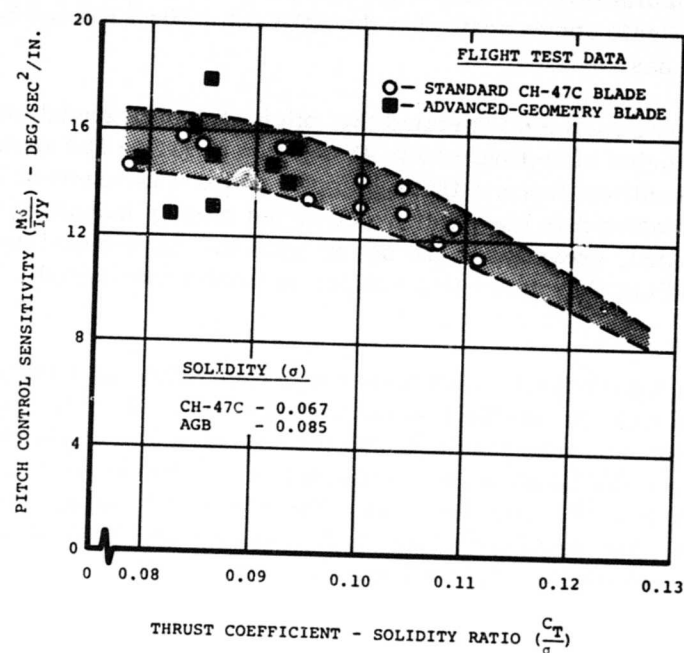


Figure 313. Longitudinal Control Sensitivity of CH-47C and Advanced-Geometry Blades.

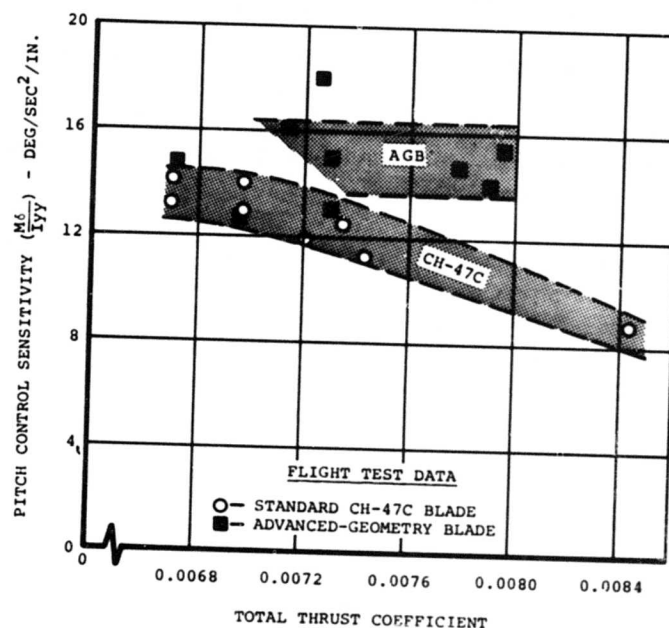


Figure 314. Longitudinal Control Sensitivity of CH-47C and Advanced-Geometry Blades.

Data scatter prohibits precise sensitivity interpretation, but the shaded areas reflect the best estimate and indicate that the AGB rotor limit has not been approached as the "C" blade has.

Pilot reports during AGB testing stated that pitch control degradation occurred at maximum bank angles of approximately 45 degrees at 115 to 130 knots. Calculations at these conditions indicate that maximum power was required for trim. Although the quantitative data was interpreted as not clearly indicating that pitch sensitivity was reduced, operating at the power limit in a high-speed turn could very well display handling characteristics similar to those experienced at the rotor limit.

The fact that the longitudinal cyclic trim was not operating as a function of dynamic pressure (q) has little or no effect on the testing conducted for this section. The cyclic was set for each trim condition, and the " q " variation associated with the dynamic inputs was insignificant within the data acquisition time frame. The aircraft from which the "C" blade data was gathered was not equipped with the pitch stability system. The tests conducted on the AGB aircraft were with the pitch stability system off and therefore are directly comparable.

ACOUSTIC MEASUREMENTS

Comparison of CH-47B and CH-47C/AGB Rotor Noise Signatures

External rotor noise measurements were obtained during the flight test program of the CH-47C aircraft, serial number 66-19103 configured with the advanced geometry blades. The purpose of the measurements was to compare the AGB noise signature with the previously measured CH-47B with V23010-1.58 cambered airfoil blades.

The data was recorded on the port side of the aircraft under the forward rotor disc (area of maximum rotor noise generation) using a Bruel and Kjaer quarter-inch condenser microphone. The microphone was attached to a support boom extending 30 inches from the fuselage skin line at Station 220 as shown in Figure 315. The output of the microphone was recorded on magnetic tape for laboratory playback and analysis using an Ampex AR 200 recorder.

The predominant factor that influences the rotor noise signature of high-speed helicopters is the advancing blade tip Mach number.

Based on the comparison of the noise signature of the AGB rotor and the CH-47B production rotor, the decided noise advantage of the AGB rotor is that it significantly delays the onset of an objectionable impulsive noise that derives from the advancing blade tip operating at high Mach numbers. An example of this objectionable impulsive noise is shown in the sound pressure waveform of Figure 316 for



Figure 315. CH-47C Helicopter With Advanced-Geometry Blades in Flight.

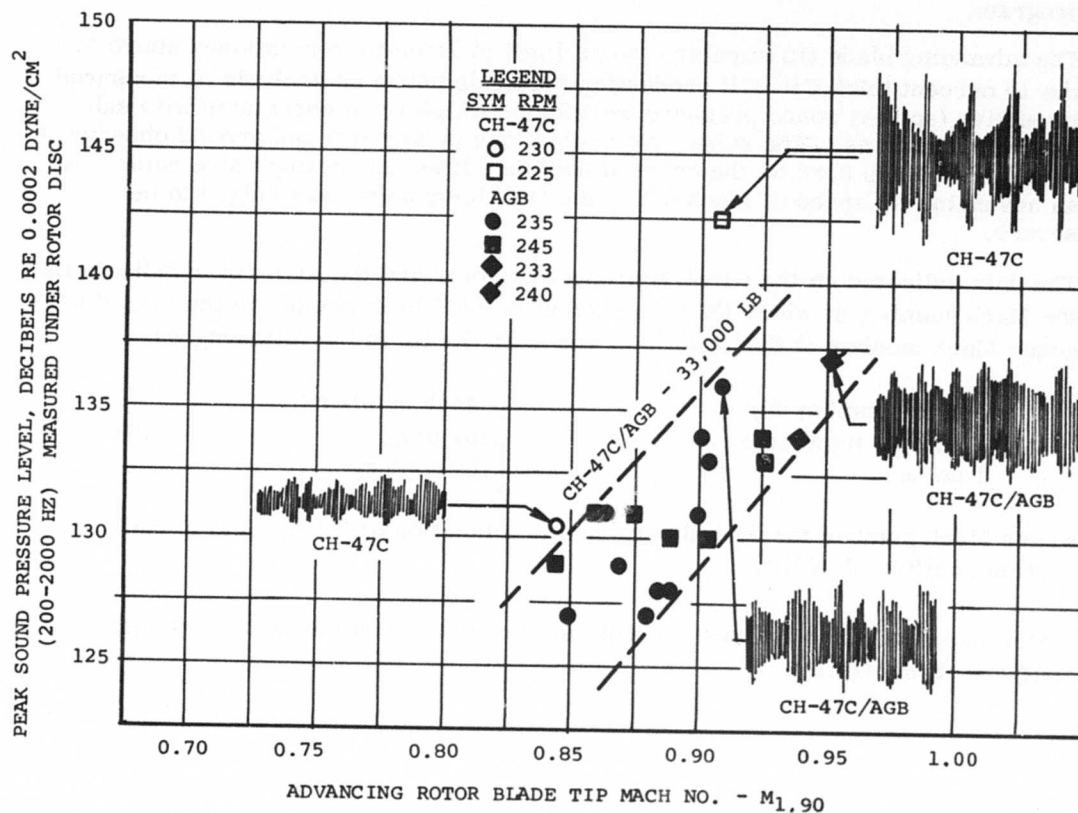


Figure 316. Forward-Flight Sound Pressure Levels - CH-47C and CH-47C/AGB.

the CH-47B production rotor, which displays a sharp pressure spike when operating at an advancing tip Mach number of 0.908. Although the critical Mach number for this occurrence depends on the particular blade tip airfoil section, indications from other experimental tests are that mild and intermittent banging occurs when the Mach number at the advancing blade tip is 0.88 for a blade with V23010-1.58 cambered airfoil, and that severe banging occurs at Mach 0.91. The sound pressure waveform of the AGB rotor at Mach number 0.908 shown in Figure 316 is not dominated by the sharp spike that was present in the CH-47B rotor at the same Mach number. In addition, the AGB rotor demonstrated the ability to operate at advancing tip velocities of Mach 0.95 without the objectionable impulsive (spikey) characteristics appearing in the sound pressure waveform.

From the comparison of the sound pressure waveforms, the conclusion is drawn that the thin tip of the AGB rotor extends the impulsive noise limit of a helicopter rotor from Mach 0.88, which is the limit for a 10 percent thick CH-47 production blade, to Mach 0.95, which is judged to be the limit for the thin-tip AGB rotor, which has thickness taper over the outer 30 percent of the blade span. This conclusion is corroborated by pilot comments collected during the AGB test program.

The advancing blade tip impulsive noise limit of Mach 0.88 mentioned above for the 10 percent thick CH-47B production blades is based on analysis of measured impulsive (spikey) sound pressure waveforms which were correlated with subjective evaluations. The subjective evaluations by aircrew and ground observers established Mach 0.88 as the onset of audible advancing tip impulsive noise. At an advancing tip speed of Mach 0.90, the impulsive noise was judged to be severe.

The data collected on the CH-47B production rotor and the AGB rotor indicate that the Mach number at which the noise becomes audible is related to the drag divergence Mach number of the airfoils at and near the tip in the following way:

$$\left(\begin{array}{c} \text{Mach number for} \\ \text{audible impulsive} \\ \text{noise} \end{array} \right) = \left(\begin{array}{c} \text{Mach number} \\ \text{for drag} \\ \text{divergency} \end{array} \right) + 0.045$$

where Mach number for drag divergence is a function of the critical blade section coefficient of lift.

The discussion which follows presents further details on the test description and analysis of the data.

Test Conditions

Data was obtained during the following CH-47C/AGB flight conditions:

1. Flight 254, 33,000 pounds gross weight
 - a. Airspeed sweep of 120, 130, 140, 145, 150, 155, 157, 160, 165 and 167 KTAS with a rotor speed of 235 rpm.
 - b. Airspeed sweep of 100, 110, 120, 130, 140, 153, and 157 KTAS with a rotor speed of 245 rpm.
2. Flights 282 and 283, 40,000 pounds gross weight
 - a. High-speed runs of 193 KTAS, 233 rotor rpm and 185 KTAS, 240 rotor rpm.

To obtain a rotor noise signature comparison with the CH-47B and the cambered airfoil blades, the following previously recorded flight data was utilized. This data was also measured on the port side of the aircraft at STA 220.

1. CH-47B, 25,000 pounds gross weights
 - a. Airspeed sweep of 26, 50, 68, 86, 105, 125, 134, 143, 153, and 164 KTAS with a rotor RPM of 225.
 - b. Airspeed sweep of 26, 50, 68, 86, 105, 126, 134, and 143 KTAS with a rotor RPM of 230.

Rotor Noise Analysis

The impulsive waveform characteristics of rotor blade noise prohibit the use of conventional RMS slow-response sound analysis equipment; therefore, to assess the noise signature adequately, a high-speed oscillograph for providing waveform time histories was used. In addition, all frequencies below 200 Hz containing unrelated wind noise were filtered out. The resulting sound pressure level amplitudes, measured peak-to-peak, represent the sound quantity of a "banging" rotor noise signature as experienced by the observer (listener).

The frequency response sensitivity of the galvanometers used with the oscillograph imposed the upper 2000 Hz limit.

The recorded data is presented in Figure 316 as the peak-to-peak sound pressure level in decibels (reference 0.0002 dyne/cm^2) within the frequency band 200-2000 Hz. Also included are actual rotor noise waveforms for three of the data points.

CONCLUSIONS

General

1. Composite materials can be successfully employed in a complex loading environment and offer a structurally efficient solution for the design of large rotor blades. However, additional research, development and testing are required before specifying composite materials for primary structure in production rotor blades. Areas requiring further effort include: (a) manufacturing technology, (b) development of a rain, erosion and environmental protection system, (c) development of a lightning and static electricity protection system, and (d) demonstration in simulated or actual service environment.
2. A development program is needed to demonstrate that interchangeable, composite material rotor blades of consistent quality can be economically fabricated in production quantities.

Specific

1. Differences in twist distribution and trailing-edge cusp angle of the experimental blades (apparently induced by variations in cure cycle and assembly) caused high one/rev cockpit vertical vibrations in some high-speed high-rpm flight conditions.
2. Test vehicle operational limits and rotor hub stress rpm limitations precluded demonstration of the AGB rotor at relatively efficient combinations of high advancing blade tip Mach numbers and high advance ratios.
3. The figure of merit for a CH-47C hovering OGE is higher with the AGB rotor than with the equivalent solidity standard rotor at thrust coefficients above 0.006. At thrust coefficients below 0.006, the standard rotor of equal solidity is more efficient. The standard rotor without a solidity adjustment ($\sigma = 0.067$) produces a higher total aircraft figure of merit up to a thrust coefficient of 0.007. Figure-of-merit trends show the AGB rotor would widen its advantage over the standard rotor at higher thrust coefficients and higher tip speeds than those demonstrated.
4. The increased nondimensional power requirements of the AGB rotor over the standard CH-47C rotor at high advance ratio, high thrust coefficients, and low tip Mach numbers are attributed to the stall characteristics of thin airfoils near the tip and the large root cutout. At high advancing-tip Mach numbers, gross weights, and tip speeds, the AGB rotor provides a slight increase in speed over a standard CH-47C rotor with equivalent solidity, due to the decreased compressibility power with the thin tips.
5. The pitch link load growth rate for the AGB rotor was slower after reaching stall than the standard rotor. Possible explanations for this difference are: increased aerodynamic or structural damping, a change in the pitch axis, different torsional natural frequencies, spanwise taper, or a combination of the preceding factors.

6. The increased solidity of the AGB rotor and slow control load growth rate after stall were the most important factors in permitting the CH-47C operational envelope to be expanded at high-gross-weight/high-altitude conditions.
7. The audible impulsive noise threshold on the AGB rotor occurs at an advancing blade tip Mach number of 0.95, compared to 0.88 for the production CH-47C rotor. The improvement is attributed to the thickness ratio taper and thin tip of the AGB.

RECOMMENDATIONS

1. A manufacturing technology development program be conducted to demonstrate manufacturing capability with emphasis on producing composite material blades of uniform characteristics at reasonable cost.
2. Materials technology programs be continued to obtain physical and mechanical properties of composite materials for use in preliminary design efforts to establish the optimum cost-effective material mix for rotor blade applications.
3. Environmental and electrical protection system for composite material blades be developed.
4. Testing techniques for composite material be improved to insure that results are economical and predictable as well as technically valid.
5. Tests be conducted to demonstrate the suitability of composite material in a typical rotor blade service environment.

LITERATURE CITED

1. MIL-S-8698 (ASG), STRUCTURAL DESIGN REQUIREMENTS, HELICOPTERS, Amendment 1, February 1958.
2. Kuest, H.L., BTWT867, A HIGH-SPEED TEST OF VR820M-1, A TWO-DIMENSIONAL ROTOR BLADE SECTION, The Boeing Company, Seattle, Washington, D2-2375-1.
3. Gabriel, E. A., ANALYSIS OF TWO-DIMENSIONAL WIND TUNNEL TESTS OF ROTOR BLADE AIRFOILS OF VARYING CAMBER AND LEADING EDGE RADIUS, The Boeing Company, Vertol Division, Philadelphia, Pa., Aerodynamics Investigation II-288, 1965.
4. Leone, P.F., THEORY OF ROTOR BLADE UNCOUPLED FLAP-BENDING AERO-ELASTIC VIBRATIONS, Proceedings 10th Annual Forum of the American Helicopter Society, May 1954.
5. Leone, P.F., THEORY OF ROTOR BLADE UNCOUPLED LAG BENDING AERO-ELASTIC VIBRATIONS, Proceedings 11th Annual Forum of the American Helicopter Society, April 1955.
6. Leone, P.F., THEORETICAL AND EXPERIMENTAL STUDY OF THE COUPLED FLAP BENDING AND TORSION AERO-ELASTIC VIBRATIONS OF A HELICOPTER ROTOR BLADE, Proceedings 13th Annual Forum of the American Helicopter Society, May 1957.
7. Fletcher, J., ADVANCED-GEOMETRY BLADE MASTER DIMENSIONING DATA, The Boeing Company, Vertol Division, Philadelphia, Pa., D8-0223, June 1966.
8. Pinckney, R., FABRICATION OF POSITIVE PRESSURE CURED, RESIN BONDED GLASS FIBER ALUMINUM HONEYCOMB ROTOR BLADES, The Boeing Company, Vertol Division, Philadelphia, Pa., D8-0133, January 1965.
9. NONDESTRUCTIVE TEST PLAN FOR THE ADVANCED-GEOMETRY ROTOR BLADE, The Boeing Company, Vertol Division, Philadelphia, Pa., D8-0280-1, October 1966.
10. INSPECTION PLANNING GUIDE FOR THE ADVANCED-GEOMETRY ROTOR BLADE, The Boeing Company, Vertol Division, Philadelphia, Pa., D8-0280, August 1966.
11. CH-47 ADVANCED-GEOMETRY BLADE FLIGHT TEST PROCEDURE, The Boeing Company, Vertol Division, Philadelphia, Pa., 114-FT-028-1, May 1968.
12. FLIGHT TEST SECTION STANDARD PLANS OF TEST, The Boeing Company, Vertol Division, Philadelphia, Pa., D8-1087, 1966.

LITERATURE CITED (Continued)

13. Porterfield, J. D., and Maloney, P. F., EVALUATION OF HELICOPTER FLIGHT SPECTRUM DATA, Kaman Aircraft Division, Kaman Corporation; USAAVLABS Technical Report 68-68, U.S. Army Aviation Materiel Laboratories, Fort Eustis, Virginia, October 1968, AD680280.
14. PERFORMANCE CHARACTERISTICS OF THE AGB-65-1 ROTOR BLADE ON THE BASIS OF MODEL ROTOR WIND TUNNEL TESTS, The Boeing Company, Vertol Division, Philadelphia, Pa., D8-0317, 1966.
15. ROTOR AIRLOADS AND PERFORMANCE ANALYSIS WITH NON-UNIFORM INDUCED FLOW (PROGRAM B-67), The Boeing Company, Vertol Division, Philadelphia, Pa., D8-0312, December 1967.
16. ROTOR PERFORMANCE CALCULATION METHOD WITH NON-UNIFORM INFLOW APPROXIMATION, The Boeing Company, Vertol Division, Philadelphia, Pa., D8-2073, December 1968.
17. DETAIL SPECIFICATION FOR THE MODEL CH-47C HELICOPTER, The Boeing Company, Vertol Division, Philadelphia, Pa., 114-PJ-803, December 1967.
18. DATA REDUCTION HANDBOOK FOR FLIGHT TEST DATA, The Boeing Company, Vertol Division, Philadelphia, Pa., D8-0822, December 1967.
19. ANALYSIS OF CH-47C PERFORMANCE FLIGHT TEST, Revision A, The Boeing Company, Vertol Division, Philadelphia, Pa., 114-FT-712, January 1969.
20. DETERMINATION OF THE POWER OUTPUT OF LYCOMING T55-L-7/11 ENGINES AND SIGNIFICANT HELICOPTER PERFORMANCE PARAMETERS, Revision A, The Boeing Company, Vertol Division, Philadelphia, Pa., Aero Investigation III-308, January 1968.
21. ANALYSIS OF PROPELLER AND ROTOR PERFORMANCE IN STATIC AND AXIAL FLIGHT BY AN EXPLICIT VORTEX INFLUENCE TECHNIQUE, Revision A, The Boeing Company, Vertol Division, Philadelphia, Pa., R-372, December 1967.
22. SUMMARY OF UNIVERSAL HELICOPTER MODEL WIND TUNNEL TEST RESULTS - NOVEMBER 1968 TO DECEMBER 1969, The Boeing Company, Vertol Division, Philadelphia, Pa., D210-10077, December 1969.

APPENDIX I
BLADE TRACKING HISTORY

1. All blade tracking results obtained by using the Chicago Aerial electronic blade tracking system are presented with the vertical out of track displacements being given relative to the appropriate forward rotor head or aft rotor head master blade.
2. To maintain a consistent system of presenting blade tracking results, the same procedure with the same two master blades, used in presenting Chicago Aerial blade tracking results, is employed in presenting Strobex blade tracking results.
3. The position at which a track was obtained, relative to the tip path circle formed by the rotating blades, is identified using clock positions, with the center being the appropriate rotor hub and the 12 o'clock position on the tip path being located on the centerline of the aircraft looking forward.
4. All airspeeds at which Strobex blade tracking was conducted are given as boom indicated airspeeds.
5. The following symbols will be utilized in presenting the blade tracking results and corresponding pitch link adjustments:

Fwd. Blade Color Code: Y - Yellow (S/N 105-1) - Master
 G - Green (S/N 104-1)
 R - Red (S/N 106-1)

Aft Blade Color Code: Y - Yellow (S/N 103-2)
 G - Green (S/N 102-2) - Master
 R - Red (S/N 104-2)

Out-of-track condition relative to the master blade:

H - High
L - Low

6. Where information is not shown in the following presentation, one of the following explanations applies:
 - 6.1 The data was not recorded on the blade tracking card as in the case of rotor rpm and/or airspeed.

- 6.2 Blade tracking was conducted on either the forward or the aft set of blades, and hence pitch link adjustments were made only on the corresponding rotor head.
- 6.3 Pitch link adjustments were not deemed necessary based on the results of the blade track.
- 6.4 Pitch link adjustments were made based on criteria other than blade tracking results, such as aircraft autorotational characteristics.
7. In the following presentation, where more than one blade track was conducted during a flight, the corresponding pitch link adjustments based on all the tracking results are shown following the last blade track of that flight.
8. The scope of blade track investigations and corresponding pitch link adjustments can be attributed to the use of prototype composite rotor blades exhibiting greater sensitivity to pitch link adjustments as compared to standard metal blade practice, and to continuing efforts to alleviate the 1/rev vibration constraints.

TABLE XLVII. BLADE TRACKING RESULTS AND CORRESPONDING PITCH LINK ADJUSTMENTS						
Test No.	Track Type	Rotor RPM Airspeed (kt)	Blade Tracking Results		Corresponding Pitch Link Adjustment (marks)	
			Fwd (clock pos)	Aft (clock pos)	Fwd	Aft
			Pitch links adjusted nominally for initial AGB track		Y inc 6	G dec 10
GR22	Chicago Aerial and Strobex	-	missing		Y dec 36 G dec 24	Y dec 21
GR23	Chicago Aerial	-	G 1½ in. low (3)	Y 4½ in. high (3)	Y inc 3	G inc 30
TK1	collective track	-	R ½ in. high	R 5 in. high	G inc 12	
	Chicago Aerial	-	R 1 3/4 low (3)	Y ½ in. low (3)	Y dec 8	Y inc 2
TK2	collective track	-	G 1/8 in. low	R 1/8 in. low	G dec 8	
	Chicago Aerial	225-240	G 1 in.-1 3/8 in. high(3)	R 3/8 in.-½ in. low (3)	G dec 8	G dec 3
TK3		-	R ½ in. low to 1/8 in. high	Y 3/8 in.-3/4 in. low		
GR24	Chicago Aerial	225-240	R 1 in.-1½ in. high(3)	R 1 1/8 in.-1½ in. high(3)	Y inc 5	Y inc 2
TK1	collectic track	-	G ½ in.-3/8 in. high	and ½ in.-3/4 in. high	G inc 4	G inc 5
	Chicago Aerial	-	G 1½ in. high (3)	R 1 3/4 in. high(3)	Y inc 10	G inc 10
TK2	collective track	-	R 1 3/4 in. high	Y 2 in. high		
	Chicago Aerial	225 & 243	G 1 in.-1½ in. low (3)	R 5/8 in.-7/8 in. high(3)	Y dec 5	G inc 3
TK3		-	R 1 1/8 in.-1½ in. low	Y 5/8 in.-7/8 in. high		
GR25	Chicago Aerial	225-240	R ½ in. low to 1/8 in. high(3)	R 1 in.-1 1/8 in. high(3)	R,G and Y-inc. each 15	R and G-dec. ea 15-Y dec 18
X242	collective track	-	G 1/8 in. low to 1/8 in. high	Y 1 1/8 in.-1½ in. high		
X243	-	-	-	-	R,G and Y-inc each 15	R,G and Y-dec each 15
X244		-	R 1½ in. low (1)			
TK1	Strobex	-	G 1½ in. low	-		
		-	R ½ in. low (1)		G inc 6	
TK2	Strobex	-	G 2½ in. low	-		

TABLE XLVII - Continued						
Test No.	Track Type	Rotor RPM Airspeed (kt)	Blade Tracking Results		Corresponding Pitch Link Adjustment (marks)	
			Fwd (clock pos)	Aft (clock pos)	Fwd	Aft
X245	Strobex-flat		R 1 in.high(1)			
TK1	pitch gnd track	-	G 1½ in.high			
	Strobex	-	R ½ in.high(1)			
TK2	ground track	-	G 1 in.high			
	Strobex	-	R ¾ in.high(1)			
TK3	hover track	-	G 1½ in.high	-		
		-	R 2 in.high(1)		G dec 3	
TK4	Strobex	100	G 4 in.high		Y inc 2	
X246		-	R ½ in.high(1)	Y 4 in.high(11)		
TK1	Strobex	80	G 2 in.high	R 4½ in.high		
		-	R - (1)			
TK2	Strobex	106	B 2 in.high	-		
		-		Y 4 in.high(11)		
TK3	Strobex	80 to 128	-	R 5 in.high		
		-	R 0-½ in.high(1)	-		
TK4	Strobex	115	G 3 in.-4 in.high			
		-	G - (1)	-	G dec 2	G inc 3
TK5	Strobex	128	R 3 in.low			
X249		-	G - (1)	-		
TK1	Strobex	Static	R ¾ in.high			
		-		Y 0-½ in.high(11)		
TK2	Strobex	Taxi	-	R 1 in.-1½ in.high	Y inc 2	R dec 1
X251	Strobex		G - (1)	Y ½ in.high(11)		
TK1	ground track	-	R ½ in.high	R ¾ in.high		
	Strobex	-	G - (1)	Y - (11)		
TK2	hover	-	R -	R ¾ in.high		
		-	G - (1)	Y - (11)		
TK2	Strobex	73	R -	R ½-¾ in.high		
		-	G - (1)	Y 3 in.-4 in.high(11)		
TK3	Strobex	100	R -	R 4in.-5in.high		
		-	G - (1)	R 4in.-6in.high(11)		
TK4	Strobex	140	R -	Y 4in.-6in.high	-	G inc 6

TABLE XLVII - Continued						
Test No.	Track Type	Rotor RPM Airspeed (kt)	Blade Tracking Results		Corresponding Pitch Link Adjustment (marks)	
			Fwd (clock pos)	Aft (clock pos)	Fwd	Aft
X252	Chicago Aerial	Min.to 243	R 1/2 in.-3/4 in.low	R 0-1/8 in.low(3)		
TK1	flat and C/P	-	(3)			
	Strobex		G 1/2 in.-5/8 in.low	Y 5/8 in.-7/8 in.low		
TK2	ground track		R - (1)	R 1 in.low (11)		
	Strobex		G - (1)	Y 2 in.low		
TK3	hover		R - (1)	R 2 in.low (11)		
	Strobex	-	G - (1)	Y 2 1/2 in.low		
TK4		80	R - (1)	R - (11)		
	Strobex	-	G - (1)	Y - (11)		
TK5		100,120 & 130	G -	R 1/2 in.high		
	Strobex		R - (1)	Y - (11)		R dec 1
TK6		140	G -	R 1 in.high		
X253	Strobex		R - (1)	R 1/2 in.low(11)		
TK1	ground track		G -	Y 1 in.low		
	Strobex	-	-	Y - (11)		
TK2		110		R 1/2 in.high		
X254	Strobex		R 1/2 in.low(1)	R 1 1/2 in.low(11)		
TK1	ground track		G 1/2 in.low	Y 2 1/2 in.low		
	Strobex		R 1/2 in.low(1)	R 1/2 in.low(11)		
TK2		140	G 1/2 in.low	Y 1/2 in.low		
	Strobex	-	R - (1)			
TK3		140	G -			
		-		R 1 in.high(11)		
TK4	Strobex	124		Y -		
		-		R 1/2 in.-3/4 in.high(11)		
TK5	Strobex	137 & 146		Y -		
	Strobex	235	R 1 in.low(1)	R - (11)		
TK6	climb	100	G 1 in.low	Y 3/4 in.low		
X254	Strobex	225	G - (1)	Y - (11)		
TK7	autorotation	120	R 3/4 in.low	R 3/4 in.high		
X255	Strobex		G - (1)			
			R 1/2 in.-1/2 in.low			

TABLE XLVII - Continued						
Test No.	Track Type	Rotor RPM Airspeed (kt)	Blade Tracking Results		Corresponding Pitch Link Adjustment (marks)	
			Fwd (clock pos)	Aft (clock pos)	Fwd	Aft
X259	Strobex	110	G - (1)			
X260	Strobex		R 0-2 in.low			
	ground track		G ½ in.low (1)	R 2 in.high (11)		
X261	Strobex		R 2½ in.low			
TK1	Strobex	60	G ½ in.low (1)			
			G ½ in.low			
TK2	Strobex	100	R - (1)			
			G ½ in.low			
TK3	Strobex	120	R - (1)			
			G 1 in.low			
TK4	Strobex	130		Y - (11)		
				R 1 in.high		
TK5	Strobex	140	G - (1)	Y - (11)		
			R 1 in..high	R - (11)		
TK6	hover			R - (11)		
X262				Y 2 in.low		
	Chicago Aerial	Min. Beeps			R,G and Y	R,G and Y
	flat	- 290	R 1 5/8 in.low(3)	Y 4 in.low (3)	dec each 30	dec each 30
X263	Strobex		G ½ in.low	R 2 in-2½ in.low		
X264	Strobex		G 3 in.low (1)	R 4 in.low (11)		
TK1	ground track		R 4 in.low	Y 8 in.low		
	Strobex		G 1 in.low (1)	R 8 in.-10 in.low(11)	G dec 3	G dec 4
TK2	hover		R 7 in.low	Y 10 in.-12 in.low	Y dec 2	Y inc 2
X265	Strobex	235	G 1 in.low(5)	R 2 in.low (11)		
TK1	ground track	-	R 1 in.low	Y 4 in.low		
	Strobex	240	G 2 in.low (5)	R 2 in.low (11)		
TK2	ground track	-	R 2 in.low	Y 4 in.low		
	Strobex	245	G 2 in.low (5)	R 2 in.-3 in.low(11)		
TK3	ground track	-	R 2 in.low	Y 4 in.-6 in.low		
	Strobex	235	R 2½ in.-3 in.low(5)	R 2 in.-4 in.low(11)		
TK4	hover	-	G 3½ in.-4 in.low	Y 3 in.-6 in.low		
	Strobex	240	R 3 in.low(5)	R 3 in.-4 in.low(11)		
TK5	hover	-	G 4 in.low	Y 4 in.-5 in.low		

TABLE XLVII - Continued						
Test No.	Track Type	Rotor RPM Airspeed (kt)	Blade Tracking Results		Corresponding Pitch Link Adjustment (marks)	
			Fwd (clock pos)	Aft (clock pos)	Fwd	Aft
TK6	Strobex	245	R 3in.low (5)	R 4in.low (11)	Y dec 2	G dec 4
	hover	-	G 4 $\frac{1}{2}$ in.low	Y 5 $\frac{1}{2}$ in.low		Y inc 2
X266	Chicago Aerial	-	R 2 1/8in.low(3)	R 2 $\frac{1}{2}$ -2 $\frac{1}{2}$ in.low(3)		
TK1	Strobex	235	G 2-2 $\frac{1}{2}$ in.low	Y 3 7/8-4in.low		
	ground track	-	G - (1)	R 1in.low (11)		
TK2	Strobex	235	R $\frac{1}{2}$ in.low (5)	R $\frac{1}{2}$ in.low (7)		
	ground track	-	G 3/4 in.low	Y 1 in.low		
TK3	Strobex	235	R $\frac{1}{2}$ in.low (9)	R $\frac{1}{2}$ in.low (3)		
	ground track	-	G $\frac{1}{2}$ in.low	Y 1in.low		
TK4	Strobex	245	R 3/4in.low (1)	R 1in.low (11)		
	ground track	-	G 3/4in.low	Y 1 $\frac{1}{2}$ in.low		
TK5	Strobex	245	R $\frac{1}{2}$ in.low (5)	R $\frac{1}{2}$ in.low (7)		
	ground track	-	G 1in.low	Y 1in.low		
TK6	Strobex	245	R $\frac{1}{2}$ in.low (9)	R $\frac{1}{2}$ in.low (3)		
	ground track	-	G 1in.low	Y 1in.low		
TK7	Strobex	235	R 1in.low (1,5&9)	R 2in.low (11)		
	hover	-	G 2in.low	Y 2in.low		
X266	Strobex	240		R 2in.low (11)		
TK9	Strobex	245	R 1in.low (1)	R 2-3in.low (11)		
	hover	-	G 1 $\frac{1}{2}$ in.low	Y 2-3in.low		
TK10	Strobex	245	R 2in.low (5)			
	hover	-	G 3in.low			
TK11	Strobex	245	R 1in.low (9)		Y dec 2	G dec 1
	hover	-	G 2in.low			
X267	Strobex		R 1in.low (1)	R $\frac{1}{2}$ -3/4in.low(11)		
TK1	Strobex		G 2in.low	Y 1 $\frac{1}{2}$ -1 3/4in.low		
	Strobex		R 1in.low (9)		G inc 1	G dec 1
			G 2in.low		Y dec 1	Y inc 1
X268	Strobex	245	G - (1)	Y - (11)		
TK1		70	R 1 in.high	R $\frac{1}{2}$ in.high		
	Strobex	245	G - (5)			
TK2		70	R $\frac{1}{2}$ in.low			

TABLE XLVII - Continued						
Test No.	Track Type	Rotor RPM Airspeed (kt)	Blade Tracking Results		Corresponding Pitch Link Adjustment (marks)	
			Fwd (clock pos)	Aft (clock pos)	Fwd	Aft
TK3	Strobex	245	G - (9)			
X269	Strobex	70	R -			
TK1	Strobex	235	G - (1)	Y - (11)		
		100	R 3/4 in. high	R 3/4 in. high		
TK2	Strobex	235	G - (5)			
		100	R 1/2 in. low			
TK2	Strobex	235	G - (5)			
		100	R 1/2 in. low			
TK3	Strobex	235	G - (9)			
		100	R -			
TK4	Strobex	235	G - (5)			
	mid target	100	R 1/2 in. high			
TK5	Strobex	235	G - (9)		R dec 1	R dec 1
X270	Strobex	100	R 1 in. high			
TK1	Strobex	245	G - (1)	Y - (11)		
		100	R 1/2 in. high	R 1/2 in. high		
TK2	Strobex	245	G - (5,9)			
		100	R -			
TK3	Strobex	245	G - (5)			
	mid target	100	R 1/2 in. high			
TK4	Strobex	245	G - (9)		R dec 1	R dec 1
	mid target	100	R 3/4 in. high			
X271	Strobex	245	G - (1)			
TK1	Strobex	100	R 1 in. low			
TK2	Strobex	245	G - (5)			
		100	R 1/2-3/4 in. low			
TK3	Strobex	245	G - (9)			
		100	R -			
TK4	Strobex	245	G - (5)			
	mid target	100	R 1/2-3/4 in. high			
TK5	Strobex	245	G - (9)		R dec 1	
	mid target	100	R 1/2 in. high			
X272	Strobex		G 3 in. low (11)	Y - (11)		
TK1			R 4 in. low	R 1 in. low		

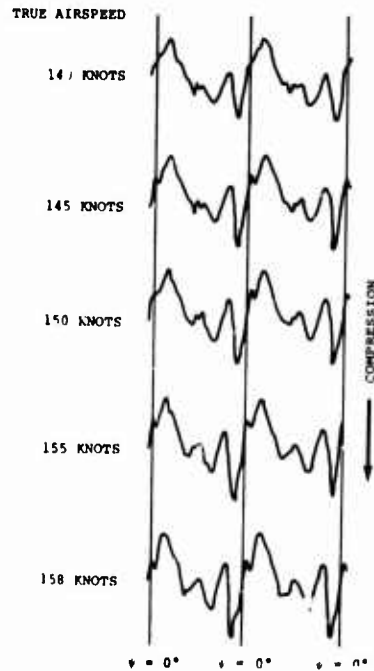
TABLE XLVII - Continued						
Test No.	Track Type	Rotor RPM Airspeed (kt)	Blade Tracking Results		Corresponding Pitch Link Adjustment (marks)	
			Fwd (clock pos)	Aft (clock pos)	Fwd	Aft
TK2	Strobex		G 2in.low (1)			
	Strobex		R 2½in.low			
TK3	mid target		R ¾in.low (11)		Y dec 3	R inc 1
X280	Strobex	235	G ¾in.low		R inc 1	
TK1		135	G - (1)	Y - (11)		
	Strobex	235	R ½in.low	R ½-¾in.high		
TK2		135	G - (5,9)			
X280	Strobex	235	R -			
TK3	mid target	135	G - (5)			
	Strobex	235	R ½in.high			
TK4	mid target	135	G - (9)			
			R ½in.high			
NOTES: 1. R = red 2. Y = yellow 3. G = green 4. inc = increase (length of pitch link) 5. dec = decrease						

APPENDIX II

PITCH LINK LOAD WAVEFORMS

This appendix contains a display of the pitch link waveforms examined in the process of establishing waveform characteristics and moment stall inception for the AGB flight program. Waveforms have been included for flights 255, 270, 271, 272, 284, 285, and 286.

- NOTES: 1. FLIGHT 255
2. RUNS 9 THROUGH 13
3. CG = 6.2 IN. AFT
4. ALTITUDE = 6,000 FT



- NOTES 1. FLIGHT 253
2. RUNS 29 THROUGH 33
3. CG = 6.7 IN. AFT
4. ALTITUDE = 7,500 FT

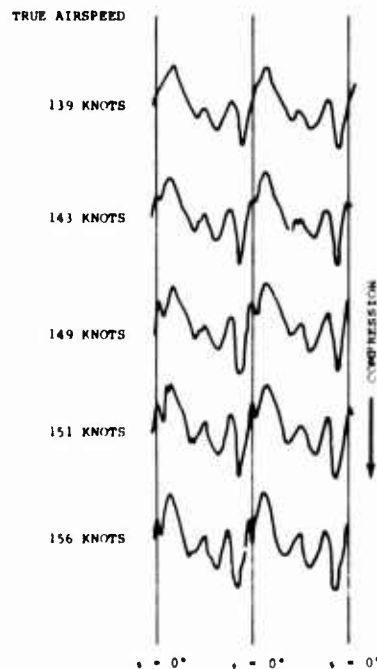
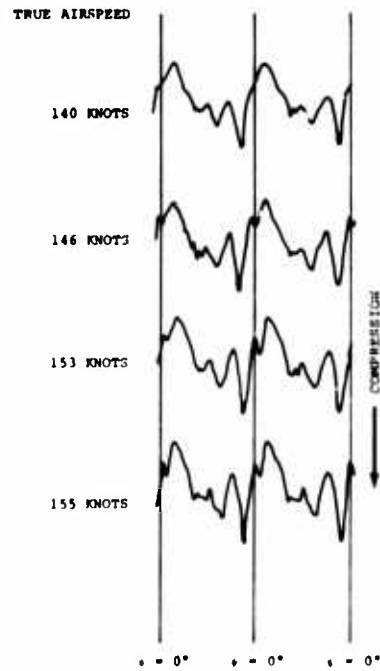


Figure 317. CH-47C/AGB Pitch Link Load Waveforms, Gross Weight = 40,000 Pounds, Rotor RPM = 235, Density Altitude = 6,000-7,500 Feet.

- NOTES: 1. FLIGHT 270
2. RUNS 12 THROUGH 15
3. CG = 4.9 IN. AFT
4. ALTITUDE = 3,000 FT



- NOTES: 1. FLIGHT 284
2. RUNS 4 THROUGH 8
3. CG = 4.4 IN. AFT
4. ALTITUDE = 5,600 FT

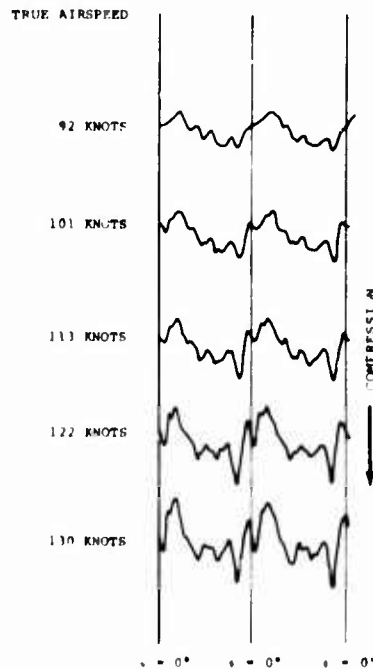
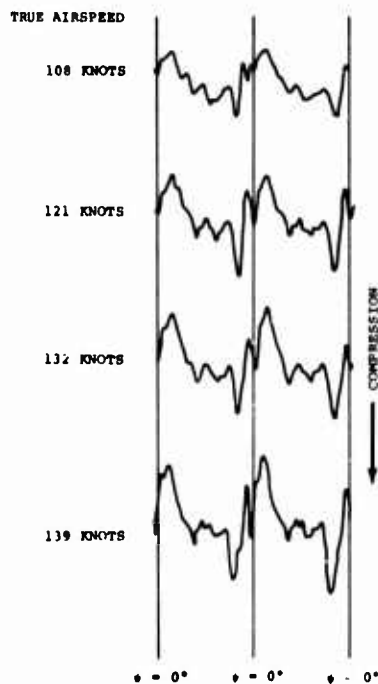


Figure 318. CH-47C/AGB Pitch Link Load Waveforms, Gross Weight = 46,000 Pounds, Rotor RPM = 235, Density Altitude = 3,000-5,600 Feet.

- NOTES: 1. FLIGHT 272
2. RUNS 15 THROUGH 18
3. CG = 4.3 IN. AFT
4. ALTITUDE = 6,000 FT



- NOTES: 1. FLIGHT 284
2. RUNS 10, 12, 14, 16
3. CG = 4.7 IN. AFT
4. ALTITUDE = 7,500 FT

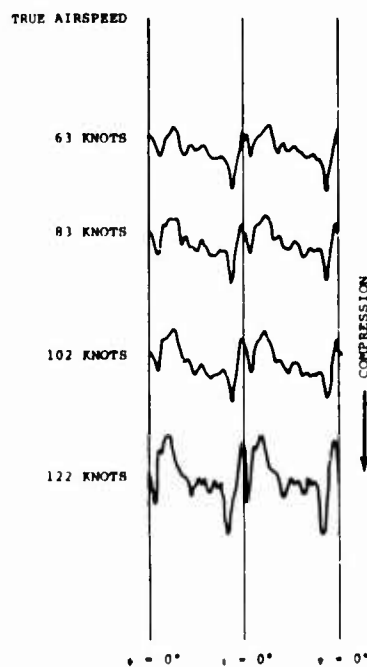
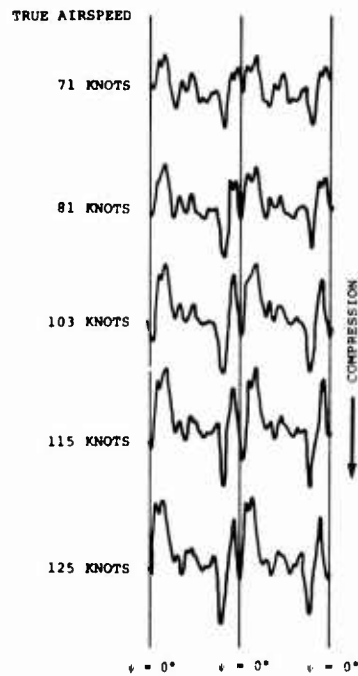


Figure 319. CH-47C/AGB Pitch Link Load Waveforms, Gross Weight = 46,000 Pounds, Rotor RPM = 235, Density Altitude = 6,000-7,500 Feet.

- NOTES: 1. FLIGHT 271
2. RUNS 16, 17, 19, 21, 23
3. CG = 4.1 IN. AFT
4. ALTITUDE = 10,400 FT



- NOTES: 1. FLIGHT 272
2. RUNS 6, 8, 10, 12
3. CG = 4.3 IN. AFT
4. ALTITUDE = 6,000 FT

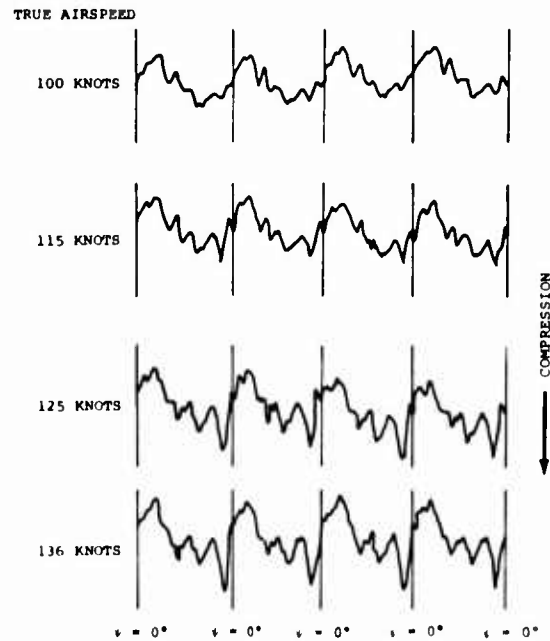
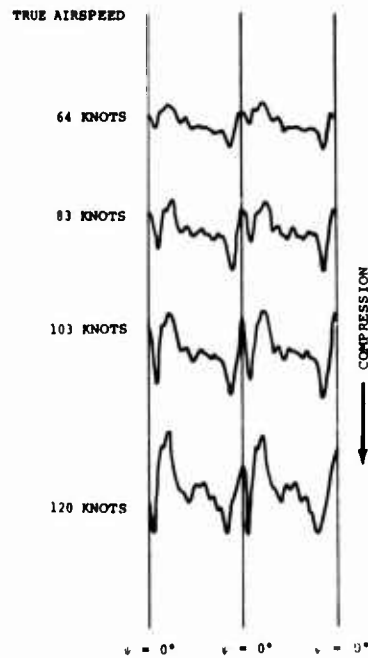


Figure 321. CH-47C/AGB Pitch Link Load Waveforms, Gross Weight = 46,000 Pounds, Rotor RPM = 245, Density Altitude = 6,000-10,400 Feet.

- NOTES: 1. FLIGHT 284
2. RUNS 19, 21, 23, 25
3. CG = 4.7 IN. AFT
4. ALTITUDE = 9,400 FT



- NOTES: 1. FLIGHT 284
2. RUNS 28, 30, 32, 34
3. CG = 5.3 IN. AFT
4. ALTITUDE = 11,000 FT

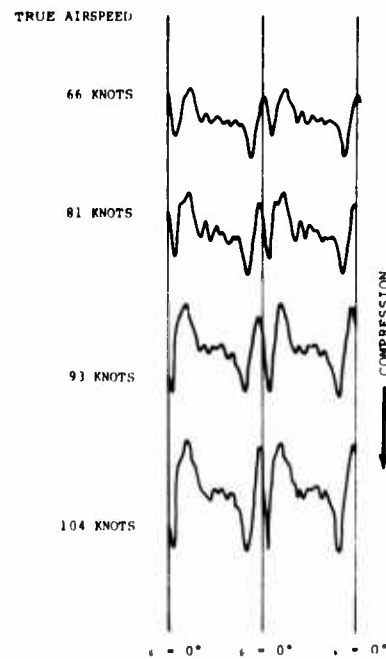
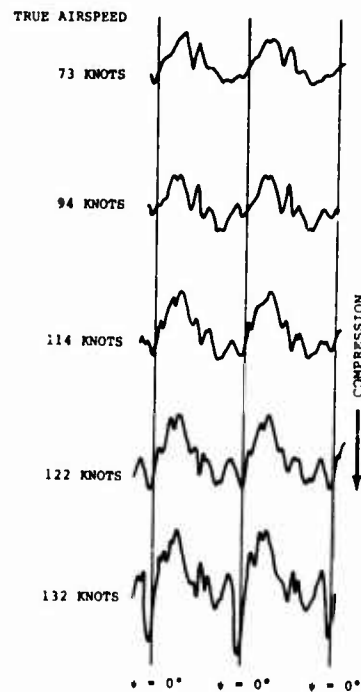


Figure 320. CH-47C/AGB Pitch Link Load Waveforms, Gross Weight = 46,000 Pounds, Rotor RPM = 235, Density Altitude = 9,400-11,000 Feet.

NOTES: 1. FLIGHT 285
2. RUNS 7, 9, 11, 12, 14
3. CG = 0.5 IN. AFT
4. ALTITUDE = 2,500 FT



NOTES: 1. FLIGHT 286
2. RUNS 17 THROUGH 20
3. CG = 0.5 IN. AFT
4. ALTITUDE = 10,000 FT

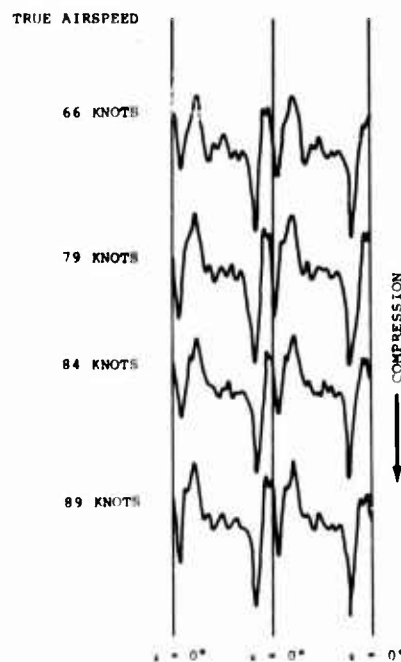


Figure 322. CH-47C/AGB Pitch Link Load Waveforms, Gross Weight = 50,000 Pounds, Rotor RPM = 245, Density Altitude = 2,500-10,000 Feet.

APPENDIX III

CONTROL AND ROTOR SHAFT LOADS

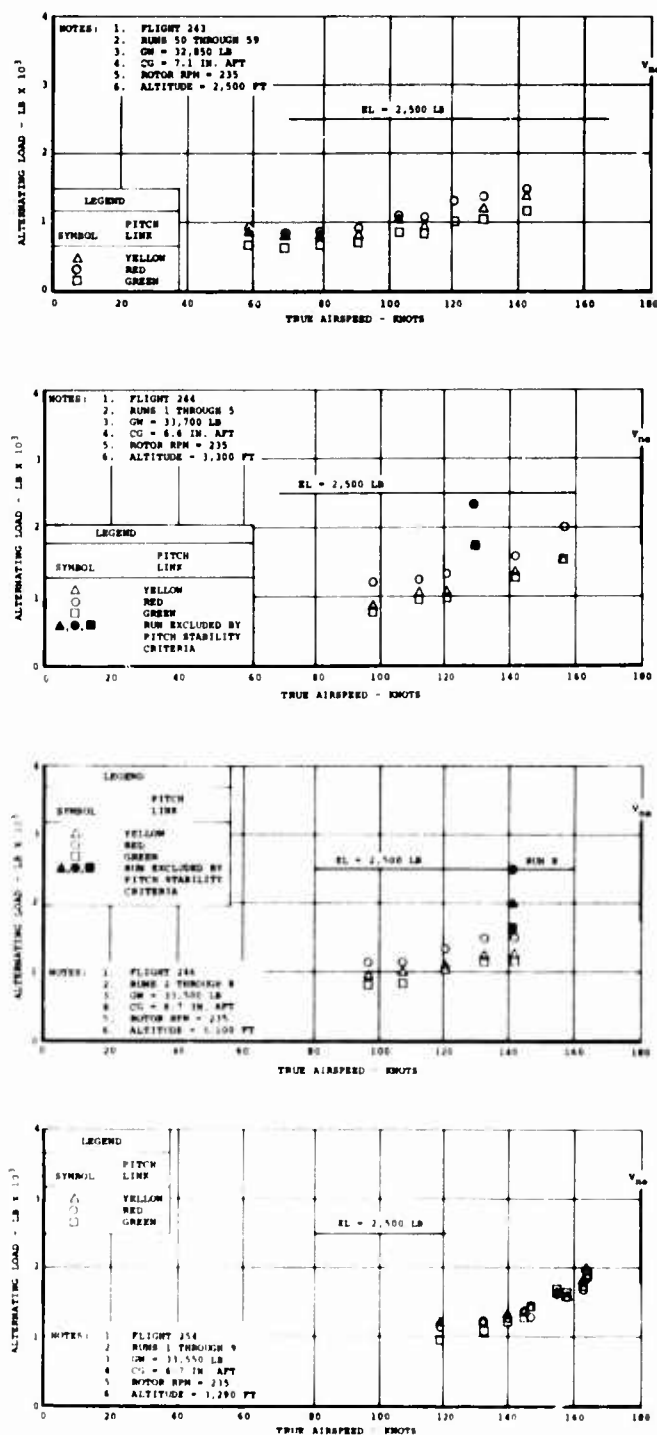


Figure 323. Aft Pitch Link Loads on CH-47C Helicopter Equipped With Advanced-Geometry Blades.

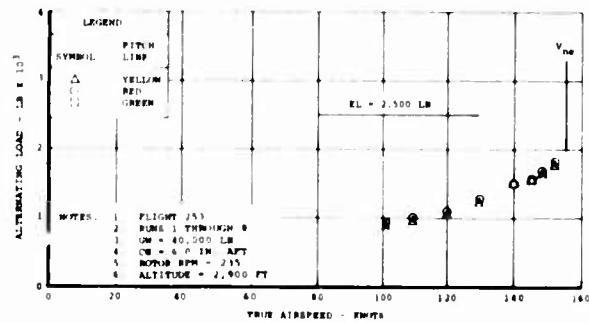
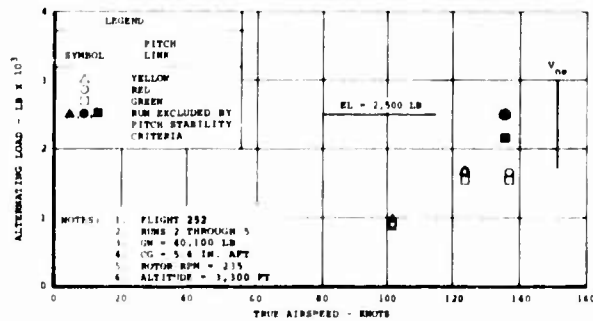
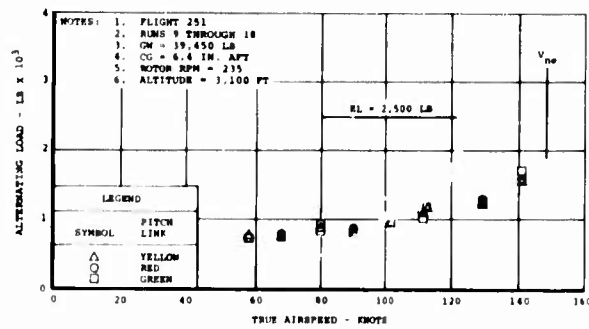
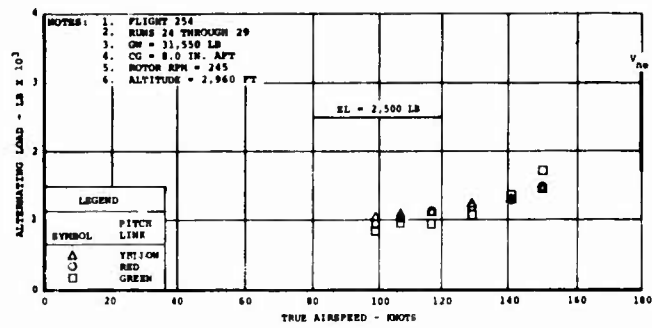


Figure 324. Aft Pitch Link Loads on CH-47C Helicopter Equipped With Advanced-Geometry Blades.

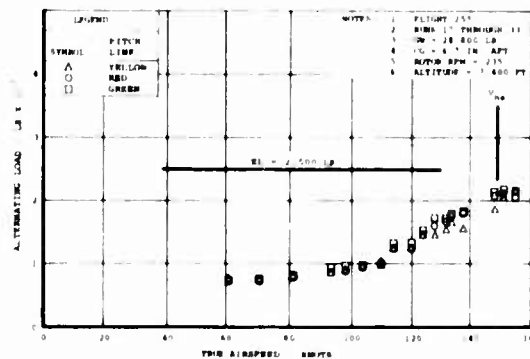
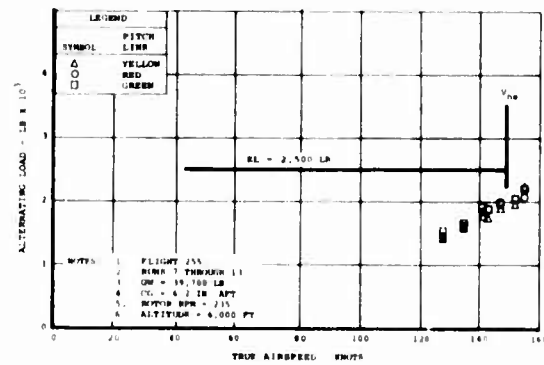
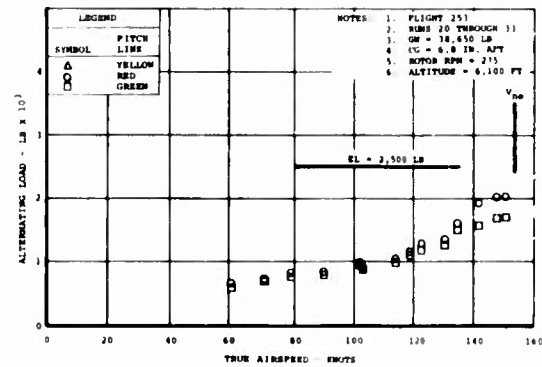
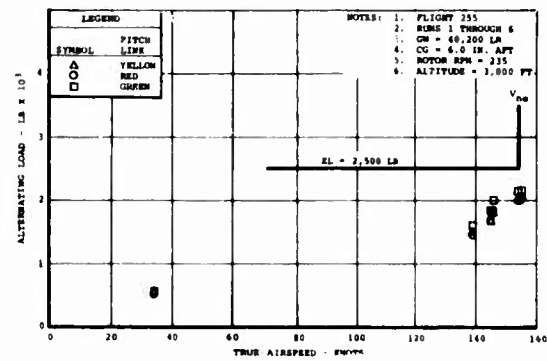


Figure 325. Aft Pitch Link Loads on CH-47C Helicopter Equipped With Advanced-Geometry Blades.

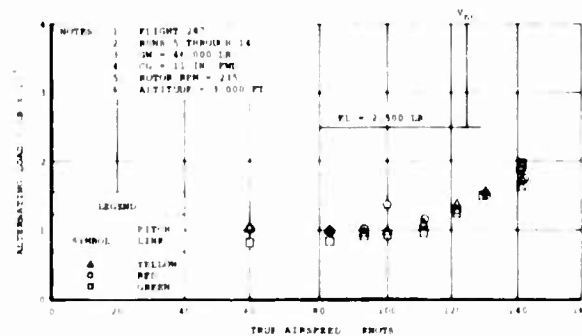
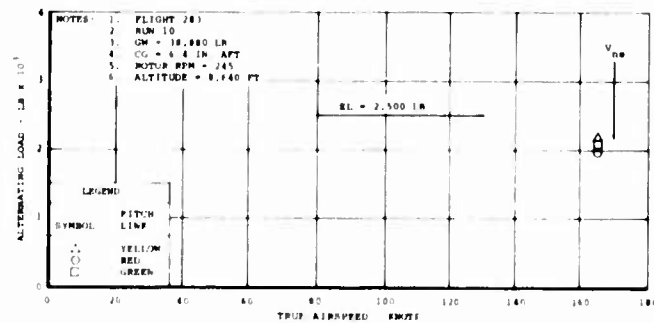
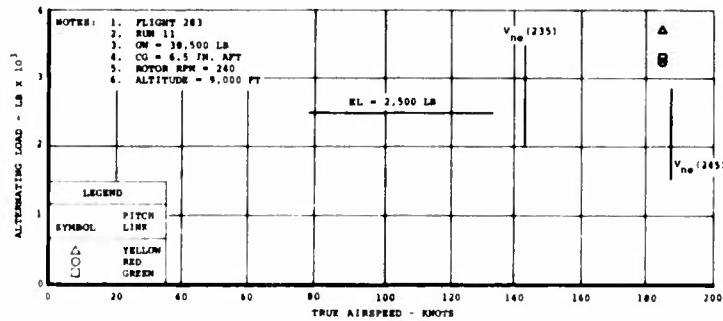
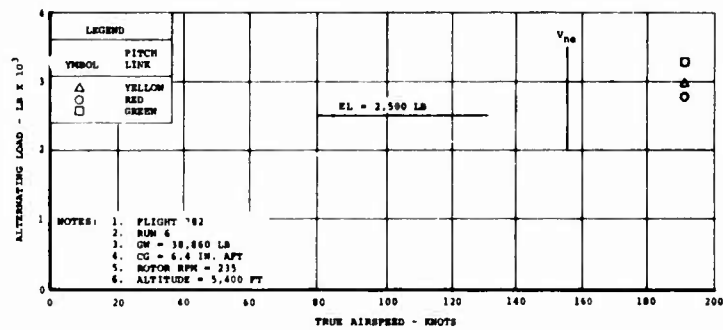


Figure 326. Aft Pitch Link Loads on CH-47C Helicopter Equipped With Advanced-Geometry Blades.

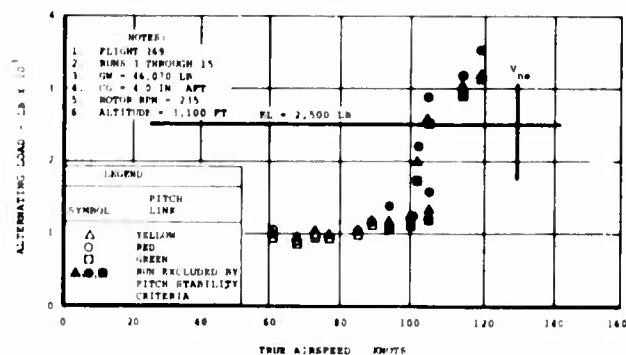
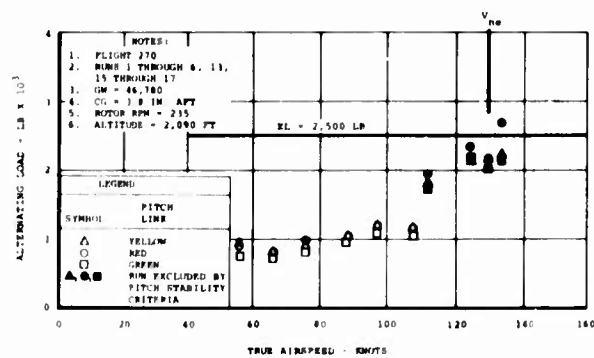
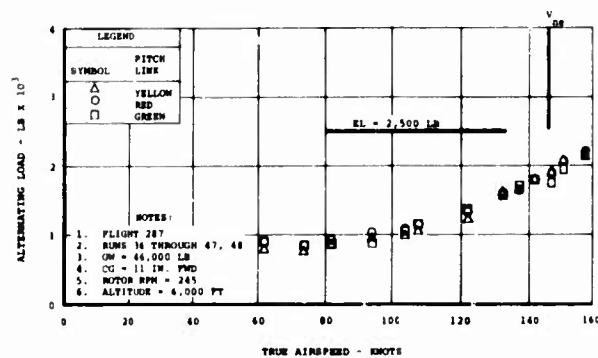
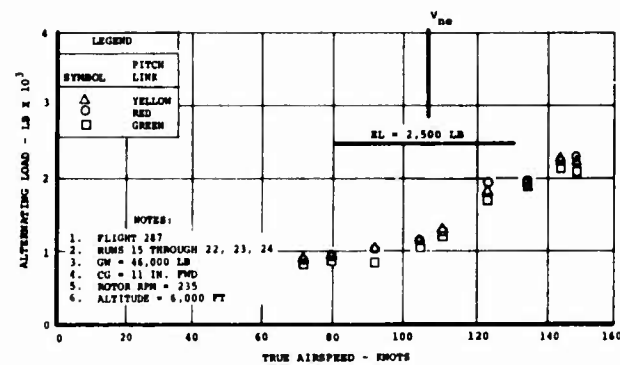


Figure 327. Aft Pitch Link Loads on CH-47C Helicopter Equipped With Advanced-Geometry Blades.

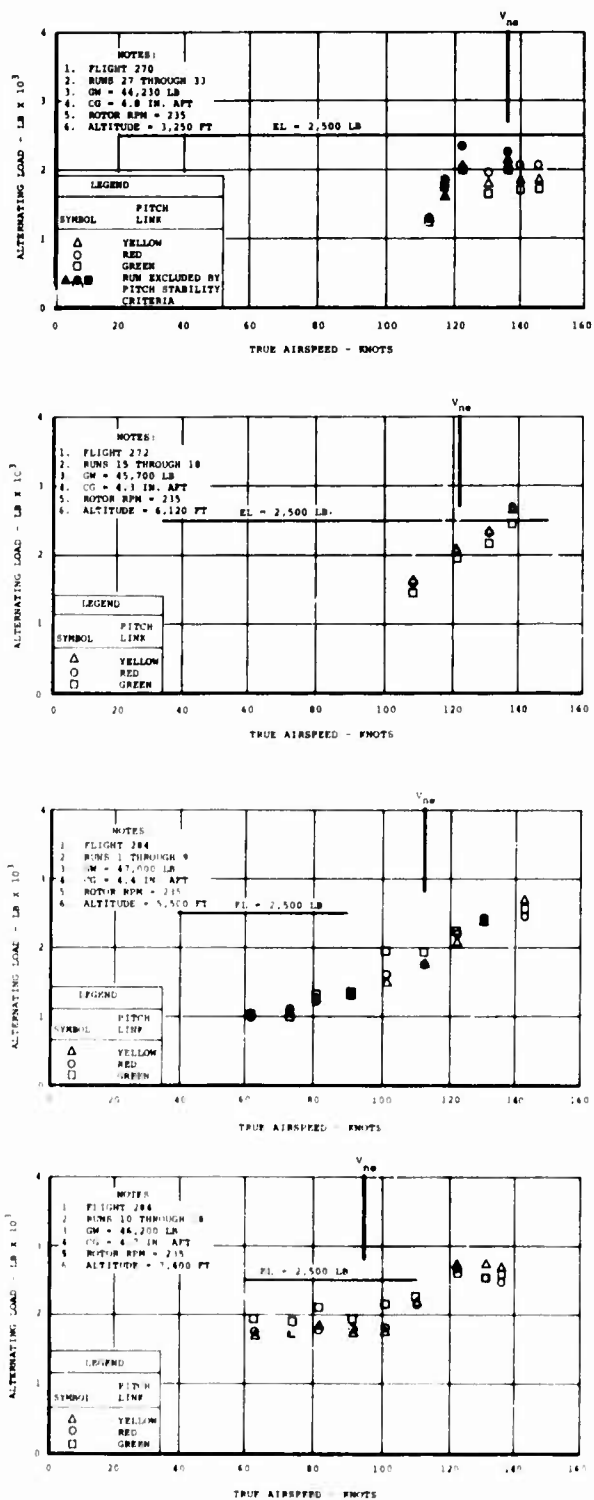


Figure 328. Aft Pitch Link Loads on CH-47C Helicopter Equipped With Advanced-Geometry Blades.

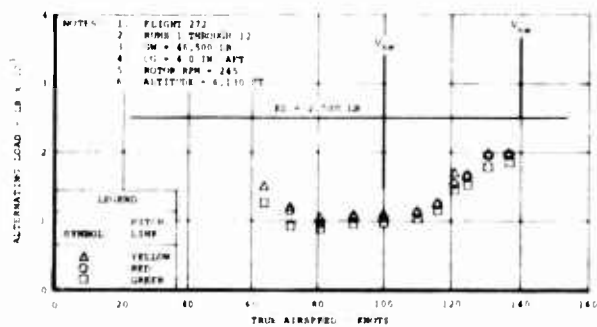
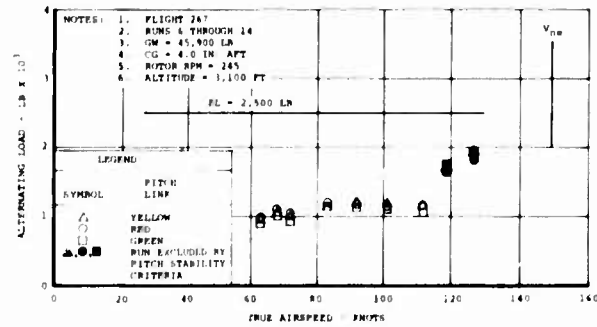
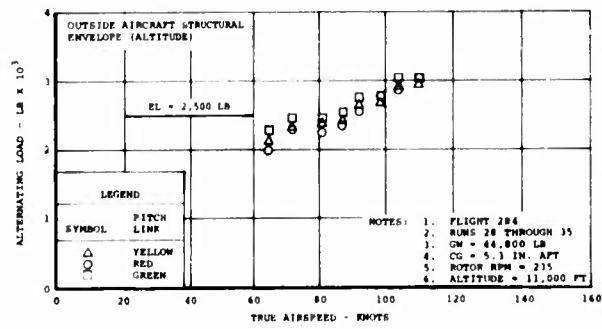
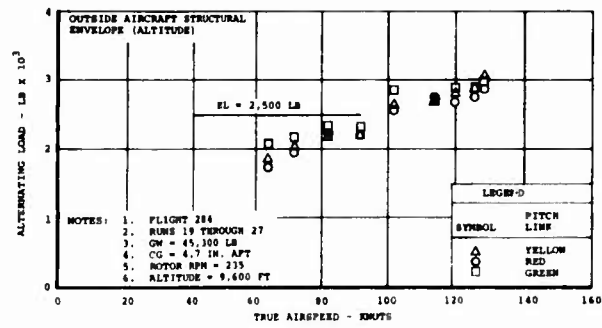


Figure 329. Aft Pitch Link Loads on CH-47C Helicopter Equipped With Advanced-Geometry Blades.

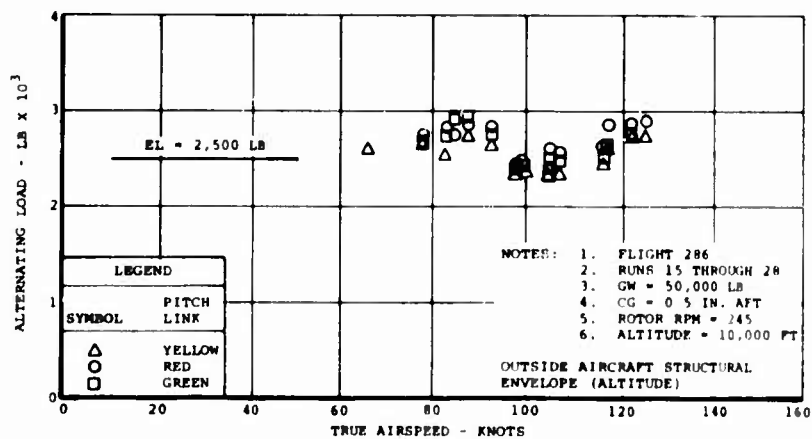
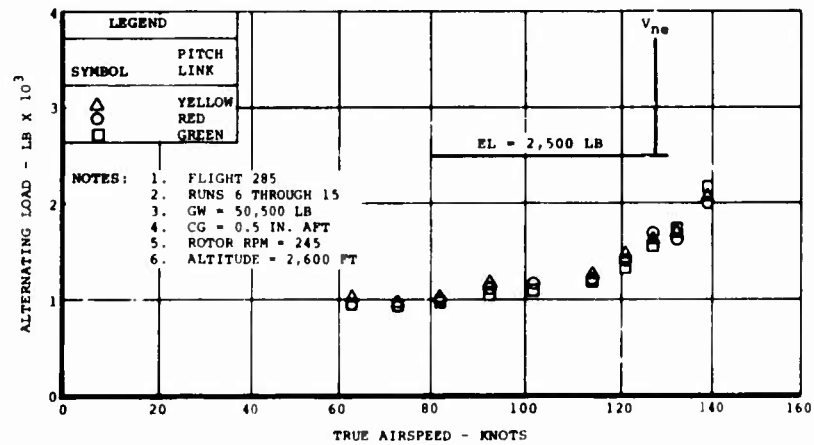
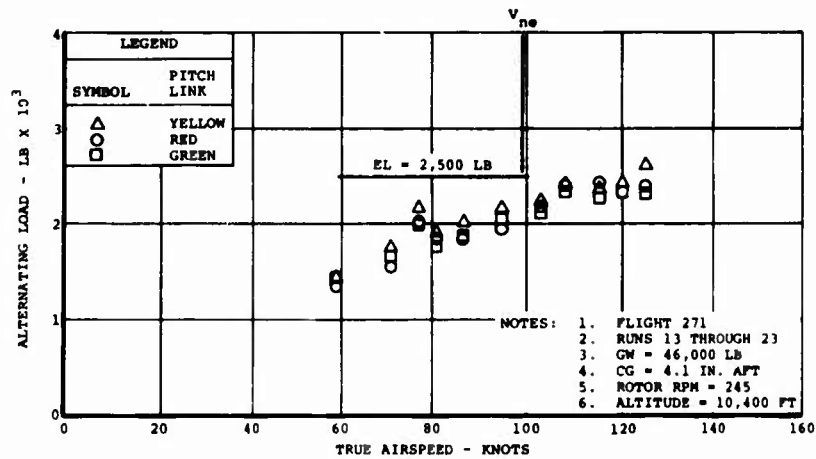


Figure 330. Aft Pitch Link Loads on CH-47C Helicopter Equipped With Advanced-Geometry Blades.

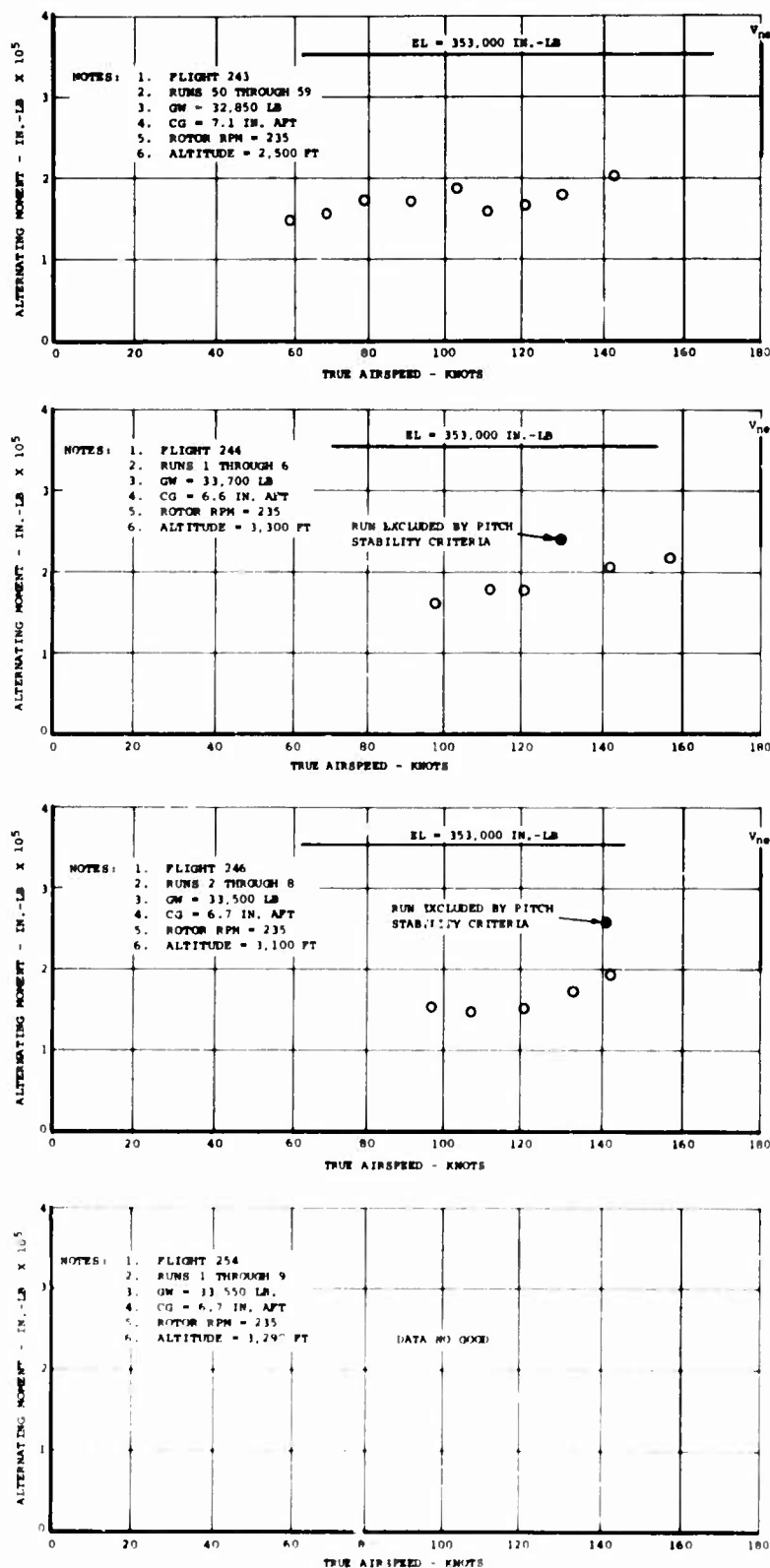


Figure 331. Aft Rotor Shaft Bending Loads on CH-47C Helicopter Equipped With Advanced-Geometry Blades.

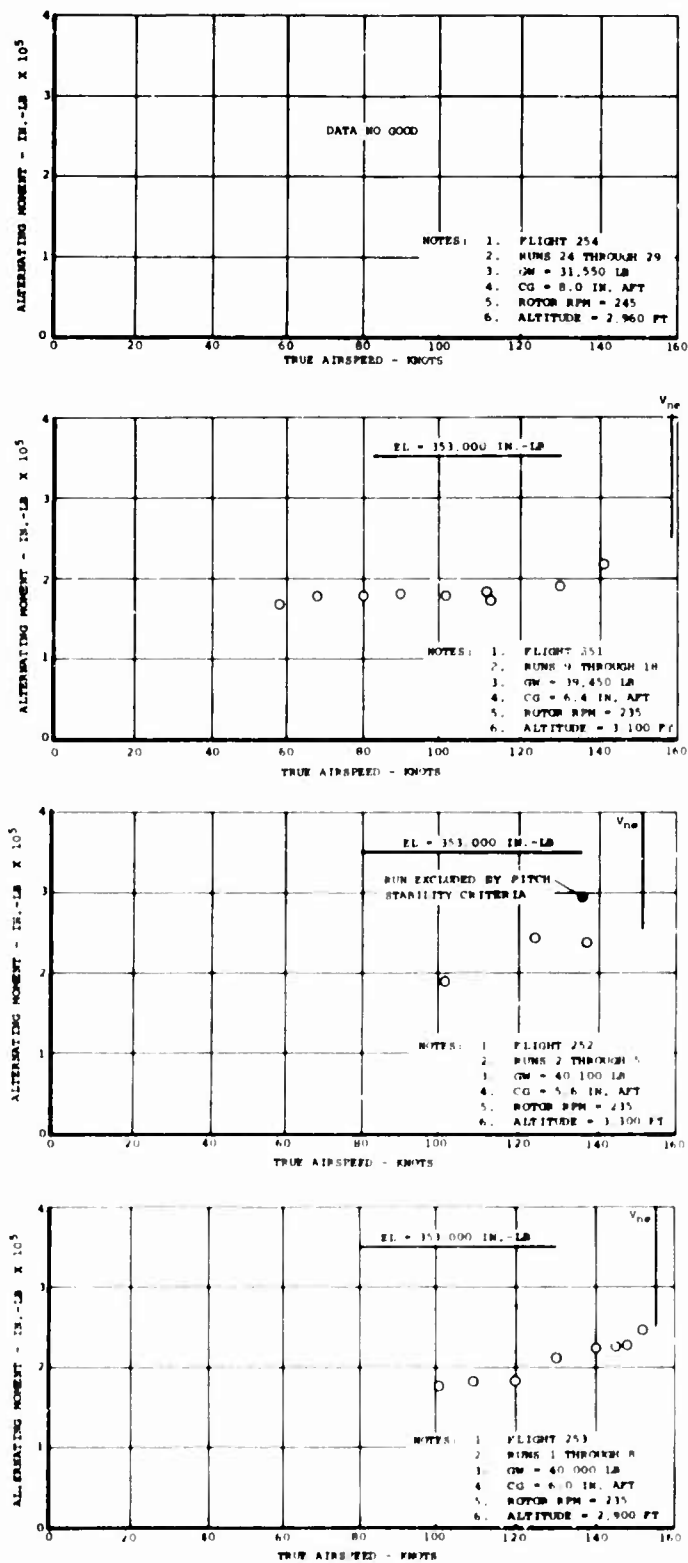


Figure 332. Aft Rotor Shaft Bending Loads on CH-47C Helicopter Equipped With Advanced-Geometry Blades.

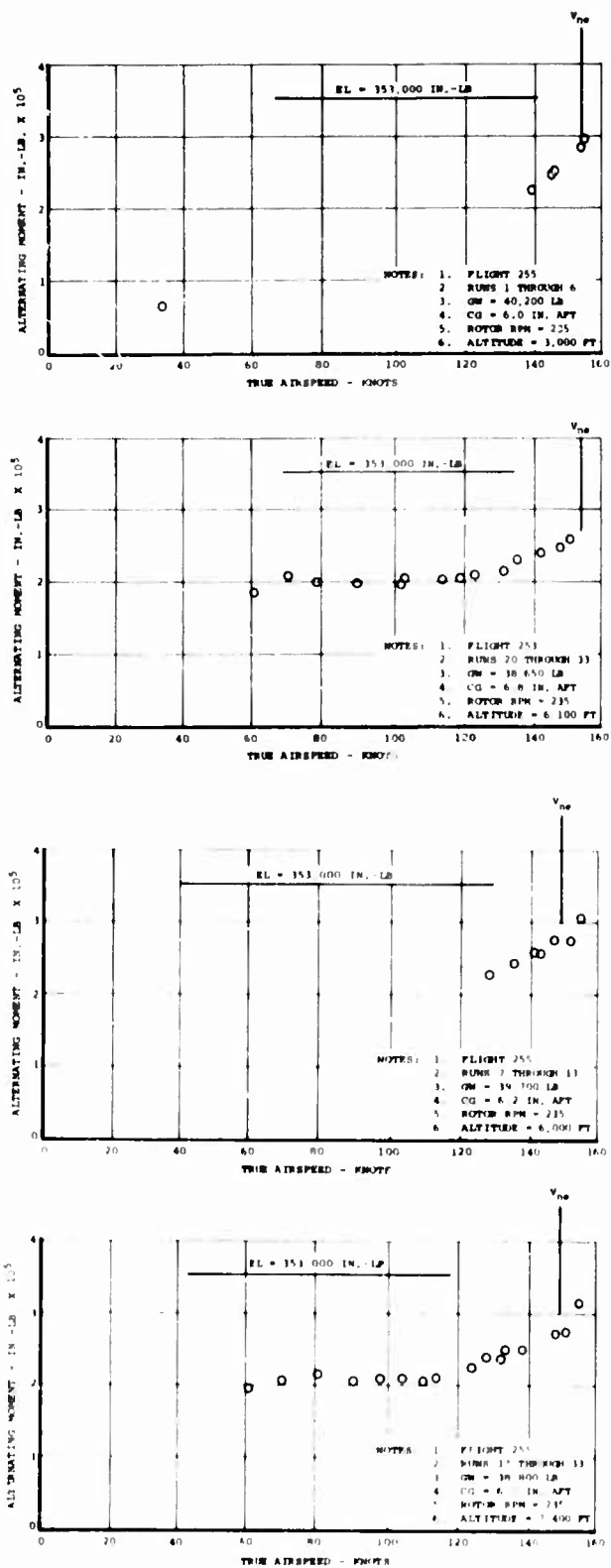


Figure 333. Aft Rotor Shaft Bending Loads on CH-47C Helicopter Equipped With Advanced-Geometry Blades.

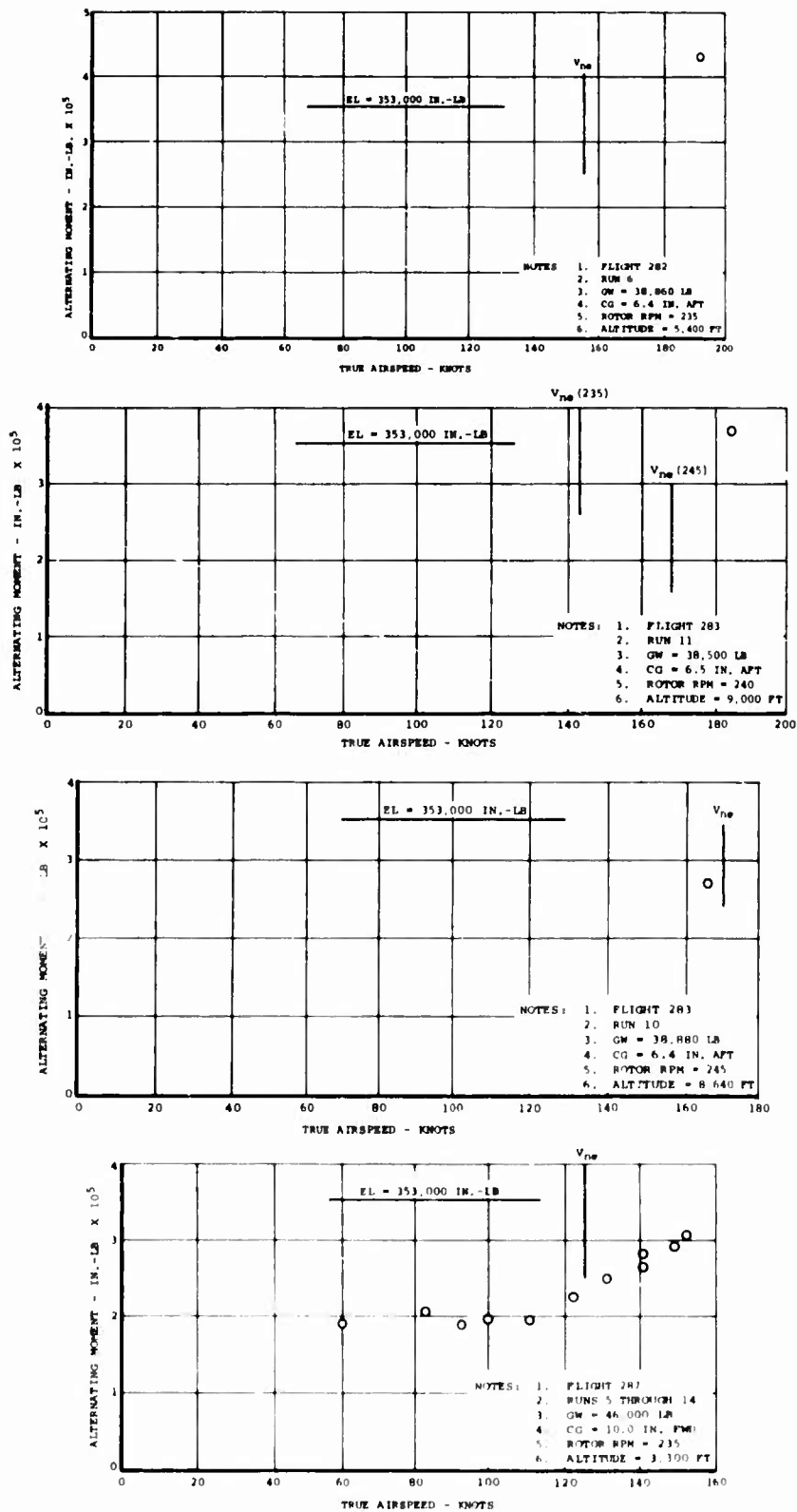


Figure 334. Aft Rotor Shaft Bending Loads on CH-47C Helicopter Equipped With Advanced-Geometry Blades.

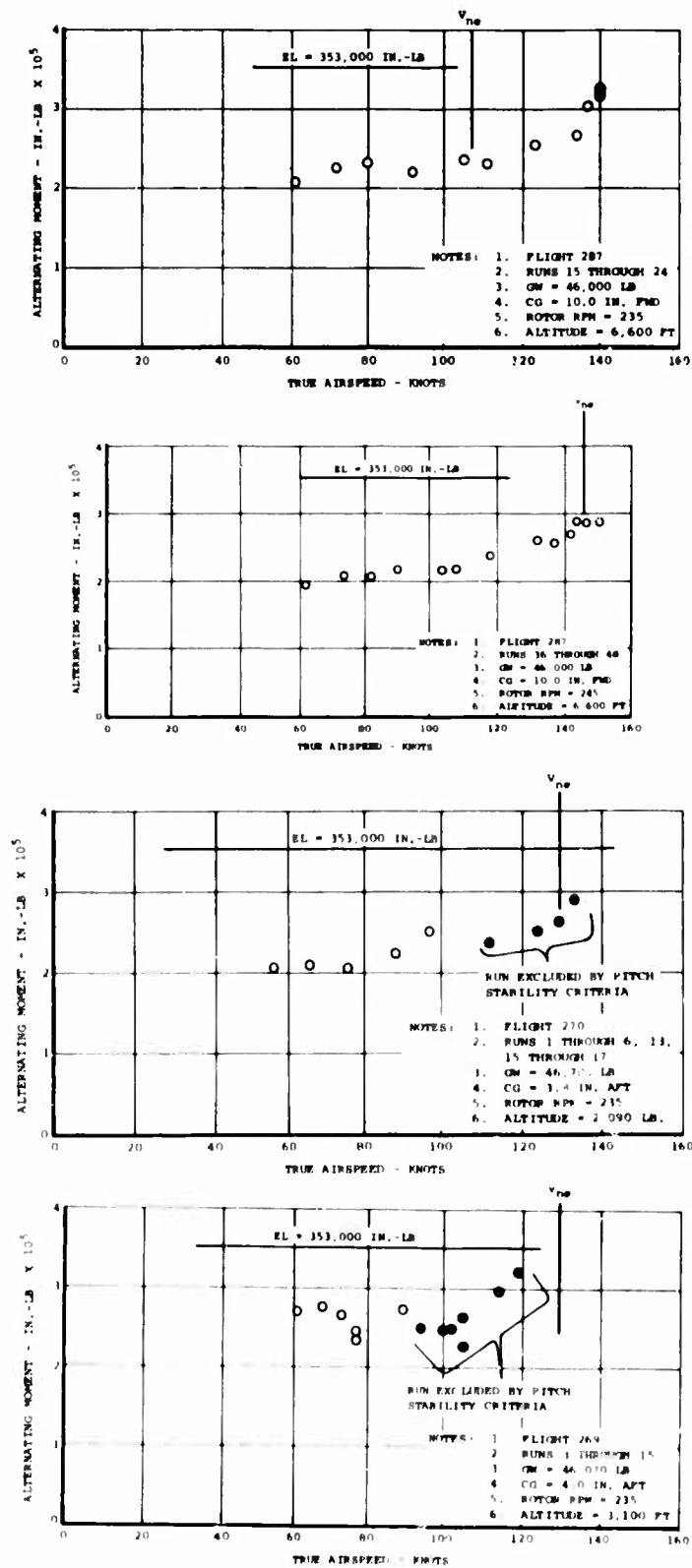


Figure 335. Aft Rotor Shaft Bending Loads on CH-47C Helicopter Equipped With Advanced-Geometry Blades.

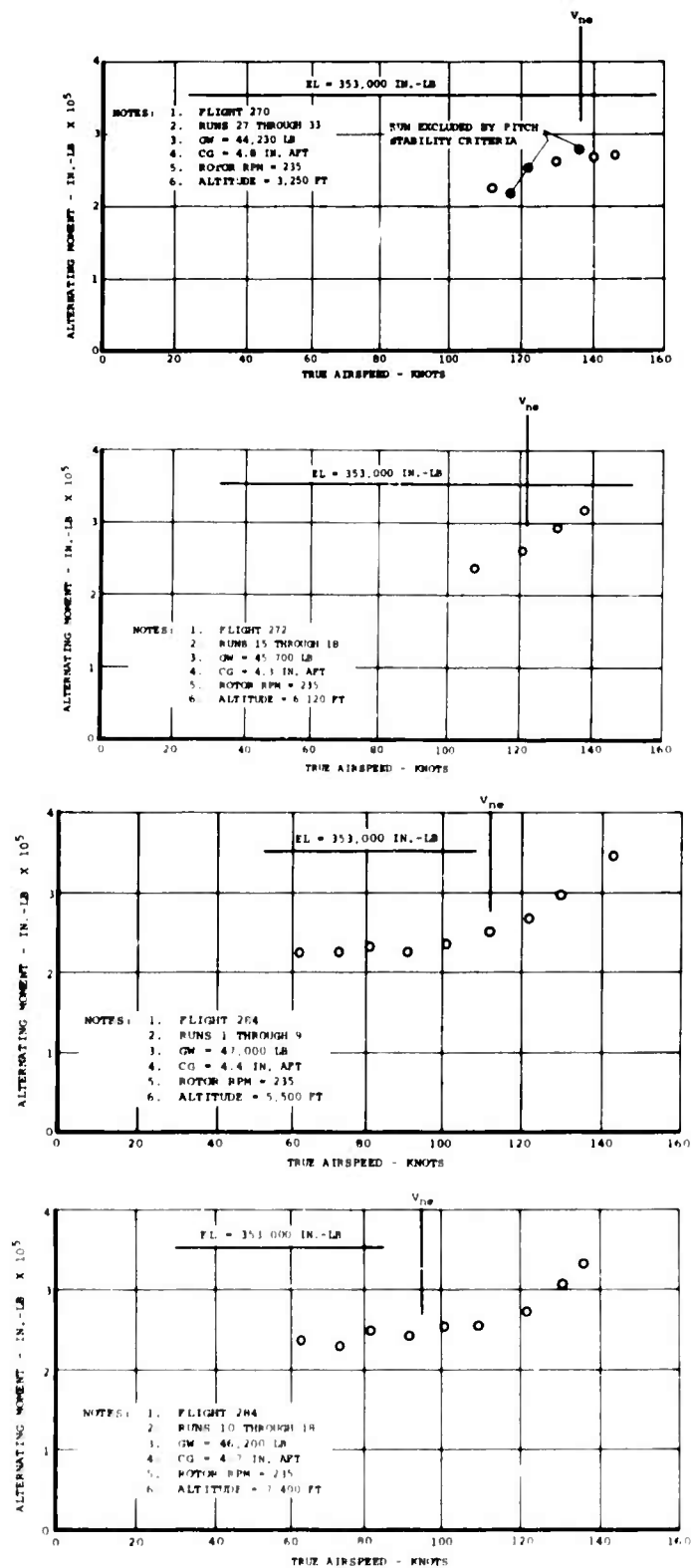


Figure 336. Aft Rotor Shaft Bending Loads on CH-47C Helicopter Equipped With Advanced-Geometry Blades.

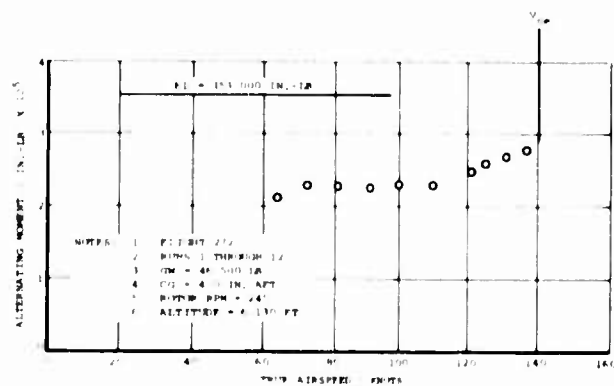
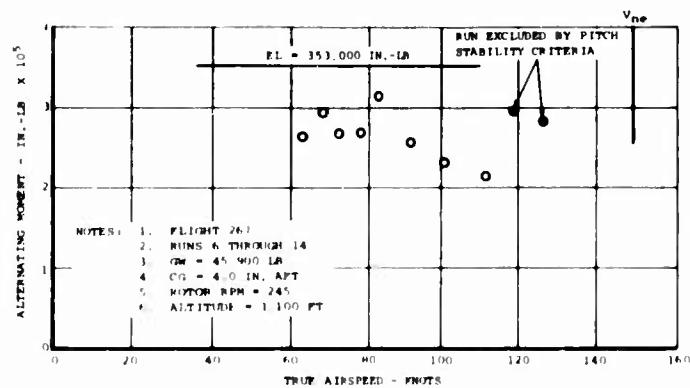
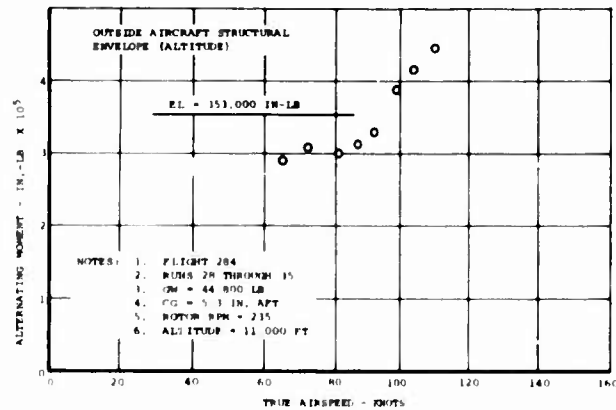
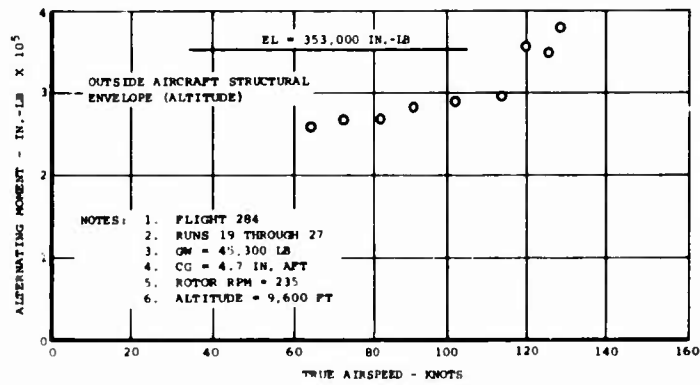


Figure 337. Aft Rotor Shaft Bending Loads on CH-47C Helicopter Equipped With Advanced-Geometry Blades.

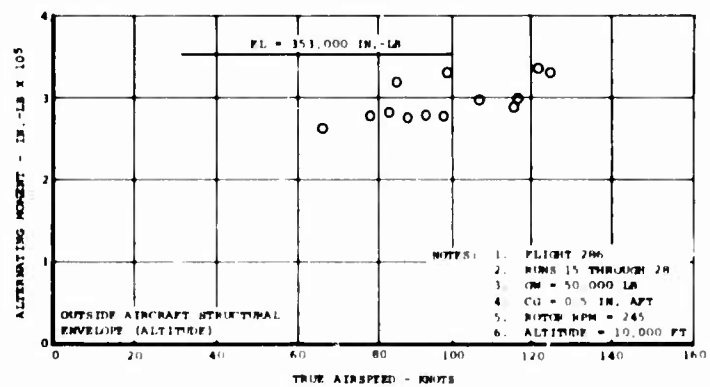
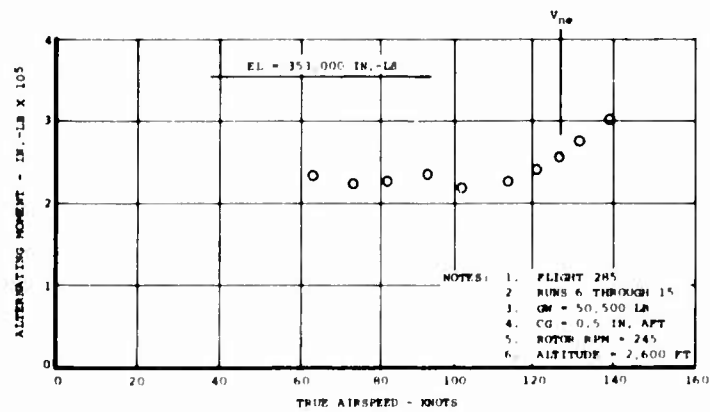
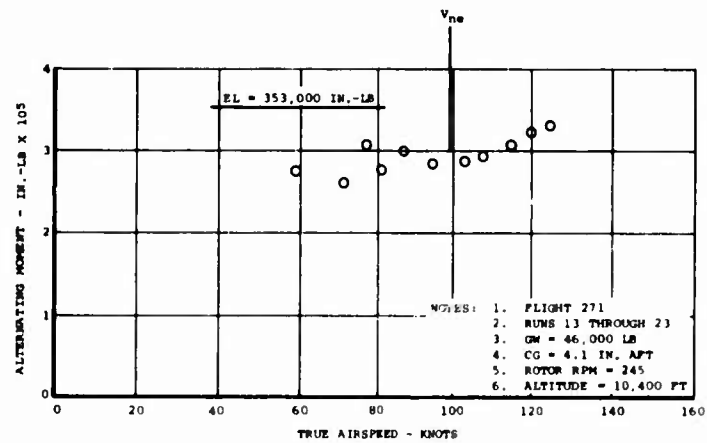


Figure 338. Aft Rotor Shaft Bending Loads on CH-47C Helicopter Equipped With Advanced-Geometry Blades.

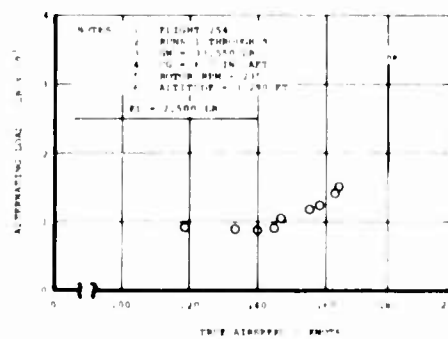
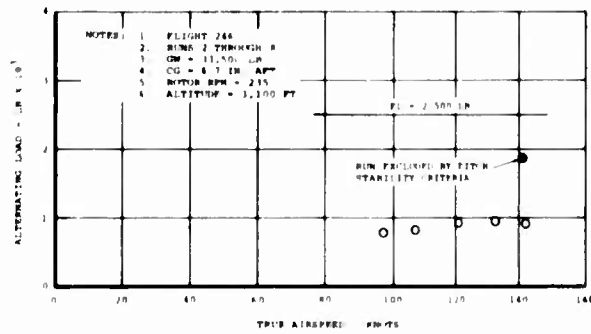
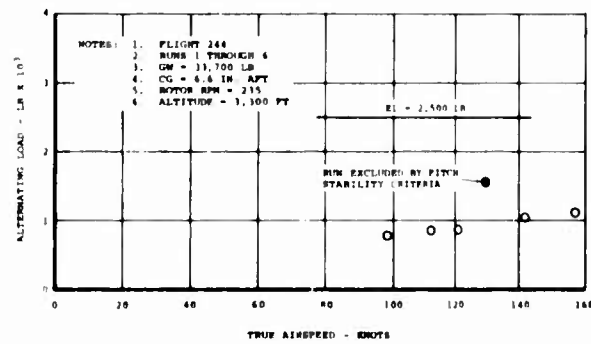
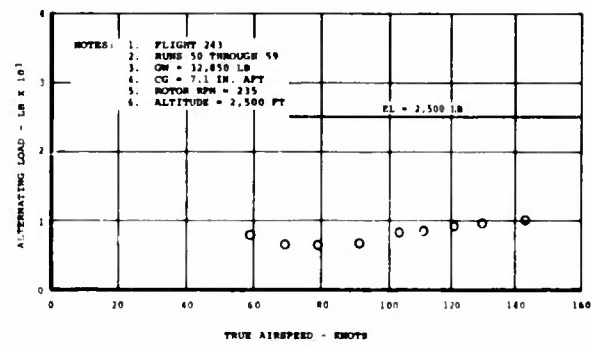


Figure 339. Aft Fixed Link Loads on CH-47C Helicopter Equipped With Advanced-Geometry Blades.

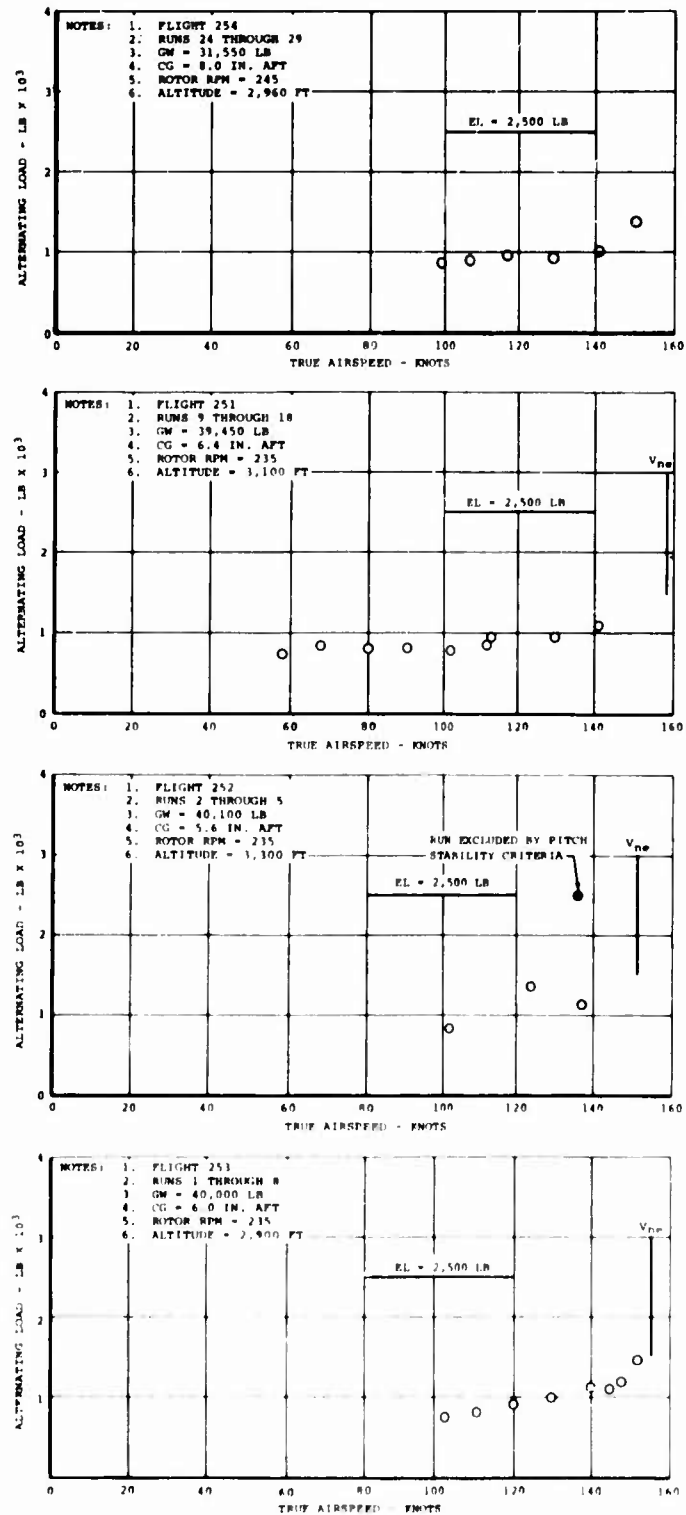


Figure 340. Aft Fixed Link Loads on CH-47C Helicopter Equipped With Advanced-Geometry Blades.

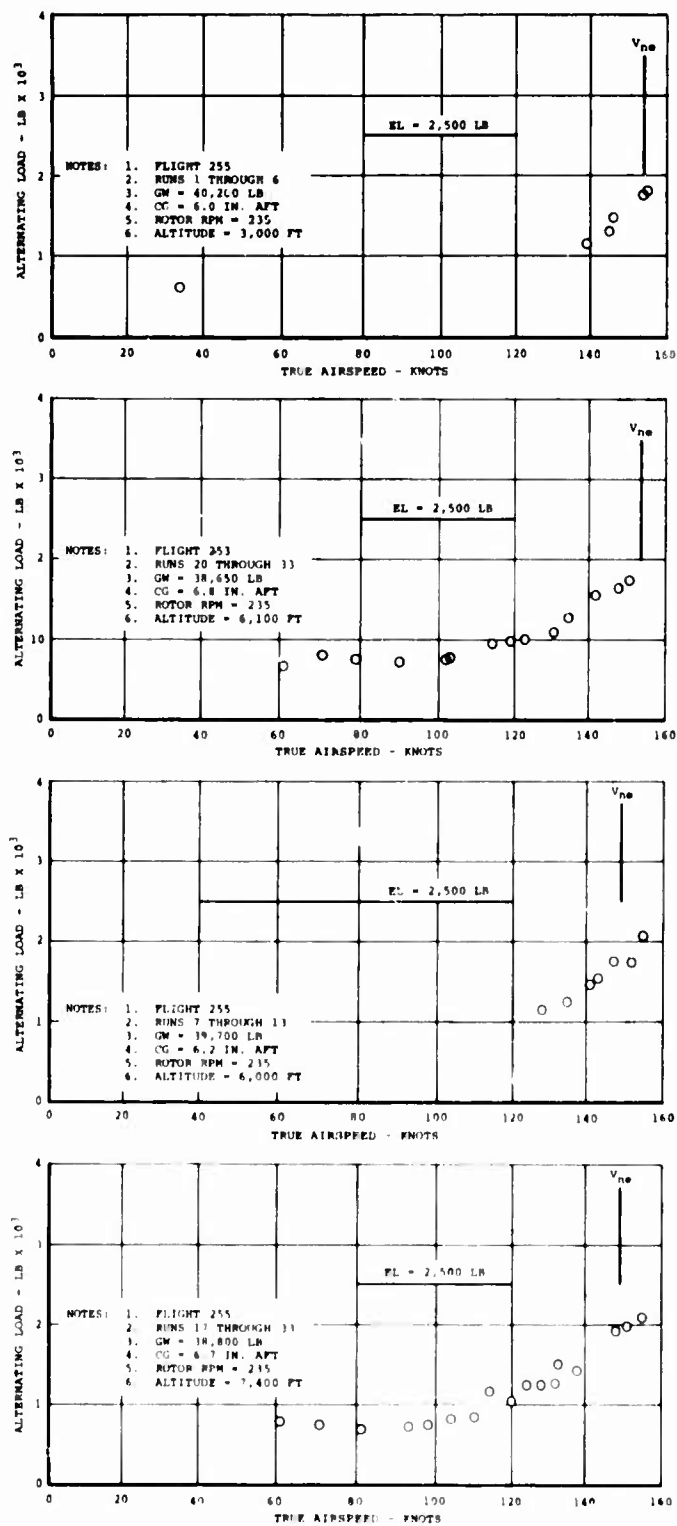


Figure 341. Aft Fixed Link Loads on CH-47C Helicopter Equipped With Advanced-Geometry Blades.

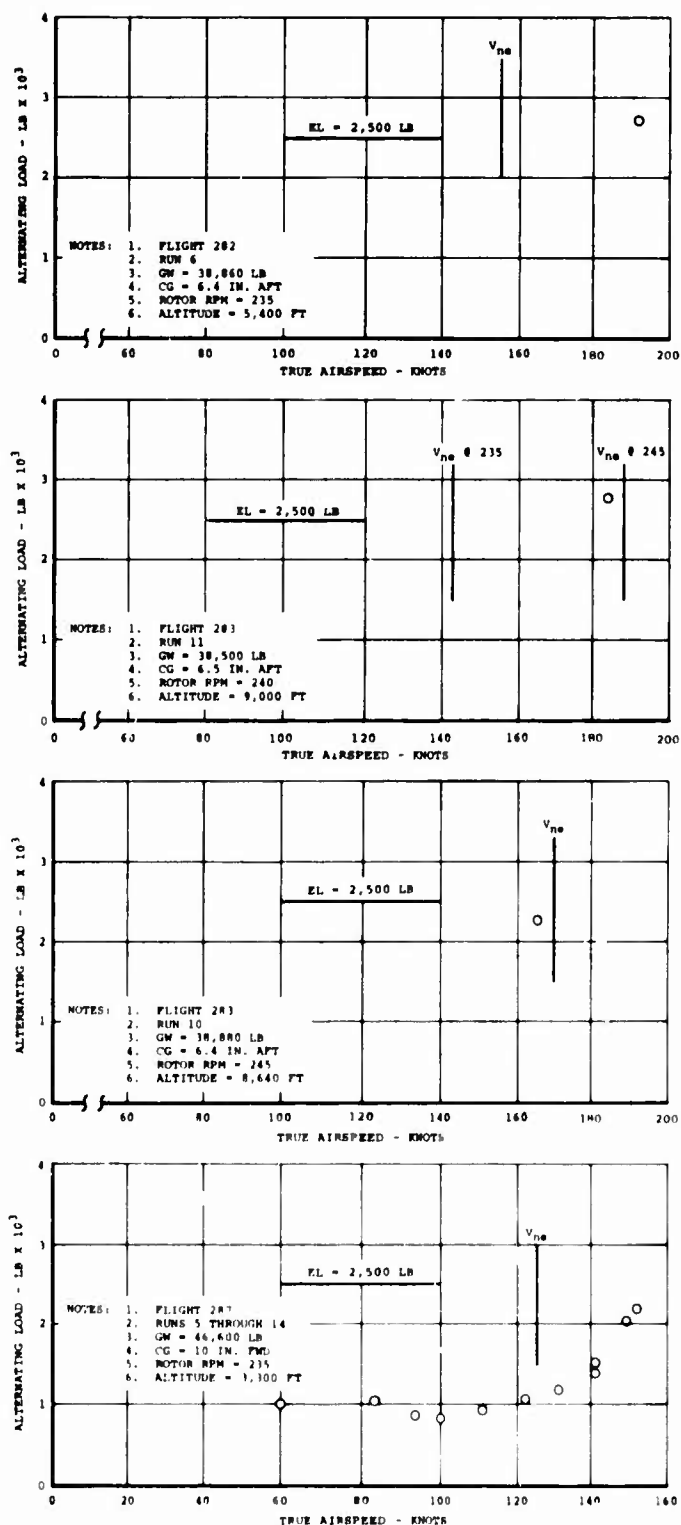


Figure 342. Aft Fixed Link Loads on CH-47C Helicopter Equipped With Advanced-Geometry Blades.

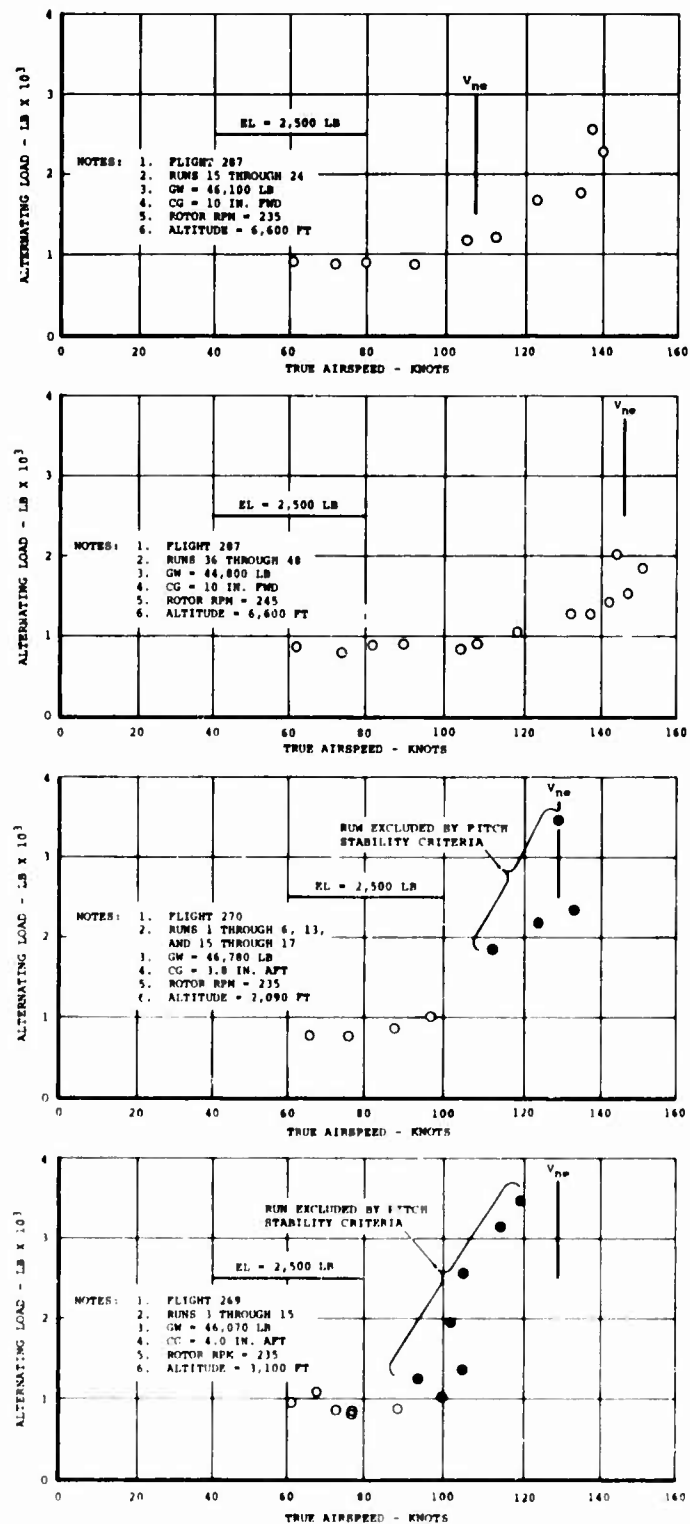


Figure 343. Aft Fixed Link Loads on CH-47C Helicopter Equipped With Advanced-Geometry Blades.

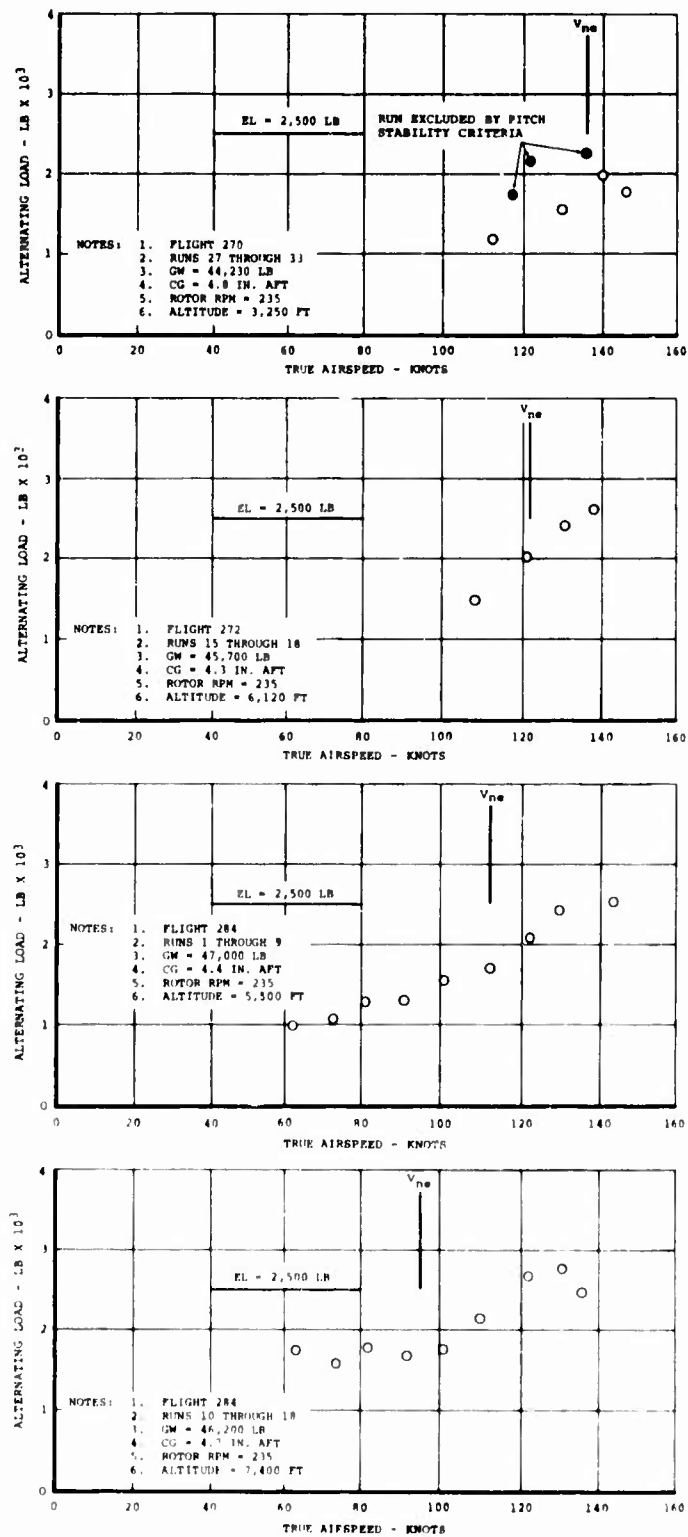


Figure 344. Aft Fixed Link Loads on CH-47C Helicopter Equipped With Advanced-Geometry Blades.

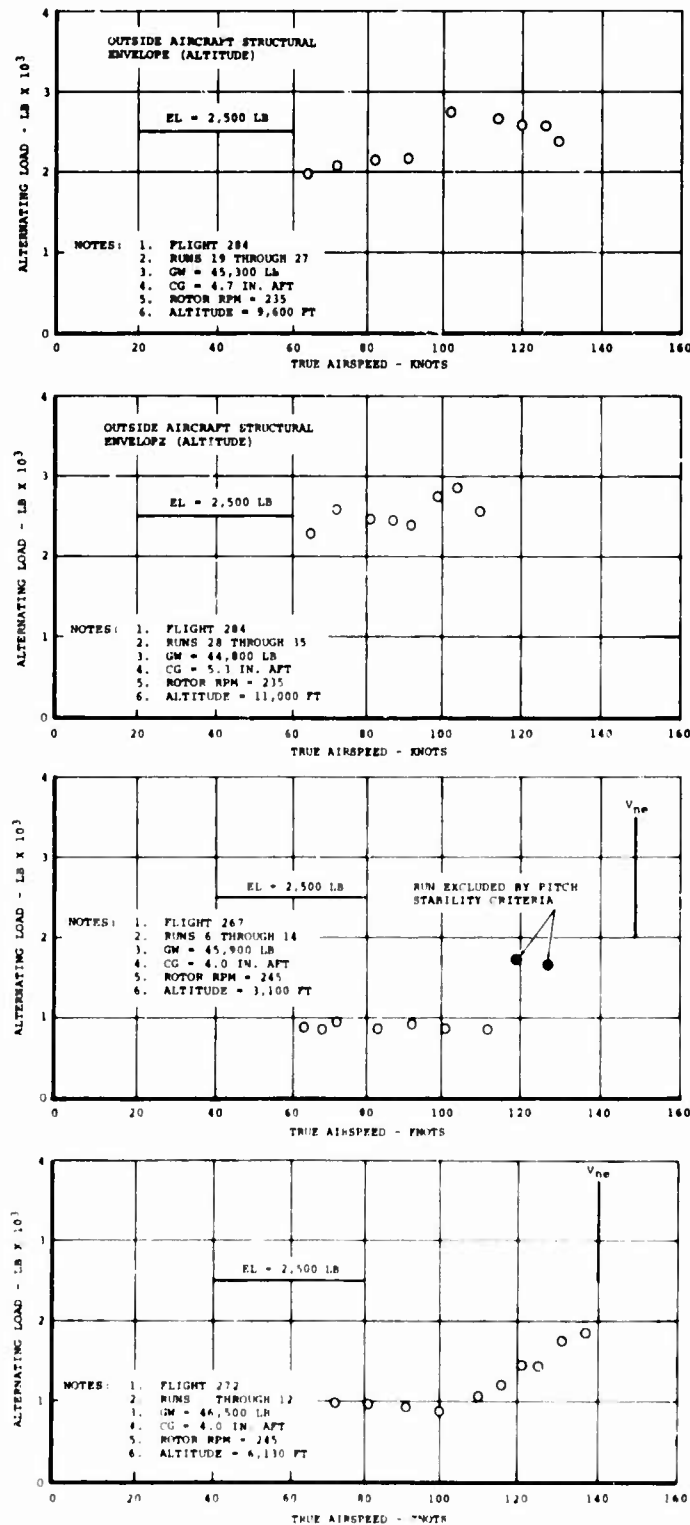


Figure 345. Aft Fixed Link Loads on CH-47C Helicopter Equipped With Advanced-Geometry Blades.

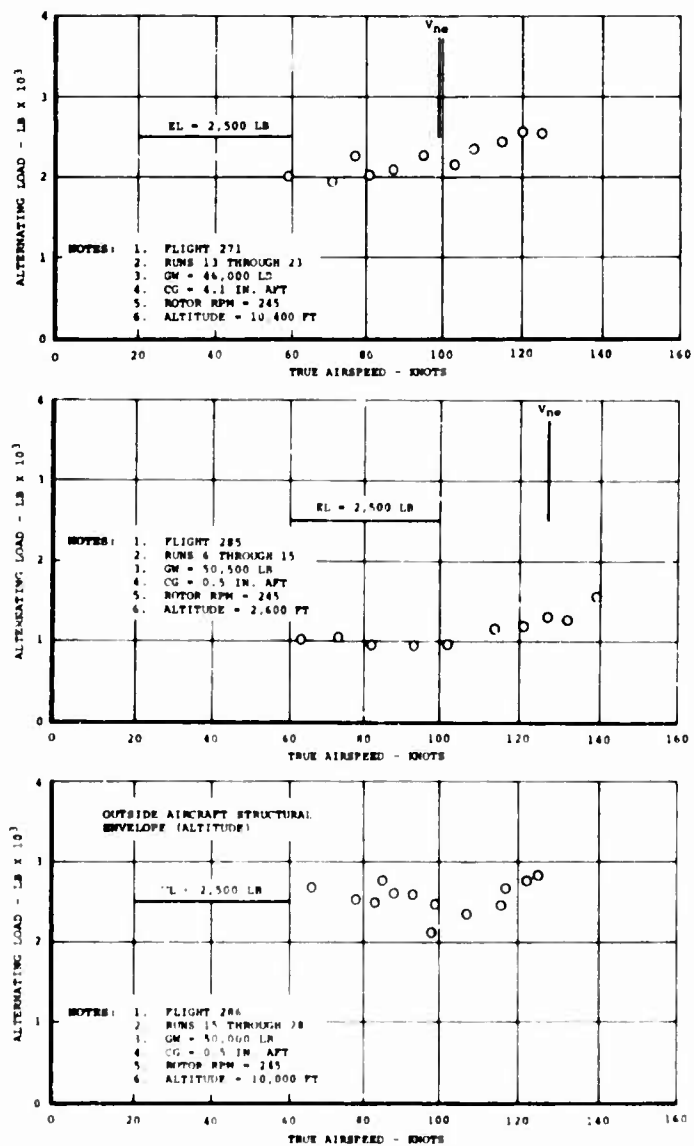


Figure 346. Aft Fixed Link Loads on CH-47C Helicopter Equipped With Advanced-Geometry Blades.

APPENDIX IV
SUMMARY OF MANEUVERING
FLIGHT TEST CONDITIONS

TABLE XLVIII. HOVER AND TRANSITION							
Hover							
Nominal Gross Weight (lb)	CG (in.)	Rotor RPM	Nominal H _D (ft)	Flight Run	Actual Gross Weight (lb)	Actual H _D (ft)	
33,000	- 7	235	IGE	243-46	43,000	880	
40,000	- 6	235	IGE	255-1	40,800	0	
46,000	+10	245	IGE	287-2	48,800	740	
	- 4	245	IGE	267-2	46,900	1500	
Transitions							
Nominal Gross Weight (lb)	CG (in.)	Rotor RPM	Nominal H _D (ft)	Flight Run	Actual Gross Weight (lb)	Actual H _D (ft)	TAS (MAX) (kt)
33,000	- 7	235	IGE	243-49	34,000	880	34
				243-66	32,500	200	
40,000	- 6	235	IGE	251-8	40,200	140	24
46,000	+10	245	IGE	287-50	44,400	970	39
	- 4	245	IGE	267-5	46,600	1600	73
				268-2	46,900	1010	29
				271-48	43,200	1730	70
50,000	0	245	IGE	285-5	51,500	1370	28

TABLE XLIX. CLIMB									
Nominal Gross Weight (lb)	CG (in.)	Rotor RPM	Nominal H _D (ft)	Flight Run	Actual Gross Weight (lb)	Actual H _D (ft)	TAS (kt)	V _{ne} (kt)	V _{ne} %
33,000	-7	235	4,000	254-19	32,000	2,910	96	180	53
				254-21	31,900	2,910	98	180	55
40,000	-6	235	4,000	253-11	39,600	2,840	99	159	62.5
			7,000	253-12	39,500	4,090	95	157	61
46,000	-4	245	2,000	270-18	45,400	2,400	102	153	67
				271-1	47,600	2,500	91	141	65
			3,000	271-2	47,600	3,490	91	139	65
			4,000	271-3	47,500	4,300	87	137	63.5
			5,000	271-4	47,500	5,230	92	135	68
			6,000	271-5	47,400	6,340	89	133	67
			8,000	271-6	47,400	7,510	90	120	75
			9,000	271-7	47,300	8,640	88	107	82
			10,000	271-8	47,200	9,700	90	95	95
			11,000	271-9	47,100	10,730	91	83	110
			12,000	271-10	47,000	11,290	94	N.C.*	-
				271-11	47,000	11,540	93	N.C.	-
50,000	0	245	4,000	286-2	51,300	4,050	79	119	66.5
			5,000	286-3	51,300	4,580	89	117	76
			6,000	286-4	51,200	5,170	93	113	82
				286-5	51,200	5,620	93	107	87
			7,000	286-6	51,100	6,230	95	102	93
				286-7	51,100	7,000	91	90	101
			8,000	286-8	51,000	7,510	87	85	102
			9,000	286-9	51,000	8,600	94	N.C.	-
			10,000	286-10	50,900	9,160	88	N.C.	-
				286-11	50,900	9,910	88	N.C.	-
			11,000	286-12	50,700	10,400	91	N.C.	-
				286-13	50,700	10,720	92	N.C.	-
				286-14	50,600	10,980	91	N.C.	-
* N.C. - No Capability									

TABLE L. LEFT TURN												
Nominal Gross Weight (lb)	CG (in.)	Rotor RPM	Nominal H _D (ft)	Flight Run	Actual Gross Weight (lb)	Actual H _D (ft)	TAS (kt)	V _{ne} (kt)	V _{ne} %	Bank Angle		
33,000	-7	235	3,000	244-10	33,000	3,540	118	180	65.5	14.4		
				244-11	32,900	3,520	113	180	62.5	24.2		
				244-12	32,900	3,630	122	180	67.5	34.6		
				244-13	32,900	3,680	117	180	65	39.4		
				244-14	32,800	3,560	115	180	64	44.9		
				244-15	32,800	3,690	116	180	64	49.2		
				254-15	32,300	3,250	100	180	55.5	28.1		
				254-17	32,200	3,350	154	180	85.5	27.2		
40,000	-6	235	IGE	251-6	40,300	160	18	161	11	3.5		
				3,000 252-6	40,300	3,310	138	153	90	15		
			6,000	253-9	39,800	3,120	151	155	97.5	27.2		
				255-15	39,400	6,240	149	150	99	35.3		
				8,000 255-34	38,600	7,500	155	151	102	29.3		
				9,000 283-1	39,600	8,640	108	-	-	7.6		
			230	283-2	39,600	8,690	108	-	-	17.0		
				283-3	39,500	8,690	115	-	-	28.5		
		283-4		39,500	8,760	113	-	-	35.7			
		283-5		39,400	9,090	61	-	-	7.6			
		283-6		39,300	9,280	65	-	-	19.2			
		283-7		39,200	9,190	66	-	-	30.1			
		283-8		39,200	9,330	71	-	-	39.4			
		283-9		39,100	8,600	83	-	-	40.7			
		46,000	+10	235	2,000	287-25	45,800	1,900	121	132	91.5	30.3
						5,000 287-29	45,600	4,940	110	126	87.5	35.1
245	IGE			287-3	47,800	2,730	40	140	28.5	3.6		
				245 IGE	267-3	46,800	3,110	61	145	42	4.0	
-4	245			3,000	267-15	45,800	3,330	119	149	80	21.8	
					267-16	45,100	1,260	64	159	40	29.5	
					267-17	44,900	3,600	107	152	70	37.3	
	5,000			270-39	43,400	4,990	101	157	64.5	10.1		
			270-41	43,300	4,890	99	158	62.5	16.9			
			270-43	43,300	4,810	98	158	62	17.1			
			270-45	43,200	4,740	95	159	60	23.7			
	6,000		272-21	45,100	6,030	108	146	74	29.2			
10,000	271-26		45,600	10,300	103	105	98	19.3				
	271-27		45,500	10,470	101	104	97	28.5				
50,000	0		245	IGE	285-3	51,800	1,220	34	124	27.5	5.2	
					2,000 285-16	50,600	2,750	115	126	91	33.6	
		285-18			50,400	2,730	106	125	85	39.2		
		10,000 286-30			49,100	10,100	105	N.C.	-	29.7		

TABLE LI. RIGHT TURN												
Nominal Gross Weight (lb)	CG (in.)	Rotor RPM	Nominal H D (ft)	Flight Run	Actual Gross Weight (lb)	Actual H D (ft)	TAS (kt)	V ne (kt)	V ne %	Bank Angle (deg)		
33,000	-7	235	3,000	254-16	32,300	3,350	100	180	55.5	31.2		
				254-18	32,200	3,380	157	180	87	31.2		
40,000	-6	235	IGE	251-7	40,200	160	-	161	-	4.8		
			3,000	253-10	39,700	3,110	153	155	99	30.2		
			6,000	255-14	39,500	6,100	147	149	99	27.1		
			8,000	255-35	38,600	7,580	151	151	100	29.5		
46,000	+10	235	6,000	287-26	45,700	5,840	138	120	115	24.3		
				287-27	45,700	6,370	126	114	111	31.2		
				287-28	45,600	6,480	118	120	98	35.5		
	-4	245	IGE	287-4	47,700	2,730	36	141	25.5	3.2		
			IGE	267-4	46,700	3,120	68	145	47	4.5		
			3,000	267-18	44,800	3,690	117	153	76.5	19.7		
		245	6,000	267-19	44,700	3,730	115	154	75	30.0		
				267-20	44,600	3,480	118	155	76	34.7		
				272-22	45,000	6,000	110	146	75	28.5		
			10,000	271-28	45,400	10,450	101	105	96	23.5		
50,000	0	245	IGE	285-4	51,700	1,250	48	125	38.5	6.3		
			2,000	285-17	50,500	2,740	115	127	90.5	28.0		
				285-19	50,300	2,770	118	128	92	35.5		
			10,000	286-29	49,200	9,970	128	N.C.	-	26.6		

TABLE LII. SIDESLIP

Nominal Gross Weight (lb)	CG (in.)	Rotor RPM	Nominal H _D (ft)	Flight Run	Actual Gross Weight (lb)	Actual H _D (ft)	TAS (kt)	V _{ne} (kt)	V _{ne} %	Sideslip Angle (deg)
33,000	-7	235		No Data						
40,000	-6	235	3,000	255-45	38,000	2,920	147	163	90	8.9L
				255-47	37,900	2,840	149	163	91	2.1R
				255-46	37,900	2,910	147	163	90	12.2L
			6,000	253-16	39,300	5,640	58	152	38	6.3R
				253-17	39,300	5,740	65	151	43	5.7L
				253-15	39,300	5,630	59	152	39	10.8R
				253-18	39,200	5,590	59	152	39	10.2L
				253-14	39,300	5,630	65	152	43	15.9R
				253-19	39,200	5,590	61	152	40	18.2L
				255-42	38,100	5,720	141	156	90	2.9R
				255-40	38,200	5,630	142	155	92	7.4R
				255-43	38,100	5,710	141	156	90	8.1R
				255-41	38,200	5,740	141	157	90	13.2L
			8,000	255-38	38,400	7,510	144	151	95	1.9R
				255-36	38,500	7,530	143	150	95	8.7L
				255-39	38,300	7,440	143	151	95	6.4R
				255-37	38,500	7,540	142	150	95	12.0L
46,000	+10	235	6,000	287-33	45,400	6,520	61	114	53.5	4.1R
				287-30	45,500	6,610	60	112	53.5	4.9L
				287-34	45,400	6,520	65	113	57.5	11.3R
				287-31	45,500	6,610	62	112	55	10.9L
				287-35	45,300	6,520	62	116	53.5	14.3R
				287-32	45,400	6,590	62	113	55	16.0L
	-4	235	1,000	272-41	43,000	2,700	137	142	96.5	4.1R
				272-39	43,200	2,760	130	141	92	6.5L
				272-42	42,900	2,560	136	143	93	9.9R
				272-40	43,100	2,720	134	142	94	14.2L
		245	3,000	270-24	44,900	3,010	58	154	38	3.2R
				270-21	45,100	2,850	61	153	40	7.1L
				270-25	44,800	2,880	57	154	37	7.8R
				270-22	45,100	2,970	59	152	39	11.7L

TABLE LII - Continued

Nominal Gross Weight (lb)	CG (in.)	Rotor RPM	Nominal H _D (ft)	Flight Run	Actual Gross Weight (lb)	Actual H _D	TAS	V _{ne} (kt)	V _{ne} %	Sideslip Angle (deg)
46,000	-4	245	3,000	270-26	44,800	2,990	59	154	38	13.8R
				270-23	45,000	2,890	58	153	38	18.8L
				272-28	44,600	5,920	59	148	40	6.2R
				272-23	44,900	5,860	57	147	39	3.9L
				272-27	44,600	5,860	56	148	38	7.9L
			6,000	272-29	44,500	5,920	56	149	37.5	10.3R
				272-24	44,800	5,810	59	147	40	5.2L
				272-26	44,700	5,840	56	148	38	10.8L
				272-30	44,400	5,930	57	149	38	14.0R
				272-25	44,800	5,830	57	147	39	17.8L
				272-33	44,200	6,070	124	150	83	5.4R
				272-31	44,300	6,140	125	149	84	6.0L
				272-34	44,100	6,010	128	150	85	9.2R
				272-32	44,200	6,150	125	149	84	11.2L
			10,000	271-32	45,200	10,190	61	110	55	3.8R
				271-29	45,300	10,390	59	105	56	7.0L
				271-33	45,100	10,170	62	110	56	8.1R
				271-30	45,300	10,250	61	108	56	11.7L
				271-34	45,100	10,150	62	110	56	13.7R
				271-31	45,200	10,340	60	107	56	17.8L
				271-37	44,900	10,320	115	111	104	3.2R
				271-35	45,000	10,430	115	108	106	7.7L
				271-38	44,900	10,210	116	112	103	7.5R
				271-36	44,900	10,280	116	111	105	12.8L
50,000	0	245	10,000	286-17	50,100	9,990	66	N.C.	-	0
				286-31	48,900	9,940	63	N.C.	-	5L
				286-32	48,900	9,900	67	N.C.	-	10L
				286-33	48,800	10,040	66	N.C.	-	15L
				286-34	48,800	9,980	67	N.C.	-	5R
				286-35	48,700	9,990	69	N.C.	-	10R
				286-36	48,600	9,880	68	N.C.	-	15R

TABLE LIII. PARTIAL POWER DESCENT AND AUTOROTATION

Partial Power Descent										
Nominal Gross Weight (lb)	CG (in.)	Rotor RPM	Nominal H D (ft)	Flight Run	Actual Gross Weight (lb)	Actual H D (ft)	TAS (kt)	V ne (kt)	V ne %	Rate of Descent (fpm)
33,000	- 7	235	3,000	244-7	33,300	3,810	98	179	55	500
				244-8	33,200	3,990	98	179	55	1000
				244-9	33,200	3,780	105	180	58	1500
40,000	- 6	235	6,000	253-13	39,500	6,420	99	149	66	1000
46,000	- 4	245	6,000	271-39	44,800	10,330	108	112	96	1000
50,000	0	245	10,000	286-37	48,600	9,380	105	86	122	1000
Autorotations										
Nominal Gross Weight (lb)	CG (in.)	Rotor RPM	Nominal H D (ft)	Flight Run	Actual Gross Weight (lb)	Actual H D (ft)	TAS (kt)	V ne (kt)	V ne %	
33,000	- 7	235	3,000	254-20	32,000	4,780	94	180	52	
40,000	- 6		No	Data						
46,000	- 4	245	7,000	271-40	44,700	7,180	106	145	73	
50,000	0		No	Data						

TABLE LIV. COLLECTIVE PULL-UP AND FLARE										
Collective Pull-Ups										
Nominal Gross Weight (lb)	CG (in.)	Rotor RPM	Nominal H _D (ft)	Flight Run	Actual Gross Weight (lb)	Actual H _D (ft)	TAS (kt)	V _{ne} (kt)	V _{ne} %	Load Factor "G"
33,000	-7	235	3,000	254-22	31,900	2,750	98	180	55	1.82
				254-23	31,800	2,830	145	180	80	1.97
40,000	-6			No	Data					
46,000	-4			No	Data					
50,000	0			No	Data					
Flares										
Nominal Gross Weight (lb)	CG (in.)	Rotor RPM	Nominal H _D (ft)	Flight Run	Actual Gross Weight (lb)	Actual H _D (ft)	TAS (kt)			
33,000	-7	235	IGE	244-23	32,200	1,380	94			
40,000	-6	235	IGE	251-20	38,700	350	74			
46,000	+10	235	IGE	287-49	44,500	880	76			
				287-51	43,700	1,000	62			
	-4	235	IGE	284-36	43,700	2,130	72			
		245	IGE	267-22	43,400	1,930	65			
				267-23	43,400	1,930	0			
				268-5	45,800	890	52			
				269-16	44,900	1,260	64			
				270-49	42,400	940	62			
				272-43	42,700	1,520	44			

APPENDIX V PERFORMANCE SUPPORT DATA

INTRODUCTION

This appendix contains the derivation of nondimensional and generalized performance parameters, a definition of terms, and a tabulation of pertinent hover and level-flight performance data (Tables LV through LXXIII). The tabulated performance was calculated from the various data collected during both performance and rotor strain survey flights of the CH-47C/AGB rotor flight test program. The data is presented as actual measured power and weight in terms of nondimensional or generalized values.

NONDIMENSIONAL AND GENERALIZED PERFORMANCE PARAMETERS

There are two common methods of presenting rotorcraft performance data: dimensionless C_p , C_T , μ , and tip Mach number; or generalized $\text{SHP}/\delta\sqrt{\theta}$, GW/δ , $V/\sqrt{\theta}$, and $N/\sqrt{\theta}$. The equivalence of these two methods can be shown as follows:

The rotorcraft thrust coefficient is defined as

$$C_T = \frac{\text{GW}}{\rho A V_T^2} \quad (1)$$

where GW = gross weight, lb

ρ = air density, slugs/ft³

A = total rotor swept area, ft²

V_T = rotor tip speed, fps

and by using the standard definition of $\rho = \sigma_A \rho_o$, the following form is obtained:

$$C_T = \frac{\text{GW}}{\sigma_A \rho_o A V_T^2} \quad (2)$$

σ_A is equal to δ/θ and the tip speed can be expressed as a function of rotor speed, N , by $\frac{\pi R}{30}$ (N). Thus,

$$C_T = \frac{\text{GW}/\delta}{\rho_o A \left(\frac{\pi R}{30}\right)^2 \left(\frac{N}{\sqrt{\theta}}\right)^2} = \left(\frac{900}{\rho_o A \pi^2 R^2}\right) \left(\frac{\text{GW}/\delta}{(N/\sqrt{\theta})^2}\right) \quad (3)$$

Since the grouped terms are constant for a specific configuration, it can be concluded that generalized data presented at constant GW/δ and constant $N/\sqrt{\theta}$ is equivalent to presenting data at constant C_T as in the dimensionless method.

In a similar manner, it can be shown that the dimensionless power coefficient, C_p , is equivalent to

$$C_p = \frac{550 \text{ SHP}}{\rho A V_T^3} = \left(\frac{550 (30)^3}{\rho_o A \Pi^3 R^3} \right) \left(\frac{\text{SHP}/\delta \sqrt{\theta}}{(N/\sqrt{\theta})^3} \right) \quad (4)$$

and again the grouped terms are constant for a specific configuration, and data presented in generalized method is equivalent to the dimensionless method.

The final comparison of the two methods is made with respect to forward speed and advancing tip Mach number. The advance ratio, μ , is defined as the ratio of forward speed, V , to rotor tip speed, V_T :

$$\mu = \frac{V}{V_T} = \left(\frac{30}{\Pi R} \right) \left(\frac{V/\sqrt{\theta}}{N/\sqrt{\theta}} \right) \quad (5)$$

Thus, data generalized in terms of $V/\sqrt{\theta}$ and $N/\sqrt{\theta}$ can be related directly to advance ratio for a specific configuration. The advancing tip Mach number, $M_{(1) (90)}$ is given by

$$M_{(1) (90)} = M_o (1 + \mu) \quad (6)$$

and since M_o is equal to V_T/a and $a = a_o \sqrt{\theta}$, the following expression is obtained:

$$M_{(1) (90)} = \frac{V_T}{a} (1 + V/V_T) = \frac{\Pi R}{30 a_o} \left(\frac{N}{\sqrt{\theta}} \right) \left(1 + \frac{30}{\Pi R} \left[\frac{V/\sqrt{\theta}}{N/\sqrt{\theta}} \right] \right) \quad (7)$$

Again it is shown that the advancing tip Mach number, which is experienced at a given value $V/\sqrt{\theta}$ and $N/\sqrt{\theta}$, can be expressed in terms of the corresponding μ and M_o in the dimensionless system.

The above discussion shows that the two methods can be used interchangeably and will give equal performance values for a given flight speed, gross weight, and rotor speed, provided that the rotational tip Mach number M_o is held constant. To obtain model or flight test power polars for a series of gross weight conditions to be used at a specified ambient temperature condition, it is necessary to hold a constant test tip Mach number M_o .

Even though the two methods are shown to be equivalent, the generalized method is becoming increasingly popular, primarily due to two reasons:

1. The generalized method uses quantities that are of a familiar magnitude.
2. A significant number of performance comparisons are made at sea level standard conditions where δ and σ have values of unity, and thus the performance figures can be used directly in dimensional form. The dimensionless method requires elaborate calculations even for the standard-day condition.

DEFINITION OF TERMS:

<u>Symbol</u>	<u>Definition</u>	
A	rotor disc area, ft ²	
a	speed of sound, fps	
C _d	drag coefficient,	$\frac{D}{\rho/2V^2S}$ (nd)
C _L	lift coefficient,	$\frac{L}{\rho/2V^2S}$ (nd)
C _P	power coefficient,	$\frac{550 \text{ SHP}}{\rho A (V_{TIP})^3}$ (nd)
C _T	thrust coefficient,	$\frac{GW}{\rho A (V_{TIP})^2}$ (nd)
C _T '/ σ	rotor lift coefficient,	$\frac{C_T (\text{Gross Weight})}{\text{Rotor Solidity}}$ (nd)
GW	gross weight, lb	
GW/ δ	generalized gross weight, lb	
K _p	climb efficiency factor	(nd)
M(1)(90)	advancing tip Mach number	
	$= \frac{V_{TIP} + 1.69 V}{a}$	(nd)

<u>Symbol</u>	<u>Definition</u>	
N	rotor speed, rpm	
$N/\sqrt{\theta}$	generalized rotor speed, rpm	
R	rotor radius, ft	
SHP	shaft horsepower (at engine), hp	
$SHP/\delta\sqrt{\theta}$	generalized shaft horsepower, hp	
V	true airspeed of forward flight, kt	
V_{TIP}	rotor tip speed, $N \left(\frac{2\pi}{60} \right) R$, fps	
$V/\sqrt{\theta}$	generalized true airspeed, kt	
δ	altitude pressure ratio, $\frac{P}{P_{SL. STD.}}$	(nd)
$\sqrt{\theta}$	square root of absolute temperature ratio	
	$\frac{T}{T_{SL. STD.}}$	(nd)
μ	rotor advance ratio, V/V_{tip}	(nd)
ρ	air density at altitude/temperature, slugs/ft ³	
ρ_o	air density at sea level, standard temp. .00238 slug/ft ³	
σ	rotor solidity, $\frac{\text{blade area}}{\text{disc area}}, \frac{bC_e}{\pi R}$	(nd)
a	altitude density ratio $\frac{\rho}{\rho_o}$	(nd)
(nd)	nondimensional	

TABLE LV. CH-47C/AGB ROTOR HOVER POWER REQUIRED (OUT OF GROUND EFFECT)									
Aircraft: S/N 66-19103				Ext Load #2: 16,986 lb		Flight No. X-280			
Aft Wheel Height: 150 ft				Takeoff GW: 33,697 lb		Date: 8/12/69			
Ext. Load #1: 10,964 lb				CG: 0.9-in. Fwd					
Rec. No.	Gross Weight (lb)	Hp (ft)	OAT (°C)	Rotor Speed N (rpm)	$\frac{N}{\sqrt{\theta}}$ (rpm)	SHP Test Rotor Shaft Torque	C _T Test (x 10 ⁻⁴)	C _P Test (x 10 ⁻⁵)	$\frac{M_{Tip}}{V_{Tip}}$ Test
External Load No. 1									
2-0	42,973	280	20.3	227.1	225.0	5,593	64.59	64.83	0.633
2-1	42,954		20.1	227.1	225.0	5,525	64.57	64.08	0.633
2-2	42,934		20.4	226.6	224.5	5,648	64.84	65.92	0.632
2-3	42,914		20.2	226.6	224.6	5,650	64.76	66.02	0.632
5-0	42,570	300	20.3	235.8	233.7	5,621	59.39	58.87	0.656
5-1	42,526		20.1	236.4	234.3	5,549	58.99	57.02	0.660
5-2	42,482		20.0	236.0	234.0	5,583	59.11	57.64	0.658
5-3	42,437		20.0	236.0	234.0	5,157	59.04	53.25	0.658
6-0	42,360	300	20.4	240.5	238.3	5,552	56.83	54.24	0.671
6-1	42,334		20.2	240.3	238.2	5,619	56.85	55.00	0.670
6-2	42,325		20.2	240.5	238.4	5,520	56.74	53.89	0.671
6-3	42,281		20.0	240.3	238.2	5,592	56.74	54.69	0.670
7-0	42,190	300	20.1	245.4	243.2	5,665	54.31	52.04	0.684
7-1	42,161		20.2	245.7	243.5	5,615	54.16	51.32	0.685
7-2	42,133		20.1	245.8	243.6	5,585	54.06	51.06	0.685
7-3	42,104		20.0	246.0	243.9	5,505	53.92	50.19	0.686

TABLE LV - Continued									
Aircraft: S/N 66-19103			Ext Load #2: 16,986 lb			Flight No. X-280			
Aft Wheel Height: 150 ft			Takeoff GW: 33,697 lb			Date: 8/12/69			
Ext. Load #1: 10,964 lb			CG: 0.9-in. Fwd						
Rec. No.	Gross Weight (lb)	H _P (ft)	OAT (°C)	Rotor Speed N (rpm)	$\frac{N}{\sqrt{\theta}}$ (rpm)	SHP Test — Rotor Shaft Torque	C _T Test (x 10 ⁻⁴)	C _P Test (x 10 ⁻⁵)	$\frac{M_{Tip} Test}{V_{Tip} a}$
External Load No. 1 (continued)									
8-0	42,032	310	20.3	245.5	243.3	5,642	54.12	51.82	0.684
8-1	42,006		20.3	245.7	243.5	5,662	54.00	51.88	0.685
8-2	41,979		20.3	245.8	243.6	5,561	53.92	50.90	0.685
8-3	41,952		20.3	245.6	243.4	5,537	53.97	50.80	0.684
9-0	41,894	290	20.3	230.9	237.7	5,505	56.45	54.15	0.668
9-1	41,867		20.3	240.0	237.8	5,478	56.36	53.81	0.668
9-2	41,841		20.2	240.0	237.9	5,447	56.31	53.50	0.669
9-3	41,814		20.3	240.3	238.1	5,400	56.15	52.86	0.670
10-0	41,747	280	20.2	234.8	232.7	5,310	58.68	55.67	0.654
10-1	41,721		20.2	234.7	232.6	5,377	58.69	56.44	0.654
10-2	41,695		20.2	234.8	232.7	5,353	58.60	56.12	0.654
10-3	41,670		20.2	234.8	232.7	5,367	58.57	56.27	0.654
11-0	41,598	300	20.0	231.0	229.0	5,417	60.41	59.64	0.644
11-1	41,572		20.0	230.7	228.7	5,238	60.53	57.90	0.643
11-2	41,547		19.9	230.5	228.6	5,300	60.58	58.72	0.643
11-3	41,521		20.0	230.4	228.4	5,330	60.51	59.14	0.642

TABLE IV - Continued

TABLE LV - Continued									
Aircraft: S/N 66-19103			Ext Load #2: 16,986 lb			Flight No. X-280			
Aft Wheel Height: 150 ft			Takeoff GW: 33,697 lb			Date: 8/12/69			
Ext Load #1: 10,964 lb			CG: 0.9-in. Fwd						
Rec. No.	Gross Weight (lb)	Hp (ft)	OAT (°C)	Rotor Speed N (rpm)	$\frac{N}{\sqrt{\theta}}$ (rpm)	SHP Test Rotor Shaft Torque	C _T Test (x 10 ⁻⁴)	C _P Test (x 10 ⁻⁵)	$\frac{M_{Tip} \text{ Test}}{V_{Tip}^a}$
External Load No. 1 (continued)									
12-0	41,435	320	19.9	226.5	224.6	5,271	62.61	61.59	0.622
12-1	41,409		19.7	226.5	224.7	5,274	62.53	61.58	0.622
12-2	41,381		19.9	226.6	224.7	5,270	62.48	61.50	0.622
12-3	41,356		19.9	226.5	224.6	5,262	62.49	61.48	0.622
External Load No. 2									
13-0	46,730	200	19.3	245.9	244.1	6,288	59.53	57.05	0.687
13-1	46,700		19.3	245.6	243.8	6,382	59.64	58.12	0.685
13-2	46,668		19.3	245.6	243.8	6,352	59.60	57.84	0.685
13-3	46,637		19.2	245.6	243.8	6,353	59.54	57.83	0.685
14-0	46,623	200	19.2	245.6	243.8	6,357	59.52	57.87	0.685
14-1	46,590		19.3	245.8	244.0	6,311	59.40	57.33	0.686
14-2	46,558		19.2	245.6	243.8	6,343	59.43	57.74	0.685
14-3	46,525		19.2	245.8	244.0	6,339	59.30	57.57	0.686
15-0	46,444	200	19.3	240.1	238.3	6,285	62.06	61.25	0.671
15-1	46,415		19.3	240.1	238.3	6,292	62.02	61.33	0.671
15-2	46,386		19.3	240.3	238.5	6,258	61.88	60.84	0.671
15-3	46,356		19.3	240.3	238.5	6,274	61.84	61.00	0.671

TABLE IV - Continued									
Aircraft: S/N 66-19103 Aft Wheel Height: 150 ft Ext Load #1: 10, 964 lb				Ext Load #2: 16,986 lb Takeoff GW: 33,697 lb CG: 0.9-in. Fwd		Flight No. X-280 Date: 8/12/69			
Rec. No.	Gross Weight (lb)	Hp (ft)	OAT (°C)	Rotor Speed N (rpm)	$\frac{N}{\sqrt{\theta}}$ (rpm)	$\frac{SHP_{Test}}{\text{RotorShaftTorque}}$	$C_{T_{Test}}$ (x 10 ⁻⁴)	$C_{P_{Test}}$ (x 10 ⁻⁵)	$\frac{M_{Tip}}{V_{Tip}^2}$
External Load No. 2 (continued)									
16-0	46,350	200	19.3	240.4	238.6	6,255	61.78	60.74	0.671
16-1	46,322		19.3	240.1	238.4	6,249	61.87	60.89	0.671
16-2	46,293		19.2	240.5	238.8	6,180	61.63	59.91	0.672
16-3	46,265		19.2	240.8	239.1	6,147	61.44	59.37	0.673
17-0	46,167	200	19.1	235.8	234.1	6,179	63.91	63.53	0.659
17-1	46,135		-	235.8	-	6,200	-	-	-
17-2	46,102		19.2	236.1	234.4	6,138	63.68	62.90	0.660
17-3	46,070		19.1	235.6	233.9	6,211	63.89	64.02	0.658
18-0	46,060	200	19.2	236.0	234.3	6,176	63.68	63.36	0.660
18-1	46,029		19.2	235.9	234.2	6,178	63.69	63.47	0.659
18-2	46,003		19.3	236.0	234.2	6,154	63.62	63.16	0.659
18-3	45,974		19.3	235.8	234.1	6,152	63.69	63.31	0.659
19-0	45,903	200	19.2	230.2	228.5	6,057	66.70	66.97	0.643
19-1	45,875		18.8	230.2	228.7	6,068	66.57	66.99	0.643
19-2	45,847		19.2	229.7	228.0	6,166	66.91	68.62	0.642
19-3	45,819		19.2	230.0	228.3	6,073	66.69	67.31	0.643

TABLE LV - Continued

TABLE LV - Continued									
Aircraft: S/N 66-19103				Ext Load #2: 16,986 lb		Flight No. X-280			
Aft Wheel Height: 150 ft				Takeoff GW: 33,697 lb		Date: 8/12/69			
Ext. Load #1: 10, 964 lb				CG: 0.9-in. Fwd					
Rec. No.	Gross Weight (lb)	H _p (ft)	OAT (°C)	Rotor Speed N (rpm)	$\frac{N}{\sqrt{\theta}}$ (rpm)	$\frac{SHP_{Test}}{\text{Rotor Shaft Torque}}$	C _T Test (x 10 ⁻⁴)	C _P Test (x 10 ⁻⁵)	$\frac{M_{Tip Test}}{\frac{VTIP}{a}}$
External Load No. 2 (continued)									
20-0	45,813	200	19.3	230.2	228.5	6,055	66.59	66.97	0.643
20-1	45,785		19.2	-	-	-	-	-	-
20-2	45,756		19.0	230.0	228.4	6,057	66.56	67.09	0.643
20-3	45,728		19.2	229.9	228.2	6,060	66.62	67.25	0.642
22-0	45,521	200	19.2	225.4	223.8	5,973	68.99	70.34	0.630
22-1	45,494		18.6	225.3	223.9	5,910	68.87	69.54	0.630
22-2	45,465		19.1	225.5	223.9	5,824	68.82	68.47	0.630
22-3	45,436		18.9	225.3	223.8	5,929	68.85	69.84	0.630

TABLE LVI. CH-47C/AGB ROTOR - LEVEL FLIGHT POWER REQUIRED										
Rec. No.	$\frac{GW}{8}$ Test (lb)	$\frac{N}{\sqrt{\theta}}$ Test (rpm)	$\frac{V}{\sqrt{\theta}}$ Test (kt)	$\frac{SHP}{8\sqrt{\theta}}$ Test Rotor Shaft Torque	Target GW/8: 37,500 lb CG: 6.1 in. Aft Target $N\sqrt{\theta}$: 235 rpm				Flight No. X-254 Date: 5/21/69	
					$\frac{\Delta SHP}{8\sqrt{\theta}}$ Cor. To Target GW/8	$\frac{\Delta SHP}{8\sqrt{\theta}}$ Cor. To Target $N\sqrt{\theta}$	$\frac{\Delta SHP}{8\sqrt{\theta}}$ Cor. To Zero R/C	$\frac{\Delta SHP}{8\sqrt{\theta}}$ Cor. To Zero Accel.	$\frac{\Delta SHP}{8\sqrt{\theta}}$ Cor. To CH-47C Ext. Drag	$\frac{SHP}{8\sqrt{\theta}}$ Cor- rected
1	37,947	236.2	119.3	4,287	-39	-34	N.A.	N.A.	-55	4,159
2	37,752	236.8	128.8	4,257	-23	-47			-68	4,119
3	37,752	236.6	138.6	4,664	-24	-61			-86	4,493
4	37,669	236.2	142.9	5,233	-17	-51			-94	5,071
5	37,586	233.8	147.1	5,392	-9	+58			-102	5,339
6	37,613	234.8	152.7	6,093	-13	+11			-115	5,976
7	37,613	233.8	158.2	6,288	-14	+82			-127	6,229
8	37,447	236.8	162.4	7,000	+7	-135			-137	6,735
9	37,502	234.8	164.8	7,172	0	+16			-143	6,995

TABLE LVII. CH-47C/AGB ROTOR - LEVEL FLIGHT POWER REQUIRED

Aircraft: S/N 66-19103 Takeoff GW: 34,835 lb				Target GW/8: 35,700 lb CG: 6.1 in. Aft Target $N/\sqrt{\theta}$: 245 rpm		Flight No. X-254 Date: 5/21/69				
Rec. No.	$\frac{GW}{8}$ Test (lb)	$\frac{N}{\sqrt{\theta}}$ Test (rpm)	$\frac{V}{\sqrt{\theta}}$ Test (kt)	$\frac{SHP}{8\sqrt{\theta}}$ Test Rotor Shaft Torque	$\frac{\Delta SHP}{8\sqrt{\theta}}$ Cor. To Target GW/8	$\frac{\Delta SHP}{8\sqrt{\theta}}$ Cor. To Target $N/\sqrt{\theta}$	$\frac{\Delta SHP}{8\sqrt{\theta}}$ Cor. To Zero R/C	$\frac{\Delta SHP}{8\sqrt{\theta}}$ Cor. To Zero Accel.	$\frac{\Delta SHP}{8\sqrt{\theta}}$ Cor. To CH-47C Ext. Drag	$\frac{SHP}{8\sqrt{\theta}}$ Cor- rected
24	35,744	244.9	100.0	3,434	-3	0	N.A.	N.A.	-32	3,399
25	35,688	245.3	109.8	3,879	0	-7			-42	3,830
26	35,741	246.3	119.6	3,920	-3	-30			-55	3,832
27	35,658	247.9	129.3	4,432	+3	-70			-70	4,295
28	35,711	246.9	139.2	5,058	0	-74			-88	4,896
29	35,708	245.9	151.2	6,140	0	-50			-110	5,980

TABLE LVIII. CH-47C/AGB ROTOR - LEVEL FLIGHT POWER REQUIRED										
Aircraft: S/N 66-19103 Takeoff GW: 32,662 lb			Target GW/8: 33,000 lb CG: 2 in. Aft Target N/√θ: 235 rpm			Flight No. X-258 Date: 6/12/69				
Rec. No.	$\frac{GW}{8}$ Test (lb)	$\frac{N}{\sqrt{\theta}}$ Test (rpm)	$\frac{V}{\sqrt{\theta}}$ Test (kt)	$\frac{SHP}{8\sqrt{\theta}}$ Test Rotor Shaft Torque	$\frac{\Delta SHP}{8\sqrt{\theta}}$ Cor. To Target GW/8	$\frac{\Delta SHP}{8\sqrt{\theta}}$ Cor. To Target N/√θ	$\frac{\Delta SHP}{8\sqrt{\theta}}$ Cor. To Zero R/C	$\frac{\Delta SHP}{8\sqrt{\theta}}$ Cor. To Zero Accel.	$\frac{\Delta SHP}{8\sqrt{\theta}}$ Cor. To CH-47C Ext. Drag	$\frac{SHP}{8\sqrt{\theta}}$ Cor-rected
9	33,214	234.4	49.8	2,994	-26	+14	-39	0	-4	2,939
10	33,172	234.0	58.4	2,722	-21	+23	+10	0	-6	2,737
11	32,275	234.4	70.3	2,707	-33	+14	0	+4	-11	2,681
12	33,184	234.5	80.9	2,712	-19	+12	0	+9	-18	2,696
13	33,247	234.0	91.0	2,826	-24	+21	0	+14	-24	2,813
14	33,324	233.8	102.4	3,016	-28	+20	-30	+1	-36	2,943
15	33,403	234.6	114.1	3,309	-33	+10	-35	+17	-50	3,218
16	33,230	234.1	126.2	3,776	-19	+18	-64	+9	-69	3,651
17	33,048	233.9	136.5	4,165	-4	+43	0	-3	-88	4,113
18	32,954	233.8	146.4	4,734	+5	+73	-41	0	-108	4,662
19	32,828	233.8	157.4	5,688	+21	+108	0	-8	-117	5,692

TABLE LIX. CH-47C/AGB ROTOR-ACCELERATION CORRECTION							
$\frac{\Delta \text{SHP}}{8\sqrt{\theta}} = - \left(\frac{\text{GW}}{8} \right) \left(\frac{\Delta V}{\sqrt{\theta}} \right) \left(\frac{V}{\sqrt{\theta}} \right) \left(\frac{1}{\sqrt{\theta}} \right)$				Target GW/8: 33,000 lb Target N/√θ: 235 rpm		Flight No. X-258 Date: 6/12/69	
Accel				Δ Time			
Rec. No.	$\frac{V}{\sqrt{\theta}}$ Test Avg (kt)	$\frac{\Delta V}{\sqrt{\theta}}$ (kt)	Δ Time (min)	$\frac{\text{GW}}{8}$ Test (lb)	$\sqrt{\theta}$ Test	$\frac{\Delta \text{SHP}}{8\sqrt{\theta}}$ Accel (hp)	
9	49.8	0	-		1.011	0	
10	58.4	0	-		-	0	
11	70.3	-0.6	1.0	33,275	1.011	4	
12	80.9	-1.22	1.0	33,184	1.012	9	
13	91.0	-1.70	1.0	33,247	1.012	14	
14	102.4	-0.1	1.0	33,324	1.012	1	
15	114.1	-1.66	1.0	33,403	1.012	17	
16	126.2	-0.79	1.0	33,230	1.013	9	
17	136.5	+0.23	1.0	33,048	1.013	-3	
18	146.4	0	-	-	-	0	
19	157.4	+0.57	1.0	32,828	1.014	-8	

TABLE LX. CH-47C/AGB ROTOR - RATE OF CLIMB CORRECTION										
$\frac{\Delta \text{SHP}}{\delta \sqrt{\theta}}$		$\frac{\text{R/C}}{\sqrt{\theta}} \times \frac{\text{GW}}{\delta}$ = $\frac{\text{Climb}}{33,000 \text{ Kp}}$			Kp: 0.87		Target GW/ δ : 33,000 lb Target N/ $\sqrt{\theta}$: 235 rpm		Flight No. X-258 Date: 6/12/69	
Rec. No.	Rate of Climb Test (fpm)	Hp (ft)	OAT Test (°C)	OAT Std (°C)	$\frac{\text{OAT}_T + 273}{\text{OAT}_S + 273}$ (fpm)	R/C Tapeline (fpm)	$\sqrt{\theta}$ Test	$\frac{\text{R/C T.L.}}{\sqrt{\theta}}$ (fpm)	$\frac{\text{SHP}}{\delta \sqrt{\theta}}$ Climb (hp)	
9	33	2,492	21	10	1.040	34	1.011	34	-39	
10	-16	2,536	22	10	1.043	-17	1.012	-16	-19	
11	0	2,698	21	10			1.011		0	
12	0	2,697	22	10			1.012		0	
13	0	2,833	22	10			1.012		0	
14	25	2,979	22	9	1.047	26	1.012	26	-30	
15	29	3,131	22	9	1.047	30	1.012	30	-35	
16	54	3,150	22	9	1.047	56	1.012	56	-64	
17	0	3,197	22	9			1.012		0	
18	34	3,264	23	9	1.049	36	1.013	35	-41	
19	0	3,328	23	9			1.013		0	

TABLE LXI. CH-47C/AGB ROTOR - LEVEL FLIGHT POWER REQUIRED										
Aircraft: S/N 66-19103 Takeoff GW: 45,756 lb			Target GW/8: 63,000 lb CG: 1.7 in. Fwd Target $N/\sqrt{\theta}$: 245 rpm			Flight No. X-274 Date: 7/31/69				
Rec. No.	$\frac{GW}{8}$ Test (lb)	$\frac{N}{\sqrt{\theta}}$ Test (rpm)	$\frac{V}{\sqrt{\theta}}$ Test (kt)	$\frac{SHP}{8\sqrt{\theta}}$ Test Rotor Shaft Torque	$\frac{\Delta SHP}{8\sqrt{\theta}}$ Cor. To Target GW/8	$\frac{\Delta SHP}{8\sqrt{\theta}}$ Cor. To Target N/ $\sqrt{\theta}$	$\frac{\Delta SHP}{8\sqrt{\theta}}$ Cor. To Zero R/C	$\frac{\Delta SHP}{8\sqrt{\theta}}$ Cor. To Zero Accel	$\frac{\Delta SHP}{8\sqrt{\theta}}$ Cor. To CH-47C Ext. Drag	$\frac{SHP}{8\sqrt{\theta}}$ Cor- rected
1-4	62,147	244.6	123.2	6,773	+157	0	-92	+14	-60	6,792
5-8	62,202	245.5	116.3	6,456	+135	0	+92	0	-50	6,633
9-12	63,008	246.2	106.4	6,608	0	0	-139	+11	-38	6,442
13- 16	63,469	245.8	95.3	6,455	-83	0	-117	0	-27	6,228
17- 20	63,585	245.8	81.7	6,459	-112	0	+94	+24	-17	6,448

TABLE LXII. CH-47C/AGB ROTOR - ACCELERATION CORRECTION							
$\frac{\Delta \text{SHP}}{8\sqrt{\theta}} = - \left(\frac{\text{GW}}{8} \right) \left(\frac{\Delta V}{\sqrt{\theta}} \right) \left(\frac{V}{\sqrt{\theta}} \right) (\sqrt{\theta})$				Flight No. X-274 Date: 7/31/69			
Accel Δ Time							
Target GW/8: 63,000 lb							
Target N/√θ : 245 rpm							
Rec. No.	$\frac{V}{\sqrt{\theta}}$ Test Avg. (kt)	$\frac{\Delta V}{\sqrt{\theta}}$ (kt)	Δ Time (min)	$\frac{\text{GW}}{8}$ Test (lb)	$\sqrt{\theta}$ Test	$\frac{\Delta \text{SHP}}{8\sqrt{\theta}}$ Accel (hp)	
1-4	123.2	-0.7	1.0	62,147	0.99	+14	
5-8	116.3	0				0	
9-12	106.4	-0.9	1.5	63,008	0.985	+11	
13-16	95.3	0				0	
17-20	81.7	-2.6	1.5	63,585	0.983	+24	

TABLE LXIII. CH-47C/AGB ROTOR - RATE OF CLIMB CORRECTION

$\frac{\Delta \text{SHP}}{8\sqrt{\theta}} = \frac{\text{R/C} \times \text{GW}}{\sqrt{\theta}} \times \frac{\text{Kp}}{8}$					Climb 33000 Kp		Kp: 0.87		Target GW/8: 63,000 lb Target N/√θ : 245 rpm		Flight No. X-274 Date: 7/31/69	
Rec. No.	Rate of Climb Test (fpm)	Hp (ft)	OAT Test (°C)	OAT Std (°C)	$\frac{\text{OAT}_T + 273}{\text{OAT}_S + 273}$	R/C Tapeline (fpm)	√θ Test	$\frac{\text{R/C}_{\text{T.L.}}}{\sqrt{\theta}}$ (fpm)	$\frac{\Delta \text{SHP}}{8\sqrt{\theta}}$ Climb (hp)			
1-4	40	9,000	9	-3	1.044	41.8	0.99	42.2	-92			
5-8	-40	9,200	8	-3	1.04	-41.6	0.988	-42.2	+92			
9-12	+60	9,660	7	-4	1.04	62.4	0.985	63.4	-139			
13-16	+50	10,000	6	-5	1.041	52.1	0.984	53	-117			
17-20	-40	10,100	5	-5	1.037	-41.5	0.983	-42.2	+94			

TABLE LXIV. CH-47C/AGB ROTOR - LEVEL FLIGHT POWER REQUIRED										
Aircraft: S/N 66-19103			Takeoff GW: 33,643 lb Target GW/8: 33,000 lb		CG: 0.9 in. Fwd Target N/√θ: 235 rpm		Flight No. X-276 Date: 8/7/69			
Rec. No.	GW δ Test (lb)	N √θ Test (rpm)	V √θ Test (kt)	SHP δ√θ Test Rotor Shaft Torque	ASHP δ√θ Cor. to Target GW/8	ASHP δ√θ Cor. to Target N/√θ	ASHP δ√θ Cor. to Zero R/C	ASHP δ√θ Cor. to Zero Accel	ASHP δ√θ Cor. to CH-47C Ext. Drag	SHP δ√θ Corrected
23	33,186	232.8	68.0	2,858	-18	+63	-71	0	-10	2,822
25	33,248	233.4	78.6	2,686	-22	+43	+101	0	-15	2,793
26	33,272	233.9	90.2	2,943	-22	+30	0	0	-23	2,928
27	33,136	233.5	111.9	3,388	-11	+15	-76	+25	-45	3,296
28	33,140	233.3	128.1	3,945	-12	+34	0	0	-68	3,899
29	33,101	233.2	146.5	5,013	-10	+94	-32	0	-101	4,964
30	33,188	234.2	67.0	2,708	-19	+22	+98	+16	-10	2,815
31	33,156	234.6	77.7	2,936	-14	+11	-163	+19	-15	2,774
32	33,232	234.2	91.5	2,963	-20	+22	0	-12	-24	2,929
33	33,186	234.1	115.2	3,471	-15	+9	-126	+17	-46	3,310
34	33,240	234.7	135.1	4,256	-21	+9	0	+20	-79	4,185
35	33,130	234.6	145.5	4,971	-12	+21	0	0	-99	4,881

TABLE LXV. CH-47C/AGB ROTOR-ACCELERATION CORRECTION							
$\frac{\Delta \text{SHP}}{8\sqrt{\theta}} = - \left(\frac{\text{GW}}{8} \right) \left(\frac{\Delta V}{\sqrt{\theta}} \right) \left(\frac{V}{\sqrt{\theta}} \right) \left(\frac{\sqrt{\theta}}{\sqrt{\theta}} \right)^{-6} 2.684 \times 10^{-6}$		Target GW/8: 33,000 lb Target N/8: 235 rpm		Flight No. X-276 Date: 8/7/69			
Rec. No.	$\frac{V}{\sqrt{\theta}}$ Test Avg (kt)	$\frac{\Delta V}{\sqrt{\theta}}$ (kt)	ΔTime (min)	$\frac{\text{GW}}{8}$ Test (lb)	$\sqrt{\theta}$ Test	$\frac{\Delta \text{SHP}}{8\sqrt{\theta}}$ Accel (hp)	
23	68.0	0				0	
25	78.6	0				0	
26	90.2	0				0	
27	111.9	-2.5	1.0	33,136	1.016	+25	
28	128.1	0				0	
29	146.5	0				0	
30	67.0	-2.6	1.0	33,188	1.012	+16	
31	77.7	-2.6	1.0	33,156	1.012	+19	
32	91.5	+1.5	1.0	33,232	1.012	-12	
33	113.2	-1.7	1.0	33,186	1.013	+17	
34	135.1	-1.6	1.0	33,240	1.014	+20	
35	145.5	0				0	

TABLE LXVI. CH-47C/AGB ROTOR - RATE OF CLIMB CORRECTION										
$\frac{\Delta \text{SHP}}{8\sqrt{\theta}} = \frac{R/C}{\sqrt{\theta}} \times \frac{GW}{8}$ Climb 33,000 Kp			Kp: 0.87		Target GW/8 : = 33,000 lb Target N/ $\sqrt{\theta}$: 235 rpm		Flight No. X. 276 Date: 8/7/63			
Rec. No.	Rate of Climb Test (fpm)	H _p (ft)	OAT Test (°C)	OAT Std (°C)	$\frac{OAT_T + 273}{OAT_S + 273}$	R/C Tapeline (fpm)	$\sqrt{\theta}$ Test	$\frac{R/C_{T.L.}}{\sqrt{\theta}}$ (fpm)	$\frac{\Delta \text{SHP}}{8\sqrt{\theta}}$ Climb	(hp)
23	+60	2400	24	10	1.05	+63	1.016	+62	-71	
25	-85	2500	24	10	1.05	-89	1.016	-88	+101	
26	0	2642	24						0	
27	+64	2600	24	10	1.05	+67	1.016	+66	-76	
28	0	2720	24						0	
29	+27	2900	25	9	1.056	+29	1.017	+28	-32	
30	-82	3100	22	9	1.045	-86	1.012	-85	+98	
31	+138	3100	22	9	1.045	+144	1.012	+142	-163	
32	0	3250	22						0	
33	+106	3300	23	9	1.05	+111	1.014	+110	-126	
34	0	3390	23						0	
35	0	3410	23						0	

TABLE LXVII. CH-47C/AGB ROTOR - LEVEL FLIGHT POWER REQUIRED											
Aircraft: S/N 66-19103			Takeoff GW: 45,065 lb Target GW/8: 60,000 lb 60,000 lb			CG: 0.6 in. Fwd Target N/√θ: 235 rpm 245 rpm			Flight No. X-279 Date: 8/11/69		
Rec. No.	GW 8 Test (lb)	N √θ Test (rpm)	V √θ Test (kt)	SHP 8√θ Test Rotor Shaft Torque	ASHP 8√θ Cor. to Target GW/8	ASHP 8√θ Cor. to Target N/√θ	ASHP 8√θ Cor. to Zero R/C	ASHP 8√θ Cor. to Zero Accel	ASHP 8√θ Cor. to CH-47C Ext. Drag	SHP 8√θ Corrected	
1	60,276	234.8	64.1	6,422	-65	-3	0	0	-9	6,345	
2	60,192	235.3	77.3	6,111	-43	+4	0	-53	-15	6,004	
3	60,170	234.9	88.2	5,991	-38	-1	0	0	-22	5,930	
4	60,252	236.0	101.7	6,015	-57	+12	0	+19	-34	5,955	
5	60,206	234.6	113.7	6,437	-48	-10	-98	+25	-47	6,259	
6	59,904	233.4	125.8	7,355	+25	-100	-144	+23	-64	7,095	
7	59,796	234.4	137.6	8,087	+67	-57	0	-13	-83	8,001	
9	60,040	244.7	114.1	6,426	-6	0	-128	0	-48	6,244	
10	60,041	245.3	126.5	6,949	-7	0	+40	0	-65	6,917	

TABLE LXVIII. CH-47C/AGB ROTOR-ACCELERATION CORRECTION						
$\frac{\Delta \text{SHP}}{\delta \sqrt{\theta}}$ Accel		$-\left(\frac{CW}{8}\right)\left(\frac{\Delta V}{\sqrt{\theta}}\right)\left(\frac{V}{\sqrt{\theta}}\right)\left(\frac{\Delta \text{Time}}{\sqrt{\theta}}\right)$ 2.684×10^{-6}		Target $\frac{GW}{8} \delta : 60,000$ Target $N/\sqrt{\theta} : 235$ 245		Flight No. X-279 Date: 8/11/69
Rec. No.	$\frac{V}{\sqrt{\theta}}$ Test Avg (kt)	$\frac{\Delta V}{\sqrt{\theta}}$ (kt)	ΔTime (min)	$\frac{GW}{8}$ Test (lb)	$\sqrt{\theta}$ Test	$\frac{\Delta \text{SHP}}{\delta \sqrt{\theta}}$ Accel (hp)
1	64.1	0				0
2	77.3	+4.3	1.0	60,192	0.987	-53
3	88.2	0				0
4	101.7	-1.2	1.0	60,252	0.986	+19
5	113.7	-1.4	1.0	60,206	0.987	+25
6	125.8	-1.7	1.5	59,904	0.99	+23
7	137.6	+0.6	1.0	59,796	0.988	-13
9	114.1	0				0
10	126.5	0				0

TABLE LXIX. CH-47C/AGB ROTOR - RATE OF CLIMB CORRECTION									
$\frac{\Delta \text{SHP}}{\delta \sqrt{\theta}}$		$= \frac{R/C}{\sqrt{\theta}} \times \frac{GW}{\delta}$		Kp: 0.87		Target GW/ δ : 60,000 lb Target N/ $\sqrt{\theta}$: 235 rpm 245 rpm		Flight No. X-279 Date: 8/11/69	
Climb		33,000 Kp							
Rec. No.	Rate of Climb Test (fpm)	Hp (ft)	Oat Test (°C)	Oat Std (°C)	$\frac{OAT_T + 273}{OAT_S + 273}$	R/C Tapeline (fpm)	$\sqrt{\theta}$ Test	$\frac{R/C_{T.L.}}{\sqrt{\theta}}$ (fpm)	$\frac{\Delta \text{SHP}}{\delta \sqrt{\theta}}$ Climb (hp)
1	0	8,523	8						0
2	0	8,554	8						0
3	0	8,653	8						0
4	0	8,781	7						0
5	+44	9,080	+7	-3	1.038	+46	0.986	+46	-98
6	+65	8,900	9	-3	1.044	+68	0.99	+69	-144
7	0	8,969	8						
9	+58	9,200	8	-3	1.041	+60	0.988	+61	-128
10	-18	9,300	7	-3	1.038	-19	0.986	-19	+40

TABLE LXX. CH-47C/AGB ROTOR - LEVEL FLIGHT POWER REQUIRED										
Aircraft: S/N 66-19103			Takeoff GW: 52,282 lb Target GW/8: 68,000 lb		CG: 0.2 in. Aft Target N/√θ: 245 rpm		Flight No. X-286 Date: 8/20/69			
Rec. No.	GW/8 Test (lb)	N/√θ Test (rpm)	V/√θ Test (kt)	SHP/8√θ Test Rotor Shaft Torque	ΔSHP/8√θ Cor. to Target GW/8	ΔSHP/8√θ Cor. to Target N/√θ	ΔSHP/8√θ Cor. to Zero R/C	ΔSHP/8√θ Cor. to Zero Accel	ΔSHP/8√θ Cor. to CH-47C Ext. Drag	SHP/8√θ Corrected
17	68,416	245.9	67.5	8,120	-127	0	N.A.	N.A.	-10	7,983
18	68,128	244.9	79.3	7,780	-36	0			-15	7,729
19	67,901	244.9	84.1	7,730	+27				-19	7,738
20	67,956	247.9	88.9	7,635	+12				-23	7,624
21	67,856	246.9	93.7	7,348	+36				-26	7,358
22	67,788	246.9	98.4	7,655	+50				-31	7,674
24	67,783	245.9	106.9	7,438	+54				-39	7,453
26	67,657	246.4	116.5	7,596	+88				-51	7,633
27	67,536	245.9	121.3	7,846	+124				-57	7,913
28	67,516	245.4	128.6	8,348	+164				-69	8,443

TABLE LXXI. CH-47C/AGB ROTOR - LEVEL FLIGHT POWER REQUIRED											
Aircraft: S/N 66-19103			Takeoff GW: 40,080 Target GW/8 : 50,000		lb CG: 3.1 in. Fwd lb Target N/√θ: 235 rpm		Flight No. X-288 Date: 8/21/69				
Rec. No.	GW/8 Test (lb)	N/√θ Test (rpm)	V/√θ Test (kt)	SHP/8√θ Test Rotor Shaft Torque	ΔSHP/8√θ Cor. to Target GW/8	ΔSHP/8√θ Cor. to Target N/√θ	ΔSHP/8√θ Cor. to Zero R/C	ΔSHP/8√θ Cor. to Zero Accel	ΔSHP/8√θ Cor. to CH-47C Ext. Drag	SHP/8√θ Corrected	
1	50,095	234.2	51.8	5,247	-13	+7	+164	+6	-5	5,406	
2	50,029	233.8	64.1	4,797	-4	+11	0	-22	-9	4,773	
5	50,050	234.8	73.7	4,594	-6	+2	+106	-50	-13	4,633	
6	50,139	233.3	86.1	4,570	-15	+15	0	0	-20	4,550	
8	50,252	233.5	98.1	4,542	-26	+8	+73	-34	-30	4,533	
9	50,158	234.3	110.4	4,837	-17	+7	-99	0	-43	4,683	
11	50,060	233.4	121.7	5,196	-7	+19	-40	+11	-58	5,121	
12	50,013	233.6	133.9	5,833	-2	+17	0	-10	-77	5,761	
14	49,717	234.1	145.5	6,454	+40	+8	0	+62	-98	6,466	
15	49,752	233.4	155.4	7,629	+41	0	0	0	-120	7,550	

TABLE LXXII. CH-47C/AGB ROTOR - ACCELERATION CORRECTION

$\frac{\Delta \text{SHP}}{8\sqrt{\theta}} = - \left(\frac{\text{GW}}{8} \right) \left(\frac{\Delta V}{\sqrt{\theta}} \right) \left(\frac{V}{\sqrt{\theta}} \right) \left(\frac{\sqrt{\theta}}{\sqrt{\theta}} \right) \frac{2.684 \times 10^{-6}}{\Delta \text{Time}}$							Target GW/8: 50,000 lb Target N/√θ: 235 rpm	Flight No. X-288 Date: 8/21/69
Accel								
Rec. No.	$\frac{V}{\sqrt{\theta}}$ Test Avg (kt)	$\frac{\Delta V}{\sqrt{\theta}}$ (kt)	Δ Time (min)	$\frac{\text{GW}}{8}$ Test (lb)	$\sqrt{\theta}$ Test	$\frac{\Delta \text{SHP}}{8\sqrt{\theta}}$ Accel (hp)		
1	51.8	-0.8	1.0	55,095	0.996	+6		
2	64.1	+2.5	1.0	50,029	0.996	-22		
5	73.7	+5.0	1.0	50,050	0.996	-50		
6	86.1	0				0		
8	98.1	+2.6	1.0	50,252	0.996	-34		
9	110.4	0				0		
11	121.7	-0.7	1.0	50,060	0.996	+11		
12	133.9	+0.6	1.0	50,013	0.997	-10		
14	145.5	-1.6	0.5	49,717	0.997	+62		
15	155.4	0						

TABLE LXXIII. CH-47C/AGB ROTOR - RATE OF CLIMB CORRECTION									
$\frac{\Delta \text{SHP}}{8\sqrt{\theta}} = \frac{\text{R/C}}{\sqrt{\theta}} + \frac{\text{GW}}{8}$ Climb 33,000 Kp			Kp: 0.87		Target GW/8 : 50,000 lb Target N/√θ : 235 rpm		Flight No. X-288 Date: 8/21/69		
Rec. No.	Rate of Climb Test (fpm)	Hp (ft)	OAT Test (°C)	OAT Std (°C)	$\frac{\text{OAT}_T + 273}{\text{OAT}_S + 273}$	R/C Tapeline (fpm)	√θ Test	$\frac{\text{R/C T.L.}}{\sqrt{\theta}}$ (fpm)	$\frac{\Delta \text{SHP}}{8\sqrt{\theta}}$ Climb (hp)
1	-90	6,500	13	+2	1.04	-94	0.996	-94	+164
2	0	6,560	13						0
5	-58	6,800	13	+2	1.04	-60	0.996	-61	+106
6	0	6,940	12						0
8	-40	7,100	13	1	1.045	-42	0.996	-42	+73
9	+54	7,200	13	1	1.045	+56	0.996	+57	-99
11	+22	7,200	13	1	1.045	+23	0.996	+23	-40
12	0	7,345	13						0
14	0	7,402	14						0
15	0	6,570	14						0